Journal of Engineering for Gas Turbines and Power

Published Bimonthly by ASME

VOLUME 131 • NUMBER 4 • JULY 2009

RESEARCH PAPERS

Gas Turbines: Ceramics

Gas Turbines: Combustion, Fuels, and Emissions

Gas Turbines: Controls, Diagnostics, and Instrumentation

Gas Turbines: Cycle Innovations

Gas Turbines: Structures and Dynamics

Internal Combustion Engines

(Contents continued on inside back cover)

ASME
SETTING THE STANDARD

Editor
D. R. BALLAL (2011)
Assistant to the Editor
S. D. BALLAL
Associate Editors
Gas Turbine (Review Chairs)
K. BRUN (2009)
T. SATTELMAYER (2009)
Coal, Biomass & Alternative Fuels
K. ANNAMALAI (2010)
Combustion & Fuels
N. K. RIZK (2009)
T. SATTELMAYER (2009)
Controls, Diagnostics, & Instrumentation
A. VOLPONI (2010)
Cycle Innovation
P. PILIDIS (2010)
Electric Power
P. CHIESA (2011)
Structures and Dynamics
P. S. KEOGH (2010)
J. SZWEDOWICZ (2009)
D. P. WALLS (2009)
Advanced Energy Systems
J. KAPAT (2010)
Internal Combustion Engines
C. RUTLAND (2009)
T. RYAN III (2009)
J. WALLACE (2011)
M. WOOLDRIDGE (2011)
Nuclear Engineering
J. KUNZE (2011)
I. PIORO (2011)

PUBLICATIONS COMMITTEE
Chair, **B. RAVANI**

OFFICERS OF THE ASME
President, **A. E. HOLT**
Executive Director,
T. G. LOUGHLIN
Treasurer,
T. D. PESTORIUS

PUBLISHING STAFF

Managing Director, Publishing
P. DI VIETRO
Manager, Journals
C. MCATEER
Production Coordinator
J. SIERANT

Transactions of the ASME, Journal of Engineering for Gas Turbines and Power (ISSN 0742-4795) is published bimonthly (Jan., Mar., May, July, Sep, Nov.) by The American Society of Mechanical Engineers, Three Park Avenue, New York, NY 10016. Periodicals postage paid at New York, NY and additional mailing offices. POSTMASTER: Send address changes to Transactions of the ASME, Journal of Engineering for Gas Turbines and Power, c/o THE AMERICAN SOCIETY OF MECHANICAL ENGINEERS, 22 Law Drive, Box 2300, Fairfield, NJ 07007-2300. **CHANGES OF ADDRESS** must be received at Society headquarters seven weeks before they are to be effective. Please send old label and new address.

STATEMENT from By-Laws. The Society shall not be responsible for statements or opinions advanced in papers or ... printed in its publications (B7.1, par. 3). **COPYRIGHT © 2009** by the American Society of Mechanical Engineers. For authorization to photocopy material for internal or personal use under circumstances not falling within the fair use provisions of the Copyright Act, contact the Copyright Clearance Center (CCC), 222 Rosewood Drive, Danvers, MA 01923, Tel: 978-750-8400, www.copyright.com.

Canadian Goods & Services Tax Registration #126148048

This journal is printed on acid-free paper, which exceeds the ANSI Z39.48-1992 specification for permanence of paper and library materials. ∞™
♲ 85% recycled content, including 10% post-consumer fibers.

Downloaded 03 Jun 2010 to 171.66.16.160. Redistribution subject to ASME license or copyright; see http://www.asme.org/terms/Terms_Use.cfm

(**Contents continued**)

Journal of Engineering for Gas Turbines and Power **JULY 2009**

Volume 131, Number 4

Nuclear Power

Thermodynamic Properties

TECHNICAL BRIEFS

The ASME Journal of Engineering for Gas Turbines and Power is abstracted and indexed in the following:

AESIS (Australia's Geoscience, Minerals, & Petroleum Database), Applied Science & Technology Index, Aquatic Sciences and Fisheries Abstracts, Civil Engineering Abstracts, Compendex (The electronic equivalent of Engineering Index), Computer & Information Systems Abstracts, Corrosion Abstracts, Current Contents, Engineered Materials Abstracts, Engineering Index, Enviroline (The electronic equivalent of Environment Abstracts), Environment Abstracts, Environmental Science and Pollution Management, Fluidex, INSPEC, Mechanical & Transportation Engineering Abstracts, Mechanical Engineering Abstracts, METADEX (The electronic equivalent of Metals Abstracts and Alloys Index), Pollution Abstracts, Referativnyi Zhurnal, Science Citation Index, SciSearch (The electronic equivalent of Science Citation Index), Shock and Vibration Digest

Downloaded 03 Jun 2010 to 171.66.16.160. Redistribution subject to ASME license or copyright; see http://www.asme.org/terms/Terms_Use.cfm

Rémy J. L. Steenbakker
National High Temperature Surface Engineering Centre,
Cranfield University,
Bedfordshire MK43 0AL, UK
e-mail: r.steenbakker.2003@cranfield.ac.uk

Jörg P. Feist[1]
Southside Thermal Sciences (STS) Ltd.,
c/o Imperial Innovations, Level 12,
Electrical Engineering,
Imperial College London,
London SW7 2AZ, UK
e-mail: j.feist@stscience.com

Richard G. Wellman

John R. Nicholls

National High Temperature Surface Engineering Centre,
Cranfield University,
Bedfordshire MK43 0AL, UK

Sensor Thermal Barrier Coatings: Remote In Situ Condition Monitoring of EB-PVD Coatings at Elevated Temperatures

*Thermal barrier coatings (TBCs) are used to reduce the actual working temperature of the high pressure turbine blade metal surface. Knowing the temperature of the surface of the TBC and at the interface between the bondcoat and the thermally grown oxide (TGO) under realistic conditions is highly desirable. As the major life-controlling factors for TBC systems are thermally activated, therefore linked with temperature, this would provide useful data for a better understanding of these phenomena and to assess the remaining lifetime of the TBC. This knowledge could also enable the design of advanced cooling strategies in the most efficient way using minimum amount of air. The integration of an on-line temperature detection system would enable the full potential of TBCs to be realized due to improved precision in temperature measurement and early warning of degradation. This, in turn, will increase fuel efficiency and reduce CO_2 emissions. The concept of a thermal-sensing TBC was first introduced by Choy, Feist, and Heyes (1998, "Thermal Barrier Coating With Thermoluminescent Indicator Material Embedded Therein," U.S. Patent U.S. 6974641 (B1)). The TBC is locally modified so it acts as a thermographic phosphor. Phosphors are an innovative way of remotely measuring temperatures and also other physical properties at different depths in the coating using photo stimulated phosphorescence (Allison and Gillies, 1997, "Remote Thermometry With Thermographic Phosphors: Instrumentation and Applications," Rev. Sci. Instrum., **68**(7), pp. 2615–2650). In this study the temperature dependence of several rare earth doped EB-PVD coatings will be compared. Details of the measurements, the influence of aging, the composition, and the fabrication of the sensing TBC will be discussed in this paper. The coatings proved to be stable and have shown excellent luminescence properties. Temperature detection at ultrahigh temperatures above 1300°C is presented using new types of EB-PVD TBC ceramic compositions. Multilayer sensing TBCs will be presented, which enable the detection of temperatures below and on the surface of the TBC simultaneously.* [DOI: 10.1115/1.3077662]

Keywords: thermal barrier coating, sensor TBC, phosphorescence, luminescence, YAG, heat flux gauge, thermographic phosphor, remote monitoring

1 Introduction

1.1 Industrial Need. Gas turbines are widely used to provide aircraft propulsion and increasingly to generate electricity. The efficiency of such plant is linked to the maximum gas temperatures that occur in the hot gas section of the engine. Higher efficiencies and hence higher temperatures are constantly being sought, both for commercial reasons (lower operating costs) and environmental reasons (lower CO_2 emissions). The downside of operating at higher temperatures is the greater stress it places on components, which then creates the need for improved materials and also for improved monitoring tools.

In addition to new alloys and cooling methods, thermal barrier coatings have played a major role in this development. These coatings were first used on jet engines in the 1970s and are now a common feature on power generation turbines. Temperatures in today's turbines are above the melting point of the metal components—vanes and blades—in the hot section, the most expensive part of the turbine. TBCs allow components to survive in higher temperatures, while having acceptable lifetimes. It is claimed that a 1% improvement in engine efficiency can save $20 million in fuel over the lifetime of a typical industrial, gas fired, 400–500 MW combined cycle power plant [1]. In fact GE claims that its dominance in worldwide gas turbine production is due to its leadership in TBC technology resulting in improved efficiencies of their engines [1].

The prediction of the durability of a TBC is strongly dependent on the absolute temperature the coating system experiences. The thickness of the thermally grown oxide (TGO) layer, underneath the TBC ceramic layer, determines one of the prime failure mechanisms of a TBC: the spallation of the ceramic top coating. The increase in temperature from 1010°C to 1064°C can triple the growth rate of the TGO leading to a rapid premature failure [2]. Reliable temperature detection in an operating turbine has not yet been achieved and consequently lifetime prediction models remain uncertain. Thus, uncertainties in current temperature measurement systems [3] do not allow operators to run their engines at maximum efficiency without compromising on reduced material life and safety. The proposed sensor coating technology will provide more accurate temperature data inside the hot section of the engine, and this knowledge might be used to reduce safety margins by 50°C or even more. Current safety margins are be-

---

[1] Corresponding author.

Contributed by the International Gas Turbine Institute of ASME for publication in the JOURNAL OF ENGINEERING FOR GAS TURBINES AND POWER. Manuscript received April 9, 2008; final manuscript received April 9, 2008; published online April 10, 2009. Review conducted by Dillip R. Ballal. Paper presented at the ASME Turbo Expo 2008: Land, Sea and Air (GT2008), Berlin, Germany, June 9–13, 2008.

Copyright © 2009 by STS Ltd. and Cranfield University

Downloaded 02 Jun 2010 to 171.66.16.109. Redistribution subject to ASME license or copyright; see http://www.asme.org/terms/Terms_Use.cfm

lieved to be as high as 200°C giving a great potential for an increase in operating temperatures [4]. A rule of thumb says a 50°C increase in the firing temperature corresponds to 1% efficiency gain, which is considerable regarding the size of the market [5].

1.2 Thermographic Phosphors. The concept of using phosphorescent materials for temperature detection in gas turbine applications has been studied for more than 20 years, and it is usually known as *phosphor thermography*. When applied as paints, these materials have a limited lifetime of a few hundred hours or less when exposed to high temperatures and harsh environments. These materials are usually doped ceramics mixed with high temperature binders. After excitation of the phosphor with ultra violet (UV) light, the subsequent emission is recorded using a photomultiplier or a camera system in order to observe the decay time, which is temperature dependent [6–26]. Alternatively, the intensity ratio technique can be utilized for specific phosphor materials, looking at the ratio of temperature dependency of two different emission lines simultaneously [6,16,22–24,27–31]. A more in-depth study of the theoretical aspects of the technique can be found in the literature [6,16,32].

1.3 Thermal Barrier Sensor Coating. Early work by Amano et al. [33] considered the integration of luminescent materials as erosion sensors in TBCs. In 1998 Choy et al. [34] introduced the notion of a *thermal barrier sensor coating* (sensor TBC) for temperature detection. Instead of applying a phosphor layer on the surface where the temperature needs to be measured, they proposed to locally modify the composition of the TBC so that it acts as a thermographic phosphor and as a protective thermal barrier. This technique enables surface temperature measurement but also could provide a means to measure temperature within the TBC and at the metal/topcoat interface, hence enabling the manufacturing of an integrated heat flux gauge. They first published results on yttria stabilized zirconia co-doped with europia (YSZ:Eu) powders in 2000 [15]. They also demonstrated for the first time the detection of subsurface measurements looking through a 50 μm undoped YSZ layer and detecting the phosphorescence of a thin ($\approx$10 μm) YSZ:Eu layer (bi-layer system) underneath using the ESAVD technique to produce the coating [8]. The first results on EB-PVD TBCs were published in 2001 by Feist et al. [27]. The coating tested was a monolayer coating of standard YSZ co-doped with dysprosia (YSZ:Dy). Later in 2004 and 2005, Gentleman and Clarke [35,36] reported the temperature sensitivity of YSZ:Eu phosphors as well as erbium doped YSZ and europia doped pyrochlore zirconates, which could be seen as a potential replacement for YSZ materials due to their lower thermal conductivity. They also showed that the temperature at the TGO/TBC interface could be measured with thermographic phosphors using a bi-layer EB-PVD coating (10 μm YSZ:Eu bottom layer) in a thermal gradient [37]. First work on industrial air plasma sprayed (APS) sensor coating systems commenced around 2002 and were first published in 2005 [26,38]. Heyes et al. [26] demonstrated the capabilities of APS sensor coatings for in situ two-dimensional temperature measurements in burner rigs using a high speed camera system. Further, Feist et al. [39] showed the temperature measurement capabilities of APS sensor coatings beyond 1400°C. The application of thermographic paints on conventional free standing APS coatings was studied by Eldridge et al. [25] to demonstrate its use for depth-penetrating studies.

While the previously mentioned studies were focusing on the temperature detection capability as the main industrial driver for this technology, it became apparent that the inclusion of phosphorescent materials into the thermal barrier coating can also work as a microprobe to detect the aging mechanisms or changes to other physical parameters that affect the local atomic surroundings of the optical active ion. This was first stated by Choy et al. [34], later by Srivastava et al. [40] and then by Feist and Heyes [41]. The latter proved the viability of detecting hot corrosion processes in YSZ due to vanadium attack. Most recently, Eldridge and co-workers [42,43] studied the effect of delamination and erosion on the luminescence response, showing that sensor TBCs can have multiple applications.

The top surface of a TBC can experience temperatures as high as 1300°C [1], and therefore the challenge is to find luminescent materials, which are sensitive at very high temperatures and are compatible with the TBC structure and chemistry. In the selection of high temperature phosphors, the most straightforward approach is to co-dope standard YSZ material with rare earth oxides (YSZ:RE). First because YSZ:RE materials have been shown to luminesce at high temperatures [23,27,35,44]. Second, small additions of dopants should not dramatically change the properties of the TBC, an important factor when it comes to industry acceptability. It has been shown by Nicholls et al. [45] that a 4 mol % addition of rare earth dopant could significantly reduce the thermal conductivity of TBCs and that such compositions could be easily deposited by the EB-PVD process.

In this contribution, rare earth doped yttrium aluminum garnet (YAG:RE) phosphors were also investigated in order to improve the temperature capabilities of currently proposed smart TBC system. In fact, undoped yttrium aluminum garnet (YAG) materials have been suggested as a potential replacement for the standard YSZ TBC by Klemens and co-workers [46,47] because of some particularly favorable material properties. YAG has also been incorporated into an APS coating as an oxygen diffusion barrier by Su et al. [48]. The high temperature luminescence capabilities of doped YAG has been reported by various researchers to show temperature sensing capabilities up to a maximum of 1700°C [6,39,49,50]. It is also being suggested to the authors that YAG becomes a more acceptable TBC constituent at higher temperatures.

Finally, the results on multilayer sensing TBCs, enabling simultaneous temperature measurements below and on the surface of the coating, are presented. Such a multilayer coating could also be used as a heat flux gauge in order to monitor the thermal gradient and also to determine the heat flux through the thickness of the TBC under realistic service conditions.

2 Theory

When a rare earth phosphor is excited its electrons move from a ground state to higher energy states. The allowed energy levels are described by the *Dieke diagram* (Fig. 1) and the corresponding optical emissions are characterized by a finite lifetime, which is temperature dependent. Indeed, relaxation from an excited state cannot only take place by direct transition to a lower state via the emission of photons but also by releasing energy in the form of phonons to the surrounding crystal. Consequently the luminescence lifetime can be expressed as a function of the probability of the occurrence of these two processes, as follows:

$$\tau = \frac{1}{P_R + P_{\mathrm{NR}}} \tag{1}$$

where τ is the lifetime and P_R and P_{NR} the radiative and nonradiative components, respectively.

A simple relationship can be determined for P_{NR} using the theory of multiquantum emission [52–55]:

$$P_{\mathrm{NR}}(n,T) = P_{\mathrm{NR}}(n,T=0)\left[1 - \exp\left(-\frac{E_{\mathrm{phonon}}}{kT}\right)\right]^{-n} \tag{2}$$

where $P_{\mathrm{NR}}(n,T=0)$ is the probability of a spontaneous emission of n phonons at $T=0$ K, and E_{phonon} is the energy of the phonon under consideration. $E_{\mathrm{phonon}}=\hbar\omega$, where $\hbar$ is the *Dirac* constant and ω is the angular frequency.

The radiative rate P_R does not depend on temperature and is usually small compared with P_{NR}. The nonradiative component P_{NR} increases with temperature; consequently, the lifetime decay τ becomes smaller as temperature is increased. This temperature

Downloaded 02 Jun 2010 to 171.66.16.109. Redistribution subject to ASME license or copyright; see http://www.asme.org/terms/Terms_Use.cfm

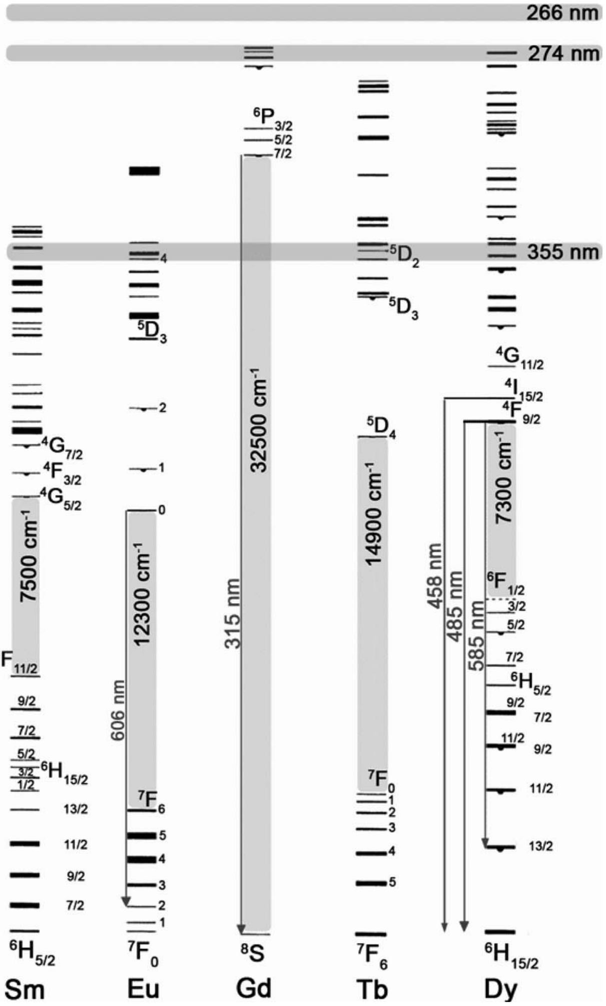

Fig. 1 Dieke diagram; energy levels of the 4*f* configuration of rare earth trivalent ions [51]

dependence leads to the *lifetime decay method* for temperature measurement. The number of phonons n involved in the process can be determined from $n=\Delta E/\hbar\omega$, where ΔE is the energy gap that has to be bridged [56]. The energy gap between two levels is typically 1000 cm^{-1}. The maximum phonon energy being about 500 cm^{-1}, then nonradiative decay takes place by a multiphonon process.

It is worth noting that the constant $P_{\mathrm{NR}}(n,T=0)$ is highly dependent on the order n of the process. Weber [52], Henderson and Imbusch [56], Hufner [55], and Risenberg and Moos [57] calculated the values of $P_{\mathrm{NR}}(n,T=0)$ for various levels of different trivalent rare earth ions in different host materials, and they found that there is an exponential dependence on the energy gap to the next lowest level (ΔE), as follows:

$$P_{\mathrm{NR}}(n,T=0)=A\ \exp(-\alpha\Delta E)) \tag{3}$$

Consequently, the bigger the energy gap that has to be bridged, the lower $P_{\mathrm{NR}}(n,T=0)$. Therefore, important light emissions are observed for transitions between energy levels that are separated by a large gap, and one might expect that these transitions might have longer high temperature lifetimes. As mentioned, the lifetime of the phosphorescence decreases with increasing temperature. This temperature dependence of the phosphorescence process is most commonly used to perform temperature measurements. The lifetime decay method involves the calibration of the phosphor materials in order to determine its temperature sensitivity. The calibration process is generally performed under isothermal conditions in a furnace. The decay time is recorded from room temperature until the complete temperature quenching of the phosphorescence signal. From this experiment, a calibration curve, that is to say the lifetime of the phosphorescence as a function of temperature, can be plotted. A phosphor is characterized by the temperature range over which it is sensitive and its maximum operating temperature. Obviously, the maximum temperature capability of a phosphor also depends on the minimum decay time that can be recorded by the measurement device. In order to determine the temperature, the lifetime decay of the phosphorescence is recorded and the temperature is read from the calibration curve and therefore calibration curves reflect the temperature measurement capabilities of a particular phosphor.

3 Experimentation

As mentioned previously, rare earth phosphors with a high energy band gap should be quenched at a higher temperature; therefore, according to the Dieke diagram in Fig. 1, Sm_2O_3, Eu_2O_3, Gd_2O_3, Tb_2O_3, and Dy_2O_3 are potentially the best candidates to dope YSZ from the luminescence point of view. In this work, only YSZ co-doped with dysprosia, gadolinia, and europia were studied. The dopant concentration was chosen so that the total amount of stabilizer (rare earth oxide plus yttria) remained in a range that guaranteed the formation of the metastable tretagonal t' phase after deposition. Three different concentrations of dysprosia—0.3 mol %, 1 mol %, and 2 mol %—were chosen in order to determine the influence of dopant concentration on the phosphorescence. Compositions with 2 mol % of Eu_2O_3 and Gd_2O_3 were also investigated to compare the temperature capabilities of these three phosphors at the same dopant concentration level.

All the coatings were deposited at Cranfield University, UK, on alumina substrates using a single source EB-PVD evaporator. High purity single crystal alumina substrates were used, rather than a nickel based superalloy, in order not to be limited by the melting point of the superalloy during the phosphorescence furnace calibration.

All the phosphorescence measurements were undertaken at Southside Thermal Sciences Limited (STS) at the Imperial College, London, UK. The calibration curves of the EB-PVD coatings, that is to say the decay time of the phosphorescence as a function of temperature, were determined using a similar experimental setup to that described in Ref. [15]. All the samples were tested under the exact same conditions.

4 Results and Discussion

4.1 Temperature Sensitivity of YSZ Phosphors. The calibration curves for the three different YSZ phosphors are represented in Fig. 1. The YSZ:Dy(2%) EB-PVD TBC was excited at 355 nm and the phosphorescence lifetime was calculated from the emission line with the highest intensity at 585 nm. The temperature sensitivity range of YSZ:Dy(2%) phosphor was between around 500°C and 950°C. The maximum temperature capability was found at 950°C for a lifetime of around 0.3 μs. The detection limit of the experimental setup is governed by the response time of the photomultiplier-amplifier system, which was determined by calculation and measurement, and is between 0.3 μs and 0.4 μs [16]. Therefore, by using a detection system with a faster response time, temperatures in excess of 1000°C could be measured with the YSZ:Dy phosphor.

The YSZ:Gd(2%) coating was excited at 274 nm using a dye laser and the luminescence line at 315 nm was observed to determine the lifetime decay as a function of the temperature (Fig. 2). Contrary to the YSZ:Dy(2%) coating, where the lifetime decay remains relatively constant up to around 400°C, for the YSZ:Gd(2%) phosphor rapid quenching is observed as soon as the temperature starts to increase. Lifetime decay of up to around

Downloaded 02 Jun 2010 to 171.66.16.109. Redistribution subject to ASME license or copyright; see http://www.asme.org/terms/Terms_Use.cfm

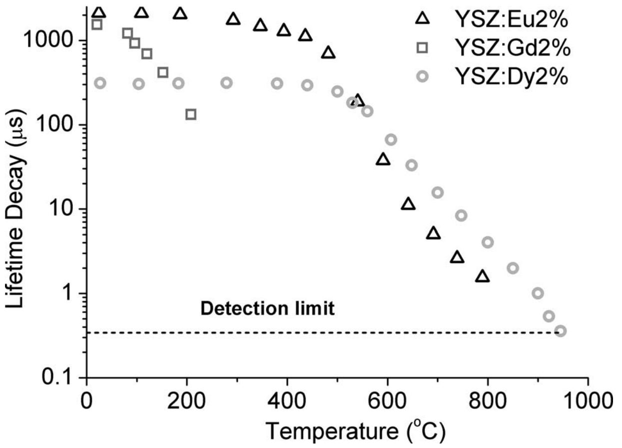

Fig. 2 Calibration curves of YSZ:Eu2%, YSZ:Gd2%, and YSZ:Dy2% EB-PVD TBCs

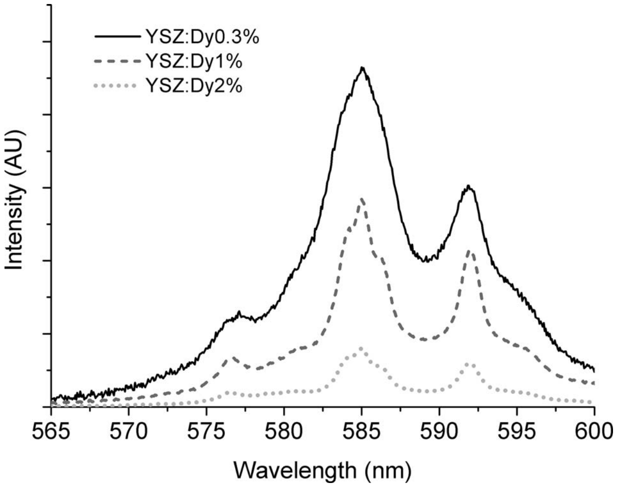

Fig. 3 Effect of dysprosia concentration on the luminescence intensity of YSZ:Dy EB-PVD TBCs at room temperature

200°C was measured, meaning that the temperature capabilities of YSZ:Gd phosphor are rather poor, although it could be used as a low temperature thermographic phosphor. This is rather surprising since the large energy gap between the radiating level and the ground level would suggest an improved high temperature measurement range, due to a small probability for multiple phonon quenching. The current result suggests that the quenching mechanism for YSZ:Gd is of a different kind to that for the YSZ:Eu phosphor.

The YSZ:Eu phosphor was excited using a 266 nm radiation and the luminescence at 606 nm was observed. As can be seen in Fig. 2, the YSZ:Eu phosphor can be used to measure temperatures from 500°C up to around 800°C. In this study, the detection limit of 0.3 μs, for the system used, could not be reached because the YSZ:Eu phosphorescence was quenched at 800°C, and consequently the luminescence could not be recorded above this temperature and the decay time calculated.

However, Gentleman and co-workers [37,58] have reported temperature measurements of up to 1100°C with the YSZ:Eu phosphor. The difference in the maximum temperature measurement capability between this study and that of Gentleman and co-workers is believed to be due to the following.

- The use of a sapphire fiber by Gentleman et al. [58] to collect the phosphorescent signal very close to the sample therefore improving the signal-to-noise ratio. In the current setup the collection optic is situated at around 30–40 cm from the sample, looking through a 25 mm diameter optical access window in the furnace. Above 800°C, the intensity of the phosphorescent signal of YSZ:Eu decreases rapidly and makes it difficult to detect the decay remotely.
- The remote detection of the signal requires that the photomultiplier is operated using an amplifier system, and, as explained above, this limits the response time and hence restricts the lifetime decay, which can be detected. Gentleman and co-workers [37,58] did not use an amplifier system as the signal strength directly measured at the sample is sufficient for detection with the optical fiber system. It is believed, however, that the photomultiplier capability is only limited by the transient time, which is typically of the order of 20 ns for standard Hamamatsu photomultipliers or similar types.
- Differences in the fitting routine used to determine the luminescence lifetime from the decay curve may also influence detectability.

It should be noted that for detection in an operating engine the distance between the sensor coating and the optic will be a few centimeters, hence the detection system must have an amplifier system in place. Even though the results obtained in this study might not show the maximum temperature capabilities of the various YSZ:RE phosphors, it still provides a consistent criterion for comparison purposes between the phosphors studied.

It is believed that the extinction of the YSZ:Eu phosphorescence is caused by the depopulation of the excited energy level via charge transfer state (CTS) at high temperature. The mechanisms involved in the emptying of these energy levels by charge transfer state were described by Struck and Fonger [59,60]. Because Eu^{3+} has a $4f^6$ configuration (electron shell half-filled, less one), an electron from the YSZ valence band can be favorably promoted to the $4f$ shell. The charge transfer state of YSZ:Eu has the lowest energy of all lanthanides (about 18,000 cm^{-1} lower than Dy^{3+}, which has a $4f^9$ configuration [61]), hence providing a good nonradiative path for electron relaxation at high temperatures. In fact, the CTS of Eu^{3+} and Yb^{3+} are known to be the only ones to be that low that they can interact with the luminescence $4f$ states. This is not the case for Dy^{3+}. It is therefore most likely that Dy^{3+} will show a different quenching route and hence can potentially achieve higher temperature readings.

It was found that YSZ:Dy phosphor offers the best potential in terms of temperature sensitivity and luminescence intensity at high temperatures compared with YSZ:Eu and YSZ:Gd and was further investigated in this study.

4.2 Dysprosia Doped YSZ Phosphor.

The emission spectra of as deposited coatings co-doped with 0.3 mol %, 1 mol %, and 2 mol % of dysprosia are reproduced in Fig. 3. The intensity of the emission peak at 585 nm was used for the lifetime decay measurements and decreases linearly with increasing dysprosia concentration. As the concentration of dysprosia is increased from 0.3 mol % to 2 mol %, the luminescence intensity of the 585 nm emission line is almost six times lower. The influence of dysprosia concentration on the luminescence lifetime is represented in Fig. 4. At temperatures below 500°C lower dopant concentrations give longer decay times, however at higher temperatures, the temperature measurement capabilities are very similar for the different concentrations. Lowering the concentration of dysprosia also shifts the onset of thermal quenching to lower temperatures extending slightly the range of the temperature sensitivity of the phosphor.

These results show that the temperature measurement will not be affected when dysprosia concentration ranges from 0.3 mol % to 2 mol %. However, low dysprosia contents should be preferred as they give higher luminescence intensities. As the surface of the TBC will get dirty during service, this will further reduce the

Downloaded 02 Jun 2010 to 171.66.16.109. Redistribution subject to ASME license or copyright; see http://www.asme.org/terms/Terms_Use.cfm

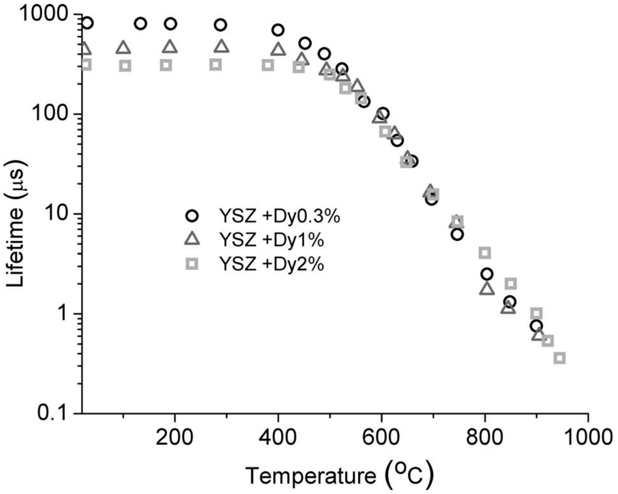

Fig. 4 Influence of dysprosia concentration on the luminescence lifetime of YSZ:Dy EB-PVD TBCs

intensity of the phosphorescence that could be detected and therefore it is very desirable to maximize the brightness of the phosphorescence. It is believed that the decrease in phosphorescence intensity and lifetime at low temperatures with increasing dysprosia concentration is caused by concentration quenching. Indeed, at high dopant concentrations there is a greater interaction between activator atoms increasing the probability of nonradiative energy transfers between dopant atoms. As the temperature increases, temperature quenching becomes predominant, and above 500°C the calibration curves for the different compositions are very similar.

As represented in Fig. 5, YSZ:Dy has several emission lines corresponding to different transitions, which could be used to build a calibration curve. Lifetime measurements were carried out using the emissions at 458 nm, 485 nm, and 585 nm. The corresponding electronic transitions are represented on the energy level diagram in Fig. 1. The emission peak at 458 nm corresponding to $^4I_{15/2} \rightarrow {}^6H_{15/2}$ transitions is not visible in room temperature luminescence spectrum. Indeed, after excitation at low temperatures the electrons relax nonradiatively down to the $^7F_{9/2}$ energy level, therefore, only emissions coming from this state are visible. Because the $^7F_{9/2}$ and $^4I_{15/2}$ states are closely spaced (around 930 cm^{-1}) the $^4I_{15/2}$ energy level is thermally populated at elevated temperatures and consequently the relative intensity of the 458 nm emission line increases with increasing temperature. Hence, at temperatures below 400°C, it was not possible to detect the decay of the luminescence at 458 nm and therefore lifetime measurements could not be performed using this emission line. The intensity ratio between the peaks at 485 nm and 585 nm can be used for temperature measurements (intensity ratio technique [27,28]).

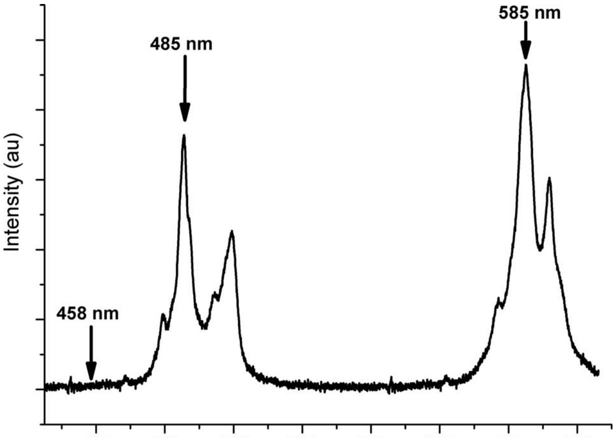

Fig. 5 Emission spectrum of YSZ:Dy at room temperature

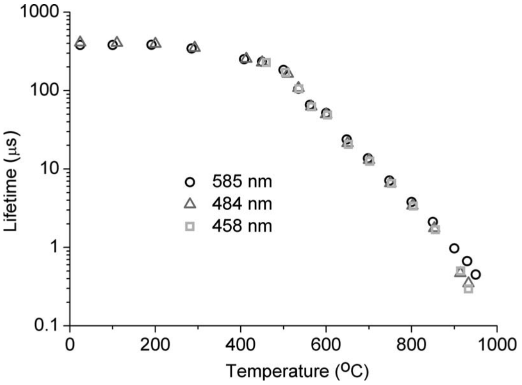

Fig. 6 Lifetime decay measurements using three different emission wavelengths

Figure 6 shows the excellent agreement of the values obtained with the three different wavelengths. Emissions at 485 nm and 585 nm both come from transitions from the $^4F_{9/2}$ state, however, this is not the case for the emission at 458 nm, although the same temperature sensitivity was still obtained. Having the possibility of using three different wavelengths offers more flexibility, if there is any overlapping with emissions from the burning fuel or from another phosphor layer in the TBC, then, another wavelength could be used to measure the temperature. These results imply that the three transitions have the same quenching mechanisms. The fact that the lifetime of the emissions coming from the $^4I_{15/2} \rightarrow {}^6H_{15/2}$ and $^7F_{9/2} \rightarrow {}^6H_{13/2-15/2}$ transitions has the same temperature dependence suggests that the thermal population of higher energy levels at high temperature do not account for the decrease in lifetime. Decay by energy transfers to other activator ions is also negligible at high temperature since, for the dysprosia concentrations investigated, the temperature quenching was identical.

During aging the coating undergoes phase transformations from the as deposited metastable t' phase to a mixture of tetragonal and cubic phases, and upon cooling the tetragonal phase can transform to monoclinic. A YSZ:Dy(2%) coating was tested in the as deposited condition and after a heat treatment of 300 h at 1500°C, followed by a slow cooling in the furnace to ensure the formation of the monoclinic phase [62], in order to determine whether the transformations in the crystal structure would affect the lifetime of the luminescence. The detection and the collection of the luminescence were not affected by the heat treatment, and the calibration curves for the aged and as deposited TBCs are similar as plotted in Fig. 7.

Thus, temperature measurements are insensitive to high temperature aging and the associated phase transformations even though the formation of the monoclinic phase changes the crystal field surrounding the activator atoms. These variations in the crystal field do not seem to have a noticeable effect on the lifetime of the $^4F_{9/2} \rightarrow {}^6H_{13/2}$ electronic transitions, highlighted by the fact that aging during service does not change the temperature measurement capabilities of the coating. Chambers and Clarke [63] reported the same behavior for high temperature aging of a YSZ:Eu phosphor.

Phosphors based on a YSZ matrix and a rare earth activator have not been found to have a temperature sensitivity above 1200°C, therefore, they cannot be used as a top layer to measure the surface temperature of the TBC. Consequently, a different

Downloaded 02 Jun 2010 to 171.66.16.109. Redistribution subject to ASME license or copyright; see http://www.asme.org/terms/Terms_Use.cfm

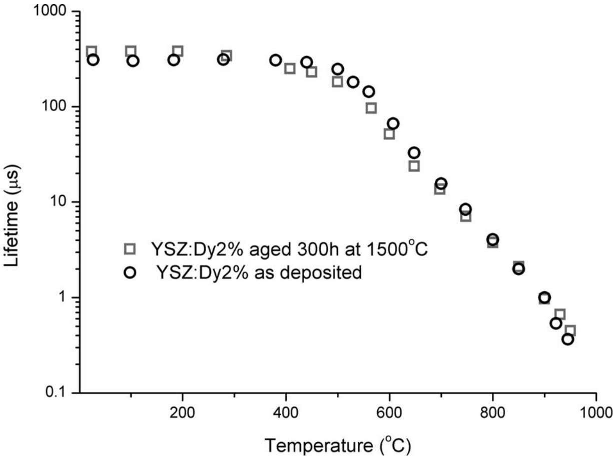

Fig. 7 Influence of aging on the phosphorescence lifetime of YSZ:Dy 2% EB-PVD TBCs

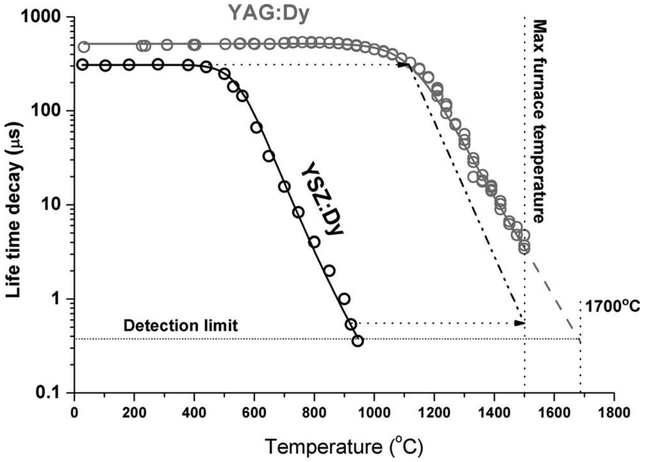

Fig. 9 Calibration curves of YSZ:Dy and YAG:Dy EB-PVD coatings

phosphor based on a different matrix, with temperature capabilities above 1200 °C, must be used as the top layer. YAG compositions would be potential candidates, from the phosphorescence point of view, and phosphors such as YAG:Dy have been reported to luminesce up to 1500 °C [6,50]. However, they have never been used as TBC material and they have never been deposited by EB-PVD before.

4.3 YAG Phosphorescent Coating. EB-PVD coatings containing the YAG:Dy phase were successfully deposited at Cranfield University and the phosphorescence spectrum of such coatings was recorded between 470 nm and 610 nm when excited at 355 nm. It is compared with YAG:Dy powder in Fig. 8 and shows that all the peaks of the YAG:Dy coating spectrum correspond to YAG:Dy emission lines. The calibration curve of the EB-PVD coating was determined for an excitation at 355 nm recording the lifetime of the 585 nm emission line (Fig. 9). It was found that YAG:Dy has a temperature sensitivity ranging from 1080 °C to at least 1500 °C. Indeed the lifetime decay measurements were limited by the maximum temperature capabilities of the furnace (1500 °C). The extrapolation of the lifetime results to the detection limit of the measurement setup (0.3–0.4 μs) shows that the YAG:Dy coating could be used to measure temperatures of up to around 1700 °C, compared with 1000 °C for the YSZ:Dy phosphor. Additionally, because the slope of the YAG:Dy calibration curve is less steep compared with that of YSZ:Dy, it can be used to measure a broader range of temperatures.

$$\text{YSZ:Dy:}\ \ 500\,^\circ\text{C} \rightarrow 950\,^\circ\text{C}(450\,^\circ\text{C})$$

$$\text{YAG:Dy:}\ \ 1080\,^\circ\text{C} \rightarrow 1700\,^\circ\text{C}(620\,^\circ\text{C})$$

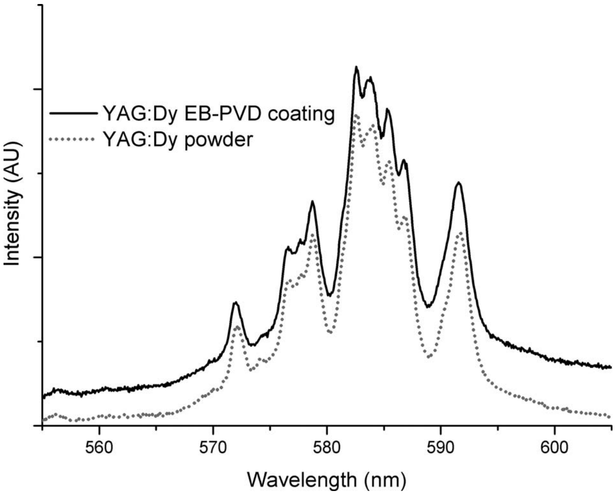

Fig. 8 Luminescence spectra of the YAG:Dy EB-PVD coating and YAG:Dy powder

4.4 Multiphonon Quenching at Elevated Temperatures. In Fig. 9 the calibration data for both materials YAG:Dy and YSZ:Dy are fitted using Eq. (2) and a commercial data processing routine based on the Levenberg–Marquardt algorithm. The authors assume that the energy gap ΔE between the lowest radiative energy level and the highest nonradiating level remains the same at 7300 cm^{-1} in the different hosts. This is due to the well shielded $4f$ levels, therefore minimizing the affect of the different atomic environments. Table 1 shows the results of both fits.

While the phonon energies are in an expected range, the number of phonons involved in the quenching process is remarkably high. Multiphonon processes are usually not expected to involve more than ten phonons at a time [54,56,64] for trivalent rare earth dopants. This assumption holds usually only for the weak coupling scheme between electrons and lattice such as for Dy^{3+} and other rare earth ions [65]. The authors speculate that for elevated temperatures the weak coupling scheme changes into a strong coupling, providing more interaction between the electrons and the lattice. This is supported by the fact that for transition metals ions, which are usually described with the strong coupling scheme, the nonradiative decay rates can be much higher than for trivalent rare earth ions. Such processes can generally involve large values for the number of phonons involved in a single decay event, in some cases more than 20 [56]. This provides a strong indicator that at elevated temperatures the quenching mechanism might be strongly affected by the decreased shielding of the $4f$ levels of the rare earth ions.

4.5 Heat Flux Gauge. In order to determine the temperature gradient and the heat flux through the thickness of the TBC under

Table 1 Fitting results for Eq. (2) for YSZ:Dy and YAG:Dy phosphors

Phosphor	n	E_{phonon} (cm^{-1})
YSZ:Dy	18	390
YAG:Dy	23	315

Downloaded 02 Jun 2010 to 171.66.16.109. Redistribution subject to ASME license or copyright; see http://www.asme.org/terms/Terms_Use.cfm

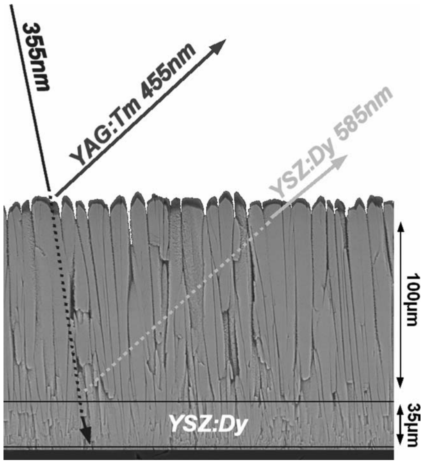

Fig. 10 SEM micrograph of the multilayer sensing EB-PVD TBC with the excitation and emission wavelengths

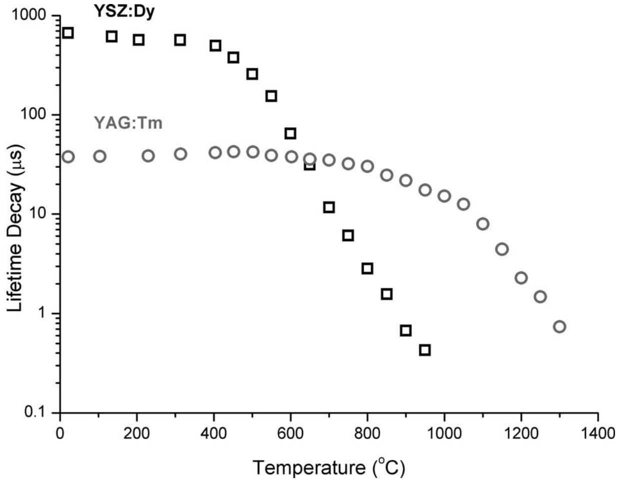

Fig. 11 Calibration curves of the YAG:Tm and YSZ:Dy layers of the multilayer EB-PVD TBC

realistic conditions using luminescence, the coating must contain at least two different phosphor layers at two different depths. Because the phosphorescence spectra of YSZ:Dy and YAG:Dy overlap, YAG:Dy cannot be used to measure the temperature at the surface of the TBC if the coating already contains a YSZ:Dy inner layer. YAG:Eu and YAG:Tb phosphors also have a temperature sensitivity above 1300°C [39,49,50] and therefore are potential candidates to be used as a top layer. However, if one of these phosphors was to be used, two different laser sources would be required in order to excite the top and inner phosphor layers. Research conducted at STS Ltd. showed that the lifetime of YAG doped with thulium oxide (YAG:Tm) can be measured also up to at least 1300°C, when excited at 355 nm (the same wavelength as for YSZ:Dy). Consequently, in order to test a multilayer sensing EB-PVD coating and to be able to measure the temperature at two different depths in the TBC using the STS setup, a multilayer coating comprising a standard 7YSZ and a YAG:Tm layer was deposited by EB-PVD. A micrograph of the sensing TBC is represented in Fig. 10. The position of the YSZ:Dy layer in the coating was determined by energy dispersive X-ray spectroscopy (EDX) analysis.

The multilayer sensing EB-PVD TBC was isothermally tested in a furnace in order to obtain the luminescence calibration curves of YSZ:Dy and YAG:Tm. For both phosphors the data were recorded during the same experiment using 355 nm excitation and switching between the YAG:Tm to the YSZ:Dy emission wavelength. There was no problem either with the YSZ:Dy phosphor excitation or with the detection of luminescence through the YAG:Tm and the 100 μm undoped layers.

The results in Fig. 11 show that the inner YSZ:Dy phosphorescent layer has a temperature sensitivity ranging from about 400°C to 950°C and the YAG:Tm top layer from 1000°C to 1300°C. As mentioned earlier, the YSZ:Dy phosphor has an emission line at 458 nm, which can also be used for temperature measurements. This luminescence peak overlaps with the 455 nm emission of the YAG:Tm phosphor. However the decay of the YSZ:Dy 458 nm line is very fast at 900°C and quenches at about 950°C; therefore, it will not affect the surface temperature measurements at higher temperatures. These results show that such an EB-PVD TBC could be used as a heat flux gauge in order to perform measurements in the temperature range that is experienced by a TBC during service.

The multilayer sample was heat treated for 1000 h at 1200°C and analyzed with X-ray diffraction (XRD) in order to determine the high temperature stability of the TBC and more particularly how the YAG:Tm layer would behave when aged for a long period of time. The as deposited YAG:Tm layer was found to be amorphous and only the diffraction peaks corresponding to the standard YSZ layer were recorded. The as deposited YAG top layer recrystallized when heat treated for 3 h at 1100°C and, as shown in Fig. 12, the XRD pattern is characteristic of the YAG phase and the YSZ tetragonal phase coming from the underlying standard YSZ layer. After 300 h at 1200°C the XRD peaks corresponding to the YAG phase become sharper and have a higher intensity. Moreover, the XRD pattern shows that the coating contains alumina. It is believed that the YAG phase in the coating aged 3 h at 1100°C was not completely crystalline and that the YAG:Tm layer did not reach its equilibrium phase composition. More importantly, longer heat treatments do not seem to cause any phase transformations in the top layer. The intensity and the width of the XRD peaks of the YAG phase do not change significantly after a heat treatment of 1000 h at 1200°C. The relative intensity of the alumina, YSZ and YAG diffraction peaks, remains constant between 300 h and 1000 h at 1200°C, which suggests good stability of the various phases present in the multilayer coating.

The presence of alumina in the YAG:Tm layer is explained by the fact that alumina has a higher vapor pressure compared with yttria. Consequently it tends to evaporate faster and it is deposited slightly in excess compared with the YAG stoichiometry. However it was found that the presence of alumina does not affect the phosphorescence and that the YAG phase remains stable for the

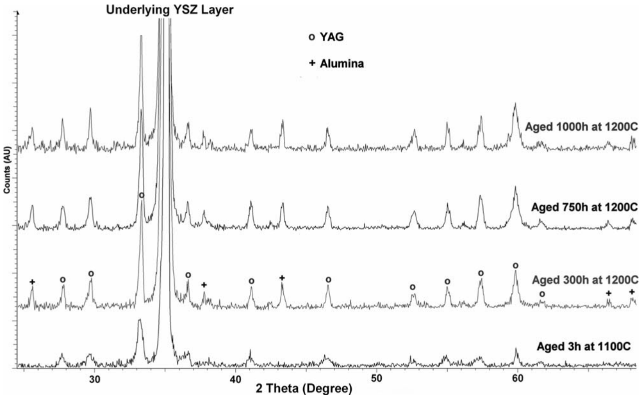

Fig. 12 XRD graphs of the multilayer coating aged 3 h at 1100°C and 300 h, 750 h, and 1000 h at 1200°C

Downloaded 02 Jun 2010 to 171.66.16.109. Redistribution subject to ASME license or copyright; see http://www.asme.org/terms/Terms_Use.cfm

heat treatments carried out.

It is worth noting that EDX analysis revealed that there was no significant diffusion of elements from the YAG:Tm and the standard YSZ layer after 1000 h at 1200°C.

5 Summary and Conclusion

- *Selection*. Phosphorescence measurement showed that YSZ:Dy, YSZ:Eu, and YSZ:Gd phosphors could be used to measure temperatures of up to 950°C, 800°C, and 250°C, respectively. It was noted that these temperature sensitivities could be further improved by using a detection system with a higher sensitivity.
- *Concentration*. For sensing purposes, low concentrations of dysprosia are preferred as they give higher luminescence intensities. However the temperature measurements will not be affected when the concentration of dysprosia ranges from 0.3 mol % to 2 mol %.
- *Aging*. Temperature measurements are insensitive to the high temperature aging and the associated phase transformations that could occur during service.
- *Multiple emission lines*. Different emission lines from the YSZ:Dy phosphorescence spectrum can be used for temperature measurements.
- *YAG coating*. A luminescent YAG:Dy coating was deposited by EB-PVD. Such a coating has a temperature sensitivity of at least 1500°C and potentially 1700°C.
- *Sublayer*. A multilayer EB-PVD TBC comprising a YSZ:Dy inner layer was successfully deposited by EB-PVD and tested. There was no problem in exciting and detecting the inner layer phosphorescence through a 100 μm thick YSZ layer.
- *Multiphonon quenching*. The fitted data suggest that up to 23 phonons were involved in the quenching process. This very large number could indicate that the weak coupling scheme for trivalent rare earth ions such as Dy^{3+} changes into strong coupling at elevated temperatures.
- *Heat flux gauge*. A multilayer phosphorescent TBC comprising an outer YAG:Tm and an inner YSZ:Dy layers was deposited by EB-PVD. The coating was successfully tested and showed that temperature measurements could be **simultaneously performed** at two different depths in the TBC with such system using a single excitation source. The YAG:Tm layer had a temperature sensitivity of at least 1300°C, and the luminescence of YSZ:Dy was not affected by the YAG top layer.
- *Good thermal stability*. The high temperature stability of the multilayer sensing TBC was investigated. It showed that the YAG phase remained stable when heat treated up to 1000 h at 1200°C.

This work describes the progress made over the past years in the manufacturing and detection of temperatures inside thermal barrier sensor coatings using the EB-PVD coating technique. The capability of making remote temperature measurements based on phosphorescence beyond 1300°C in the laboratory opens up new opportunities to provide more accurate temperature reading systems for the gas turbine industry. The coatings proved to be stable and have shown excellent luminescence properties. Further it realizes the concept of a heat flux gauge, proposed in 1998 by Choy et al. [34], and enables the accurate measurement of temperatures at different depths in a thermal barrier coating for the first time ever.

Next steps will include the application of a heat flux gauge sensor on STS's thermal gradient cycling test bed, which is designed for TBC testing under more realistic thermal gradient test conditions. The authors believe that, with recent successes, the sensor coating technology could be transferred to a real engine test bed in less than two years [66].

Acknowledgment

The work and data presented in this paper were partly sponsored by the European Community under the project ASTERIXE and by The Carbon Trust under the project SATURN. We are grateful to Dr. Andrew L. Heyes, Imperial College London, Mechanical Engineering Department, for providing essential laboratory equipment for characterizing the luminescence. We wish also to thank Tony Gray at Cranfield University for his skilled assistance in helping to produce the TBC systems. The authors would also like to thank Southside Thermal Sciences (STS) Ltd., UK, which provided the matching funding for these programs and permitted the publication of this work.

References

[1] Ruud, J., Lau, Y. C., and Kwasniewski, V., 2003, "Increased Fuel Efficiency and Decreased Emissions Through TBCs," available at http://statusreports.atp.nist.gov/reports/95-07-0018TEXT.html

[2] Cheruvu, N. S., Chan, K. S., and Viswanathan, R., 2006, "Evaluation, Degradation and Life Assessment of Coatings for Land Based Combustion Turbines," Energy Mater.: Mater. Sci. Eng. Energy Syst., **1**(1), pp. 34–47.

[3] Kerr, C., and Ivey, P., 2002, "An Overview of the Measurement Errors Associated With Gas Turbine Aeroengine Pyrometer Systems," Meas. Sci. Technol., **13**, pp. 873–881.

[4] Singh, R., 2003, *Civil Aero Gas Turbines: Technology & Strategy*, Aero India, Bangalore, India.

[5] Boyce, M. P., 2001, *Gas Turbine Engineering Handbook*, 2nd ed., Gulf Professional Publishing, Houston.

[6] Allison, S. W., and Gillies, G. T., 1997, "Remote Thermometry With Thermographic Phosphors: Instrumentation and Applications," Rev. Sci. Instrum., **68**(7), pp. 2615–2650.

[7] Noel, B. W., Borella, H. M., Lewis, W., Turley, W. D., Beshears, D. L., Capps, G. J., Cates, M. R., and Tobin, K. W., 1991, "Evaluating Thermographic Phosphors in an Operating Turbine Engine," ASME J. Eng. Gas Turbines Power, **113**(2), pp. 242–245.

[8] Choy, K.-L., Feist, J. P., Heyes, A. L., and Su, B., 1999, "Eu-Doped Y_2O_3 Phosphor Films Produced by Electrostatic-Assisted Chemical Vapor Deposition," J. Mater. Res., **14**(7), pp. 3111–3114.

[9] Bird, C., Mutton, J. E., Shepherd, R., Smith, M. D. W., and Watson, H. M. L., 1997, "Surface Temperature Measurement in Turbines," *Advanced Non-Intrusive Instrumentation for Propulsion Engines*, AGARD Conference Proceedings, Brussels, Belgium, Vol. 598, pp. 21.4–21.10.

[10] Tobin, K. W., Jr., Beshears, D. L., Noel, B. W., Turley, W. D., and Lewis, W., III, 1991, "Fiber Sensor Design for Turbine Engines," *Proc. SPIE*, Ninth Fiber Optic and Laser Sensors, Boston, MA, Vol. 1584, pp. 23–31.

[11] Noel, B. W., Borella, H. M., Franks, L. A., Marshall, B. R., Allison, S. W., Stange, W. A., and Cates, M. R., 1986, "Proposed Laser-Induced Fluorescence Method for Remote Thermometry in Turbine Engines," Jet Propul., **2**(6), pp. 565–568.

[12] Tobin, K. W., Allison, S. W., Cates, M. R., Capps, G. J., Beshears, D. L., Cyr, M., and Noel, B. W., 1990, "High-Temperature Phosphor Thermometry of Rotating Turbine Blades," AIAA J., **28**(8), pp. 1485–1490.

[13] Ranson, R. M., Thomas, C. B., and Craven, M. R., 1998, "A Thin Coating for Phosphor Thermography," Meas. Sci. Technol., **9**, pp. 1947–1950.

[14] Mannik, L., Brown, S. K., and Campbell, S. R., 1987, "Phosphor-Based Thermometry of Rotating Surfaces," Appl. Opt., **26**(18), pp. 4014–4017.

[15] Feist, J. P., and Heyes, A. L., 2000, "Europium-Doped Yttria-Stabilized Zirconia for High-Temperature Phosphor Thermometry," Proc. Inst. Mech. Eng., IMechE Conf., **214**, pp. 7–11.

[16] Feist, J. P., 2001, "Development of Phosphor Thermometry for Gas Turbines," Ph.D. thesis, University of London, London, UK.

[17] Alaruri, S., McFarland, D., Brewington, A., Thomas, M., and Sallee, N., 1995, "Development of Fiber-Optic Probe for Thermographic Phosphor Measurements in Turbine Engines," Opt. Lasers Eng., **22**, pp. 17–31.

[18] Alaruri, S., Bonsett, T., Brewington, A., McPheeters, E., and Wilson, M., 1999, "Mapping the Surface Temperature of Ceramic and Superalloy Turbine Engine Components Using Laser-Induced Fluorescence of Thermographic Phosphor," Opt. Lasers Eng., **31**, pp. 345–351.

[19] Brübach, J., Zetterberg, J., Omrane, A., Li, Z. S., Aldén, M., and Dreizler, A., 2006, "Determination of Surface Normal Temperature Gradients Using Thermographic Phosphors and Filtered Rayleigh Scattering," Appl. Phys. B, **84**, pp. 537–541.

[20] Chyu, M. K., and Bizzak, D. J., 1994, "Surface Temperature Measurement Using a Laser-Induced Fluorescence Thermal Imaging System," ASME J. Heat Transfer, **116**, pp. 263–266.

[21] Feist, J. P., Heyes, A. L., Choy, K. L., and Su, B., 1999, "Phosphor Thermometry for High Temperature Gas Turbine Applications," *18th International Congress on Instrumentation in Aerospace Simulation Facilities*, Toulouse, France, pp. 6.1–6.7.

[22] Feist, J. P., and Heyes, A. L., 2000, "The Characterization of $Y_2O_2S:Sm$ Powder as a Thermographic Phosphor for High Temperature Applications," Meas. Sci. Technol., **11**, pp. 942–947.

[23] Feist, J. P., Heyes, A. L., and Seefeldt, S., 2002, "Thermographic Phosphors

Downloaded 02 Jun 2010 to 171.66.16.109. Redistribution subject to ASME license or copyright; see http://www.asme.org/terms/Terms_Use.cfm

for Gas Turbines: Instrumentation Development and Measurement Uncertainties," 11th International Symposium on Application of Laser Techniques to Fluid Mechanics, Lisbon, Portugal.

[24] Feist, J. P., Heyes, A. L., and Seefeldt, S., 2003, "Thermographic Phosphor Thermometry for Film Cooling Studies in Gas Turbine Combustors," Proc. Inst. Mech. Eng., Part A, **217**, pp. 193–200.

[25] Eldridge, J. L., Bencic, T. J., Allison, S. W., and Beshears, D. L., 2004, "Depth-Penetrating Temperature Measurements of Thermal Barrier Coatings Incorporating Thermographic Phosphors," J. Therm. Spray Technol., **13**, pp. 44–50.

[26] Heyes, A. L., Seefeldt, S., and Feist, J. P., 2006, "Two-Colour Thermometry for Surface Temperature Measurement," Opt. Laser Technol., **38**, pp. 257–265.

[27] Feist, J. P., Heyes, A. L., and Nicholls, J. R., 2001, "Phosphor Thermometry in an Electron Beam Physical Vapour Deposition Produced Thermal Barrier Coating Doped With Dysprosium," Proc. Inst. Mech. Eng., Part G, J. Aerosp. Eng., **215**, pp. 333–341.

[28] Goss, L. P., Smith, A. A., and Post, M. E., 1989, "Surface Thermometry by Laser-Induced Fluorescence," Rev. Sci. Instrum., **60**(12), pp. 3702–3706.

[29] Allison, S. W., Boatner, L. A., and Gillies, G. T., 1995, "Characterization of High-Temperature Thermographic Phosphors: Spectral Properties of $LuPO_4$:Dy(1%), Eu(2%)," Appl. Opt., **34**(25), pp. 5624–5627.

[30] Omrane, A., Ossler, F., and Aldén, M., 2004, "Temperature Measurements of Combustible and Non-Combustible Surfaces Using Laser Induced Phosphorescence," Exp. Therm. Fluid Sci., **28**(7), pp. 669–676.

[31] Edge, A. C., Laufer, G., and Krauss, R. H., 2000, "Surface Temperature-Field Imaging With Laser-Induced Thermographic Phosphorescence," Appl. Opt., **39**(4), pp. 546–553.

[32] Heyes, A. L., 2004, *Thermographic Phosphor Thermometry Applications in Engineering* (VKI Lecture Series on Advanced Measurement Techniques for Aero and Stationary Gas Turbines), von Karman Institute, Rhode St. Genese, Belgium.

[33] Amano, K., Takeda, H., Suzuki, T., Tamatani, M., Itoh, M., and Takahashi, Y., 1987, "Thermal Barrier Coating" U.S. Patent No. 4,774,150.

[34] Choy, K.-L., Heyes, A. L., and Feist, J., 1998, "Thermal Barrier Coating With Thermoluminescent Indicator Material Embedded Therein," U.S. Patent No. 6,974,641.

[35] Gentleman, M. M., and Clarke, D. R., 2005, "Luminescence Sensing of Temperature in Pyrochlore Zirconate Materials for Thermal Barrier Coatings," Surf. Coat. Technol., **200**, pp. 1264–1269.

[36] Gentleman, M. M., and Clarke, D. R., 2004, "Concepts of Luminescence Sensing of Thermal Barrier Coatings," Surf. Coat. Technol., **188–189**, pp. 93–100.

[37] Gentleman, M. M., Eldridge, J. I., Zhu, D. M., Murphy, K. S., and Clarke, D. R., 2006, "Non-Contact Sensing of TBC/BC Interface Temperature in a Thermal Gradient," Surf. Coat. Technol., **201**, pp. 3937–3941.

[38] Chen, X., Mutasim, Z., Price, J., Feist, J. P., Heyes, A. L., and Seefeldt, S., 2005, "Industrial Sensor TBCs: Studies on Temperature Detection and Durability," Int. J. Appl. Ceram. Technol., **2**(5), pp. 414–421.

[39] Feist, J. P., Nicholls, J. R., Fraser, M. J., and Heyes, A. L., 2006, "Luminescent Material Compositions and Structures Incorporating the Same," Patent No. PCT/GB2006/003177.

[40] Srivastava, A. M., Setlur, A. A., Comanzo, H. A., Devitt, J. W., Ruud, J. A., and Brewer, L. N., 2001, "Apparatus for Determining Past-Service Conditions and Remaining Life of Thermal Barrier Coatings and Components Having Such Coatings," U.S. Patent No. 6730918B2.

[41] Feist, J. P., and Heyes, A. L., 2003, "Coatings and an Optical Method for Detecting Corrosion Process in Coatings," Patent EP1660757 (A1).

[42] Eldridge, J. I., Bensic, T. J., Spuckler, C. M., Singh, J., and Wolfe, D. E., 2006, "Delamination-Indicating Thermal Barrier Coatings Using YSZ:Eu Sublayer," J. Am. Ceram. Soc., **89**(10), pp. 3246–3251.

[43] Eldridge, J. I., Singh, J., and Wolfe, D. E., 2006, "Erosion-Indicating Thermal Barrier Coating Using Luminescent Sublayers," J. Am. Ceram. Soc., **89**(10), pp. 3252–3254.

[44] Choy, K.-L., Mei, J., Feist, J. P., and Heyes, A. L., 2000, "Microstructure and Thermoluminescent Properties of ESAVD Produced Eu Doped $Y_2O_3-ZrO_2$ Coatings," Surf. Eng., **16**(6), pp. 469–472.

[45] Nicholls, J. R., Lawson, K. J., Johnstone, A., and Rickerby, D. S., 2002, "Methods to Reduce the Thermal Conductivity of EB-PVD TBCs," Surf. Coat. Technol., **151–152**, pp. 383–391.

[46] Padture, N. P., Gell, M., and Klemens, P. G., 2000, "Ceramic Materials for Thermal Barrier Coatings," U.S. Patent No. 6,015,630.

[47] Klemens, P. G., and Gell, M., 1998, "Thermal Conductivity of Thermal Barrier Coatings," Mater. Sci. Eng., A, **245**, pp. 143–149.

[48] Su, Y. J., Trice, R. W., Faber, K. T., Wang, H., and Porter, W. D., 2004, "Thermal Conductivity, Phase Stability and Oxidation Resistance of $Y_3Al_5O_{12}$ (YAG)/$Y_2O_3-ZrO_2$ (YSZ) Thermal-Barrier Coatings," Oxid. Met., **61**(3/4), pp. 253–271.

[49] Noel, B. W., Turley, W. D., and Lewis, W., 1992, "Non-Intrusive Temperature Measurements on Advanced Turbomachinery Components," *Second Latin American Conference on Turbomachinery*, Guernavaca, Mexico, p. 23.

[50] Cates, M., and Allison, S., 2002, "Phosphor Thermometry Tutorial," available at http://www.ornl.gov/sci/phosphors/Pdfs/tutorial.pdf

[51] Blasse, G., 1979, "Chemistry and Physics of R-Activated Phosphors," *Handbook on the Physics and Chemistry of Rare Earths*, K. A. Gschneidner, Jr. and L. Eyring, eds., North-Holland, Amsterdam, pp. 237–255.

[52] Weber, M. J., 1968, "Radiative and Multiphonon Relaxation of Rare-Earth Ions in Y_2O_3 ," Phys. Rev., **171**(2), pp. 283–291.

[53] Orbach, R., 1975, *Optical Properties of Ions in Solids*, B. Di Batolo, ed., Plenum, New York.

[54] Miyakawa, T., and Dexter, D. L., 1970, "Phonon Sidebands, Multi-Phonon Relaxation of Excited States, and Phonon-Assisted Energy Transfer Between Ions in Solids," Phys. Rev. B, **1**, pp. 2961–2969.

[55] Hufner, S., 1978, *Optical Spectra of Transparent Rare Earth Compounds*, Academic, New York.

[56] Henderson, B., and Imbusch, G. F., 1989, *Optical Spectroscopy of Inorganic Solids*, Oxford University Press, New York.

[57] Riseberg, L. A., and Moos, H. W., 1968, "Multiphonon Orbit-Lattice Relaxation of Excited States of Rare-Earth Ions in Crystals," Phys. Rev., **174**(2), pp. 429–438.

[58] Gentleman, M. M., Lughi, V., Nychka, J. A., and Clarke, D. R., 2006, "Noncontact Methods for Measuring Thermal Barrier Coating Temperatures," Int. J. Appl. Ceram. Technol., **3**(2), pp. 105–112.

[59] Struck, C. W., and Fonger, W. H., 1976, "Quantum Mechanical Treatment of Eu^{+3} $4f^{--}>4f$ and 4f Charge-Transfer-State Transitions in Y_2O_2S and La_2O_2S," J. Chem. Phys., **64**, pp. 1784–1790.

[60] Struck, C. W., and Fonger, W. H., 1970, "Role of the Charge-Transfer States in Feeding and Thermally Emptying the ^5D States of Eu^{+3} in Yttrium and Lanthanum Oxysulfides," J. Lumin., **1–2**, pp. 456–469.

[61] Hoshina, T., 1983, "Luminescence of Rare Earth Ions," Sony Research Centre Report.

[62] Vanvalzah, J. R., and Eaton, H. E., 1991, "Cooling Rate Effects on the Tetragonal to Monoclinic Phase Transformation in Aged Plasma-Sprayed Yttria Partially Stabilized Zirconia," Surf. Coat. Technol., **46**, pp. 289–300.

[63] Chambers, M. D., and Clarke, D. R., 2006, "Effect of Long Term, High Temperature Aging on Luminescence From Eu-Doped YSZ Thermal Barrier Coatings," Surf. Coat. Technol., **201**, pp. 3942–46.

[64] Weber, M. J., 1979, *Handbook on the Physics and Chemistry of Rare Earths*, K. A. Gschneidner, Jr. and L. Eyring, eds., North-Holland, Amsterdam, pp. 275–315.

[65] Blasse, G., and Grabmaier, B. C., 1994, *Luminescent Materials*, Springer-Verlag, Berlin.

[66] Mehta, R., 2006, "Sensing a Solution," Mater. World, **4**(6), p. 12.

Downloaded 02 Jun 2010 to 171.66.16.109. Redistribution subject to ASME license or copyright; see http://www.asme.org/terms/Terms_Use.cfm

Combustion Characteristics of a Can Combustor With a Rotating Casing for an Innovative Micro Gas Turbine

Hsin-Yi Shih[1]
Assitant Professor
e-mail: hyshih@mail.cgu.edu.tw

Chi-Rong Liu

Department of Mechanical Engineering,
Chang Gung University,
Taoyuan 333, Taiwan

A can type combustor with a rotating casing for an innovative micro gas turbine has been modeled, and the combustion characteristics were investigated. The simulations were performed using commercial code STAR-CD*, in which a three-dimensional compressible k-ε turbulent flow model and a one-step overall chemical reaction between methane/air were used. The results include the detailed flame structure at different rotation speeds of outside casing, ranging from stationary to the maximum speed of 58,000 rpm of the design point. The airflows are baffled when entering the combustor through the linear holes due to the centrifugal force caused by the rotating casing, and the inlet flow angle is inclined. When the rotation is in the opposite direction of the swirling flows driven by the designed swirler, a shorter but broader recirculation zone and a concave shape flame are found at a higher rotating speed. At maximum rotating speed, the swirling flows are dominated by the rotating flows caused by the casing, especially downstream of the combustor. The combustor performance was also analyzed, indicating a higher combustion efficiency and higher exit temperature when the casing rotates, which benefits the performance of the gas turbine, but the cooling and possible hot spots for turbines are the primary concerns.* [DOI: 10.1115/1.3043807]

Keywords: *gas turbine combustion, can combustor, micro gas turbine*

1 Introduction

The gas turbine engine operates on the Brayton cycle, which begins with compression, heat addition, and terminates in expansion. The intake air is compressed in a compressor and delivered through the diffuser to the combustor, where fuel is injected and burned to raise the gas temperature to a higher value. The hot high-pressure combustion gases then expand through the rotating turbines, where work is extracted to produce shaft power, propulsive thrust, or the combination of these two. Recently, micro gas turbines, with a power range of 25–300 kW, have gained a lot of interest due to the market potential for distributed power generation. A lot of research programs have been initiated since late 1999 [1]. For a high-speed micro gas turbine, it is difficult to improve the rigidity of the core shaft with a limited diameter. The vibration due to resonance is also a serious problem and it is more apparent in micro gas turbines at high-speed operations. One of the inventions related to the engine core rotor shaft structure for use in a gas turbine engine is to greatly enlarge the diameter of the shaft to increase the rigidity and avoid vibration from resonance of the shaft. This invention has granted the United States and Republic of China patents [2,3], and the idea is schematically shown in Fig. 1. As illustrated, the innovative engine core rotor is mounted inside a casing, which has a compression section, a combustion section, and a turbine section. The shaft of the engine core rotor comprises an outer annular shaft body, an inner annular shaft body, a front annular shaft body, compressor and turbine blades, and a combustor. The innovation is to attach the turbine blades inside an enlarged outer annular shaft. Therefore, the shaft body has a high rigidity and can be operated under a high critical speed to improve the stability of the system and to prolong the service life. Also, the hollow shaft accommodates a can type combustor for compactness, so as to reduce heat dissipation and to increase the thermal efficiency of the gas turbine engine.

However, unlike the conventional gas turbine engine, the stationary combustor is mounted inside the rotating shaft of the innovative gas turbine engine, and the hollow shaft becomes the casing of the combustor. During operation, the entrance air between the combustor liner and the casing then flows both axially and circumferentially due to the centrifugal effect as the shaft rotates, causing a swirling flow outside the combustor liner. This is quite different from the conventional flow patterns for a gas turbine combustor, where entrance air moves downstream most axially until it meets the liner holes and flows into the combustor. Although the swirling flows have been widely used in gas turbine combustors for promoting rapid mixing, improving flammability limits, shortening flame size, and reducing pollutant emissions [4,5], it was produced for the combustion zone, which is inside the liner and not outside it. So far, there is no study for such combustor with a rotating casing. It apparently set the purpose of this work to investigate the combustion characteristics of the can combustor with a rotating casing and the subsequent influence on the innovative micro gas turbine.

2 The Innovative Micro Gas Turbine

According to the present invention, a micro gas turbine with a power output of 60 kW was proposed, and the feasibility study of the system was made [6]. The schematic of the engine is shown in Fig. 2, which includes the centrifugal compressor, can combustor, axial turbine, and the enlarged hollow shaft. Because the combustor is mounted directly inside the shaft, the proposed system greatly reduces the dimensions and weight of the engine core rotor, in comparison with conventional designs of equal power. Based on the feasibility study, the dimensions and weight of the invention can be about 80% of a convectional gas turbine engine.

---

[1] Corresponding author.

Manuscript received June 5, 2008; final manuscript received July 7, 2008; published online April 15, 2009. Review conducted by Dilip R. Ballal. Paper presented at the ASME Turbo Expo 2008: Land, Sea and Air (GT2008), Berlin, Germany, June 9–13, 2008.

Copyright © 2009 by ASME

Downloaded 02 Jun 2010 to 171.66.16.109. Redistribution subject to ASME license or copyright; see http://www.asme.org/terms/Terms_Use.cfm

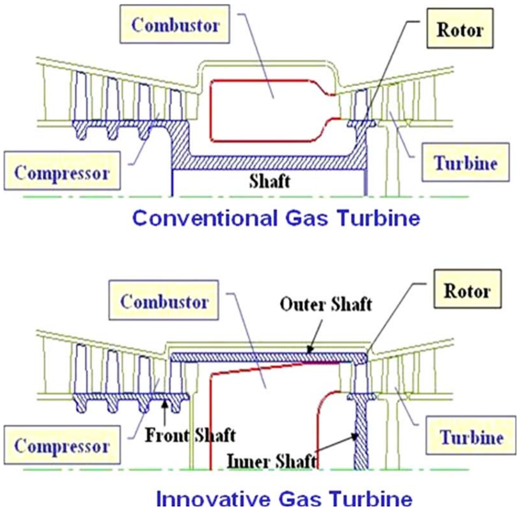

Fig. 1 The schematic of innovative rotor shaft structures

The thermodynamic cycle analysis and the gas turbine performance were simulated by the software GASTURB™ [7] and the results on the mass-flow rate, temperature, and pressure *P* at each station (the inlet and outlet of the component) were analyzed. For the proposed micro gas turbine engine to have power output near 60 kW, the total airflow rate is 0.49 kg/s and the fuel supply rate (natural gas) is 0.0096 kg/s. The designed efficiencies for the compressor, combustor, and turbine are 0.81, 0.9, and 0.84, respectively. The compression ratio is 3.28, and the expansion ratio is 1.73. The overall thermal efficiency without any heat recuperation will be 12.8% at a nominal speed of 58,000 rpm. Here the target combustion efficiency of 90% is set lower than the normal application in a gas turbine engine because a conservative design was considered for the newly proposed system in compact size.

3 The Can Combustor

Figure 3 shows the picture of the can combustor inside the rotating shaft, which was designed using the in-house preliminary design code PRECOMB [8] based on the design method for a conventional combustor. From the previous cycle analysis for the proposed micro gas turbine, the airflow rate at the inlet of the combustor is 0.473 kg/s at 431 K and 3.2 atm. The fuel is a natural gas (methane, CH_4) with a flow rate of 0.0096 kg/s. The overall equivalence ratio is 0.35, and the Reynolds number is around 3.4×10^5. The design criterion for the can combustor is to achieve a combustion efficiency of 90% with an exit gas temperature of 1200 K and a 6% pressure drop.

The combustor, made of stainless steel, is 75 mm in diameter and 180 mm in length, consisting of primary, secondary, and dilution zones, followed by a bullet nosed cap to form a transition duct. The diameter of the rotating casing is 95 mm. The air admission holes are determined by evaluating the air distribution to achieve the highest flame temperature in the primary zone, a weaker reaction zone in the secondary zone, and an extinction region in the dilution zone. The air holes are distributed equally around the combustor; eight for the primary zone, each 7 mm in diameter, eight for the secondary zone, each 5 mm in diameter, and six for the dilution zone, each 11 mm in diameter. Most of the main air stream flow through the gap between the casing and the combustor liner and then enter the combustor through the holes. Only about 10% of the entrance air flow directly into the combustor through a swirler.

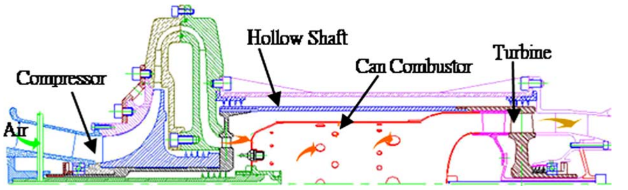

Fig. 2 The schematic of the proposed innovative micro gas turbine

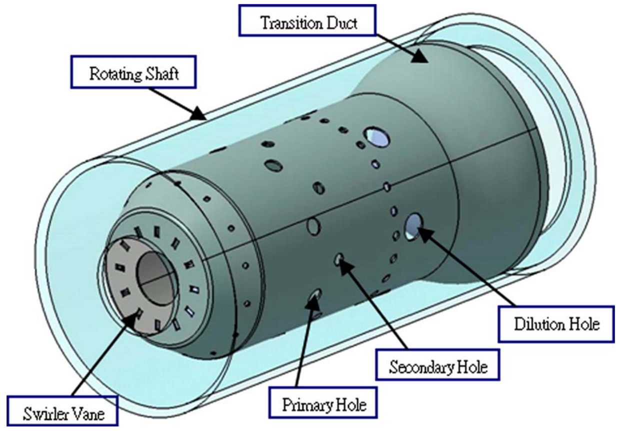

Fig. 3 The designed can combustor inside the rotating shaft

To accommodate the combustor inside the shaft, a simple and compact design with heavy combustion loading was made. Therefore, the swirler was simply designed as 12 rectangular slots circling around the inlet of the combustor with a vane angle of 30 deg. The swirl number is estimated to be near 1. The film cooling was replaced with two rows of small cooling holes located at the combustor dome and dilution zone just ahead of the dilution holes. We think the swirling outside the liner could contribute to the cooling by circulating around the combustor. The gaseous fuel nozzle is inserted axially, and the fuel is injected radially from the small holes that are equally spaced around the circumference of the nozzle. Viewing downstream, the swirling flows caused by the swirler rotate counterclockwise, and the casing rotates in the opposite direction.

4 The Modeling

The commercial computational fluid dynamics (CFD) software STAR-CD [9] is used to model the combustor. The computational domain includes the interior of the can combustor, the combustor liner, and the space between the liner and the rotating casing. The grids are generated using the multiblock method. The meshes for fuel injection holes and the liner holes are created and refined in centric coordinates. Finer cells are located in the primary zone where a strong reaction is expected, and also around the air entrance holes where the physical properties change more dramatically.

One layer of zero-thickness cells called "baffles" simulates the liner of the combustor. The baffles are assumed to be smooth, stationary, impermeable walls with a no-slip condition. Thermal resistance is also specified at the baffle, so the amount of heat transferred across the liner can be calculated. The total amount of grids are 302,139. The grid structure and the baffle representing the combustor liner are shown in Fig. 4.

The theoretical model consists of a three-dimensional compressible k-ε/high Reynolds number turbulent flow model and a one-step overall reaction between methane and air. The steady-state Navier–Stokes equations are solved using the finite-volume method and SIMPLE algorithm [10]. The chemical reaction mechanism adopts the presumed probability density function (PPDF) for diffusion flames in the chemical module to simulate the combustion process. Gravitational effect is ignored. Although the model does not represent the state-of-art in modeling gas tur-

Downloaded 02 Jun 2010 to 171.66.16.109. Redistribution subject to ASME license or copyright; see http://www.asme.org/terms/Terms_Use.cfm

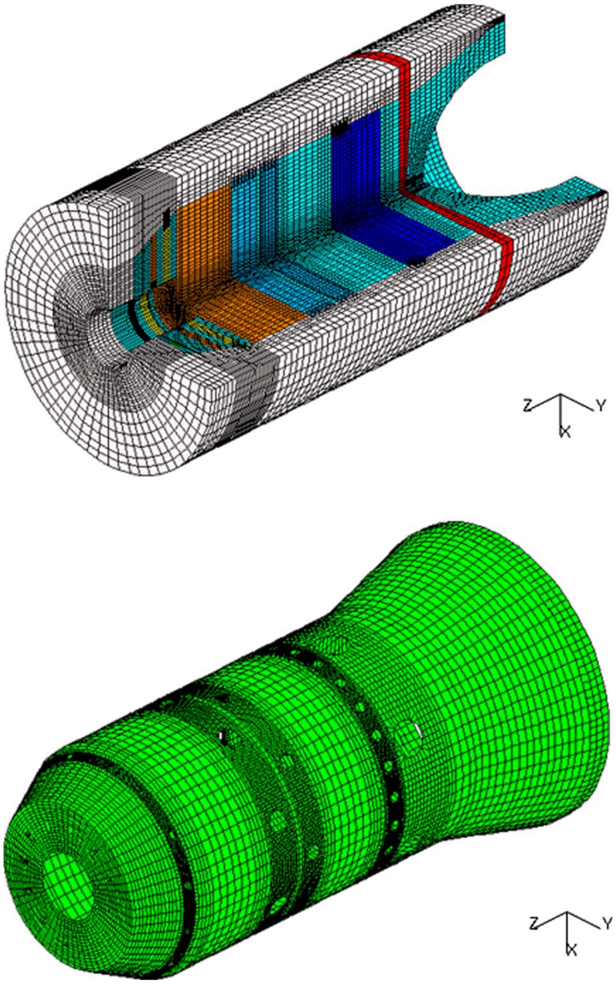

Fig. 4 The grid structure and the combustor liner represented by a baffle

bine reacting flows, it could provide a qualitative trend prediction of the casing rotation effects in the early developing stage.

The boundary conditions for the casing wall need to be specified. Aside from being no-slip, smooth, and impermeable, the wall is assumed nonadiabatic with an ambient temperature of 300 K. Besides this, an angular velocity that describes the rotation speed of the casing is required. In this work, computations were made for a casing rotating between 0 rpm and 58,000 rpm, which is the maximum nominal speed.

5 Results and Discussions

5.1 Cold Flow Field. The cold flow fields for the combustor with and without a rotating casing are compared first to demonstrate the change in flow pattern. In Fig. 5, the whole flow field inside and outside the combustor liner is shown on the axial centerline plane through the middle of the primary holes. As you can see, there is a flow recirculation in the primary zone; it is induced by the vortex breakdown in swirling flows when the rotation imparted to the flow is high. The swirling flows are produced by the swirler, which sits around the fuel injector. This type of recirculation promotes better mixing and has been widely used in industrial burners and gas turbine combustors.

With the rotation of the casing (at 58,000 rpm), the axial flow velocity is smaller and the recirculation zone seems to be shorter but a little broader. Interestingly, there is a second recirculation region downstream near the dilution zone with a stationary casing. However, it disappears when the casing rotates. It is believed that as the casing rotates, the flows outside the liner also rotate. Consequently, the flows entering the combustor are not going straight toward the center, but with an angle into the liner holes. Figure 6 illustrates where the velocity profiles are shown on the radial plane through the eight primary holes. Viewing downstream, the swirling flows produced by the swirler rotate counterclockwise, and the inlet flows between the combustor liner and the casing enter vertically into the combustor through the air holes. However, with the casing rotating clockwise at 58,000 rpm, it is very obvious that flows outside the liner rotate clockwise at a high speed. Due to the rotation, the flows enter the combustor with an angle, and it dominates the flow motion inside the combustor. As a result, the flows inside the combustor also rotate in the clockwise direction, a reversal from the case without a rotating casing. The

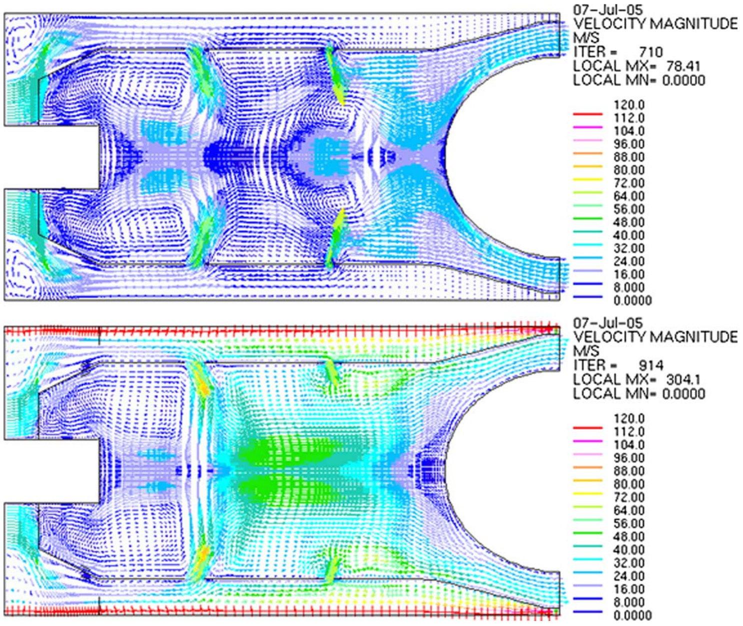

Fig. 5 The velocity profiles on the axial centerline for 0 rpm (top) and 58,000 rpm (bottom)

Downloaded 02 Jun 2010 to 171.66.16.109. Redistribution subject to ASME license or copyright; see http://www.asme.org/terms/Terms_Use.cfm

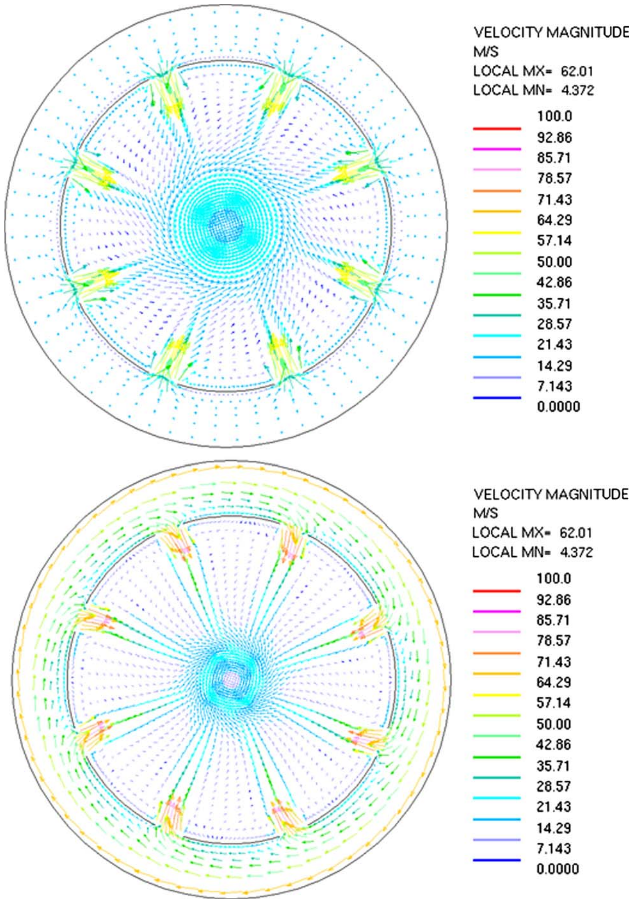

Fig. 6 The velocity profiles on the radial planes through the primary holes for 0 rpm (top) and 58,000 rpm (bottom)

motion of rotation increases further downstream and diminishes the second recirculation zone. Besides this, the centrifugal force caused by the rotation prohibits the air stream from penetrating into the middle of the combustor. Compared with the case without a rotating casing, a lesser amount of air is admitted in the primary zone, but with more air going to the rear part of the combustor.

5.2 Effects of Rotating Casing on Combustion. The three-dimensional combustion simulation for the combustor was then performed to study the influence of the rotating casing on combustion behaviors. Figure 7 shows velocity stream lines and temperature profiles on three selected planes of the combustor for the cases at 0 rpm (stationary casing) and 58,000 rpm. As we can see, near the primary zone upstream, the swirling flows caused by the swirler at 0 rpm are much stronger than that at 58,000 rpm. When the casing rotates at 58,000 rpm, the recirculation flow is a little bit twisted, and the entrance air basically flows downstream spirally because of the rotating motion of the casing. More entrance air flows into the combustor downstream near the dilution zone. In addition, the temperature profiles indicate that the combustion zone is in the primary zone upstream. Near the air holes and going downstream, the temperature is lower due to air cooling. However, a high temperature region is wider, but is shorter when the casing rotates at 58,000 rpm compared with that at 0 rpm.

The combustion characteristics of the can combustor with the casing rotating at different speeds are then investigated. Figure 8 shows the temperature profiles on the axial centerline plane sliced through one of the primary holes for rotating speeds of 0 rpm, 20,000 rpm, 40,000 rpm, and 58,000 rpm. The flame is stabilized in the core region of the primary zone since the fuel and air mix rapidly in the recirculation zone there. The highest temperature is around 2400 K, which is close to the adiabatic flame temperature for a methane-air mixture at an equivalence ratio near 1. Going downstream, the temperature decreases due to air cooling and dilution. However, when the casing begins to rotate, the flame shape alters. As we can see, when the rotating speed increases from 0 rpm to 20,000 rpm, the high temperature zone seems to be a little wider, and the maximum temperature is increased by 10 K. As the rotating speed increases further to 40,000 rpm, the high temperature zone in the core region shrinks and the flame becomes shorter, but it expands becoming wider and longer on the side. As a result, the flame changes to a concave shape downstream. At the maximum rotating speed of 58,000 rpm, the flame shape is basically similar to that at 40,000 rpm, but the high temperature zone is enlarged, especially on the side of the primary zone.

The flow patterns in the primary zone for rotating speeds of 0 rpm and 58,000 rpm are shown and compared in Fig. 9. The recirculation zone seems to be shorter but shifts to the side when the casing rotates. Besides this, the flows move upstream in the middle of the primary zone, which push the flame backward. Consequently, a shorter but wider concave flame is observed at a

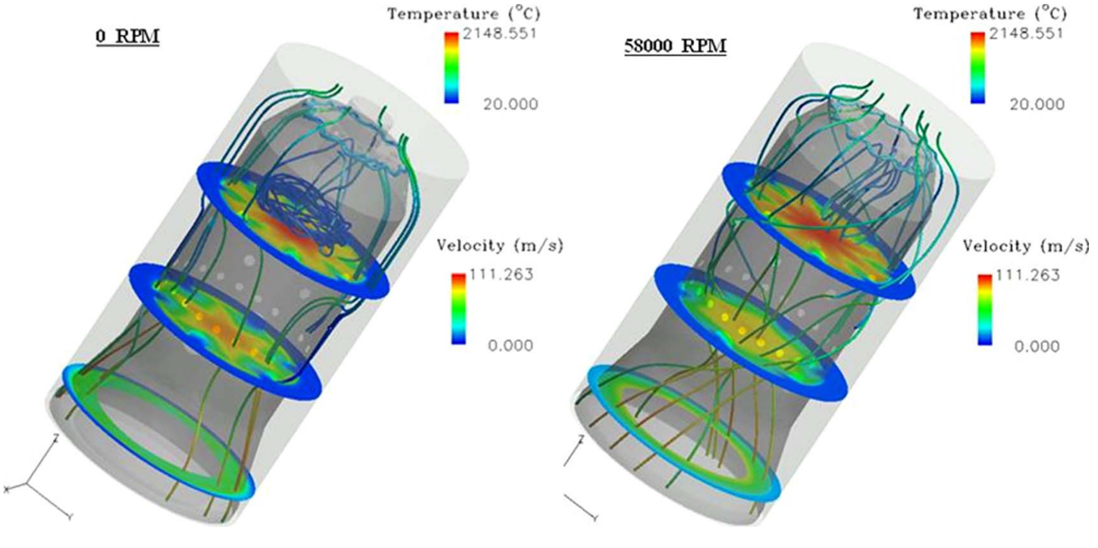

Fig. 7 The three-dimensional combustion simulation of the combustor

Downloaded 02 Jun 2010 to 171.66.16.109. Redistribution subject to ASME license or copyright; see http://www.asme.org/terms/Terms_Use.cfm

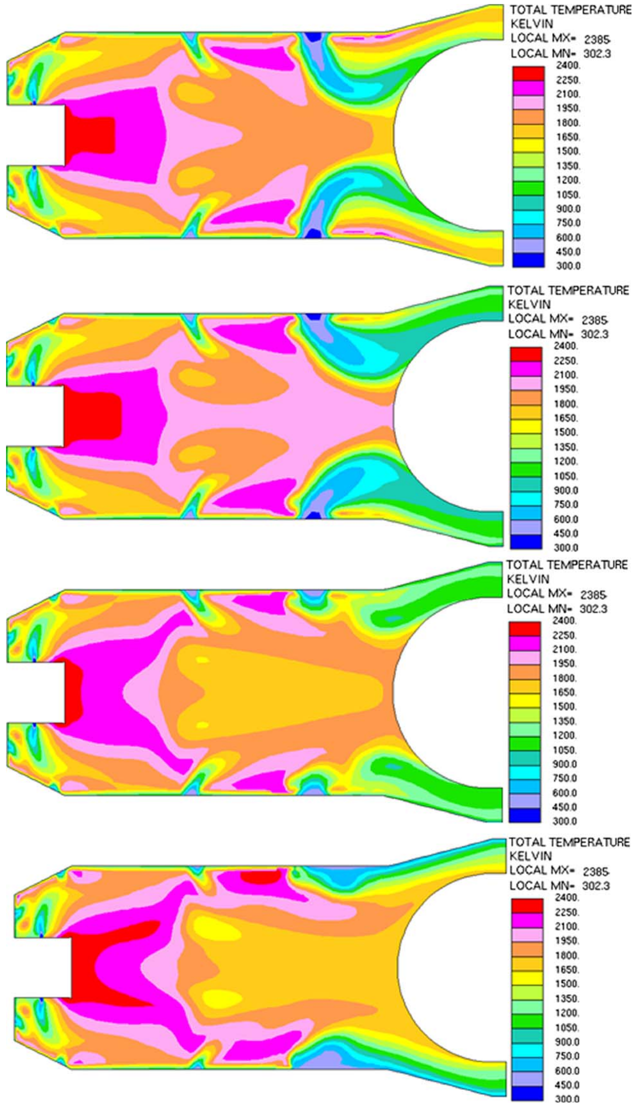

Fig. 8 The temperature profiles on the centerline planes for 0 rpm, 20,000 rpm, 40,000 rpm, and 58,000 rpm (from top to bottom)

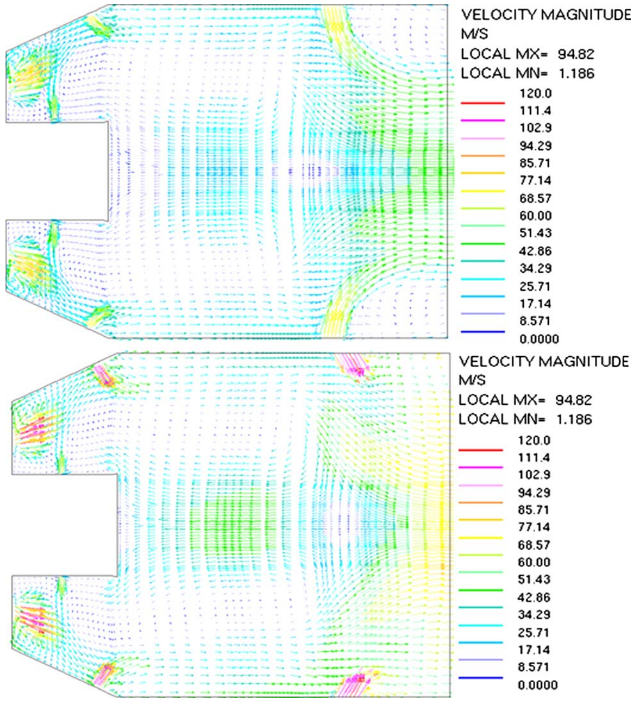

Fig. 9 The velocity profiles on the centerline planes for 0 rpm (top) and 58,000 rpm (bottom)

higher rotating motion. However, near the secondary zone, the axial flow velocity increases tremendously because of the thermal expansion of the hot combustion products, and the velocity is larger when the rotating speed is higher. Even for the case at 0 rpm, the flow acceleration going downstream due to thermal expansion suppresses the second flow recirculation appearing in the cold flow case near the dilution zone.

The corresponding velocity profiles on the radial planes through primary holes are shown in Fig. 10. This can help understand why the flame shape and the flow recirculation change in the primary zone. For the 0 rpm case, we can see that the air flows enter straight into the combustor through the liner holes. The flows then rotate counterclockwise in the core of the combustor in the primary zone due to the designed swirler. As mentioned earlier, the casing rotates in the opposite direction and the driven flows counter the swirling flows inside the combustor. The inlet flows then slant to the right slightly and affect the swirling flows. The swirling in the core region is depressed by the motion; therefore the flows move upstream and push the recirculation aside. The impact is more pronounced downstream at a higher rotating speed. Consequently, the flame shape becomes concave and the flame is

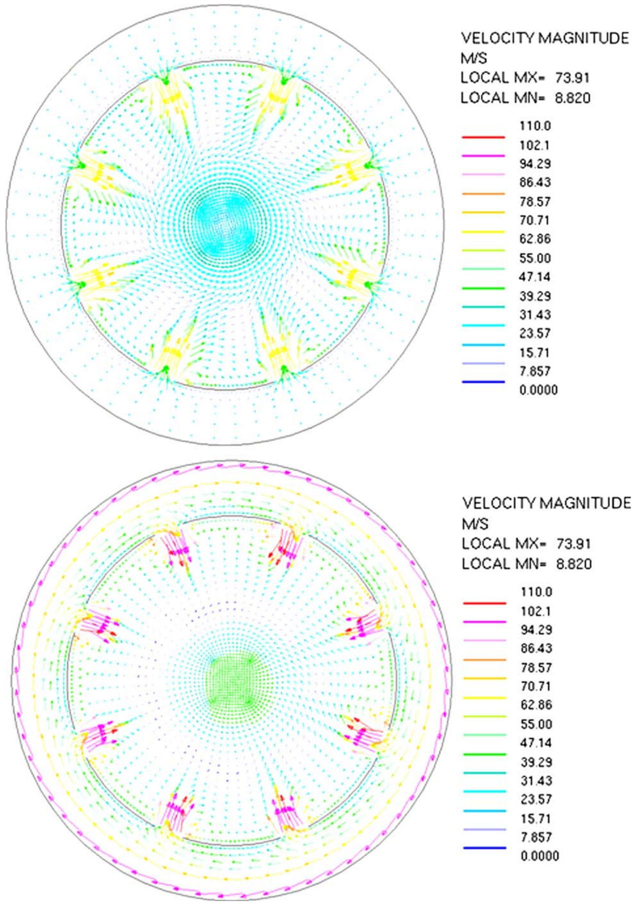

Fig. 10 The velocity profiles on radial planes through the primary holes for 0 rpm (top) and 58,000 rpm (bottom)

Downloaded 02 Jun 2010 to 171.66.16.109. Redistribution subject to ASME license or copyright; see http://www.asme.org/terms/Terms_Use.cfm

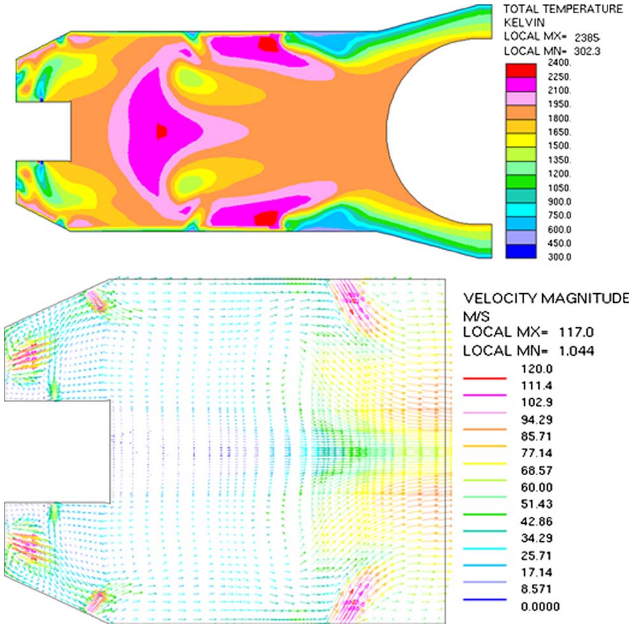

Fig. 11 The temperature and velocity profiles on the centerline plane at −58,000 rpm

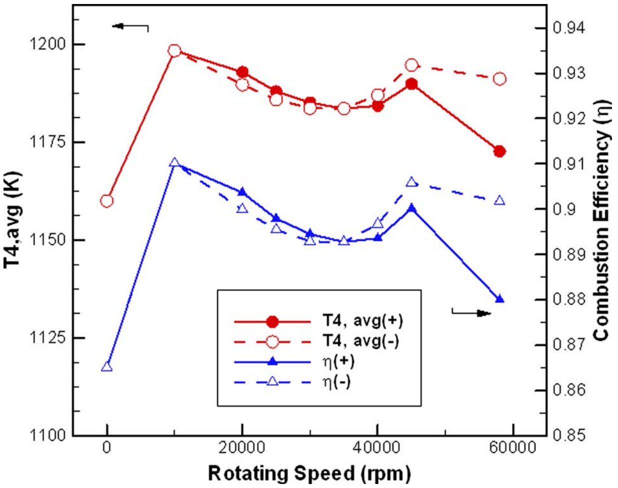

Fig. 12 The exit temperature and combustion efficiency of the combustor

long on the side due to the rotation. At the maximum speed of 58,000 rpm, the rotating flows caused by the casing seem to neutralize the swirling flows inside the combustor.

Apparently, the rotating speed, as well as the rotating direction of the casing, affects the flow structure and flame behavior. Here we make a calculation that the casing rotates in the same direction of the swirling flows caused by the swirler. That is, viewing downstream, the casing rotates counterclockwise as that of the designed swirler. The results of the temperature and flow profiles on the axial plane at −58,000 rpm are shown in Fig. 11 (the rotating speed is shown as a negative value to represent the counterclockwise direction). As the rotation speed increases, the flame seems to become narrower in the core region, and the high temperature zone moves downstream. However, at a maximum rotation speed of −58,000 rpm, the flame stabilizes downstream toward the secondary zone, as shown in the figure. The flow profile at −58,000 rpm indicates that the recirculation in the primary zone is split into two small recirculation flows. The flame moves downstream and stabilizes between these two recirculation zones. Further examination of the radial velocity profile in the plane through the primary holes shows that the rotation in the counterclockwise direction is more severe by the augmentation of the rotating casing.

5.3 Combustor Performance. Generally speaking, the combustion performance parameters of prime importance to the gas turbine are combustion efficiency, stability, and ignition. The stability map, which involves a wide range of equivalence ratios, is not studied in this work. Also, the ignition is not an issue for steady-state simulation. So only the combustion efficiency of the combustor will be discussed. Besides, in order to achieve a satisfactory and consistent distribution of temperature in the efflux gases discharging into the turbines, the most important parameters are the turbine inlet temperature ($T_{4\mathrm{avg}}$) and the pattern factor. In Fig. 12, the $T_{4\mathrm{avg}}$, which is calculated by the mass-flow-weighted mean of all the exit temperatures and the corresponding combustion efficiency at different rotating speeds of the casing, are shown. The positive mark (+) represents the results with the casing rotating clockwise (but in the opposite direction of the swirler), and the negative sign (−) indicates otherwise. We can see that the average exit temperature is around 1160 K when the casing is stationary. As the casing rotates, the average exit temperature jumps to 1198 K at 10,000 rpm, which is close to the target exit temperature of 1200 K. When the rotating speed increases further, the exit temperature drops a little bit, but the values are rather close for different rotating speeds and directions, except for the case of maximum rotating speed in the clockwise direction (+58,000 rpm), which is approximately 15 K lower than the others. The higher average exit temperature means that the combustion efficiency is better, since the efficiency is defined as the ratio of the heat released over the heat available. So the profile of combustion efficiency resembles that of the average exit temperature in Fig. 12, which is expected. The combustion efficiency can reach 90% with a relatively higher exit temperature at 10,000 rpm, but the combustion efficiency is lowest (86.5%) for stationary casing.

However, too high a temperature or too severe a temperature fluctuation at the exit is a problem for turbines. Therefore, the pattern factor, which highlights the maximum exit temperature, is normally defined as $(T_{4\,\max}-T_{4\mathrm{avg}})/(T_{4\mathrm{avg}}-T_{3\mathrm{avg}})$ to indicate the temperature fluctuation or the possible hot spots at the exit. The pattern factor and the pressure drop through the combustor at different rotating speeds are shown in Fig. 13. The pressure drop continually decreases with increasing rotating speeds, but the values (near 11%) are larger than the designed target of 6%. The

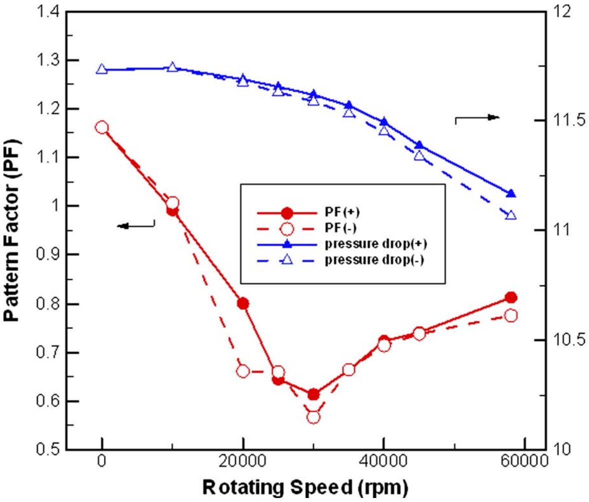

Fig. 13 Pattern factor and pressure drop of the combustor

Downloaded 02 Jun 2010 to 171.66.16.109. Redistribution subject to ASME license or copyright; see http://www.asme.org/terms/Terms_Use.cfm

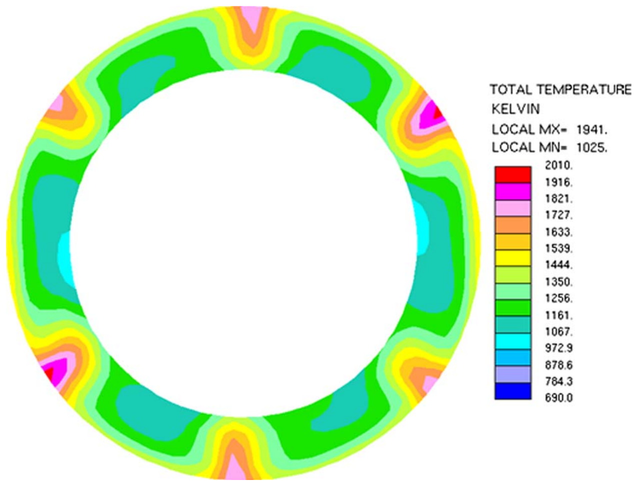

Fig. 14 The exit temperature distribution at 0 rpm

pattern factor is greater than 1 for stationary casing, indicating a severe temperature fluctuation at the combustor exit and a worse condition for the turbine. The temperature distribution at the combustor exit is shown in Fig. 14. Six hot spots are clearly found at several places near the outside circumference, and the temperature can be as high as 1900 K. This demonstrates the serious problem of cooling for the current combustor design with six large dilution holes. However, with the casing rotating, the pattern factor first decreases and then increases as the rotating speed increases. The cooling problem improves, but the values are still too high for a combustor to be satisfactory. The corresponding temperature distribution at the exit for 58,000 rpm is shown in Fig. 15. The higher temperature regions now shift to the inside circumference due to the swirling flows caused by the rotating casing, and the highest temperature drops to 1700 K. The temperature continually decreases from the inner periphery outward.

Two things are noticed in the performance analysis. First, even with the stationary casing like that in the convectional gas turbine combustor, the exit temperature, combustion efficiency, and pressure drop do not reach the target values for the current combustor designs, and the severe temperature fluctuation at the exit could cause damage to the turbine since the pattern factor is high. This indicates that the combustion loading of the compact sized combustor is too heavy, and the cooling strategy in the dilution zone needs to be reconsidered. It is the consequence of trying to minimize the size of the combustor in order to fit into the hollow shaft. Within the limited space, the performance can be improved in the future with a longer combustor, more dilution holes, and film cooling in the dilution zone. Second, with a rotating casing, the combustion efficiency and pattern factor are better than those with a stationary casing, no matter what direction the casing rotates. It shows that the swirling flows circulating outside the liner could help the mixing, combustion, and cooling. However, the effects and benefits are varied at different rotating speeds. From 10,000 rpm to 45,000 rpm, the flames first shrink, become concave shape, and then enlarge again with increasing rotating speeds, as shown in previous flame temperature profiles (Fig. 8). Consequently, the combustion efficiency (and exit temperature) and pattern factor first decrease and then increase with increasing rotating speed, exhibiting a nonmonotonic behavior with a minimum value at a certain rotating speed (near 30,000 rpm). In this study, the direction of the rotation begins to take effect over 50,000 rpm. When the casing rotated clockwise and countered the swirler, the swirling flows were depressed and even reversed that the combustion efficiency dropped. On the other hand, when the casing rotated in the same direction as the designed swirler, the flame stabilized much downstream (in Fig. 11). As a result, the combustion efficiency (and exit temperature) is higher than in the case of the clockwise rotation at the maximum rotation speed of 58,000 rpm.

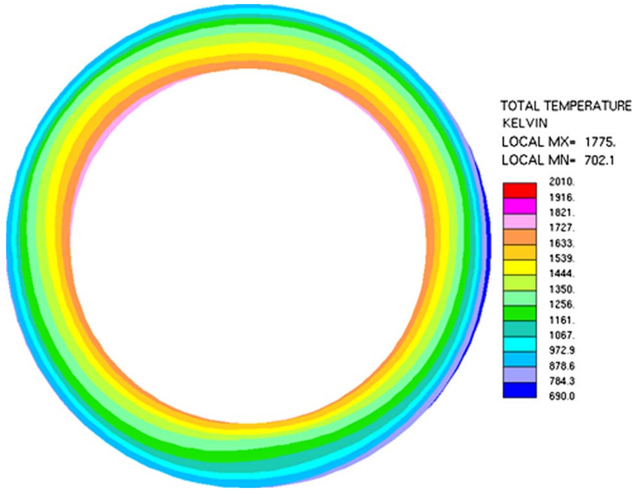

Fig. 15 The exit temperature distribution at 58,000 rpm

6 Conclusions

The can type combustor was modeled and the effects of the rotating casing on combustion performance were studied and characterized qualitatively. Compared with the conventional gas turbine combustor, the centrifugal force caused by the rotation makes the air flows more difficult to enter the liner holes in the primary zone. This alters the air distribution and also the combustion behavior. Not only did the amount of air change, but the inclined angle that the air flows into the combustor made the flow pattern inside the combustor really complex. A shorter but wider recirculation zone and a concave shape were found in the primary zone. At a higher speed of rotation, the influence of the swirling flows outside the combustor can exceed the effect of the designed swirler.

The rotating casing produces a centrifugal force on airflows. The effects of centrifugal acceleration on combustion have been previously studied [11]. The flame speed increases with increasing acceleration up to approximately 800 g. Yonezawa et al. [12] applied the concept to design a swirl-stabilized combustor by using a series of injection ducts inclined both axially and circumferential to drive swirling flows within the combustor liner. It demonstrated that the rate of combustion could be sufficiently enhanced, so that the swirl combustor had a higher efficiency with an extremely short flame. This effect is similar to what we have here. However, the situation in our combustor is more complicated if the outer swirling flows driven by the rotating casing are in the opposite direction of the inner swirling flows induced by a designed swirler. The flow interactions at different rotating speeds plus the combustion phenomenon are both of fundamental and practical interest.

The combustor performance was also analyzed with the modeling results. The exit temperature and the combustion efficiency are increased with the casing rotation. This will benefit the performance of the gas turbine. However, the cooling and possible hot spots for the turbine are the primary concerns, although the pattern factors are decreased compared with the case with a stationary casing. Further design modifications or redesigns for the combustor are needed, especially for the cooling strategy in the dilution zone. Before the invention can be employed in the future, the experimental testing of these combustion concepts is required. The comparisons of the simulation results and the performance measurements of the combustor should be done first for the case with a stationary casing to validate the model quantitatively.

Downloaded 02 Jun 2010 to 171.66.16.109. Redistribution subject to ASME license or copyright; see http://www.asme.org/terms/Terms_Use.cfm

Acknowledgment

This work was funded by NSC of Taiwan under Grant No. NSC95-13231. The authors would like to thank all the excolleagues in ITRI for their valuable suggestions.

References

[1] Little, A. D., 2000, "Opportunity of Micropower and Fuel Cell/Gas Turbine Hybrid Systems in Industrial Applications," DOE Report No. 85X–TA009V.
[2] 2003, U.S. Patent No. US2003/0121270 A1.
[3] 2003, R.O.C. Patent No. 00525708.
[4] Gupta, A. K., Lilley, D. G., and Syred, N., 1984, *Swirl Flows*, Abacus, Cambridge, England.
[5] Lefebvre, A. H., 1999, *Gas Turbine Combustion*, 2nd ed., Taylor & Francis, Philadelphia, PA.
[6] 2003, ITRI Foresight Project Report No. 92-EC-2-A-17-0337.
[7] Kurzke, J., 1995, "Advanced User-Friendly Gas Turbine Performance Calculations on a Personal Computer," ASME Paper No. 95-GT147.
[8] Shih, H. Y., 2003, "An Empirical Based Preliminary Design Code for Gas Turbine Combustor," *13th Annual Conference on Combustion*, Combustion Institute of R.O.C., Taipei.
[9] STAR-CD, Computational Fluid Dynamics Software, CD Adapco Group.
[10] Patankar, S. V., 1980, *Numerical Heat Transfer and Fluid Flow*, Taylor & Francis, London.
[11] Lewis, G. D., 1973, "Centrifugal-Force Effects on Combustion," Proc. Combust. Inst., **14**, pp. 413–419.
[12] Yonezawa, Y., Toh, H., Goto, S., and Obata, M., 1990, "Development of the Jet-Swirl High Loading Combustor," 26th AIAA/SAE/ASME/ASEE Joint Propulsion Conference, Orlando, FL, Paper No. AIAA-90-2451.

Downloaded 02 Jun 2010 to 171.66.16.109. Redistribution subject to ASME license or copyright; see http://www.asme.org/terms/Terms_Use.cfm

Properties, Characteristics, and Combustion Performance of Sasol Fully Synthetic Jet Fuel

Clifford A. Moses
Southwest Research Institute,
San Antonio, TX 78228

Petrus N. J. Roets
Sasol Technology Fuels Research,
Houston, TX 77224

In 1999, as the only inland petroleum refinery in South Africa was reaching capacity, Sasol gained approval of a semisynthetic jet fuel (SSJF) for civil aviation to augment production and meet the growing demand for jet fuel at the airport in Johannesburg. Prior to this, all jet fuel had to be refined from petroleum sources. SSJF consists of up to 50% of an isoparaffinic kerosene produced from coal using Fischer–Tropsch processes. The production of SSJF remains vulnerable to the production capacity of conventional jet fuel, however. To ensure supply, Sasol has proposed producing a fully synthetic jet fuel (FSJF) using synthetic kerosene streams that contain aromatics and satisfy all the property requirements of international specifications for jet fuel. Being fully synthetic, it was necessary to demonstrate that the fuel is "fit-for-purpose" as jet fuel, i.e., behaves like conventional jet fuel in all aspects of storage and handling as well as air worthiness and flight safety. Four sample blends were developed, covering the practical range of production. Extensive tests on chemistry and physical properties and characteristics demonstrated that Sasol FSJF will be typical of conventional jet fuel. As a final demonstration, the engine manufacturers requested a series of engine and combustor tests to evaluate combustion characteristics, emissions, engine durability, and performance. The performance of the synthetic test fuel was typical of conventional jet fuel. This paper identifies the tests and presents the results demonstrating that Sasol fully synthetic jet fuel is fit-for-purpose as jet fuel for civilian aviation. Sasol FSJF is the first fully synthetic jet fuel approved for unrestricted use. [DOI: 10.1115/1.3028234]

1 Introduction

Prior to the introduction of Sasol's semisynthetic jet fuel (SSJF) at Johannesburg International Airport, now named OR Thambo International Airport (ORTIA), in July 1999, all commercial aviation fuel had been derived solely from petroleum sources. The specifications controlling the quality of jet fuel has evolved around the historical characteristics and properties of jet fuels, assuming a relatively constant, or slowly evolving, range of crude resource and refining techniques. The Sasol request for the use of synthetic hydrocarbons derived from coal through their Fischer–Tropsch (FT) processing was a significant departure from experience. Since many of the inherent properties of kerosenes that make them "fit-for-purpose" as jet fuels are not a part of the specification and quality control system, and are rarely measured, the British Aviation Fuels Committee (AFC), which guides the Defense Standard (DEF STAN) 91-91 [1] fuel specification for Jet A-1, developed a new set of guidelines for fuels containing synthetic products as blending stocks. The concept of fit-for-purpose will be discussed later in this paper.

If accepted under DEF STAN 91-91, specific synthetic kerosenes can now be used in civil aviation in concentrations up to 50%, providing the fuel has adequate lubricity and there are at least 8% aromatics in the final blend, all of which must come from the petroleum-derived blending stream [1].

Initially SSJF was defined as a blend of the synthetic isoparaffinic kerosene (IPK) with a Merox-treated kerosene from petroleum [2]. At that time, this Merox-treated kerosene was one of three kerosene streams used by Sasol in the production of conventional Jet A-1 along with a mild hydrotreated kerosene and a hydrocracked kerosene. It was recognized that should something happen to the Merox unit, not only would the production of petroleum-derived Jet A-1 be severely curtailed, but the shortfall could not be made up by SSJF. Sasol then demonstrated the ability to successfully incorporate the hydrotreated and hydrocracked kerosenes into the production of SSJF. The use of these blending streams for semisynthetic jet fuel was approved in DEF STAN 91-91 (Issue 4, dated June 14, 2002).

In 2002, the government of South Africa issued new regulations for low-sulfur diesel fuel. To meet this requirement, Sasol has had to use much of the output from the hydrotreater for diesel fuel so that the hydrotreated product is no longer available for jet fuel. This means that the Merox-treated kerosene is once again the critical stream in producing both conventional Jet A-1 and semisynthetic Jet A-1.

In order to ensure a reliable supply of jet fuel to Johannesburg International Airport (JIA), in the event of a disruption in the Merox process stream, Sasol then proposed to use its refinery at Secunda to provide a second refinery source in the Johannesburg area. This refinery makes synthetic gasoline and diesel fuel, lubricants, and other hydrocarbons from coal via a Fisher–Tropsch process and is the source of the IPK currently used in making semisynthetic jet fuel. While IPK does not contain the necessary aromatics to be considered fit-for-purpose as a jet fuel, the refinery has four other synthetic kerosene streams that do contain single-ring aromatics in the jet fuel boiling range. These are mature refinery streams currently used in the production of gasoline and diesel fuel and will be discussed later in regard to the new fully synthetic jet fuel.

This paper describes the process for demonstrating that the Sasol fully synthetic jet fuel is fit-for-purpose as jet fuel for civil aviation and presents results of both the properties and characteristics of the fuel as well as performance characteristics in engine and combustor tests. As the world's first fully synthetic jet fuel, this approval process will be the basis for the approval of future synthetic jet fuels.

Manuscript received May 7, 2008; final manuscript received May 25, 2008; published online April 16, 2009. Review conducted by Dilip R. Balla. Paper presented at the ASME Turbo Expo 2008: Land, Sea and Air (GT2008), June 9–13, Berlin, Germany.

Copyright © 2009 by ASME

Downloaded 02 Jun 2010 to 171.66.16.109. Redistribution subject to ASME license or copyright; see http://www.asme.org/terms/Terms_Use.cfm

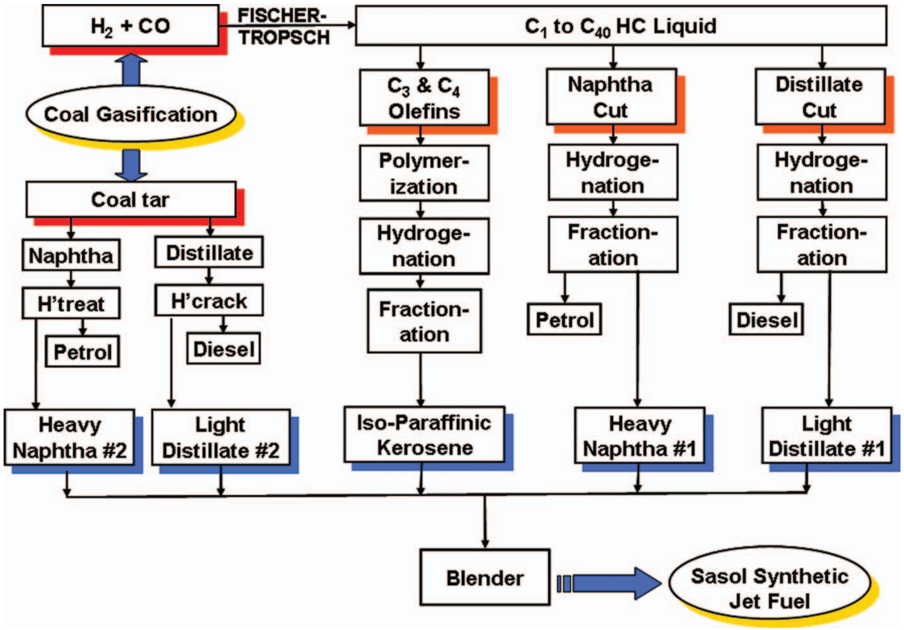

Fig. 1 Production schematic for Sasol fully synthetic jet fuel

2 Fuel Processing

Sasol makes synthetic hydrocarbons from a synthesis gas, i.e., carbon monoxide and hydrogen, using a high-temperature FT process with an iron catalyst. The synthesis gas is derived from the coal resources in South Africa. The Sasol process is unique in that distillate fractions are produced which contain aromatic hydrocarbons. This difference is due to the historical need by Sasol to produce gasoline and diesel fuel from their coal resource. Hence, the catalysts and operating conditions have a different focus than other plants currently online and/or being developed.

Other refiners, e.g., Shell, Exxon-Mobil, Chevron-Texaco, and Syntroleum, have developed, or are in the process of developing, FT plants to make synthetic hydrocarbons from synthesis gas derived from natural gas. The latter are commonly known as "gas-to-liquid" (GTL) fuels. A low-temperature FT process with a cobalt catalyst is used and the resulting distillate fractions are comprised of normal paraffins and isoparaffins. Because they contain no aromatic hydrocarbons, under the current understanding of fit-for-purpose, these fuels would not be appropriate as jet fuels but would be excellent blending streams in the same way that Sasol uses IPK to make semisynthetic jet fuel.

Figure 1 illustrates the production scheme of the Sasol FSJF. In addition to IPK, there are four distillate streams from which kerosene fractions can be distilled. The initial step, of course, is the gasification of coal to synthesis gas, hydrogen (H_2), and carbon monoxide (CO). The synthesis gas is then passed over an iron-based catalyst according to the Fischer–Tropsch process to yield a wide-boiling-range synthetic crude oil.

The IPK stream in the middle of the schematic is the kerosene that is used for making semisynthetic jet fuel. It is the dominant stream in making fully synthetic jet fuel. The other streams are either the heavier fractions of a naphtha stream normally used for making gasoline or the lighter fractions of a distillate stream normally used for making diesel fuel. One set of each comes from the FT crude oil on the right or from the by-product of the coal gasification process shown on the left of the diagram. These are all mature streams used for making gasoline, diesel fuel, or illuminating kerosene.

Four sample blends of synthetic jet fuel were blended to emphasize different combinations of the synthetic kerosenes and to cover a practical range of aromatics from about 8% to 17%. (Note: Only four of the five blend streams were used as the light naphtha 2 was not available at the time.) The blend ratios and aromatic analyses are summarized in Table 1; the petroleum-derived Jet A-1 from Sasol's Natref refinery is included for comparison. Figure 2 presents the results of an analysis by two-dimensional gas chromatography (2D GC). These figures demonstrate that the synthetic fuels are made up of a large number of hydrocarbons that are well-distributed across the jet-fuel boiling range. They are not made by simply blending together a few pure compounds or solvents.

These four fuels demonstrate that there is considerable flexibility in using the four synthetic kerosenes to produce candidate jet fuels. All four of these fuels were certified by Sasol as meeting the property requirements of Table 1 in DEF STAN 91-91 for Jet A-1 fuel.

3 Concept of Fit-For-Purpose

Fuel specifications are merely controls on fuel quality for the purpose of purchase. They do not define all the properties and characteristics that are important for the design and function of aircraft, engine, and ground-handling fuel systems. Many of these

Table 1 Sample blends of Sasol synthetic kerosene

Synthetic kerosene stream	FSJF Blend 1	FSJF Blend 2	FSJF Blend 3	FSJF Blend 4	Natref Jet A-1
Heavy naphtha 1	15	15	13	59	—
Light distillate 1	18	—	10	—	—
Light distillate 2	—	30	20	36	—
Isoparaffinic kerosene	67	55	57	5	—
Chemistry	**FSJF Blend 1**	**FSJF Blend 2**	**FSJF Blend 3**	**FSJF Blend 4**	**Natref Jet A-1**
Aromatics, v %	7.2	13.6	12.5	16.9	22.9
Saturates, v %	92.8	86.4	8705	83.1	77.1

Downloaded 02 Jun 2010 to 171.66.16.109. Redistribution subject to ASME license or copyright; see http://www.asme.org/terms/Terms_Use.cfm

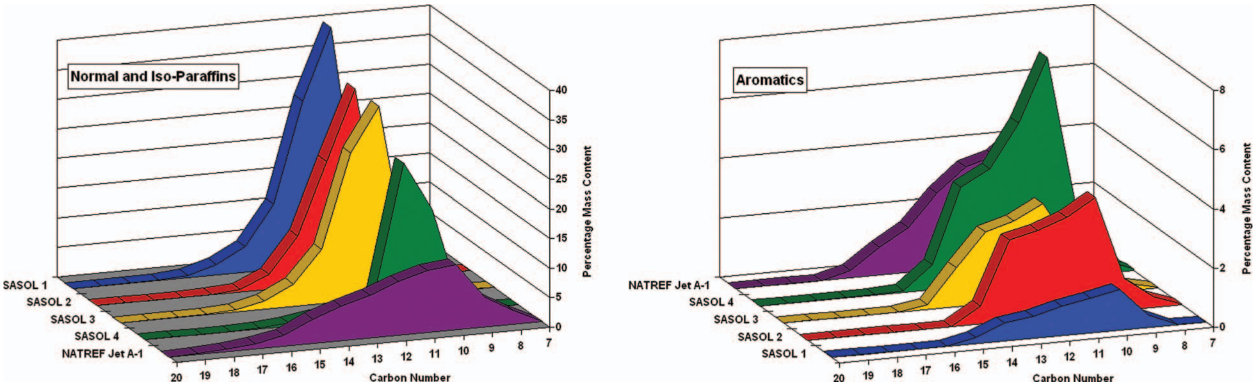

Fig. 2 Distribution of saturates and aromatics in Sasol synthetic kerosene blends

properties and characteristics are not a part of the specification and quality control system and are, therefore, rarely measured.

The *issues and concerns* used in this project were based on the criteria defined in DEF STAN 91-91: Annex D entitled "Additional Requirements Applicable to Fuels Containing Synthetic Compounds." These requirements were first defined by the AFC in the UK to ensure that SSJF using the synthetic IPK was fit-for-purpose. This Committee includes engine and airframe manufacturers, refiners, and other stakeholders in the use of aviation fuels. Table 2 provides a general overview of these critical issues. All of the elements except the chemistry apply to the final fuel. The results of this evaluation on the four blends are presented in Sec. 4.

Table 2 General areas of issues and concerns

- Chemistry of synthetic components
  - Hydrocarbons
  - Organics
  - Metals
- Bulk physical properties versus temperature
- Boiling point distribution
- Lubricity
- Water separation
- Compatibility
  - Fuels
  - Additives
  - Materials
- Stability
  - Thermal
  - Storage

4 Properties and Characteristics of Sasol FSJF

Three of the most important characteristics to engine manufacturers are the thermal stability, lubricity, and material compatibility. The results of these evaluations are presented along with representative bulk physical properties.

4.1 Thermal Stability. The thermal stability of jet fuel is rated by the color of the deposit after the fuel has passed over a heated tube for 2.5 h using the Jet Fuel Thermal Oxidation Test (JFTOT) according to ASTM D 3241 [3]. The standard tube temperature for this test is 260°C (500°F). To pass the test, the deposit must have a color rating less than 3. (Darker deposits have a higher number.) The Sasol synthetic blends not only passed the test at the standard temperature but also demonstrated superior thermal stability by easily passing the test at 300°C (572°F), a significantly higher temperature.

The possibility that the synthetic fuels might generate deposits that have a different color than conventional fuels was considered. As a precaution, the deposit thickness was measured using the Phillips Analytical Fuel Qualifier, formerly known as the Ellipsometric Tube Analyzer (ETA). Figures 3 and 4 compare deposit maps for one of the Sasol blends and a Code 3 deposit from a petroleum-derived fuel. The deposit from the Sasol fuel was uni-

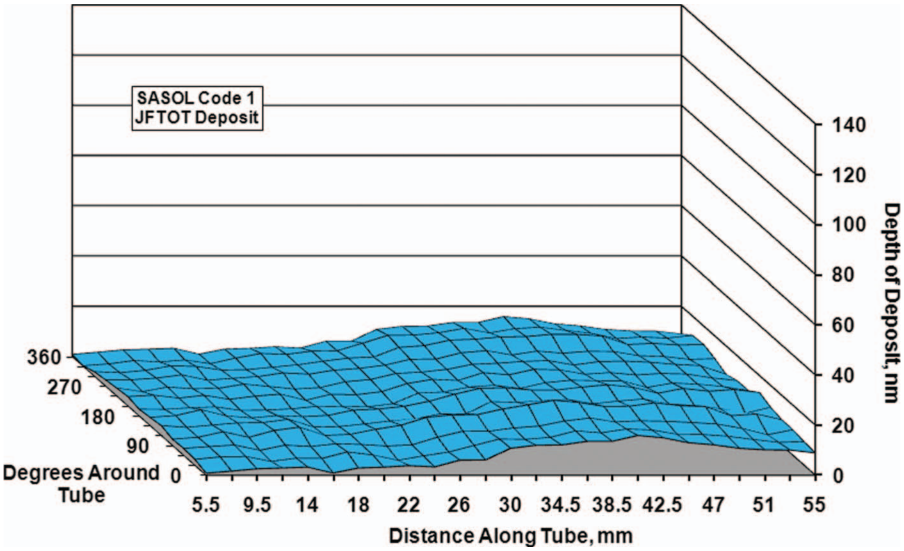

Fig. 3 JFTOT deposit map for Sasol FSJF with Code 1 deposit

Downloaded 02 Jun 2010 to 171.66.16.109. Redistribution subject to ASME license or copyright; see http://www.asme.org/terms/Terms_Use.cfm

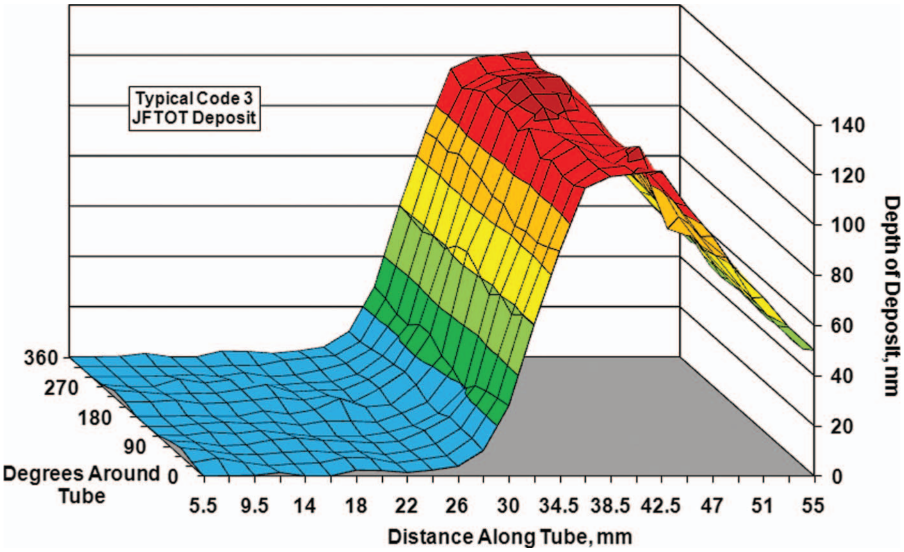

Fig. 4 JFTOT deposit map for conventional fuel with Code 3 deposit

form around the tube and had a maximum thickness just under 20 nm. This is consistent with the thickness of Code 1 deposits generated by conventional fuels. The Code 3 deposit was also very uniform around the tube and had a maximum thickness of about 120 nm. Experience with conventional fuels shows that Code 3 deposits start around 100 nm. Therefore, it was concluded that the JFTOT deposits from Sasol FSJF will be just like those of conventional fuels, and the current rating system is valid.

4.2 Evaluation of Elastomer Compatibility. Elastomer compatibility is considered one of the key areas for demonstrating that any alternative fuel is fit-for-purpose because the chemistry is potentially somewhat different and could affect the response and durability of some elastomeric compounds that are sensitive to fuel chemistry.

4.2.1 Selection of Test Materials. There are three basic materials used in fabricating sealing items, such as O-rings, gaskets, diaphragms, bladders, and hose linings, used in aviation fuel systems:

1. nitrile (Buna-N)
2. fluorocarbon (Viton)
3. fluorosilicone

Of these three materials, only nitrile materials exhibit any significant sensitivity to fuel chemistry. This is due to the solvent activity of aromatics on the acrilonitrile plasticizer that is used in this class of materials. The amount of acrilonitrile used in the formulation is a balance between fuel sensitivity and low-temperature capability. One of the major reasons aromatics are limited to 25 vol % in jet fuel is to prevent the fuel from being too strong a solvent on nitrile elastomers.

On the other hand, some consistent level of aromatics is thought to be necessary in jet fuel. Nitrile elastomers can swell and shrink as the aromatic content changes. For this reason a minimum aromatic level of 8 vol % was placed on semisynthetic jet fuel in DEF STAN 91-91. The aviation community does not agree on whether a minimum aromatic level is required or what it should be; there is a lack of data in this area. The choice of 8% was considered a conservative safeguard.

It was shown in Fig. 2 that the aromatics in FSJF blends are in the jet-fuel boiling range. There really is limited variability in the molecular structures available in this range. Thus, the real issue is to demonstrate that the Sasol synthetic fuels behave like petroleum-derived fuels when in contact with these three elastomer types.

4.2.2 Elastomer Property Tests for Fuel Compatibility. Three properties were tested as indicators or measures of fuel effects. Reference [4] discusses the relevance of these tests to fuel resistance.

1. Volume change: Excessive volume shrinkage can cause leakage; swell is usually accompanied by a decrease in hardness. For static O-ring applications, a 50% increase in volume can usually be tolerated. For dynamic applications, 15–20% is considered a reasonable maximum.
2. Hardness: Hardness relates to the ability of the material to flow, and the desired level varies with the application. In static applications, a softer material fills in the microgrooves more easily to generate a seal; on the other hand, the material can extrude out of the cavity more easily. In dynamic applications, a harder compound may allow some leakage but will reduce sliding friction; softer compounds may tend to abrade, wear, and extrude. It is important that contact with fuel does not alter the hardness too much.
3. Tensile strength: This property is primarily used for production quality control; it also is useful as an indicator of deterioration after fuel contact.

These tests were conducted on four new O-rings of each material according to the appropriate ASTM standards following a 14-day soak in the test fuel at $23.9 \pm 2.8^\circ\mathrm{C}$ ($75 \pm 5^\circ\mathrm{F}$). The results reported are the averages for the four samples.

4.2.3 Test Results. In the graphical presentations of the results, the effects of the synthetic fuels are compared to that of the petroleum-derived Jet A-1 from Sasol's Natref refinery; the results are ordered according to increasing aromatic content in the fuel.

Figure 5 compares the fuel effects on the swell of the O-rings expressed as the percentage change in volume according to ASTM D 471 [5]. As expected, the fluorosilicone and fluorocarbon O-rings were relatively insensitive to the various fuels as the differences are only a percent or so and of the same order of magnitude as the Natref Jet A-1. The nitrile tests, however, showed the expected increase in volume that was directly related to the aro-

Downloaded 02 Jun 2010 to 171.66.16.109. Redistribution subject to ASME license or copyright; see http://www.asme.org/terms/Terms_Use.cfm

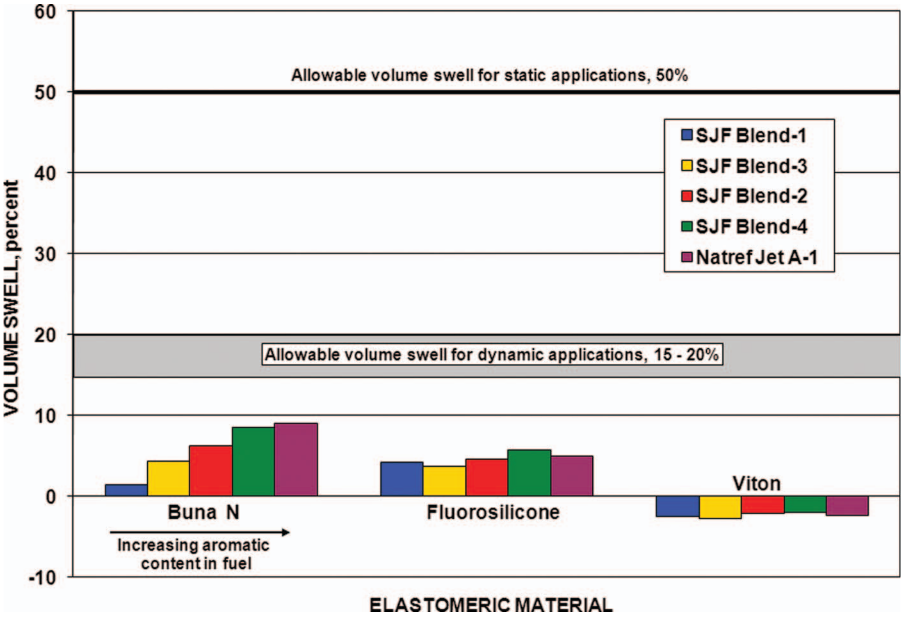

Fig. 5 Effect of Sasol synthetic jet fuel on swell of common fuel-system elastomers

matic content. Also shown in this graph are the limits of allowable swell for static and dynamic applications [4]. These results show that the swell produced by the Sasol synthetic fuels is both acceptable and typical.

Figure 6 presents data on the fuel effects on the hardness of the elastomers according to ASTM D 2240 [6]. It is important to note that the hardness rating is only good to ±5 durometer numbers. The hardness ratings of the fluorosilicone and fluorocarbon O-rings were essentially unaffected by fuel soaking. The nitrile O-rings were slightly softer following fuel soaking than their original values in air; although small, the effect was directly related to increasing aromatic content. The effects of the Sasol synthetic fuels are no different than the effect of the Natref fuel.

Tensile strength is important in dynamic seals where a minimum tensile strength of 6900 kPa (1000 psi) is considered necessary [4]. Tensile strength was determined according to ASTM D 412 [7]. Figure 7 shows that all of the nitrile and fluorocarbon elastomers had tensile strengths well over this minimum before and after the soakings in the synthetic fuels; fluorosilicone elastomers are not used for dynamic seals, so this minimum does not apply. After the soakings in the synthetic fuels, the tensile strength of the fluorosilicone elastomers are essentially the same as the Natref Jet A-1. The nitrile elastomers exhibited a decrease in ten-

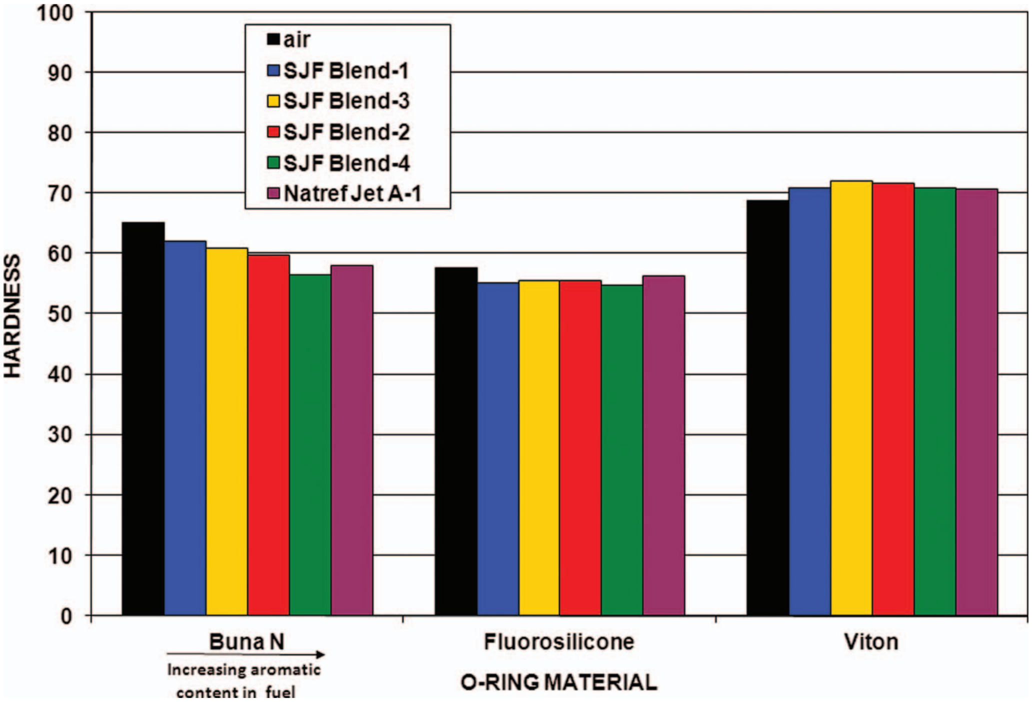

Fig. 6 Effect of Sasol synthetic jet fuel on hardness of common fuel-system elastomers

Downloaded 02 Jun 2010 to 171.66.16.109. Redistribution subject to ASME license or copyright; see http://www.asme.org/terms/Terms_Use.cfm

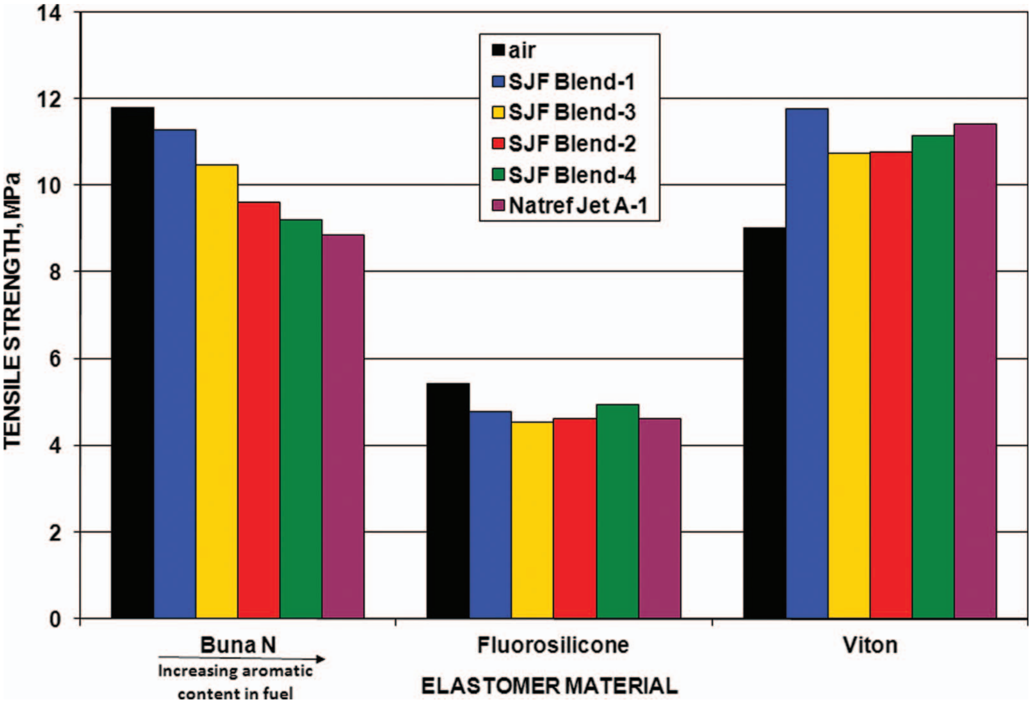

Fig. 7 Effect of Sasol synthetic jet fuel on the tensile strength of common fuel-system elastomers

sile strength with increasing aromatic content that was consistent with the Natref fuel.

While there were some minor changes in these properties with the fluorocarbon (Viton) and fluorosilicone materials, the response to the synthetic fuels was essentially the same as the response for the petroleum-derived Jet A-1 from the Natref refinery.

As expected, the nitrile (Buna-N) elastomers were more fuel sensitive then the other two materials, and the changes were in direct proportion to the aromatic content of the fuel. The variation in swell with aromatic content was shown to be in line with previous data. Limited tests with used nitrile O-rings showed the same sensitivity to the aromatic content as the new O-rings. Swell with both new and used nitrile O-rings was well within the design guidelines for both static and dynamic applications.

4.3 Lubricity. It is important to demonstrate that the Sasol synthetic fuels either have good inherent lubricity or respond to lubricity improving additives (LIA). This issue comes from a general concern for lubricity in fuels of low-sulfur and aromatic content. Severely hydrotreated fuels and synthetic fuels may not have the trace organic species that provide lubricity. In the case of Sasol's semisynthetic jet fuel, the lubricity is derived from the conventional Natref Jet A-1.

Lubricity for jet fuel is evaluated with the Ball-on-Cylinder Lubricity Evaluator (BOCLE) in accordance with ASTM D 5001 [8]. A wear scan is generated on the ball during the test. A wear scar diameter of less than 0.85 mm is required [1].

Figure 8 compares the BOCLE lubricity ratings of the four synthetic blends with that of the Natref Jet A-1. The lubricity ratings of all four synthetic blends are significantly less than the limit of 0.85 mm. This suggests that there are some natural lubricity improvers in one or more of the synthetic kerosene streams and that lubricity additives may not be necessary with the Sasol synthetic jet fuels. It was shown, however, that the FSJF blends respond to lubricity additives, and they could be used if necessary.

4.4 Bulk Physical Properties. The following fuel properties are important to aircraft/engine design:

- viscosity
- density
- bulk modulus
- specific heat
- thermal conductivity

Viscosity and density are part of the fuel specification, but only at a single temperature as a control. For design considerations, it is necessary to consider the variations in these properties with temperature or pressure, as appropriate. Data are presented and compared with data from Refs. [9,10], where data exist.

4.4.1 Viscosity Versus Temperature. The most important aspect of viscosity is that it is the fuel property that controls atomization; density and surface tension are also important, but they do not vary with temperature as much as viscosity does. Viscosity is also used in calculating pressure drops when designing fuel systems.

Turbine engines are required to cold start on fuels with viscosity of 12 cS. Therefore, the fuel viscosity must be less than 12 cS as the fuel temperature approaches the freezing point, which is −40°C for Jet A and −47°C for Jet A-1. It is difficult to measure the viscosity close to the freezing point, so it is measured at −20°C with a maximum of 8 cS. It was therefore necessary to demonstrate that the viscosity-temperature function of the Sasol fuels was the same as that of conventional fuel to verify the sufficiency of the single viscosity data point in the specification.

The viscosity of the synthetic blends was measured at five temperatures from −40°C to 100°C. These results are graphed on the standard ASTM viscosity-temperature chart in Fig. 9. For reference, the characteristics for the fuels with the highest and lowest viscosities from Ref. [10] are included along with the characteristics for a "typical Jet A-1" from Ref. [9]. The viscosity-temperature characteristics of the synthetic blends are seen to be very linear on this transformed graph, verifying that the viscosity characteristics of the Sasol synthetic jet fuels are normal regardless of the actual blending ratios of the synthetic streams.

It is concluded that the Sasol synthetic fuels have viscosity characteristics that are identical to conventional fuels. As such, the

Downloaded 02 Jun 2010 to 171.66.16.109. Redistribution subject to ASME license or copyright; see http://www.asme.org/terms/Terms_Use.cfm

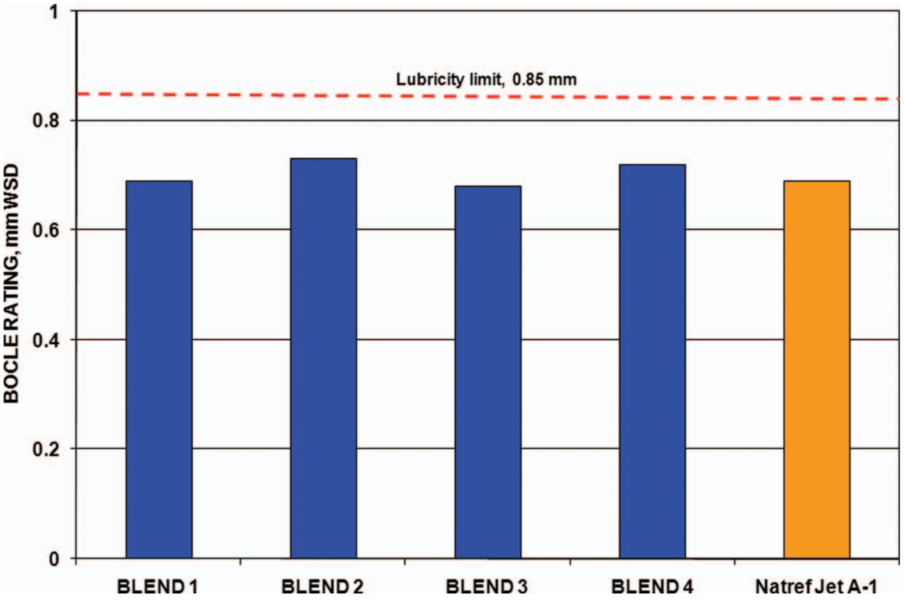

Fig. 8 Lubricity of Sasol FSJF blends

use of these fuels will not cause any deterioration in ignition or relight limits and will not increase pumping losses in the fuel system.

4.4.2 Density Versus Temperature. Density is important to the design and operations of aircraft because it can determine loaded fuel weight and range. Density is also used in flow calculations, tank gauging, fuel metering devices, and structural design of fuel tanks.

As discussed earlier, most FT jet fuels are comprised of normal and isoparaffins with no aromatics. The lack of aromatics results

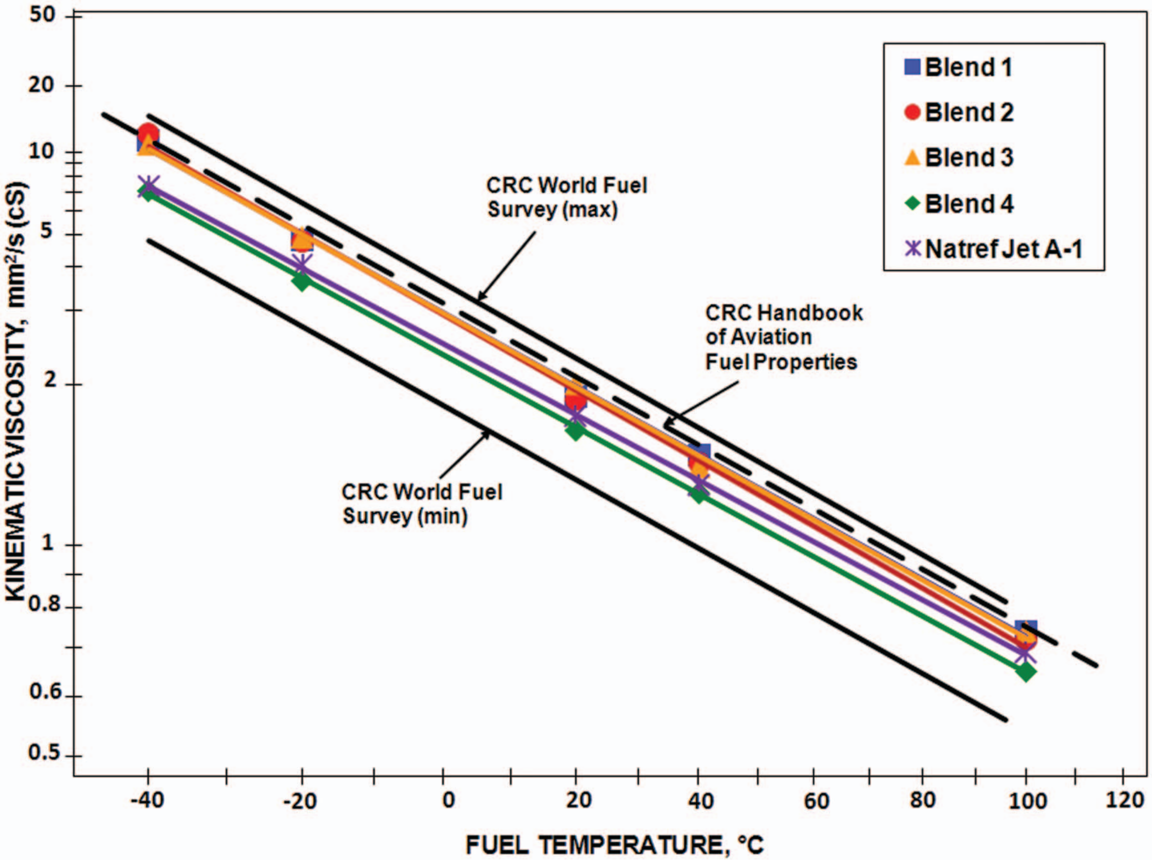

Fig. 9 Viscosity characteristics of Sasol FSJF blends

Downloaded 02 Jun 2010 to 171.66.16.109. Redistribution subject to ASME license or copyright; see http://www.asme.org/terms/Terms_Use.cfm

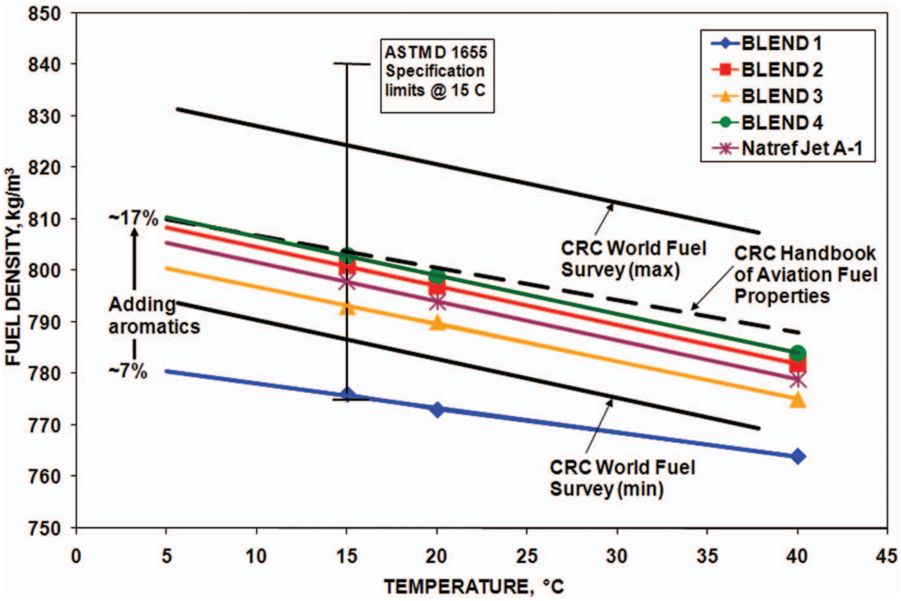

Fig. 10 Density characteristics of Sasol FSJF blends

in a fuel that cannot meet the minimum specification requirement for a density of 775 kg/m^3 at 15°C. This results in a lower energy density of the fuel as well. It is also important that the density-temperature function be typical for operations throughout the flight.

Figure 10 compares the density-temperature data of the FSJF blends with that of Ref. [10]. The test fuels are all seen to lie within the fuel specification limits; however, Blend 1 is right at the minimum. The other three blends fall well within the results of the Boeing survey. These results also demonstrate that increasing the aromatic content increases the fuel density.

Table 3 Summary of energy density and specific energy

Fuel	Energy density (MJ/m^3)	Specific energy (MJ/kg)
CRC WFS (avg)[a]	34,736	43.26
Blend 1	33,865	43.81
Blend 2	34,558	43.36
Blend 3	34,373	43.51
Blend 4	34,437	43.10
NATREF Jet A-1	34,317	43.22

[a] CRC World Fuel Survey.

Although the energy density, MJ/m^3, is lower for the blends, the specific energy, MJ/kg, is virtually unchanged. These are summarized in Table 3.

4.4.3 Bulk Modulus Versus Pressure. In many modern aircraft engines, the fuel is used to activate hydraulic equipment. In order to make the system responsive, it is desirable to have a fuel that is difficult to compress. Such a fluid will have a high bulk modulus.

Currently there is no standardized method for determining bulk modulus for jet fuels. The test fuels were submitted to the Phoenix Laboratories, Inc. (Chicago, IL) for the determination of bulk modulus using a procedure that is under consideration as a new ASTM standard. The results are presented in Fig. 11. The bulk modulus characteristics of the Sasol synthetic fuels are essentially identical to each other and to that of the Natref Jet A-1. These data

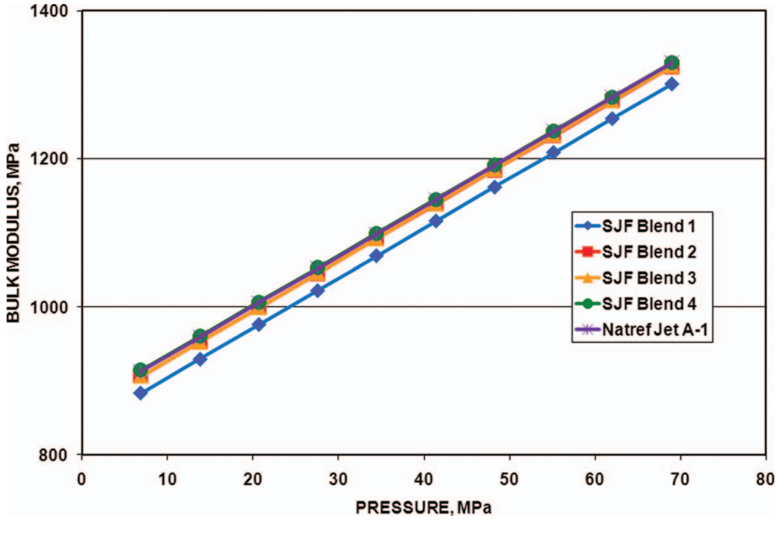

Fig. 11 Bulk modulus of Sasol FSJF blends

Downloaded 02 Jun 2010 to 171.66.16.109. Redistribution subject to ASME license or copyright; see http://www.asme.org/terms/Terms_Use.cfm

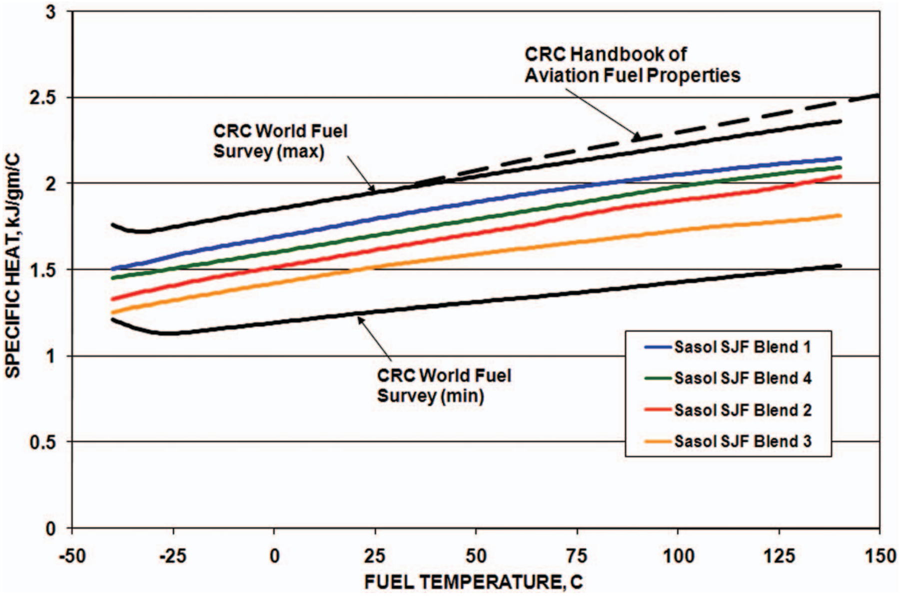

Fig. 12 Specific heat characteristics of Sasol FSJF blends

demonstrate that the bulk modulus and, therefore, the compressibility characteristics of the Sasol synthetic jet fuel are the same as those of conventional jet fuel.

4.4.4 Specific Heat Versus Temperature. Specific heat is especially important in the design of modern engines as the fuel is increasingly used as a coolant or heat sink.. The specific heats of the five Sasol test fuels were determined using ASTM E 1269 [11] over the temperature range of −40°C to 100°C. The results are compared in Fig. 12 with data from Refs. [9,10].

The Sasol synthetic fuels all have the same temperature sensitivity as the other fuels and lie totally within the data band of the world survey. The data from Ref. [9] is significantly higher than most fuels. If the values from Ref. [9] were used in the design of a fuel-cooled heat exchanger, the result would be higher fuel temperatures than predicted; however, this is the fault of Ref. [9] not a shortcoming of the Sasol fuels, and will be true for all jet fuels. The thermal conductivity data showed similar results, and it was concluded that the Sasol FSJF will have thermodynamic and transport properties that are typical of conventional jet fuels.

4.5 Summary of Fit-for-Purpose Tests. The four sample blends of synthetic jet fuel prepared by Sasol had excellent qualities as jet fuels and were very similar in nature to the petroleum-derived Jet A-1 from Sasol's Natref refinery. The fuels were blended from four mature synthetic distillate streams in the jet-fuel boiling range; they were not streams from pilot plants. The data demonstrated that Sasol synthetic jet fuels will have physical and chemical properties and characteristics that are indistinguishable from conventional fuels refined from petroleum crude oils.

Since the thermodynamic and transport properties of the samples were typical of conventional fuels to the extent that data were available, it was concluded that parameters that provide guidance on fluid mechanics and heat transfer regimes, e.g., Reynold's number, Prandtl number, and Weber number, will also be typical of conventional fuels. These conclusions are independent of the blending ratio of the four synthetic distillates.

5 Engine and Combustor Performance Testing

5.1 Overview. Although satisfied with the demonstrated properties and characteristics of the Sasol synthetic kerosenes, the engine original equipment manufacturers (OEMs) requested the following component tests to demonstrate that Sasol synthetic jet fuel would have no adverse effect on engine performance and operation as an essential precondition of approval and certification of Sasol synthetic jet fuel under DEF STAN 91-91:

- engine endurance
- low-temperature atomization
- cold-day ignition and altitude relight
- exhaust emissions
- lean blowout (LBO)

These tests were mutually defined by the engine OEMs and conducted at their facilities as appropriate. Individual test reports [12–15] were written by the performing organization for review by all the OEMs as part of the approval process. A single fuel was produced by Sasol and was provided for all of the tests. The results presented here are normalized for proprietary reasons to the engine companies.

5.2 Test Fuel. The volume requirements for the requested tests totaled 1000 m^3 (250,000 gal). As the refinery would not be reconfigured to make jet fuel until the approval is granted, it was necessary to use streams that were available in suitable quantities. Also it was necessary to use the existing configuration of the distillation columns rather than optimize them for kerosene production.

The test fuel was a blend of approximately 70% IPK and 30% heavy naphtha 2, as indicated in Fig. 1. The two light distillate streams were not available for use in making the test fuel as the entire production was needed for making low-sulfur diesel. The properties and characteristics most important to the engine and combustor tests are summarized in Table 4.

The boiling point distribution is shown in Fig. 13. It was significantly "flatter" than the petroleum-derived Jet A-1 that Sasol produces at the Natref refinery. This is primarily due to the lack of heavier fractions that would have come from the light distillate if it had been available. This will have implications in the results of the ignition and altitude relight test (Sec. 5.6). It must be noted, however, that the boiling point distribution was within the range of commercial jet fuels on the market today.

5.3 Engine Endurance Test

5.3.1 Objective. The engine endurance test was to evaluate the effect of the Sasol synthetic jet fuel on the overall performance

Downloaded 02 Jun 2010 to 171.66.16.109. Redistribution subject to ASME license or copyright; see http://www.asme.org/terms/Terms_Use.cfm

Table 4 Selected properties and characteristics of the test fuel

Fuel property	Specification limits	Value
Aromatics, vol %	8.0–25.0	10.9
Sulfur, wt %	0.3 max	<0.01
Smoke point, mm	25.0 min	28
Viscosity, cS	8.0 max	4.09
Density, kg/m^3	771.0–836.0	781.2
Freezing point, °C	–47.0 max	–55.0
Flash point, °C	38.0 min	51.0
Heat of combustion, kJ/kg	42.8	43.7

and operation of a commercial jet engine [12]. The test was conducted at the engine overhaul facilities of South African Airways (SAA) at OR Thambo International Airport in Johannesburg, South Africa using a completely refurbished Pratt & Whitney (P&W, East Hartford, CT) JT-9D engine. The test was conducted by SAA personnel and monitored by a field representative of Pratt & Whitney (P&W) and the local regulating authority. The engine selection was agreed upon by the engine OEMs as representing a high-pressure-ratio fan engine with an annular combustor [12]. Conducting the tests at the SAA facilities in Johannesburg significantly reduced the logistic problems of transporting 950 m^3 (250,000 gal) of fuel to the test site.

5.3.2 Test Description. The test was developed by the engine OEMs. The test was cyclic, consisting of 500 modified landing and takeoff cycles as illustrated in Fig. 14 with shutdown and ignition events every 25 cycles. Prior to the endurance test, a performance test was run on the test engine using a petroleum-derived Jet A-1 fuel. This was followed by a performance test using Sasol FSJF. Following the endurance test, performance tests were repeated using the same two fuels to determine if any degradation of performance as a result of the cyclic test on the synthetic fuel. At intervals during the test, videos of the hot section were made using a boroscope; special attention was given to the fuel nozzles and air swirlers. There was also a periodic removal of the fuel control to inspection selected O-ring seals.

5.3.3 Results. The performance tests prior to the cyclic test showed no differences between the two fuels; furthermore, the post-cyclic-test performance evaluations showed no degradation in performance as a result of the test on the Sasol fuel. The engine performed satisfactorily during the cyclic test. The boroscope inspections showed no unusual changes in the fuel nozzles, swirlers, and hot-section components, and there was no deterioration of the O-rings inspected from the fuel control. The test results were reviewed by P&W chief engineers, discipline chiefs, and performance system analysis, combustion, and turbine groups. The consensus was that there was no discernible difference between the baseline petroleum Jet A-1 and Sasol 100% synthetic Jet A-1.

5.4 Low-Temperature Atomization Tests

5.4.1 General Comments. Onboard auxiliary power units (APUs) are required to start immediately if there is an in-flight shutdown of a main engine. The environment during APU altitude starting is different from that of the main engines, however, be-

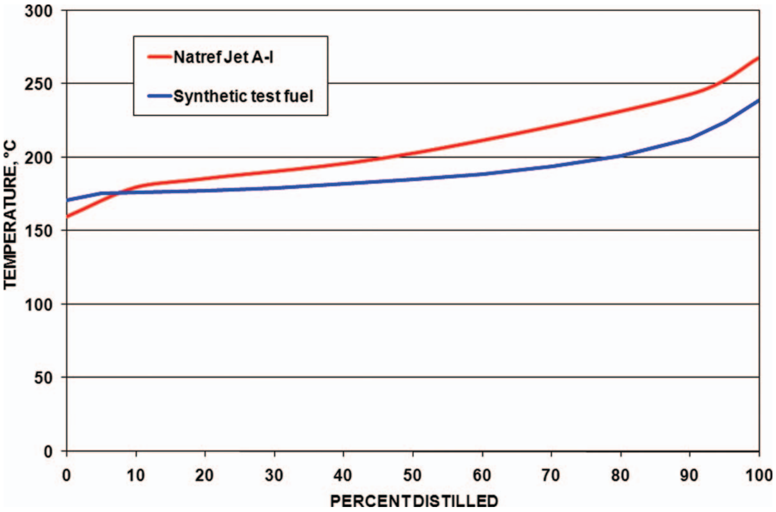

Fig. 13 Boiling point distribution of test fuel

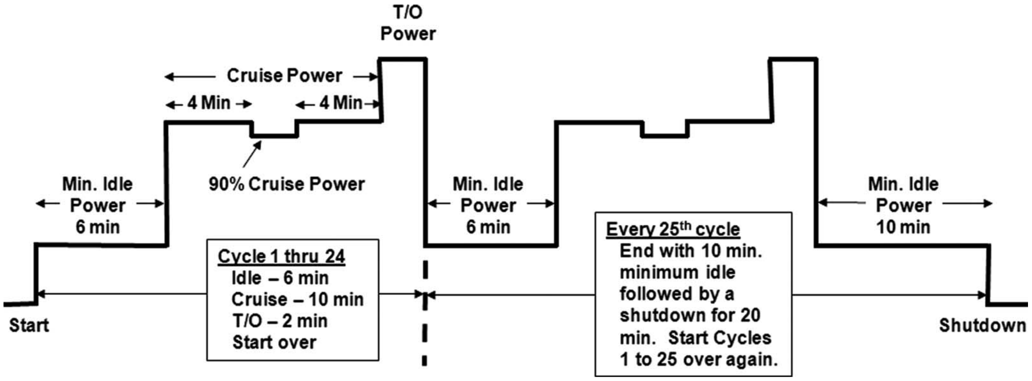

Cycle 1 thru 24
Idle – 6 min
Cruise – 10 min
T/O – 2 min
Start over

Every 25th cycle
End with 10 min. minimum idle followed by a shutdown for 20 min. Start Cycles 1 to 25 over again.

Fig. 14 Test cycle for JT-9D performance/endurance test of SSJF

Downloaded 02 Jun 2010 to 171.66.16.109. Redistribution subject to ASME license or copyright; see http://www.asme.org/terms/Terms_Use.cfm

Table 5 Physical properties of test fluids for atomization

Test fuel	Specific gravity At 25°C	Specific gravity At test temp.[a]	Viscosity At 25°C	Viscosity Test temp.[a]	Surface tension At 25°C	Surface tension At test temp.[a]
7024-II	0.766	0.758	1.17	1.15	22.3	22.1
Viscor	0.878	0.878	12.2	12.2	24.7	24.7
Jet A	0.816	0.858	1.72	10.0	27.1	29.5
FSJF	0.782	0.824	1.56	7.9	25.0	27.4

[a] The test temperature for FSJF and Jet A was −40°C; the temperature for Viscor and 1074-II was ambient.

cause the APU and its fuel supply are cold soaked. Therefore, it was considered necessary to demonstrate that the Sasol fuel would not affect low-temperature starting characteristics of APU [13]. This demonstration was conducted by Honeywell Aerospace (Phoenix, AZ) , a major manufacturer of APUs, using atomizer bench tests with cold Sasol synthetic fuel to verify if the fuel would have no adverse effect on atomization or spray quality, and by inference, on low-temperature ignition. Pressure atomizers typical of those used on APUs and an air blast atomizer typical of those used on small propulsion engines were selected for testing. Atomizer performance parameters, including flow number and spray characteristics, were measured over a range of conditions.

5.4.2 *Test Atomizers*. Atomizer A had a low flow number (FN) typical of the primary atomizers used on newer transport and military APUs. Atomizer B was a larger FN atomizer typical of primary atomizers used on older commercial and military transport APUs and smaller APUs used on a regional aircraft. Atomizer C was a small thin-sheet-type air blast atomizer, typical of those used on small propulsion engines.

5.4.3 *Test Fuels/Fluids*. Four fluids were used for the atomization tests:

- Jet A (ASTM D 1655)
- Sasol FSJF (DEF STAN 91-91)
- standard calibrating fluid (MIL-PRF-7024 Type II)
- a 12 cS calibrating fluid (Viscor)

The last fluid is a special test fluid that allows Honeywell to evaluate atomization quality at the 12 cS limit at ambient temperatures, thus avoiding subzero test conditions.

Table 5 lists the physical properties important to atomization for the four test fluids. At the test conditions, the Weber number for the Sasol FSJF and Jet A differed by about 3%; the Weber numbers of the other two fluids were about 20% higher.

5.4.4 *Test Conditions*. Each atomizer was tested over a range of conditions representative of an APU during typical engine start conditions. For the pressure atomizers, this required a range of inlet fuel pressures. The air blast atomizer was tested over a range of fuel flows and air pressure drops representative of light-off and acceleration conditions. The performance evaluation was based on the Sauter mean diameter (SMD) as a measure of atomization and the spray angle.

5.4.5 *Results*. For the pressure atomizers, the Sasol FSJF and Jet A had similar spray opening pressures, spray angles, and spray quality. This is illustrated in Fig. 15 for Atomizer B showing that at −40°C (−40°F), the Sasol fuel produced a smaller drop-size distribution than the Jet A at all flow rates. Similar results were produced for the other pressure atomizer. Figure 16 compares the sprays for cold Jet A and Sasol FSJF at 50 psi (gauge). The pictures show that the sprays are both fully developed with similar spray angles. The spray of the Sasol fuel appears denser than that of the Jet A fuel, suggesting many more small droplets; the spray of the Jet A fuel appears to contain numerous large drops.

For air blast Atomizer C, the SMD for cold FSJF was similar to that of cold Jet A and Viscor with very little fuel effect. The FSJF and Jet A fuel had similar spray angles and spray quality at all test conditions. Figure 17 shows the correlation of SMD with the following parameter for air blast atomizers from Lefebvre [16]:

$$\mathrm{XPAR} = (1 + W_f/W_a)/(\rho_a V_a)$$

where W_f/W_a is the atomizer fuel/air ratio, ρ_a is the air density,

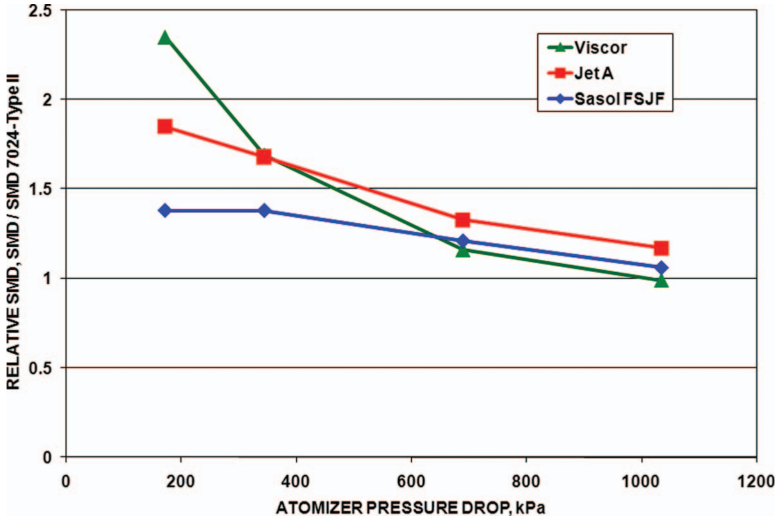

Fig. 15 Atomization of Sasol FSJF compared with Jet A at −40°C (−40°F) in a pressure atomizer

Downloaded 02 Jun 2010 to 171.66.16.109. Redistribution subject to ASME license or copyright; see http://www.asme.org/terms/Terms_Use.cfm

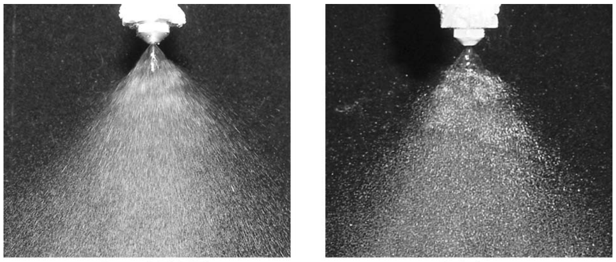
Sasol FSJF
Jet A

Fig. 16 Comparison of fuel sprays at −40°C (−40°F) and 50 psi (gauge) for Sasol fuel and jet a

and V_a is the air velocity.

In summary, the atomization and spray characteristics using cold FSJF were the same, or better than, for cold Jet A fuel due to lower fuel specific gravity and viscosity. Honeywell concluded that the FSJF fuel would provide a well-defined spray and an adequate spray droplet size for reliable cold starting.

5.5 Exhaust Emissions

5.5.1 Objective and Scope. The objective of the emission test was to determine the effect of using Sasol synthetic jet fuel on the exhaust emissions of a commercial combustor [14]. The following emissions were sampled and analyzed:

- CO
- unburned hydrocarbons (UHCs)
- NO_x
- smoke number

5.5.2 Test Description. The emission test was conducted by Pratt & Whitney at the United Technologies Research Center Jet Burner Test Stand using an 80 deg, four-nozzle arc sector rig of a commercial combustor. Exhaust samples were collected at the combustor exit. The data reported were averages of the samples from the center two sectors. The results were compared with emission data from a petroleum-derived Jet A fuel that were taken after the synthetic fuel tests using the same procedures and conditions. Both fuels were analyzed to ensure that they conformed to ASTM D 1655.

The combustor was tested over a range of pressures, $P_3 = 0.3-1.7$ MPa (50–250 psi (absolute)), and inlet temperatures, $T_3 = 200-480°C$ (460–890°F). Fuel/air ratios were varied, $f/a = 0.005-0.035$, at each of four pressure/temperature conditions used to cover a range of operating conditions for an engine. Combustor flow parameter variations were also conducted for scaling purposes. Emission data were collected at these conditions and then scaled to flight conditions representative of an engine with an overall pressure ratio (OPR) of 30. Data are presented for idle, cruise, approach, and sea-level takeoff (SLTO).

5.5.3 Analysis and Results. When an engine is certified, it must meet emission standards recommended by the International Civil Aviation Organization (ICAO) Committee on Aviation Environmental Protection (CAEP). Therefore, Pratt & Whitney considered it important to determine the effect of a fuel change on the standard emission parameter. The recommended parameter is the total amount of pollutant created per unit of net thrust from the engine (F_{00}) for a simulated landing takeoff (LTO) cycle consisting of four operating modes: 0.7 min at SLTO, 2.2 min at climb, 4.0 min at approach, and 26.0 min at idle. The parameter is calculated by

$$\text{Emission for LTO cycle} = \text{EPAP} = \sum (\text{EI}_{\text{species}} w_{\text{fuel}} t_{\text{mode}})/F_{00}$$

For these tests, the parameter was calculated for a simulated LTO cycle of an engine with an overall pressure ratio of 30.

The results of the emissions tests are illustrated in Figs. 18–20 for NO_x, CO, and smoke number (SN), respectively. In the LTO cycle, the Sasol synthetic fuel produced 4% less NO_x and 19% less CO than the Jet-A fuel. These emission levels for both fuels were lower than the limits of CAEP/6. At the individual power points, the NO_x emissions were virtually unchanged. The CO emissions from the Sasol synthetic fuel were lower than that of the conventional Jet A, especially at idle, in line with the lower viscosity of the Sasol fuel, recalling from the Honeywell atomization tests that fuels of lower viscosity produce a finer spray.

In Fig. 20, the data for smoke number, SN, are normalized to the Jet A results. The Sasol synthetic fuel produced lower smoke than the Jet A fuel as expected because of the higher hydrogen content, i.e., lower aromatic content, of the Sasol fuel. The outlier at SLTO at a fuel/air ratio of 0.018 was due to a low SN for the Jet-A. The differences in CO_2 emissions and combustion efficiency were negligible.

UHCs were only reported for the idle condition. At approach, climb, and takeoff, the levels on both fuels were very low and within the uncertainty of the measurement technique. The UHC results at the idle condition are presented in Table 6 showing that there was no significant difference in the amount of unburned hydrocarbons.

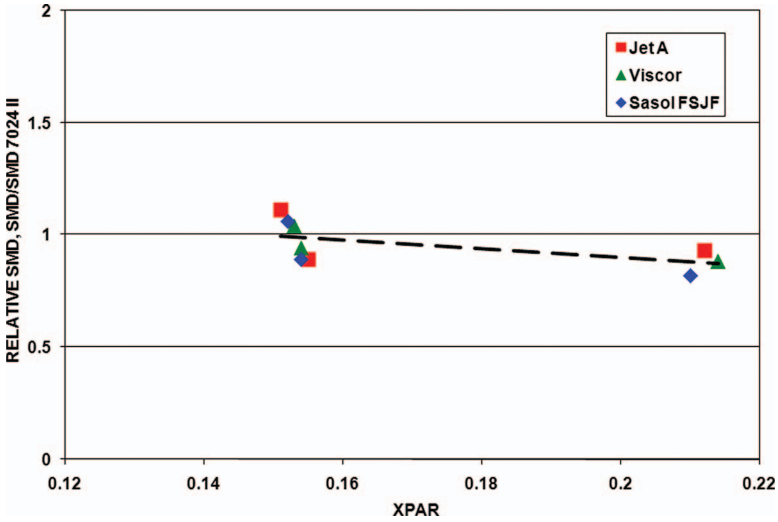

Fig. 17 Spray characteristics of Sasol FSJF in an air blast atomizer

Downloaded 02 Jun 2010 to 171.66.16.109. Redistribution subject to ASME license or copyright; see http://www.asme.org/terms/Terms_Use.cfm

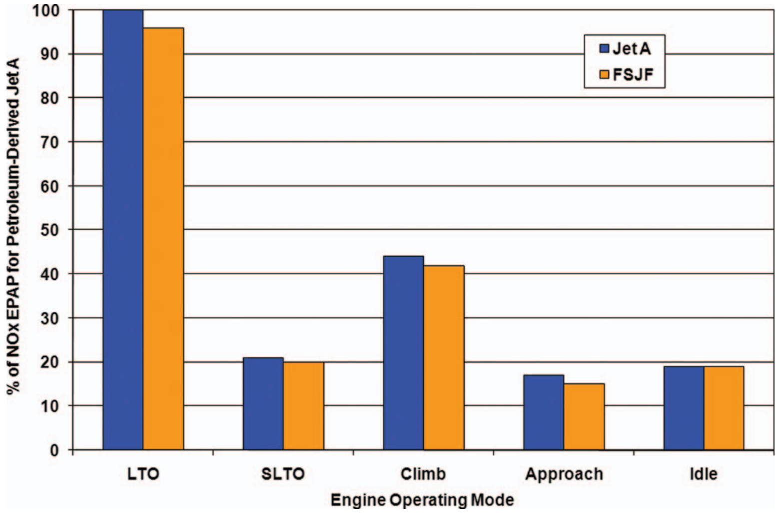

Fig. 18 Comparison of NO_x production for Sasol fuel and conventional Jet A

5.5.4 Summary of Emission Tests. The Pratt & Whitney engineers concluded that the use of synthetic Jet-A instead of petroleum-derived Jet-A did not adversely affect the combustion efficiency and emissions of the test combustor. They concluded that the combustor would operate at the same fuel-air ratio on the synthetic fuel as on the conventional Jet-A.

5.6 Cold-Day Ignition and Altitude Relight Test

5.6.1 Objective. The objective of these tests was to compare the cold-day ignition and altitude relight performance of the Sasol fully synthetic jet fuel with a conventional fuel in a state-of-the-art combustor [15].

5.6.2 Test Description. The ignition and altitude relight tests were conducted by Rolls-Royce (Derby, UK) using a full-annular Trent combustor, which has air blast atomizers. The other OEMs agreed that the results should be translatable to other engines.

Figure 21 is a map of the test points for ignition and extinction, both cold-day ground and altitude relight. Ground ignition testing was conducted at −40°C (−40°F). Altitude relight tests were conducted over altitudes ranging from about 8.5 km to 11 km (28,000–35,000 ft) over a range of Mach numbers from 0.6 to 1 to cover the windmill envelope. Some additional points at higher altitude and Mach number were added for blowout tests. Overall, tests were conducted at more than 200 operating conditions.

The fuel of reference was a Jet A-1 (AVTUR) fuel in compliance with DEF STAN 91-91. Flash point and energy density were very comparable for the two fuels; however, there was a significant difference in the boiling point distribution of the two fuels, as shown in Fig. 22. The slope of the Jet A-1 line was quite typical of jet fuels in the UK and elsewhere while that of the Sasol FSJF was much flatter.

5.6.3 Results. All baseline testing with Jet A-1 fuel, including both the simulated high altitude and the ground ambient cold-day conditions, agreed with the expectations based on previous Rolls-Royce engines and combustor tests.

Figure 23 is a schematic representation of the results of the cold-day ground ignition and extinction limits showing that there were no significant differences between the performance limits of the Sasol FSJF and the Jet A-1 fuels. The difference between the extinction limits and the fueling line is the available margin for sudden throttle maneuvers. Similarly, Fig. 24 illustrates the results for the altitude ignition limits of the two test fuels. (There are no

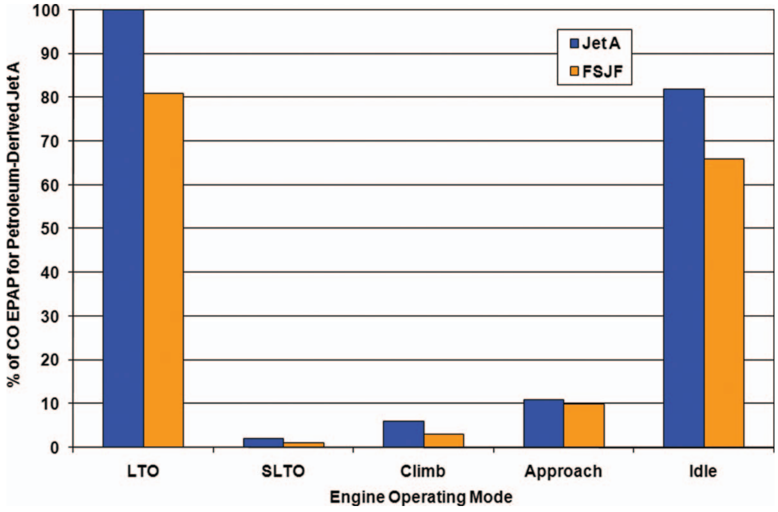

Fig. 19 Comparison of CO production for Sasol fuel and conventional Jet A

Downloaded 02 Jun 2010 to 171.66.16.109. Redistribution subject to ASME license or copyright; see http://www.asme.org/terms/Terms_Use.cfm

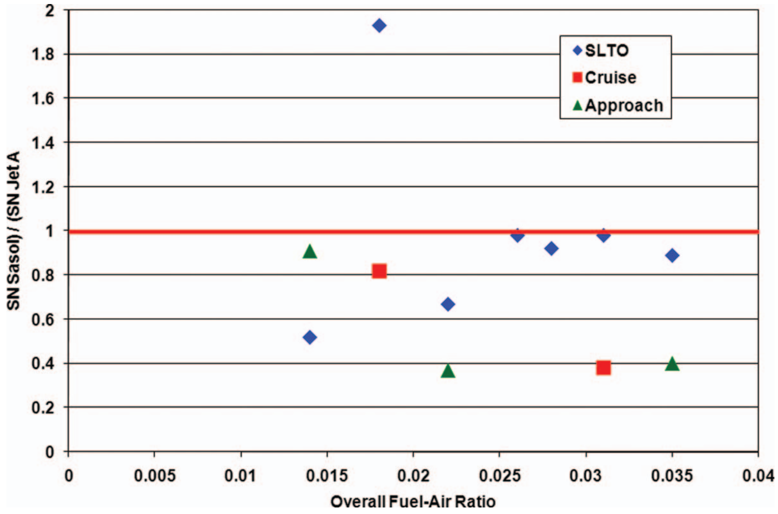

Fig. 20 Comparison of smoke number for Sasol fuel and conventional Jet A

values given on these figures for proprietary reasons.)

The weak and rich extinction limits at altitude were also satisfactory; however, close to the blowout limit at higher altitude condition, the difference began to increase. The blowout characteristic was worse for the Sasol fuel; i.e., the blowout point was at a lower combustor mass flow compared to the Jet A-1 fuel. Since lean blowout is considered to be evaporation limited [16], it was thought that this last result was due to differences in boiling point distribution, as noted in Fig. 20. However, the possibility had to be considered that the difference in lean blowout limit might be due to changes in fuel chemistry. As a result, further testing was requested by the engine manufacturers to resolve the issue.

Table 6 Comparison of unburned hydrocarbons at idle

Fuel	UHC, ppm
Sasol FSJF	11.8
Jet A	16.0

5.6.4 Summary of Ignition and Relight Tests. Other than the issue of extinction at high altitude, Rolls-Royce concluded that the Sasol fuel met the expectations of an aviation kerosene fuel. Based on the differences in the lean blowout characteristics at the high-altitude condition, LBO tests were then conducted at conditions more relevant to descent where throttle maneuvers are more likely to cause lean combustion.

5.7 Lean Blowout Test

5.7.1 Objective. Lean blowout tests were conducted by Honeywell to resolve the question of the blowout characteristics found in the altitude extinction tests described in Sec. 5.6 [13]. The goal was to verify that lean blowout characteristics of the Sasol synthetic jet fuel are due to the particular boiling point distribution of the test fuel and its effect on evaporation.

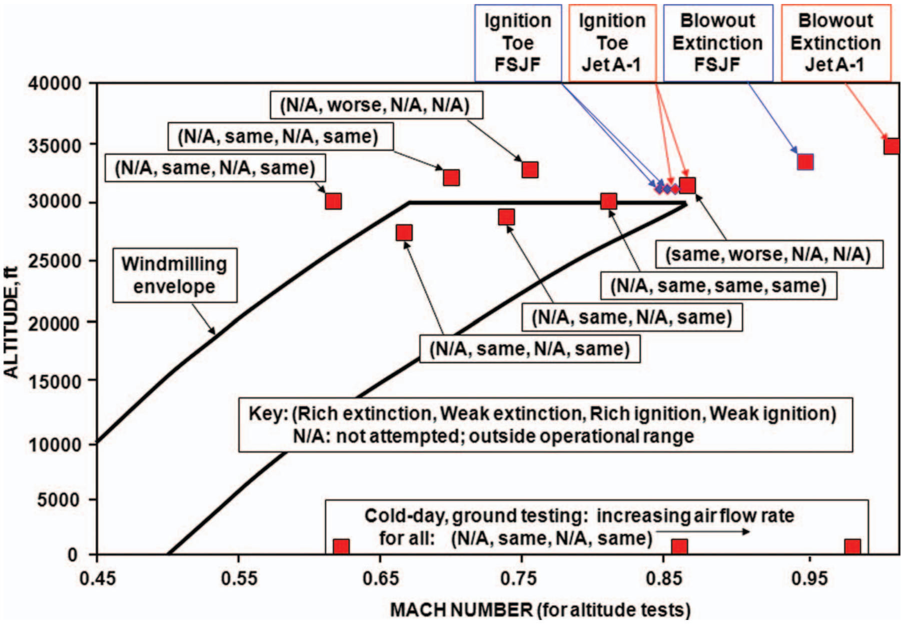

Fig. 21 Map of test conditions for ignition and extinction tests

Downloaded 02 Jun 2010 to 171.66.16.109. Redistribution subject to ASME license or copyright; see http://www.asme.org/terms/Terms_Use.cfm

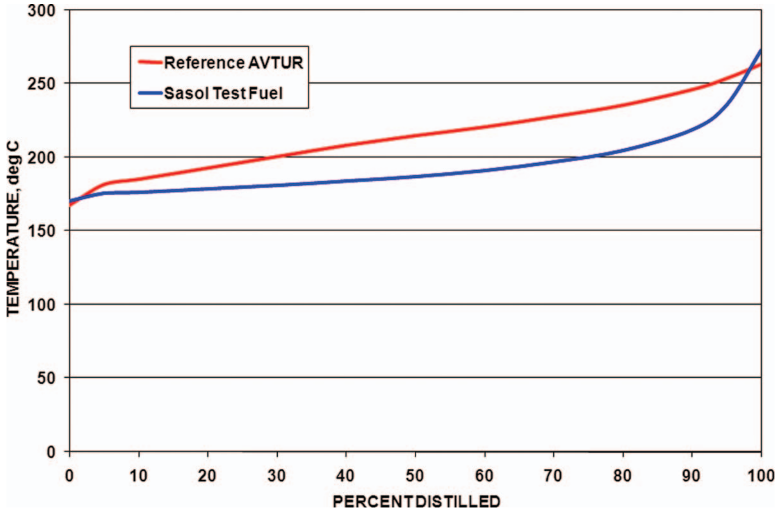

Fig. 22 Boiling point distributions of test fuels for ignition and altitude relight tests

5.7.2 Combustor Description. The lean stability tests were conducted with a full-scale annular combustor rig from a small turboshaft (helicopter) engine. The combustion system features a reverse-flow annular combustor and axially inserted dual-orifice fuel atomizers. The engine pressure ratio at SLTO conditions is approximately 10.

5.7.3 Test Fuels. Three test fuels were used in this evaluation:

- Sasol synthetic jet fuel (DEF STAN 91-91)
- Jet A (ASTM D 1655)
- JP-5 (MIL-DTL-5624)

The Jet A and JP-5 test fuels were selected on the basis of their boiling point distribution to specifically address the question raised in the Rolls-Royce altitude tests. JP-5 had "weathered" and lost some of its lighter fractions; as a result it had a flat boiling point distribution like the Sasol fuel, but a higher flash point. Jet A had the same flash point as the Sasol fuel, but the slope of the boiling point distribution was similar to the AVTUR used by Rolls-Royce. The flash points of the test fuels are compared in Table 7, and the boiling point distributions are compared in Fig. 25.

5.7.4 Test Conditions. The LBO tests were conducted at four deceleration conditions from the sea level to a 7.6 km (25,000 ft) altitude and from a standard day to −40°C (−40°F). The tests were conducted with conditioned, nonvitiated air to the rig inlet at actual engine operating conditions (not scaled).

5.7.5 Results. The test results showed that the Sasol FSJF had no adverse effect on lean stability (lean blowout). The lean stability test results are presented in Fig. 26, with test fuel data normalized to the baseline Jet A data. The data are very tightly grouped, indicating very little differences among the fuels. At higher altitude conditions, there was some limited fuel effect noted, with FSJF results between the Jet A and JP-5 results in accordance with the differences in the boiling point distributions. The flash point and front end distillation temperatures of FSJF were between the Jet A and JP-5 fuels. Previous testing at Honeywell on other engines has shown combustor lean stability characteristics to correlate with these fuel properties.

5.7.6 Conclusions on LBO Tests. These results demonstrate that the Sasol FSJF had no adverse effect on the lean stability characteristics. The lean stability characteristics of the FSJF were

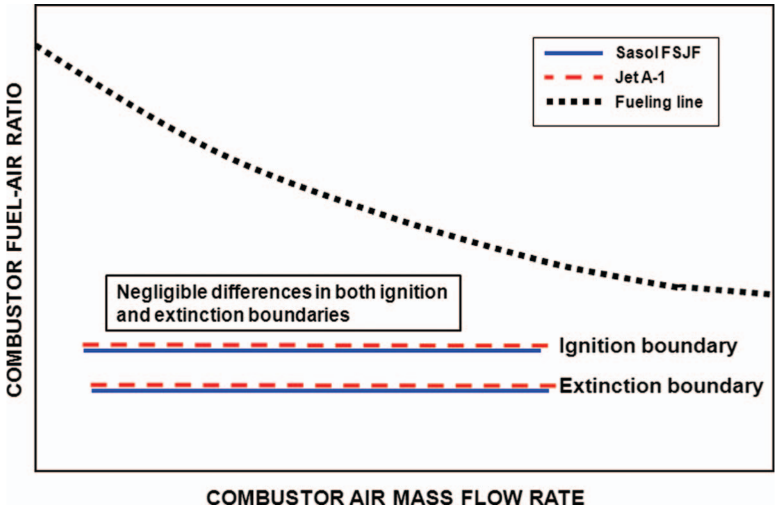

Fig. 23 Schematic representation of the extinction and ignition performance for a ground ambient cold-day (−40°C) condition

Downloaded 02 Jun 2010 to 171.66.16.109. Redistribution subject to ASME license or copyright; see http://www.asme.org/terms/Terms_Use.cfm

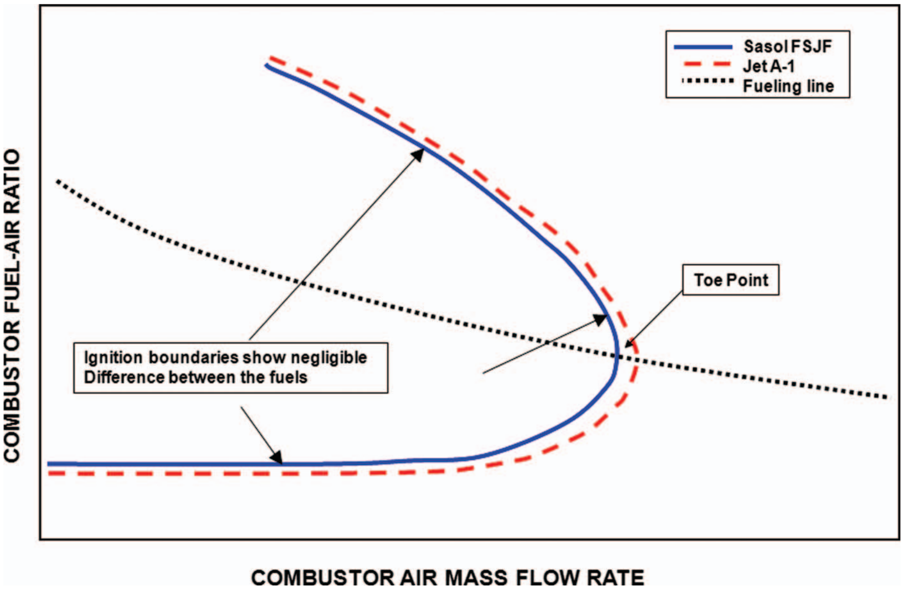

Fig. 24 Schematic representation of the altitude ignition results

similar to the Jet A and JP-5 fuels. Differences at the higher altitude conditions were due to the particular boiling point distributions of the test fuel and not to chemistry.

6 Summary and Conclusions

The Sasol synthetic kerosene is unique among distillates from Fischer–Tropsch processes in that it contains aromatic hydrocarbons. Within the current understanding, the presence of the aromatics makes the Sasol FT kerosene more suitable as a complete jet fuel than the more common FT distillates, which are comprised of normal paraffins and isoparaffins and contain no aromatics. Nevertheless, this fuel is a radical departure from experience as this is the first completely synthetic jet fuel to be approved. It was, therefore, necessary to demonstrate that the fuel is fit-for-purpose as jet fuel and will have no adverse impact on performance, durability, and safety. This paper has documented the process of demonstrating that an alternative fuel is fit-for-purpose as a fuel for commercial aviation. The methodology used to demonstrate that the Sasol FSJF is fit-for-purpose was the same as that used to evaluate the original Sasol semisynthetic fuel except for the addition of the engine and combustor tests. The process is now being refined and codified by the major specification-writing bodies to produce an approval protocol for alternative aviation fuels in the future.

Four samples of the fuel representing practical extremes of production were given a thorough evaluation to demonstrate that the Sasol FSJF will have properties and characteristics that fall within the experience of conventional jet fuels from petroleum. Not all of the tests for physical properties and characteristics are presented in this paper.

Sasol then produced a large volume of synthetic kerosene for

Table 7 Flash point comparison of fuels for honeywell LBO tests

Test fuel	Flash point
Jet A	47°C (117°F)
Sasol FSJF	47°C (117°F)
JP-5	56°C (133°F)

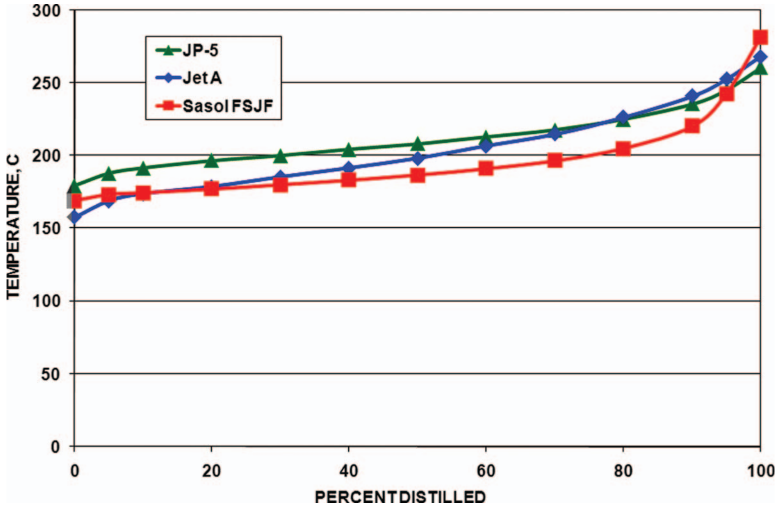

Fig. 25 Comparison of boiling point distributions of the test fuels used in the Honeywell LBO tests

Downloaded 02 Jun 2010 to 171.66.16.109. Redistribution subject to ASME license or copyright; see http://www.asme.org/terms/Terms_Use.cfm

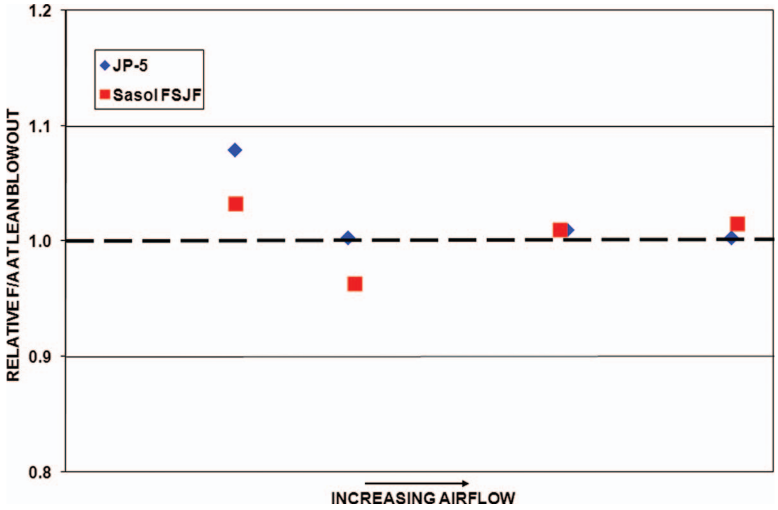

Fig. 26 Comparison of fuel effects on lean blowout characteristics

engine and combustor tests to evaluate the effects on performance, emissions, and operability. The combustion characteristics of Sasol FSJF were found to be the same as that of petroleum-derived jet fuel having the same properties. Differences were within the normal variations found in jet fuel. These engine and combustor tests also served to validate the conclusions from the tests on the properties and characteristics of the fuels.

The results of these tests have been presented to the aviation community at technical meetings and industry forums and in formal reports [17,18]. The engine manufacturers have critically reviewed the data and have concluded that the Sasol synthetic jet fuel will have no adverse impact on air-worthiness and safety and is fit-for-purpose as jet fuel for civilian aviation.

Based on the results of this evaluation and the recommendations of the aircraft engine manufacturers, the UK Aviation Fuels Committee approved the acceptance of Sasol FSJF in DEF STAN 91-91, Issue 6 in April 2008 [1]. Sasol FSJF is the first fully synthetic jet fuel approved for unrestricted use in aviation.

References

[1] Defense Standard 91-91, Turbine Fuel, Aviation Kerosene Type, Jet A-1 NATO Code: F-35 Joint Service Designation: AVTUR, www.dstan.gov.uk

[2] Moses, C. A., and Stavinoha, L. L., 1997, "Qualification of Sasol Semi-Synthetic Jet A-1 As Commercial Jet Fuel," Southwest Research Institute, Report No. 8531.

[3] ASTM D 3241, "Standard Test Method for Thermal Oxidation Stability of Aviation Turbine Fuels (JFTOT Procedure)," ASTM International, 100 Barr Harbor Drive, P.O. Box C700, West Conshohocken, PA.

[4] Parker Seal Company, 1992, *Parker O-Ring Handbook*, O-Ring Division, Lexington, KT, pp. A3-7 and A3-8.

[5] ASTM D 471, "Standard Test Method for Rubber Property—Effect of Liquids," ASTM International, 100 Barr Harbor Drive, P.O. Box C700, West Conshohocken, PA.

[6] ASTM D 2240, "Standard Test Method for Rubber Property—Durometer Hardness," ASTM International, 100 Barr Harbor Drive, P.O. Box C700, West Conshohocken, PA.

[7] ASTM D 412, "Standard Test Methods for Vulcanized Rubber and Thermoplastic Elastomers-Tension," ASTM International, 100 Barr Harbor Drive, P.O. Box C700, West Conshohocken, PA.

[8] ASTM D 5001, "Standard Test Method for Measurement of Lubricity of Aviation Turbine Fuels by the Ball-on-Cylinder Lubricity Evaluator (BOCLE)," ASTM International, 100 Barr Harbor Drive, P.O. Box C700, West Conshohocken, PA.

[9] Coordinating Research Council, Inc., 2004, *Handbook of Aviation Fuel Properties*, 3rd ed., Alpharetta, GA.

[10] Hadaller, O. J., and Johnson, J. M., 2006, "World Fuel Sampling Program," Coordinating Research Council, Inc., CRC Report No. 647.

[11] ASTM E 1269, "Standard Test Method for Determining Specific Heat Capacity by Differential Scanning Calorimetry," ASTM International, 100 Barr Harbor Drive, P.O. Box C700, West Conshohocken, PA.

[12] Biddle, T., 2007, "JT9D Engine Endurance Test for Investigating Impact of Sasol Synthetic Fuel on Engine Performance, P&W Review and Conclusions," Pratt & Whitney, East Hartford, CT.

[13] Williams, R., 2007, "Final Report Evaluation of Sasol Fully Synthetic Jet Fuel for Approval for Use as Jet A-1 Fuel," Honeywell Aerospace, Report No. 21-13781.

[14] Biddle, T., 2007, "Pratt & Whitney Emissions Test to Determine the Effect of Sasol Fully Synthetic Jet-A Fuel on the Emissions of a Commercial Combustor," Southwest Research Institute, Pratt & Whitney, Final Report.

[15] Herman, F., 2007, "Cold Day Ignition and Altitude Relight Testing of SASOL Fully Synthetic Aviation Kerosene—External Report," to Southwest Research Institute, Rolls-Royce PLC, Report No. DNS 126274.

[16] Lefebvre, A. H., 1983, *Gas Turbine Combustion*, Hemisphere Publishing, New York.

[17] Moses, C., Wilson, G., and Roets, P., 2003, "Evaluation of Sasol Synthetic Kerosene for Suitability as Jet Fuel," Southwest Research Institute, Report No. 04438-1.

[18] Moses, C., 2007, "Evaluation of Sasol Synthetic Kerosene for Suitability as Jet Fuel—Phase II: Engine and Combustor Tests," Southwest Research Institute, Report No. 04438-2.

Downloaded 02 Jun 2010 to 171.66.16.109. Redistribution subject to ASME license or copyright; see http://www.asme.org/terms/Terms_Use.cfm

Benefits of Active Compressor Stability Management on Turbofan Engine Operability

Yuan Liu

Manuj Dhingra

J. V. R. Prasad

School of Aerospace Engineering,
Georgia Institute of Technology,
Atlanta, GA 30332

Active compressor stability management can play a significant role in the intelligent control of gas turbine engines. The present work utilizes a computer simulation to illustrate the potential operability benefits of compressor stability management when actively controlling a turbofan engine. The simulation, called the modular aeropropulsion system simulation (MAPSS) and developed at NASA Glenn, models the actuation, sensor, controller, and engine dynamics of a twin-spool, low-bypass turbofan engine. The stability management system is built around a previously developed stability measure called the correlation measure. The correlation measure quantifies the repeatability of the pressure signature of a compressor rotor. Earlier work has used laboratory compressor and engine rig data to develop a relationship between a compressor's stability boundary and its correlation measure. Specifically, correlation measure threshold crossing events increase in magnitude and number as the compressor approaches the limit of stable operation. To simulate the experimentally observed behavior of these events, a stochastic model based on level-crossings of an exponentially distributed pseudorandom process has been implemented in the MAPSS environment. Three different methods of integrating active stability management within the existing engine control architecture have been explored. The results show that significant improvements in the engine emergency response can be obtained while maintaining instability-free compressor operation via any of the methods studied. Two of the active control schemes investigated utilize existing scheduler and controller parameters and require minimal additional control logic for implementation. The third method, while introducing additional logic, emphasizes the need for as well as the benefits of a more integrated stability management system.

[DOI: 10.1115/1.3028565]

Introduction

An intelligent control system is one that adapts itself to changes in its surrounding environment. When applied to gas turbine engines, the benefits of an intelligent control system include optimized performance and increased engine life [1]. Engine simulations have greatly aided research and development in this area. Detailed engine models have been implemented in a real-time environment to enable investigations into model-based control [2]. Moreover, these simulations have been used as inexpensive testbeds to evaluate various novel active engine control schemes [3]. In this paper, a modular aeropropulsion system simulation (MAPSS) developed at the NASA Glenn Research Center is used to demonstrate the benefits of an active compressor stability management system.

The operating envelope of modern gas turbine engines is limited by, among other things, aerodynamic instabilities in the compression system. On a compressor map (Fig. 1), this stability limit is represented by the surge line. The precise location of the surge line is uncertain due to effects such as inlet distortion, aging, manufacturing tolerances, and thermal and speed transients. Consequently, the engine control system is designed with a conservative safety margin, called the stall margin, ensuring system operation well within the safe region. The conservative margins translate into penalties on the engine performance. For instance, as engine accelerations require transient excursions of the compressor operating point toward the surge line, acceleration rates are limited to maintain stall margin requirements. An active stability management system would alleviate the need for stacked worst-case scenarios, enabling optimal utilization of available stall margins.

Moore and Greitzer [4,5] first developed a model for poststall transients about two decades ago. The model captured the essentials of rotating stall and spurred numerous stall control studies [6–11] to evaluate the benefits of active control and stabilize part of the unstable region. However, experimental work by Day [12] and Camp and Day [13] revealed an alternative route to stall via "spikes" that was not captured by the analytical model. In fact, further studies [14,15] showed that under certain conditions, the spikelike stall inception is dominant. Thus, active control techniques based on the analytical model are insufficient for complete avoidance of compressor instabilities.

Experiments conducted by Inoue et al. [16] determined that stall precursors could be detected by the deterioration of blade spacing periodicity. However, the similarity coefficient that was proposed is unsuitable for rapid engine transients since it utilized 200 rotor revolutions of data. Dhingra et al. [17] introduced active compressor stability management through the use of a correlation measure based on the unsteady flow field characteristics in the tip region of the compressor rotor. The correlation measure has been demonstrated on laboratory compressor rigs as well as on a modern aircraft engine [18]. A stochastic model has also been developed that captures the statistical characteristics of the correlation measure [19].

This work continues the evaluation of active compressor stability management with the application of the system to the MAPSS environment. Three different methods of implementation have been investigated. All three schemes are successful in preventing stall during a severe transient at sea-level static conditions. Two of them, direct manipulation of fuel and indirect manipulation through the acceleration scheduler, are relatively simple and re-

---

Manuscript received May 8, 2008; final manuscript received May 23, 2008; published online April 14, 2009. Review conducted by Dilip R. Ballal. Paper presented at the ASME Turbo Expo 2008: Land, Sea and Air (GT2008), June 9–13, Berlin, Germany.

Copyright © 2009 by ASME

Downloaded 02 Jun 2010 to 171.66.16.109. Redistribution subject to ASME license or copyright; see http://www.asme.org/terms/Terms_Use.cfm

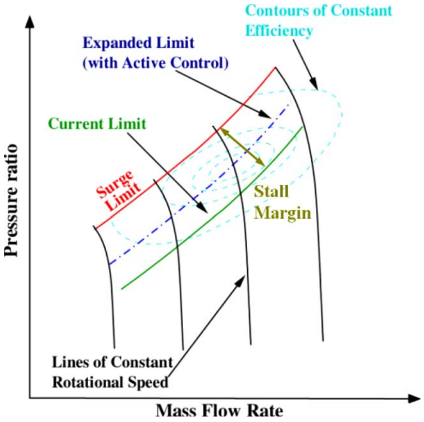

Fig. 1 Potential performance improvements

quire a minimal amount of additional control logic. The results from these two methods demonstrate the applicability and benefits of stability management to existing engine lines. The third method of implementation models a more sophisticated integration of the stability management system with the digital engine controller. This advanced control system not only improves on the advantages introduced by the previous two; it is also capable of controlling the engine in the harshest conditions where its simpler counterparts fail.

Engine Simulation

The engine model used in this work is MAPSS. Developed at NASA Glenn Research Center, MAPSS is a graphical implementation of a previously validated FORTRAN simulation of a low-bypass military turbofan engine and control system. MAPSS was developed in the block diagram-based MATLAB/SIMULINK environment to allow easy access to various engine parameters and to facilitate control and diagnostic systems research.

The MAPSS environment is a nonlinear, non-real-time, and multirate system consisting of the component level model (CLM) and the controller and actuator dynamics (CAD) modules. The CLM is a dynamic simulation of a low-bypass, high-pressure ratio, and dual-spool military-type turbofan engine (Fig. 2). Engine components are represented by different submodules inside the CLM. The components modeled include the fan, booster, high-pressure compressor (HPC), combustor, high-pressure turbine (HPT), low-pressure turbine (LPT), mixer, afterburner, and nozzle. Also modeled are forward blocker doors, aft variable area bypass injector, bypass duct air flow, and compressor bleed and cooling flows. The state variables of the engine model are fan spool speed, core spool speed, and average hot section metal temperature. The CLM has an update rate of 2500 Hz [20].

The CAD module consists of a digital engine controller and an actuator submodule that emulates the required dynamics to determine actuator positions for guide vanes, areas (such as nozzle area), and fuel flow. The digital controller, which has a sampling rate of 50 Hz, takes power lever angle (PLA), Mach number, and altitude as its inputs. The controller uses these inputs, open-loop schedules, and signals from sensors collecting data on various engine parameters from the CLM to calculate demands to the actuator submodule. For instance, maps are used to determine actuator commands for the fan, booster, and HPC guide vane positions. Other actuator demands, particularly burner fuel flow, are obtained from five proportional-integral control action regulators, each corresponding to a particular mode tailored to regulating certain engine parameters and operating limits. Three of the control modes are related to PLA power settings (low, medium, and high), while the other two are the fan stall margin and fan spool overspeed modes. Values calculated from the modes are blended based on engine operating conditions to obtain the final demands sent to the actuator submodule [21].

It is important to note that although MAPSS is a dynamic engine model capable of simulating transient performance, it is unable to capture stall or poststall engine characteristics. However, the CLM module calculates stall margins of the fan, booster, and HPC based on the stall pressure ratio of each component. The onset of compressor instabilities is taken to be the instant any of the three stall margins is less than or equal to zero. The objective of the present work is avoidance of compressor instabilities, and therefore the lack of a surge-capable model is not considered to be a significant limitation.

Correlation Measure

The detection of compressor operation in the proximity of its stability limits is essential to active stability management. This can be accomplished via the correlation measure developed at the School of Aerospace Engineering, Georgia Institute of Technology. This measure quantifies the repeatability of pressure signals over a compressor rotor. For a sampled signal, the correlation measure [17] is defined as

$$C(n) = \frac{\sum_{i=n-\mathrm{wnd}}^{n} p_i p_{i-\mathrm{shaft}}}{\sqrt{\sum_{i=n-\mathrm{wnd}}^{n} p_i^2 \sum_{i=n-\mathrm{wnd}}^{n} p_{i-\mathrm{shaft}}^2}} \tag{1}$$

where $C(n)$=correlation measure, n=sample index, i=index, shaft=number of samples per shaft rotation, and wnd=window size in number of samples.

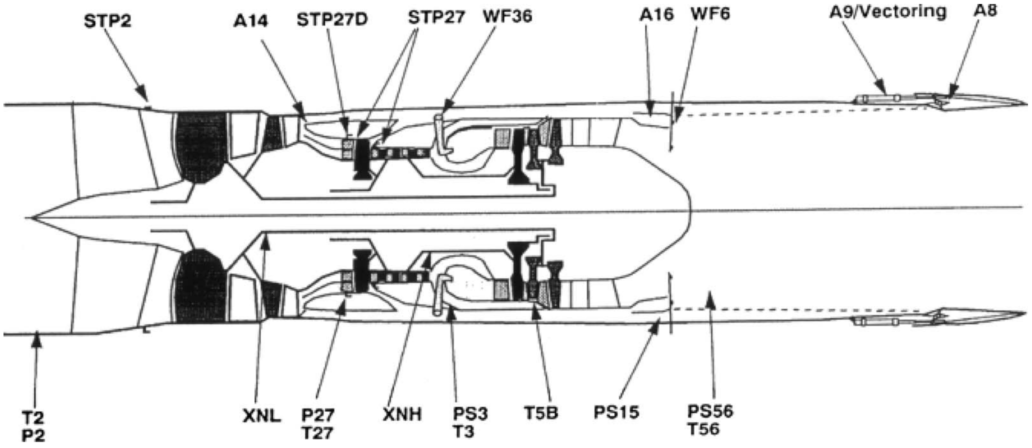

Fig. 2 Schematic of the MAPSS low-bypass turbofan engine (Parker and Guo [21])

Downloaded 02 Jun 2010 to 171.66.16.109. Redistribution subject to ASME license or copyright; see http://www.asme.org/terms/Terms_Use.cfm

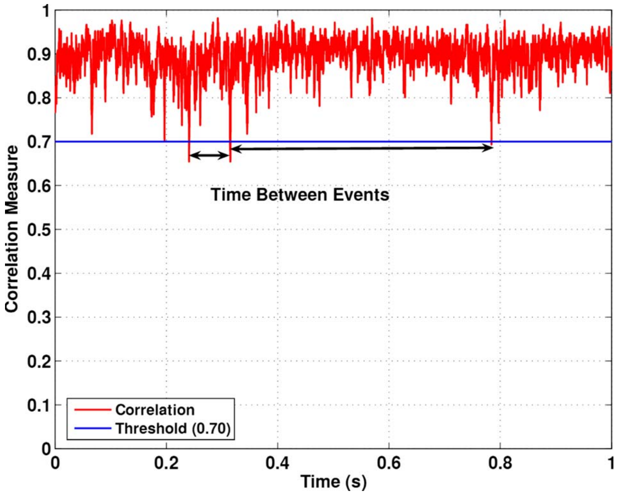

Fig. 3 TBE: An event occurs when correlation measure drops below some specified threshold

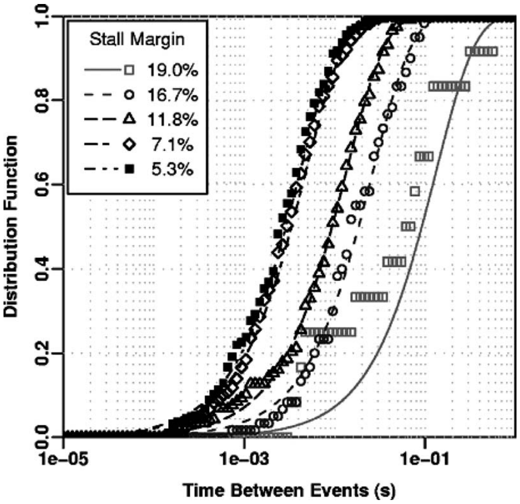

Fig. 4 The cumulative distribution function of TBE when correlation measure is calculated at various stall margins is approximately exponential

It has been experimentally observed that the periodicity of the pressure over the rotor, as measured by a sensor fixed to the casing, deteriorates when the compressor loading is increased toward its stability limits. From Eq. (1), the correlation measure is bounded by −1 and 1, with the latter representing a perfectly repeatable signal. For a typical compressor operation, the correlation measure stays between 0 and 1, with lower values indicating operation near the stability limit. When applied to engine control, the correlation measure is calculated and actively monitored for any drops below a specified threshold. Such a drop is defined as an "event." Control action, such as bleed air or fuel flow actuation, is taken in response to these events.

Stochastic Model

The evaluation of correlation-measure-based stability management for different control strategies and/or engine platforms requires the replication of the observed correlation measure behavior in a simulation environment. In particular, it is necessary to generate correlation measure threshold crossing events in a fashion that is representative of experimental data. As engine dynamic models do not capture details at the scale of pressure fluctuations over a compressor rotor, the correlation measure cannot be directly calculated. Instead, the engine simulation is paired with a previously developed stochastic model [19]. The model captures the relationship between the compressor stall margin, readily available in the simulation environment, and the distribution of the time between successive events (TBE). This metric is illustrated in Fig. 3.

An analysis of experimental data obtained on different compressor platforms has shown that for a fixed threshold level, the TBE follows an exponential distribution,

$$F_{\mathrm{TBE}}(\tau) = P(\mathrm{TBE} < \tau) = 1 - e^{-\mu_{cm}\tau} \qquad (2)$$

In this expression, μ_{cm} is the average number of events per second. A comparison of predicted (solid lines) and observed (markers) distributions for a representative case is reproduced in Fig. 4. The parameter μ_{cm} is a function of stall margin and can be determined from experimental data (Fig. 5).

Cramer and Leadbetter [22] showed that for any given random process (e.g., a sequence from a random number generator) and a threshold value, the distribution of the time between threshold crossings is

$$F_{\mathrm{TBE}}(\tau) = 1 + \mu^{-1}D^{+}u_0(\tau) \qquad (3)$$

Here, μ is the average number of threshold crossings, D^{+} is the right hand derivative, and u_0 is the probability that no threshold crossings are observed in the time interval of $0-\tau$. To simulate the TBE characteristics of the correlation measure, a random process with an exponentially decaying probability of "no event," i.e., $u_0 = e^{-\mu\tau}$, has to be found. Numerical experiments show that level-crossings of a pseudorandom number generator with an exponential distribution yield the required form of $u_0(\tau)$. Further, if the threshold level for this pseudorandom number generator is set based on the natural logarithm of μ_{cm}, μ equals μ_{cm}, reducing Eq. (3) to Eq. (2). In the present work, this empirical observation is used to generate events with the appropriate TBE distribution in the MAPSS environment.

Description of Experiments

A number of factors impact the susceptibility of an engine to compressor instabilities. This work focuses on severe engine accelerations, a scenario common to the low-bypass ratio turbofan

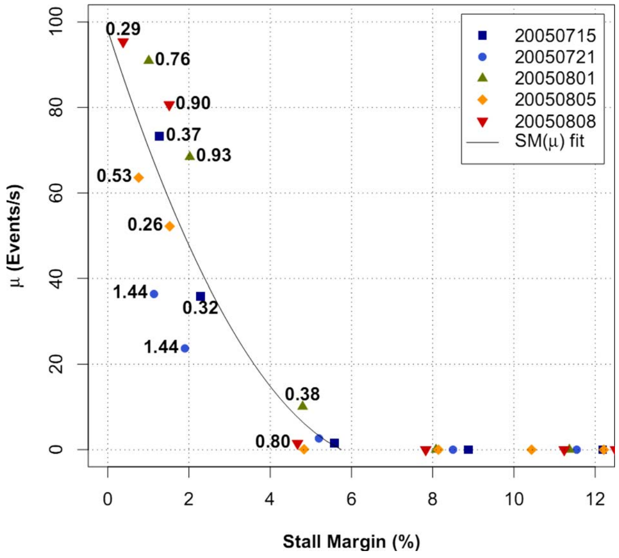

Fig. 5 Curve fit of average number of events versus stall margin used for the stochastic model based on experimental data from a laboratory compressor rig at Georgia Tech. The labels denote the error in the stall margin of the curve fit from each data point.

Downloaded 02 Jun 2010 to 171.66.16.109. Redistribution subject to ASME license or copyright; see http://www.asme.org/terms/Terms_Use.cfm

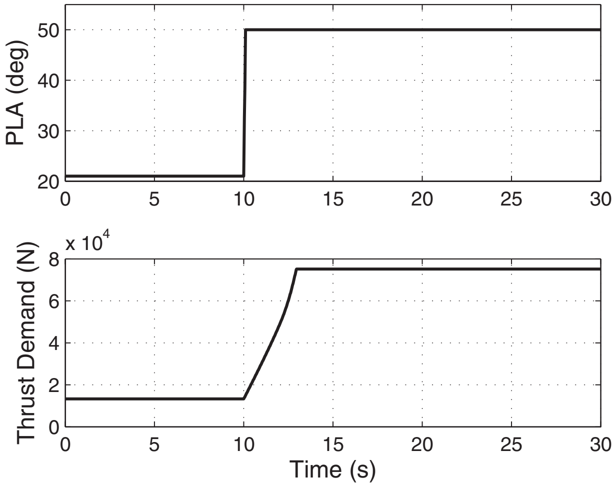

Fig. 6 PLA input for all simulation runs and corresponding net thrust demand after PLA rate limiter

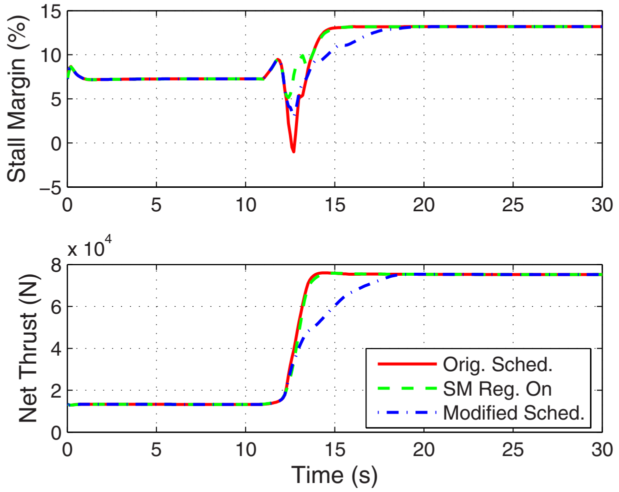

Fig. 7 Stall margin and net thrust responses to PLA step input command. The original fuel scheduler is unable to prevent stall without the stall margin regulator. The modified scheduler prevents stall but degrades transient performance.

engines on fighter aircraft and thus appropriate to analyze using the MAPSS environment. Each case described in this paper consists in using MAPSS to simulate a 30 s transient with a step PLA command from idle (21 deg) to maximum power (50 deg) at the 10 s mark (Fig. 6). The corresponding demands in net thrust are slightly less austere since the CAD module incorporates a time lag and a PLA rate limiter. This component of the controller model is left unmodified throughout this study. Furthermore, although MAPSS gives information on the stall margins of the fan, booster, and HPC, it has been observed that for all runs performed, the fan stall margin is the limiting case (i.e., consistently reaches zero first). Therefore, the stochastic model is applied only to the fan; the booster and HPC stall margins are checked for each case to ensure that they either are greater than zero for the entirety of the run or reach zero only after the fan has stalled.

The typical method of compressor control is an open-loop scheme utilizing a fuel scheduler. The scheduler places a limit on fuel flow based on certain measured engine parameters and inlet conditions. This prevents compressor stall at nearly all operating conditions but sometimes at the cost of engine performance. However, it has been seen that the acceleration scheduler in the CAD module of MAPSS is unable to prevent fan stall during relatively fast and demanding engine transients, such as the PLA step command from idle to full power (Fig. 7). The simulation contains a fan stall control mode that addresses this issue. This mode is essentially a stall margin regulator that is designed to drive the engine to a preset stall margin. The difference between the actual stall margin and the preset value is used to calculate actuator demands. When activated, this mode can successfully prevent stall for the PLA command under consideration. However, as stall margin is not a measurable quantity on a gas turbine engine, this is an unrealistic solution. To estimate the performance of the engine within current control practice, the fan stall margin mode is not utilized. The acceleration scheduler has been scaled down by a value that consistently prevents stall during severe engine acceleration. However, it is recognized that the scaling factor has been determined by trial and error, and the resulting scheduler is not optimized. Although this modified scheduler has been utilized as part of the active stability management system, its performance is not used as a basis of any comparison. The simulation runs using the stall margin regulator, though unrealistic, represent the ideal case scenario for an active compressor control scheme and thus serve well as a benchmark for this study.

Three different methods of implementing the stability management system have been investigated. For all cases, the stall margin regulator is turned off and the fuel scheduler is bypassed, unless otherwise indicated.

Direct Fuel Manipulation. The fuel flow has the highest impact among the available control inputs in a gas turbine engine. A relatively simple active control scheme can be constructed by using the stability management system to directly manipulate fuel flow (Fig. 8). In the presence of an event generated by the stochastic model, the fuel command calculated by the engine controller is reduced by 10%. To minimize chatter in the fuel command, a low-pass filter is applied to the signal before it is sent to the actuator submodule. It is important to note that these actions take place inside the engine controller, which precedes any time delays simulated by the CAD module.

Fuel Scheduler Manipulation. The fuel scheduler is central to conventional engine compressor control, and, as such, the scheduler encapsulates invaluable experimental data on the limits of safe engine operation. Whereas the direct manipulation of fuel flow command is simple to implement, it does not utilize this information. In fact, the percentage of fuel to reduce in response to an event is open to experimentation. An alternative approach, manipulation of the fuel scheduler, attempts to leverage the experience embedded in the scheduler. In this approach, depicted in Fig. 9, the limits imposed by the scheduler are nominally bypassed. However, an event from the stochastic model triggers the scheduler limit for that particular time step. The controller defaults back to bypassing the scheduler at the next time step unless another event is detected. The scaled fuel scheduler has been used for this work. In essence, this method is an indirect manipulation of commanded fuel flow. It uses the fuel scheduler to determine the reduced fuel flow, thus utilizing the existing information.

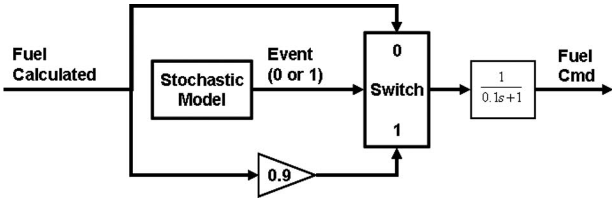

Fig. 8 Schematic of the direct fuel manipulation control scheme

Downloaded 02 Jun 2010 to 171.66.16.109. Redistribution subject to ASME license or copyright; see http://www.asme.org/terms/Terms_Use.cfm

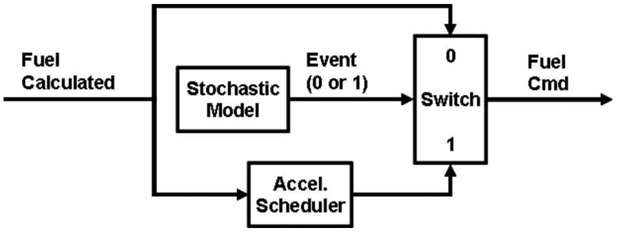

Fig. 9 Schematic of the fuel scheduler manipulation control scheme

Integrated Stability Management. The fuel flow and scheduler manipulation techniques represent relatively simple methods of implementing the stability management system. In both cases, the active control system is an “add-on” component, utilizing existing modules to integrate with the engine controller. Such approaches are perhaps more suitable for existing platforms due to minimal addition of control logic. For new designs, on the other hand, it may be desirable to fully integrate active stability management into the controller design. The stall margin regulator in MAPSS provides a unique opportunity to evaluate the potential benefits of such an integrated active compressor control scheme (Fig. 10).

The stall margin regulator generates actuator commands that are a function of a stall margin error signal. Further, the outputs of this regulator are activated, as well as blended with other controller modes, based on the available stall margin. The unobservability of the stall margin of a gas turbine engine renders this regulator an unrealistic approach to engine control in its current form. For the integrated stability management approach explored in this work, the gains and structure of the original regulator are retained. To eliminate the need for stall margin measurement, the error term is set to a constant value (for example, 2%). This slightly modified regulator defaults to an inactive state but is activated by the occurrence of an event. Thus, in combination with the stochastic model, an implementable form of the stall margin regulator can be used to simulate an engine controller with an integrated active stability management system.

Results and Discussion

The three approaches to stability management are successful in maintaining stall-free engine operation for the severe acceleration at state sea-level conditions. In order to evaluate the impact on engine transient performance, a “rise time” metric has been introduced. The rise time is defined as the time taken by the engine to attain 99% of the final thrust and is measured relative to the PLA step input. As noted earlier, the performance of the new control strategies is compared to that of the stall margin regulator. This regulator yields a rise time of 4.1 s. On the other hand, the engine takes twice as long, a rise time of 8.2 s, to complete the same transient with the scaled fuel scheduler in place.

Events based on the correlation measure have a stochastic nature. To gauge the impact of this stochastic nature on the control strategies under consideration, a Monte Carlo simulation has been performed for each case. Specifically, the engine response to the step PLA command is evaluated for 100 different seed values of the stochastic model for each stability management approach. This ensures that no two runs are identical as far as the correlation measure stochastic model is concerned. In the results that follow, to illustrate the variation in rise times, the raw values for the 100 trials are shown along with their mean. The transient behavior is illustrated via time traces of stall margin, event triggers, and fuel flow command for a representative run. Finally, for each method, the thrust response of the engine is compared to the stall margin regulator case.

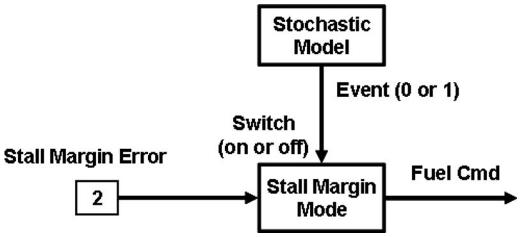

Fig. 10 Schematic of the integrated stability management using a built-in stall margin regulator

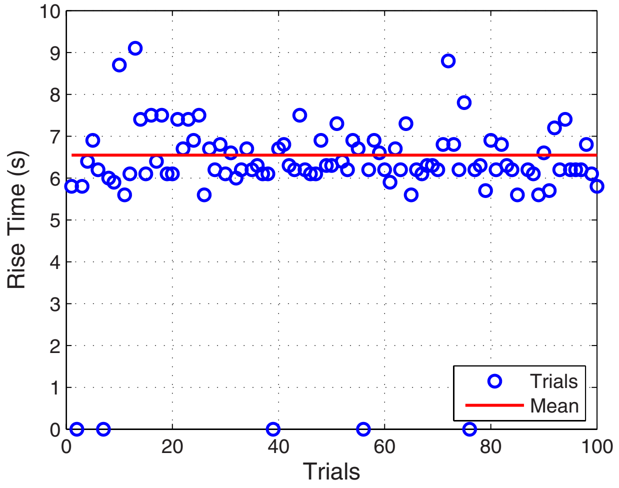

Fig. 11 Fuel manipulation results: rise time values for 100 runs. The average rise time is 6.55 s. 95% success rate (rise time of 0 s indicates a failed run).

Direct Fuel Manipulation. The fuel manipulation scheme operates the engine in the absence of the fuel scheduler and reduces fuel command by 10% at each occurrence of an event. The rise times observed in the 100 trials are summarized in Fig. 11. The average rise time for the successful trials is approximately 6.5 s. The results show relatively large variation, with a worst-case rise time of about 8.9 s. The five runs with 0 s rise times are failed transients in the sense that the engine did not achieve the desired final thrust level. The control system prevented the stall margin from reaching zero in every case.

Figures 12 and 13 show the results of a representative successful transient. The low-pass filter is unable to completely eliminate the chatter in the fuel flow command (Fig. 12). This characteristic is a direct consequence of the simplistic Boolean (event or no event) signal from the stability management system. Due to the strong dependence of the engine operating condition on the fuel flow rate, this chatter translates into significant fluctuations in the net engine thrust (Fig. 13).

The disadvantages of this simple control scheme are further evident in Figs. 14 and 15, which depict the outcome of a failed transient. The ad hoc fuel reduction, coupled with the stochastic nature of the events, leads to a limit cycle-like oscillation in the commanded fuel flow rates. The result, contrary to the demanded acceleration, is an eventual deceleration of the engine. Although the percentage reduction in fuel flow rate could be tuned to achieve successful results for the scenario under consideration, this method is not robust enough to be a feasible active control approach.

Fuel Scheduler Manipulation. As mentioned earlier, this approach activates and deactivates the scheduled fuel limits as necessary. Nominally bypassed, these limits are enforced whenever a correlation-measure-based event is detected. In every simulated trial, the application of this approach led to a stall-free transient engine operation. In regard to performance, the average value of the rise time over 100 trials is approximately 4.6 s. Additionally,

Downloaded 02 Jun 2010 to 171.66.16.109. Redistribution subject to ASME license or copyright; see http://www.asme.org/terms/Terms_Use.cfm

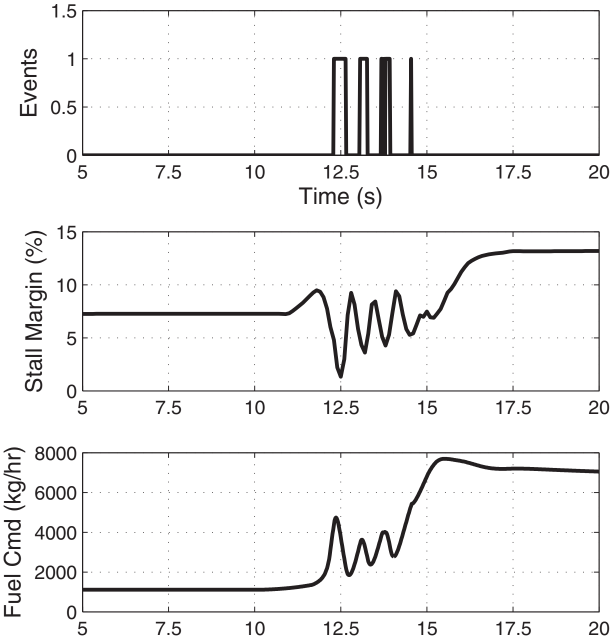

Fig. 12 Fuel manipulation results: stall margin, events, and fuel command signals for a representative successful run

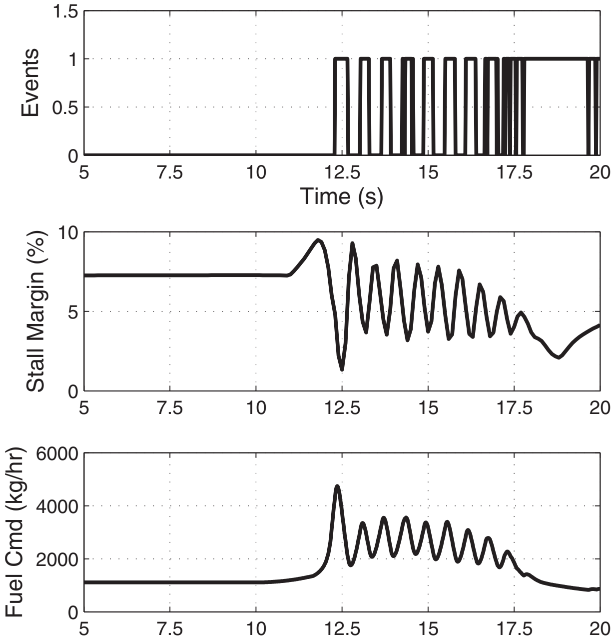

Fig. 14 Fuel manipulation results: stall margin, events, and fuel command signals for a representative failed run

as seen in Fig. 16, there is a relatively low variation in the rise times, with the worst rise time at about 5 s. These numbers compare favorably to the 4.1 s rise time observed with the stall margin regulator.

The manipulation of the fuel scheduler supersedes direct fuel modulation in every aspect. The transient behavior of variables of interest for a representative run is shown in Figs. 17 and 18. In contrast to the direct fuel modulation, there is no chatter in the commanded fuel flow rate. As evidenced by their location relative to the events, the sharp clips in the fuel flow rate visible in Fig. 17 are due to the activation of fuel scheduler limits. It may be noted that these dips do not cause any fluctuations in the engine thrust profile (Fig. 18). The abruptness of the changes in commanded fuel is mitigated by fuel metering valve dynamics. However, the impact of these dips on combustor thermoacoustic stability could be a potential concern.

Integrated Stability Management. The results discussed thus far show that manipulation of the fuel scheduler is a viable method of implementing active stability management on existing engines with minimal modification to the original engine controller. This section presents the benefits of a more fully integrated stability management system.

Although it reuses the control structure and gain values of the stall margin regulator, this approach essentially emulates an advanced stall margin limiter (the stall margin error term is replaced by a constant number). This control mode is nominally inactive, is activated by the occurrence of an event, and directly determines the actuator demands when active. Due to the compatible nature of the stall margin regulator, the transition to and from this stall avoidance mode is fairly smooth. This fact is illustrated by the fuel flow rate results presented in Fig. 19, which shows results for a representative run. The initial activation of stability management logic leads to a small change in the slope of the fuel command

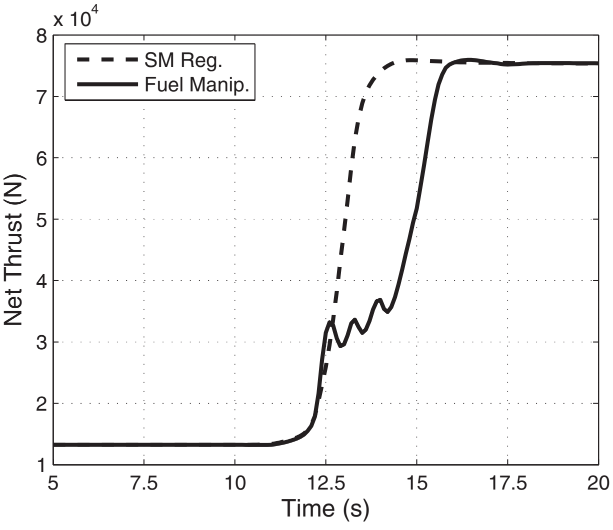

Fig. 13 Fuel manipulation results: engine thrust response for a representative successful run

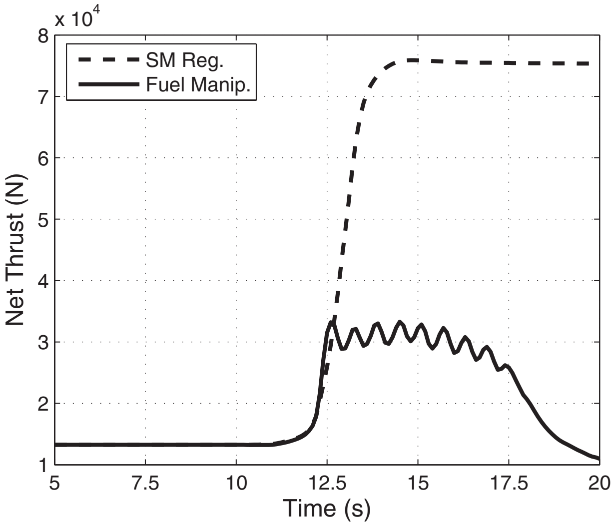

Fig. 15 Fuel manipulation results: engine thrust response for a representative failed run

Downloaded 02 Jun 2010 to 171.66.16.109. Redistribution subject to ASME license or copyright; see http://www.asme.org/terms/Terms_Use.cfm

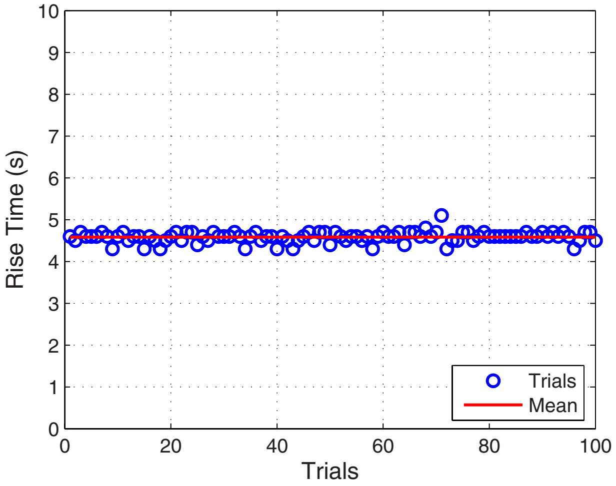

Fig. 16 Scheduler manipulation results: rise time values for 100 runs. The average rise time is 4.58 s. 100% success rate.

signal, but there are no abrupt changes in the fuel flow rate. The engine net thrust (Fig. 20) shows that the transient performance is better than the benchmark stall margin regulator case.

A similar observation can be made based on the rise time calculations. The average value of the rise time over 100 runs is 3.9 s, which is faster than the stall margin regulator case. Additionally, as evident in Fig. 21, there is relatively low variation in rise times from one trial to another. The slowest response among the 100 trials yields a rise time of 4.5 s. The reference stall margin regulator is a deterministic control mode. It is switched on at a given stall margin and is designed to drive the engine to a preset stall margin. In the current integrated stability management approach, the stall margin limiting mode is triggered by stochastic events. Whereas the exact stall margin at which this occurs varies from run to run, the overall results of the 100 trials suggest that this value is lower than that of the reference stall margin mode.

In order to further investigate the capabilities of this control approach, another set of Monte Carlo simulations have been performed. As before, the PLA command is stepped from idle to full power but at cruise conditions of 0.8 Mach and 35,000 ft (10,688 m) altitude. This speed could represent an aggressive inflight engine restart, a worst-case operational scenario for the aircraft as well as the engine control system. The integrated stability management approach is found to be reasonably reliable in this extreme condition. Of the 100 trials that are simulated (Fig. 22), the control approach was unsuccessful in only one case. The average rise time of 17.8 s compares favorably to the 18.7 s obtained with the stall margin regulator. The time traces for a representative run are shown in Figs. 23 and 24. The engine operates for a longer duration near the compressor stability limits. The time taken for the completion of the transient is significantly longer than the sea-level case.

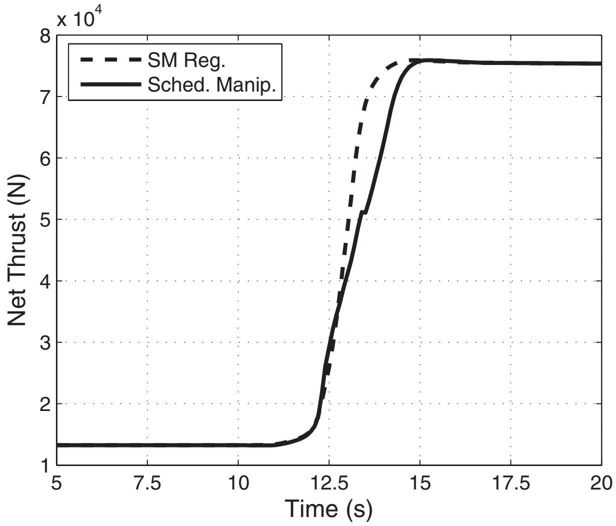

Fig. 18 Scheduler manipulation results: engine thrust response for a representative run

The other two methods, direct fuel and scheduler manipulation, are unsuccessful in this extreme case. The lack of sophistication in the direct fuel manipulation causes continual fuel reduction until the engine essentially shuts down. Even when always active, the scaled down acceleration scheduler is unable to maintain a posi-

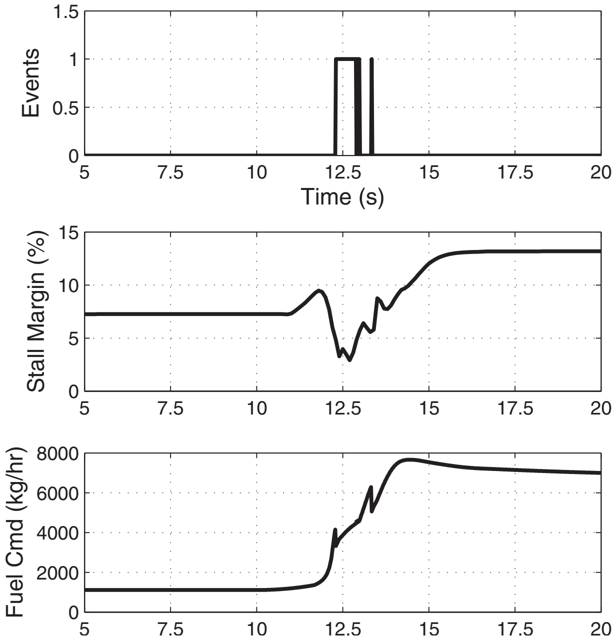

Fig. 17 Scheduler manipulation results: stall margin, events, and fuel command signals for a representative run

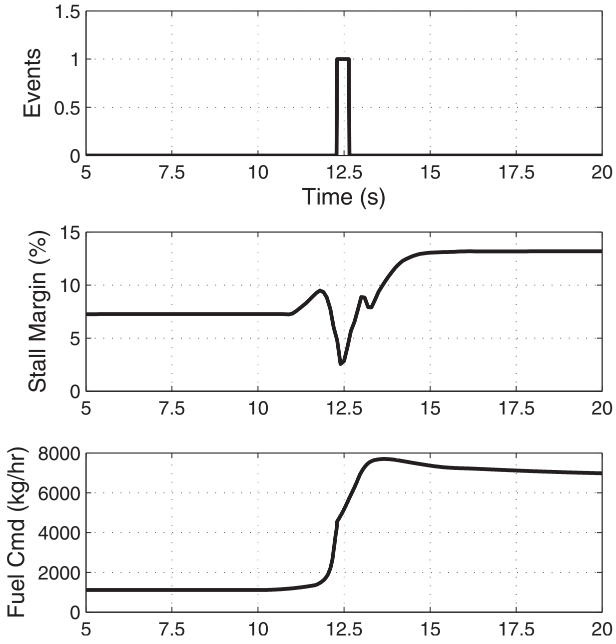

Fig. 19 Integrated stability management results: engine thrust response for a representative run

Downloaded 02 Jun 2010 to 171.66.16.109. Redistribution subject to ASME license or copyright; see http://www.asme.org/terms/Terms_Use.cfm

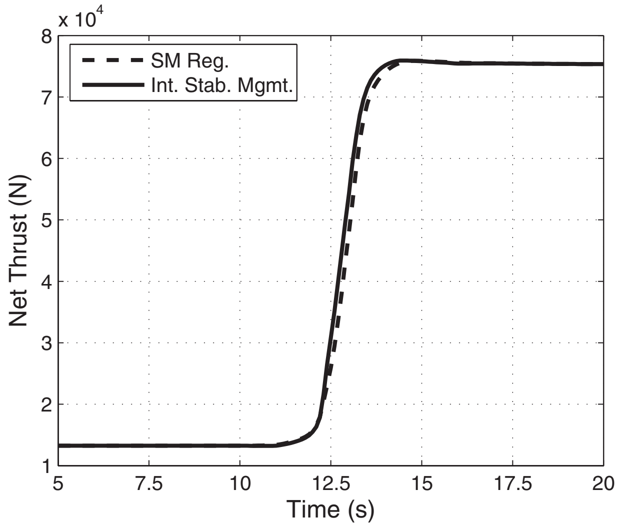

Fig. 20 Integrated stability management results: rise time values for 100 runs. The average rise time is 3.91 s. 100% success rate.

tive stall margin through the duration of the transient. Consequently, it also fails when used in the fuel scheduler manipulation approach.

Discussion. The results to date show the potential operability benefits of active compressor stability management. An advantage of the current approach is its physical foundation. The correlation measure, which forms the core of stability management, quantifies the cycle-to-cycle periodicity of blade-level pressure oscillations. This periodicity deteriorates as the compressor is loaded toward its stability limits. The self-normalization nature of the technique allows it to accommodate engine-to-engine variations, manufacturing tolerances, and different compressors. Dhingra et al. [17] showed the sensitivity of the correlation measure to the aerodynamic health of the blade as well as tip clearances. Hence, the measure is expected to reflect engine deterioration, but the impact on the controller performance needs further analysis.

Correlation-measure-based stability management is relatively simple to implement. Other approaches to intelligent engine control, such as model-based control where engine parameters are estimated from an on-board model, are relatively complex and may have significant computational requirements. Model-based control requires both a high-fidelity engine simulation that can run at least in real-time and the ability to reliably tune the simulation to account for engine-to-engine differences due to factors such as deterioration and operating condition uncertainties [23]. If such a model can be reliably implemented, its application extends beyond stability management. The correlation measure is a physical measure of the compressor stability limits and has been validated on different platforms. The issue at hand is to optimally utilize this measure in an integrated engine controller.

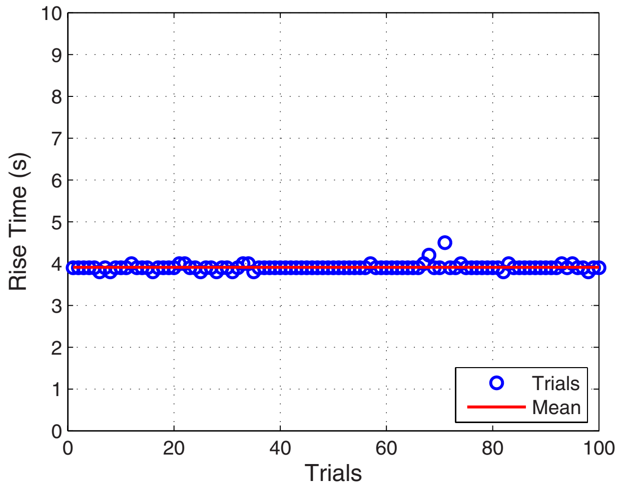

Fig. 21 Integrated stability management results: stall margin, events, and fuel command signals for a representative run

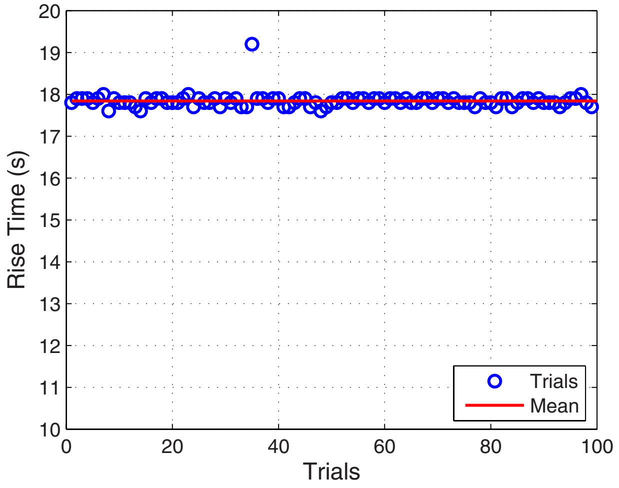

Fig. 22 Integrated stability management at cruise conditions: rise time values for 100 runs. The average rise time is 17.84 s. 99% success rate (failed run not shown).

Conclusions

Active compressor stability management is a viable route toward intelligent engine control. The system is based on the correlation measure developed at the School of Aerospace Engineering, Georgia Institute of Technology. Past research has established the strong relationship between the correlation measure and proximity to the compressor stability limit. An experimentally verified stochastic model of the correlation measure has also been developed.

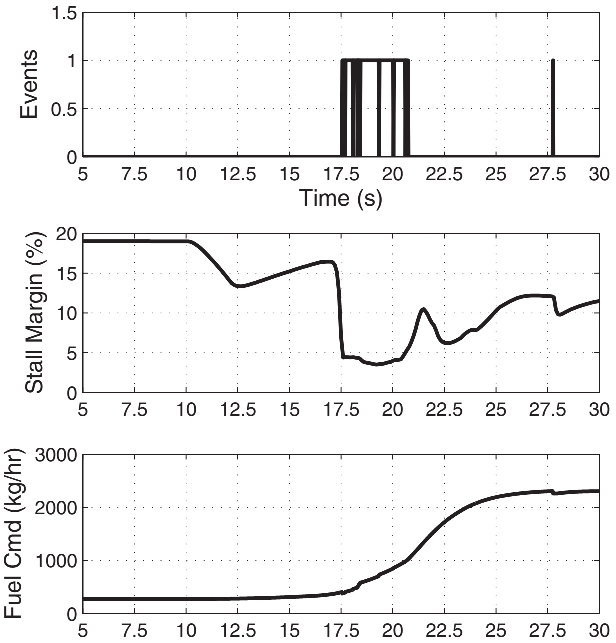

Fig. 23 Integrated stability management at cruise conditions: stall margin, events, and fuel command signals for a representative successful run

Downloaded 02 Jun 2010 to 171.66.16.109. Redistribution subject to ASME license or copyright; see http://www.asme.org/terms/Terms_Use.cfm

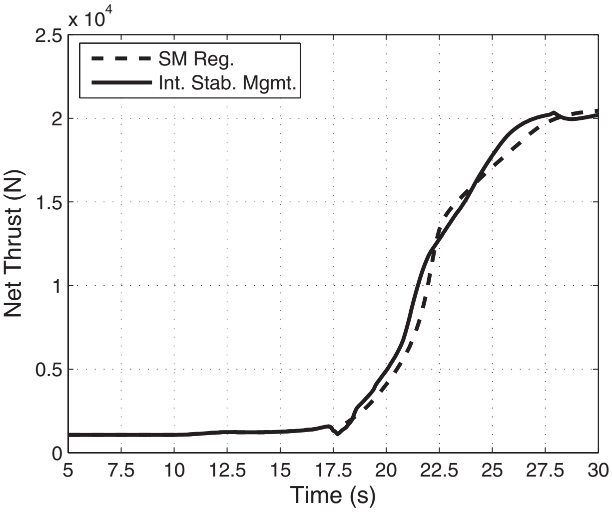

Fig. 24 Integrated stability management at cruise conditions: engine thrust response for a representative successful run

This work describes the use of the stochastic model and the MAPSS environment to evaluate three different methods of implementing the stability management system on a military-type turbofan engine. The methods were tested with a severe PLA step command from idle to full power at static sea-level conditions. The results demonstrate both the benefits of the system on engine operability and its applicability to current and future engine platforms.

Direct manipulation of the fuel flow command is sufficient to avoid stall during the engine acceleration. However, the simplicity of the control logic causes fluctuations in the net thrust response and can even prevent the engine from reaching the desired thrust level. Manipulation of the fuel scheduler is a promising alternative. In contrast to the fuel manipulation method, this control scheme indirectly modulates the fuel command through activation-deactivation of the acceleration scheduler and hence the fuel flow limits. As a result, the undesirable characteristics in the control channel and engine response are all but eliminated. Yet, its simplicity facilitates implementation of the active control scheme with a minimal amount of additional control logic and thus would be useful for existing engine lines.

Finally, a modified stall margin regulator feeding off a somewhat arbitrary constant error has been shown to be a successful method for integrating a compressor stability management system into an advanced intelligent engine controller. This work has shown the benefits of the integrated approach over the simple add-on method. Further analysis as well as numerical experiments would be necessary to fully comprehend the capabilities and limitations of this approach before implementation in a production environment.

Acknowledgment

This work was funded by the NASA University Research Engineering Technology Institute (URETI) on Aeropropulsion and Power Technology (UAPT) and the GE Aircraft Engines University Strategic Alliance (GEUSA) program for compressor stability management at the Georgia Institute of Technology. MAPSS was provided by NASA Glenn Research Center. The authors gratefully acknowledge Jonathan S. Litt and Dr. Sanjay Garg of NASA Glenn for their help and support with the engine simulation.

Nomenclature

$C(n)$ = correlation measure
i = index
n = sample index
p = pressure signal
shaft = number of samples per shaft rotation
wnd = window size in the number of samples
μ_{cm} = number of events per second

References

[1] Litt, J. S., Simon, D. L., Garg, S., Guo, T., Mercer, C., Millar, R., Behbahani, A., Bajwa, A., and Jensen, D. T., 2004, "A Survey of Intelligent Control and Health Management Technologies for Aircraft Propulsion Systems," Journal of Aerospace Computing, Information, and Communications, **1**(12), pp. 543–563.

[2] Curry, T., and Behbahani, A., 2004, "Propulsion Directorate/Control and Engine Health Management (Cehm): Real-Time Turbofan Engine Simulation," *IEEE Aerospace Conference Proceedings*, pp. 3414–3423.

[3] Guo, T., Chen, P., and Jaw, L., 2004, "Intelligent Life-Extending Controls for Aircraft Engines," AIAA First Intelligent Systems Technical Conference, Paper No. AIAA-2004-6468.

[4] Moore, F., and Greitzer, E., 1986, "Theory of Post-Stall Transients in Axial Compression Systems: Part 1—Development of Equations," ASME J. Eng. Gas Turbines Power, **108**(1), pp. 68–76.

[5] Moore, F., and Greitzer, E., 1986, "Theory of Post-Stall Transients in Axial Compression Systems: Part 2—Application," ASME J. Eng. Gas Turbines Power, **108**(2), pp. 231–239.

[6] Epstein, A. H., Williams, J. E. F., and Greitzer, E., 1989, "Active Supression of Aerodynamic Instabilities in Turbomachines," J. Propul. Power, **5**(2), pp. 204–211.

[7] Weigl, H. J., Paduano, J. D., Frechette, L. G., Epstein, A. H., Greitzer, E., Bright, M. M., and Strazisar, A. J., 1998, "Active Stabilization of Rotating Stall and Surge in a Transonic Single-Stage Axial Compressor," ASME J. Turbomach., **120**, pp. 625–636.

[8] Badmus, O. O., Chowdhury, S., Eveker, K. M., Nett, C. N., and Rivera, C. J., 1995, "Simplified Approach for Control of Rotating Stall, Part 1: Theoretical Development," J. Propul. Power, **11**(6), pp. 1195–1209.

[9] Badmus, O. O., Chowdhury, S., Eveker, K. M., Nett, C. N., and Rivera, C. J., 1995, "Simplified Approach for Control of Rotating Stall, Part 2: Experimental Results," J. Propul. Power, **11**(6), pp. 1210–1223.

[10] Gysling, D. L., and Greitzer, E., 1995, "Dynamic Control of Rotating Stall in Axial Flow Compressors Using Aeromechanical Feedback," ASME J. Turbomach., **117**(3), pp. 307–319.

[11] D'andrea, R., Behnken, R. L., and Murray, R. M., 1997, "Rotating Stall Control of an Axial Flow Compressor Using Pulsed Air Injection," ASME J. Turbomach., **119**(4), pp. 742–752.

[12] Day, I. J., 1993, "Stall Inception in Axial Flow Compressors," ASME J. Turbomach., **115**(1), pp. 1–9.

[13] Camp, T. R., and Day, I. J., 1998, "A Study of Spike and Modal Stall Phenomena in a Low-Speed Axial Compressor," ASME J. Turbomach., **120**(3), pp. 393–401.

[14] Escuret, J. F., and Garnier, V., 1996, "Stall Inception Measurements in a High-Speed Multistage Compressor," ASME J. Turbomach., **118**(4), pp. 690–696.

[15] Hoss, B., Leinhos, D., and Fottner, L., 2000, "Stall Inception in the Compressor System of a Turbofan Engine," ASME J. Turbomach., **122**(1), pp. 32–44.

[16] Inoue, M., Kuroumaru, M., Iwamoto, T., and Ando, Y., 1991, "Detection of a Rotating Stall Precursor in Isolated Axial Flow Compressor Rotors," ASME J. Turbomach., **113**(2), pp. 281–289.

[17] Dhingra, M., Neumeier, Y., Prasad, J. V. R., and Shin, H., 2003, "Stall and Surge Precursors in Axial Compressors," 39th AIAA/ASME/SAE/ASEE Joint Propulsion Conference and Exhibit, AIAA Paper No. 2003-4425.

[18] Christensen, D., Cantin, P., Gutz, D., Szucs, P., Wadia, A., Armor, J., Dhingra, M., Neumeier, Y., and Prasad, J. V. R., 2006, "Development and Demonstration of a Stability Management System for Gas Turbine Engines," ASME Paper No. GT-2006-90324.

[19] Dhingra, M., Neumeier, Y., Prasad, J. V. R., Breeze-Stringfellow, A., Shin, H., and Szucs, P., 2007, "A Stochastic Model for a Compressor Stability Measure," ASME J. Eng. Gas Turbines Power, **129**(3), pp. 730–737.

[20] Parker, K. I., and Guo, T., 2003, "Development of a Turbofan Engine Simulation in a Graphical Simulation Environment," NASA Technical Report No. TM-2003-212543.

[21] Parker, K. I., and Melcher, K. J., 2004, "The Modular Aero-Propulsion System Simulation (Mapss) Users' Guide," NASA Technical Report No. TM-2004-212968.

[22] Cramer, H., and Leadbetter, M. R., 1967, *Stationary and Related Stochastic Processes*, Wiley, New York.

[23] Adibhatla, S., and Lewis, T. J., 1997, "Model-Based Intelligent Digital Engine Control (Mobidec)," 33rd AIAA/ASME/SAE/ASEE Joint Propulsion Conference and Exhibit, AIAA Paper No. 1997-3192.

Downloaded 02 Jun 2010 to 171.66.16.109. Redistribution subject to ASME license or copyright; see http://www.asme.org/terms/Terms_Use.cfm

R. M. Kavanagh
Hopkinson Laboratory,
Department of Engineering,
Cambridge University,
Trumpington Street,
Cambridge, CB2 1PZ, UK
e-mail: ronan.kavanagh@power.alstom.com

G. T. Parks
Department of Engineering,
Cambridge University,
Trumpington Street,
Cambridge, CB2 1PZ, UK
e-mail: gtp@eng.cam.ac.uk

A Systematic Comparison and Multi-Objective Optimization of Humid Power Cycles—Part I: Thermodynamics

The steam injected gas turbine (STIG), humid air turbine (HAT), and TOP Humid Air Turbine (TOPHAT) cycles lie at the center of the debate on which humid power cycle will deliver optimal performance when applied to an aeroderivative gas turbine and, indeed, when such cycles will be implemented. Of these humid cycles, it has been claimed that the TOPHAT cycle has the highest efficiency and specific work, followed closely by the HAT, and then the STIG cycle. In this study, the systems have been simulated using consistent thermodynamic and economic models for the components and working fluid properties, allowing a consistent and nonbiased appraisal of these systems. Part I of these two papers focuses purely on the thermodynamic performance and the impact of the system parameters on the performance; Part II will study the economic performance. The three humid power systems and up to ten system parameters are optimized using a multi-objective Tabu Search algorithm, developed in the Cambridge Engineering Design Centre. [DOI: 10.1115/1.3026561]

1 Introduction

The analysis of humid power cycles presents a challenge in multi-objective optimization for three reasons. First, as with any power system, there may be a trade-off between cycle efficiency (η_{cycle}), specific work (w), and cost of electricity (COE). Second, the added plant complexity in a humid power cycle increases the need for rigorous thermodynamic and economic evaluation, optimization, and risk analysis. Third, the increased complexity means humid cycles require careful design and analysis as well as a thorough understanding of potential constraints on the systems. In this first paper, the focus is on two objectives: η_{cycle} and w. The second paper studies a third objective: COE.

The HAT cycle was patented in the 1980s [1,2] and the first pilot plant was constructed in Lund University in 2000 [3]. The first full-scale demonstration advanced HAT plant is currently under construction by Hitachi Ltd. (Hitachi-Shi, Japan) [4]. The thermodynamic advantage of the HAT cycle over its simple cycle competitors is that heat in the exhaust is used for both recuperation of the gas precombustion and for heating water in preparation for the humidification process. The heat and mass transfer processes from the water to the gas in a humidification tower increase the mass flow rate of the working fluid in the turbine, which increases both w and η_{cycle} and, assuming additional plant cost is not prohibitively expensive, decreases COE.

Some recent thermodynamic studies have introduced more complex heat exchanger networks [5,6] and demonstrated performance improvements over the basic HAT configuration. The current study will focus on the basic cycle layout, which has been modeled by several authors [7–9] and is illustrated in Fig. 1(*a*).

The STIG cycle (Fig. 1(*b*)) is more commonplace in the industry, since the system is relatively simple compared to the HAT cycle. Steam, generated in a heat recovery steam generator (HRSG), is injected at or before combustion—the latter for power augmentation and the former to suppress NO_x emissions. As for the HAT cycle, the increased mass flow rate and specific heat capacity of the working fluid increase the power output of the turbine. However, the combination of the HRSG and steam injection at high pressure is a more irreversible process than the humidification process in the HAT cycle, as investigated by El-Masri [10].

The TOPHAT cycle is the most ambitious of proposed humid power cycles; the configuration originally proposed by Van Liere [11] is illustrated in Fig. 1(*c*). An economizer generates hot water for the spray-compression process and a recuperator heats the low temperature compressor outlet gas to ensure fuel demand is not excessive. The use of water sprayed between compressor stages to reduce compressor work demand was originally suggested by Utamura et al. [12]—the evaporation of a fine spray of hot water in the working fluid effectively cools the working fluid temperature and, therefore, reduces the work demand. Van Liere patented the swirl-flash technology, which ensures that the water instantaneously evaporates (*flash atomization*) by injecting a very fine spray of hot water. Increasing the water temperature seems counterintuitive if the objective is to reduce the working fluid temperature; however, the latent heat of vaporization is the primary thermodynamic mechanism that reduces the working fluid temperature and increasing the water temperature increases the mass of water that can be evaporated. Christodoulou and Farrugia [13] suggested that water temperatures of 90–120 K above the working fluid saturation temperature ensure effective flash atomization without any nozzle flow instability, which can lead to reduced flow at high temperatures.

A multi-objective Tabu search (TS) algorithm was chosen for its proven robustness and flexibility in handling highly constrained and multivariate problems. This algorithm, developed by Jaeggi et al. [14], generates a Pareto-optimal set of candidate designs, allowing the designer to analyze the trade-off between multiple objectives (for example, η_{cycle}, w, and COE) when selecting the desired system operating point. This optimizer was implemented on the humid air turbine by Kavanagh et al. [15] and is discussed in more detail in the Appendix.

This is a thermodynamic study and, therefore, some of the design implications cannot be fully considered. For instance, higher mass flow rates in the turbine could lead to off-design behavior and high humidity air in the combustion chamber could lead to lower NO_x and reduce flame stability [4]. Commercial applica-

---

Manuscript received April 7, 2008; final manuscript received August 11, 2008; published online April 13, 2009. Review conducted by Dilip R. Ballal.

Copyright © 2009 by ASME

Downloaded 02 Jun 2010 to 171.66.16.109. Redistribution subject to ASME license or copyright; see http://www.asme.org/terms/Terms_Use.cfm

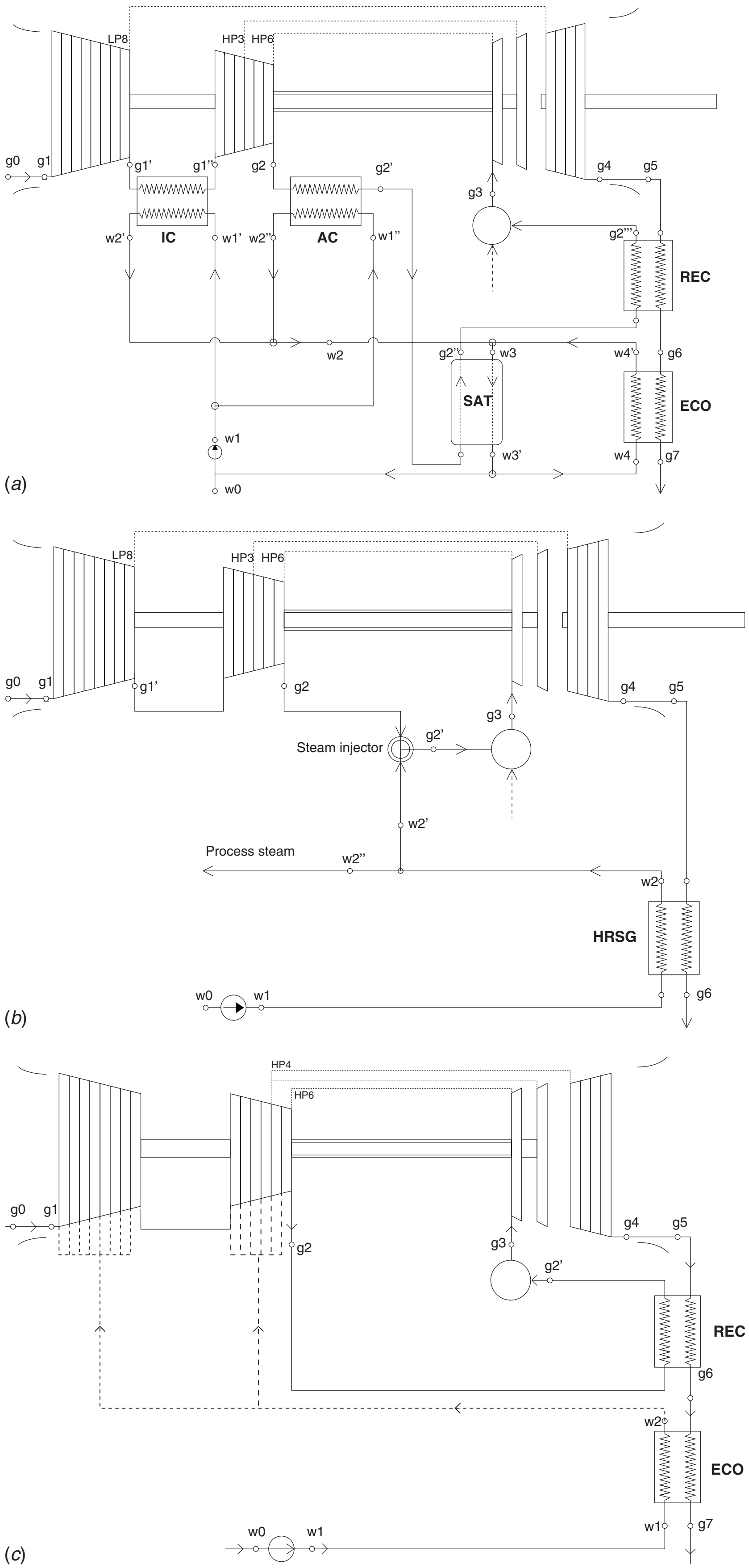

Fig. 1 Humid cycle configurations: (*a*) HAT cycle configuration, (*b*) STIG cycle configuration, and (*c*) TOPHAT cycle configuration

Downloaded 02 Jun 2010 to 171.66.16.109. Redistribution subject to ASME license or copyright; see http://www.asme.org/terms/Terms_Use.cfm

Table 1 Parameters: Gas turbine components

Basic gas turbine components			
Compressor			
$\dot{m}_g$ (kg/s)	100.0		
$n_{\text{stage(IP/HP)}}$	8/6		
$\eta_{p\text{(LP/HP)}}$	0.9		
η_{mech} $(-)$	0.99		
Combustor			
TIT (K)	1573		
Δp_g (%)	5.0		
Turbine			
$n_{\text{stage(IP/HP/FPT)}}$	1/1/4		
$\eta_{p\text{(HP/LP)}}$	0.87		
$\eta_{p\text{(FPT)}}$	0.91		
Stage loading	1.4		
Cooling	Stage 1 Stator/Rotor		Stage 2 Stator/Rotor
$T_{m,\max}$ (K)	1075/1025		1025/1025
K_{comb}	0.5/0.35		0.20/0.15
K_{swirl}		0.5	
$\eta_{c,\text{int}}$		0.7	
ϵ_{film}		0.3	
Exhaust			
Δp_g (%)		5.0	
Generator			
η_{gear} $(-)$		0.993	
η_{elec} $(-)$		0.99	
Disk cooling HP/LP/FPT			
$\dot{m}_{\text{disk}}/\dot{m}_g$ $(-)$		0.02/0.01/0.01	
Humid gas turbine components			
$\Delta p_{g,\text{ic}}$ (%)	6.0		
$\Delta p_{g,\text{eco}}$ (%)	3.0		
$\Delta p_{g,h,\text{rec}}$ (%)	8.5		
$\Delta p_{g,c,\text{rec}}$ (%)	6.0		
$\Delta p_{g,\text{HRSG}}$ (%)	3.5		
$\Delta p_{w,\text{HRSG}}$ (%)	2.5		
T_{w0} (K)	288.15		
p_{w1} (bar)	$p_{g2}+1$		(HAT)
	$p_{g2}+10$		(STIG)
	200		(TOPHAT)

Table 2 Variables, bounds, and constraints

Constraints			
$\Delta T_{\min,hx} > 10$ K		$T_{\text{exhaust}} > 373.15$ K	$\Delta p_{\text{cool}} > 0$ bar
$\Delta T_{\text{approach}} > 10$ K		$\Delta T_{\text{boil}} > 10$ K	
General cycle variables and bounds			
β	10–40	Π	0.2–0.8
STIG cycle variables and bounds			
ΔT_p (K)	10–30	$\bar{m}_{w2}$ (%)	0–100
ΔT_{sh} (K)	0–400	Δp_w (bar)	10–100
HAT cycle variables and bounds			
ε_{rec}	0.50–0.95	ΔT_p (K)	3–7
ε_{ic}	0.50–0.85	$\bar{m}_{\text{ic}}$ $(-)$	0.2–0.8
ε_{ac}	0.50–0.85	$\bar{m}_{\text{eco}}$ $(-)$	0.2–0.8
ε_{eco}	0.50–0.85	$\bar{m}_{\text{sat}}$ (kg_w/kg_g)	0.2–2.0
TOPHAT cycle variables and bounds			
ε_{rec}	0.20–0.95	ε_{eco}	0.20–0.85

tions of the humid cycles are generally in the medium power range, with particular suitability to decentralized energy systems or combined heat and power, as the infrastructure to generate hot water or steam is already in place.

The component performances, listed in Table 1, were selected in collaboration with Rolls-Royce plc (Derby, UK) and are typical for an aeroderivative gas turbine and industrial heat exchanger equipment.

For comparison, simple, intercooled, and intercooled-recuperated cycles were modeled. Two reference combined cycles, using performance data from Gas Turbine World [16], are also used for comparison: CC1 is a combined cycle of similar power output to the cycles studied (65 MW, 53%) and CC2 is a large scale combined cycle (650 MW, 56%). The pressure ratio (β) and pressure ratio split (Π) were optimized for the simple, intercooled, and intercooled-recuperated cycles using the TS algorithm. For the simple cycle, $\beta^*_\eta=32$ and $\beta^*_w=15$. For the intercooled cycle, $\beta^*_\eta=\beta^*_w=40$, $\Pi^*_\eta=0.27$, and $\Pi^*_w=0.51$. For the intercooled-recuperated cycle, $\beta^*_\eta=19.1$, $\beta^*_w=32.3$, and $\Pi^*_\eta=\Pi^*_w=0.5$.

Where possible, parametric studies of the system variables and associated analyses are presented and compared to the optimization results for the humid power cycles to assist interpretation of the optimization results. When performing the parametric studies for all three cycles, constraints are frequently met, which prevents the optimal performance from being located. This phenomenon is common in advanced cycle studies where constraints on pinch points, water temperatures, and exhaust temperature are necessary. The Tabu Search optimization tool allows the designer to overcome this problem by adjusting all the system parameters rather than just addressing a single parameter at a time.

2 Thermodynamic Modeling

The thermodynamic modeling for the humid air turbine and its components has been examined by Kavanagh and Parks [17] and will not be covered here. For the STIG cycle, a HRSG and a steam injector are simulated. The HRSG is defined by its pinch point (ΔT_p) and superheat (ΔT_{sh}), and the steam injector model performs a heat and mass balance to calculate the properties of the steam/air mixture. The steam utilizaton ($\bar{m}_{w2}$) is defined as the percentage of steam generated that is used for injection. For the TOPHAT cycle, the recuperator and economizer are modeled as counterflow gas-gas and gas-liquid heat exchangers, defined by a temperature effectiveness (ε). The wet compression process is modeled as a constant pressure evaporation process, defined by a saturation ratio ($\Phi_{\text{sat}}=\omega/\omega_{\text{sat}}$). The cooling model for these cycles was developed by Young and Wilcock [18,19], and the cooling architecture for each cycle is illustrated in Figs. 1(*a*)–1(*c*).

2.1 STIG Cycle Results. Six variables were optimized for the STIG cycle: β ΔT_{sh}, Π, ΔT_p, Δp_w, and $\bar{m}_{w2}$. Their bounds and the system constraints are listed in Table 2—the exhaust temperature has been constrained to ensure that the gas temperature is above the dew point in the economizers. The Pareto-optimal set for the STIG cycle is illustrated in Fig. 2(*a*) and compared to a parametric study of β and ΔT_{sh} in Fig. 2(*b*)—a maximum efficiency of 49.12% and a maximum specific work of 625 kJ/kg are observed. The design values *selected* for the first three parameters are illustrated in Figs. 2(*c*)–2(*e*). The last three variables all adopted their minimum ($\Delta T^*_p=10$ K and $\Delta p^*_w=10$ bar) or maximum ($\bar{m}^*_{w2}=100\%$) values.

From the parametric study in Fig. 2(*b*), it is clear that β and ΔT_{sh} play an important role in the η_{cycle}/w trade-off. $\beta=25-28$ yields maximum efficiency, while lower β yields maximum specific work. Decreasing β increases the exhaust gas temperature

Downloaded 02 Jun 2010 to 171.66.16.109. Redistribution subject to ASME license or copyright; see http://www.asme.org/terms/Terms_Use.cfm

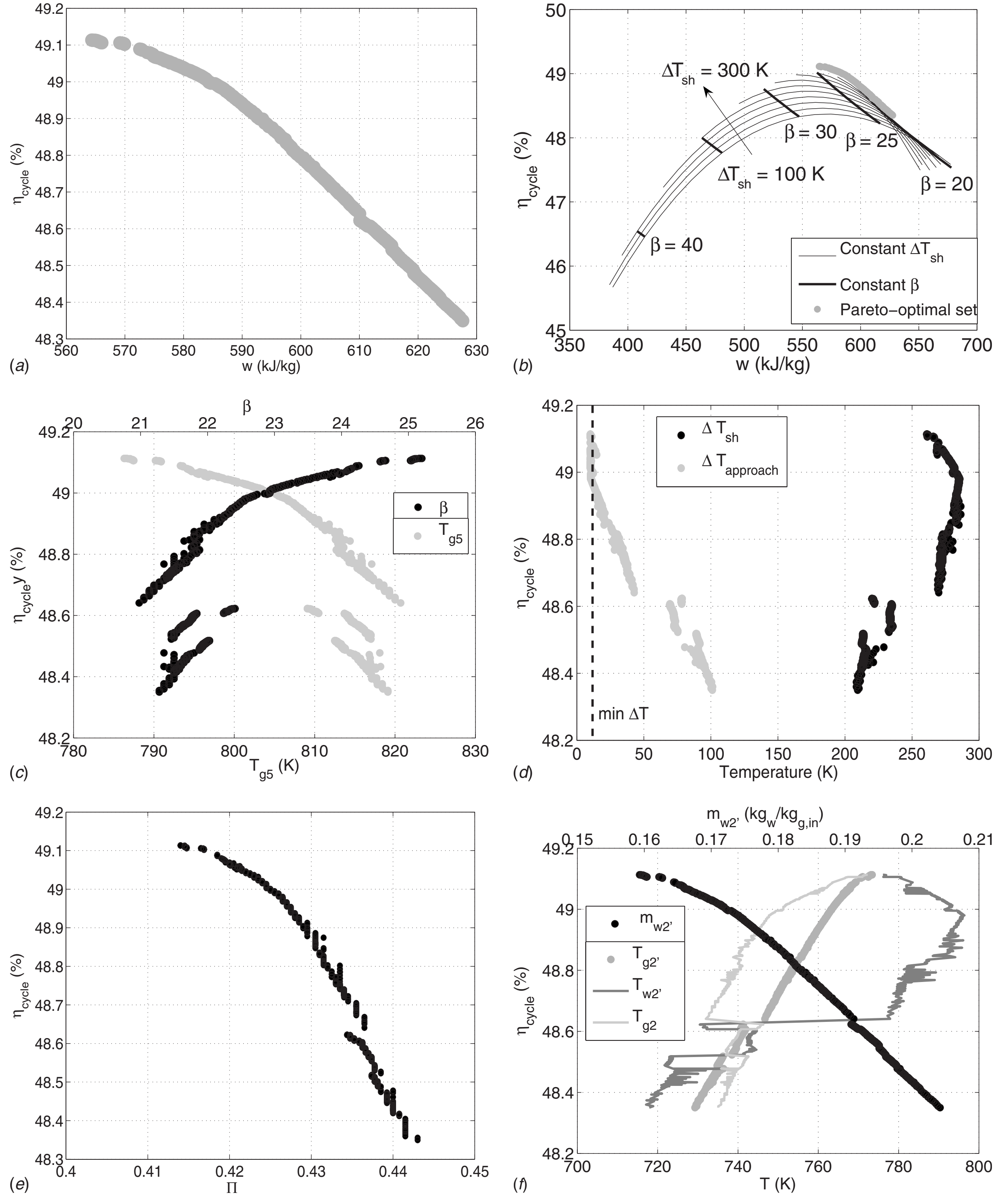

Fig. 2 Results for STIG TS optimization: (*a*) η_{cycle}/w Pareto-optimal set, (*b*) parametric study: $\beta/\Delta T_{sh}$, (*c*) β^* selection and T_{g5} calculated, (*d*) ΔT_{sh} selection and ΔT_{app} calculated, (*e*) Π^* selection, and (*f*) $\dot{m}_{w2'}$ and steam injector temps

and, therefore, the steam injection rate, pushing the maximum efficiency to lower β compared to the simple cycle. For fixed β, increasing ΔT_{sh} reduces the quantity of steam that can be generated and, therefore, reduces w. However, increasing ΔT_{sh} increases the combustor inlet temperature and increases η_{cycle}.

Design values for the Pareto-optimal set of $\beta^*=21-25.2$ are evident in Fig. 2(*c*), with the lowest values yielding maximum w and highest values yielding maximum η_{cycle}. In agreement with the parametric study, Fig. 2(*d*) illustrates that higher ΔT_{sh} favors efficiency, however, ΔT_{sh} reduces from a maximum 286 K at 49% to 260 K at 49.1%. Below η_{cycle}=49%, a steady decrease in ΔT_{sh} to 210 K is observed. To explain the decrease in ΔT_{sh} at high efficiency, it is instructive to compare $\Delta T_{approach}$ and ΔT_{sh} in Fig. 2(*d*). Increasing ΔT_{sh} from 210 K to 276 K reduces $\Delta T_{approach}$ from 100 K to 10 K. Hence, to increase efficiency any further, β must be increased to increase work output, which reduces the

Downloaded 02 Jun 2010 to 171.66.16.109. Redistribution subject to ASME license or copyright; see http://www.asme.org/terms/Terms_Use.cfm

steam generator inlet temperature and, therefore, ΔT_{sh} must be reduced accordingly to ensure that the constraint on $\Delta T_{\mathrm{approach}}$ is not exceeded.

Π^* is illustrated in Fig. 2(*e*), which demonstrates that $\Pi < 0.5$ favors η_{cycle} and w. For a fixed β the HPC coolant flow cannot be changed; however, reducing Π (i.e., β_{LPC}) reduces the LPC coolant temperature and, therefore, the cooling demands, although the coolant pressure is contrained ($\Delta p_{\mathrm{cool}} > 0$). Hence, Π^* increases at low β (low η_{cycle}).

A discontinuity is evident in β^*, ΔT^*_{sh}, and Π^* at $\eta_{\mathrm{cycle}} = 48.65\%$. First, it should be emphasized that two factors contribute to increasing steam generation and, therefore, work output: decreasing β *and* decreasing ΔT_{sh}. Initially, decreasing β *and* ΔT_{sh} yield the best η_{cycle}/w trade-off. However, at a certain point, characterized by the discontinuity, reducing ΔT_{sh} (to increase the steam generation) and increasing β (to increase the work output) yield a superior trade-off than if β were continuously decreased. The turbine exit temperature (T_{g5}), illustrated in Fig. 2(*c*), clearly exhibits the same discontinuity and is a strong function of β. Despite this discontinuity, the steam injection rate ($\dot{m}_{w2'}$ in Fig. 2(*f*)) increases continuously as w increases/η_{cycle} decreases. Also, the steam/air mixture temperature increases steadily as η_{cycle} increases ($T_{g2'}$ in Fig. 2(*f*)), despite the discontinuity in the steam and gas temperatures into the mixer. It is these two metrics which drive the continuous trade-off in efficiency and specific work and this emphasizes that, although there may be a discontinuity in some of the design variables, they are adopted to ensure that the critical performance drivers are carefully selected to generate the optimal η_{cycle}/w trade-off.

Steam injection rates of up to $0.204\ \mathrm{kg}_w/\mathrm{kg}_g$ were achieved at $\Delta T^*_{\mathrm{sh}} = 210$ K and $\beta^* = 21.3$ (where T_{g5} is maximum), yielding the highest work output. For the highest efficiency, steam injection rates of $0.157\ \mathrm{kg}_w/\mathrm{kg}_g$ were achieved at $\Delta T^*_{\mathrm{sh}} = 260$ K and $\beta^* = 25.2$ (minimum T_{g5}).

2.2 HAT Cycle Results. Figure 3(*a*) illustrates the Pareto-optimal set for the HAT cycle and compares it to a $\beta/\varepsilon_{\mathrm{rec}}$ parametric study in Fig. 3(*b*). A maximum efficiency of 51.7% and a specific work of 680 kJ/kg are achieved. The TS optimization tool has clearly pushed the performance of the cycle well beyond the capabilities of the parametric study and these improvements are significantly greater than those found when optimizing the STIG cycle. This is for two reasons. First, throughout the parametric study, constraints were encountered ($\Delta T_{\mathrm{min},hx}$ or ΔT_{boil}). Second, the number of design variables has increased from six to ten.

From the parametric study in Fig. 3(*b*) it is clear that β and $\varepsilon_{\mathrm{rec}}$ play an important role in the η_{cycle}/w trade-off. β^*_η is a strong function of $\varepsilon_{\mathrm{rec}}$ (β^*_η increases from 25 to 35 as $\varepsilon_{\mathrm{rec}}$ decreases from 0.95 to 0.70) and β^*_w is always the maximum in the range studied. Increasing β increases the temperature of the working fluid in IC and AC, thereby increasing the water temperatures and improving the heat and mass transfer processes in the saturator, which increases the work output. However, as β increases, the quantity of heat available for recuperation falls, pushing β^*_η to lower values, where $\varepsilon_{\mathrm{rec}}$ is high and more heat can be recuperated. On the other hand, decreasing $\varepsilon_{\mathrm{rec}}$ reduces the influence of recuperation on η_{cycle} and increases the heat transfer in ECO, thus pushing β^*_η to higher values where higher temperature water is generated.

Figures 3(*c*) and 3(*d*) outline the results for six of the ten variable. $\varepsilon_{\mathrm{ic}}$, $\varepsilon_{\mathrm{ac}}$, $\varepsilon_{\mathrm{eco}}$, and ΔT_p are not illustrated as they all adopted their maximum ($\varepsilon_{\mathrm{ic}}$, $\varepsilon_{\mathrm{ac}}$, $\varepsilon_{\mathrm{eco}}$) or minimum values ($\Delta T_p$). A trial optimization was executed where these variables were set to their maximum values, but the TS algorithm was unable to achieve comparable performance as the system was too highly constrained—this emphasizes the importance of considering multiple variables to overcome apparent constraints.

The design values for β and $\varepsilon_{\mathrm{rec}}$ are illustrated in Fig. 3(*c*). As anticipated from the parametric study, a trade-off between efficiency and power is found when β is decreased from 26.7 to 38.1; $\varepsilon_{\mathrm{rec}}$ behaves as expected by decreasing from its maximum value of 0.95 at maximum η_{cycle} to 0.87 at minimum η_{cycle}.

The design values of Π^* are illustrated in Fig. 3(*d*)—values of 0.59—0.61 agree with a parametric study of β and Π in Fig. 4(*a*). A perfect gas analysis of the HAT cycle was also performed, and the following equation was derived:

$$\Pi^*_\eta = 0.5 + \frac{\ln\left(1 + \frac{(T_{w1}/T_{w0} - 1)}{1/\eta_s + 1/\varepsilon_{\mathrm{rec}} - 1/\eta_s\varepsilon_{\mathrm{rec}}}\right)^{\gamma/2(\gamma-1)}}{\ln(\beta)} \qquad (1)$$

Inserting typical values for the HAT cycle yields $\Pi^*_\eta = 0.61 - 0.62$. These results agree with the findings by Lindquist [3], who suggested $\Pi^*_\eta = 0.597$.

Figure 3(*d*) also exhibits the choice of intercooler ($\bar{m}_{\mathrm{ic}}$) and economizer ($\bar{m}_{\mathrm{eco}}$) flow ratios, which both adopt values slightly below and slightly above 0.5, respectively. We can see from Fig. 3(*e*) that $\bar{m}_{\mathrm{ac}}$ ($\bar{m}_{\mathrm{ac}} = 1 - \bar{m}_{\mathrm{ic}}$) follows the same trend as Π. This would be expected since, if the optimization has been successful and the water temperatures have been maximized, the water flow rates into the intercooler and aftercooler would have to adjust as Π and, therefore, the heat exchanger inlet temperatures change.

Figure 4(*b*) shows a parametric study of $\bar{m}_{\mathrm{sat}}$ and $\bar{m}_{\mathrm{eco}}$, which shows that increasing $\bar{m}_{\mathrm{eco}}$ and decreasing $\bar{m}_{\mathrm{sat}}$ increase η_{cycle} and w. Reducing the saturator water flow rate reduces the water flow rate throughout the system, which increases the water temperature and, therefore, improves the heat and mass transfer processes in the saturator. Increasing the economizer flow rate increases the amount of heat recovered from the exhaust, whereas sending hot water back to the intercooler increases the compressor work. However, decreasing $\bar{m}_{\mathrm{sat}}$ increases the vulnerability of the HAT cycle to boiling. This reduces the range of valid water flow rates into the economizer, as indicated by the narrowing lines as we move from left to right in Fig. 4(*b*). Design values of $\bar{m}^*_{\mathrm{sat}} = 0.9 - 0.93$ are illustrated in Fig. 3(*d*), which are below the minimum values that could be achieved in Fig. 4(*b*) without meeting constraints.

The maximum water temperature reached in the system is illustrated in Fig. 3(*f*), where it is compared to the saturation temperature (boiling point) of the water and the saturator inlet temperature (T_{w3}). Clearly, the whole system has been optimized to ensure that the water temperature is as high as possible without reaching the constraint on ΔT_{boil}—the maximum water temperature is always 10 K below the saturation temperature of the water. Since the saturation temperature is dictated by the system pressure, its behavior and, therefore, the behavior of the maximum water temperature in the system trace the behavior of β. However, the maximum temperature is not always located at the same point in the system, but instead shifts from IC exit to the AC exit throughout the Pareto set, as illustrated in Fig. 3(*g*).

For the heat and mass transfer processes, the saturator inlet temperature (T_{w3}) is a critical variable. In Fig. 3(*f*) T_{w3} follows a similar pattern to the maximum temperature, but lies $1 - 3$ K lower due to the addition of the lower temperature economizer water (not illustrated). The repercussions of the higher water temperature on improving the heat and mass transfer processes and therefore the mass of water added are clear in Fig. 3(*h*).

Two phenomena contribute to the increase in T_{w3} at low η_{cycle}/high w (see Fig. 3(*i*)). First, β increases, which increases the gas temperature into IC ($T_{g1'}$) and AC (T_{g2}). Second, although higher β reduces the exhaust temperature (T_{g5}), $\varepsilon_{\mathrm{rec}}$ decreases, which increases the temperature into the economizer (T_{g6}).

As well as being strongly dependent on the water temperature, the mass flow of water added will also be dependent on $\bar{m}_{\mathrm{sat}}$ and

Downloaded 02 Jun 2010 to 171.66.16.109. Redistribution subject to ASME license or copyright; see http://www.asme.org/terms/Terms_Use.cfm

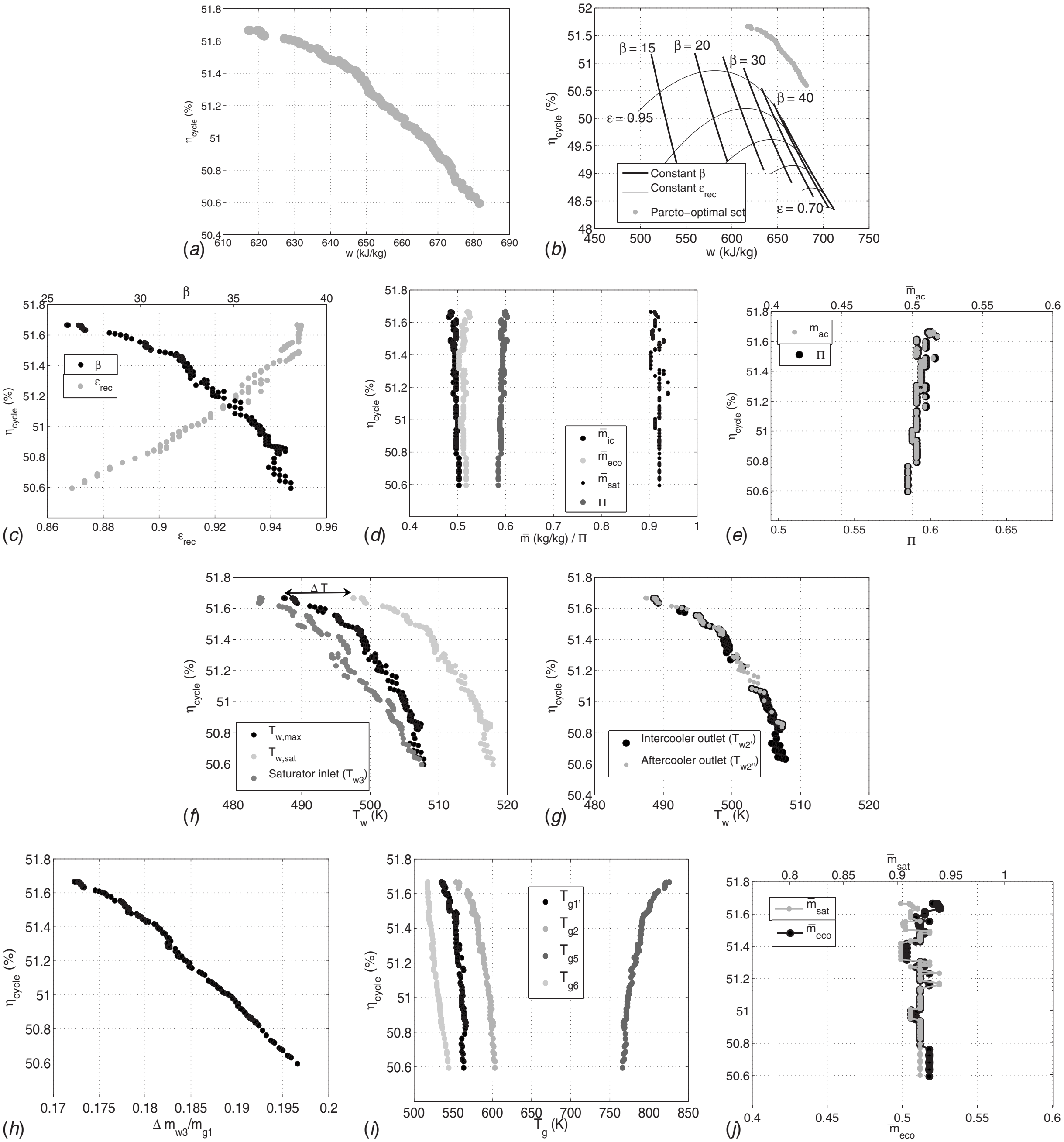

Fig. 3 Results for HAT TS optimization: (*a*) η_{cycle}/w Pareto-optimal set, (*b*) parametric study: β/ε_{rec}, (*c*) β^* and ε^*_{rec}, (*d*) $\bar{m}^*_{eco}$ $\bar{m}^*_{ic}$, $\bar{m}^*_{sat}$, and Π^*, (*e*) $\bar{m}^*_{ac}$ and Π^*, (*f*) T_{max} calculated, (*g*) location of T_{max}, (*h*) $\dot{m}_{w0}$ calculated, (*i*) gas temperature hot/cold end, and (*j*) $\bar{m}^*_{eco}$ and $\bar{m}^*_{sat}$

ΔT_p. Decreasing the pinch point always increases the mass of water added and hence it is always minimized. A study by Kavanagh and Parks [17] revealed that the mass of water added actually increases as water flow rate into the saturator increases (for a constant water temperature), which seems to contradict what has been discussed thus far. However, this study neglected the impact of reducing the water flow rate in the system on water temperature, which will clearly increase as water flow rate is reduced, thus driving up the mass of water added.

It was already identified that increasing $\bar{m}_{eco}$ favored both efficiency and work output, but as $\bar{m}_{sat}$ was decreased, the range of values decreased due to the susceptibility to boiling. So the optimizer should try and increase the economizer flow rate toward the values found in the parametric study, but it will be constrained by the values for $\bar{m}_{sat}$. This is confirmed in Fig. 3(*j*), where the values of $\bar{m}_{eco}$ follow the trend of $\bar{m}_{sat}$ quite closely.

2.3 TOPHAT Results. The optimization variables, bounds, and constraints are listed in Table 2. When optimized using the TS algorithm, a maximum cycle efficiency of 53.4% and a maximum work output of 709 kJ/kg were observed. The Pareto-optimal set is illustrated in Fig. 5(*a*) and compared to a parametric study of β/ε_{rec} in Fig 5(*b*).

In the parametric study it was found that maximizing β maximized efficiency, except for ε_{rec}=0.95, where β^*_η=30 was identified. Generally, high β favors η_{cycle} and w for similar reasons to

Downloaded 02 Jun 2010 to 171.66.16.109. Redistribution subject to ASME license or copyright; see http://www.asme.org/terms/Terms_Use.cfm

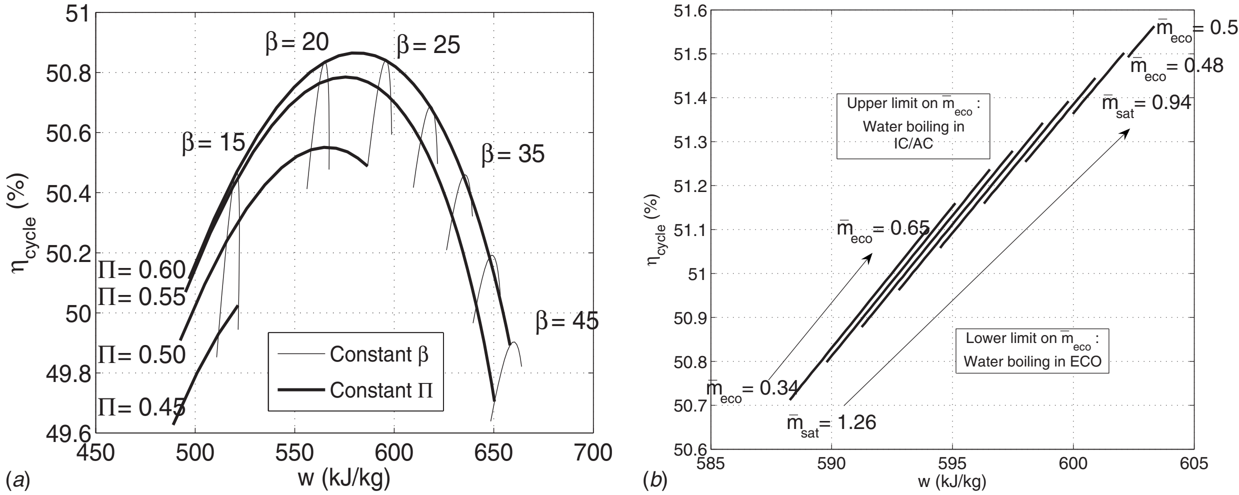

Fig. 4 HAT: Parametric studies of β, Π, and mass flow rates: (*a*) β and Π, and (*b*) $\bar{m}_{eco}$ and $\bar{m}_{sat}$

the intercooled cycle—low compressor demand ensures that increasing overall β continuously increases the net work output. However, for $\varepsilon_{rec}=0.95$, more emphasis is placed on recuperation, and this results in a slight reduction in the optimal β to utilize the exhaust heat and reduce fuel consumption.

Values for Π^* of 0.6–0.78 were found in a parametric study of Π and the water spray temperature, with higher values corresponding to higher water temperatures (Fig. 6(*a*)). $\Pi_w^*=1.0$ for all water temperatures and a minimum compressor demand was located at $\Pi=0.45-0.50$ (not illustrated). As Π increases, the temperature at which water is sprayed in the HPC increases and this

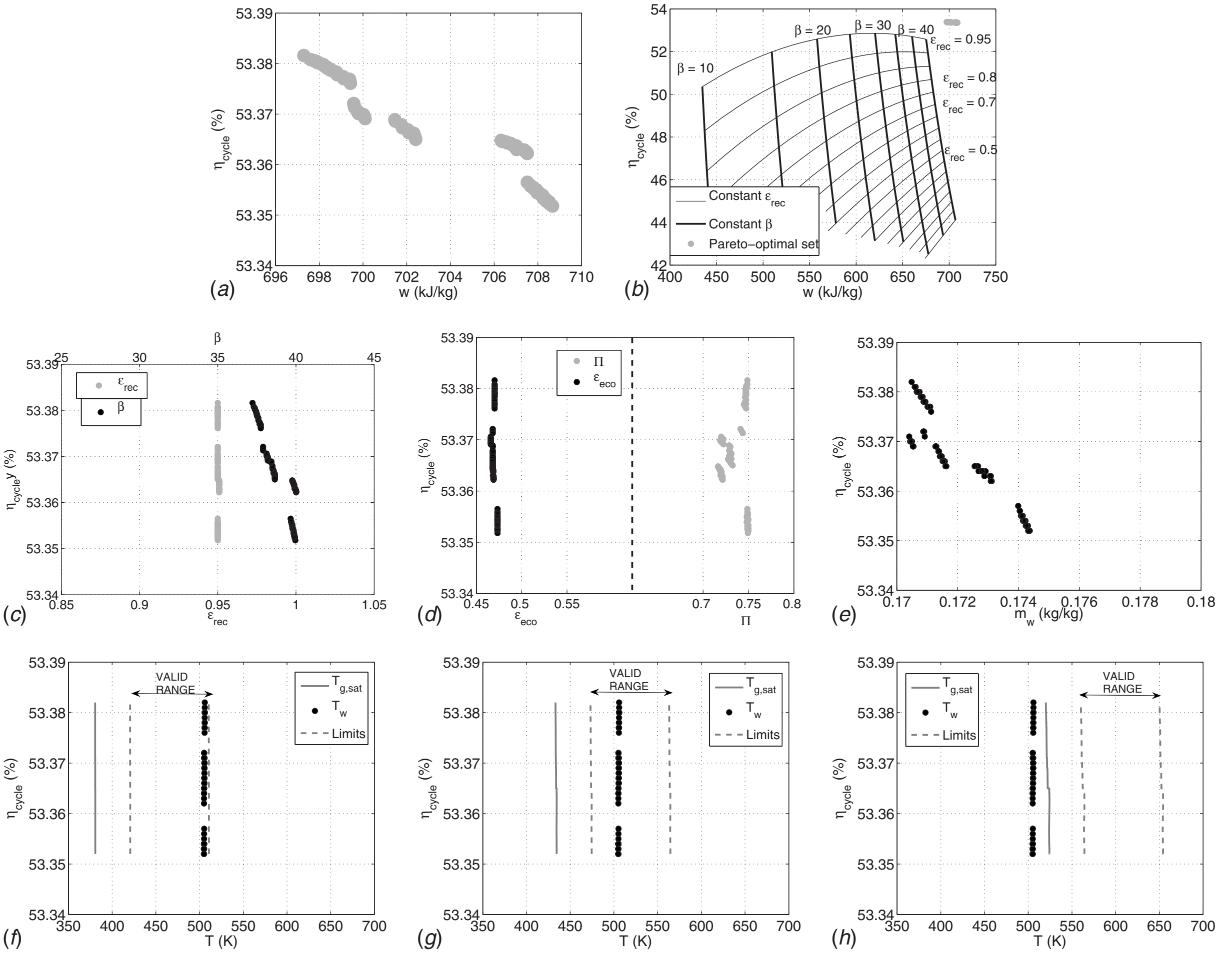

Fig. 5 Results for TOPHAT TS optimization: (*a*) η_{cycle}/w Pareto-optimal set, (*b*) parametric study: $\beta/\Delta\varepsilon_{rec}$, (*c*) β^* selection, (*d*) Π^* selection, (*e*) $\dot{m}_{w0}$ calculated, (*f*) water temperatures in first stage, (*g*) water temperatures in middle stage, and (*h*) water temperatures in last stage

Downloaded 02 Jun 2010 to 171.66.16.109. Redistribution subject to ASME license or copyright; see http://www.asme.org/terms/Terms_Use.cfm

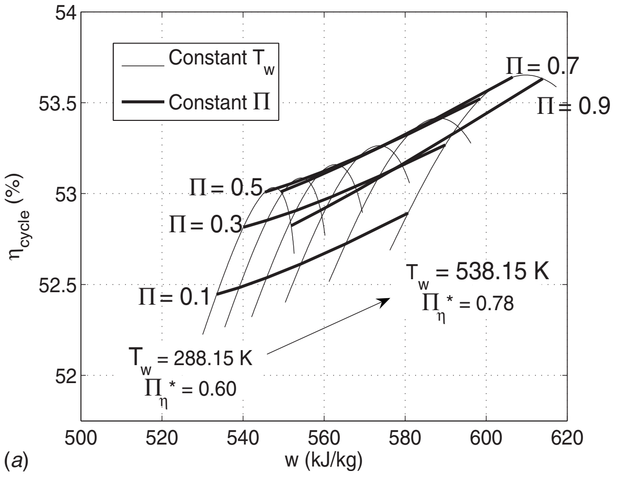

Fig. 6 TOPHAT: Parametric study of Π and T_w: Π and T_w, and (*b*) mass flow-rate of water

increases the mass of water that can be evaporated (Fig. 6(*b*))—this drives the increase in work output as the mass flow rate in the turbines increases. However, increasing Π decreases the compressor outlet temperature, driving up the fuel demand. For $\Pi > 0.50$ the compressor work demand also increases—this results in Π^* between 0.5 and 1. Higher water temperatures reduce the compressor demand, shifting Π^*_η to higher values where the turbine work output is higher. A parametric study (not shown) revealed that ε_{eco} is constrained to values below 0.40 due to a constraint on the maximum water temperature to allow saturation—if the water is too hot, the spray model cannot satisfy the heat and mass balance for the spray stage. Furthermore, for higher values of ε_{eco}, it was found that β also becomes constrained to higher values to ensure that the exhaust gas temperature is not too high, which leads to high water temperatures and the same constraint being met.

The relatively small Pareto-optimal set in Fig. 5(*a*) indicates that the set of parameters that maximize η_{cycle} also maximize w. The values adopted (see Figs. 5(*c*) and 5(*d*)) are as follows: $\beta^* = 37-40$, $\Pi^* = 0.72-0.75$, $\varepsilon^*_{rec} = 0.95$, and $\varepsilon^*_{eco} = 0.468-0.472$. Slightly lower β yields maximum efficiency, in agreement with the parametric study. ε^*_{eco} is higher than the maximum value of 0.40 found previously, which has increased the work output and efficiency. This leads to a reduction in the range of valid β and, therefore, the maximum efficiency is pushed to $\beta = 37$ due to the constraint on the maximum water temperature. Figure 5(*e*) exhibits water consumption rates of 0.17 $kg_w/kg_{g,in}$.

Figures 5(*f*)–5(*h*) compare the water temperature to the saturation temperature of the working fluid and the implications of potential constraints on the water temperature, as suggested by Christodoulou and Farrugia [13], although slightly more relaxed constraints were chosen $(30 < T_w - T_{g,sat} < 140)$. Clearly, for the first and middle stages, the water temperature lies within this constraint, but not for the last stage, where the water temperature is below the saturation temperature of the working fluid. This suggests that additional heat exchangers may be required in order to achieve adequate temperatures for the LPC and HPC.

3 Conclusions

In this paper the TS multi-objective algorithm was applied to the STIG, HAT, and TOPHAT cycles. The results of this optimization are summarized in Fig. 7, where a mass flow rate of 100 kg/s is assumed to calculate the power output. It is notable how the variation in efficiency is significantly lower than the dry cycles. They are compared to optimized simple, intercooled, and intercooled-recuperated cycles as well as to the reference combined cycles.

The maximum STIG cycle efficiency just exceeds 49%, with a corresponding specific work output of 564.3 kJ/kg, which represents an efficiency gain of 10% over the simple cycle and a 72% increase in specific work output. To achieve this ΔT_{sh} is increased to 261 K and $\beta = 25.2$. The work output can be maximized by reducing β to 21.3 and ΔT_{sh} to 210 K, increasing specific work output to 627.6 kJ/kg, which is a 91% increase over the simple cycle although efficiency falls to 48.3%.

The maximum HAT cycle efficiency is 51.7%, with a corresponding specific work output of 617.2 kJ/kg, which represents an efficiency gain of 12.7% over the simple cycle and an 88% increase in specific work output ($\beta = 26$). The work output can be maximized by increasing β to 37.5 (note that this is a reversal of the trend observed for the STIG and, indeed, the simple cycle), increasing the specific work output to 681.6 kJ/kg, which is a 108% increase over the simple cycle although efficiency falls to 50.6%.

The maximum TOPHAT cycle efficiency is 53.4%, with a corresponding specific work output of 706.3 kJ/kg, which represents an efficiency gain of 14.4% over the simple cycle and a 115%

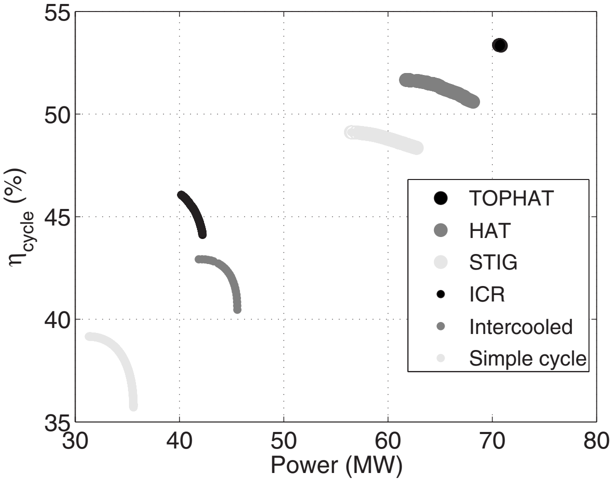

Fig. 7 Comparison of humid cycle Pareto-optimal sets

Downloaded 02 Jun 2010 to 171.66.16.109. Redistribution subject to ASME license or copyright; see http://www.asme.org/terms/Terms_Use.cfm

Table 3 Optimizer parameters

Parameter	Description	Value
n_{stm}	Size of the STM	10
n_{regions}	Search space split into $n_{\text{var}} \times n_{\text{regions}}$ regions in the LTM	4
n_{sample}	No. of points randomly sampled at each move	6
$i_{\text{intensify}}$	No. of iterations after a successful addition to the MTM at which an intensification move is performed	25
$i_{\text{diversify}}$	No. of iterations after a successful addition to the MTM at which a diversification move is performed	45
i_{reduce}	No. of iterations after a successful addition to the MTM at which a step-size reduction move is performed	90
h	Step size (as a percentage of the range of each variable)	8%
δh	Step-size reduction factor	0.5

increase in specific work output (β=39.8). The maximum work output and maximum efficiency coincide closely and the parameters vary only marginally.

On a thermodynamic basis, the TOPHAT cycle competes with the medium scale combined cycle and is followed closely by the HAT cycle. Although there remain technical challenges to overcome for these two cycles (especially the TOPHAT cycle), if careful consideration is given to their design and optimization, they can be very competitive with efficiencies of 52–53%. The STIG cycle performance lags slightly, with efficiencies of 46–49%, however, the STIG cycle carries relatively low technical and investment risks for the industry.

Acknowledgment

This work was carried out in the Hopkinson Laboratory of the Cambridge University Engineering Department. R.M.K. gratefully acknowledges support by grants from the Cambridge European Trust, the EPSRC, and Rolls-Royce plc.

Nomenclature

$\dot{m}$ = mass flow rate (kg/s)
p = pressure (bar)
P = power output (MW)
T = temperature (K)
w = specific work (kJ/kg)
β = pressure ratio
γ = ratio of specific heat capacities (c_p/c_v)
Δ = change in property (%)
ε = heat exchanger effectiveness
η_{cycle} = cycle efficiency (%)
η_p = polytropic efficiency
η_s = isentropic efficiency
Π = pressure ratio split exponent
Φ_{sat} = saturation ratio
$T_{m,\text{max}}$ = maximum metal temperature (K)
K_{comb} = combustion pattern factor
K_{swirl} = combustion swirl factor
$\eta_{c,\text{int}}$ = internal blade cooling efficiency
ϵ_{film} = film cooling effectiveness

Subscripts

c = cold side
cool = cooling air
ECO = economizer
h = hot side
p = pinch point property
sat = saturated state
sh = superheat
turb = turbine
w = water

Superscripts

$*$ = design values selected for Pareto-optimal set
β_w^*, β_η^*, etc. = design values for β at maximum η_{cycle} and w

Acronyms

AC = aftercooler
FPT = free power turbine
IC = intercooler
L/HPT = low/high pressure turbine
L/HPC = low/high pressure compressor
TIT = turbine inlet temperature (K)
TS = tabu search

Common Relations

$\bar{m}_{\text{eco}} = \dot{m}_{w4}/\dot{m}_{w3'}$(HAT)
$\bar{m}_{\text{ic}} = \dot{m}_{w1'}/\dot{m}_{w1}$(HAT)
$\bar{m}_{\text{sat}} = \dot{m}_{w3}/\dot{m}_{g1}$(HAT)
$\bar{m}_{w2} = 100 \times \dot{m}_{w2'}/\dot{m}_{w2}$ (%) (STIG)
$\Delta p_{\text{cool}} = p_{\text{cool}} - p_{\text{turb}}$
$\Delta p_w = p_{w1} - p_{g2}$
$\beta_{\text{LPC}} = \beta^{\Pi}$
$\Delta T_{\text{boil}} = T_{w,\text{sat}} - T_{w,\text{max}}$
$\Delta T_{\text{approach}} = T_{g,\text{in}} - T_{w,\text{out}}$

Appendix: Tabu Search Description and System Parameters

The method combines a local direct-search (Hooke–Jeeves) method with a heuristic method. The *short-term memory* (STM) stores the most recently visited points, which are then tabu and cannot be revisited. When the optimizer proceeds with an optimization step and evaluates a number of designs, the optimizer selects the *nondominated* designs from those evaluated, which are then added to the *medium-term memory*—this defines the Pareto-optimal set of candidate designs. The *long-term memory* stores all designs evaluated and ensures that unexplored regions of the search space are not neglected and that the algorithm does not terminate at local optima. The "Pareto-optimal" set, therefore, offers the designer a host of designs, which reveal the optimal trade-off between multiple objectives, rather than just a single design for each objective. More details can be found in Refs. [14,15]. Table 3 lists the optimizer parameters used in the current research.

References

[1] Nakamura, H., 1981, "Regenerative Gas Turbine With Water Addition and Method of Operation Thereof," European Patent No. 0,053,045.
[2] Rao, A., 1989, "Process for Producing Power," U.S. Patent No. 4,289,763.
[3] Lindquist, T., 2002, "Evaluation, Experience and Potential of Gas Turbine Based Cycles With Humidification," Ph.D. thesis, Lund University, Sweden.
[4] Kuroki, H., Shibata, T., Koganezawa, T., Kizuka, N., Hatamiya, S., and Marushima, S., 2006, "Development of Elemental Technologies for Advanced Humid Air Turbine System," ASME Paper No. GT2006–90639.
[5] Lazzaretto, A., and Segato, F., 2001, "Thermodynamic Optimization of the HAT Cycle Plant Structure Part II: Structure of Heat Exchanger Network," ASME J. Eng. Gas Turbines Power, **123**, pp. 8–16.
[6] Parente, J. O., Traverso, A., and Massardo, A. F., 2003, "Saturator Analysis for an Evaporative Gas Turbine Cycle," Appl. Therm. Eng., **23**, pp. 1275–1293.
[7] Chiesa, P., Lozza, G., Macchi, E., and Consonni, S., 1994, ASME Paper No. 94-GT-424.
[8] Gallo, W. L. R., 1997, "A Comparison Between the HAT Cycle and Other Gas Turbine Based Cycles: Efficiency, Specific Power and Water Consumption," Energy Convers. Manage., **38**, pp. 1595–1604.
[9] Xiao, Y., Cai, R., and Lin, R., 1997, "Modelling HAT Cycle and Thermodynamic Evaluation," Energy Convers. Manage., **38**, pp. 1606–1612.
[10] El-Masri, M., 1988, "A Modified, High Efficiency, Recuperated Gas Turbine Cycle," ASME J. Eng. Gas Turbines Power, **110**, pp. 233–242.
[11] Liere, V., 2001, "The TOPHAT Turbine Cycle," Modern Power Systems, pp. 35–37.
[12] Utamura, M., Takehara, C., and Karasawa, H., 1998, "MAT, a Novel, Open Cycle Gas Turbine for Power Augmentation," Energy Convers. Manage., **39**, pp. 1631–1642.
[13] Christodoulou, M., and Farrugia, N., 2001, "Inlet Fog Boost Advanced

Downloaded 02 Jun 2010 to 171.66.16.109. Redistribution subject to ASME license or copyright; see http://www.asme.org/terms/Terms_Use.cfm

Nozzles Research Project," Rolls Royce plc. Technical Report.
[14] Jaeggi, D., Parks, G., Kipouros, T., and Clarkson, P., 2005, The Third International Conference of Evolutionary Multi-Criterion Optimisation.
[15] Kavanagh, R., Parks, G., and Obana, M., 2007, "Multi-Objective Optimisation of the Humid Air Turbine," ASME Paper No. GT2007–27456.
[16] *Gas Turbine World*, 2006, Pequot, Southport, CT.
[17] Kavanagh, R., and Parks, G., 2006, *Proceedings of the ETN Third International Conference on the Future of Gas Turbine Technology*.
[18] Young, J., and Wilcock, R., 2001, "Modelling the Air-Cooled Gas Turbine: Part I—General Thermodynamics," ASME J. Eng. Gas Turbines Power, **124**, pp. 207–213.
[19] Young, J., and Wilcock, R., 2001, "Modelling the Air-Cooled Gas Turbine: Part II—Coolant Flows and Losses," ASME J. Eng. Gas Turbines Power, **124**, pp. 214–222.

Downloaded 02 Jun 2010 to 171.66.16.109. Redistribution subject to ASME license or copyright; see http://www.asme.org/terms/Terms_Use.cfm

A Systematic Comparison and Multi-Objective Optimization of Humid Power Cycles—Part II: Economics

R. M. Kavanagh
Hopkinson Laboratory,
Department of Engineering,
Cambridge University,
Trumpington Street,
Cambridge CB2 1PZ, UK
e-mail: ronan.kavanagh@power.alstom.com

G. T. Parks
Department of Engineering,
Cambridge University,
Trumpington Street,
Cambridge CB2 1PZ, UK
e-mail: gtp@eng.cam.ac.uk

The steam injected gas turbine (STIG), humid air turbine (HAT), and TOP Humid Air Turbine (TOPHAT) cycles lie at the center of the debate on which humid power cycle will deliver optimal performance when applied to an aeroderivative gas turbine and, indeed, when such cycles will be implemented. Of these humid cycles, it has been claimed that the TOPHAT cycle has the highest efficiency and specific work, followed closely by the HAT and then the STIG cycle. In this study, the systems have been simulated using consistent thermodynamic and economic models for the components and working fluid properties, allowing a consistent and nonbiased appraisal of these systems. Part I of these two papers focused on the thermodynamic performance and the impact of the system parameters on the performance, Part II studies the economic performance of these cycles. The three humid power systems and up to ten system parameters are optimized using a multi-objective Tabu Search algorithm, developed in the Cambridge Engineering Design Centre. [DOI: 10.1115/1.3026562]

1 Introduction

This is Part II of a multi-objective optimization of the steam injected gas turbine (STIG), humid air turbine (HAT), and TOPHAT cycles, which are illustrated in Fig. 1. Part I addressed the optimal thermodynamic performance of these systems and explored the system parameters, which achieved this performance as well as the associated constraints. Only two objectives were considered: η_{cycle} and w. The Pareto-optimal sets for these systems, compared with the simple, intercooled, and intercooled-recuperated cycles are illustrated in Fig. 2.

In Part II, the cost of electricity (COE) is considered as a third objective, which leads to two additional Pareto-optimal sets: $\eta_{\text{cycle}}/\text{COE}$ and COE/w. In order to help understand the interpretation and implications of these results, a simple cycle is also optimized.

2 Economic Modeling

The economic models for the cycles studied were presented by Traverso et al. [1], which originated in Ref. [2], and are summarized in the Appendix. However, it was found that the basic gas turbine engine could be undercosted by up to 60% when multispool engines were studied, therefore the factors outlined in the Appendix were developed for multispool engines to avoid this phenomenon.

Cost modeling for humid cycles can be a challenging prospect since so few systems has been developed in the industry. Therefore, a *factor of safety* will also be calculated, which will provide the designer with a range of capital costs, which will ensure the systems remain cost competitive with medium and large-scale combined cycles. The economic comparison assumes the technologies are *mature* and, therefore, neglects R&D costs. In addition, constant annual running hours of 7500 h are assumed. In Ref. [3] the implication of peaking operation is studied.

The COE is the cost per kilowatt hour of fuel, capital, operations and maintenance, and carbon tax (Eq. (1)). The *internal rate of return* (IRR) is the return on an investment and is a useful measure when comparing different investment options. It is found by calculating the rate of return that would result in a zero *net present value* (NPV). The NPV is the difference between the capital investment and the cash-flow over the economic life of the plant (see Eq. (6)). This requires a sales cost of electricity, which for this study will be assumed to be 9 c/kW h.

$$\text{COE} = \frac{\dot{C}_{\text{TCI}} + \dot{C}_{\text{CO}_2} + \dot{C}_f + \dot{C}_{\text{O\&M}}}{P/3600} \tag{1}$$

$$\dot{C}_{\text{TCI}} = \frac{\Xi_{\text{TCI}} \cdot \text{CRF}}{t \cdot 3600} \tag{2}$$

$$\dot{C}_f = \dot{m}_f \cdot c_f \tag{3}$$

$$\dot{C}_{\text{CO}_2} = \dot{m}_{\text{CO}_2} \cdot c_{\text{CO}_2} \tag{4}$$

$$\text{CRF} = \frac{(1+i)^n \cdot i}{(1+i)^n - 1} \tag{5}$$

$$\text{NPV} = \text{TCI} + \sum_{j=1}^{n} \frac{C_j}{(1+\text{IRR})^j} \tag{6}$$

2.1 Simple Cycle. Before proceeding to the multi-objective optimization of humid cycles, it is instructive to optimize the simple cycle. Figure 3(*a*) plots the η_{cycle}/w contours for a range of pressure ratios and turbine inlet temperature (TIT) for the simple cycle with COE contours superimposed. For TIT=1573 K: $\beta^*_\eta=32$, $\beta^*_{\text{COE}}=28$, and $\beta^*_w=15$.

The location of the optimal pressure ratio for minimum COE (β^*_{COE}) is an important one for designers—for the simple cycle $\beta^*_w < \beta^*_{\text{COE}} < \beta^*_\eta$, and β^*_{COE} lies close to β^*_η. Two factors contribute to this behavior. First, decreasing β lowers the capital costs and, therefore, the capital cost-rate ($\dot{C}_{\text{TCI}}$), in Eq. (2), which therefore lowers the contribution to COE ($\dot{C}_{\text{TCI}} \times 3600/P$), in Eq. (1)—this pushes the minimum COE to lower pressure ratios. Furthermore,

---

Manuscript received April 7, 2008; final manuscript received August 11, 2008; published online April 13, 2009. Review conducted by Dilip R. Ballal.

Copyright © 2009 by ASME

Downloaded 02 Jun 2010 to 171.66.16.109. Redistribution subject to ASME license or copyright; see http://www.asme.org/terms/Terms_Use.cfm

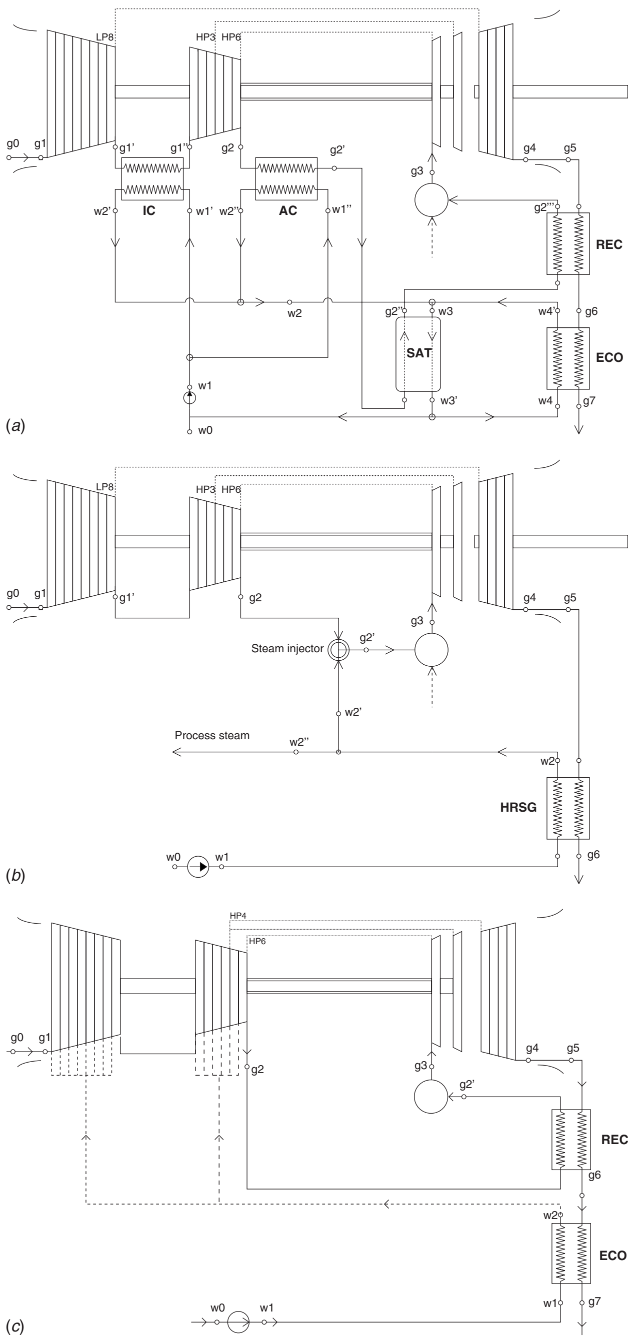

Fig. 1 Humid cycle configurations: (*a*) HAT cycle configuration, (*b*) STIG cycle configuration, and (*c*) TOPHAT cycle configuration

decreasing β increases the work output and, therefore, dilutes the capital contribution to COE—this also pushes the minimum COE to lower pressure ratios. However, because of the dominance of fuel costs when calculating COE (Eq. (1)), β^*_{COE} lies closer to β^*_η than to β^*_w (maximum work output), or to $\beta_{\min}=10$ (minimum capital cost).

Applying the Tabu search (TS) optimization algorithm yields the three Pareto-optimal sets in Figs. 4(*a*)–4(*c*). They are superimposed in the η_{cycle}/w domain in Fig. 3(*b*) and compared with the parametric contours from Fig. 3(*a*). Pareto 2 ($\eta_{\mathrm{cycle}}/\mathrm{COE}$) and Pareto 3 ($\mathrm{COE}/w$) are clearly subsets of Pareto 1 (η_{cycle}/w). Pareto 1 defines the set of designs between maximum η_{cycle} and maximum w, Pareto 2 defines the set of designs between maximum η_{cycle} and minimum COE, and Pareto 3 defines the set of designs between minimum COE and maximum w. The *inflection point* is the location of minimum COE and separates Paretos 2 and 3.

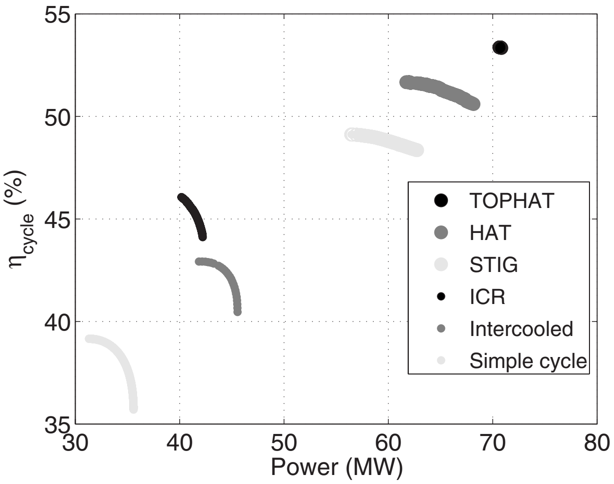

Fig. 2 Comparison of humid cycle Pareto-optimal sets

The design values for β are shown in Figs. 4(*d*)–4(*f*). For Pareto 1, $15<\beta^*<32$; for Pareto 2, $28<\beta^*<32$; and for Pareto 3, $15<\beta^*<32$. The minimum COE (the inflection point) is clearly defined at $\beta^*_{\mathrm{COE}}=28$. This is quite a rudimentary optimization compared with humid cycles but serves to aid interpretation of later optimization results.

2.2 STIG Cycle. The three Pareto-optimal sets for the STIG cycle are superimposed in Fig. 5(*a*) in the η_{cycle}/w domain. As for the simple cycle, there is a clear inflection point, however, unlike the simple cycle, Paretos 2 and 3 are not subsets of Pareto 1. Pareto 1 is the same Pareto-optimal set as in Part I of these two papers.

Paretos 2 and 3 are plotted separately in Figs. 5(*b*) and 5(*c*) with the associated design variables in Figs. 5(*d*)–5(*i*). For Pareto 2 (Fig. 5(*d*)), a pressure ratio of 23.7 yields the minimum COE and, as for Pareto 1, 25.3 yields the maximum efficiency. For Pareto 3 (Fig. 5(*g*)), a pressure ratio of 21.3 yields the maximum work output and 23.7 yields the minimum COE. Figure 5(*j*) compares the adopted pressure ratios for the three Pareto-optimal sets. From this figure, the inflection point at $\beta=23.7$ is obvious. There is a very clear divergence between the pressure ratios adopted for Paretos 1 and 3, with higher pressure ratios being adopted for Pareto 3. Since COE and w are the emphasis of Pareto 3, this seems to be counterintuitive since higher pressure ratios increase capital costs—the key to this phenomenon lies in the design values for the superheat.

$\Delta T^*_{\mathrm{sh}}=260-270$ K are identified for Pareto 2 in Fig. 5(*e*), with the inflection point to Pareto 3 occurring at 265 K. Decreasing the superheat below this value in Pareto 3 toward 210 K (Fig. 5(*h*)) increases COE and specific work. The superheat selection for Paretos 2 and 3 diverge considerably in Fig. 5(*k*) at the inflection point, with lower superheat favoring lower COE. Figure 6, which plots a parametric study of ΔT_{sh} and β, provides the explanation for this behavior. For constant β, increasing the superheat increases η_{cycle} and reduces w. However, a minimum COE is located at slightly lower ΔT_{sh} since, to maintain a low COE, a higher work output is favorable. This follows similar logic to the location of β^*_{COE} for the simple cycle. Also, recall that for Pareto 1, the superheat was increased as far as possible in order to maximize efficiency, which required a reduction in pressure ratio in order to achieve sufficiently high exhaust temperatures. Now a

Downloaded 02 Jun 2010 to 171.66.16.109. Redistribution subject to ASME license or copyright; see http://www.asme.org/terms/Terms_Use.cfm

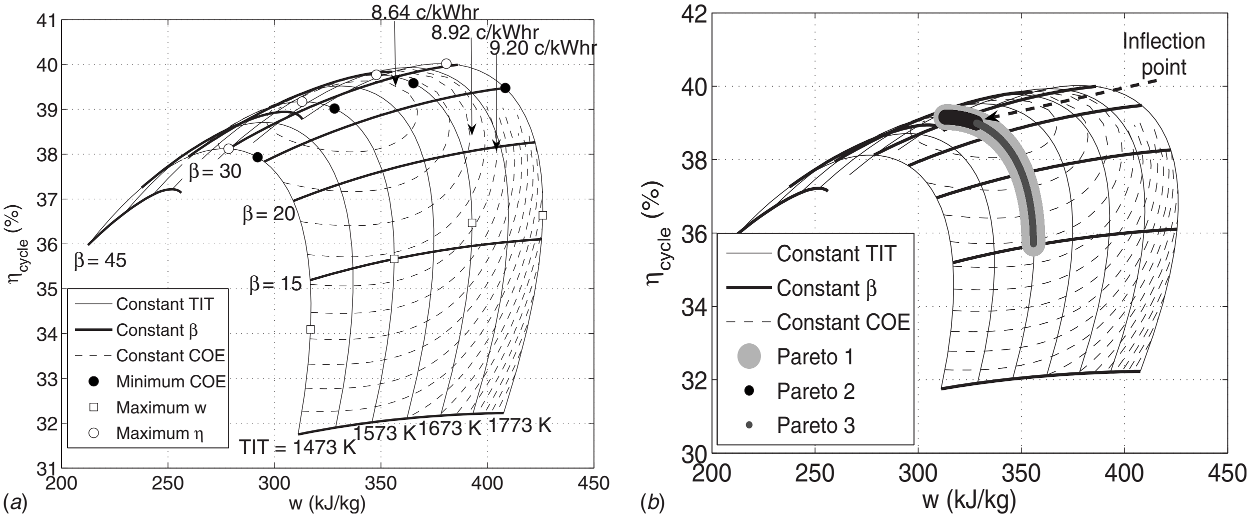

Fig. 3 Comparison of Pareto-optimal sets. (*a*) Parametric contours:*β* and TIT. (*b*) Pareto-optimal sets and parametric contours.

simultaneous increase in pressure ratio and a decrease in superheat increase the work output and lower COE. Hence, for Pareto 1, the TS optimizer is constantly pushing ΔT_{sh} to its maximum value to reduce fuel input, but for Pareto 3, a slightly lower ΔT_{sh} and higher β to ensure higher work output and lower COE. Figure 7 plots the three Pareto-optimal sets in the COE/w domain emphasizing the superior COE/w set for Pareto 3 compared with Pareto 1.

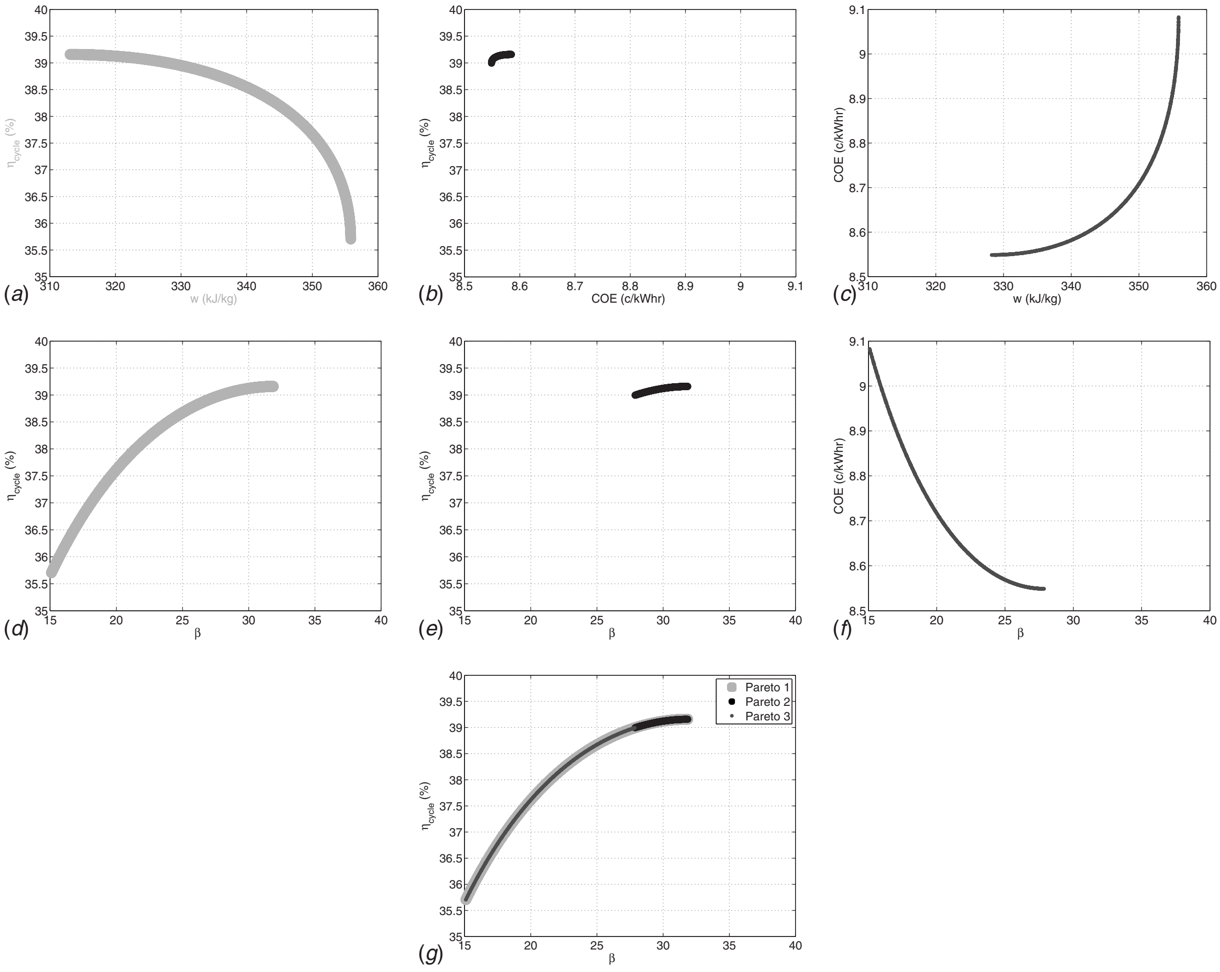

Fig. 4 Results for simple cycle TS optimization. (*a*) Pareto 1: η_{cycle}/w Pareto-optimal set; (*b*) Pareto 2: η_{cycle}/COE Pareto-optimal set; (*c*) Pareto 3: COE/w Pareto-optimal set; (*d*) Pareto 1: β^* selection; (*e*) Pareto 2: β^* selection; (*f*) Pareto 3: β^* selection; and (*g*) P1–3: β^* selection.

Downloaded 02 Jun 2010 to 171.66.16.109. Redistribution subject to ASME license or copyright; see http://www.asme.org/terms/Terms_Use.cfm

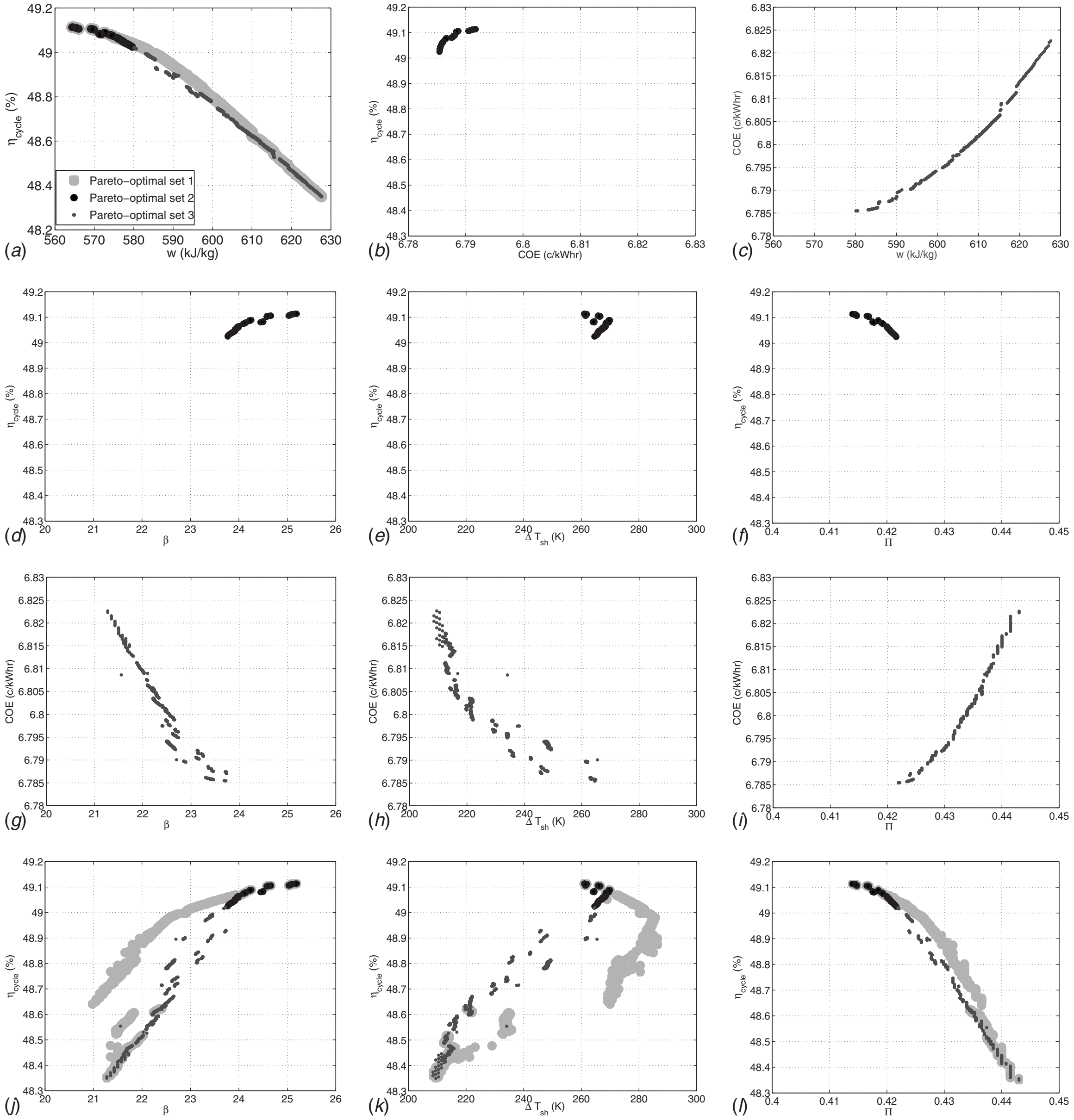

Fig. 5 Results for STIG cycle TS optimization. (*a*) Paretos 1–3 in η_{cycle}/COE domain; (*b*) P2: η_{cycle}/COE Pareto-optimal set; (*c*) P3: COE/*w* Pareto-optimal set; (*d*) P2: β^* selection; (*e*) P2: ΔT^*_{sh} selection; (*f*) P2: Π^* selection; (*g*) P3: β^* selection; (*h*) P3: ΔT^*_{sh} selection; (*i*) P3: Π^* selection; (*j*) P1–3: β^* selection; (*k*) P1–3: ΔT^*_{sh} selection; and (*l*) P1–3: Π^* selection.

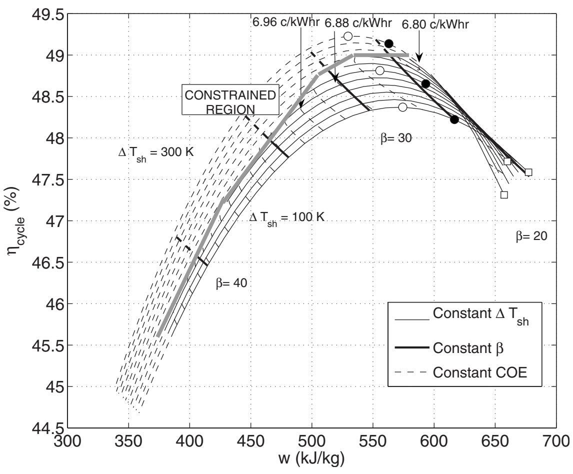

Fig. 6 STIG cycle parametric contours: β and ΔT_{sh}

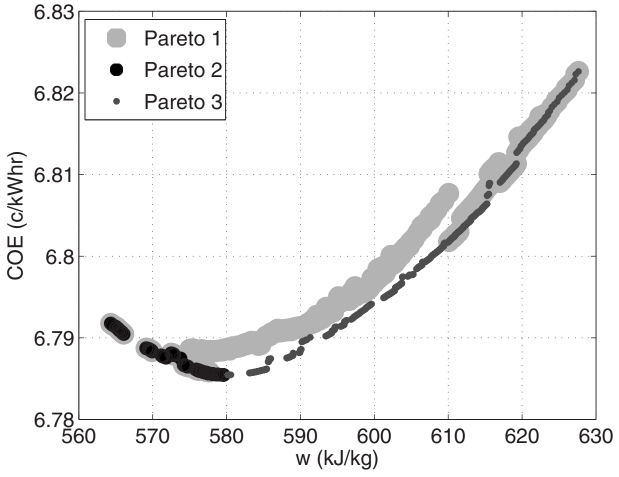

Fig. 7 STIG cycle: three Pareto-optimal sets in COE/*w* domain

Downloaded 02 Jun 2010 to 171.66.16.109. Redistribution subject to ASME license or copyright; see http://www.asme.org/terms/Terms_Use.cfm

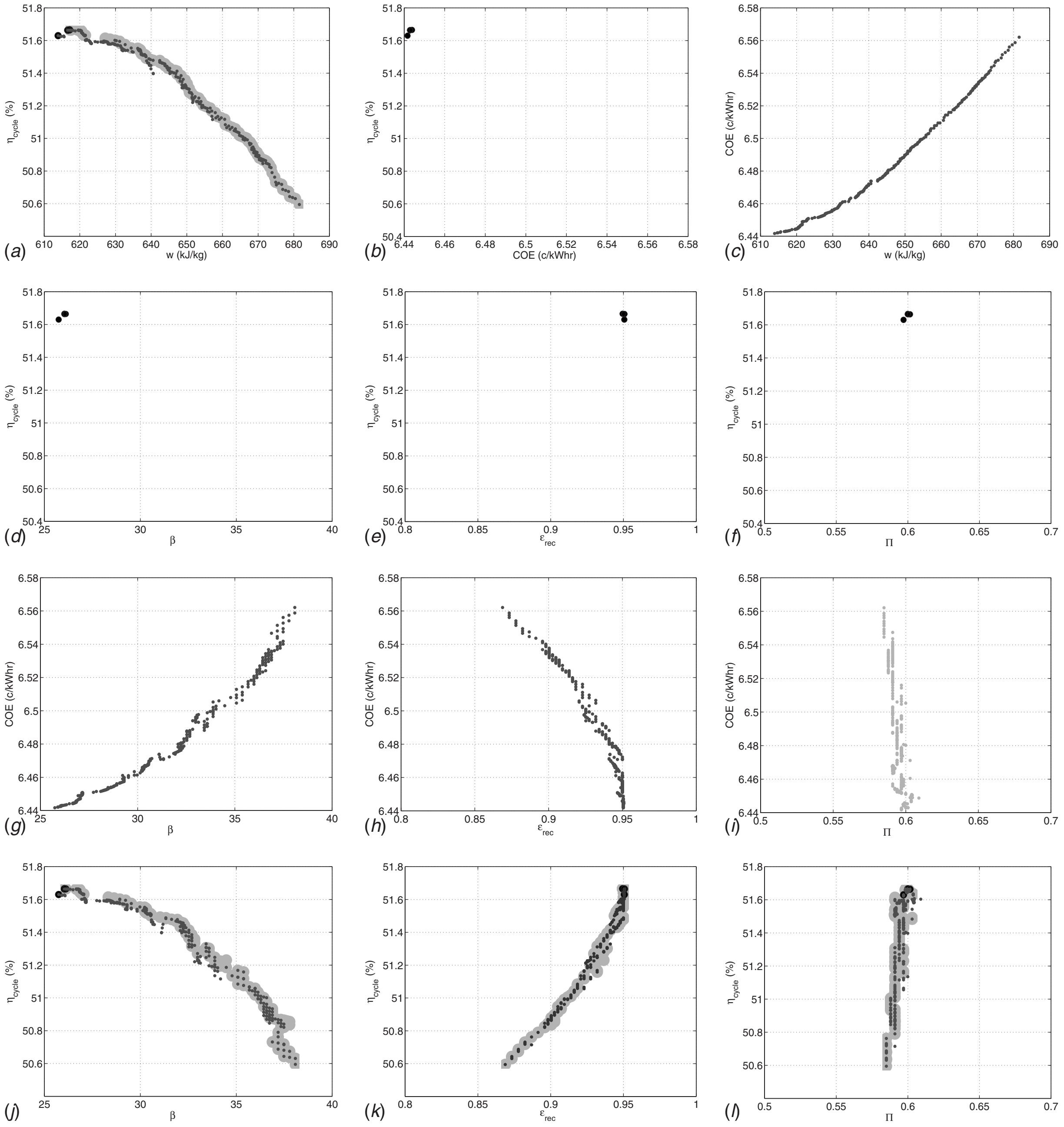

Fig. 8 Results for HAT cycle TS optimization. (*a*) Paretos 1–3 in η_{cycle}/COE domain; (*b*) P2: η_{cycle}/COE Pareto-optimal set; (*c*) P3: COE/*w* Pareto-optimal set; (*d*) P2: β^* selection; (*e*) P2: $\varepsilon^*_{\text{rec}}$ selection; (*f*) P2: Π^* selection; (*g*) P3: β^* selection; (*h*) P3: $\varepsilon^*_{\text{rec}}$ selection; (*i*) P3: Π^* selection; (*j*) P1–3: β^* selection; (*k*) P1–3: $\varepsilon^*_{\text{rec}}$ selection; and (*l*) P1–3: Π^* selection.

2.3 HAT Cycle. The three Pareto-optimal sets for the HAT cycle are superimposed in Fig. 8(*a*). There is no obvious inflection point, which implies that the maximum η_{cycle} and the minimum COE coincide. Paretos 2 and 3 are subsets of Pareto 1, so the design variable, which tends to maximize η_{cycle} also minimizes COE, unlike in the STIG cycle where maximizing ΔT_{sh} would increase η_{cycle} but not the COE due to the reduction in w.

Figure 9(*a*) plots a parametric study of $\beta/\varepsilon_{\text{rec}}$. Now, $\beta^*_{\text{COE}} < \beta^*_{\eta} < \beta^*_{w}$ unlike the STIG and simple cycles where $\beta^*_{w} < \beta^*_{\text{COE}} < \beta^*_{\eta}$. Also, β^*_{COE} and β^*_{η} are much closer together than for the STIG and simple cycles. As discussed in the simple cycle study, decreasing β lowers $\dot{C}_{\text{TCI}}$ and, therefore, the contribution to COE—this pushes β^*_{COE} to lower values. However, unlike the STIG and simple cycles, decreasing β decreases the work output and this increases the contribution to COE—this pushes β^*_{COE} much closer to β^*_{η}, and this results in a small set of designs in Pareto 2.

Figures 8(*d*)–8(*f*) illustrate the design values for Pareto 2—for this set η_{cycle} is increasing, but COE also increases due to the reduction in work output at low β and high ε_{rec}. The designs for Pareto 3 in Figs. 8(*g*)–8(*i*) are essentially identical to Pareto 1, as illustrated by Figs. 8(*j*)–8(*l*).

2.4 TOPHAT. The three Pareto-optimal sets for TOPHAT in the η_{cycle}/w domain are illustrated in Fig. 10(*a*). As for the HAT cycle, there is no obvious inflection point, as illustrated by the very small Pareto 2 in Fig. 10(*b*). This is confirmed in the parametric study in Fig. 9(*b*), where the minimum COE lies very close

Downloaded 02 Jun 2010 to 171.66.16.109. Redistribution subject to ASME license or copyright; see http://www.asme.org/terms/Terms_Use.cfm

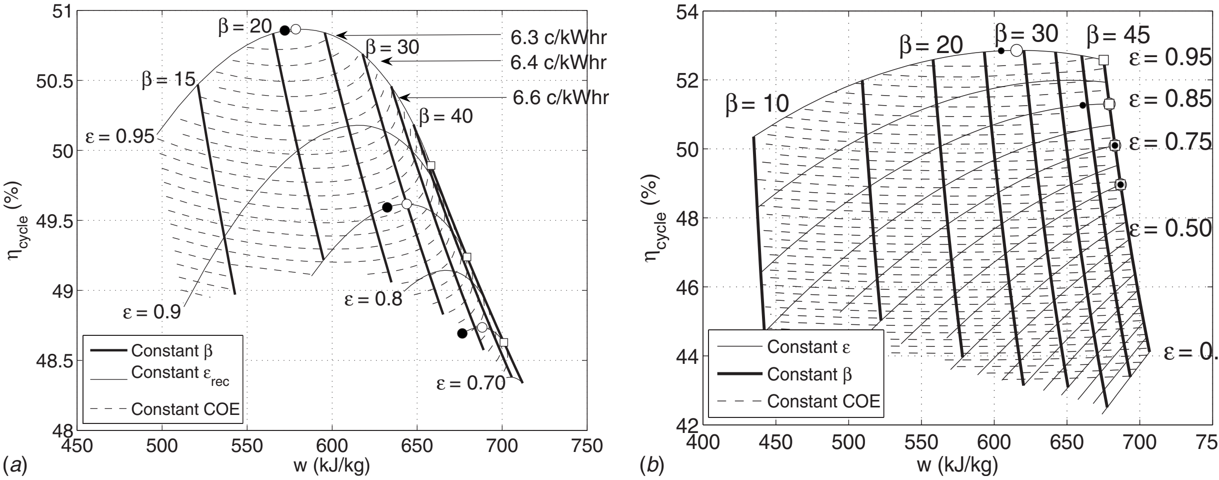

Fig. 9 Parametric contours: β and ε_{rec}. (*a*) HAT cycle, and (*b*) TOPHAT cycle.

to the maximum efficiency, for identical reasons to the HAT cycle. The remaining plots in Fig. 10 confirm that Paretos 2 and 3 are subsets of Pareto 1.

3 Economic Comparison of Cycles

Summaries of the Pareto-optimal sets are illustrated in Figs. 11(*a*) and 11(*b*) and compared with the performance of a medium-scale (CC1: $\eta_{cycle}=53\%$, $P=65$ MW, COE=7.0 c/kWh) and large-scale combined cycle (CC2: $\eta_{cycle}=56\%$, $P=650$ MW, COE=6.5 c/kWh).

The TOPHAT and HAT cycles compete with both CC1 and CC2 on a COE basis, and the STIG cycle competes with CC1 only. The advantage over the simple and the advanced dry cycles is also quite apparent.

The *purchased equipment cost* (PEC) for the humid cycles are illustrated in Fig. 12—costs of $16–18M for the HAT and STIG cycles are evident, which includes $2–2.5M for the equipment necessary for humidification/steam generation (13–14% of bare gas turbine cost). Note that PEC consists of the bare gas turbine components, heat exchangers, ancillaries, and packaging, as outlined in the Appendix. The typical cost increase, identified in Gas Turbine World 2006 [4], for STIG cycles compared with their dry counterparts is, on average, 52%. Therefore, the additional cost of equipment for injection, component adjustment, and other ancillaries can account for up to 38% of the bare gas turbine costs. For the HAT cycle, the cost of ancillary humidification equipment has also been neglected since very few reliable data exist. The TOPHAT cycle has been undercosted ($9–11M) as there are no reliable cost models for the additional equipment for spraying water in the compressor and, also, the low working fluid temperature in the compressor pushes down the costs considerably—low temperatures and, therefore, high density working fluid imply low cost in the compressor cost models.

The specific capital cost is worth comparing to data in the literature. Note that in the following paragraphs, the costs quoted are for the *total capital investment* (TCI)—this includes costs for land, labor, construction, etc. Bejan et al. [5] cited scaling factors of 4.16–6.32 of the PEC to calculate TCI, depending on whether

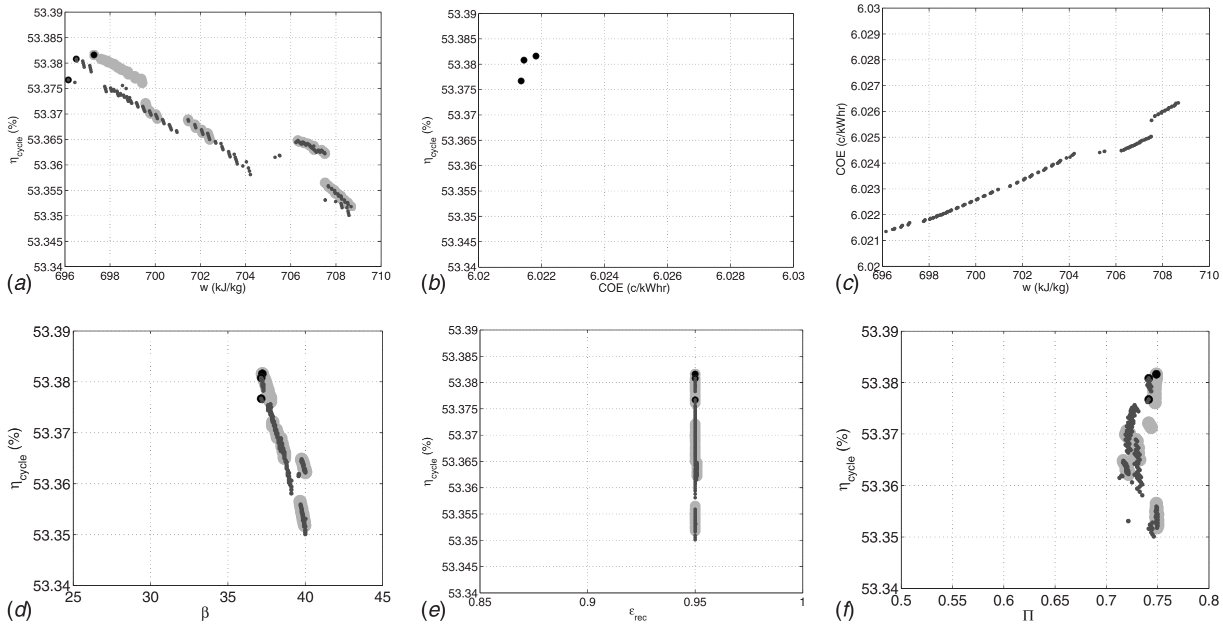

Fig. 10 Results for TOPHAT cycle TS optimization. (a) Paretos 1–3 in η_{cycle}/COE domain; (*b*) P2: η_{cycle}/COE Pareto-optimal set; (c) P3: COE/*w* Pareto-optimal set; (*d*) P1–3: β^* selection; (*e*) P1–3: ε^*_{rec} selection; and (*f*) P1–3: Π^* selection.

Downloaded 02 Jun 2010 to 171.66.16.109. Redistribution subject to ASME license or copyright; see http://www.asme.org/terms/Terms_Use.cfm

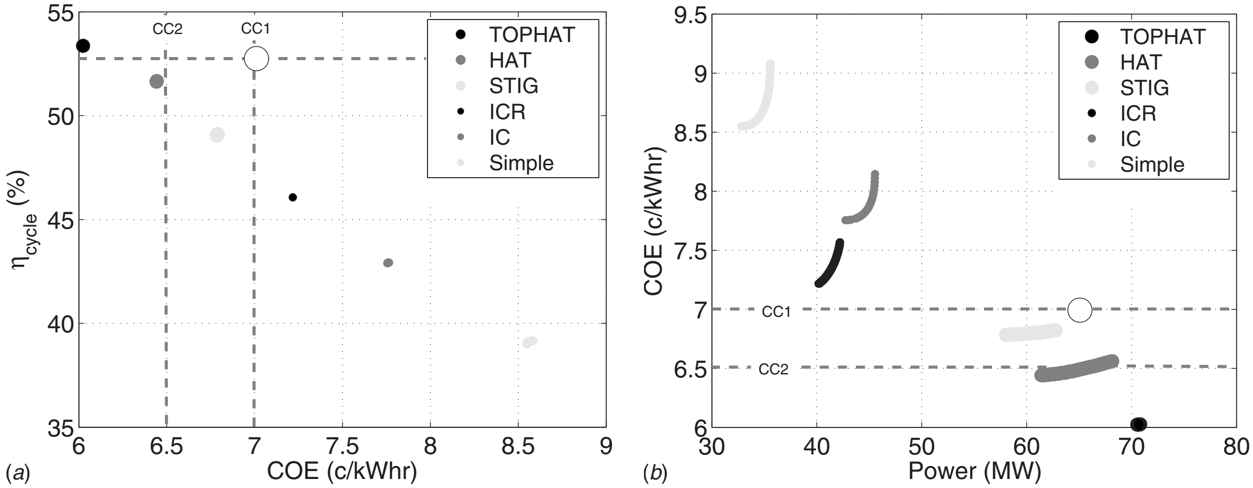

Fig. 11 Comparison of Pareto-optimal sets: (*a*) Pareto 2, and (*b*) Pareto 3

it is for a plant expansion or a completely new build. In this study, a reverse costing methodology is instead applied—λ_{TCI} is calculated, which scales the PEC to a value that maintains the economic competitiveness of the plant.

In a study by Jonsson and Yan [6], specific costs of 538 \$/kW (\$38.74M) for the 72 MW Trent HAT and 525 \$/kW (\$34.13M) for the 65 MW Trent STIG were calculated. For the 52.4 MW GTX100 HAT and 54.4 MW STIG, specific costs of 575 \$/kW (\$30.13M) and 530 \$/kW (\$28.83M) were calculated. These are compared with the combined cycle reference case of 604 \$/kW (\$44.8M) and 665 \$/kW (\$31.03M) for the 74.2 MW Trent and 62 MW GTX100, respectively.

Kakaras et al. [7] published specific costs of 500 \$/kW for the simple cycle, 700 \$/kW (\$26M) for the 37.25 MW STIG, 880 \$/kW (\$32.15M) for the 36.55 MW HAT, and 932 \$/kW (\$38.53M) for the 41.3 MW combined cycle (costs quoted in euro, assuming 1.244 \$/euro [8]). The ranges of specific TCI are superimposed on Fig. 12(*b*), which plots the specific PEC from the simulation (* refers to cycle designs for minimum COE). The lower bounds on the specific TCI for the STIG and HAT are from the study of Jonsson and Yan, which have similar power output to the cycles in the current analysis (60–70 MW). This indicates that a scaling factor of 1.25–1.8 for the PEC calculated from the current analysis would yield a similar TCI to that in Ref. [6].

Clearly, from the discussion above, there exist significant challenges in costing these systems due to the lack of reliable data, so a factor of safety (λ_{TCI}) is used to determine the potential repercussions of additional capital expense on the COE. It was found that $\lambda_{TCI}=1.9$ for the STIG cycle, and $\lambda_{TCI}=2.85$ for the HAT cycle ensured that the plants remained competitive on a COE basis with CC1, as illustrated in Fig. 13. $\lambda_{TCI}=3.5$ for the TOPHAT cycle ensured the plant remained competitive on a COE basis with CC2.

Figure 14(*a*) plots the IRR and TCI for the humid power cycles using the factors found above; they are compared with CC1 and CC2, which have an IRR of 5% and 33%, respectively. The STIG and TOPHAT are very competitive with CC2, and the HAT cycle is competitive with CC1. Since the factors chosen were purely based on COE competitiveness, it is more insightful to consider a range of capital costs and the impact on IRR.

Due to the uncertainty in the economic models, these data are more useful at providing the designer with absolute limits on capital cost, assuming the systems can achieve the performance expected. Figure 14(*b*) plots the total capital investment against IRR.

Clearly, increasing capital expenditure will reduce the return on investment and, for a fixed capital expenditure, selecting the TOPHAT or HAT cycle over the STIG cycle will yield a higher return. It is worthwhile noting that, for an IRR comparable to the medium-scale combined cycle (CC1)—which was budgeted at nearly \$70M (assuming $\lambda_{TCI}=2.0$)—the designer can spend \$100M on the TOPHAT (72 MW) or \$70M on the STIG (58 MW) cycle to yield a similar return. The 62 MW HAT cycle should be costed at \$80M to be competitive with CC1. To be competitive

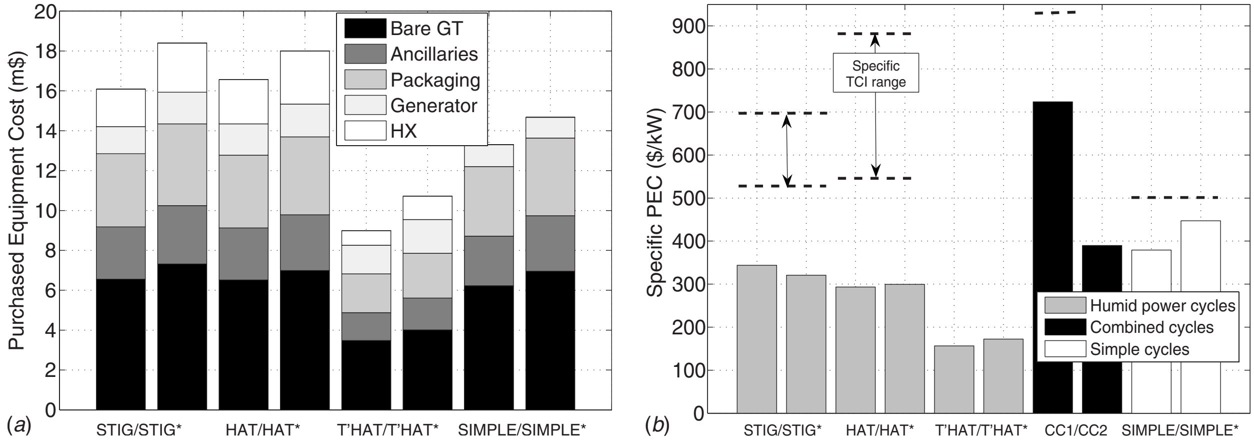

Fig. 12 PEC and specific PEC: (*a*) purchased equipment costs, and (*b*) specific PEC

Downloaded 02 Jun 2010 to 171.66.16.109. Redistribution subject to ASME license or copyright; see http://www.asme.org/terms/Terms_Use.cfm

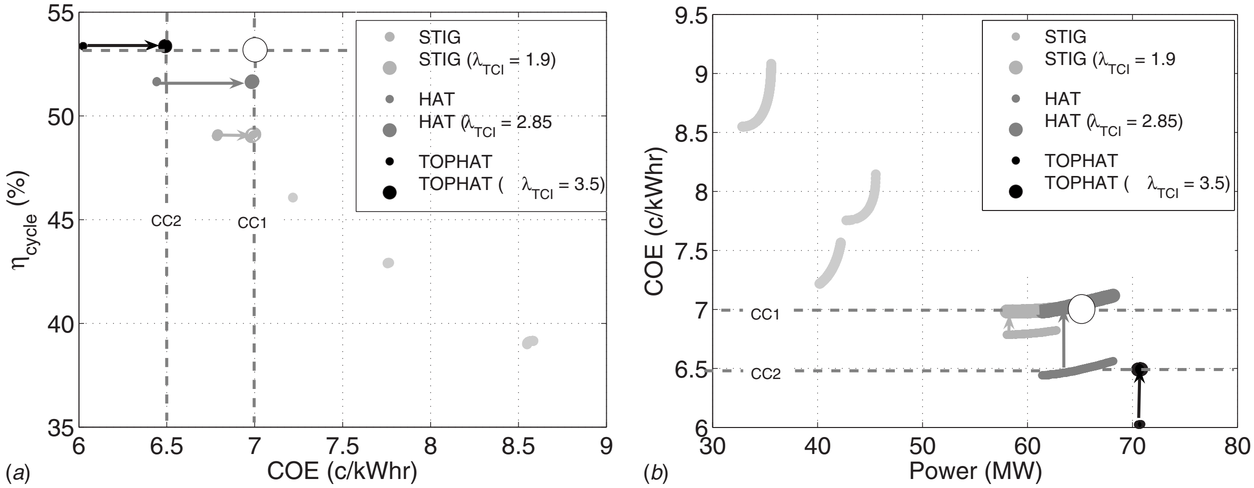

Fig. 13 Comparison of adjusted Pareto-optimal sets: (*a*) Pareto 2—adjusted TCI, and (*b*) Pareto 3—adjusted TCI

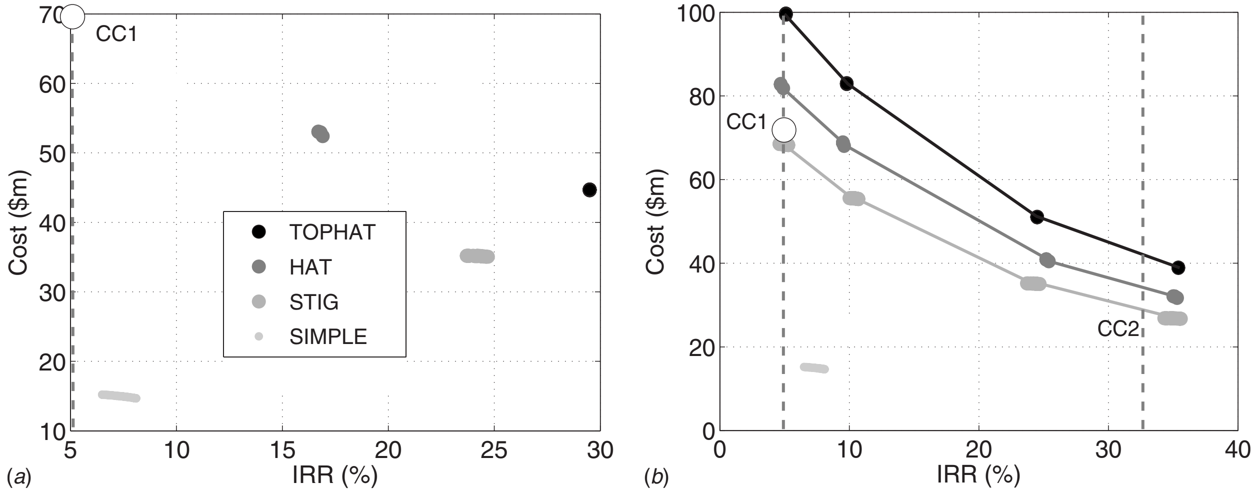

Fig. 14 IRR for humid cycles: (*a*) IRR for Pareto 2, and (*b*) TCI versus IRR for Pareto 2

with CC2, a much tighter budget is necessary. Just over $40M for the TOPHAT, $30M for the STIG cycle, and just over $35M for the HAT cycle can maintain an IRR of 33%. This provides the designer with a range of costs for these cycles, which will maintain their cost competitiveness; a desired IRR and maximum capital expenditure can be matched.

4 Conclusions

In Part II of these two papers, two additional Pareto-optimal sets (incorporating COE) for the humid power cycles and their associated design variables were studied. For the STIG cycle the emphasis shifted away from maximizing superheat but instead toward increasing the power output in order to reduce COE by increasing the steam injection. This emphasized how optimizing for COE instead of η_{cycle} can yield alternative design variables. For the remaining humid cycles, maximizing η_{cycle} tended to minimize COE, as characterized by the very small $\eta_{\text{cycle}}/\text{COE}$ Pareto-optimal sets (Pareto 2). The primary cause of this was that power decreased as pressure ratio decreased, unlike the STIG and simple cycles, which pushed the minimum COE close to the maximum η_{cycle}.

Due to the uncertainty in cost modeling, a range of capital costs were studied, which would ensure that the humid cycles remained cost competitive. For the 58 MW STIG cycle, costs of $30–70M would be desirable; for the 62 MW HAT cycle, costs of $35–80M were preferable; and finally costs of $40–100M for the 70 MW TOPHAT cycle keep the plant highly competitive.

These cost ranges are an invaluable guideline when designing new plants where there is more uncertainty about costs than the thermodynamic performance.

Acknowledgment

This work was carried out in the Hopkinson Laboratory of the Cambridge University Engineering Department. R.M.K. gratefully acknowledges the support by grants from the Cambridge European Trust, the EPSRC, and Rolls-Royce plc.

Nomenclature

$\dot{C}$ = cost-rate ($/s)
C_j = cash-flow in year j ($)
c = unit cost ($/kg)
i = discount rate (%)
$\dot{m}$ = mass flow-rate (kg/s)
n = economic life (years)
p = pressure (bar)
P = power (MW)
T = temperature (K)
ν = specific volume (m^3/kg)
ρ = density

Downloaded 02 Jun 2010 to 171.66.16.109. Redistribution subject to ASME license or copyright; see http://www.asme.org/terms/Terms_Use.cfm

t = run-hours (h)
w = specific work (kJ/kg)
β = pressure ratio
γ = ratio of specific heats (c_p/c_v)
Δ = change in property (%)
ε = heat exchanger effectiveness
η_{cycle} = cycle efficiency (%)
η_p = polytropic efficiency
Π = pressure ratio split exponent
Ξ = capital cost ($)
ζ = cost scaling for multispool engines

Subscripts

ac = aftercooler
comb = combustor
comp = compressor
cr = critical
eco = economizer
f = fuel
g = gas
gen = generator
hx = heat exchanger
ic = intercooler
in = property into component
out = property out of component
p = pinch point property
rec = recuperator
w = water
sat = saturated state
sh = superheat
turb = turbine

Superscripts

$*$ = design values selected for Pareto-optimal set
β^*_{COE} etc. = design values for β at minimum COE

Acronyms

CRF = capital recovery factor
FPT = free power turbine
IRR = internal rate of return
L/HPT = low/high pressure turbine
L/HPC = low/high pressure compressor
NPV = net present value
O&M = operations and maintenance
PEC = purchased equipment cost
TCI = total capital investment
TIT = turbine inlet temperature

Appendix: Cost Equations

The cost models developed by Traverso et al. [1] were used to cost the compressor, combustor, turbine, and generator (see Table 1). The heat exchanger costs were calculated using proprietary data. The bare gas turbine cost consists of the compressor, combustor, turbine, and on-engine ancillaries. The system *ancillaries* are approximated as 40% of the compressor/combustor/turbine system, and the *packaging* cost is 40% of the bare gas turbine cost. The PEC and TCI are calculated below.

$$\Xi_{\text{comp}} = a_1 \left[\frac{\left(\dfrac{\dot{m}_{\text{in}} \sqrt{R_{\text{in}} T_{\text{in}}}}{p_{\text{in}} \cdot m_{\text{cr}}} \right)}{\left(\dfrac{\dot{m} \sqrt{R \cdot T}}{p \cdot m_{\text{cr}}} \right)_{\text{ref}}} \right]^{a_3} \frac{\beta^{a_4} \ln(\beta)}{(1 - \eta_p)^{a_2}}$$

$$\Xi_{\text{comb}} = b_1 \left[\frac{\dot{m}_{\text{out}} v_{\text{out}}}{(m \cdot v)_{\text{ref}}} \right]^{b_5} \cdot [1 + e^{(b_3 \cdot (T_{\text{out}}/T_{\text{ref}}) - b_4)}] \frac{1}{\Delta p^{b_2}}$$

$$\Xi_{\text{turb}} = c_1 \left[\frac{\dot{m}_{\text{out}} v_{\text{out}}}{(\dot{m} \cdot v)_{\text{ref}}} \right]^{c_5} \cdot [1 + e^{(c_3 \cdot (T_{\text{in}}/T_{\text{ref}}) - c_4)}] \frac{\ln \beta}{(1 - \eta_p)^{c2}}$$

Table 1 Cost factors and assumptions

Economic assumptions	
Economic life (years), n	20.0
Discount rate, i (%)	7.0
Annual hours of operation, t (h)	7500
Fuel price, $\bar{c}_f$ ($/GJ)	0.07
Carbon price, c_{CO_2} ($/kg)	0.01

Economic factors

a_1	5095.9	b_1	1857.0	c_2	5979.1	f_1	72176.0
a_2	0.15	b_2	0.995	c_2	0.29	f_2	0.7605
a_3	0.85	b_3	5.479	c_3	4.185	g_1	1.5758
a_4	0.30	b_4	34.36	c_4	23.60	g_2	0.7879
d_{hx}	$\text{f(UA, mat)}_{\text{hx}}$	b_5	0.6	c_5	0.75		
T_{ref}	298.15	p_{ref}	1.013×10^5	$\dot{m}_{\text{ref}}$	1.0		

$$\Xi_{\text{hx}} = d_{\text{hx}} \cdot \frac{\dot{Q}}{\Delta T_{LM}}$$

$$\Xi_{\text{gen}} = f_1 (P/P_{\text{ref}})^{f_2}$$

$$\Xi_{\text{SAT}} = g_1 \cdot c_{\text{material}} \cdot m_{\text{tower}} + g_2 \cdot c_{\text{packing}} \cdot m_{\text{packing}}$$

$$\Xi_{\text{BARE-GT}} = \Xi_{\text{comp}} + \Xi_{\text{comb}} + \Xi_{\text{turb}} + \Xi_{\text{ancillaries}}$$

$$\Xi_{\text{GT}} = \Xi_{\text{BARE-GT}} + \Xi_{\text{packaging}}$$

$$\Xi_{\text{PEC}} = \Xi_{\text{GT}} + \sum (\Xi_{\text{hx}}) + \Xi_{\text{gen}} \Xi_{\text{sat}}$$

$$\Xi_{\text{TCI}} = \lambda_{\text{TCI}} \cdot \Xi_{\text{PEC}}$$

$$m_{\text{cr}} = \frac{\sqrt{\gamma}}{((\gamma + 1)/2)^{\gamma + 1/2(\gamma - 1)}}$$

In order to avoid the undercosting of the compressors in the case of multispool engines, an additional cost factor was derived by the author. The compressor costs for a single-spool and twin-spool engine are calculated from Eqs. (A1) and (A2) respectively, where $\omega = (\gamma(1 - 2\eta) - 1)/2\gamma\eta$.

$$\Xi_{\text{comp},I} = a_1 \left[\frac{\bar{m}_{g,\text{in}}}{\bar{m}_{\text{ref}}} \right]^{a_3} \frac{\beta^{a_4} \ln(\beta)}{(1 - \eta_p)^{a_2}} \tag{A1}$$

$$\Xi_{\text{comp},II} = a_1 \left[\frac{\bar{m}_{g,\text{in}}}{\bar{m}_{\text{ref}}} \right]^{a_3} \frac{\beta_{\text{LP}}^{a_4} \ln(\beta) + (\beta_{\text{LP}}^{\omega})^{a3} \beta_{\text{HP}}^{a_4} \ln(\beta_{\text{HP}})}{(1 - \eta_p)^{a_2}} \tag{A2}$$

By dividing Eq. (A1) into Eq. (A2), the cost factor can be calculated. Dividing ζ_{comp} into the cost of any compressor in a twin-spool engine will ensure the compressors are not undervalued. This factor will equate the costs of twin-spool and single-spool compressors for the same parameters.

$$\zeta_{\text{comp}} = \Pi \left[\frac{1}{\beta^{a_4(1-\omega)}} + \left(\frac{1 - \Pi}{\Pi} \beta^{\Pi(\omega a_3 - a_4)} \right) \right] \tag{A3}$$

This was also completed for turbine costs where there are two (Eq. (A4)) or three (Eq. (A5)) turbines.

$$\zeta_{\text{turb}} = \frac{\ln \beta_{\text{HP}}}{\ln \beta} \times \left[\frac{(\dot{m}_{g,\text{out}}/\rho_{g,\text{out}})_{\text{HP}}}{(\dot{m}_{g,\text{out}}/\rho_{g,\text{out}})_{\text{LP}}} \right] + \frac{\ln \beta_{\text{LP}}}{\ln \beta} \times \left[\frac{1 + \exp\left(c_3 \dfrac{T_{\text{HP,in}}}{T_0} - c_4 \right)}{1 + \exp\left(c_3 \dfrac{T_{\text{LP,in}}}{T_0} - c_4 \right)} \right] \tag{A4}$$

Downloaded 02 Jun 2010 to 171.66.16.109. Redistribution subject to ASME license or copyright; see http://www.asme.org/terms/Terms_Use.cfm

$$
\begin{aligned}
\zeta_{\mathrm{turb}} = {} & \frac{\ln \beta_{\mathrm{HP}}}{\ln \beta} \times \left[\frac{(\dot{m}_{g,\mathrm{out}}/\rho_{g,\mathrm{out}})_{\mathrm{HP}}}{(\dot{m}_{g,\mathrm{out}}/\rho_{g,\mathrm{out}})_{\mathrm{LP}}} \right] + \frac{\ln \beta_{\mathrm{IP}}}{\ln \beta} \times \left[\frac{(\dot{m}_{g,\mathrm{out}}/\rho_{g,\mathrm{out}})_{\mathrm{IP}}}{(\dot{m}_{g,\mathrm{out}}/\rho_{g,\mathrm{out}})_{\mathrm{LP}}} \right] \\
& \times \left[\frac{1 + \exp\left(c_3 \dfrac{T_{\mathrm{IP,in}}}{T_0} - c_4 \right)}{1 + \exp\left(c_3 \dfrac{T_{\mathrm{LP,in}}}{T_0} - c_4 \right)} \right] + \frac{\ln \beta_{\mathrm{LP}}}{\ln \beta} \\
& \times \left[\frac{1 + \exp\left(c_3 \dfrac{T_{\mathrm{HP,in}}}{T_0} - c_4 \right)}{1 + \exp\left(c_3 \dfrac{T_{\mathrm{LP,in}}}{T_0} - c_4 \right)} \right] \qquad \text{(A5)}
\end{aligned}
$$

References

[1] Traverso, A., Massardo, A. F., Cazzola, W., and Lagoria, G., 2004, “WIDGET-TEMP: A Novel Web-Based Approach for Thermoeconomic Analysis and Optimization of Conventional and Innovative Cycles,” ASME Paper No. GT2004-54115.

[2] Agazzani, A., and Massardo, A. F., 1997, “A Tool for Thermoeconomic Analysis and Optimization of Gas, Steam, and Combined Plants,” ASME J. Eng. Gas Turbines Power, **119**, pp. 885–892.

[3] Kavanagh, R., 2008, “Analysis and Optimisation of Humidified Power Cycles,” Ph.D. thesis, University of Cambridge, Cambridge.

[4] Gas Turbine World, 2006, *Gas Turbine World*, Pequot, Southport, CT.

[5] Bejan, A., Tsatsaronis, G., and Moran, M., 1996, *Thermal Design and Optimization*, Wiley, New York.

[6] Jonsson, M., and Yan, J., 2003, “Economic Assessment of Evaporative Gas Turbine Cycles with Optimized Part Flow Humidification Systems,” ASME Paper No. GT2003-38009.

[7] Kakaras, E., Doukelis, A., Leithner, R., and Aronis, N., 2004, “Combined Cycle Power Plant With Integrated Low Temperature Heat (LOTHECO),” Appl. Therm. Eng., **24**, pp. 1677–1686.

[8] U.S. Federal Reserve, 2004, *Federal Reserve Historical Exchange Rates*, www.federalreserve.gov/releases/(2007).

Downloaded 02 Jun 2010 to 171.66.16.109. Redistribution subject to ASME license or copyright; see http://www.asme.org/terms/Terms_Use.cfm

Mechanical Investigation of a Failed Lock-Pin

E. Poursaeidi[1]
Department of Mechanical Engineering,
Zanjan University,
Zanjan, Iran;
Research and Lab Division,
Iran Power Plant Repair Co.,
P.O. Box 31585-381,
Karaj, Iran
e-mail: epsaeidi@znu.ac.ir
e-mail: epsaeidi@gmail.com

A. A. Pirmohammadi
Department of Mechanical Engineering,
Zanjan University,
Zanjan, Iran

M. R. Mohammadi Arhani
Research and Lab Division,
Iran Power Plant Repair Co.,
P.O. Box 31585-381,
Karaj, Iran

This paper presents the outcomes of computational mechanics applied in the root-cause investigation on hot section failure of a 25 MW gas turbo generator in the domestic power plant after 2228 start-stops and 52,586 h operation. The failure includes the complete damage of the first and the second stage of nozzles, blades, seals, shroud segments, and also a peripheral damage on the disk of first stage. Several reported cases from the different power plants with similar events evidenced that the failure is a serious common type in the mentioned gas turbine engine. A previous study on complete metallurgical analysis of disk, moving blades, and lock-pins, was done by Poursaeidi and Mohammadi (2008, "Failure Analysis of Lock-Pin in a Gas Turbine Engine," Eng. Fail. Anal., ***15****(7), pp. 847–855), which concluded that the mechanical specification of applied materials had been satisfied. Nevertheless, some problems were found in the fractographic results of lock-pins: the typical fatigue fracture surfaces in the neck of failed lock-pins and frankly localized pitting signs near the head of lock-pin. The lock-pins are kinds of small devices that lock the buckets after inserting them into disk grooves. In this work, a 3D finite element model (FEM) of a blade, a disk, and a lock-pin are made and analyzed by the* ANSYS *software. The results of the FEM showed a reasonable agreement between the analysis and position of fracture on lock-pins. Also, the results showed that the second vibrational mode of the bucket is a possible cause of failure because in this mode the peak stress occurs on the head of the lock-pin. However, inadequate design and long time service reduced the performance of lock-pins for sustaining a severe hot condition in the first stage of the turbine section.* [DOI: 10.1115/1.3077660]

Keywords: lock pin, FEM, vibration analysis, gas turbine component failure

1 Introduction

Gas turbine blade and disk assemblies are subjected to high centrifugal, thermomechanical and vibrational load and contain high stressed components. Bucket loss can be contained within the engine casing, while the catastrophic failure of a turbine wheel could cause a whole destruction of turbine section by the first larger fragments. The consequences of such failure are particularly costly resulting in destruction of the engine.

In the engine that was studied in this paper, the bladed-disk assembly (Fig. 1) basically has three critical regions for which lifetime certification is necessary: the fir-tree region of blades, the assembly grooves of disk, and the head of locking-pins. The loads associated with these regions are the centrifugal forces of the blades, the self-generated loads applied by blade vibration, and thermal stresses. These detrimental loads are not constant and they vary during each start-stop. Thus, these components are exposed to fatigue phenomena. In the majority of cases, cracks are initiated in the lock-pin's head due to the vibrating action at the assembly interface [1].

The stress analysis of the blade assembly area of the gas turbo engine has received the attention of several investigators. Of particular interest to this study are the works of Kenny et al. [2] and Nurse and Patterson [3]. Their works were concerned with second stage fatigue crack growth paths in fir-tree fixtures; however, the fir-tree damage is not the subject of this investigation. Boddington et al. [4] also treated the numerical analysis at dovetail joints. In their work, a technique was developed to model the relative motion at the interface of the assembly.

Parks and Sanford [5,6] conducted two- and three-dimensional photoelastic analyses of the blade/disk fir-tree region of a turbine disk and blade assembly. Centrifugal, circumferential, and antiplane bending loads were applied at the centroid of the blade for the three-dimensional model, while only centrifugal loads were applied to the two-dimensional model. Their results revealed that the stresses at the central region of the three-dimensional disk were approximately twice those found in the two-dimensional study and the stress concentration in the central region is balanced by a large reduction in the stress at the ends of the fillet. This reduction was associated with the flexibility of the dovetail joint at the both ends. Durelli et al. [7] conducted a comprehensive study on turbine blade attachments. They concluded that the most important forms of loading are the radial centrifugal force due to blade loading and the bending of the blade due to the gas pressure.

Overall, the blade assembly locking devices have never been investigated as important and causative components of hot section failures. In fact, they have low safety in parts due to poor considerations of design or manufacturing errors. Numerous reports of some consistent cases of failure represent good evidences for this subject. Pilicy and Dundas [8] pointed that such failure of gas turbines is often the consequence of faulty design.

This paper presents the outcomes of computational mechanics applied in the root-cause investigation of hot section failures of a 25 MW gas turbo generator in a domestic power plant after 2228 start-stops and 52,586 h operation. The failure occurred on July 1, 2005. Table 1 shows a detailed history of the turbine blades and the overhaul.

Similar failures have been reported previously for three other gas turbine engines installed in different power plants with the same signs. Mazur and Kubiak reported the first major accident, which had occurred in a power plant in Mexico in June 1998 [9]. The second and third events with the exact similar failures were reported in the autumn of 2000 and the summer of 2002, respectively. The failed gas turbo generators were operating in Shariati power plant, northeast of Iran [10]. Hence, the research program

---

[1] Corresponding author.

Contributed by the International Gas Turbine Institute of ASME for publication in the Journal of Engineering for Gas Turbines and Power. Manuscript received December 14, 2007; final manuscript received November 11, 2008; published online April 9, 2009. Review conducted by David Walls.

Copyright © 2009 by ASME

Downloaded 02 Jun 2010 to 171.66.16.109. Redistribution subject to ASME license or copyright; see http://www.asme.org/terms/Terms_Use.cfm

(*a*) (*b*)

Fig. 1 (*a*) View of disk grooves after plastically deformations in the failed gas turbo generator. (*b*) A typical failed lock-pin. The knocked edges are visible on the remaining head.

was defined for the investigation of these failures. The first investigation by the authors were focused on metallurgy and fractography of the disk, blade, and lock-pins [11]. The outcome of works showed that lock-pin weakness has been the main agent of turbine failure. Nevertheless, the research group continued the investigation of failure from a mechanical aspect to find more problems or contributed reasons.

2 Background

The failed gas turbines are single shaft units with power ranges of 20–25 MW and used in electrical generation. The engine type has a 17-stage compressor with variable inlet guide vanes and ten combustion chambers. Combustors are ringed around the outside of the compressor and are slightly offset. They are designed to consume oil, gas, or dual-fuels.

It has two axial stages, which drive the gas generator and the integral output shaft. Long-shank bucket casts of high nickel-based alloy are used to provide a substantial temperature drop between the airfoil and the root area. First-stage blades are hollow cored to reduce centrifugal stress but are not cooled. The second stage with increased diameter has an integrated tip shroud. First-stage nozzles are cooled by air directed through the individual nozzle partitions and out from small holes near the trailing edge [12]. The weights of the first and the second stage bucket are approximately 1.2 kgf and 2.1 kgf, respectively. The nominal turbine speed is 5100 rpm and the acceleration time during start-up is 4 min.

In Fig. 1 the general view of failed gas turbine rotor disk and lock-pin is shown. Certainly, in this typical case of hot section failure, the damage have started in the first stage of the turbine section. It seems the event has started by failure of a lock-pin's head. Serrations of two disk grooves were identically destroyed by moving the blades toward the first stage of nozzle cascade, and then due to the reduction in contacted area (increasing of stress), the groove teeth were deformed plastically in the radial direction. There are unchanged portions at the corner of disk slots that demonstrates dual step processes of blade displacement inside the disk root grooves. Fracture surface investigation and impact test results showed that there were not any problems in the microstructure and mechanical properties of disk. The metallography of samples taken from blades showed that there are not any signs of fatigue, creep, or hot corrosion in their microstructure [11].

The fractographic investigation of lock-pins, as the last suspect components, showed that they could be considered as the main agent for the starting of gas turbine failure. Figure 2(*a*) shows the magnified view of the fracture surface of the failed lock-pin. It consists of a small portion as crack nucleation area, a smooth portion as a crack propagation zone in the middle area, and finally a rough portion as final fracture zone. Figure 2(*b*) is the schematic view of the same fractured surface that is divided into three zones. The crack initiation zone is marked with letter A. The crack propagation zone is shown by a dashed vector and marked with letter B. The final fracture zone is colored gray and marked with letter C. Also, two angles are shown significantly less than 90 deg at two intersection points. The angles are between peripheral borderline of the fractured section and the tangent line of the final fracture curvature (the last Beach Mark). According to ASM Standards, these figures demonstrate the existence of severe stress concentration with a low nominal tensile stress for a unidirectional bending case during failure time [13].

Commonly there were some coincidental indications as listed below:

1. the fracture of three adjacent blades from the platform section
2. the serious damage of all buckets and nozzles of first and second stages
3. the damage of shroud segments and other elements of the hot section
4. the tip-rubbing of compressor moving and stator blades consequent of rotor unbalancing
5. the extensive fretting corrosion products (reddish oxide particles) inside of disk grooves in the turbine section

Table 1 Turbine blades and overhaul history

Items	From first utilization (turbine life)	From last overhaul (turbine life)	First-stage buckets	Second-stage buckets
Operating hours	52,586	3414	45,023	52,586
No. of start-stops	2,228	641	1,861	2,228

Downloaded 02 Jun 2010 to 171.66.16.109. Redistribution subject to ASME license or copyright; see http://www.asme.org/terms/Terms_Use.cfm

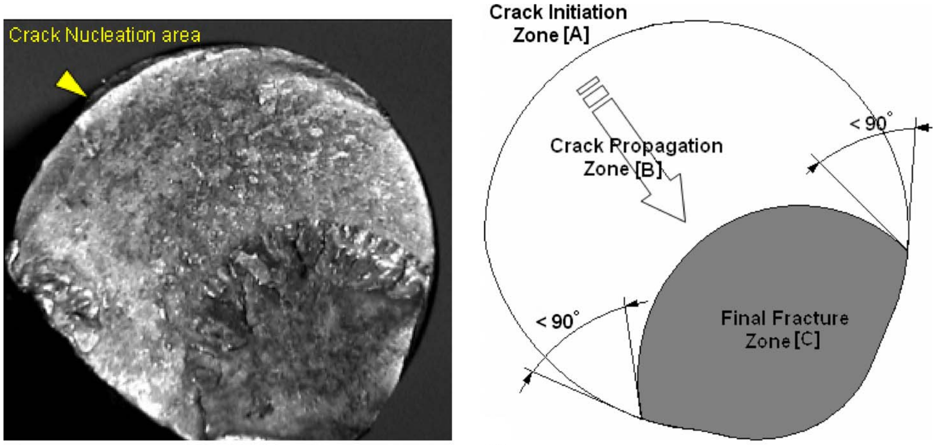

(*a*)

(*b*)

Fig. 2 (*a*) Stereomicroscope view shows the fracture surface of a failed lock-pin (10×). (*b*) The schematic feature in accordance to view (*a*) presents distinct rapture areas.

3 Mechanical Analysis

3.1 Material Specifications. The mechanical specification of applied materials for each part is presented in Table 2. Figure 3 shows the hot section area of failed gas turbine, which is detailed to show the mean temperature of some special points at the peak load. The temperature of combustion products around the surfaces of airfoil of the first stage blades arises up to 795°C on the leading edge and 756°C on the trailing edge. According to power plant records, the maximum temperature around lock-pins and root grooves goes up to 450°C due to hot gas leakage.

Table 2 Material properties of alloys at the ambient temperature [14–16]

Component	Material	Mass density	Tensile yield strength (min)	Tensile ultimate strength
Bucket	IN-738LC	8110.0 kg/m^3	9.5×108 Pa	1.1×109 Pa
Disk	A471-Cl.10	7800.0 kg/m^3	6.2×108 Pa	7.25×108 Pa
Lock-pin	AISI 403	7750.0 kg/m^3	2.7×108 Pa	5.86×108 Pa

3.2 Mechanical Forces. One of the most unfavored loads at rotating components of gas turbines is the centrifugal force. It depends on two variable parameters: the whirling rotor speed and the distance of each element from the rotating axis [17].

Hence, by applying a nominal rotating speed of 5100 rpm (85 rps), the centrifugal force was simulated on the elements of FE geometric model. In addition, the centrifugal force can be estimated from the following formula [18]:

$$F_c = mV^2/r = 4\pi^2 mrN_s^2 \tag{1}$$

where m is the mass, V is the surface velocity, r is the radius of center of gravity from the rotation axis, N_s is the turbine speed in rps.

As predictive assessment, by assuming a concentrated mass equal to 1.2 kg in the center of gravity of a single bucket, the centrifugal force is calculated about 216,000 N, so this huge force

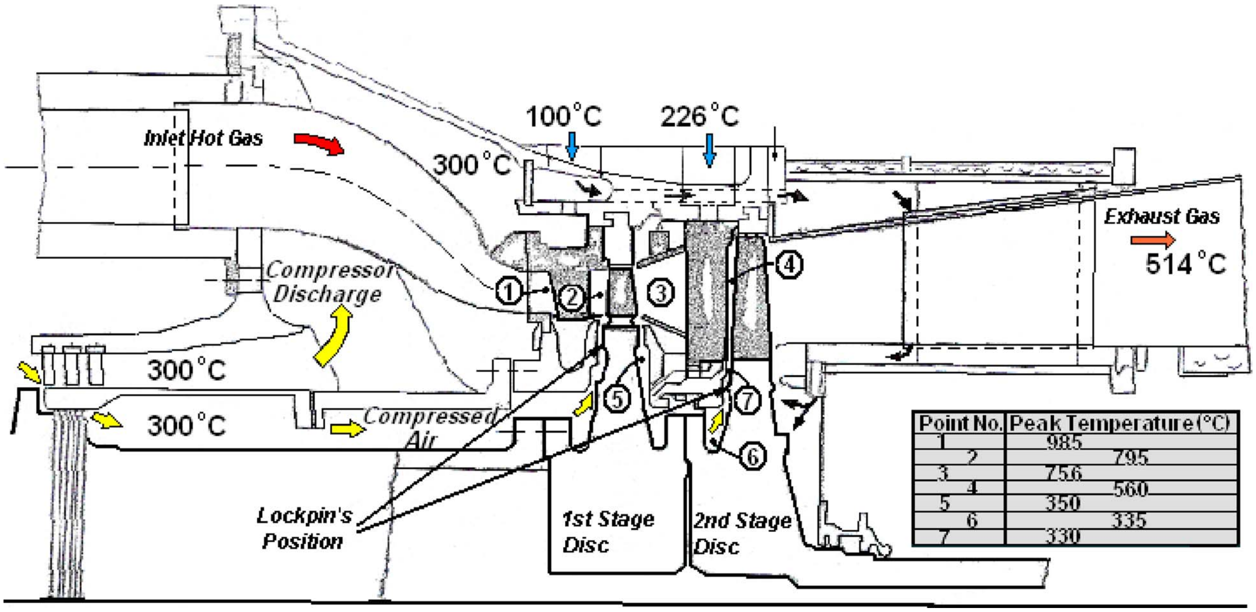

Point No.	Peak Temperature (°C)
1	985
2	795
3	756
4	560
5	350
6	335
7	330

Fig. 3 The sketch view of turbine's hot section with temperatures of some special points (presented by the manufacturer)

Downloaded 02 Jun 2010 to 171.66.16.109. Redistribution subject to ASME license or copyright; see http://www.asme.org/terms/Terms_Use.cfm

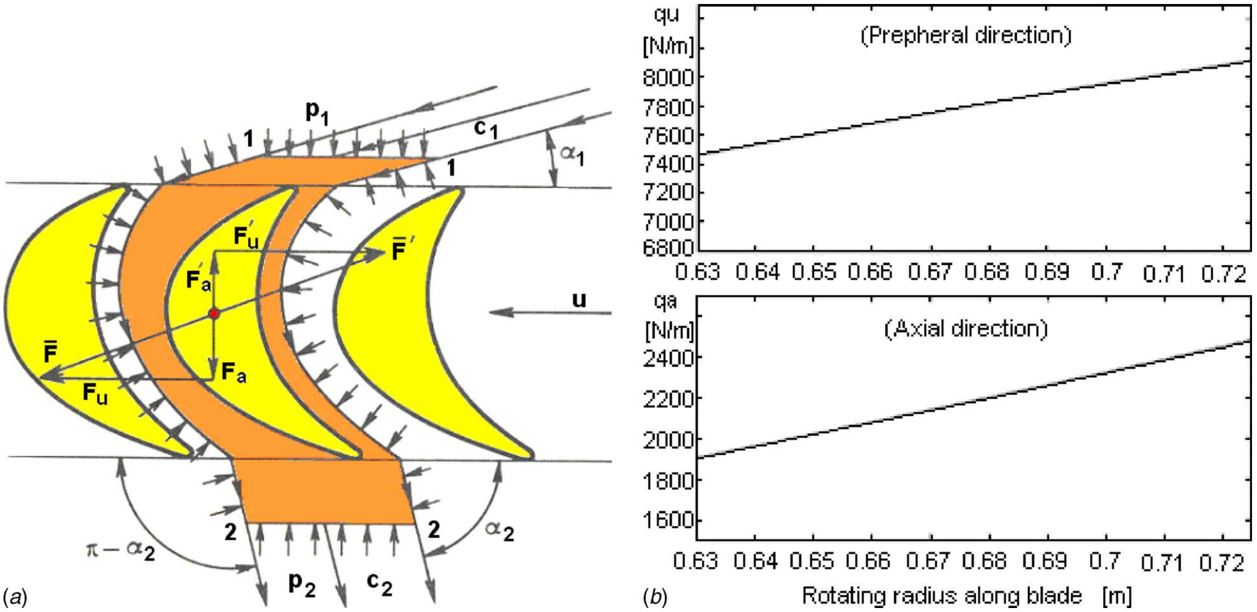

Fig. 4 (*a*) Scheme of loads applied to blades. (*b*) Aerodynamic load distribution graphs along the blade length.

results strict attachments in the fir-tree areas [19]. This subject on contribution of blade vibration makes harmful phenomena as fretting corrosion and fatigue effects.

The aerodynamic loads on the surface of moving blades can be calculated by using the turbo-machine theory. By attention to Fig. 4(*a*) and considering a control volume around a moving blade in a turbine cascade and using the equation of momentum in two directions, the aerodynamic loads distribution along the blade length can be calculated [17]:

$$q_u = \rho_b \cdot C_{2a} \cdot (C_{1u} + C_{2u}) \cdot t_b \tag{2}$$

$$q_a = [\rho_b \cdot C_{2a} \cdot (C_{1a} - C_{2a}) + \Delta P] \cdot t_b \tag{3}$$

where q is the linearized aerodynamic load, ρ_b is the hot gas density between the blades (assumed to be constant), C is the hot gas velocity, t_b is the pitch of the moving blades cascade, ΔP is the pressure drop, a is the axial direction index, and u is the peripheral direction index. All of these parameters are functions of rotating radius.

By using Eqs. (4) and (5), the values of force components were calculated and their results were presented in Fig. 4(*b*). Because of the complexity of the mentioned formula, MATLAB software was used to solve them. Mathematically, the areas under the load curves are equal to the concentrated load vectors that are imposed on the concave surface of blade.

$$F_u = \int_{\text{hub}}^{\text{tip}} q_u dr \tag{4}$$

$$F_a = \int_{\text{hub}}^{\text{tip}} q_a dr \tag{5}$$

According to the above-mentioned procedure, the axial component was calculated at about 209 N as the agent of thrust generation force. And the peripheral component was calculated at about 740 N as the agent of rotational torque.

Supposing a problem has focused on the root of blades, the resultant of aerodynamic forces was loaded on the point of application on the airfoil by a single vector.

3.3 FE Modeling. The bladed-disk is a kind of cyclic-symmetric structure, which consists of 120 buckets. The buckets are inserted into the steeples on the disk via straight, axial, fir-tree shaped roots, and are blocked by locking-pins. However, for simplifying the analysis of FE model, an assembly of a single bucket on a small portion of disk was created by using the MDT software package. The study was continued by utilizing the ANSYS finite element code. Figure 5 shows both of the geometries of assembled and meshed models. The generated FE model consists of 16,534 solid elements, which were defined in a Cartesian coordinate system. Types of applied elements are listed below.

(a) 10-node quadratic tetrahedron (solid 187) elements were used to mesh the blade and lock-pin.
(b) 20-node quadratic hexahedron (solid 186) elements were used to mesh the disk section.

In addition to the model of the mechanical interface of adjacent surfaces between lock-pin and both the disk section and root of blade, the high-order surface to surface contact element was defined.

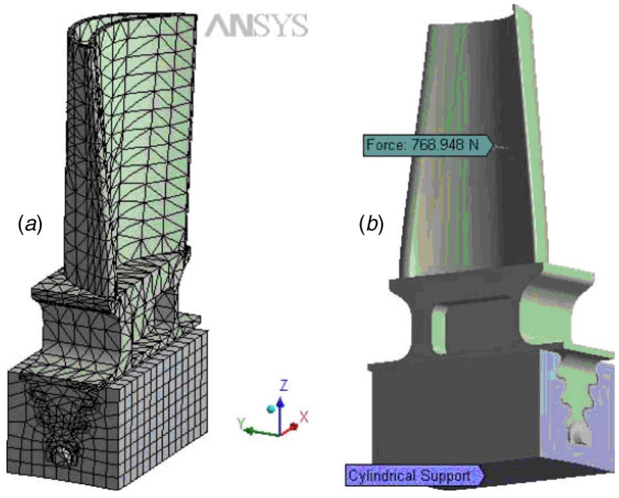

Fig. 5 The preprocessing of FE model. (*a*) Meshing feature of three components separately. (*b*) Assembled model of the disk section, blade, and lock-pin after applying boundary conditions.

Downloaded 02 Jun 2010 to 171.66.16.109. Redistribution subject to ASME license or copyright; see http://www.asme.org/terms/Terms_Use.cfm

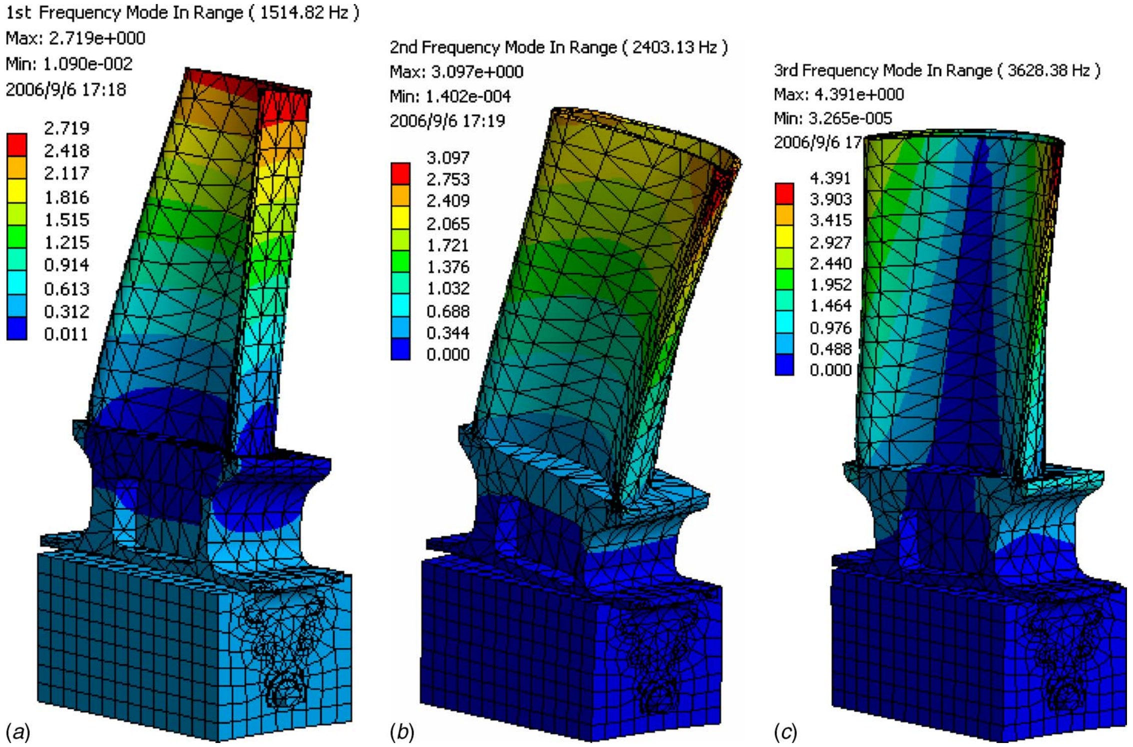

Fig. 6 Modal analysis. (*a*) The first frequency mode is bending type, 1514.82 Hz. (*b*) The second frequency mode is bending type in the axial direction, 2403.13 Hz. (*c*) The third frequency mode is torsion type, 3628.38 Hz.

Due to the circular symmetry of the problem, the lowest surface of disk portion consisting of 150 nodes was selected to fix the model radially in a cylindrical coordinate. Centrifugal force was simulated by defining a rotating condition with a constant speed equal to 5100 rpm around the center axis of previously defined cylindrical support (Fig. 5(*b*)). In addition, aerodynamic load was defined on the blade with its quantity shown in Fig. 4(*b*).

To examine the dynamic behaviors of the lock-pin between the blades and the disk, the created FE model was investigated with two methods of vibrational analysis, modal and harmonic analysis. Via modal analysis some natural mode shape and frequency were calculated.

Substantially, the short blades are often suffered to the first three natural modes in a resonant state. According to Fig. 6, the first mode is bending type in the peripheral direction that can be caused by the exciting frequency of 1514.82 Hz. The second mode shows a bending type in the axial direction with the natural frequency equal to 2403.13 Hz. The third mode shape is a torsional type that can be caused by the exciting frequency equal to 3628.38 Hz.

The result of harmonic analysis has been presented in Fig. 7. Included are the frequency responses of lock-pin according to maximum tensile stress and the acceleration of blade root in the axial direction. It seems that the two investigated parameters can help to determine the main reason of the failure. The maximum stress value of lock-pin and acceleration of blade root correspondingly occurred at a frequency of 2403.13 Hz. However, there were smaller peaks at frequencies of 1514.82 Hz and 3628.38 Hz, respectively, for the first and third vibration modes.

The stress distribution contours were correspondingly calcu-

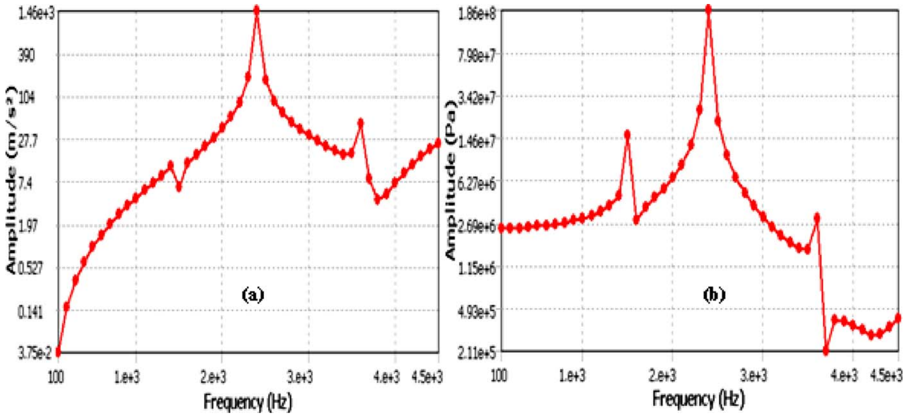

Fig. 7 The frequency response graphs show the three critical points between 100 Hz and 4500 Hz. Graph (*a*) shows the acceleration of blade root in the axial direction. Graph (*b*) shows the values of tensile stress along the lock-pin.

Downloaded 02 Jun 2010 to 171.66.16.109. Redistribution subject to ASME license or copyright; see http://www.asme.org/terms/Terms_Use.cfm

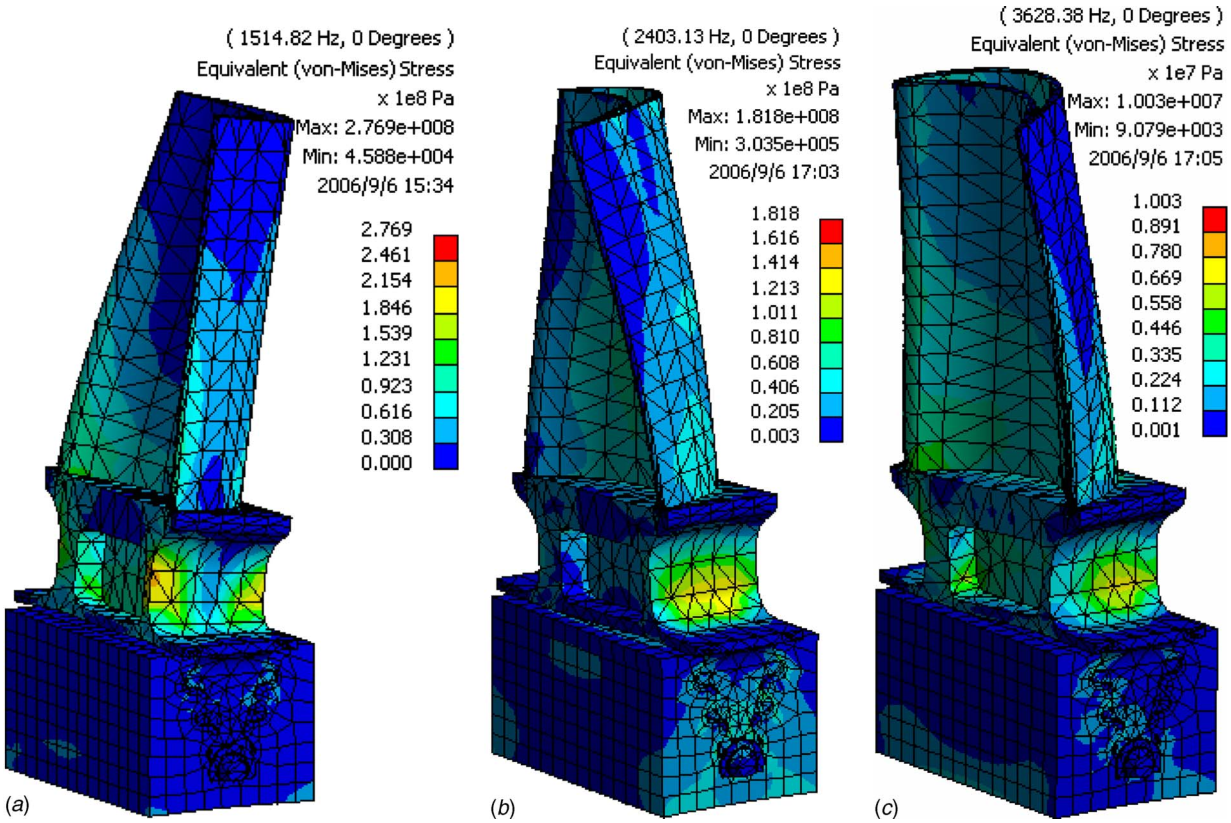

Fig. 8 Harmonic analysis. (*a*) First bending mode (peripheral direction), (*b*) second bending mode (axial direction), and (*c*) third torsional mode.

lated for the three natural modes. To compare the actual service condition of buckets, the stress distributions according to first, second, and third vibrational mode shapes are shown in Fig. 8. The maximum stress of the lock-pin corresponding to the second vibrational mode is concentrated in the neck of lock-pin's head, where the failures have happened. Therefore, it is concluded that the first bending and the third torsional vibration mode are not the significant contributors to the failure of lock-pins.

Figure 9 presents the focus view of lock-pin inside the fir-tree area. The position of local stress concentration at the fillet portion

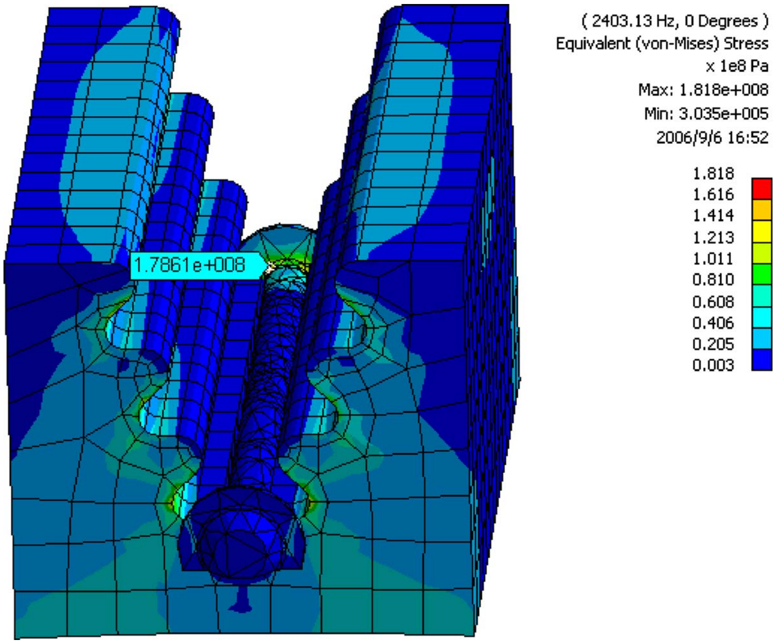

Fig. 9 The magnified views of the second natural mode in Fig. 8(*b*)

Downloaded 02 Jun 2010 to 171.66.16.109. Redistribution subject to ASME license or copyright; see http://www.asme.org/terms/Terms_Use.cfm

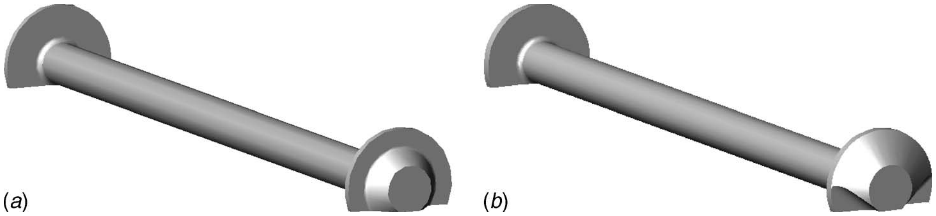

Fig. 10 (*a*) The view of a damageable lock-pin with week profile at the ends. (*b*) A lock-pin with the advanced head profiles.

of lock-pin demonstrates a very good agreement of the predicted stress distribution and crack location. The value of stress is labeled 178.6 MPa in the neck of lock-pin.

3.4 Discussion of the Excitation Factors. Along this study, it was found that the locking-pins were the starter agent of all events. In fact, they are designed to inhibit the axial displacement of buckets in disk grooves. Thus, the lock-pins that encounter to fatigue phenomena with corrosive and high temperature condition cannot sustain the affected loads and after a few operating times will fail and result in lots of damage.

Consistently, due to the excessive vibration of the first failed bucket, the next one will undergo the same critical conditions. Subsequently, before setting the third adjacent buckets to similar events, the fractured parts of the first and the second failed blades impact to the other blades and they will fracture. However, the vibration control of gas turbo generators can help to reduce the amount of risks effectively, but some vibrating sources are the inherent specifications of turbo engines. In this manner, investigation of important parts is very essential. Substantially, during the operation of gas turbines, there are complicated vibrational systems, which can be excited by disturbing agents. For example, bladed-disks in turbine stages are important components for vibrational considerations.

Although most excitations in turbo machinery are sinusoidal forms, impactlike excitations are common. Surge and volute tongue pressure distribution are examples of such loading. Marscher [20] grouped the excitations factors into three categories: those involving free vibration, those creating forced vibrations, and those involving self-excited instability phenomena.

Usually the parameter N (rotor speed) is defined by rps for calculating the excitation frequencies. The aerodynamic loads are one of the exciting agents. Therefore, by taking into account the 50 nozzle guide vanes of the first stage, the base frequency of the gas dynamic fluctuations on a blade can be calculated by the following formula [21]:

$$\text{Vane passing frequency} = \text{Number of nozzles in cascade} \times \text{rps} = 50 \times 85 = 4250 \text{ Hz} \qquad (6)$$

As aforementioned, the frequency of second mode is about 2403 Hz, which consequently along every start-stop of the turbine engine will be resonated at 2884 rpm of rotor speed. It seems there are two remedies to avoid from destroying of components, first, reduce the number of start-stops and second, decrease the time interval of engine start-ups. By applying these two policies, the total time of resonances and related excitations will be decreased effectively and so the number of fatigue cycles.

4 Conclusions

Because of the complex nature of the turbine part failure, numerous aspects were examined. This paper has focused specifically on the possible causes of fatigue failure, which may occur as a direct consequence of anomalies in the mechanical behavior of the lock-pins in conflict with both the blade's root and disk. Some related conclusions that were found are summarized below.

The fractography of failed lock-pin shows that the crack has been initiated and propagated in one side of lock-pin by fatigue mechanism and the kind of loading has been bending type. To find the distribution of the mechanical stresses, the finite element method was carried out for all related components. The results showed that the second vibrational mode of buckets caused the most severe loading on the head of the lock-pin to make higher stress levels. During each start-stop, the second vibrational mode, depending on the excitation frequency, could be occurred.

As a correlated conclusion, the likely causes of catastrophic failure in the hot section are mainly considered to be high cycle fatigue phenomena due to blade root/head of lock-pin impact. The cause of such impact may be increased in clearance of disk serrations as a consequence of fretting wear and local microscopic fusions between the blade root and the lock-pin's stem, after an extended period in service. In this case, the risk of failure would clearly be exacerbated by improper operation due to the destruction of sealing and hot gas leakage in these areas and finally inadequate design of lock-pins to sustain a severe hot condition in the first stage of turbine section. On the other hand, there was no report of similar failures for the second stage of these gas turbine types.

In the fir-tree area, most of the corrosion damage are located on the slot surfaces of the disk fir-tree. This is consequent of more rigidity of blade material rather than the disk. Because of this undesired over clearance, the bucket is exposed to new conditions with an inadmissible degree of freedom. Consequently, the meridional vibration of blade will be as enough as to make a harmful engagement between lock-pin ends, root of the blade, and lateral surfaces of the disk, which provides a fatigue process for the weakest mechanical device, "the locking-pins."

5 Recommendations

(a) Provide a better preventive method to inhibit any hot gas leakages around the lock-pins.
(b) Improve the mechanical properties of lock-pin by changing the applied material.
(c) Reduce the time interval of start-ups to avoid from any resonance conditions.
(d) Modify the geometric profile of the lock-pin heads according to Fig. 10(*b*).

Acknowledgment

The authors would like to thank Mr. Kalouti and Mr. Gharib for their financial support through investigation of the projects. In addition, they would also like to acknowledge Mr. Vahedi, Aghajanlu, Farrahi, Hatami, and Garjani for their contributions to gather the metallurgical data and Mr. Oghbaee for his contribution to prepare the failure photos.

References

[1] Papanikos, P., Meguid, S. A., and Stjepanovic, Z., 1998, "Three-Dimensional Nonlinear Finite Element Analysis of Dovetail Joints in Aeroengine Discs," Finite Elem. Anal. Design, **29**, pp. 173–186.
[2] Kenny, B., Patterson, E., Said, M., and Aradhya, K., 1991, "Contact Stress

Downloaded 02 Jun 2010 to 171.66.16.109. Redistribution subject to ASME license or copyright; see http://www.asme.org/terms/Terms_Use.cfm

Distributions in a Turbine Disc Dovetail Type Joint—A Comparison of Photo Elastic and Finite Element Results," Strain, **27**, pp. 21–24.

[3] Nurse, A. D., and Patterson, E., 1993, "Experimental Determination of Stress Intensity Factors for Cracks in Turbine Discs," Fatigue Fract. Eng. Mater. Struct., **16**, pp. 315–325.

[4] Boddington, P. H. B., Chen, K., and Ruiz, C., 1985, "The Numerical Analysis of Dovetail Joints," Comput. Struct., **20**, pp. 731–735.

[5] Parks, V. J., and Sanford, R. J., 1977, "Experimental Stress Analysis of the TF-30 Turbine Engine Third-Stage Fan-Blade/Disc Dovetail Region," NRL Report No. NRL 8149.

[6] Parks, V. J., and Sanford, R. J., 1978, "Three-Dimensional Photo Elastic Stress Analysis of the Dovetail Region of the TF-30 Turbine Engine Third-Stage Fan," NRL Report No. NRL 8276.

[7] Durelli, A. J., Dally, J. W., and Riley, W. F., 1957, "Stress and Strength Studies on Turbine Blade Attachment," SESA Proceedings, Vol. XVI(1), pp. 171–186.

[8] *Sawyer's Turbo Machinery Maintenance Handbook*, 1980, Vol. 1, 1st ed., Turbo Machinery International, Norwalk, CT, Chaps. 1 and 12.

[9] Mazur, Z., and Kubiak, J., 1998, "Gas Turbine Rotor Disc Repair—Case History," ASME Paper No. 98-GT-547.

[10] Poursaeidi, E., Aghajanlu, M., Farrahi, Gh. H., Hatami, Sh., and Garjani, I., 2000, "Failure Analysis of Unit 4 and 5 Gas Turbines of Shariati Power-Plant," Iran Power Plant Repair Company, Internal Report No. 96.

[11] Poursaeidi, E., and Mohammadi, M. R., 2008, "Failure Analysis of Lock-Pin in a Gas Turbine Engine," Eng. Failure Anal., **15**(7), pp. 847–855.

[12] *Sawyer's Gas Turbine Engineering Handbook*, 1985, Vol. 3, 3rd ed., Turbo Machinery International, Norwalk, CT, Chap. 5.

[13] *ASM Metals Hand Book: Failure Analysis and Prevention*, 1987, Vol. 11, 9th ed., ASM International, Materials Park, OH, p. 111.

[14] *ASM Specialty Hand Book: Stainless Steels*, 1999, The Materials Information Society, ASM International, Materials Park, OH.

[15] *CASTI Metals Black Book: North American Ferrous Data*, 2003, 5th ed., Casti Publishing, Inc., Canada.

[16] Donachie, M. J., and Donachie, S. J., 2002, *Super Alloys: A Technical Guide*, 2nd ed., The Materials Information Society, ASM International, Materials Park, OH.

[17] Kostyuk, A., and Frolov, V., 1988, *Steam and Gas Turbines*, Mir, Moscow.

[18] Mukhopadhyay, N. K., Ghosh Chowdhury, S., Das, G., Chattoraj, I., Das, S. K., and Bhattacharya, D.K., 1998, "An Investigation of the Failure of Low-Pressure Steam Turbine Blades," Eng. Failure. Anal., **5**(3), pp. 181–193.

[19] Rao, J. S., 2000, *Turbine Blade Life Estimation: High Cycle Fatigue Life Estimation by Stress Based Theories*, Alpha Science International Ltd., Oxford, UK.

[20] *Sawyer's Gas Turbine Engineering Handbook*, 1985, Vol. 3, 3rd ed., Turbo Machinery International, Norwalk, CT, Chap. 7.

[21] Rao, J. S., 2005, *Turbomachine Blade Vibration*, New Age International, New Delhi, India.

Downloaded 02 Jun 2010 to 171.66.16.109. Redistribution subject to ASME license or copyright; see http://www.asme.org/terms/Terms_Use.cfm

Daejong Kim[1]
Mechanical and Aerospace Engineering,
University of Texas at Arlington,
500 West 1st Street,
Arlington, TX 76019
e-mail: daejongkim@uta.edu

Andron Creary
Department of Mechanical Engineering,
Texas A&M University,
3123 TAMU,
College Station, TX 77843

Suk Sang Chang

Jong Hyun Kim

Pohang Accelerator Laboratory,
POSTECH,
San-31 Hyojadong,
Pohang 790-784, Republic of Korea

Mesoscale Foil Gas Bearings for Palm-Sized Turbomachinery: Design, Manufacturing, and Modeling

Palm-sized microturbomachinery have broad potential applications in micropower generation areas, such as air/fuel management systems for various fuel cells, propulsion engine for unmanned micro-air vehicles, power generation turbines for robots, small satellites, etc. This paper introduces design and manufacturing processes of mesoscale foil gas bearings applicable to the microturbomachinery and also presents its performances predicted from nonlinear orbit simulations. X-ray and ultraviolet lithography were explored as promising manufacturing tools of elastic foundations for the mesoscale foil gas bearings. Designed and manufactured mesoscale foil gas bearings have unique design features that precision-machined foil bearings cannot provide, such as easy control of mechanical properties of elastic foundations, a simple assembly process, and easy control of bearing preload through lithographic pattern. The manufactured bearing performance was predicted using a time-domain orbit simulation, and results are presented. [DOI: 10.1115/1.3077643]

Keywords: power MEMS, mesoscale foil gas bearing, palm-sized microturbomachinery

1 Introduction

Palm-sized microturbomachinery has broad potential applications in micropower generation areas, such as air/fuel management system for small fuel cells, propulsion engines for unmanned air vehicles, micropower generation for robots, small satellites, etc. These very small microturbomachinery cannot use ball bearings due to their limited reliability at extremely high speeds. Considering the reliability issue and the well-known high surface area/volume ratio in small system, gas-lubricated bearings are the most feasible solution.

An approach using silicon as a structural material for the gas bearings constrains design features to solid wall geometry [1] with limited reliability during rotor crashes. Furthermore, structural and manufacturing limitations of silicon microturbomachinery mandate very small length to diameter (L/D) ratio of the silicon microgas bearings. Recent progress on the silicon microgas bearings [2] partially owes to precisely-controlled pressure drop across the bearing length and nonsymmetrical bearing stiffness. However, the precise control of pressure drop across the bearing length requires a complicated flow path, and control of the required pressure difference may not be feasible in certain microturbomachinery applications. A miniaturization of the existing small turbomachinery to microturbomachinery, of which examples can be found in Refs. [3–7], can eliminate the structural limitation inherent to the silicon microturbomachinery. This approach can reduce the rotor speed below 1,000,000 rpm because the impeller size can be increased up to 10–12 mm for bearing size of 5–6 mm. However, the required operating speeds of these three-dimensional palm-sized microturbomachineries are still above 500,000 rpm to achieve target performance.

Macroscale foil gas bearings, shown in Fig. 1, are the most widely-accepted form of stable gas bearings for various oil-free turbomachinery applications. A corrugated bump foil supports the smooth top foil providing elastic cushion as well as damping when the bump foils slide against the bearing sleeve and top foil. The bump foils and top foil are welded at one end and whole foil assembly is assembled to the bearing sleeve. The damping provided by the bump foil is believed to be beneficial to suppress hydrodynamic instability, which has been a chronic problem in gas-lubricated bearings. Furthermore, the compliant structure of the foil bearing can accommodate rotor-bearing misalignment and debris in some extent. Due to the promising feature of the foil bearings, they have been investigated extensively for decades, and currently foil bearings are used in air management systems [8] for aircraft, microgas turbines as independent power generators [9], turbo compressors [10], etc.

However, miniaturization of the macroscale foil bearing into its mesoscale counterpart is not easy due to the complicated structure of bump foils and the difficulty in forming the tiny precision bump foils using very thin metal sheets. Furthermore handling and assembly of the tiny bump foils onto the bearing is very laborious. In addition, the continuous bump foil structure makes the analysis and performance prediction very difficult. Due to the difficulties in designing (analysis and prediction) and manufacturing into mesoscale, applications of the foil bearing into palm-sized microturbomachinery are very limited. Only exploratory experimental investigations on mesoscale foil gas bearing made by precision machining have been reported in Refs. [7,11].

Successful deployment of mesoscale foil gas bearings into the industry requires innovative an approach in designing and manufacturing. Continuous bump foils are not universal solution for the foil bearing, and any appropriate elastic foundation that provides both stiffness and damping can support the top foil. However, potential high temperature applications prohibit the usage of elastomers. Furthermore, due to the continuous elastic motion of the elastic foundation during the operation, semiconductor materials are also excluded in the material selection. Only metallic or metal/ceramic composite structures are feasible as the elastic foundation. Manufacturing process should be simple and dimensions should be accurately controllable and repeatable with very smooth surfaces.

---

[1] Corresponding author.

Manuscript received December 16, 2007; final manuscript received November 17, 2008; published online April 10, 2009. Review conducted by Patrick S. Keogh.

Copyright © 2009 by ASME

Downloaded 02 Jun 2010 to 171.66.16.109. Redistribution subject to ASME license or copyright; see http://www.asme.org/terms/Terms_Use.cfm

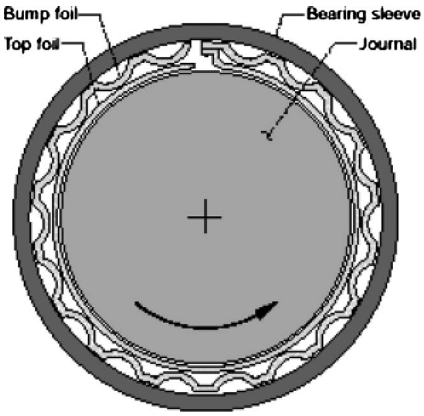

Fig. 1 Schematics of macroscale foil bearing; figure adopted from Ref. [15]

Considering the above constraints, the LIGA—German acronym for lithography, electroplating and molding—process [12] involving X-ray lithography or ultraviolet (UV) lithography is a feasible process to manufacture the mesoscale foil gas bearings using metals. Submillimeter scale gas bearings fabricated using X-ray lithography and electroplating have been reported earlier [13,14] and the process can be applied to mesoscale gas bearings.

2 Scope of the Paper

This paper introduces the design and manufacturing process of mesoscale foil gas bearings with a bearing (journal) diameter of 5 mm and length of 4 mm made of Ni. The manufacturing process combines lithography of polymer mold, electroplating of Ni, and precision forming of the top foil. Unique design features of the mesoscale foil bearings and performance analysis results are also presented. The performance analyses involve solving transient Reynolds equations for the gas film and nonlinear dynamic simulation of rotor motion supported by the designed mesoscale foil gas bearings.

3 Design Features

Lithographically manufactured mesoscale foil gas bearings have unique design features that precision-machined foil bearings [7,11] cannot provide. Figure 2 shows the design of an elastic foundation used in the designed mesoscale foil gas bearing. Unlike continuous bump foils shown in Fig. 1, the manufactured elastic foundation is comprised of multiple independent bump sets. Each bump set consists of an inner bump (IB), outer bump (OB), and a partial arc beam (AB).

A unique feature of mesoscale foil gas bearings manufactured through the method in this work is that various compliant wall structures that cannot be made via traditional precision machining can be made. For example, each bump set in Fig. 2 provides independent stiffness and damping to the top foil unlike macroscale foil bearings in Fig. 1, where bump foils are continuous, and it is difficult to analyze overall characteristics. Each bump can be engineered and designed differently along the circumferential direction for improved bearing performance. The IB and OB provide parallel stiffnesses combined with the AB in a series to the IB and OB. Stiffness of these spring elements can be calculated using elementary beam theory.

Figure 3 shows overall assembly procedure of mesoscale foil gas bearing. The multiple elastic foundation layers are assembled into the top foil (made of thin sheet metals via hot forming) through the grooves on the elastic foundation layers, which are formed as an integral process of lithography. A precision-machined bearing sleeve encloses the top foil-elastic foundation assembly to complete the bearing. Because each elastic foundation layer provides independent support to the top foil along the axial direction, they do not have to be bonded together. This adds another benefit and advantage to the proposed design/manufacturing approach over the traditional precision machining; each elastic foundation layer can be engineered and manufactured independently with different stiffnesses and dampings along the bearing length.

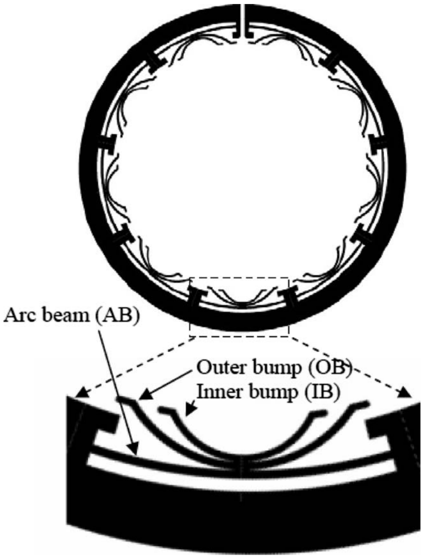

Fig. 2 Design of elastic foundation layer for mesoscale foil gas bearings

Parametric studies on macroscale foil bearings [16] indicate that the foil gas bearings with three top foil pads with noncircular geometry have superior rotor dynamic performance to the bearings with cylindrical continuous top foil. In macroscale foil gas bearings, the bearing sleeve can be machined with certain geometry such that the final bearing surface on the top foil follows a noncircular geometry. However, in the mesoscale foil gas bearings, the noncircular bearing geometries cannot be achieved easily using traditional precision machining. Adopting lithography techniques for the elastic foundations can overcome this kind of problem without any difficulty.

Another important design feature of the manufactured mesoscale foil bearings is a self-generated preload. It is well-known that the lightly-loaded gas bearings are unstable due to large cross-coupled stiffness [13,17]. Traditionally external loading has been the most effective mechanism to stabilize any fluid film bearings, which would be unstable otherwise. External loading is not practical and is very difficult in very small rotating machines, thus the bearings should be designed such that they are self-preloaded when installed on a machine. In the manufacturing process, the

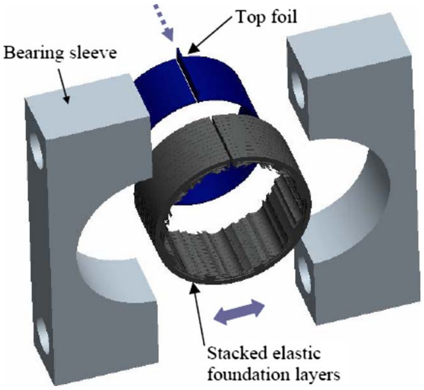

Fig. 3 Assembly scheme of mesoscale foil gas bearing

Downloaded 02 Jun 2010 to 171.66.16.109. Redistribution subject to ASME license or copyright; see http://www.asme.org/terms/Terms_Use.cfm

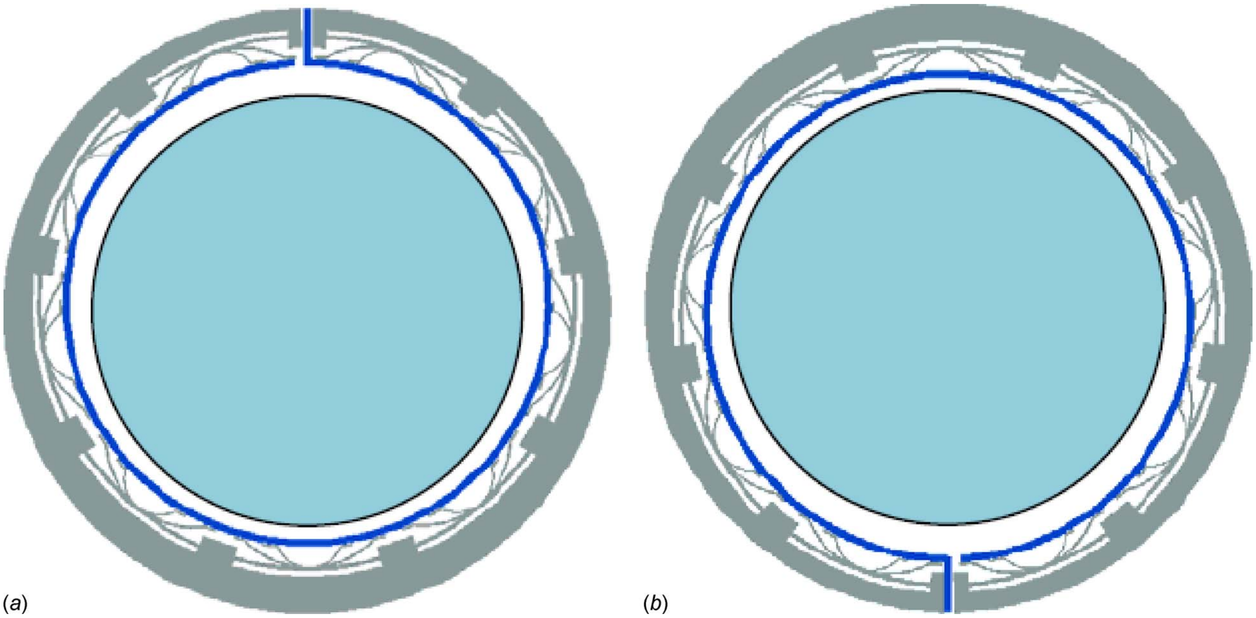

Fig. 4 Exaggerated schematic description of elastic foundation with different shell thicknesses along the circumferential direction: (*a*) front half sub-bearing, and (*b*) rear half sub-bearing

solid shell thickness was made different along the circumferential direction via the lithography mask pattern as exaggerated in Fig. 4(*a*). When the two sub-bearings (each 2 mm long) in Fig. 4 are arranged to a back-to-back configuration, 180 deg offset of top foil leading edges, the total bearing assembly (4 mm long) has a finite amount of self-generated hydrodynamic preload as illustrated in Fig. 5. The preloading direction is in vertical direction in Fig. 5, and the amount of preload is the same as the difference of minimum and maximum solid shell thicknesses in the bearings. It is also noteworthy that the self-generated preload could also be implemented within one bearing through the lithography pattern of the elastic foundation. However, the back-to-back arrangement of two sub-bearings was chosen to easily control the preload by clocking one sub-bearing with respect to another. Furthermore, manufacturing circular top foils is much easier than lemon-shaped top foil in mesoscale.

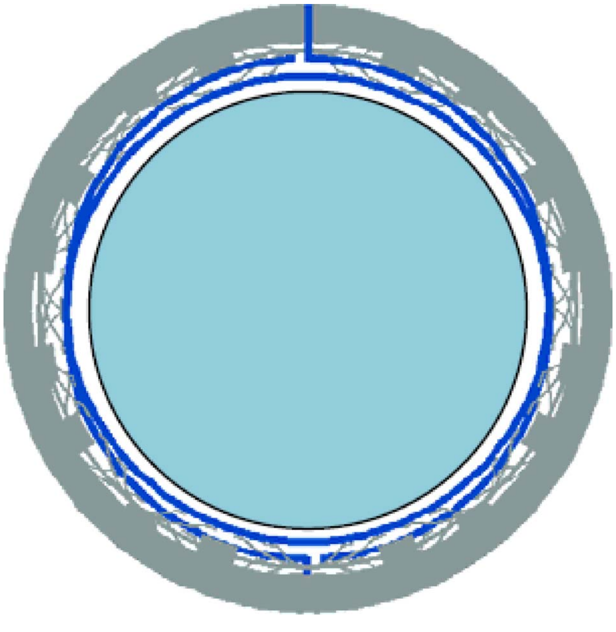

Fig. 5 Schematic description of the mesoscale foil gas bearing with a hydrodynamic preload in vertical direction; two sub-bearings are arranged as back-to-back configuration

4 Manufacturing Process

200 μm and 1 mm thick elastic foundation layers were made through UV lithography on SU-8 (negative photo resist available from MicroChem, Inc. [18]) and X-ray lithography on polymethyl-methacrylate (PMMA), respectively, and successive electroplating on the SU-8 and PMMA plating molds.

For specific bearing length, the number of elastic foundation layers should be decided depending on their thickness. Advantages of using UV lithography on SU-8 are low cost and easy design change by redesigning the UV mask. However, maximum thickness that can be achieved by UV lithography is limited because high precision (vertical sidewall) is required on the elastic foundation layers. X-ray lithography can produce very thick layers but requires expensive X-ray mask. If, however, full LIGA process [12] is combined with X-ray lithography, the electroplated Ni inserts can be used to replicate the plastic molds for successive metal sintering or electroplating without repeating the expensive X-ray lithography.

In this work, as a preliminary research, the original electroplated Ni structures were used as elastic foundation layers for the bearings without further seeking for full LIGA process. Detailed processes of UV lithography on 200 μm thick SU-8 are as follows: Silicon wafer was cleaned in a Piranha etching solutions which is comprised of a 3:1 volumetric ratio of H_2SO_4 and H_2O_2 at 100 °C for 1 h, followed by O_2 plasma cleaning. As a seed layer for electroplating, 50 nm thick Cr and 50 nm thick Au layers were evaporated on the silicon wafer using a BOC Edwards Auto 306 metal evaporation system. Because the adhesion of SU-8 is not good on the Au seed layer, an adhesion promoter, OmniCoat (from MicroChem, Inc. [18]), was spin-coated on top of the Cr/Au seed layers to improve adhesion of the SU-8. 200 μm thick SU-8 was spin coated and soft baked at 65 °C for 7 min and 95 °C for an additional 39 min. Slow temperature ramp of 6 °C/min was used between 65 °C and 95 °C. Quintel Q4000 MA was used for UV exposure. The required dose was 315 mJ/cm^2 with an exposure time of 26.3 s with I-line intensity at 12 mW/cm^2. The postexposure bake was done at 65 °C for 5 min followed by addi-

Downloaded 02 Jun 2010 to 171.66.16.109. Redistribution subject to ASME license or copyright; see http://www.asme.org/terms/Terms_Use.cfm

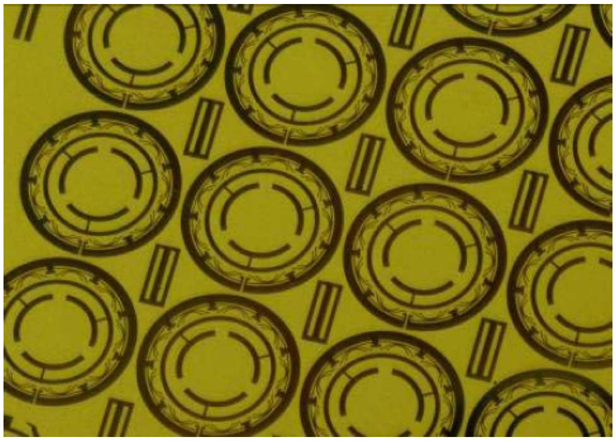

Fig. 6 **Photo of an X-ray mask for manufacturing of the mesoscale foil gas bearings. The dark area is the X-ray transparent material (represents the areas for bearing structures) and the bright area is with the X-ray absorber (Au film)**

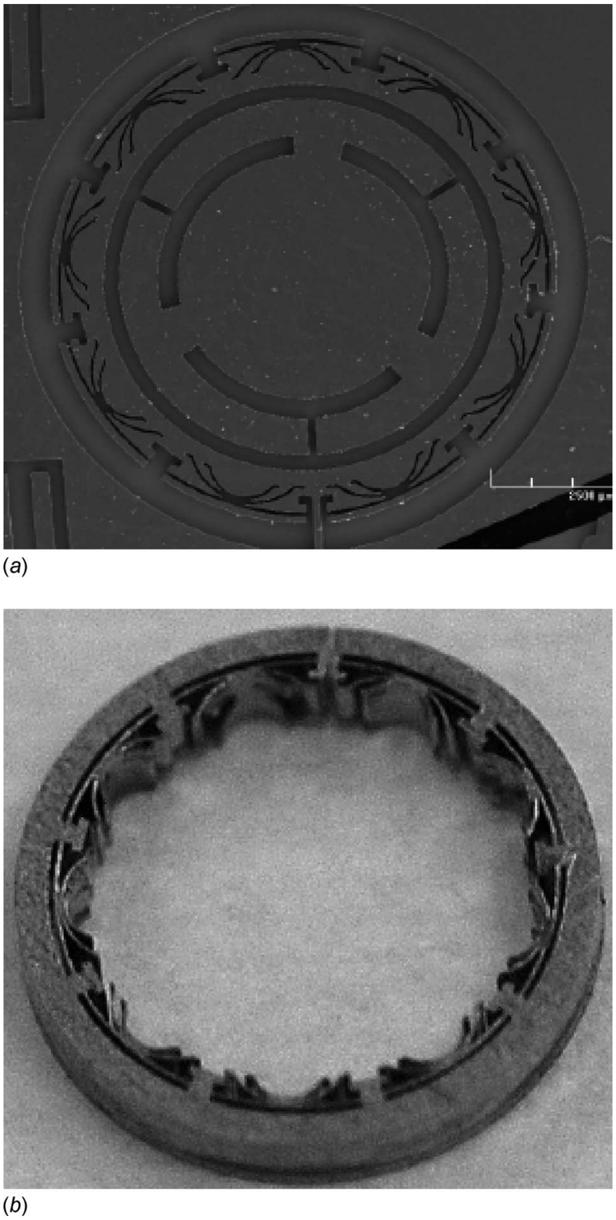
(*a*)

(*b*)

Fig. 7 **SEM image of 1 mm thick PMMA mold and the optical image of an elastic foundation layer: (*a*) PMMA mold, and (*b*) elastic foundation layer**

tional baking at 95 °C for 16 min. Slow temperature increase similar to soft-baking was necessary to avoid thermal shock to the SU-8. For the same reason, the SU-8 was cooled down slowly for about 12hrs after postexposure bake. The SU-8 was developed for 16 min in SU-8 developer, cleaned with isopropyl alcohol, and dried with filtered air.

1 mm thick PMMA plating mold was also fabricated using X-ray lithography. Figure 6 is a photo of the fabricated X-ray mask. The dark areas without Au film in Fig. 6 have images of the bearings to be manufactured. The X-ray mask was fabricated at Pohang University of Science and Technologies (POSTECH), and the PMMA plating mold was developed through successive exposure to X-ray and development in a G-G solution, which is composed of 60 vol % of 2-(2-butoxyethoxy)ethanol, 20 vol % of morpholine, 5 vol % of 2-aminoethanol, and 15 vol % of deionized water.

After the SU-8 or the PMMA mold was manufactured, Ni was electroplated in a sulfamate bath for room temperature applications as initial studies. The current density was 10 $\mathrm{mA/cm^2}$ at 50 °C. Figure 7 shows scanning electron microscope (SEM) images of the 1 mm thick PMMA mold and an optical image of the 1 mm thick elastic foundation layer made of Ni. The top foil made of 75 μm thick stainless steel sheet was manufactured using a hot-forming process at 500 °C.

5 Performance Analysis of the Designed Bearing

To understand the dynamic behavior of the mesoscale foil gas bearing, a mathematical model was developed to simulate the rotordynamic behavior of a rotor supported by the mesoscale foil gas bearings.

5.1 Model for Elastic Foundations. Although the layers are not bonded, the total elastic foundation is assumed to be one piece with a length corresponding to the sum of each elastic foundation layer. In the computational model for the pressure calculation, the bearing surface (on the top foil) is modeled with multiple grid points along the circumferential and axial directions. Note that the number of grid points along the axial direction does not have to be the same as the number of elastic foundation layers because the elastic foundation is assumed one piece in physical domain. Because the pressure is different along the axial direction, the elastic foundation undergoes different deflections along the axial direction. Therefore, for the simplicity of the computational model, it is assumed that the total elastic foundation can be modeled as multiple independent layers corresponding to the number of computational grid points along the axial direction, and each layer provides independent support to the top foil. The thickness of each elastic foundation layer can be chosen such that the physical number of layers within the foundation matches with the number of grid points along the axial direction. However, because different bearing designs (and fabrication methods) can have different thicknesses of elastic foundation layers and total bearing lengths, it is more convenient to separate the physical and computational domains.

Because the elastic foundation is modeled as multiple layers, each bump set within the layer is consisted of two bumps (IB and OB) with contact patches with the top foil and one partial AB fixed to the structure (see Fig. 2). The stiffnesses of IB, OB, and AB can be calculated using elementary beam theory [19], assuming the contact patches of IB and OB are free to move. The thickness of all the beam structures is 50 μm.

Figure 8(*a*) shows presumed motions of one bump set under dynamic pressure through the top foil. The simplified model represented by the two spring-viscous dampers (one spring-damper

Downloaded 02 Jun 2010 to 171.66.16.109. Redistribution subject to ASME license or copyright; see http://www.asme.org/terms/Terms_Use.cfm

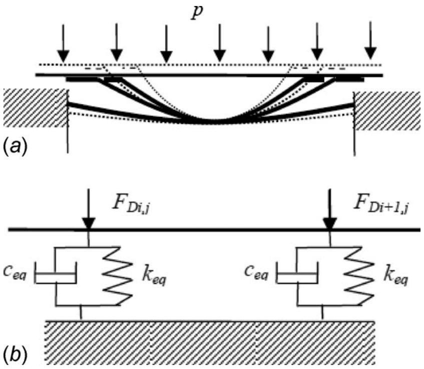

Fig. 8 Presumed motions of one bump set and equivalent spring-damper models: (*a*) presumed motions of one bump set, and (*b*) two spring-damper models for each bump set

combination will be called "elastic support" hereafter) assumes that the top foil and bumps sets are massless. Dotted lines and curves represent the structure and the top foil before deflection and solid lines represent the deformed shapes. The design of the mask in Fig. 6 was made such that the distances between individual elastic supports are nearly equally-spaced. Because each bump set is modeled as two elastic supports, the equivalent stiffness of one elastic support can be found from the following equation:

$$\frac{1}{2k_{\mathrm{eq}}} = \frac{1}{(k_{\mathrm{IB}} + k_{\mathrm{OB}})} + \frac{1}{k_{\mathrm{AB}}} \tag{1}$$

where k_{AB} is a stiffness of AB, k_{IB} and k_{OB} are the stiffnesses of IB and OB, respectively

The bump foils are modeled as spring-viscous dampers with equivalent damping coefficient, $c_{\mathrm{eq}}=\gamma_b k_{\mathrm{eq}}/\omega$, assuming the bump motion is sinusoidal by imbalance excitations. The structural loss factor can be found experimentally, and many experimental studies on damping measurements of the bump foils [20–23] show that the loss factor is in the range of 0.15–0.25 depending on the design.

Adopting the spring-viscous damper model, the equation of motion for each elastic support is

$$c_{\mathrm{eq}}\dot{\delta}_{Di,j} + k_{\mathrm{eq}}\delta_{Di,j} = F_{Di,j} \tag{2}$$

The proposed model would render a negative film thickness at the bearing edges where net pressure becomes zero whenever the bearing is loaded beyond the original clearance. Therefore, the top foil deflections at the edge region adopt a linear extrapolation from the values evaluated near the edge of the bearing. The accuracy and appropriateness of the independent elastic support model along the axial direction and the extrapolation model toward the edge regions were validated in previous studies on macroscale foil gas bearings by the authors [16,21,24].

5.2 Model for Hydrodynamic Pressure on the Top Foil. The dynamic forces $F_{Di,j}$ on each elastic support (see Fig. 8(*b*)) can be found by solving a simplified Navier–Stokes equation applied to thin gas film, i.e., Reynolds equation [17], given by

$$\frac{\partial}{R^2\,\partial\theta}\left(\frac{ph^3}{12\mu}\frac{\partial p}{\partial\theta}\right) + \frac{\partial}{\partial z}\left(\frac{ph^3}{12\mu}\frac{\partial p}{\partial z}\right) = \frac{R\omega}{2}\frac{\partial}{R\,\partial\theta}(ph) + \frac{\partial}{\partial t}(ph) \tag{3}$$

where μ is the viscosity, p is the pressure, h is the local gas film thickness, ω is the angular velocity of the rotor, θ is the circumferential coordinate described in Fig. 9, z is the axial direction, and x is the circumferential direction of the unwrapped bearing. Equation (3) can be nondimensionalized as

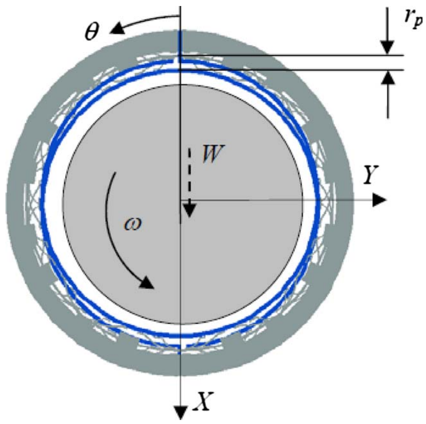

Fig. 9 Coordinate systems for analyses. r_p is the hydrodynamic preload offset distance.

$$\frac{\partial}{\partial\theta}\left(PH^3\frac{\partial P}{\partial\theta}\right) + \frac{\partial}{\partial Z}\left(PH^3\frac{\partial P}{\partial Z}\right) = \Lambda\frac{\partial(PH)}{\partial\theta} + 2\Lambda\frac{\partial(PH)}{\partial\tau} \tag{4}$$

where $\Lambda=(6\mu\omega/p_a)(R/C)^2$, $\theta=x/R$, $Z=z/R$, $\tau=\omega t$, $H=h/C$, and $P=p/p_a$. Λ is the bearing number, R is the bearing radius, C is a nominal radial clearance of the bearing, and p_a is an atmospheric pressure.

As described earlier, assembled bearings have a hydrodynamic preload along the X-direction in Fig. 9 when two sub-bearings are arranged as back-to-back arrangement. If the preload offset distance is denoted as r_p, local film thickness at the front and rear sub-bearings considering rotor centrifugal growth can be described as

$$\begin{aligned} &H(\theta,Z) = 1 - r_g/C + (\varepsilon_X + r_p/C)\cos\theta + \varepsilon_Y\sin\theta + W(\theta,Z), \\ &\qquad 0 < Z < L/2R \\ &H(\theta,Z) = 1 - r_g/C + (\varepsilon_X - r_p/C)\cos\theta + \varepsilon_Y\sin\theta + W(\theta,Z), \\ &\qquad L/2R < Z < L/R \end{aligned} \tag{5}$$

where $W(\theta,Z)$ is a normalized top foil deflection by clearance C, ε_X and ε_Y are nondimensional rotor eccentricities in the X- and Y-directions, respectively, r_g is a rotor centrifugal growth. The front sub-bearing $(0<Z<L/2R)$ has a hydrodynamic preload in $+X$-direction while rear sub-bearing $(L/2R<Z<R/L)$ has a hydrodynamic preload in $-X$-direction. The rotor centrifugal growth can be predicted from

$$r_g = \frac{R\rho\omega^2}{4E}[R_i^2(\nu+3) + R^2(1-\nu)] \tag{6}$$

where ρ is the rotor material density, E is Young's modulus, ν is Poisson's ratio, and R_i is the rotor inner radius. Equation (6) was derived from the plane stress model of a rotating cylinder [25] but the model agrees very well with finite element results [26] because the rotor is not constrained along the axial direction.

5.3 Model for Top Foil Sagging. Because the thin top foil is supported by multiple elastic supports separated by a certain distance, as depicted in Fig. 8, the top foil may undergo a certain level of sagging between the elastic supports, as exaggerated in Fig. 10.

The detailed sagging model is fully described in Ref. [27], and only essential elements of the model are repeated in this paper. In Fig. 10, a local sagging function $v_{Di,j}(\zeta)$ is defined with respect to the local coordinate ζ (same direction as x) attached to the point where $F_{Di,j}$ is applied. Because the top foil sagging effect is considered, nodal points for pressure calculations are assigned, as shown in Fig. 11, where three computational nodal points are

Downloaded 02 Jun 2010 to 171.66.16.109. Redistribution subject to ASME license or copyright; see http://www.asme.org/terms/Terms_Use.cfm

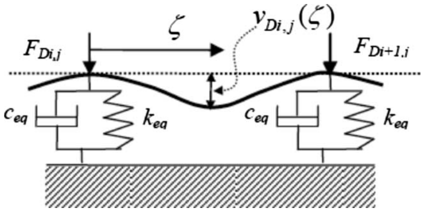

Fig. 10 Exaggerated description of a top foil sagging effect

assigned between two adjacent elastic supports.

From Ref. [27], the total force acting on the bump with an index Di,j, and the maximum sagging amount of the top foil at the center between the two elastic supports is given by the following:

$$F_{Di,j} = \frac{\Delta x \Delta z}{24}(-p_{4Di-5,j} - 2p_{4Di-4,j} + 12p_{4Di-3,j} + 26p_{4Di-2,j} + 26p_{4Di-1,j} + 26p_{4Di,j} + 12p_{4Di+1,j} - 2p_{4Di+2,j} - p_{4Di+3,j}) \tag{7}$$

$$v_{Di,j}(2\Delta x) = \frac{\Delta x^4 \Delta z}{15EI}(3p_{4Di+2,j} + p_{4Di+1,j} + 1.5p_{4Di+3,j} + 3p_{4Di-2,j} + 1.5p_{4Di-3,j} + p_{4Di-1,j} - p_{4Di,j}) \tag{8}$$

The total top foil deflection can be found by adding the local sagging function $v_{Di,j}(\zeta)$ to the linear interpolation between $\delta_{Di,j}$ and $\delta_{Di+1,j}$, which are found from Eq. (2).

$$w_{Di,j}(\zeta) = \left(1 - \frac{\zeta}{2\Delta x_1}\right)\delta_{Di,j} + \frac{\zeta}{2\Delta x_1}\delta_{Di+1,j} + v_{Di,j}(\zeta) \tag{9}$$

Finally, normalizing Eq. (9) by the nominal clearance C yields $W(\theta,Z)$ in Eq. (5).

A sagging coefficient α_f is defined as normalized maximum sagging term from Eq. (8) by clearance C for unit gauge pressures at all the nodal points.

$$\alpha_f = \left.\frac{v_{Di,j}(2\Delta x)}{C}\right|_{\text{all nodal pressures}=1\ \text{atm}} = \frac{10\Delta x^4 \Delta z}{15CEI} = \frac{3.125 \times 10^{-2}}{E}\frac{p_b^4}{Ct_b^3} \propto \frac{p_b^4}{Ct_b^3} \tag{10}$$

where $I=\frac{1}{12}\Delta z t_b^3$ and $p_b=4\Delta x$ is a pitch between two elastic supports. α_f can evaluate relative magnitude of sagging effect between two different bearing designs in different size scales. α_f for the mesoscale foil bearing in this paper is 3.3×10^{-3} times that of typical macroscale foil bearing introduced in Refs. [21,27–31]. Therefore, the actual sagging effect is much less significant compared with the macroscale foil bearings. The negligible sagging effect is due to relatively large clearance and top foil thickness compared with the size of the bearing (see Table 1). It is clear from Eq. (10) that miniaturization of every single physical variable (except stiffness of the elastic support) will render the identical sagging coefficients. However, as scaling analyses on tilting pad gas bearings [32] shows, reducing the bearing clearance in proportion to the size of the bearing renders the bearing rotordynamically very unstable regardless of the gas bearing type. Furthermore, handling very thin top foil is not easy. Due to the above two reasons, the mesoscale foil bearing in this paper has a relatively large clearance and thick top foil compared with the size of the bearing. Even if the sagging coefficient was defined in this paper, actual sagging amount of the top foil is negligible and it was not considered in the subsequent simulation studies.

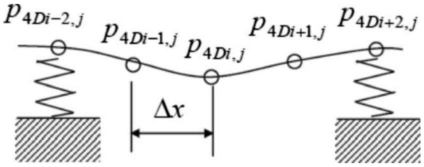

Fig. 11 Index for nodal pressures

Table 1 Geometry of the bearing and simulation parameters

Parameter	Value
Inner bearing diameter ($2R$)	5 mm
Bearing length (L)	4 mm
Preload offset distance (r_p)	22 μm
Nominal clearance (C)	25 μm
Top foil thickness (t_b)	75 μm
Number of bumps	9
Stiffness of elastic support per unit area	54 N/mm^3
Pitch of elastic supports (p_b)	0.873 mm
Rotor mass per bearing	4 g
Loss factor	0.15, 0.20, 0.25

5.4 Orbit Simulation. A widely used method to predict bearing performance is to find bearing stiffness and damping coefficients as a function of a rotor speed and fractional excitation frequency of the rotor speed and performing linear stability analyses [16,33–36]. However, as shown in Refs. [16,32,37], the linear stability analyses only provide natural frequency of rotor-bearing system and does not provide exact onset speed of instability.

In this paper, stability characteristics and overall bearing performance are evaluated using orbit method to characterize the overall performance of the manufactured mesoscale foil gas bearings. In the current frame of work, only cylindrical rigid body mode is investigated.

For the simulations, a virtual rotor, which mimics a palm-sized gas turbine generator supported by three mesoscale foil gas bearing sets is envisioned as in Fig. 12. The rotor consists of a solid shaft (diameter=5 mm, length=50 mm) and inertias (compressor, turbine, permanent magnet (PM) generator, and thrust disk), and the total mass of the virtual rotor is estimated at about 12 g. Assuming the rotor weight is evenly distributed to three bearing sets, the equivalent rotor mass to each bearing set is 4 g. From a simplified rotor model with lumped masses of compressor and turbine impellers, the rotor's first bending critical speed was estimated over 1.5×10^6 rpm, far above the maximum target design speed (600,000 rpm). Therefore, rotor is assumed to be pseudorigid, allowing only cylindrical/conical rigid body modes.

To investigate characteristics of the individual bearing set, the cylindrical mode of a pseudorigid rotor is simulated. Nondimensional rotor equations of motion are given by

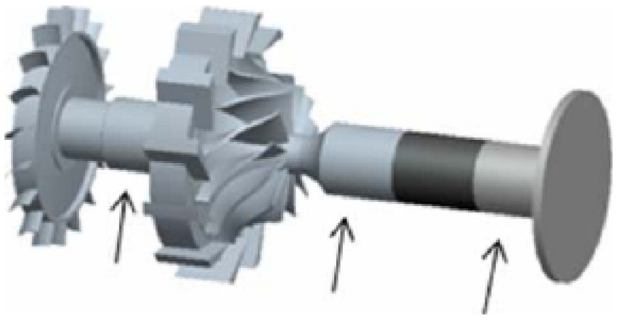

Fig. 12 Conceptual description of palm-sized gas turbine generator; the arrows indicate bearing locations

Downloaded 02 Jun 2010 to 171.66.16.109. Redistribution subject to ASME license or copyright; see http://www.asme.org/terms/Terms_Use.cfm

$$m_r C\omega^2 \frac{d^2\varepsilon_X}{d\tau^2} = F_{bX} + F_{eX} \tag{11}$$

$$m_r C\omega^2 \frac{d^2\varepsilon_Y}{d\tau^2} = F_{bY} + F_{eY} \tag{12}$$

where m_r is the rotor mass, $F_{eX,Y}$ are the external loads applied to the bearing including rotor weight, and $F_{bX,Y}$ are the dynamic bearing reaction forces integrated over the bearing surface.

In the orbit simulation, the trajectory of the rotor center is found by solving Reynolds equation (Eq. (4)), bump dynamics (Eq. (2)), and rotor equation of motions (Eqs. (11) and (12)) simultaneously. The Reynolds equation is solved at every time step using the displacements and velocities of both rotor and top foil evaluated at the previous time step. The orbit method uses 360 computational time grids for one cycle. The fifth order Adams–Bashforth scheme [38] was used for the time integration. More details on the accuracy of the chosen time step and the orbit method can be found in Refs. [16,27].

It is very well-known that lightly-loaded gas bearings are very unstable. As explained earlier, the manufactured bearing has a self-generated hydrodynamic preload (see Fig. 5) when the rotor is assembled concentrically with the bearing sleeve. Each sub-bearing is 2 mm long, and the total bearing length is 4 mm. Other design variables are presented in Table 1.

Note that the bearing comprises of two sub-bearings separated with a finite gap and that the film thickness functions are also different as shown in Eq. (5). Because of the finite gap between the two sub-bearings, boundary conditions with ambient pressure are imposed at the bearing midplane and two leading edges of each sub-bearing (ambient pressure at $\theta=0$ deg for the front half bearing and $\theta=180$ deg for the rear half bearing).

The calculated equivalent stiffness of one elastic support from the geometries of the design is 188.660 mN/mm for the entire bearing length ($L=4$ mm). The number of grid points along the circumferential direction is 72, assigning 3 nodal points between 2 elastic supports (one bump contributes to two elastic supports as shown in Fig. 8). In addition, the number of grid points along the axial direction is 20 (10 for each sub-bearing), rendering $k_{\text{eq}} = 9433$ mN/mm (=188,660/20) for each elastic support or stiffness per unit area of 54 N/mm^3.

6 Simulation Results

Parametric studies were performed for the different levels of preload offset distance and loss factor. Due to the unique design feature of the elastic foundation, the true level of damping (loss factor) is unknown without experimental measurements. The onset speed of instability, critical speeds, and steady state orbit characteristics were investigated as for different preloads and loss factors. At each speed, 2000 cycles were simulated to achieve steady state orbits. For each speed, 4096 data points from last 30 cycles were converted to frequency spectrum using fast Fourier transform (FFT) algorithm.

6.1 Effect of Preload Offset Distance. Manufactured bearings have a preload offset distance of 22 μm. However, three different levels of preload offset distances (12 μm, 17 μm, and 22 μm) were selected for comparative studies with the constant loss factor of 0.2.

Figure 13 shows the waterfall plot for the bearing with a preload distance of 12 μm. For 12 μm preload case, bounded subsynchronous vibration (i.e., limit cycles) begins to appear at around 250 krpm and its magnitude grows as speed increases up to 350 krpm, where vibration magnitude reaches about 28 μm. At 360 krpm, the subsynchronous vibration became unbounded. The whirl frequency ratio at 350 krpm is 0.055 as shown in Fig. 13. Figure 14 shows the waterfall plot with a preload distance of 17 μm. The bearing is stable for the entire simulated speed range of up to 1000 krpm. At maximum simulated speed, the bounded subsynchronous vibration is still smaller than the synchronous vibration. Figure 15 shows that critical speed is around 17,500 rpm, which is very low considering the size of the bearing. The low critical speed is due to relatively large bearing clearance compared with the size of the bearing. Rendering large hydrodynamic preload with large bearing clearance makes the bearing extremely

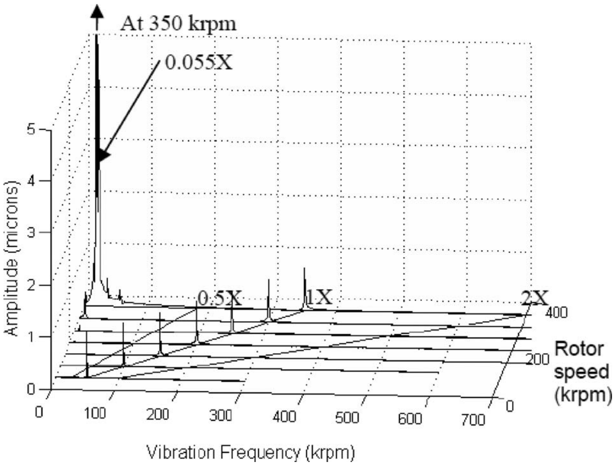

Fig. 13 Waterfall plot of simulated vibration in the *X*-direction for preload offset distance; r_p=12 μm, loss factor=0.2

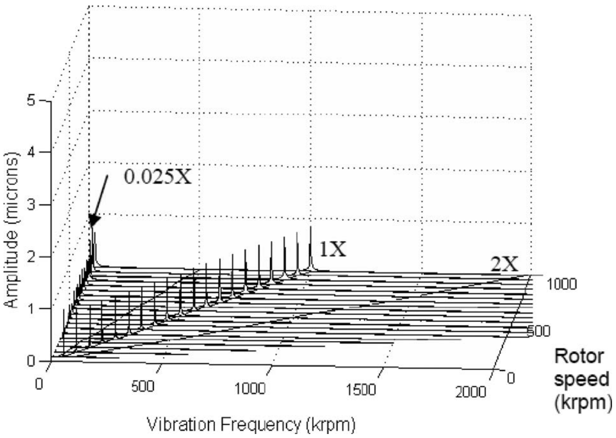

Fig. 14 Waterfall plot of simulated vibration in the *X*-direction; r_p=17 μm, loss factor=0.2

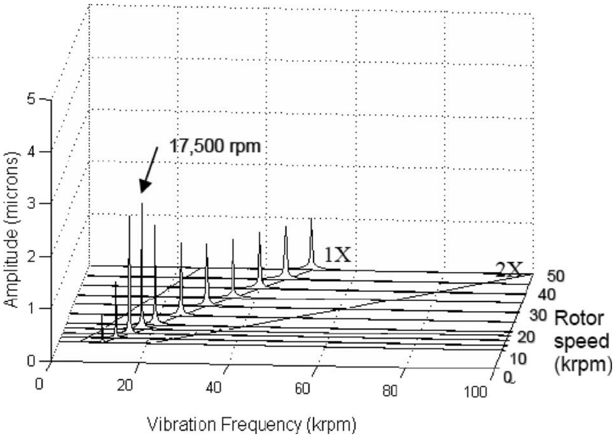

Fig. 15 Waterfall plot in the *X*-direction at low speeds; r_p=17 μm, loss factor=0.2

Downloaded 02 Jun 2010 to 171.66.16.109. Redistribution subject to ASME license or copyright; see http://www.asme.org/terms/Terms_Use.cfm

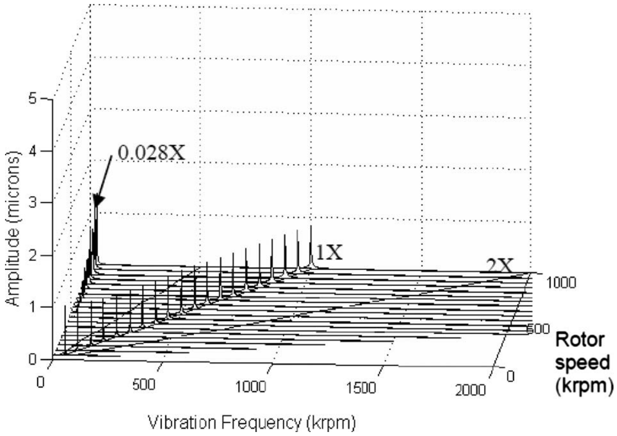

Fig. 16 Waterfall plot of a simulated vibration in the *X*-direction; $r_p=22$ μm, loss factor=0.2

stable at high speeds. Note that the large clearance does not result in a large vibration magnitude due to preload. Increasing the preload further to 22 μm does not change the overall bearing performance significantly within the speed range of interest, as shown in Fig. 16. It is noteworthy that increasing the preload from 12 μm to 17 μm stabilizes the bearing dramatically. Further increasing preload up to 22 μm does not change the overall bearing performance. However, a close look at both waterfall plots in Figs. 14 and 16 indicates that the onset of bounded subsynchronous vibration is delayed from around 400 krpm to 500 krpm as preload increases from 17 μm to 22 μm.

6.2 Effect of Loss Factor. The effect of different loss factors was investigated at the smallest preload offset distances (12 μm). Figures 17–19 show waterfall plots for preload 12 μm with different loss factors. Interestingly enough, the onset speed of bounded subsynchronous vibrations is at around 250 krpm regardless of the magnitude of the damping factors (damping of elastic supports). However, increasing the loss factor allows higher operating speed with bounded limit cycles. Figures 17–19 shows that vibration magnitude at 340 krpm decreases as loss factor is increased. For the loss factor at 0.15, subsynchronous vibration magnitude is about 4.7 μm, while they are about 3 μm for loss factor higher than 0.2. It is also observed that the maximum allowed speed with bounded subsynchronous vibration increases from about 340 krpm to about 380 krpm as loss factor is increased from 0.15 to 0.25, as shown in Fig. 20. However, considering the size of mesoscale turbomachinery and its performance requirements, the vibration magnitude should be minimized, and too high subsynchronous vibration should be avoided even if they are bounded limit cycles.

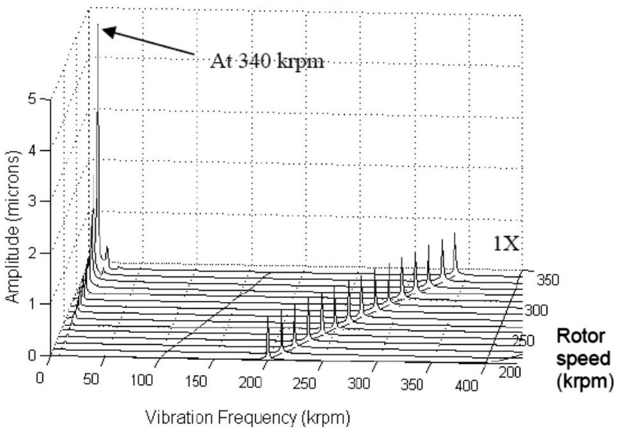

Fig. 17 Waterfall plot of simulated vibration in the *X*-direction; $r_p=12$ μm, loss factor=0.15

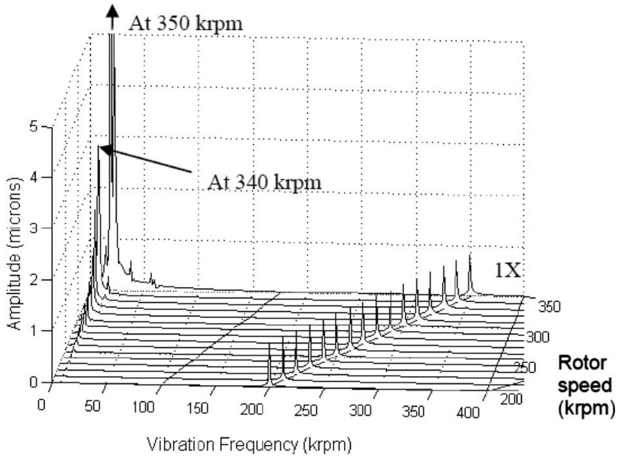

Fig. 18 Waterfall plot of a simulated vibration in the *X*-direction; $r_p=12$ μm, loss factor=0.20

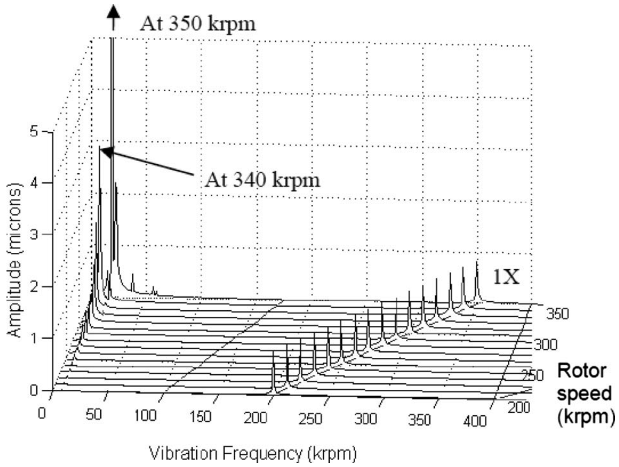

Fig. 19 Waterfall plot of a simulated vibration in the *X*-direction; $r_p=12$ μm, loss factor=0.25

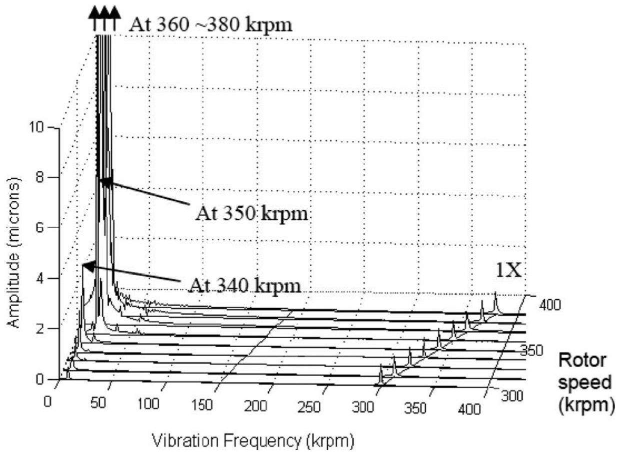

Fig. 20 Extended waterfall plot of a simulated vibration in the *X*-direction for speed range 300–380 krpm; $r_p=12$ μm, loss factor=0.25

Downloaded 02 Jun 2010 to 171.66.16.109. Redistribution subject to ASME license or copyright; see http://www.asme.org/terms/Terms_Use.cfm

7 Conclusions

X-ray and UV lithography were explored as a promising manufacturing tool of elastic foundations for the mesoscale foil gas bearings. The lithographically manufactured mesoscale foil gas bearings have unique design features that precision-machined foil bearings cannot provide, such as easy control of mechanical properties of elastic foundations, a simple assembly process, and easy control of bearing preload through lithographic pattern. 1 mm thick elastic foundation layers were manufactured and assembled with precision-formed top foil and bearing sleeve.

Preliminary simulation studies indicate that the bearing performance is affected by both preload and damping. Preload of 12 μm has a maximum operating speed of around 340 krpm with bounded subsynchronous vibration. As preload increased to 17 μm, the bounded subsynchronous vibration began to appear at around 500 krpm but remained very small comparable to a synchronous component of up to the maximum simulated speed of 1000 krpm. The fabricated bearing with preload of 22 μm shows no significant difference in bearing performance from the 17 μm case.

The effect of damping of underlying elastic support on the onset speed of subsynchronous vibration and bearing performance was investigated for the 12 μm preload case. The effect of damping of elastic foundation on the onset of subsynchronous vibration is predicted to be minimal, indicating that the source of subsynchronous vibration is a hydrodynamic interaction of circumferential gas flow with rotor motion. However, the damping of elastic support suppresses the subsynchronous vibration within bounded limit cycles allowing higher operating speeds than the onset speed of initial subsynchronous vibration.

Nomenclature

C = nominal clearance
c_{eq} = equivalent damping of one-half of a bump, as shown in Fig. 9; a combination of the Coulomb friction and squeeze film damping effect
$e_{X,Y}$ = eccentricity in the X-direction and Y-direction
$F_{bX,Y}$ = dynamic bearing reaction forces in the X- and Y-directions
$F_{Di,j}$ = dynamic force acting on an elastic support
$F_{eX,Y}$ = external forces on the rotor including the rotor weight
H = nondimensional gas film thickness $\left(H=\frac{h}{C}\right)$
h = local gas film thickness
k_{eq} = equivalent stiffness of elastic support
L = length of the bearing
m_r = mass of the rotor
P = nondimensional pressure $P=\frac{p}{p_a}$
p = pressure
p_a = ambient pressure
p_b = pitch between elastic supports
R = bearing radius
r_g = rotor centrifugal growth
t_b = thickness of top foil
$v_{Di,j}(\zeta)$ = local top foil sagging function
$W(\theta,Z)$ = nondimensional total top foil deflection, $W(\theta,Z)=\frac{w(\theta,z)}{C}$
$w(\theta,z)$ = total top foil deflection at physical domain
$w_{Di,j}(\zeta)$ = total top foil deflection in computational grid points including top foil sagging
x = circumferential direction of the unwrapped bearing, $x=R\cdot\theta$
X,Y = global inertial coordinate
Z = nondimensional axial direction, $Z=\frac{z}{R}$
z = axial direction

Greek

α_f = sagging coefficient
$\delta_{Di,j}$ = deflection of elastic support
$\varepsilon_{X,Y}$ = nondimensional eccentricity in X- and Y-directions, $\varepsilon_x=\frac{e_x}{C}$, $\varepsilon_y=\frac{e_y}{C}$
γ_b = structural loss factor of elastic supports
Λ = bearing number, $\Lambda=\left(\frac{6\mu\omega}{p_a}\right)\left(\frac{R}{C}\right)^2$
μ = gas viscosity
θ = global inertial coordinate, $\theta=\frac{x}{R}$
τ = nondimensional time, $\tau=\omega t$
ω = rotor speed, rad/s
ζ = local coordinate attached to each elastic support

References

[1] Epstein, A. H., 2004, “Millimeter-Scale, Micro-Electro-Mechanical Systems Gas Turbine Engines,” ASME J. Eng. Gas Turbines Power, **126**(2), pp. 205–226.
[2] Teo, C. J., Liu, L. X., Li, H. Q., Ho, L. C., Jacobson, S. A., Ehrich, F. F., Epstein, A. H., and Spakovszky, Z. S., 2006, “High-Speed Operation of a Gas-Bearing Supported MEMS Air Turbine,” ASME Paper No. IJTC2006-12173.
[3] Isomura, K., Tanaka, S., Togo, S., and Esashi, M., 2005, “Development of High-Speed Micro-Gas Bearings for Three-Dimensional Micro-Turbo Machines,” J. Micromech. Microeng., **15**, pp. S222–S227.
[4] Vleugels, P., Waumans, T., Peirs, J., Al Bender, F., and Reynaerts, D., 2006, “High-Speed Foil Bearings for Micro Gas Turbines: Test Set-Up,” *Proceedings of Power MEMS 2006*, Berkeley, CA.
[5] Reynaerts, D., Van Den Braembussche, J., Hendrick, P., Baelmans, M., Driesen, J., Puers, R., Al-Bender, F., Peirs, J., Waumans, T., Vleugels, P., Liu, K., Alsalihi, Z., Di Sante, A., Verstraete, T., Verstraete, D., Trilla, J., Stevens, T., Rogiers, F., Stevens, S., and Ceyssens, F., 2006, “Development of a Gas Turbine With a 20 mm Rotor: Review and Perspectives,” *Proceedings of Power MEMS 2006*.
[6] Tanaka, S., Isomura, K., Togo, S., and Esashi, M., 2004, “Turbo Test Rig With Hydroinertia Air Bearings for a Palmtop Gas Turbine,” J. Micromech. Microeng., **14**, pp. 1449–1454.
[7] Salehi, M., Heshmat, H., Walton, J. F., II, and Tomaszewski, M., 2007, “Operation of a Mesoscopic Gas Turbine Engine Simulator at Speeds in Excess of 700,000 rpm on Foil Bearing,” ASME J. Eng. Gas Turbines Power, **129**, pp. 170–176.
[8] Agrawal, G. L., 1997, “Foil Air/Gas Bearing Technology—An Overview,” ASME Paper No. 97-GT-347.
[9] “Capstone Microturbine Solutions Product Index,” available at http://microturbine.com/prodsol/products/index.asp.
[10] “Samsung Techwin Product Line,” available at http://www.samsungtechwin.com.
[11] Lee, Y., Ryu, K., and Kim, C. H., 2004, “Preliminary Test Results of Rotordynamic Characteristics for 100 Watts Class Micro Power System,” *Proceedings of Power MEMS 2004*.
[12] Ehrfeld, W., Hessel, V., Lowe, H., Schilz, C., and Weber, L., 1999, “Materials of LIGA Technology,” Springer Microsystem Technologies, **5**, pp. 105–112.
[13] Kim, D., Lee, S., Bryant, M. D., and Ling, F. F., 2004, “Hydrodynamic Performances of Gas Microbearing,” ASME J. Tribol., **126**(4), pp. 711–718.
[14] Kim, D., Lee, S., Jin, Y., Desta, Y., Bryant, M. D., and Goettert, J., 2004, “Micro Gas Bearings Fabricated by Deep X-Ray Lithography,” Microsyst. Technol., **10**, pp. 456–461.
[15] “NASA Oil Free Turbomachinery Program,” available at http://www.grc.nasa.gov/WWW/Oilfree/bearings.htm.
[16] Kim, D., 2007, “Parametric Studies on Static and Dynamic Performance of Air Foil Bearings With Different Top Foil Geometries and Bump Stiffness Distributions,” ASME J. Tribol., **129**, pp. 354–364.
[17] Hamrock, B. J., Schmid, S. R., and Jacobson, B. O., 2004, *Fundamentals of Fluid Film Lubrication*, Dekker, New York.
[18] “Description of SU-8,” available at www.microchem.com.
[19] Timoshenko, S.P., 1983, *Strength of Materials*, 3rd ed., Krieger, New York, Pts. 1 and 2.
[20] Salehi, M., Heshmat, H., and Walton, J. F., 2003, “On the Frictional Damping Characterization of Compliant Bump Foils,” ASME J. Tribol., **125**, pp. 804–813.
[21] Song, J., and Kim, D., 2007, “Foil Gas Bearing With Compression Springs: Analyses and Experiments,” ASME J. Tribol., **129**, pp. 628–639.
[22] Rubio, D., and San Andrés, L., 2007, “Structural Stiffness, Dry Friction Coefficient, and Equivalent Viscous Damping in a Bump-Type Foil Gas Bearing,” ASME J. Eng. Gas Turbines Power, **129**, pp. 494–502.
[23] Ku, C. P., and Heshmat, H., 1994, “Structural Stiffness and Coulomb Damping in Compliant Foil Journal Bearing: Parametric Studies,” STLE Tribol. Trans., **37**(3), pp. 455–462.
[24] Kim, D., Lee, A., and Kim, Y., 2008, “Hybrid Air Foil Journal Bearings with External Hydrostatic Pressure Supplies,” IP disclosure made to the University of Texas at Arlington Office of Technology, Reference No. 8-60.

Downloaded 02 Jun 2010 to 171.66.16.109. Redistribution subject to ASME license or copyright; see http://www.asme.org/terms/Terms_Use.cfm

[25] Timoshenko, S. P., and Goodier, J. N., 1970, *Theory of Elasticity*, McGraw-Hill, New York, pp. 90–92.
[26] Sim, K., and Kim, D., 2007, "Design of Flexure Pivot Tilting Pads Gas Bearings for High-Speed Oil-Free Microturbomachinery," ASME J. Tribol., **129**, pp. 112–119.
[27] Kim, D., and Park, S., 2009, "Hydrostatic Air Foil Bearings: Analytical and Experimental Investigations," Tribol. Int., **42**, pp. 413–425.
[28] Kim, D., and Kumar, M., 2009, "Load Capacity Measurements of Hydrostatic Bump Foil Bearing," ASME Paper No. GT2009-59286.
[29] Kim, T., and San Andrés, L., 2005, "Heavily Loaded Gas Foil Bearings: A Model Anchored to Test Data," ASME Paper No. GT2005-68486.
[30] San Andrés, L., Rubio, D., and Kim, T. H., 2007, "Rotordynamic Performance of a Rotor Supported on Bump Type Foil Gas Bearings: Experiments and Predictions," ASME J. Eng. Gas Turbines Power, **129**, pp. 850–857.
[31] Kumar, M., and Kim, D., 2008, "Parametric Studies on Dynamic Performance of Hybrid Airfoil Bearing," ASME J. Eng. Gas Turbines Power, **130**(6), p. 062501.
[32] Kim, D., Rimpel, A. M., Chang, S. S., and Kim, J. H., 2009, "Design and Manufacturing of Mesoscale Tilting Pad Gas Bearings for 100–200W Class Power MEMS Applications," ASME J. Eng. Gas Turbines Power **131**, p. 042503.
[33] Pan, C. H. T., and Kim, D., 2007, "Stability Characteristics of a Rigid Rotor Supported by a Gas-Lubricated Spiral-Groove Conical Bearing," ASME J. Tribol., **129**, pp. 375–383.
[34] Peng, J. P., and Carpino, M., 1993, "Calculation of Stiffness and Damping Coefficients for Elastically Supported Gas Foil Bearings," ASME J. Tribol., **115**(1), pp. 20–27.
[35] Sim, K., and Kim, D., 2006, "Stability Analyses on Flexure Pivot Tilting Pad Gas Bearings for Microturbomachinery," ASME Paper No. IJTC 2006-12158.
[36] Lund, J. W., 1968, "Calculation of Stiffness and Damping Properties of Gas Bearings," J. Lubr. Technol., **90**(4), pp. 793–803.
[37] Wilde, D., and San Andrés, L., 2003, "Comparison of Rotordynamic Analysis Predictions With the Test Response of Simple Gas Hybrid Bearings for Oil-Free Turbomachinery," ASME Paper GT-2003-38859.
[38] Chapra, S. C., and Canale, R. P., 1989, *Numerical Methods for Engineers*, McGraw-Hill, New York, pp. 631–634.

Downloaded 02 Jun 2010 to 171.66.16.109. Redistribution subject to ASME license or copyright; see http://www.asme.org/terms/Terms_Use.cfm

Design and Manufacturing of Mesoscale Tilting Pad Gas Bearings for 100–200 W Class PowerMEMS Applications

Daejong Kim[1]
Mechanical and Aerospace Engineering,
University of Texas at Arlington,
500 West First Street,
Woolf Hall,
Arlington, TX 76019
e-mail: daejongkim@uta.edu

Aaron M. Rimpel
Department of Mechanical Engineering,
Texas A&M University,
3123 TAMU,
College Station, TX 77843

Suk Sang Chang

Jong Hyun Kim

Pohang Accelerator Laboratory,
POSTECH,
San31 Hyojadong,
Pohang 790-784, Republic of Korea

This paper introduces a design and manufacturing of mesoscale flexure pivot tilting pad gas bearing with a diameter of 5 mm and a length of 1–2.5 mm for PowerMEMS (micro electromechanical systems for power generation) applications with power ranges of 100–200 W. Potential applications include power source for unmanned air vehicles, small robots, microgas turbines to be harnessed by very small solid oxide fuel cells, microblowers/compressors for microfuel cells, etc. The design studies involve scaling analysis, time-domain orbit simulations for stability analyses, and frequency-domain modal analyses for prediction of rotor-bearing natural frequencies. Scaling analysis indicates that direct miniaturization of macroscale tilting pad gas bearing can result in a large bearing number, which may render the rotor-bearing system unstable. However, the scaling analysis provides the baseline design from which the final design can be derived considering manufacturing issue. The generalized modal analysis using impedance contours predict damped natural frequencies close to those from orbit simulations, providing high fidelity to the developed numerical methods. It was predicted that the designed mesoscale tilting pad gas bearings would show very stable operation up to a maximum simulated speed of 1,000,000 rpm. The designed mesoscale tilting pad gas bearings were manufactured using X-ray lithography and electroplating.

[DOI: 10.1115/1.3077646]

Keywords: PowerMEMS, mesoscale, tilting pad gas bearing, stability, X-ray lithography

1 Introduction

The critical technical challenges involved in the small compact power sources are, among others, high power density and efficiency. The micropower generation systems based on electrochemical reaction and thermoelectric effect have very low power density and low efficiency, respectively. The system configuration of interest is a palm-sized mesoscale thermal engine, which would have three-dimensional compressor/turbine impellers with a diameter of 10–12 mm and rotational speeds of above 500 krpm. The power range of this palm-sized mesoscale turbomachinery is expected to be 100–200 W, one order of magnitude larger than silicon microturbomachinery [1,2]. With three-dimensional features on turbomachinery components and available technologies on precision casting [3,4], precision machining [5,6], and mesoscale permanent-magnet generator [7,8], the palm-sized mesoscale turbomachinery would have high efficiency and potential for commercial applications. A representative system could be microgas turbines for power and propulsion of unmanned air vehicle, small robots, small solid oxide fuel cell-microgas turbine hybrid systems (of which a macroscale version can be found in Refs. [9,10]), etc.

Beyond direct power generation system as gas turbines, the mesoscale turbomachinery may have much broader applications as auxiliary devices, such as micro-turbo-air blowers/compressors for small fuel cells, hydrogen delivery system with controlled pressure for small fuel cells, air/fuel delivery system for microcombustors [11], microcryogenic pumps for microrefrigeration systems, etc. The representative research activities on mesoscale palm-sized turbomachinery in European and Asian countries can be found in Refs. [12–16], and they are based on direct miniaturization of macroscale turbomachinery. However, even in this scale, design and manufacturing of critical components require creative and innovative approaches. Bearing system is still the most critical technical challenge. The bearing design should consider assembly issue with other components, as well as its own inherent design issues such as manufacturing, reliability, materials, and rotordynamic stability. In the mesoscale turbomachinery handling air or gas, the well-known high surface area/volume ratio renders usage of gas-lubricated bearings as the most feasible solution.

However, gas-lubricated bearings can have notorious hydrodynamic instability if they are not designed properly. The notorious rotor-bearing instability in gas bearings is the most prominent in solid-walled gas bearings due to resonance between circumferential gas flow within the bearing clearance and rotor rotation. From a rotor dynamics point of view, lightly-loaded rotors (typical in microturbomachinery) supported by rigid-walled circular gas bearings are very unstable [17]. To avoid these phenomena in macroscale gas bearings, various measures have been adopted for decades. Widely-used remedies to these problems are (1) compliant structures on the bearing surface to absorb vibrations caused by the instability and/or external impacts, and (2) mechanical structure that self-suppresses or eliminates the resonance itself. The representative bearings in the first and second categories are foil gas bearings [18–23] and tilting pad gas bearings [24,25]. Both bearings are self-acting and hydrodynamic in nature, generating the load-supporting pressure by rotor rotation itself without requiring any externally pressurized gas.

This paper introduces design studies and manufacturing process of mesoscale tilting pad gas bearing with a diameter of 5 mm and a length of 2.5 mm. Figure 1 shows the principle of tilting pad gas

---

[1] Corresponding author.

Manuscript received December 16, 2007; final manuscript received October 27, 2008; published online April 10, 2009. Review conducted by Patrick S. Keogh.

Copyright © 2009 by ASME

Downloaded 02 Jun 2010 to 171.66.16.109. Redistribution subject to ASME license or copyright; see http://www.asme.org/terms/Terms_Use.cfm

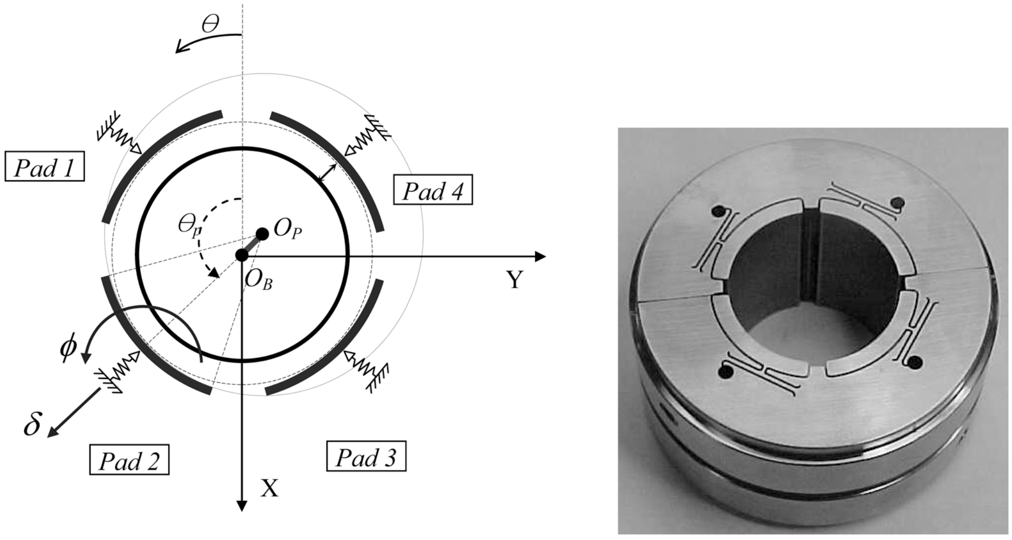

(*a*)

(*b*)

Fig. 1 Principle of tilting pad gas bearing and EDM machined four pad flexure pivot tilting pad gas bearing: (*a*) schematic of tilting pad gas bearing and (*b*) photo of flexure pivot tilting pad gas bearing

bearing and a photo of macroscale (bearing diameter of 28 mm) flexure pivot tilting pad gas bearings manufactured by wire electrodischarge machining. Hydrodynamic preload r_p is defined as the ratio of the distance d_0 between O_B and O_P in Fig. 1 to the nominal clearance C, i.e., $r_p = d_0/C$. Therefore, the bearing setbore clearance, which is the radial clearance between the circle tangent to all the pads and rotor, becomes $C(1-r_p)$. The hydrodynamic preload creates high direct stiffness and system damping (thus stability) even when the rotor is lightly loaded or positioned at the bearing center. Furthermore, due to the nonconcentric pad-rotor configuration, the contact area between the rotor and bearing is very small yielding very little start friction.

The radial compliance, which is shown as a straight beam behind the flexure pivot in Fig. 1(*b*), is for accommodating the rotor growth. Selection of the appropriate pad radial compliance requires systematic engineering in rotordynamic stability. Time-domain and frequency-domain stability analyses on the macroscale flexure pivot tilting pad gas bearing shown in Fig. 1(*b*) can be found in Refs. [24,25].

2 Design Considerations

The geometries of flexure pivot tilting pad gas bearing are 2D, and a MEMS process that can produce high aspect microstructures can be used to make this type of gas bearings. However, due to the continuous elastic motion of flexure pivots during the operation, semiconductor materials are excluded in material selection. However, manufacturing cost should be comparable to the silicon micromachining process, and high precision and dimensional repeatability should be ensured. Furthermore, geometrical accuracy and a very smooth bearing surface are crucial for proper functions. X-ray lithography and electroplating were the selected manufacturing processes for the mesoscale tilting pad gas bearings. The X-ray lithography uses X-rays with extremely small wavelength (0.2–0.4 nm), providing micromanufacturing capability of very high aspect ratio structures. For microstructures with 1 mm height, a typical deviation from the vertical sidewall would be about 1 μm [26]. Microscale gas bearings fabricated using X-ray lithography have been reported earlier with sidewall roughness of 12 nm [27], and the process can be applied to mesoscale gas bearings.

Due to the high rotational speeds, centrifugal rotor growth is a very important factor to consider in the design stage. The centrifugal growth can be accurately predicted by the elasticity theory, and it is a parabolic function of the rotor speed [28]. Thermal growth of the rotor by heat generation within the bearing clearance is also an important factor and can be bigger than the centrifugal growth in some applications. Considering these facts in mind, the mesoscale tilting pad gas bearing should have a physical mechanism to accommodate the rotor growth.

Another design consideration is an easy assembly of the bearing and rotor. Because envisioned applications are palm-sized microturbomachinery, the shaft and impellers should be preassembled. Because the journal diameter where bearings are located is usually smaller than impeller, the bearing should be split type.

Figure 2 shows the overall design of the mesoscale flexure pivot tilting pad gas bearing considering the rotor growth, manu-

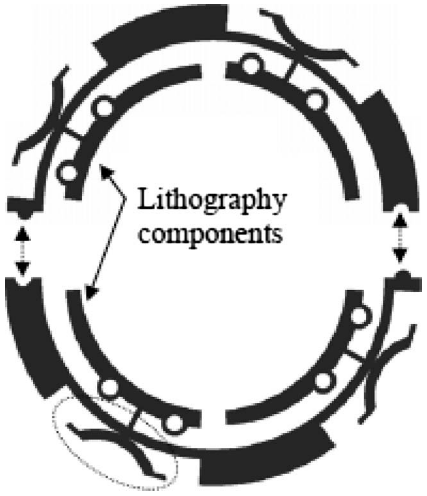

Fig. 2 Lithography components of mesoscale flexure pivot tilting pad gas bearing (bearing diameter $2R=5$ mm and length $L=2.5$ mm). The elements within the dotted ellipse represent the pad radial spring and damper.

Downloaded 02 Jun 2010 to 171.66.16.109. Redistribution subject to ASME license or copyright; see http://www.asme.org/terms/Terms_Use.cfm

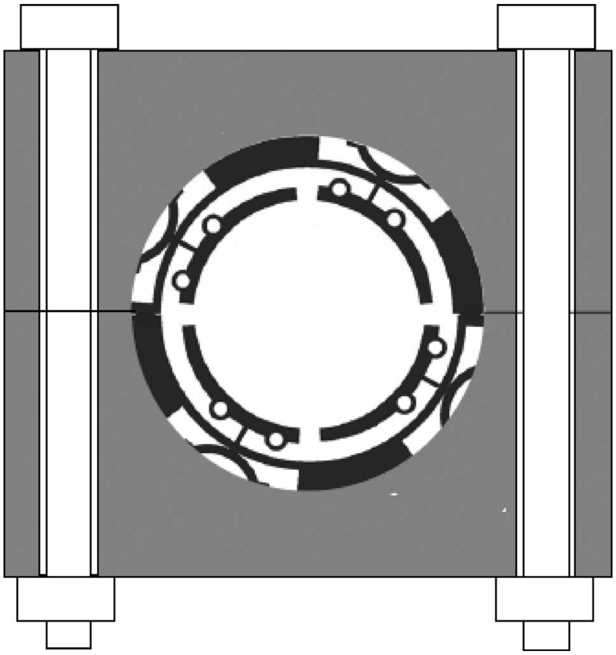

Fig. 3 Mesoscale flexure pivot tilting pad gas bearing after assembly into bearing sleeve

facturing, and assembly issues. In the figure, tilting pads and arc beam springs and dampers (elements in dotted ellipse) are made as a monolithic structure and assembled into a precision-machined split-type bearing sleeve. As illustrated in Fig. 11 in the Appendix, the sliding action between the damper and bearing sleeve generates Coulomb damping in each pad, similar to the well-known bump foil bearings [18–21]. The lithography components are designed such that they are self-aligned (via convex and concave notches) during the assembly into the sleeve, as shown in Fig. 3. The split design of the bearing allows easy assembly of the bearings and rotor. The two circular holes on the tilting pads were implemented (at the initial stage of UV mask design) as dowel pin locations to allow assembly (and bonding) of multiple pads to increase the total length of the bearing for certain applications. However, within the current frame of work, the dowel pin holes are redundant structures because all of the design variables were chosen so that one layer of 2.5 mm thick bearing structure could meet the target performance.

The designed bearings were made of electroplated Ni in a sulfamate bath for low temperature tests. More details on the manufacturing process are discussed in Sec. 5.

3 Theory

The prediction of bearing performance requires understanding the governing equations that decide the motions of the pads and rotor and pressure generation.

Because of the long pivot web, as shown in Fig. 2, the coupled behavior between the pad tangential and tilting motions should be considered. From Fig. 4, the net tangential force and moment acting on the pivot web that cause both the pad tangential and tilting motions can be found by subtracting the pad inertia effects

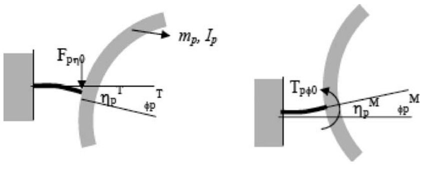

Fig. 4 Coupled behavior of pad tilting and tangential motion by pressure on a pad

$$F_{p\eta0} = F_{p\eta} - m_p \ddot{\eta}_p \tag{1a}$$

$$T_{p\phi0} = T_{p\phi} - I_p \ddot{\phi}_p \tag{1b}$$

where index p represents the pad number.

From the elementary beam theory [29], the total tangential deflection and rotation angle under both $F_{p\eta0}$ and $T_{p\phi0}$ can be represented in matrix form

$$\begin{pmatrix} \eta_p \\ \phi_p \end{pmatrix} = \begin{pmatrix} \dfrac{L_w^3}{3EI_w} & -\dfrac{L_w^2}{2EI_w} \\ -\dfrac{L_w^2}{2EI_w} & \dfrac{L_w}{EI_w} \end{pmatrix} \begin{pmatrix} F_{p\eta0} \\ T_{p\phi0} \end{pmatrix} \tag{2}$$

Rearranging for $F_{p\eta0}$ and $T_{p\phi0}$

$$\begin{pmatrix} F_{p\eta0} \\ T_{p0} \end{pmatrix} = \begin{pmatrix} k_{\eta\eta} & k_{\eta\phi} \\ k_{\phi\eta} & k_{\phi\phi} \end{pmatrix} \begin{pmatrix} \eta_p \\ \phi_p \end{pmatrix} \tag{3}$$

where $k_{\eta\eta}=12k_\phi/L_w^2$, $k_{\phi\phi}=4k_\phi$, and $k_{\eta\phi}=k_{\phi\eta}=6k_\phi/L_w$ with $k_\phi=EI_w/L_w$. Combining Eq. (3) with Eq. (1), differential equations of pad tilting and tangential motion can be derived as

$$m_p \ddot{\eta}_p + k_{\eta\eta}\eta_p + k_{\eta\phi}\phi_p = F_{p\eta} \tag{4a}$$

$$I_p \ddot{\phi}_p + k_{\phi\eta}\eta_p + k_{\phi\phi}\phi_p = T_{p\phi}. \tag{4b}$$

Introducing nondimensional parameters, $\Pi_p = \eta_p/C$, $\Phi_p=(R/C)\phi_p$, $K_{\phi\phi}=k_{\phi\phi}/I_p\omega^2$, $K_{\phi\eta}=k_{\phi\eta}R/I_p\omega^2$, $K_{\eta\eta}=k_{\eta\eta}/m_p\omega^2$, $K_{\eta\phi}=(k_{\eta\phi}/m_p\omega^2)1/R$, and $\tau=\omega t$, Eq. (4) becomes

$$\frac{d^2\Pi_p}{d\tau^2} + K_{\eta\eta}\Pi_p + K_{\eta\phi}\Phi_p = \frac{F_{p\eta}}{m_p C\omega^2} \equiv \bar{F}_{p\eta} \tag{5a}$$

$$\frac{d^2\Phi_p}{d\tau^2} + K_{\phi\eta}\Pi_p + K_{\phi\phi}\Phi_p = \frac{T_{p\phi}R}{I_p C\omega^2} \equiv \bar{T}_{p\phi} \tag{5b}$$

As shown in the dotted circle in Fig. 2, the total pad radial stiffness is provided by the circular arc spring and damper as two parallel spring elements

$$k_\delta = k_b + k_d \tag{6}$$

where k_b and k_d are the stiffness of the arc beam and damper, respectively. The expressions for the stiffnesses can be found using Castigliano's theorem [29], and they are given in the Appendix. For simplicity of analysis, the damper is modeled as a structural damper with a loss factor assuming the motion of the pad is sinusoidal with the same frequency as the rotor rotation speed. Then, the equation of motion for the pad radial motion becomes

$$m_p \ddot{\delta}_p + (k_\delta + k_d i\gamma_d)\delta_p = F_{p\delta} \tag{7a}$$

$$\frac{d^2 D_p}{d\tau^2} + \frac{k_\delta + k_d i\gamma_d}{m_p\omega^2} D_p = \frac{F_{p\delta}}{m_p C\omega^2} \equiv \bar{F}_{p\delta} \tag{7b}$$

where $i=\sqrt{-1}$, γ_d is a structural loss factor of the damper, $F_{p\delta}$ is a radial force to the pth pad, and nondimensional parameters $D_p=\delta_p/C$.

Equation of motions for rotor within the bearing can be written as

$$m_r \ddot{e}_{X,Y} = F_{eX,Y} + F_{bX,Y} \tag{8}$$

where e_X and e_Y are eccentricities of journal center along the X and Y directions. Using nondimensional eccentricity $\varepsilon=e/C$, Eq. (8) becomes

$$\frac{d^2\varepsilon_{X,Y}}{d\tau^2} = \frac{F_{bX,Y}}{m_r C\omega^2} + \frac{F_{eX,Y}}{m_r C\omega^2} \equiv \bar{F}_{bX,Y} + \bar{F}_{eX,Y} \tag{9}$$

Downloaded 02 Jun 2010 to 171.66.16.109. Redistribution subject to ASME license or copyright; see http://www.asme.org/terms/Terms_Use.cfm

The tilting moments on the pads and all the forces to the rotor and the pads are calculated by solving the nondimensional unsteady Reynolds equation [30] given by

$$\frac{\partial}{\partial\theta}\left(PH^3\frac{\partial P}{\partial\theta}\right)+\frac{\partial}{\partial Z}\left(PH^3\frac{\partial P}{\partial Z}\right)=\Lambda\frac{\partial}{\partial\theta}(PH)+2\Lambda\frac{\partial}{\partial\tau}(PH) \tag{10}$$

where, $P=p/p_a$, $Z=z/R$, $H=h/C$, C is nominal clearance, R is bearing radius, and p_a is atmospheric pressure. The nondimensional bearing number is defined as

$$\Lambda=\frac{6\mu\omega}{p_a}\left(\frac{R}{C}\right)^2 \tag{11}$$

where μ is a gas viscosity. Gas film thickness is a function of rotor and pad motions. Including rotor centrifugal growth, pad preload, pad radial motion, pad tangential motion, and pad tilting motion, nondimensional local air film thickness can be given by

$$\begin{aligned}H(\theta)&=1-R_g+\varepsilon_X\cos\theta+\varepsilon_Y\sin\theta-\Phi_p\sin(\theta-\theta_p)\\&\quad-(r_p-D_p)\cos(\theta-\theta_p)+\Pi_p\sin(\theta-\theta_p)\end{aligned} \tag{12}$$

where θ_p is a location of the pivot.

The analyses of the bearing performance involve two approaches: time-domain orbit simulation and linear perturbation analysis in the frequency domain. The orbit simulation solves Eqs. (5), (7*b*), (9), and (10) simultaneously using numerical time integration. The linear perturbation analyses calculate the bearing stiffness and damping coefficients at different excitation frequencies for a fixed rotor speed.

3.1 Linear Perturbation Analyses. In the perturbation analyses, the rotor is excited with small amplitude $(\Delta\varepsilon_X,\Delta\varepsilon_Y)$ of harmonic motion with excitation frequency, ω_{ext}, around a static equilibrium point $(\varepsilon_{X0},\varepsilon_{Y0})$ of interest. The equilibrium position of the rotor generates static film thickness (H_0) and thus static pressure field (P_0) on each pad with corresponding pad positions $(\Phi_{p0},D_{p0},\Pi_{p0})$. The dynamic motions of rotor and pads are described as

$$\varepsilon_X=\varepsilon_{X0}+\Delta\varepsilon_X e^{i\nu\tau} \tag{13a}$$

$$\varepsilon_Y=\varepsilon_{Y0}+\Delta\varepsilon_Y e^{i\nu\tau} \tag{13b}$$

$$\Phi=\Phi_0+\Delta\Phi e^{i\nu\tau} \tag{13c}$$

$$D=D_0+\Delta D e^{i\nu\tau} \tag{13d}$$

$$\Pi=\Pi_0+\Delta\Pi e^{i\nu\tau} \tag{13e}$$

where ν is an excitation frequency ratio $(=\omega_{\text{ext}}/\omega)$. The total film thickness and pad pressure field are given by

$$H=H_0+\Delta H e^{i\nu\tau} \tag{14a}$$

$$P=P_0+\Delta P e^{i\nu\tau} \tag{14b}$$

where the total perturbed film thickness and pressure field are the summation of all the contributions from the perturbed displacements of the rotor and pad motion, i.e.

$$\begin{aligned}\Delta H&=\Delta\varepsilon_X\cos\theta+\Delta\varepsilon_Y\sin\theta-\Delta\Phi_p\sin(\theta-\theta_p)+\Delta D_p\cos(\theta-\theta_p)\\&\quad+\Delta\Pi_p\sin(\theta-\theta_p)\end{aligned} \tag{15a}$$

$$\Delta P=P_X\Delta\varepsilon_X+P_Y\Delta\varepsilon_Y+P_\Phi\Delta\Phi_p+P_D\Delta D_p+P_\Pi\Delta\Pi_p \tag{15b}$$

Substitution of Eqs. (14) and (15) into the Reynolds equation, Eq. (10), leads to a zeroth order nonlinear partial differential equation (PDE) for the equilibrium pressure field and five first order linear PDEs for the perturbed pressure fields. The five first order perturbed equations are given by

$$\begin{aligned}&\frac{\partial}{\partial\theta}\left[P_0H_0^3\frac{\partial P_\alpha}{\partial\theta}\right]+\frac{\partial}{\partial Z}\left[P_0H_0^3\frac{\partial P_\alpha}{\partial Z}\right]+\frac{\partial}{\partial\theta}\left[(3H_0^2P_0H_\alpha+H_0^3P_\alpha)\right.\\&\quad\left.\times\left(\frac{\partial P_0}{\partial\theta}\right)\right]+\frac{\partial}{\partial Z}\left[(3H_0^2P_0H_\alpha+H_0^3P_\alpha)\left(\frac{\partial P_0}{\partial Z}\right)\right]\\&=\left(\Lambda\frac{\partial}{\partial\theta}+\sigma\nu i\right)(P_0H_\alpha+P_\alpha H_0)\end{aligned} \tag{16}$$

where $\alpha=X$, Y, Φ_p, D_p, and Π_p, hereafter. Here, P_α and H_α are the perturbed pressure gradients and film thickness gradients, respectively, with respect to each finite perturbation, and their expressions are given in Table 1.

Table 1 Pressure gradients and corresponding film thickness gradients in Eq. (16)

	P_α	H_α
ε_X	P_X	$\cos\theta$
ε_Y	P_Y	$\sin\theta$
Φ_p	P_Φ	$-\sin(\theta\text{-}\theta_p)$
D_p	P_D	$\cos(\theta\text{-}\theta_p)$
Π_p	P_Π	$\sin(\theta\text{-}\theta_p)$

Calculation of impedance of the tilting pad gas bearings follow the procedures developed by Delgado et al. [31], where perturbed pressures by only rotor motion (with all the pads fixed) are calculated, and all the other perturbed pressures are calculated from the principle of linear superposition, i.e., the perturbed pressures by pad tilting motion and associated impedances can be found as

$$\begin{pmatrix}P_\Phi\\P_D\\P_\Pi\end{pmatrix}=\begin{pmatrix}\sin\theta_p&-\cos\theta_p\\\cos\theta_p&\sin\theta_p\\-\sin\theta_p&\cos\theta_p\end{pmatrix}\begin{pmatrix}P_X\\P_Y\end{pmatrix} \tag{17}$$

$$\begin{pmatrix}z_{\Phi\alpha}\\z_{D\alpha}\\z_{\Pi\alpha}\end{pmatrix}=\begin{pmatrix}\sin\theta_p&-\cos\theta_p\\\cos\theta_p&\sin\theta_p\\-\sin\theta_p&\cos\theta_p\end{pmatrix}\begin{pmatrix}z_{X\alpha}\\z_{Y\alpha}\end{pmatrix},\quad\alpha=X\,,Y,\ \Phi,\ D,\ \text{and}\ \Pi \tag{18}$$

Following the algebra in Ref. [31], the final bearing impedance can be found as

$$\begin{aligned}[Z]_{XY}=\begin{bmatrix}Z_{XX}&Z_{XY}\\Z_{YX}&Z_{YY}\end{bmatrix}&=\frac{p_aR^2}{C}\sum_{\text{pads}}[[z_d]-[z_a]([z_c]-\nu^2[I]\\&\quad+[z_p])^{-1}[z_b]]\end{aligned} \tag{19}$$

where

$$[z_p]=\begin{bmatrix}K_{\phi\phi}&0&K_{\phi\eta}\\0&K_b+K_d(1+i\gamma_d)&0\\K_{\eta\phi}&0&K_{\eta\eta}\end{bmatrix}$$

$$[z_b]=\begin{bmatrix}z_{\Phi X}&z_{\Phi Y}\\z_{DX}&z_{DY}\\z_{\Pi X}&z_{\Pi Y}\end{bmatrix}$$

$$[z_c]=\begin{bmatrix}z_{\Phi\Phi}&z_{\Phi D}&z_{\Phi\Pi}\\z_{D\Phi}&z_{DD}&z_{D\Pi}\\z_{\Pi\Phi}&z_{\Pi D}&z_{\Pi\Pi}\end{bmatrix}$$

$$[z_d]=\begin{bmatrix}z_{XX}&z_{XY}\\z_{YX}&z_{YY}\end{bmatrix}$$

and

Downloaded 02 Jun 2010 to 171.66.16.109. Redistribution subject to ASME license or copyright; see http://www.asme.org/terms/Terms_Use.cfm

$$[z_a] = \begin{bmatrix} z_{X\Phi} & z_{XD} & z_{X\Pi} \\ z_{Y\Phi} & z_{YD} & z_{Y\Pi} \end{bmatrix}$$

The terms in $(z_{X\alpha} z_{Y\alpha})^T$ in Eq. (18) are calculated from

$$z_{X\alpha} = -\int P_\alpha \cos\, \theta \, d\theta \, dZ \tag{20a}$$

$$z_{Y\alpha} = -\int P_\alpha \sin\, \theta \, d\theta \, dZ \tag{20b}$$

Application of generalized modal analyses to the rotor-bearing system [32] yields the following modal impedance in forward whirling motion:

$$Z_K = K_m + j\nu\omega D_m = \frac{Z_{XX} + Z_{YY}}{2} - \sqrt{\left(\frac{Z_{XX} - Z_{YY}}{2}\right)^2 + Z_{XY} Z_{YX}} \tag{21}$$

The real and imaginary parts of Eq. (21) are the modal stiffness and damping for forward whirling, respectively. By sweeping the excitation frequency, the modal impedance versus excitation frequency ratio (ν) can be constructed for prediction of natural frequencies.

3.2 Scaling Analyses. While design features of well-designed macroscale tilting pad bearings are well-established [24,25], design guidelines for mesoscale tilting pad bearings are not available. A question that arises is whether well-designed macroscale bearing could be benchmarked or scaled down directly in order to design mesoscale bearings. The answers to the question can be made through scaling analysis of relevant equations of motion that govern the motion of pads, gas flow within the bearing, and rotor motion.

As the first step, the relative magnitudes of the stiffness coefficients in Eq. (4) are found to be

$$\frac{K_{\phi\eta}}{K_{\phi\phi}} = 1.5\frac{R}{L_w} \tag{22a}$$

$$\frac{K_{\eta\eta}}{K_{\eta\phi}} = 2\frac{R}{L_w} \tag{22b}$$

$$\frac{K_{\eta\eta}}{K_{\phi\phi}} = 6\left(\frac{R}{L_w}\right)^2 \frac{f(\theta_{\mathrm{pad}})}{\theta_{\mathrm{pad}}} \tag{22c}$$

From algebra (omitted for brevity) to derive Eq. (22*c*), it can be found that $f(\theta_{\mathrm{pad}})/\theta_{\mathrm{pad}} \sim 1$. Because the typical range of $R/L_w = 6-10$ in most flexure pivot tilting pad bearings, the nondimensional stiffness for pad tangential motion is much larger than that for tilting motion from Eq. (22*c*). Therefore, the coupled effect between the pad tilting motion and pad tangential motion is neglected in the following scaling analyses even if the orbit simulations and linear perturbation analyses retain the coupled effect. Upon neglecting the pad tangential motion, Eq. (5) is reduced to

$$\frac{d^2\Phi_p}{d\tau^2} + \frac{k_\phi}{I_p\omega^2}\Phi_p = \bar{T}_{p\phi} \tag{23}$$

3.2.1 Pad Tilting Motion. Appropriate pad tilting motion is very important to minimize cross-coupled stiffness of the bearing. For the mesoscale bearing to have similar behavior to the well-designed macroscale bearings, $k_\phi/I_p\omega^2$ in Eq. (23) should be scale-invariant. Analytical expression for pad moment of inertia can be found as a function of pad arc angle θ_{pad}, pivot offset $p_{\%}$, and pad thickness t_p, as

$$I_p = 2R^3 t_p \rho L f(\theta_{\mathrm{pad}}) \tag{24}$$

where $f(\theta_{\mathrm{pad}}) \equiv \theta_{\mathrm{pad}} - \sin((1-p_{\%})\theta_{\mathrm{pad}}) - \sin(p_{\%}\theta_{\mathrm{pad}})$. The DN (diamenter in mm times N in rpm) number of well-designed tilting pad gas bearings is about 4×10^6 (D_{N0}), which is assumed constant regardless of the bearing size. Then

$$\omega = \frac{\pi}{60R} D_{N0} \tag{25}$$

It is also assumed that the bearing length and pad thickness follow the relations, $L=R$, and the pad thickness, $t_p=\beta R$, where $\beta = 0.2-0.3$. Using these relations

$$\frac{k_\phi}{I_p\omega^2} = \alpha_\phi \left(\frac{t_w}{R}\right)^2 \frac{t_w}{L_w} \tag{26}$$

where constant

$$\alpha_\phi \equiv \frac{15E}{\beta\rho f(\theta_{\mathrm{pad}})\pi^2 D_{N0}^2}$$

3.2.2 Pad Radial Motion. In Eq. (7*b*), the nondimensional parameter that decides pad radial motion is $k_\delta/m_p\omega^2$. Using $m_p = \rho R\theta_{\mathrm{pad}} t_p L$, $L=R$, $t_p=\beta R$, and $\omega=(\pi/60R)D_{N0}$

$$\frac{k_\delta}{m_p\omega^2} \sim \alpha_\delta \frac{k_\delta}{R} \tag{27}$$

where constant

$$\alpha_\delta \equiv \frac{3600}{\beta\rho\theta_{\mathrm{pad}}\pi^2 D_{N0}^2}$$

3.2.3 Rotor Radial Motion. For scale-invariance, $\bar{F}_{bX,Y}$ should be nearly constant. If the bearing effective pressure is also scale-invariant, $F_{bX,Y} \sim R^2$, and $m_r C\omega^2 \sim R^3 C((\pi/60R)D_{N0})^2 \sim RC$. Therefore

$$\bar{F}_{bX,Y} \sim \frac{R}{C} \tag{28}$$

Summarizing the above scaling analyses related to the geometry of the bearings, the following three conditions should be satisfied.

Condition 1. From Eq. (26), for $k_\phi/I_p\omega^2$ to be scale-invariant, $(t_w/R)^2(t_w/L_w)$ should also be constant regardless of the bearing size.

Condition 2. From Eq. (27), for $k_\delta/m_p\omega^2$ to be scale-invariant, k_δ should be proportional to R.

Condition 3. From Eq. (28), for $\bar{F}_{bX,Y}$ to be scale-invariant, $\bar{F}_{bX,Y} \sim R/C$.

Equations (26)–(28) provide simple scaling laws related to the miniaturization of physical bearing dimensions. However, the assumption of scale-invariant effective pressure on the bearing surface, which was adopted to derive Eq. (28), requires another scale-invariant parameter related to the hydrodynamic pressure within the bearing clearance. In the commonly used isothermal Reynolds equation for the bearing analysis, the nondimensional number is a bearing number defined in Eq. (10). Invoking $\omega = (\pi/60R)D_{N0}$, the bearing number

$$\Lambda \sim \frac{R}{C}\frac{1}{C} \quad \text{or} \quad \Lambda \cdot \frac{C}{R} \sim \frac{1}{C} \tag{29}$$

Simple miniaturization of bearing dimensions renders C/R to be constant in Eq. (28). However, Eq. (29) states that if C/R is constant, the bearing number Λ is inversely proportional to the bearing clearance C. Therefore, direct miniaturization of every bearing design parameter maintaining the same DN number increases the bearing number significantly, rendering the rotor-bearing system to be highly susceptible to instability. However, the scaling analyses provide a general guideline in selecting initial values of tilting stiffness and pad radial stiffness.

Downloaded 02 Jun 2010 to 171.66.16.109. Redistribution subject to ASME license or copyright; see http://www.asme.org/terms/Terms_Use.cfm

4 Design

A well-designed macroscale flexure pivot tilting pad gas bearing has $t_w = 0.33$ mm and $L_w = 1$ mm to have a tilting stiffness of about 20 N m/rad for a bearing diameter of 25–30 mm with $L/D \sim 1$ [24,25]. Keeping Eq. (29) aside for a while and following the three conditions derived from the scaling analyses above, for the 1:5 scaling down to have a bearing with a 5 mm diameter with $L/D = 0.5$ will require a pivot web thickness of about 60 μm, pivot web length of 200 μm, nominal clearance of 4–6 μm, pad radial stiffness of 2–3 MN/m, and rotor mass of about 6–8 g per bearing.

However, practical difficulty in scaling down of the bearing lies in the manufacturability of the thin pivot web and in maintaining the small bearing clearance in proportion to the bearing size. Considering that the achievable diametric tolerance of the precision ground rotor is about ± 3 μm, the uncertainty of the bearing radial clearance is about ± 1.5 μm. Therefore, practically bearing clearance should be increased to the range where the clearance uncertainty does not affect the bearing performance significantly. If the pad center has the predetermined offset d_0 from the bearing center, the pad preload r_p is defined as $r_p = d_0/C$. If dimensional uncertainty of the X-ray lithography process is assumed negligible (electron-beam lithography for UV mask fabrication has a precision tolerance below 0.1 μm) compared with those of other conventional precision machining processes, the range of preload is $d_0/(C+1.5) < r_p < d_0/(C-1.5)$ from the assumed rotor tolerance. Once preload is decided, the bearing set-bore clearance, which is the minimum gap between the rotor and bearing pad, is

$$C_{\text{bore}} = C - d_0 \pm 1.5 \tag{30}$$

The rotor centrifugal growth is also an important design factor to take into consideration. The rotor growth is the actual limiting factor of maximum operating speed for a given bearing set-bore clearance and pad radial stiffness [24]. For hollow rotors, rotor centrifugal radial growth from plane stress model of rotating cylinder [28] is given by

$$r_g = \frac{\rho_r R \omega^2}{4E}[R^2(1-\nu_r) + a^2(3+\nu_r)] \tag{31}$$

where ρ_r, E, and υ_r are density, Young's modulus, and Poisson's ratio of the rotor material, respectively, and a is the inner radius of the rotor. Even if the model is for the plane stress case, the formula agrees very well with finite element method (FEM) results [24] because the rotor is not constrained along the axial direction. The parabolic function of Eq. (31) with ω indicates significant rotor centrifugal growth at high speeds, often exceeding the bearing set-bore clearance. At a design speed of 800,000 rpm (DN $= 4 \times 10^6$), the rotor radial growth is 1.46 μm assuming hollow rotor with wall thickness of 1.4 mm, which reduces effective set-bore clearance accordingly. If the rotor centrifugal growth is considered, the set-bore clearance is in the range of -0.46–2.54 μm (1.04 μm if the machining tolerance in rotor diameter is not considered), when the nominal clearance C is chosen as 5 μm with a preload of 0.5 following the scaling analyses.

The very small bearing set-bore clearance can be very problematic at actual applications because machining tolerance cannot be neglected, and the bearing and rotor are never operated at isothermal conditions. Temperature increase due to heat generation in the air film is predicted to be as high as above 50°C in macroscale tilting pad gas bearing [33], when adequate cooling is not available. Assuming the same temperature increase in the mesoscale rotor, the thermal radial growth of the rotor is about 1.25 μm if coefficient of thermal expansion of the rotor is assumed 10^{-6}. Therefore, net clearance at the pivot can be negative if the bearing does not have a mechanism to absorb the large rotor expansion. The radial springs implemented in Fig. 2 are inevitable for successful implementation of the gas bearing technology into mesoscale turbomachinery. Furthermore, heat inputs through the bearing housing from the hot section and through the rotor can be much larger than heat generation within the bearing for certain applications. These additional design factors should be considered only when actual application and configuration of the total system layout are decided. In the following design studies in this paper, thermal issue is not considered.

From the rotor centrifugal growth and manufacturing issues addressed above, larger clearance than the one from scaling analyses is desirable. Furthermore, increasing the nominal clearance minimizes the increase in the bearing number, Λ, as explained by Eq. (29). Therefore, the bearing nominal clearance C was chosen as 10 μm, twice the value from the scaling analyses. The arbitrary increase in the bearing clearance is justified because the design values from the scaling analyses are just starting points of the detailed design of all the other design parameters.

Because the radial clearance is increased, other design parameters should be adjusted to have the target DN number. Three design parameters can be varied, i.e., tilting stiffness, pad radial stiffness, and pad preload. The pad preload can be easily increased by changing the pad profile without imposing any design constraint except for the decreased set-bore clearance. The pad tilting stiffness should be as small as possible within the structural integrity of the pivot web because finite tilting stiffness generates large cross-coupled stiffness at high speeds. Therefore, the length of pivot web can be increased within a certain limit if web thickness is to be maintained at 60 μm. From preliminary design studies in macroscale tilting pad gas bearings [24,25], effect of pad preload and tilting stiffness on overall bearing performance is rather predictable compared with the complicated nature of pad radial stiffness. For example, reducing the tilting stiffness does not change critical speed because the main benefit is to decrease the cross-coupled stiffness at high speeds. Nevertheless, overall performance at high speeds is a weak function of pad tilting stiffness within a certain range of its value. Therefore, designed bearings have a preload of 0.6 and web length of 400 μm rendering a tilting stiffness of 0.0225 N m/rad, half the value of that from the scaling analyses.

Pad radial stiffness not only provides accommodation of rotor expansion but also serves as a very important design parameter in terms of rotor-bearing stability and maximum rotor vibration at critical speeds. Therefore, the pad radial stiffness should be carefully tuned from the baseline design from the scaling analyses. The general trend is as follows. A larger pad radial stiffness provides more stable bearing operation if rotor centrifugal growth is small and bearing clearance at pivot is not very small at design speeds.

5 Manufacturing Process of the Bearings

Designed mesoscale tilting pad bearing was manufactured using X-ray lithography. As an initial step, a 1 mm thick bearing was manufactured to identify any necessary design modification from the manufacturability perspective. Figure 5 is a photo of the fabricated X-ray mask using a 175 μm thick polyimide film as X-ray transparent membrane and 14–16 μm thick Au film as X-ray absorber. Because positive resist, polymethylmethacrylate (PMMA), is used as a plating mold for the electroplating of the final Ni bearings, the areas (dark) without Au film in Fig. 5 have images of the bearings to be manufactured. The X-ray mask was fabricated at Pohang University of Science and Technologies (POSTECH), and detailed lithography conditions for the X-ray mask are as follows. 30 nm thick Cr and 140 nm thick Au seed layers were evaporated on the polyimide film as a seed layer for Au electroplating using electron-beam evaporator. 25 μm thick SU-8 was used as a plating mold for Au electroplating. UV exposure on the SU-8 was made using MDE-400 M UV aligner. After development of the SU-8, Au plating was performed at growth rate of 4 μm/h at 50°C using SP-gold solution.

Once the X-ray mask is made, X-ray lithography on thick PMMA layer follows. A titanium (Ti) plate was chosen as a sub-

Downloaded 02 Jun 2010 to 171.66.16.109. Redistribution subject to ASME license or copyright; see http://www.asme.org/terms/Terms_Use.cfm

Fig. 5 Photo of X-ray mask for manufacturing of the mesoscale tilting pad gas bearings. Dark area is X-ray transparent material (represents the areas for bearing structures) and bright area is with X-ray absorber (Au film).

strate for the PMMA. The Ti plate was cleaned using oxygen plasma at 200 W for 2–3 min. Adhesion promoter S1805 diluted by acetone was spin coated at 1000 rpm and soft baked at 150°C for 5–10 min. Preparation of the 1 mm thick PMMA resist begins with spin coating of liquid PMMA on the Ti plate and baking at 180°C for 120 min. Slow ramp to the final baking temperature was necessary to achieve good adhesion without any residual stress. 1 mm thick PMMA was baked at 80°C for 4 h to decrease thermal stress. The pretreated PMMA sheet was bonded to the spin-coated PMMA layer using methylmethacrylate monomer (MMA) as a bonding material. A 1–2 kg weight was applied to promote bonding of the PMMA sheet.

X-ray exposure was performed using an X-ray beam line at POSTECH in vacuum contact mode. In the X-ray lithography, a contrast refers to absorption contrast, defined as the ratio of the total dose at the bottom of the resist under the X-ray transparent membrane to the total dose below the X-ray absorber. The absorption contrast for the fabricated X-ray mask was calculated using a dose simulation software from POSTECH. The minimum bottom dose below the polyimide membrane was chosen as $3000\ \mathrm{J/cm^3}$. The dose below the Au absorber was less than $100\ \mathrm{J/cm^3}$ yielding an absorption contrast of above 30 for excellent lithographic pattern.

PMMA was developed in a G-G solution for 50 h at room temperature to minimize cracking and to improve contrast between exposed and unexposed area [34]. The G-G solution is composed of 60 vol % of 2-(2-butoxyethoxy)ethanol, 20 vol % of morpholine, 5 vol % of 2-aminoethanol, and 15 vol % of DI water.

Final bearing manufacturing was accomplished by electroplating Ni in the PMMA mold prepared by X-ray lithography. A home-made nickel sulfamate bath was used for initial prototype bearings with current density of $10\ \mathrm{mA/cm^2}$ at 50°C. To adjust the pH, diluted sulfamic acid (H_3NO_3S) was used for $p\mathrm{H}>4$ and diluted sodium hydroxide (NaOH) was used for $p\mathrm{H}<3.5$. Figure 6 shows scanning electron microscope (SEM) images of the fabricated mesoscale tilting pad gas bearing.

After successful manufacturing of a 1 mm thick tilting pad gas bearing, X-ray lithography on a 2 mm thick PMMA was performed. X-ray exposure time was adjusted to have a similar absorption contrast ratio as a 1 mm thick PMMA. Even if minor microcracks on the sharp corners were observed (due to the large thickness of the PMMA), these microcracks do not affect the electroplating process and the integrity of electroplated structures. Figure 7 shows an optical image of 2.0 mm long mesoscale tilting pad gas bearings. Manufacturing of a 2.5 mm long bearing is still underway. Further optimization of X-ray dose and minor design change are necessary to remove sharp corners and circular holes (not used in the current design, as explained in Sec. 2) inside the tilting pads.

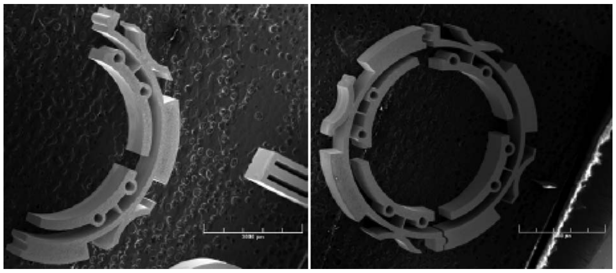

Fig. 6 SEM images of the manufactured mesoscale tilting pad gas bearing before assembly into bearing sleeve. Scale bar corresponds to 3 mm in full scale.

6 Analyses Results and Discussion

The stability characteristics and overall bearing performance were evaluated using both orbit method and linear perturbation method. The simulations assume a rigid rotor and cylindrical mode (lumped mass approximation) without consideration of conical mode and other stabilizing/destabilizing forces that can be generated in seals, impellers, etc.

Time-domain orbit methods solve multiple differential equations associated with pressure field, rotor motion, and dynamics of tilting pads simultaneously. Table 2 shows selected design parameters from the scaling analyses. The loss factor γ_d of well-designed air foil bearings with similar bump geometry as the damper in Fig. 2 is in the range of 0.15–0.25 [21–23]. In this work, $\gamma_d=0.15$ for the damper. From the scaling analyses, a total radial stiffness of 3 MN/m was chosen with $k_b=1.5\ \mathrm{MN/m}$ and $k_d=1.5\ \mathrm{MN/m}$.

For the orbit methods, the fifth order Adams–Bashforth scheme [35] solves Eqs. (5), (7*b*), and (9) in nondimensional time domain. Figure 8 is the selected nondimensional imbalance responses up to 1,000,000 rpm at steady states after transient vibrations died out. Figure 9 is a time trace of ε_X at 800,000 rpm, where damped natural frequency (low frequency oscillation) is below 100,000

Fig. 7 Optical image of 2.0 mm thick mesoscale tilting pads gas bearing (*a*) 600,000 rpm, (*b*) 800,000 rpm, and (*c*) 1,000,000 rpm

Downloaded 02 Jun 2010 to 171.66.16.109. Redistribution subject to ASME license or copyright; see http://www.asme.org/terms/Terms_Use.cfm

Table 2 Selected bearing design for simulation

Parameters	Values
I_p	3.95×10^{-2} g mm^2
m_p	2.42×10^{-2} g mm^2
k_ϕ	0.0225 N m/rad
t_w	0.06 mm
L_w	0.4 mm
C	10 μm
$D=2R$	5 mm
L	2.5 mm
r_p	0.6
$p_{\%}$	0.7
θ_{pad}	80 deg
No. of pads	4
Rotor mass	10 g per bearing

rpm, indicating a very small whirl frequency ratio below 0.1. Even if simulation results at lower rpm are not presented in the paper, the bearing is stable for the entire speed range up to the simulated maximum speed of 1,000,000 rpm.

Linear perturbation analyses were also performed for the design parameters. The zeroth order solution was found using the orbit method by applying zero imbalance and static load corresponding to the rotor weight. The bearing stiffness and damping coefficients in the Cartesian coordinate were calculated as a function of excitation frequency at different rotor speeds. Once the bearing coefficients are calculated, modal stiffness and damping coefficients are calculated using Eq. (21) as a function of the excitation frequency ratio, as shown in Fig. 10.

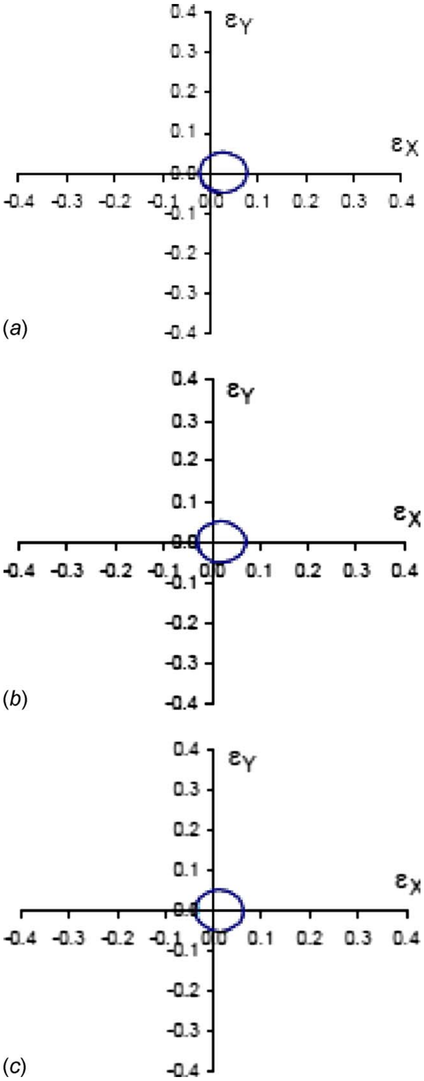

Fig. 8 Selected steady state orbits at different speeds

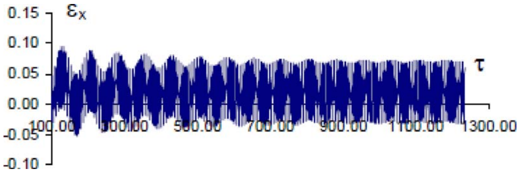

Fig. 9 Trace of ε_X in nondimensional time $\tau=\omega t$, 800,000 rpm (*a*) 500,000 rpm, (*b*) 600,000 rpm, (*c*) 700,000 rpm, and (*d*) 800,000 rpm

For given rotor mass, m_r, an approximate natural frequency of rotor-bearing system ω_N can be found by using the following equation:

$$m_r\omega_N^2 = m_r(\omega\nu_N)^2 \cong K_m(\omega_S) \tag{32}$$

where ω_S is the frequency where modal damping is zero. The approximation in Eq. (32) is based on the fact that the modal stiffness does not change much with excitation frequency near the ω_S, as shown in Fig. 10. It is possible to find more accurate ω_N by finding an intercept between the $m_r\omega^2\nu_N^2$-curve and the modal stiffness curve

$$m_r\omega_N^2 = m_r(\omega\nu_N)^2 = K_m(\omega_N) \tag{33}$$

The ω_N found using either Eq. (32) or Eq. (33) corresponds to the damped natural frequency (low frequency oscillations) observed in the transient motion in Fig. 9. Table 3 compares the damped natural frequencies using Eqs. (32) and (33) with those found from orbit simulations at different speeds.

As Table 3 shows, both orbit method and linear perturbation analyses predict reasonably close damped natural frequencies of the rotor-bearing system at each speed within 25–30%. Considering the limitation and approximation behind the linear perturbation analysis, i.e., infinitely small motion versus large vibration magnitude in the orbit simulation where nonlinear effect of gas film is included, the difference is acceptable.

Note that the excitation frequency ratio that corresponds to the interception of the modal damping curves with the horizontal axis in Fig. 10 is the whirl frequency ratio (around 0.4), which Lund's method [36] predicts. In Lund's method, the natural frequency evaluated using Eq. (32) divided by the whirl frequency ratio (around 0.4) gives the threshold speed where rotor-bearing instability occurs. The predicted threshold speed using the Lund's method is below 140,000 rpm. The threshold speed predicted by Lund's method is far below the threshold speed the orbit simulations predict. Even if experimental verification is necessary, Lund's method does not provide reasonable prediction of the threshold speed of gas bearings. Experimental studies in a different type of gas bearing [37] also provide some doubt on Lund's method in the prediction of gas bearing stability.

One interesting phenomenon is the negative modal damping in Fig. 10 at ν_N, which is contradictory to the orbit simulation results, where the bearing is stable up to 1000 krpm, which is the maximum simulated speed in this paper. One of the possible reasons for the discrepancy could be a contribution of the positive modal damping generated by synchronous imbalance excitation in the orbit simulations. However, more investigation is necessary to fully justify the speculations. Considering that any actual rotor has finite residual imbalance and complicated nonlinear behavior of gas bearings, the orbit simulation provides a more accurate prediction of rotor-bearing dynamic performance.

Downloaded 02 Jun 2010 to 171.66.16.109. Redistribution subject to ASME license or copyright; see http://www.asme.org/terms/Terms_Use.cfm

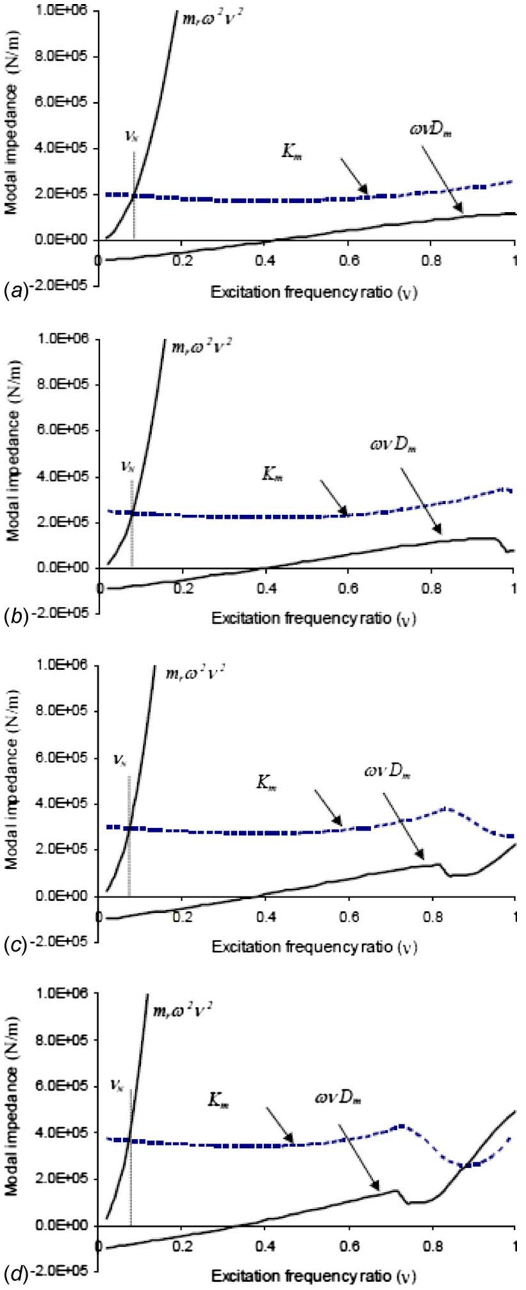

Fig. 10 Modal impedance curves at different speeds

7 Conclusions

Scaling analyses were performed to design mesoscale tilting pad gas bearings. Scaling analyses indicate that direct miniaturization of every physical dimension can result in very unstable bearing design. To ensure stable operation of the bearing, a rather larger clearance was chosen with larger hydrodynamic preload. Orbit simulation and linear perturbation analyses were used to predict the performance of the designed bearing. It was predicted that the designed mesoscale tilting pad gas bearings would show very stable operation up to a maximum simulated speed of 1,000,000 rpm. The generalized modal analysis using impedance contours predict damped natural frequencies close to those from orbit simulations, providing high fidelity to the developed numerical methods.

Designed mesoscale tilting pad gas bearings were manufactured using X-ray lithography and electroplating. Bearings up to 2 mm long were successfully manufactured. The manufacturing process is under further optimization, and minor design change is also underway to manufacture 2.5 mm long bearings.

Table 3 Natural frequencies from modal analysis and orbit simulation

	Perturbation analyses			
Speeds (krpm)	ν_N	ω_N using Eq. (33) (krpm)	ω_N using Eq. (32) (krpm)	Damped ω_N from orbit simulations (krpm)
500	0.0845	42.25	40.04	52.03
600	0.0785	47.10	44.72	55.71
700	0.0742	51.94	49.81	59.88
800	0.0720	57.60	55.62	64.73

Nomenclature

a = inner radius of hollow rotor
C = nominal clearance
C_{bore} = set-bore clearance
D_m = modal damping
D_{N0} = 4×10^6
D_p = dimensionless pad radial coordinate, $D_p=\delta_p/C$
d_0 = distance from bearing center to pad center
E = Young's modulus
$e_{X,Y}$ = rotor eccentricity
$F_{bX,Y}$ = bearing reaction force on rotor
$\bar{F}_{bX,Y}$ = dimensionless bearing reaction force on rotor, $\bar{F}_{bX,Y}=F_{bX,Y}/(m_rC\omega^2)$
$F_{eX,Y}$ = external force on rotor
$\bar{F}_{eX,Y}$ = dimensionless external force on rotor, $\bar{F}_{eX,Y}=F_{eX,Y}/(m_rC\omega^2)$
$F_{p\delta}$ = radial force on pad
$\bar{F}_{p\delta}$ = dimensionless radial force on pad, $\bar{F}_{p\delta}=F_{p\delta}/(m_pC\omega^2)$
$F_{p\eta}$ = net tangential force on pad
$\bar{F}_{p\eta}$ = dimensionless tangential force on pad, $\bar{F}_{p\eta}=F_{p\eta}/(m_pC\omega^2)$
H = dimensionless film thickness, $H=h/C$
H_α = dimensionless film thickness $(\alpha=X,Y,\Phi,D,\Pi)$
h = local film thickness
I_p = pad tilting moment of inertia
I_w = flexure pivot area moment of inertia
i = imaginary unit, $i=\sqrt{-1}$
K = dimensionless stiffness coefficients (defined in context)
K_m = modal stiffness
k = stiffness coefficients (defined in context)
L = bearing length
L_w = flexure pivot beam length
m_p = pad mass
m_r = rotor mass
P = dimensionless fluid film paper, $P=p/p_a$
P_α = dimensionless pressure gradient $(\alpha=X,Y,\Phi,D,\Pi)$
p = fluid film pressure
p_a = atmospheric pressure
R = rotor outer radius
r_g = radial growth of rotor
R_g = dimensionless rotor growth, $R_g=r_g/C$
r_p = dimensionless pad preload, $r_p=d_0/C$
t = time
t_p = pad thickness
$T_{p\phi}$ = net tilting moment on pad

Downloaded 02 Jun 2010 to 171.66.16.109. Redistribution subject to ASME license or copyright; see http://www.asme.org/terms/Terms_Use.cfm

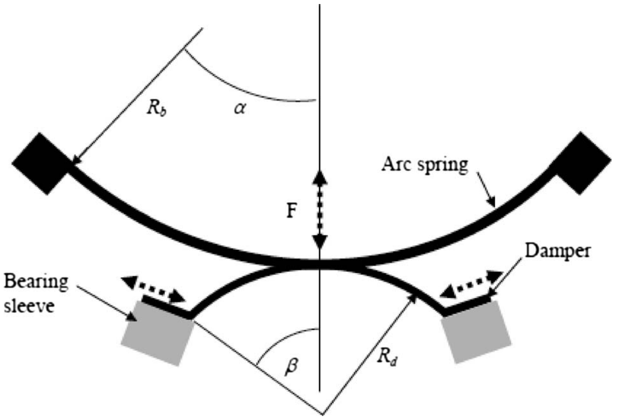

Fig. 11 Details of arc beam spring and damper (dotted ellipse in Fig. 2)

$\bar{T}_{p\phi}$ = dimensionless tilting moment on pad, $\bar{T}_{p\phi} = T_{p\phi}R/(I_pC\omega^2)$
t_w = Flexure pivot web thickness
Z = dimensionless axial coordinate, $Z=z/R$
Z_K = modal impedance
z = axial coordinate
$[Z]$ or $[z]$ = impedance matrices (defined in context)
α_ϕ, α_δ = constants defined in context of scaling
β = pad thickness ratio, $\beta=t_p/R$
δ_p = pad radial coordinate
$\varepsilon_{X,Y}$ = dimensionless rotor eccentricity, $\varepsilon_{X,Y}=e_{X,Y}/C$
Φ_p = scaled pad tilting angle, $\Phi_p=R\phi_p/C$
ϕ_p = pad tilting angle
γ_d = structural loss factor for damper
η_p = pad tangential coordinate
Λ = bearing number
μ = dynamic viscosity of fluid
ν = excitation frequency ratio, $\nu=\omega_{\text{ext}}/\omega$
ν_r = Poisson's ratio of rotor material
Π_p = dimensionless pad tangential coordinate, $\Pi_p=\eta_p/C$
θ = angular coordinate
θ_p = angular position of pad pivot
ρ = density
σ = squeeze number, $\sigma=2\Lambda$
τ = dimensionless time, $\tau=\omega t$
ω = rotor spin frequency
ω_{ext} = excitation frequency
ω_N = damped natural frequency

Appendix: Stiffness of Arc Spring and Damper

As shown in Fig. 2, the total pad radial stiffness is provided by circular arc spring with clamped ends at the bearing housing and damper, which supports the arc spring as a parallel spring element. The damper provides not only additional stiffness to the arc spring but also provides Coulomb type damping through microscopic slip of the damper against the bearing sleeve. The stiffness of the arc spring and damper depends on the overall shape of the damper. Assuming the arc spring is at clamped condition at both ends and the damper is at free-free condition, their stiffnesses can be derived using Castigliano's theorem [29]

$$k_b = \frac{4EI_b}{R_b^3}\frac{\alpha^2 + \alpha \sin \alpha \cos \alpha - 2 \sin^2 \alpha}{\alpha \cos^2 \alpha - 2 \sin(2\alpha) + 4\alpha \cos \alpha + \alpha^3 - 5\alpha + 4 \sin \alpha} \tag{A1}$$

$$k_d = \frac{4EI_d}{R_d^3 f(\beta)} \tag{A2}$$

where $f(\beta)=2\beta \sin^2 \beta - 4 \sin \beta + \beta + (3 \sin 2\beta)/2$, $I_d=Lt_d^3/12(1-\nu^2)$, and $I_b=Lt_b^3/12(1-\nu^2)$. The t_d and t_b are thicknesses of the damper and arc spring, respectively.

References

[1] Epstein, A. H., 2004, "Millimeter-Scale, Micro-Electro-Mechanical Systems Gas Turbine Engines," ASME J. Eng. Gas Turbines Power, **126**(2), pp. 205–226.
[2] Teo, C. J., Liu, L. X., Li, H. Q., Ho, L. C., Jacobson, S. A., Ehrich, F. F., Epstein, A. H., and Spakovszky, Z. S., 2006, "High-Speed Operation of a Gas-Bearing Supported MEMS Air Turbine," ASME Paper No. IJTC2006-12173.
[3] Bos, B., Gorter, H., and Dortmans, L. J. M. G., 2004, "Solid Freeform Fabrication of Piezoelectric Actuators by a Micro-Casting Method," J. Electroceram., **13**(1–3), pp. 409–412.
[4] Hung, N. P., Ngothai, Y., Yuan, S., Lee, C. W., and Ali, M. Y., 2001, "Micromolding of Three-Dimensional Components," *Initiatives of Precision Engineering at the Beginning of a Millennium, Tenth International Conference on Precision Engineering*, Kluwer, Yokohama, Japan, Jul., pp. 142–146.
[5] Honegger, A., Kapoor, S. G., and DeVor, R. E., 2006, "A Hybrid Methodology for Kinematic Calibration of Micro/Meso-Scale Machine Tools (mMTs)," ASME J. Manuf. Sci. Eng., **128**, pp. 513–522.
[6] Liu, X., DeVor, R. E., Kapoor, S. G., and Ehmann, K. F., 2004, "The Mechanics of Machining at the Microscale: Assessment of the Current State of the Science," ASME J. Manuf. Sci. Eng., **126**, pp. 666–678.
[7] Zwyssig, C., Kolar, J. W., Thaler, W., and Vohrer, M., 2005, "Design of a 100 W, 500000 rpm Permanent-Magnet Generator for Mesoscale Gas Turbines," 2005 IEEE Industry Applications Conference, 40th IAS Annual Meeting (IAS'05), Hong Kong, Oct. 2–6.
[8] Zwyssig, C., and Kolar, J. W., 2006, "Design Considerations and Experimental Results of a 100 W, 500 000 rpm Electrical Generator," J. Micromech. Microeng., **16**(9), pp. S297–S302.
[9] Veyo, S. E., Shockling, L. A., Dederer, J. T., Gillet, J. E., and Lundberg, W. L., 2002, "Tubular Solid Oxide Fuel Cell/Gas Turbine Hybrid Cycle Power Systems: Status," ASME J. Eng. Gas Turbines Power, **124**, pp. 845–849.
[10] Costamagna, P., Magistri, L., and Massardo, A. F., 2001, "Design and Part-Load Performance of a Hybrid System Based on a Solid Oxide Fuel Cell Reactor and a Micro Gas Turbine," J. Power Sources, **96**, pp. 352–368.
[11] Federici, J. A., Norton, D. G., Brüggemann, T., Voit, K. W., Wetzel, E. D., and Vlachos, D. G., 2006, "Catalytic Microcombustors With Integrated Thermoelectric Elements for Portable Power Production," J. Power Sources, **161**(2), pp. 1469–1478.
[12] Isomura, K., Tanaka, S., Togo, S., and Esashi, M., 2005, "Development of High-Speed Micro-Gas Bearings for Three-Dimensional Micro-Turbo Machines," J. Micromech. Microeng., **15**, pp. S222–S227.
[13] Tanaka, S., Hikichi, K., Watanabe, H., Togo, S., and Esashi, R., 2006, "Rotor Dynamics Test for Palmtop Gas Turbine Generator," Proceedings of Power MEMS 2006, Berkeley, CA, Nov. 29–Dec. 1.
[14] Vleugels, P., Waumans, T., Peirs, J., Al Bender, F., Reynaerts, D., 2006, "High-Speed Foil Bearings for Micro Gas Turbines: Test Set-Up," Proceedings of Power MEMS 2006, Berkeley, CA, Nov. 29–Dec. 1.
[15] Reynaerts, D., Van den Braembussche, J., Hendrick, P., Baelmans, M., Driesen, J., Puers, R., Al-Bender, F., Peirs, J., Waumans, T., Vleugels, P., Liu, K., Alsalihi, Z., Di Sante, A., Verstraete, T., Verstraete, D., Trilla, J., Stevens, T., Rogiers, F., Stevens, S., and Ceyssens, F., 2006, "Development of a Gas Turbine With a 20 mm Rotor: Review and Perspectives," Proceedings of the International Workshop on Micro and Nanotechnology for Power Generation and Energy Conversion Applications, Berkeley, CA.
[16] Tanaka, S., Isomura, K., Togo, S., and Esashi, M., 2004, "Turbo Test Rig With Hydroinertia Air Bearings for a Palmtop Gas Turbine," J. Micromech. Microeng., **14**, pp. 1449–1454.
[17] Kim, D., and Bryant, M. D., 2004, "Hydrodynamic Performance of Meso Scale Gas Journal Bearings," ASME Paper No. IMECE2004-62026.
[18] http://www.grc.nasa.gov/WWW/Oilfree/bearings.htm.
[19] www.miti.cc/foil-bearings.html.
[20] Agrawal, G. L., 1997, "Foil Air/Gas Bearing Technology-An Overview," ASME Paper No. 97-GT-347.
[21] Salehi, M., Heshmat, H., and Walton, J. F., 2003, "On the Frictional Damping Characteristics of Compliant Bump Foils," ASME J. Tribol., **125**, pp. 804–813.
[22] Rubio, D. and San Andrés, L., 2005, "Structural Stiffness, Dry-Friction Coefficient and Equivalent Viscous Damping in a Bump-Type Foil Gas Bearing," ASME Paper No. GT2005-68384.
[23] Song, J., and Kim, D., 2007, "Foil Bearing With Compression Springs: Analyses and Experiments," ASME J. Tribol., **129**(3), pp. 628–639.
[24] Sim, K., and Kim, D., 2007, "Design of Flexure Pivot Tilting Pads Gas Bearings for High-Speed Oil-Free Micro Turbomachinery," ASME J. Tribol., **129**(1), pp. 112–119.
[25] Sim, K., and Kim, D., 2006, "Stability Analyses on Flexure Pivot Tilting Pad Gas Bearings for Microturbomachinery," *Proceedings of STLE/ASME Interna-*

Downloaded 02 Jun 2010 to 171.66.16.109. Redistribution subject to ASME license or copyright; see http://www.asme.org/terms/Terms_Use.cfm

*tional Joint Tribology Conference*San Antonio, TX, Oct. 23–25, Paper No. IJTC 2006-12158.

[26] Ehrfeld, W., Hessel, V., Lowe, H., Schilz, C., and Weber, L., 1999, "Materials of LIGA Technology," Microsyst. Technol., **5**, pp. 105–112.

[27] Kim, D., Lee, S., Jin, Y., Desta, Y., Bryant, M. D., and Goettert, J., 2004, "Micro Gas Bearings Fabricated by X-Ray Lithography," Microsyst. Technol., **10**, pp. 456–461.

[28] Timoshenko, S. P., and Goodier, J. N., 1970, *Theory of Elasticity*, McGraw-Hill, New York, pp. 80–83.

[29] Gere, M. G., and Timoshenko, S. P., 1984, *Mechanics of Materials*, Brooks/Cole Engineering Division, Monterey, CA, p. 636.

[30] Hamrock, B. J., Jacobson, B. O., and Schmid, S. R., 2004, *Fundamentals of Fluid Film Lubrication*, Dekker, New York.

[31] Delgado, A., SanAndrés, L., and Justak, J. F., 2004, "Analysis of Performance and Rotordynamic Force Coefficients of Brush Seals With Reverse Rotation Ability," *Proceedings of ASME Turbo Expo 2004*, Vienna, Austria.

[32] Pan, C. P., and Kim, D., 2007, "Stability Characteristics of a Rigid Rotor Supported by a Gas Lubricated Spiral-Groove Conical Bearing," ASME J. Tribol., **129**(2), pp. 375–383.

[33] Sim, K. and Kim, D., 2008, "Thermohydrodynamic Analysis of Compliant Flexure Pivot Tilting Pad Gas Bearings," ASME J. Eng. Gas Turbines Power, **130**(3), p. 032502.

[34] Pantenburg, F. J., Achenbach, S., and Mohr, J., 1998, "Characterization of Defects in Very High Deep-Etch X-Ray Lithography Microstructures," Microsyst. Technol., **4**(2), pp. 89–93.

[35] Chapra, S. C., and Canale, R. P., 1989, *Numerical Methods for Engineers*, McGraw-Hill, New York, pp. 631–634.

[36] Lund, J. W., 1968, "Calculation of Stiffness and Damping Properties of Gas Bearings," ASME J. Lubr. Technol., **90**(4), pp. 793–803.

[37] Wilde, D. and SanAndrés, L., 2003, "Comparison of Rotordynamic Analysis Predictions With the Test Response of Simple Gas Hybrid Bearings for Oil-Free Turbomachinery," ASME Paper No. GT-2003-38859.

Downloaded 02 Jun 2010 to 171.66.16.109. Redistribution subject to ASME license or copyright; see http://www.asme.org/terms/Terms_Use.cfm

Nonlinear Identification of Mechanical Parameters in a Squeeze Film Damper With Integral Mechanical Seal

Adolfo Delgado
e-mail: adelgam@tamu.edu

Luis San Andrés
e-mail: lsanandres@mengr.tamu.edu

Mechanical Engineering Department,
Texas A&M University,
College Station, TX 77843

End seals in squeeze film dampers (SFDs) aid to increase their damping capability while maintaining low lubricant flow rates and reducing the severity of air ingestion. This paper presents measurements of the forced response in a SFD integrating a contacting end seal and with closed flow ports, i.e., no lubricant through flow. The system motion is nonlinear due to the dry-friction interaction at the mechanical seal mating surfaces. Single parameter characterization of the test system would yield an equivalent viscous damping coefficient that is both frequency and motion amplitude dependent. Presently, an identification method suited for nonlinear systems allows determining simultaneously the squeeze film damping and inertia force coefficients and the seal dry-friction force. The identification procedure shows similar (within 10%) force coefficients than those obtained with a more involved two-step procedure that first requires measurements without any lubricant in the test system. The identified SFD damping and inertia force coefficients agree well with model predictions that account for end flow effects at recirculation grooves. The overall test results demonstrate that the nonrotating end seal effectively eliminates side leakage and avoids air ingestion, thus maintaining a consistent damping performance throughout the test frequency range. The nonlinear identification procedure saves time and resources while producing reliable physical parameter estimations.

[DOI: 10.1115/1.2967498]

1 Introduction

Squeeze film dampers (SFDs) aid to reduce synchronous vibration amplitude and enhance stability characteristics in rotating machinery. Since first formally tested by Cooper [1] more than 40 years ago, SFDs have been widely researched and successfully used in rotating equipment. Della Pietra and Adilleta [2,3] reviewed most of the relevant work, analytical and experimental, conducted on SFDs up to 2002. However, despite the many advances in SFD design and practice, important issues still remain. For example, in aerogas turbines, low inlet feed pressures make SFDs prone to oil cavitation and air ingestion that degrades their damping performance. These phenomena are more pervasive with increasing rotor vibration amplitudes and operating frequencies [4]. In certain SFD configurations, end seals help to delay air ingestion, but their effectiveness is often questioned [5].

A successful industrial sealed SFD type, as shown in Fig. 1, incorporates a mechanical (contacting faces) seal at one damper end and a recirculation groove with outlet orifices regulating the lubricant through flow. In this damper, the faces in contact fully seal the damper film land, thus preventing air ingestion. However, the mechanical seal introduces a dry-friction force, which depends on the assembly preload and surfaces' conditions, thus making the seal-SFD system nonlinear. San Andrés and Delgado [6,7] presented comprehensive experiments to identify the seal-SFD force coefficients while evaluating the effectiveness of the mechanical seal in preventing air ingestion. The tests were conducted with single frequency dynamic loads that produced both circular centered orbits (CCOs) and line path motions. A laborious two-step identification procedure was established to identify the seal friction force independently from the system (SFD and seal) damping forces. Dry system shakes, i.e., without any lubricant, determined the seal frictional force. Next, with lubricant flowing through the test rig, system damping coefficients were identified. The damping coefficient from the squeeze film land alone is ascertained from the system damping less the equivalent viscous action[1] from the mechanical seal. The experimentally identified SFD coefficients, in good agreement with model predictions, show that the damper forced performance remains uniform throughout the test frequency range. In addition, dynamic pressure and flow measurements also demonstrate that the mechanical seal effectively prevents air ingestion.

A variety of parameter identification procedures are readily available to characterize mainly linear mechanical systems. Tiwari et al. [8] reviewed the most popular test techniques and analysis methods to identify linearized force coefficients in fluid film bearings. The methods include time and frequency domain procedures, while testing focuses on the types of dynamic load excitation most efficient for a particular procedure. The literature on the experimental identification of nonlinear parameters in complex lubricated systems is more scant. In the early 1990s, Rice and Fitzpatrick [9] using random force excitations introduced a technique that characterizes a simple nonlinear system as a combination of linear and nonlinear inputs with linear operators on a multiple-input/single output scheme. Cross-spectra frequency analysis using residual coherence functions decouples the linear and nonlinear force contributions [10]. The method demonstrates to be robust and computationally light.

Other identification methods rely on various techniques to discern the linear and nonlinear contributions from recorded mechanical system responses due to the random or deterministic ex-

Contributed by the International Gas Turbine Institute of ASME for publication in the Journal of Engineering for Gas Turbines and Power. Manuscript received April 2, 2008; final manuscript received April 4, 2008; published online April 13, 2009. Review conducted by Dilip R. Ballal. Paper presented at the ASME Turbo Expo 2008: Land, Sea and Air (GT2008), Berlin, Germany, June 9–13, 2008.

---

[1] The equivalent viscous damping coefficient representative of "dry friction" is inversely proportional to the amplitude of motion and excitation frequency; hence then the nonlinear character of the test SFD-mechanical seal system.

Copyright © 2009 by ASME

Downloaded 02 Jun 2010 to 171.66.16.109. Redistribution subject to ASME license or copyright; see http://www.asme.org/terms/Terms_Use.cfm

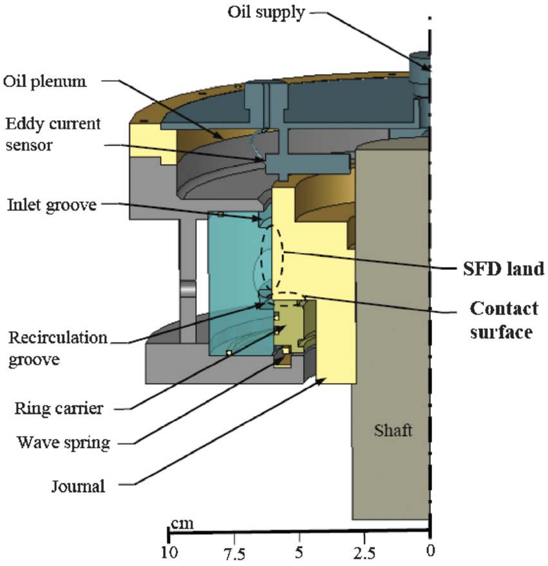

Fig. 1 Assembly cut view of SFD with mechanical seal

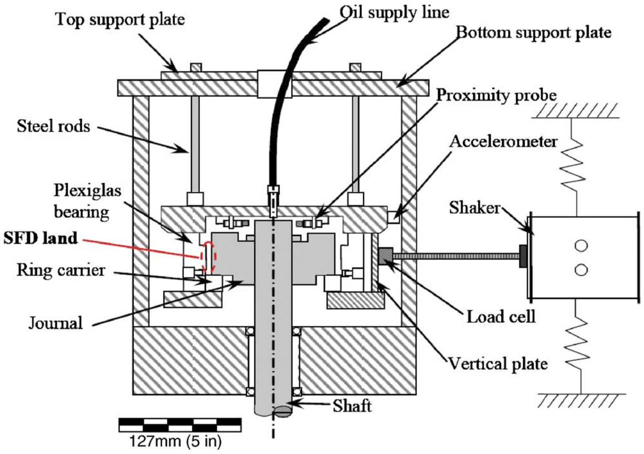

Fig. 2 Test rig for dynamic force measurements and flow visualization in a sealed end SFD (Ref. [7])

citations. More than often, however, existing methods rely on a priori knowledge of the nonlinearity functional form. Rice and Xu [11] identified nonlinear system parameters using multiple-single frequency excitations and expressing the system response in terms of Volterra functions in the frequency domain. The accuracy of the method depends on the number (order) of nonlinear kernels used on the Volterra expansion, and it only allows a qualitative evaluation of these kernels. Adams and Allemang [12] also estimated simultaneously the linear and nonlinear mechanical system parameters using a frequency domain technique that relies on the principle that the nonlinear feedback is directly linked to the spatial nature of the test nonlinear system. The method, based on an output feedback formulation, allows estimating the frequency response matrix and nonlinear coefficients simultaneously. The method is successfully tested on a numerically simulated system, but the sensitivity of the method to inherent measurement noise is yet to be studied. To identify the parameters in nonlinear systems, Yang et al. [13,14] introduced a sensitivity function defined as partial derivatives of the impedance (transfer) functions with respect to a specific system parameter (mass, damping, and stiffness). The embedded sensitivity functions are employed to characterize the type and location of the nonlinearity and then to estimate the nonlinear parameters by using Taylor expansions of the system impedances for small variations of the input signal level.

For a test mechanically sealed SFD with closed outlet ports, i.e., no through flow, this paper presents a proven technique to simultaneously extract the seal dry-friction force and the squeeze film damping force coefficients. The procedure avoids the need of an independent "dry system" shake test. The identification method, an adaptation of the Rice and Fitzpatrick [9] procedure, implements multiple-single frequency excitations with different load amplitudes. In prior art, San Andrés and Aguilar [15] using impact loads applied a similar procedure and identified the force coefficients on a hybrid gas damper-brush seal. The current SFD configuration is of special interest in unmanned aerial vehicles (UAVs). A description of the test facility and identification methodology follows.

2 Test Rig Description

References [6,7] detail the test rig, shown schematically on Fig. 2. A vertical rigid shaft, mounted on three precision ball bearings (natural frequency ~400 Hz), holds a steel journal of 127 mm (5 in.) diameter and 76.2 mm (3 in.) long. The SFD bearing assembly, shown in Fig. 1, consists of an acrylic bearing that also accommodates a metallic ring carrier and two (top and bottom) support plates. Two vertical thick steel plates clamp the support plates to the acrylic bearing. Upon assembly, a wave spring pushes the ring holder against the journal and provides a contact force between the matting surfaces, thus sealing the damper.

The top support plate includes a lubricant supply connection, a static pressure gauge displaying the feed pressure into the bearing, and four eddy current sensors facing the stationary shaft. The composite bearing housing hangs from a top frame via four steel rods that provide the structural stiffness to the test bearing section. Two sliding flat plates atop the test damper support the frame permit adjusting the position of the bearing center with respect to the shaft to simulate centered and off-centered operation conditions. The SFD configurations tested in Refs. [6,7] used four variable diameter outlet ports at the recirculation groove to regulate the lubricant through flow. In the current test setup, these ports are plugged (i.e., no through flow allowed). Figure 3 depicts the squeeze film land portion of the test bearing with relevant dimensions.

Two electromagnetic shakers, suspended from separate steel structures (90 deg apart), excite the test system. A slender stinger connects the shaker to a piezoelectric load cell attached to the vertical plate on the bearing housing. A customized data acquisition system records all the sensor signals and controls the shakers.

3 Methodology for System Parameter Identification

Controlled amplitude and phase shaker loads (F_x, F_y) of single frequency induce centered circular orbits of the test mechanical

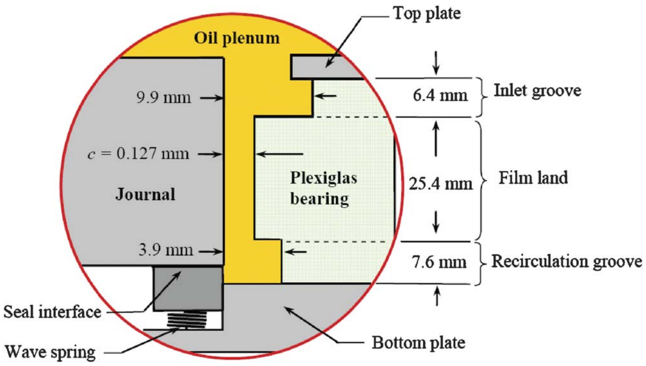

Fig. 3 Dimensions of squeeze film land (no oil throughflow condition). Film radial clearance $c=0.127$ mm.

Downloaded 02 Jun 2010 to 171.66.16.109. Redistribution subject to ASME license or copyright; see http://www.asme.org/terms/Terms_Use.cfm

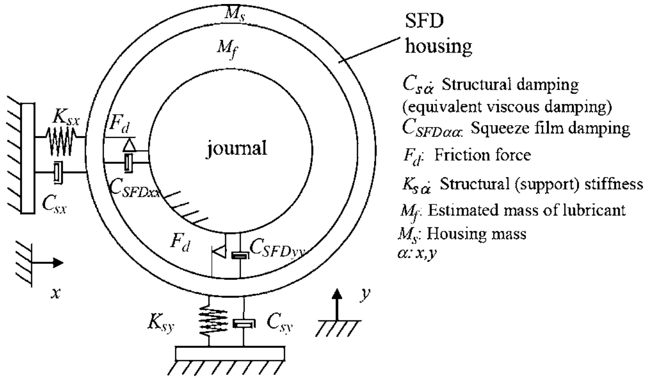

Fig. 4 Schematic of the equivalent representation of the SFD with mechanical seal

seal-SFD. Figure 4 depicts a representation of the mechanical system with its major physical parameters. The equations of motion for the test bearing section are [7]

$$(M_s+M_f)\begin{Bmatrix}\ddot{x}\\ \ddot{y}\end{Bmatrix}+\begin{Bmatrix}C_{sx}\dot{x}\\ C_{sy}\dot{y}\end{Bmatrix}+\begin{Bmatrix}K_{sx}x\\ K_{sy}y\end{Bmatrix} = \begin{Bmatrix}F_x\\ F_y\end{Bmatrix}-\begin{Bmatrix}F_x\\ F_y\end{Bmatrix}_{\text{seal}}-\begin{Bmatrix}F_x\\ F_y\end{Bmatrix}_{\text{SFD}} \tag{1}$$

where $(K_s)_{x,y}$ are the stiffnesses of the elastic support structure holding the test bearing of mass, $M_s.M_f$ is the mass of fluid enclosed in the plenum above the fluid film land section and in the recirculation groove, and $(C_s)_{x,y}$ represent the small viscous damping coefficients from the structural support. The structure stiffness and damping force coefficients, obtained from impact tests on the dry system, are $K_{sx}=853$ kN/m, $K_{sy}=885$ kN/m, and $C_{s(x,y)}=230$ N s/m, respectively [7].

The reaction forces from the squeeze film land[2] are

$$\begin{Bmatrix}F_x\\ F_y\end{Bmatrix}_{\text{SFD}}=\begin{Bmatrix}C_{\text{SFD}_{xx}}\dot{x}\\ C_{\text{SFD}_{yy}}\dot{y}\end{Bmatrix}+\begin{Bmatrix}M_{\text{SFD}_{xx}}\ddot{x}\\ M_{\text{SFD}_{yy}}\ddot{y}\end{Bmatrix} \tag{2}$$

where $\{C_{\text{SFD}\alpha}\}_{\alpha=xx,yy}\{M_{\text{SFD}\alpha}\}_{\alpha\beta=xx,yy}$ are the film damping and inertia force coefficients, respectively.

The mechanical contact seal dry-friction force, with magnitude F_d, is a nonlinear function expressed as [15]

$$\begin{Bmatrix}F_x\\ F_y\end{Bmatrix}_{\text{seal}}=F_d\begin{Bmatrix}\dot{x}\\ \dot{y}\end{Bmatrix}\frac{1}{\sqrt{\dot{x}^2+\dot{y}^2}}=F_d\begin{Bmatrix}u\\ v\end{Bmatrix} \tag{3}$$

with $\{u,v\}=\{\dot{x},\dot{y}\}/\sqrt{\dot{x}^2+\dot{y}^2}$ as the normalized velocities. The applied dynamic loads are of a single frequency and represented as

$$F_x(t)=(F_{xc}-iF_{xs})e^{i\omega t}=\bar{F}_x e^{i\omega t},\quad \bar{F}_x=(F_{xc}-iF_{xs})$$

$$F_y(t)=(F_{yc}-iF_{ys})e^{i\omega t}=\bar{F}_y e^{i\omega t},\quad \bar{F}_y=(F_{yc}-iF_{ys}) \tag{4}$$

and the ensuing bearing displacements (x,y) and accelerations are also periodic with identical frequency (ω), i.e.,

$$\begin{Bmatrix}x\\ y\end{Bmatrix}=\begin{Bmatrix}x_c-ix_s\\ y_c-iy_s\end{Bmatrix}e^{i\omega t}=\begin{Bmatrix}\bar{x}\\ \bar{y}\end{Bmatrix}e^{i\omega t},\quad \begin{Bmatrix}\ddot{x}\\ \ddot{y}\end{Bmatrix}=\begin{Bmatrix}\bar{a}_x\\ \bar{a}_y\end{Bmatrix}e^{i\omega t} \tag{5}$$

Above, $(\bar{x},\bar{y})$ and $(\bar{F}_x,\bar{F}_y)$ are the complex Fourier coefficients of the periodic displacements and forces, respectively.

In the frequency domain, the equations of motion for the test system become

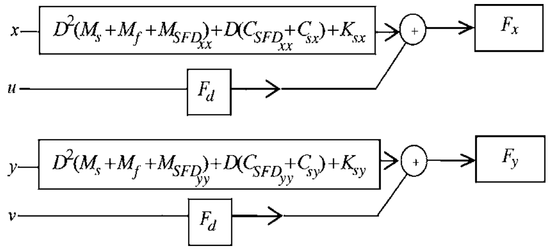

Fig. 5 Elements of a four-input/two-output representation of the nonlinear mechanical seal-SFD system [15]

$$\bar{F}_x=L_{xx}\bar{x}+F_d\bar{u},\quad L_{xx}=(K_{sx}-\omega^2 M_{S-xx}+i\omega C_{S-xx})$$

$$\bar{F}_y=L_{yy}\bar{y}+F_d\bar{v},\quad L_{yy}=(K_{sy}-\omega^2 M_{S-yy}+i\omega C_{S-yy}) \tag{6}$$

where L_{xx} and L_{yy} are the linear transfer functions containing the system stiffness, inertia, and damping force coefficients.

$(\bar{u},\bar{v})$ denote the fundamental Fourier coefficients of the normalized velocities (u,v) and obtained by building the velocity vector $(\dot{x},\dot{y})^T$ with the Fourier coefficients $(\bar{x},\bar{y})$. This procedure effectively reduces signal noise. Note that, although the system response is nonlinear (with $3x$, $5x$, … harmonics), only the first harmonic of the measured responses is included in the equations above since the applied force contains a single frequency. Thus, the identification method relies on discerning the contribution of the first harmonic of the (nonlinear) friction force from the overall system response.

In Eq. (6) above, the system (S) parameters are defined as

$$M_{S-xx}=M_{\text{SFD}_{xx}}+M_f+M_s,\quad M_{S-yy}=M_{\text{SFD}_{yy}}+M_f+M_s$$

$$C_{S-xx}=C_{\text{SFD}_{xx}}+C_{sx},\quad C_{S-yy}=C_{\text{SFD}_{yy}}+C_{sy} \tag{7}$$

Figure 5 represents the test system as a four-input/two-output equivalent model, with D denoting the time derivative operator. In the identification system, the normalized velocities u and v are regarded as nonlinear input paths derived from the two original inputs (x,y) recorded in the time domain. Recall that in the experiments, the excitation forces are the actual inputs and the displacements (x,y) and the modeled nonlinear inputs (u,v) represent the output of the system.

The dry-friction force (F_d) can be identified from Eq. (6) using two single frequency force excitations of different magnitudes provided that the force coefficients in Eq. (7) are independent of the motion amplitude. However, this is not the case for a SFD since, as theory predicts and experiments and practice demonstrate, squeeze film damping coefficients are a function of the amplitude of journal motion. Presently, the dependency of the squeeze film damping coefficient on motion amplitude is regarded as linear for small differences in motion amplitudes, as shown in prior experiments [7]. Thus, $C_{\text{SFD}xx}=a_x|\bar{x}|+b_x$ and $C_{\text{SFD}yy}=a_y|\bar{y}|+b_y$, with a and b as generic constants.

For N independent excitation load levels, $i=1,\ldots,N$,

$$H^i_{xx}=(K_{sx}-\omega^2 M_{s-xx}+i\omega C_{sx})+i\omega(a_x|\bar{x}^i|+b_x)+F_d G^i_{xx}$$

$$H^i_{yy}=(K_{sy}-\omega^2 M_{s-yy}+i\omega C_{sy})+i\omega(a_y|\bar{y}^i|+b_y)+F_d G^i_{yy} \tag{8}$$

with

$$H^i_{xx}=\frac{\bar{F}^i_x}{\bar{x}^i},\quad G^i_{xx}=\frac{\bar{u}^i}{\bar{x}^i}$$

$$H^i_{yy}=\frac{\bar{F}^i_y}{\bar{y}^i},\quad G^i_{yy}=\frac{\bar{v}^i}{\bar{y}^i} \tag{9}$$

---

[2] As demonstrated in a prior paper [6], cross-coupled force coefficients are negligible since the damper operates without oil cavitation.

Downloaded 02 Jun 2010 to 171.66.16.109. Redistribution subject to ASME license or copyright; see http://www.asme.org/terms/Terms_Use.cfm

Table 1 Test conditions for dynamic load tests. Lubricated SFD (no throughflow).

Inlet pressure (P_s)[a]	31 kPa
Discharge groove pressure (P_r)[a]	8.6–15.5 kPa
Frequency range	20–70 Hz (5 Hz step)
Lubricant temperature (T)	23–25°C (73–77°F)
Viscosity (η)	3.1–2.8 cP
Density (ρ)	800 kg/m^3
Clearance (c)	125–127 μm (4.9–5 mils)
Orbit amplitude (e)	25–50 μm (1–2 mils)

[a] Gauge pressure.

The seal friction force (F_d) is identified from three increasing load magnitudes inducing three circular orbits of dissimilar amplitudes. That is,

$$F_d = \frac{H^1_{\alpha\alpha} + H^3_{\alpha\alpha} - 2H^2_{\alpha\alpha}}{G^1_{\alpha\alpha} + G^3_{\alpha\alpha} - 2G^2_{\alpha\alpha}}, \quad \alpha{:}x,y \qquad (10)$$

Superscripts 1, 2, and 3 represent each of the three independent tests determining different excitation amplitudes. In the experiments, the displacement differences are constant, i.e., $|\bar{x}^1|-|\bar{x}^2| = |\bar{x}^2|-|\bar{x}^3| \approx 0.05c$.

Once the seal friction force is identified, it can be used directly for any other excitation amplitude without any restrictions on orbit amplitude. Recall that the friction force is only a function of the wave-spring assembly force and the condition of the surfaces in contact. The parameters from the linear transfer functions (L_{xx}, L_{yy}) are obtained from least squares fits of their real and imaginary parts, i.e.,

$$K_{s_\alpha} - \omega^2 M_{s-\alpha\alpha} = \mathrm{Re}(L_{\alpha\alpha}) = \mathrm{Re}(H_{\alpha\alpha} - F_d G_{\alpha\alpha})$$

$$\omega C_{s-\alpha\alpha} = \mathrm{Im}(L_{\alpha\alpha}) = \mathrm{Im}(H_{\alpha\alpha} - F_d G_{\alpha\alpha}), \quad \alpha = x,y \qquad (11)$$

Finally, the squeeze film added mass and damping and damping coefficients are then extracted from

$$M_{\mathrm{SFD}_{\alpha\alpha}} = M_{S-\alpha\alpha} - M_s - M_f$$

$$C_{\mathrm{SFD}_{\alpha\alpha}} = C_{S-\alpha\alpha} - C_{s\alpha}, \quad \alpha = x,y$$

3.1 Identified Force Coefficients. Single frequency loads produce circular centered orbits of the test element. Throughout the test frequency range (20–70 Hz), the excitation load amplitudes are adjusted to maintain circular orbits of a fixed radius (25 μm, 31 μm, 38 μm, and 50 μm). The tests conditions are similar to those in Ref. [7] to allow direct comparisons of the identified parameters. Table 1 presents the test conditions and lubricant properties. Figure 6, bottom graph, shows the recorded displacement bearing orbits for tests at 60 Hz.

Figure 7 depicts the dry-friction force (F_d) identified from the procedure detailed above. The results also include the dry-friction parameter (F_d=53 N) identified in Refs. [6,7] from dry system tests (i.e., with no lubricant). The test results show excellent correlation between the parameters identified with each method. The current F_d is ~2% larger than that identified from an energy method and in a lengthier two-step procedure. Furthermore, the friction force remains fairly constant throughout the test frequency range (less than a 15% change over the test frequency range). Small variations in forces along the x and y directions are apparent. However, the presently identified seal dry-frictional force appears to be unique

Figure 8 shows, for the largest amplitude of orbital motion (50 μm), the real part of the linear path transfer function (L_{xx}, L_{yy}) and the corresponding curve fit. Table 2 presents the identified values of added mass coefficients and the average identified dry-friction force. The added mass results are similar (within 15%) to those obtained in Ref. [7] for the throughflow condition. The present results, just like the previous ones, show large magnitudes of added mass coefficients (i.e., about half the whole system mass). These relatively large magnitudes are associated with

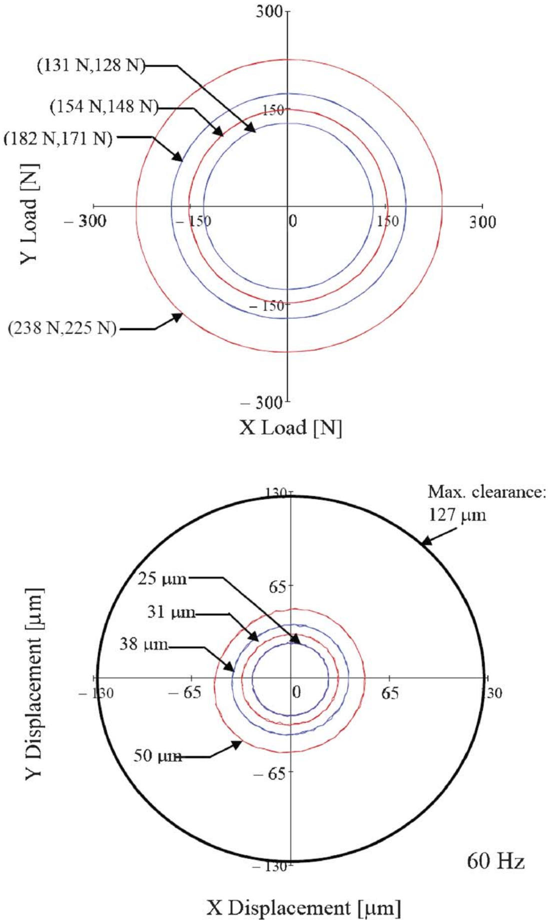

Fig. 6 Recorded load (top) and ensuing displacement orbits (bottom) for four load magnitudes. Clearance circle noted. (60 Hz, lubricated SFD, CCO).

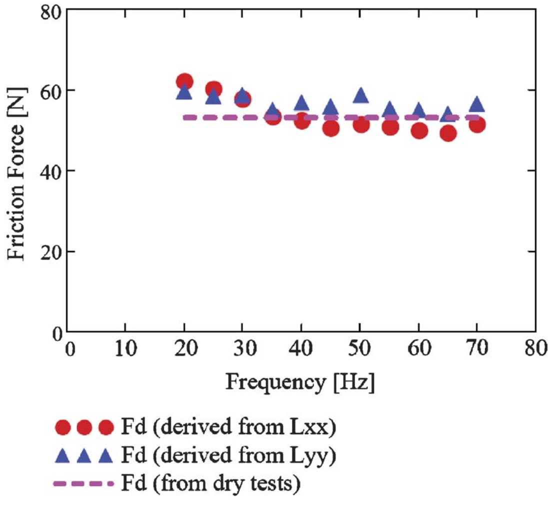

Fig. 7 Dry friction force identified from circular centered orbits. The dotted line represents dry friction estimated from energy method and tests under dry conditions.

Downloaded 02 Jun 2010 to 171.66.16.109. Redistribution subject to ASME license or copyright; see http://www.asme.org/terms/Terms_Use.cfm

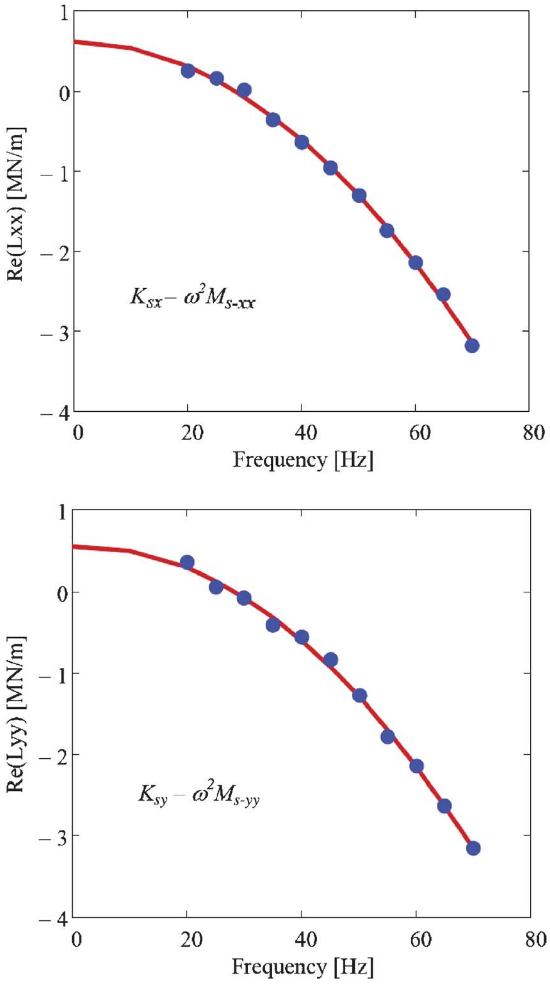

Fig. 8 Real part of dynamic stiffnesses versus frequency. Circular centered orbits of amplitude x,y: 50 μm (K_{sx}=853 kN/m, K_{sy}=885 kN/m).

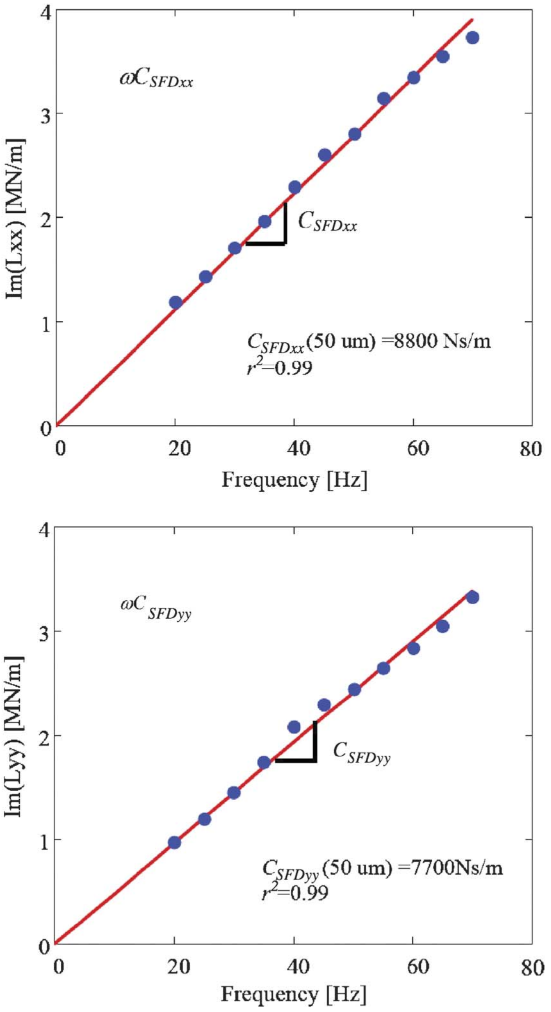

Fig. 9 Imaginary part of linear impedance function versus excitation frequency. (C_{SFDxx}) Circular centered orbits of amplitude x,y: 50 μm (no throughflow).

the development of significant dynamic pressures at the inlet and recirculation grooves, a direct evidence of the importance of fluid inertia effects in SFDs.

Figure 9 shows the imaginary part of the linear transfer function (L_{xx}, L_{yy}) and the corresponding linear fit ($\omega C_{\mathrm{SFD}xx,yy}$) for the largest amplitude circular orbit (50 μm). The slope of the linear curve fit represents the squeeze film damping coefficients ($C_{\mathrm{SFD}xx}, C_{\mathrm{SFD}yy}$). The goodness of the curve fit, $r^2=0.99$, indicates that the "viscous" damping contribution from the dry-friction force has been effectively subtracted from the system overall damping. The squeeze film damping coefficient in the x direction is ~13% larger than that along the y direction. This small discrepancy is attributed to the small structural orthotropy of the test system.

Figure 10 shows the squeeze film damping coefficient ($C_{\mathrm{SFD}yy}$) versus orbit amplitude. The figure includes the damping coeffi-

Table 2 SFD inertia coefficients and seal dry-friction force identified from circular centered orbit tests (frequency range 20–70 Hz, no throughflow)

Parameter	xx	yy
Friction fore (F_d) (average)		54 N
System mass, (M_s)	20.2 kg	20.6kg
Squeeze film inertia (M_{SFD})	9.9 kg	10.3 kg
r^2 (goodness of curve fit)	0.99	0.98
Fluid mass, (M_f) [kg]		0.62

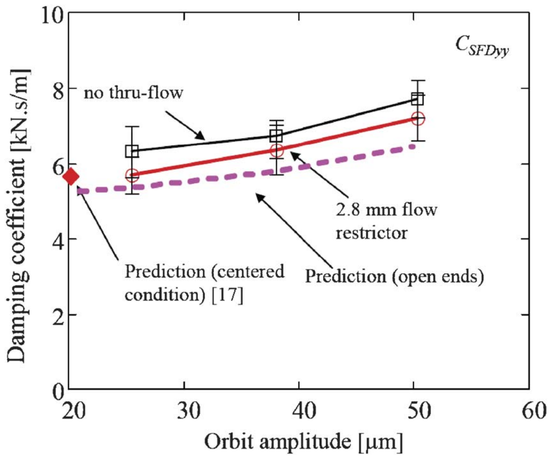

Fig. 10 Squeeze film damping coefficient ($C_{\mathrm{SFD}yy}$) versus orbit amplitude (circular centered orbits, no throughflow, flow restrictor: 2.8 mm [3])

Downloaded 02 Jun 2010 to 171.66.16.109. Redistribution subject to ASME license or copyright; see http://www.asme.org/terms/Terms_Use.cfm

cient obtained earlier with a throughflow condition using 2.8 mm flow restrictors [7] and predictions based on the short length bearing model [5].

Figure 10 also depicts an improved damping coefficient prediction advanced in Ref. [16] and adequately accounts for the contribution of the inlet and recirculation grooves on the SFD forced performance. The error bars denote the uncertainty associated with each coefficient following the uncertainty analysis detailed in Ref. [7]. The experimental squeeze film damping coefficient ($C_{\mathrm{SFD}yy}$) increases for increasing orbit amplitudes, as in the previous test configuration. Furthermore, the current damping coefficient is slightly larger (~10%) but still within the uncertainty of the coefficients reported for the throughflow condition. Thus, the damper operating with no throughflow is also effective. The improved damping prediction for a centered condition is also within the uncertainty value of the damping coefficient identified for the smallest orbit amplitude.

The experimental results are of interest in applications that need fully sealed dampers and able to contain the oil within the damper land for extended periods of time. Note, however, that the current test results correspond to laboratory conditions maintaining a relatively constant temperature, ~2°C variation within the squeeze film land and oil plenum (see Table 1). The film temperature remains nearly invariant since the experiments are of very short duration (~30 min) with low levels of energy input (a maximum power of 5.7 W). The mass of oil (0.59 kg) in the inlet plenum together with other system components account for a large thermal capacity of 4.1 kJ. In actual applications, with no lubricant through flow and with a limited oil volume, it may be necessary to consider the increase in oil temperature and the corresponding viscosity reduction when estimating the system damping forced performance.

Figure 11 depicts the identified system damping and the squeeze film damping coefficients versus the excitation frequency. The system damping coefficient, which includes the equivalent viscous action of dry friction, is frequency dependent and notably larger than the extracted squeeze film damping coefficient. Also note that the system damping is larger for the smallest amplitude (i.e., 25 μm). The noted characteristics are distinctive of systems with dry friction [17]. On the other hand, the squeeze film damping coefficients are independent of frequency, being largest for the largest amplitude (50 μm). These results show that the identification method is effective in discerning the squeeze film damping contribution from the overall system damping.

4 Conclusions

This paper presents the identification of nonlinear force coefficients in a mechanical seal-SFD test element. In the tests, to assess the effectiveness of the seal in preventing air ingestion, the damper discharge ports are closed so there is no lubricant throughflow. A nonlinear identification method is implemented to simultaneously determine the squeeze film force coefficients and the friction force from the mechanical contact seal. The squeeze film damping coefficients are accurately identified from a linear curve fit of the linear path transfer function, which evidences the effectiveness of the method in subtracting the nonlinear damping contribution of the mechanical seal.

The test squeeze film damping coefficients are a function of the circular orbit amplitude and similar (~10% larger) to those reported for the same damper with lubricant throughflow, Ref. [7]. In addition, the test damper added mass coefficients are of similar magnitude to those reported earlier [7]. The oil temperature remains relatively constant throughout the testing, in spite of the lack of lubricant throughflow. The uniform temperature is due to the small duration of the tests, the small amount of work input into the system, and the large volume of oil residing in the inlet plenum. Note that in the actual application (unmanned aerial vehicle) the SFD will only operate for a few minutes (at most). Hence, thermal effects are relatively unimportant.

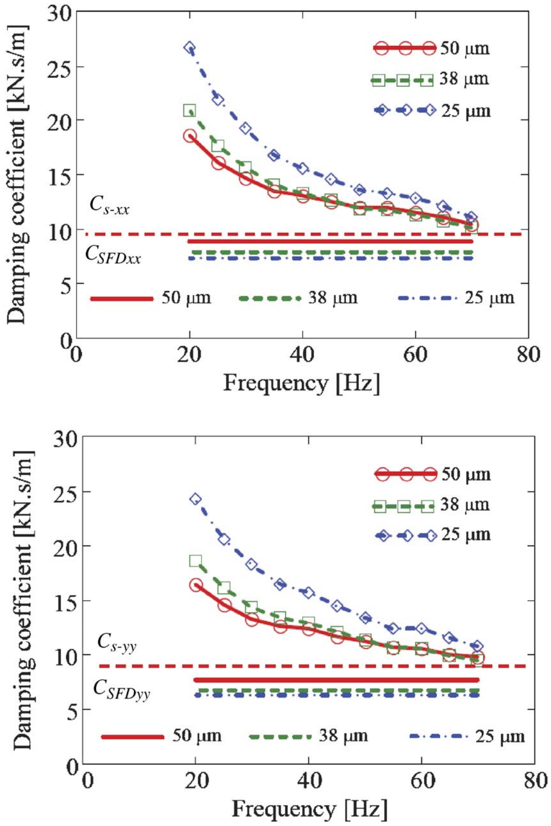

Fig. 11 Squeeze film damping coefficients ($C_{\mathrm{SFD}xx}, C_{\mathrm{SFD}yy}$) and system damping coefficients (C_{s-xx}, C_{s-yy}) versus excitation frequency for increasing orbit amplitudes (circular centered orbits, no throughflow)

The experimentation demonstrates that the mechanical seal is effective in avoiding air ingestion; even without lubricant throughflow, the test system damping performance is not greatly affected. Thus, the SFD with closed outlet ports is a viable option for a UAV application.

Current work includes multiple frequency excitations to simulate actual operating conditions in multispool engines. Other tests are being conducted with larger contact forces at the seal interface to evaluate their impact on the seal-SFD forced performance The identification method can be readily extended to obtain the system force coefficients from eccentric journal orbits, for example.

Acknowledgment

The support of the Turbomachinery Research consortium is gratefully acknowledged. Thanks to Mr. Mathew Kristley, undergraduate student, for assisting in the experimental work.

Nomenclature

$C_{s\alpha}$ = structure damping coefficients (N s/m), $\alpha=x,y$
$C_{S-\alpha\beta}$ = identified test system damping coefficients (N s/m), $\alpha,\beta=x,y$
c = SFD radial clearance, 0.127 mm
$C_{\mathrm{SFD}\alpha\beta}$ = identified squeeze film damping coefficients (N s/m), $\alpha,\beta=x,y$
e = amplitude or radius of circular orbit (m)
$F_{x,y}$ = external (shaker) forces (N)
$\bar{F}_x,\bar{F}_y$ = components of external forces in frequency domain (N)

Downloaded 02 Jun 2010 to 171.66.16.109. Redistribution subject to ASME license or copyright; see http://www.asme.org/terms/Terms_Use.cfm

F_d = dry friction force from contact in mechanical seal (N)

$H_{\alpha\beta}, L_{\alpha\beta}, G_{\alpha\beta}$ = dynamic transfer functions (N/m), $\alpha, \beta = x, y$

$K_{s\alpha}$ = structural (support) stiffnesses (N/m), $\alpha = x, y$

M_s = mass of SFD housing (kg)

M_f = lubricant mass in feed plenum and groove (kg)

$M_{\mathrm{SFD}\alpha\beta}$ = squeeze film inertia coefficients (kg), $\alpha, \beta = x, y$

$M_{S-\alpha\beta}$ = identified test system inertia coefficients (kg), $\alpha, \beta = x, y$

T = lubricant temperature (°C)

t = time (s)

u, v = $\{\dot{x}, \dot{y}\} / \sqrt{\dot{x}^2 + \dot{y}^2}$ normalized velocities

$\bar{u}, \bar{v}$ = components of normalized velocities in frequency domain

x, y = bearing X, Y dynamic motions (m)

$\bar{x}, \bar{y}$ = components of bearing motions in frequency domain (m)

$\dot{x}, \dot{y}$ = bearing velocities (m/s)

$\ddot{x}, \ddot{y}$ = bearing acceleration (m/s)

ρ, η = lubricant density (kg/m^3) and viscosity (Pa s)

ω = excitation frequency (rad/s)

References

[1] Cooper, S., 1963, "Preliminary Investigation of Oil Films for Control of Vibration," *Proceedings of the Lubrication and Wear Convention*, London, Institute of Mechanical Engineers, pp. 305–315, Paper No. 28.

[2] Della Pietra, L., and Adiletta, G., 2002, "The Squeeze Film Damper Over Four Decades of Investigations. Part I: Characteristics and Operating Features," Shock Vib. Dig., **34**(1), pp. 3–26.

[3] Della Pietra, L., and Adiletta, G., 2002, "The Squeeze Film Damper Over Four Decades of Investigations. Part II: Rotordynamic Analyses With Rigid and Flexible Rotors," Shock Vib. Dig., **34**(2), pp. 97–126.

[4] Diaz, S., and San Andrés, L., 1999, "Reduction of the Dynamic Load Capacity in a Squeeze Film Damper Operating With a Bubbly Lubricant," ASME J. Eng. Gas Turbines Power, **121**, pp. 703–709.

[5] Zeidan, F. Y., San Andrés, L., and Vance, J. M., 1996, "Design and Application of Squeeze Film Dampers in Rotating Machinery," *Proceedings of the 25th Turbomachinery Symposium*, Houston, TX, Sept. 16–19, pp.169–188.

[6] San Andrés, L., and Delgado, A., 2007, "Identification of Force Coefficients in a Squeeze Film Damper With a Mechanical End Seal. Part I: Unidirectional Load Tests," ASME J. Eng. Gas Turbines Power, **129**(3), pp. 858–864.

[7] San Andrés, L., and Delgado, A., 2007, "Identification of Force Coefficients in a Squeeze Film Damper With a Mechanical End Seal–Centered Circular Orbit Tests," ASME J. Tribol., **129**(3), pp. 660–668.

[8] Tiwari, R., Lees, A. W., and Friswell, M. I., 2004, "Identification of Dynamic Bearing Parameters: A Review," Shock Vib. Dig., **36**(2), pp. 99–124.

[9] Rice, H. J., and Fitzpatrick, J. A., 1991, "Procedure for the Identification of Linear and Non-Linear Multi-Degree-of-Freedom Systems," J. Sound Vib., **149**(3), pp. 397–411.

[10] Fitzpatrick, J. A., and Rice, H. J., 1988, "Simplified Partial Coherence Functions for Multiple Input/Output Analysis," J. Sound Vib., **122**(1), pp. 171–174.

[11] Rice, H. J., and Xu, K. Q., 1996, "Linear Path Identification of General Non-Linear Systems," Mech. Syst. Signal Process., **10**(1), pp. 55–63.

[12] Adams, D. E., and Allemang, R. J., 2000, "A Frequency Domain Method for Estimating the Parameters of a Non-Linear Structural Dynamic Model Through Feedback," Mech. Syst. Signal Process., **14**(4), pp. 637–656.

[13] Yang, C., Adams, D. E., and Ciray, S., 2005, "System Identification of Non-Linear Mechanical Systems Using Embedded Sensitivity Functions," Trans. ASME, J. Vib. Acoust., **127**(6), pp. 530–541.

[14] Yang, C., Adams, D. E., and Yoo, S. W., 2003, "Diagnosing Vibration Problems With Embedded Sensitivity Functions," J. Sound Vib., **37**(4), pp. 12–17.

[15] San Andrés, L., and Aguilar, R., 2000, "Leakage and Dynamic Response of a Hybrid Brush Seal-Gas Damper Seal," Texas A&M University, Research Progress Report No. TRC-SEAL-3-00.

[16] San Andrés, L., and Delgado, A., 2007, "Parameter Identification of an End Sealed SFD. Part II: Improved Predictions of Added Mass Coefficients for Grooved SFDs and Oil Seals," TRC, Report No. TRC-SFD-2-07.

[17] Ginsberg, J. H., 2001, *Mechanical and Structural Vibrations*, Wiley, New York, pp. 135–139.

Downloaded 02 Jun 2010 to 171.66.16.109. Redistribution subject to ASME license or copyright; see http://www.asme.org/terms/Terms_Use.cfm

Cylinder-to-Cylinder Variations in a V6 Gasoline Direct Injection HCCI Engine

Jacek Misztal

Hongming Xu

Miroslaw L. Wyszynski

Athanasios Tsolakis

Mechanical and Manufacturing Engineering,
School of Engineering,
University of Birmingham,
Birmingham B15 2TT, UK

Jun Qiao
Jaguar Cars Limited,
W/2/021 Engineering Centre,
Abbey Road,
Whitley, Coventry CV3 4LF, UK

Despite the fact that homogeneous charge compression ignition (HCCI) has been demonstrated as a combustion technology feasible for implementation with different fuels in various types of engines, cylinder-to-cylinder variations (CTCVs) in multicylinder HCCI engines remain one of the technical obstacles to overcome. A reduction in CTCV requires further developments in control technology. This study has been carried out with regard to the overall engine parameters, involving geometric differences between individual cylinders, coolant paths through the engine, combustion chamber deposits, and also the differences in the inlet temperature distributions between the cylinders. Experimental investigations on the Jaguar V6 HCCI research engine with negative valve overlapping and cam profile switching show that the differences in the rate of pressure rise between the cylinders can be larger than 1 bar/CA deg and that the load differences can be as high as 5–10%. It has been found that some individual cylinders will approach the misfiring limit far earlier than the others. The complex interaction between a number of parameters makes the control of the multicylinder engine a serious challenge. In order to avoid these differences, an active cylinder balancing strategy will be required. It has been observed that spark assistance and split injection strategy deliver the best control for the cylinder balance. However, spark assistance is restricted to low loads and low engine speeds, while split injection requires a considerable effort to optimize its possible settings. This paper defines the most important parameters influencing cylinder-to-cylinder variations in the HCCI engine and aims to put forward suggestions that can help to minimize the effect of cylinder-to-cylinder variations on the overall engine performance. [DOI: 10.1115/1.3077661]

1 Introduction

New regulation standards demand a continuous reduction in emissions from passenger cars while fuel consumption is a matter of concern for all engine users as well as for environment protection due to its relation to the production of green-house-gas CO_2. These two reasons have brought homogeneous charge compression ignition (HCCI) technology to the engine combustion researchers' attention for a number of years. In HCCI engines the homogeneous mixture is auto-ignited through compression. The advantages of HCCI combustion are in the reduction of nitric oxides (NO_x) emissions and fuel consumption (mainly through avoidance of throttling). However, the price of these benefits is lower combustion efficiency and difficulties in controlling the combustion process. NO_x reduction is a result of lower combustion temperature due to dilution and increased heat capacity by trapped internal exhaust gas. Exhaust gas trapping is commonly used to supply extra energy to enable auto-ignition and also dilute the cylinder mixture. Lower combustion efficiency leads to higher emissions of carbon monoxide (CO) and unburned hydrocarbons (UHC). Higher CO and UHC emissions are due to lower combustion temperature, which impedes the oxidation process. The lack of parameters directly triggering and defining the combustion makes HCCI difficult to control.

Controlling the start of combustion is difficult since it is strictly related to the in-cylinder temperature and pressure history. Problems with HCCI control become even more significant when one considers a multicylinder engine. Cylinder-to-cylinder variations (CTCVs) are not exclusively a matter of concern for HCCI engines. Spark ignition (SI) and diesel engines in many different ways are also affected by this phenomenon. However, CTCV has a much more serious impact on HCCI than on any other mode of operation of multicylinder engines. The speed-load operation region, which is relatively limited because of the delicately balanced nature of HCCI combustion, becomes even smaller when CTCV is taken into account. In order to create appropriate pressure and temperature for well timed auto-ignition, a number of parameters have to be strictly monitored and controlled. Some of these parameters will enhance auto-ignition while others will impede the process. Through the years of HCCI research, many efforts have been made worldwide in defining and controlling the most important parameters influencing HCCI operation [1–5]. The task is further complicated since almost all of the mentioned parameters will interact with each other.

The work presented here will be split into three main parts. First, the literature survey with respect to the most important parameters causing cylinder-to-cylinder variations will be provided. Second, a discussion with reference to CTCV on the Jaguar V6 GDI-HCCI research engine will be presented. Finally, three methods for the reduction of CTCV will be considered.

From the authors' experience and also from the discoveries made by other researchers, six important variables should be considered: inlet air temperature, effective compression ratio, coolant path, exhaust gas recirculation (EGR) distribution between cylinders, differences in the amount of injected fuel (variation of lambda), and formation of deposits in individual cylinders. Since all of these parameters have been previously discussed in numerous publications, e.g., Refs. [6–8], the discussion below will be conducted regarding V6 engines specifically.

2 Factors Critical to CTCV

Inlet Air Temperature. Inlet air temperature has a significant effect on HCCI operation. Not only does it affect the temperature at the end of the compression stroke but also the gravimetric air-

---

Manuscript received February 27, 2008; final manuscript received October 17, 2008; published online April 9, 2009. Review conducted by Dilip R. Ballal.

Copyright © 2009 by ASME

Downloaded 02 Jun 2010 to 171.66.16.109. Redistribution subject to ASME license or copyright; see http://www.asme.org/terms/Terms_Use.cfm

fuel ratio through air density, as well as through volumetric efficiency. It has been shown by Morgan et al. [9] that increasing inlet temperature to 70°C will decrease the net-mean-effective-pressure (NMEP) by 7% and it will advance the timing of 50% MFB by ~2.5 CAD while increasing the pressure rise rate (dp/dCA) by 7%.

Hyvönen et al. [6] checked the effect of inlet air temperature on the cylinder-to-cylinder variations. They found that controlling the combustion phasing in individual cylinders by adjusting inlet air temperature is the most effective method (compared, e.g., with adjusting the amount of fuel injected into individual cylinders) to decrease cylinder-to-cylinder variations. This method can lead not only to the same combustion phasing in all cylinders but can bring the highest brake efficiency and the lowest NO_x emissions. Unfortunately, air density and therefore the load will vary between individual cylinders.

On the other hand it has been shown that maintaining inlet temperature on the same level for all cylinders will not guarantee the same combustion phasing since other parameters would affect HCCI operation. Iida et al. [10] and Güralp et al. [11] have presented results on the effects of inlet air and coolant temperature on HCCI operation. Iida et al. [10] showed that higher inlet air and coolant temperature will cause an earlier start of heat release and that this effect is dependent on the engine speed. The higher the engine speed, the more pronounced the effect will be. Güralp et al. [11] stated that inlet gas temperature will affect the temperature of core gas in the charge and thus will directly affect the ignition timing. Furthermore, there is a strong correlation between ignition timing and combustion duration when inlet temperatures vary.

Effective Compression Ratio (CR). The effective compression ratio and thus maximum in-cylinder pressure have significant effects on HCCI operation. Hyvönen et al. [6] researched the effect of manufacturing tolerances on the effective compression ratio. They found that the resulting effect on combustion phasing can be up to 10–20 CA. They also stated that if the effect of these differences cannot be removed active cylinder balancing will be required. The effective compression ratio will be affected not only by these mechanical parameters, but other factors such as blow-by losses, heat transfer through cylinder walls. In addition, the effective compression ratio can be affected by volumetric efficiency.

Iida et al. [10] identified that the compression ratio—through the mixture of temperature and pressure at the end of compression stroke—has a bigger effect on the start of heat release than the temperatures of inlet air and coolant. From their experiments it was found that the start of heat release could be advanced to about 15 CAD when the compression ratio was increased by about 4 units. The effect of compression ratio on HCCI operation shows only restricted sensitivity to engine speed. Since increasing the compression ratio increases gas temperature at the end of the compression stroke, the required inlet temperature decreases.

Haraldsson et al. [7] showed the correlation between compression ratio and brake thermal efficiency as well as CO and NO_x emissions. Increasing the CR will cause higher brake thermal efficiency and lower NO_x emissions while CO emissions increase due to faster expansion, thereby shortening reaction time.

In the work presented here apart from the measurement of peak motoring pressure, no further investigation into the effective compression ratio is provided. When the engine was adapted to HCCI operation, all components have been carefully measured and all tolerances were within limits for SI engines. However, from the time when these measurements were taken to the period when the results presented here were taken, the engine was operated for a significant length of time and some changes in geometry are likely to be present. Recent observations of crank case pressure suggest that blow-by losses will be a very important factor, but at the current state of the authors' knowledge it is too early to clarify the blow-by loss effect on the effective CR and combustion phasing.

Coolant Temperature Distribution. Coolant temperature will directly affect heat transfer through cylinder walls and thus it will affect the effective compression ratio. It has been found by Flowers et al. [8] that if the coolant passes longitudinally through the engine, the coolant temperature differs between cylinders, and that differences in heat transfer will change the combustion phasing. A similar observation has been made in the V6 engine studied in this paper where the coolant passes through the engine block and returns through the cylinder head—the cylinder, which has the coldest cylinder wall, will have the hottest cylinder head.

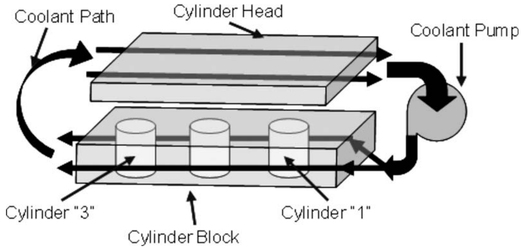

Fig. 1 Engine coolant path sketch

Iida et al. [10] defined the effect of coolant temperature on the range of HCCI operation. The tendency is similar to the effect of inlet temperature. The higher the coolant temperature, the lower the achievable equivalence ratio is. This effect is particularly pronounced at higher engine speeds. Increasing the coolant temperature extends the operating range for higher engine speeds. Coolant path and cylinder placement have effects on the heat transfer.

Persson et al. [12] found that at lower load and speed the changes in the wall temperature for cylinders located at the ends of an engine block are important. This means that cylinders not surrounded by other cylinders will be affected by ambient condition changes, which, in turn, change the wall temperature and therefore the charge temperature. This effect becomes insignificant when the engine speed increases.

The influence of coolant temperature on HCCI operation was widely studied by Milovanovic et al. [13]. Improving the fuel consumption and extending the upper operational range was possible by decreasing the coolant temperature from 90°C to 65°C. This effect was mainly due to the increased heat transfer and a further decrease in-cylinder temperature. Lower in-cylinder temperature increases the air density and air flow through the engine. Hence it increases the power density of the engine. The same mechanism applies in the opposite direction at the lower end of the HCCI range, making it possible to achieve lower load while increasing coolant temperature from 90°C to 125°C. Unfortunately, achieving the lower load implies a fuel consumption penalty.

In the engine studied in this paper, first cylinders (upstream) in the coolant path (therefore having the largest heat transfer and the lowest bulk charge temperature) will define the lower boundary of HCCI, as they are the first to misfire. Cylinders last (downstream) in the coolant path (see Fig. 1) will define the upper HCCI boundary as they operate with the highest rate of pressure rise. This is due to reduced heat transfer and the resulting highest in-cylinder temperature, which, in turn, advances combustion.

EGR Distribution. From the modeling data for the authors' engine it can be observed that the differences in residual distribution between cylinders can be smaller than 1%. On the other hand in order to change the load by about 1 bar of NMEP the amount of trapped residuals has to be changed by about 10%. From this simple relation it can be observed that differences in residual distribution should not cause serious differences in the cylinder-to-cylinder performance. Hyvönen et al. [6] showed the effect of gas dynamics in the inlet and exhaust manifolds on cylinder behavior. The difference in maximum in-cylinder pressure between the case with an inlet manifold present compared with the case when the inlet manifold was dismounted could be up to 0.5 bar. Further-

Downloaded 02 Jun 2010 to 171.66.16.109. Redistribution subject to ASME license or copyright; see http://www.asme.org/terms/Terms_Use.cfm

more, the effects of gas dynamics can cause a difference in air-fuel ratio (lambda)—which will be discussed further in this paper. The effect of gas dynamics becomes important at higher engine speeds (approximately 2000 rpm and above).

Effective Air-to-Fuel Ratio (AFR). This problem will be particularly pronounced on engines, which do not have individual lambda sensors for each cylinder. All physical phenomena, which affect the air density or the amount of air introduced into the cylinder, will have direct impact on lambda variation. These will be inlet air temperature, gas dynamics effects in inlet and exhaust manifolds, blow-by losses, and heat transfer through cylinder walls. In addition, each injector will inject somewhat different amounts of fuel for the same pulse-width signal.

Hyvönen et al. [6] stated, however, that the largest effect on lambda variations is exerted by the gas exchange process. Lambda differences could be approximately about 14% and this, in turn, will cause combustion phasing differences of up to 3–4 CA deg. Differences in the amount of fuel injected into individual cylinders do not have a large effect on combustion phasing. The nominal differences between injectors are approximately 3%, causing differences in combustion phasing of less than 1 CA deg. However, differences between injectors will grow and become a more important issue during a very long HCCI operation.

Combustion Chamber Deposits (CCDs). . Combustion chamber deposits have been a subject of concern for all types of engines. The reasons why they have become important are mainly due to their effect on increasing the NO_x and HC emissions. This is caused by their insulating effect causing increased temperature for NO_x formation and due to the deposits absorbing unburned fuel during combustion and desorbing it during exhaust, which causes increased HC emissions, pointed out by Jonkers et al. [14]. Additionally, CCD can cause physical damage to the engine. CCD can mainly result from lubricant oil, fuel, or from the combustion of both.

A recent study by Cheng [15] showed that for SI engines there is a critical wall temperature: the fuel type of deposits form at 310°C and oil type deposits form at 370°C. Above these temperatures there was little deposit growth. Cheng investigated the impact of operating conditions on CCD formation in GDI-SI engines, such as coolant temperature, spark timing, fuel-air ratio, and manifold pressure. Some effort has been put into avoiding the lubricant contribution to CCD formation in order to focus only on fuel based CCD. From this experiment it can be found that coolant temperature has a significant impact on the deposit formation—the lower coolant temperature, the more pronounced CCD is. The effect of spark (which could be important in spark-assisted HCCI) does not bring about a major increment in the amount of CCD. However, there is a significant influence on CCD distribution inside cylinders—the "spark side" of the combustion chamber has less deposit accumulated while the opposite side has more. The air-to-fuel equivalence ratio also has a large influence on CCD formation. Minimum formation appears at the equivalence ratio of 1.1; changing the equivalence ratio in any direction from that point will cause increased CCD formation. Because the air-fuel ratio in HCCI engines can change more readily, this problem can be relevant.

Finally, Güralp et al. [11] characterized the effect of combustion chamber deposits on the HCCI operation. It has been shown that the burn rate becomes significantly faster when CCD layer increases, hence the conclusion is that HCCI combustion is very sensitive to the presence of CCD. Peak heat release rates increased to about 50% between the start of the test and the end when no further variations in the combustion were observed. The analysis of the nature of the CCD effect on the HCCI operation suggests that burn rate changes more because of CCD than because of ignition phasing. Furthermore, it leads to the conclusion that CCD affects bulk burning near the wall of the combustion chamber, which, in turn, proves that the reduction in heat losses in the case of the insulating characteristic of CCD, is less important than thermal capacity and temperature swings.

As shown in the above paragraph, CCDs can significantly affect the HCCI combustion; therefore their influence on CTCV might be very important. However, measurements of this phenomenon require engine modifications (and are particularly difficult on a multicylinder engine) therefore in the work presented here their influence has not been defined.

Table 1 Research engine specification

Engine type	Jaguar research V6, 24-V, GDI
Engine speed	1500 rpm, 2000 rpm, 2500 rpm
Bore	89 mm
Stroke	79.5 mm
Fuel	Commercial gasoline
Compression ratio	11.3
Intake valve timing	Variable
Exhaust valve timing	Variable
Intake temperature	~335 K
Air/fuel ratio	14.7

3 Experiment Setup

The experimental engine is a Jaguar V6 direct injection (DI), four valves per cylinder, and three l capacity research engine. Basic engine details are shown in Table 1.This engine has been described previously in a number of publications. e.g., Refs. [16,17]. To switch between the SI and HCCI modes of operation, cam profile switching (CPS) is used. This system allows on-line switching of valve lifts from 9 mm (SI operation) to 3 mm (HCCI operation). The variable cam timing system makes it possible to change the cam timing for the inlet and exhaust cams within 60 CA deg range. The HCCI operation is achieved by internal EGR produced by negative valve overlap, which traps exhaust gases in order to deliver enough energy for auto-ignition. Valve timings are defined here by inlet valve opening (IVO) and exhaust valve closing (EVC) points, which are the crank angle measured from TDC at gas exchange denoted as 720 (0) deg. Exhaust valve timing is expressed in degrees CA before TDC, and inlet valve timing in degrees CA after TDC. The fuelling system is DI wall guided. The strategy of fuel injection during negative valve overlap (NVO) has been chosen with the end of injection set to 350 deg before TDC combustion, i.e., 10 deg after TDC recompression (except for split injection experiments).

In order to control the engine an in-house MATLAB/SIMULINK model is employed in connection with a DSPACE system. The system is a fully computer-controlled unit, which enables users to control and record all engine data. Kistler 6125A pressure transducers fitted into the wall of the combustion chambers measure in-cylinder pressures in all six cylinders with 1 CA deg resolution. Other parameters are measured with 100 Hz frequency. The amount of fuel injected is adjusted separately to each engine bank during normal operation (closed-loop lambda controller) or manually into each cylinder during cylinder balancing tests. Emission has been measured with AVL CEB1 emission bench. It is a five gas bench that measures CO, CO_2, NO_x, O_2, and HC concentration. Different analyzers use methods as follows: nondispersive infrared (CO and CO_2), chemiluminescence (NO_x), paramagnetic (O_2), and flame ionization detector (FID) (HC). The HCCI starting procedure involves a warming up period when engine is operated on SI mode for as long as necessary until the oil and coolant temperatures reach 90°C. In HCCI mode the engine is operated with wide open throttle.

The engine is fitted with a thermal management system (Fig. 2). By controlling three throttles it is possible to control the air flow and as a result the air temperature. First throttle adjusts the amount of air going through the heating box while the next two

Downloaded 02 Jun 2010 to 171.66.16.109. Redistribution subject to ASME license or copyright; see http://www.asme.org/terms/Terms_Use.cfm

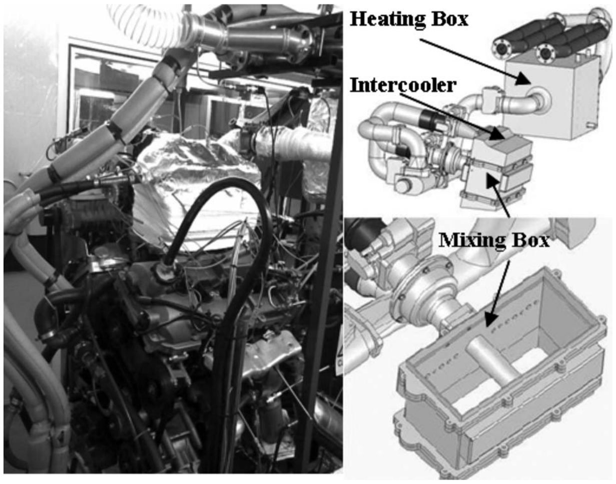

Fig. 2 Research engine with thermal management system

control the flow between intercooler and mixing box. This solution allows controlling the temperature with relatively small time constant.

Parameters such as ambient air temperature and humidity have been kept constant throughout the group of tests. In order to maintain a good quality of results every day, four samples are recorded. These samples are used for measurement validation and engine checks. Base (reference) condition is always repeated at the end of the group of tests to validate data repeatability. All of the data presented in this publication have been collected during steady-state operation and were averaged over 100 cycles.

As a criterion to define the CTCV in this publication, the value of crank angle at which 50% of MFB occurs will be used. However, in general MFB10% and MFB90% will be observed as well. This is needed for a better understanding of the combustion process when set parameters will be adjusted.

4 Characterization of CTCV

As an introduction to the CTCV, engine bank-to-bank variations will be considered. Figure 3 presents the problem of bank-to-bank variation, which has been observed on the research engine. The source of the problem was identified as a blocked three way catalyst, which, in turn, increased the back pressure on engine bank A. The source of blockage was tracked to very high UHC emissions. During initial HCCI tests when lower boundary was unknown misfires were very common. As a result a lot of unburnt fuel has been introduced into the exhaust manifold that led to catalyst blockage. From Fig. 3 it is clear that bank-to-bank load spread was about 0.5 bar NMEP. The load spread was constant for different test conditions. The back pressure on bank A was 0.15 bar higher than on bank B. Additionally, during the measurements, back pressure on bank B had higher pulsations than pressure on bank A. Higher back pressure was, in turn, increasing EGR for bank A, hence its lower load. Test 7 represents the point in time when catalysts on both engine banks were replaced by a new set. Differences in load become insignificant for a wide range of test conditions. Before the catalyst has been replaced, it was still possible to avoid bank-to-bank load differences. Retarding the exhaust valve timing for bank B by about 8 CA deg. resulted in the same effect as the increased back pressure on bank A.

Further discussion will concentrate on the CTCV variations in MFB50%, inlet port temperature, air-to-fuel ratio, in-cylinder pressure, and HC emission for different engine speeds and for fixed valve timing. The IVO was set at 85 CAaTDC gas exchange and EVC was set at 96 CAbTDC gas exchange. The engine was operated with stoichiometric air-to-fuel ratio. There is a clear trend in the combustion phasing, which is independent of engine speed. For both engine banks cylinders "1" are the most prone to misfire when cylinders "3" are least prone. This trend is related to the coolant path. Coolant flows from cylinder "1" through "2" to cylinder "3" and back through the cylinder head, independently for each engine bank (Fig. 1).

From experience cylinder A1 is the first to misfire and cylinders A2 and B1 are the next which will loose the combustion. A quick look at Fig. 4 shows that for cylinder A1 MFB50% always occurs as the latest when cylinders A2 and B1 are both next to misfire. Finding the explanation for the trend of the timing of MFB50% cannot be done straightforwardly. The inlet air temperature, compression pressure, and AFR will interact together resulting in an introduced MFB50% trend.

Figure 4 shows that at 2000 rpm bank A cylinders experience the biggest difference in combustion phasing. A closer look at the results shows that at this engine speed air flow through the engine is largest—21 g/s compared with 20 g/s and 19 g/s at 1500 rpm and 2500 rpm, respectively. This determines the load, which varies from 4.4 at 1500 rpm to 4.6 at 2000 rpm and 4.2 bar at 2500 rpm. With respect to maximum in-cylinder pressures it is possible to find that increasing the speed from 1500 rpm to 2000 rpm advances the timing of peak pressure. But different behavior for both banks can be observed with regard to the magnitude of maximum pressure. For bank B increasing the speed causes an increase in maximum pressure. In bank A for cylinders 1 and 2 the magnitude maximum pressure decreases by about 1–2 bars. It is ex-

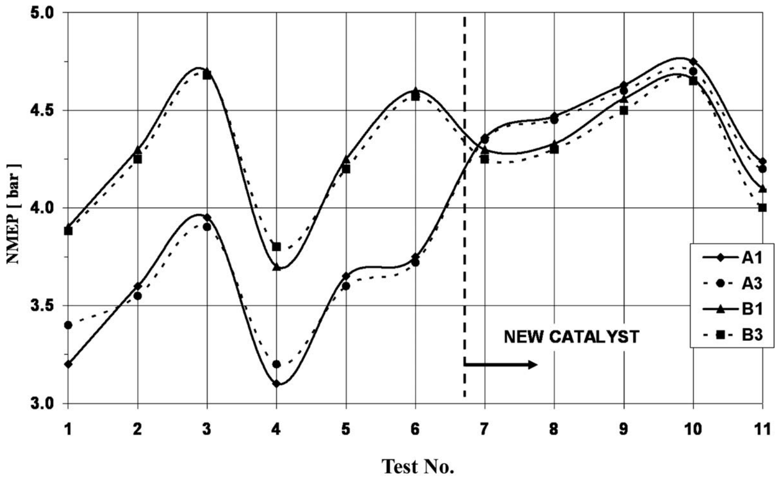

Fig. 3 Engine banks load spread caused by blocked three way catalyst

Downloaded 02 Jun 2010 to 171.66.16.109. Redistribution subject to ASME license or copyright; see http://www.asme.org/terms/Terms_Use.cfm

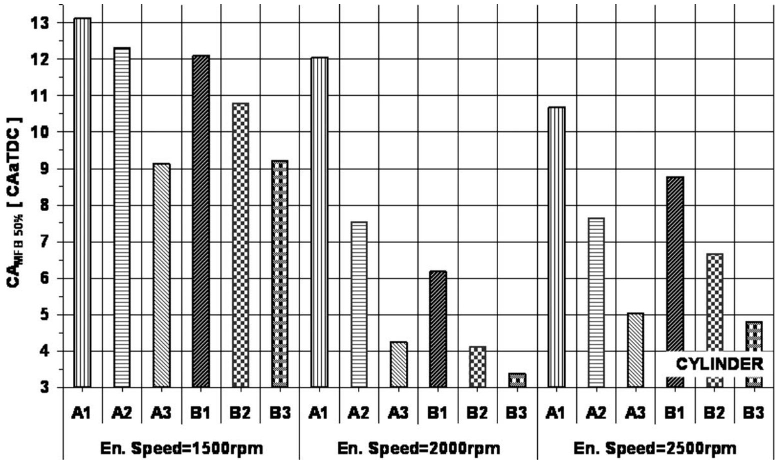

Fig. 4 $CA_{MFB50\%}$ variation in the V6 test engine

pected that the observed phenomena is due to higher heat exchange for those cylinders or to increased blow-by losses caused by increased maximum pressure.

Figure 5 presents air temperature in the inlet ports. Cylinders A2 and B2 have the highest air temperature, which is a result of two factors. First, these cylinders are in the middle of the engine and the heat losses to the environment are the lowest. Second factor is due to the arrangement of the thermal management system. The pipe supplying hot air is passing on the top of those two cylinders increasing their temperature, as seen in Fig. 2. On the other hand cylinder A1 has always the lowest temperature, which goes together with very late combustion. Unfortunately, the general temperature trend is not necessarily in tune with combustion phasing, e.g., cylinders A3 and B3 in which combustion appears early have usually one of the lowest inlet temperatures.

Interesting observations can be made when in-cylinder pressure is considered for a motored engine. As has been plotted in Fig. 6 the higher the engine speed, the more visible the trend for bank A is. Here it can be observed that the peak motoring pressure has the reversed trend compared with combustion phasing. This means that cylinder A1 with the latest combustion has the lowest peak in-cylinder pressure. The differences between cylinders increase with increasing engine speed. The trend is not the same for bank B of the engine. For this bank the maximum difference in pressure does not exceed 0.3 bar; while in bank A it reaches 1 bar. As has been pointed out in the discussion of CTCV critical parameters, the difference of 0.3 bar is not significant.

Air-to-fuel ratio distribution plotted in Fig. 7 shows that, in general, all cylinders tend to run on higher lambda than the set value (lambda set to 1.0 during the presented tests). The disagreement in lambda value between cylinders could be up to 0.07 (resulting in the spread of air-to-fuel ratio values of about 1.2). There is no clear trend between combustion phasing and lambda value for individual cylinders, but it has to be taken into account that it is due to two factors. First, the differences presented above are too small to be fully evident. Second, the method used to measure AFR affects readings as well. There are natural pulsations in injected fuel quantity, which are the result of short time fluctuation in the closed-loop lambda controller. This fluctuation extends the time required to switch the analyzer between all six cylinders since measurement has to be long enough for averaging. This long time of measurements leads only to qualitative valuation.

The NO_x CTCV can be summarized into two groups. For the low load operation the difference between cylinders is very small and does not increase beyond a single part per million (ppm). Increasing load will increase NO_x emission difference. This is due to very low emissions at low loads, which, in turn, lead to very small differences. An interesting effect has been observed for UHC emissions. As presented in Fig. 8, the HC emissions are significantly higher at low speed for cylinders A3 and B3. As has been shown earlier those two cylinders have the earliest combus-

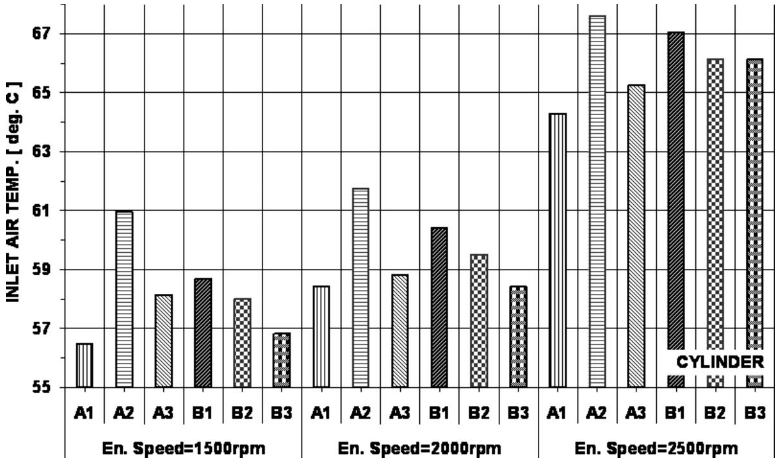

Fig. 5 Inlet port air temperature distribution in the V6 test engine

Downloaded 02 Jun 2010 to 171.66.16.109. Redistribution subject to ASME license or copyright; see http://www.asme.org/terms/Terms_Use.cfm

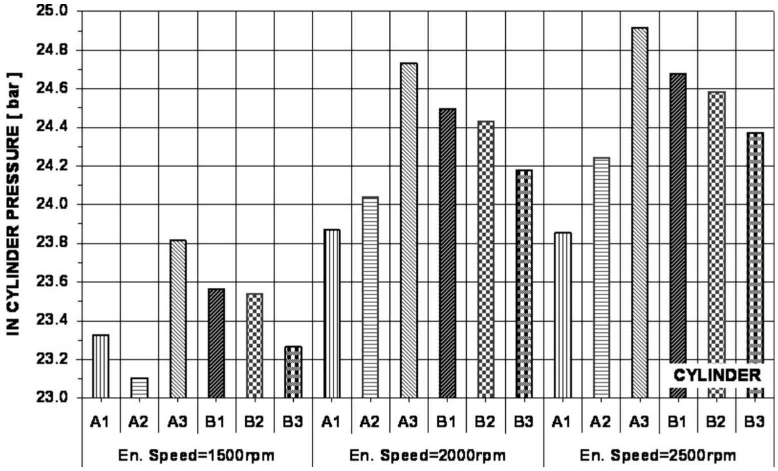

Fig. 6 Peak in-cylinder pressure distribution in motoring mode

tion phasing at all speeds. At higher engine speeds there is a trend that HC emissions from those two cylinders decrease compared with other cylinders.

In general, CTCV on bank A seems to be sensitive to compression pressure. Cylinder A3, which has always the highest compression pressure, has the shortest combustion delay as well. There is an influence of in-cylinder mixture composition. Cylinder A3 operates most of the time with air-to-fuel ratio very close to stoichiometric. Cylinders A1 and A2 quite often will have similar compression pressure. Cylinder A2 has usually higher inlet air temperature but operates with leaner mixture. This suggests that following the importance of compression pressure, inlet air temperature and AFR also become important.

CTCV on bank B presents a more complex problem. As has

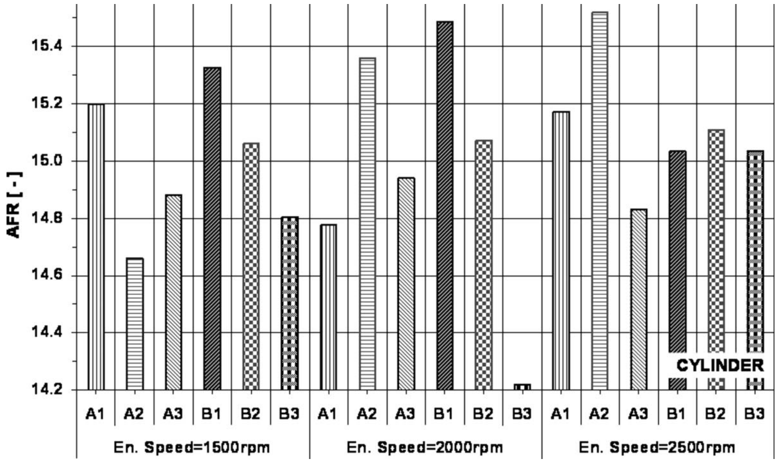

Fig. 7 AFR cylinder-to-cylinder variations for the V6 test engine

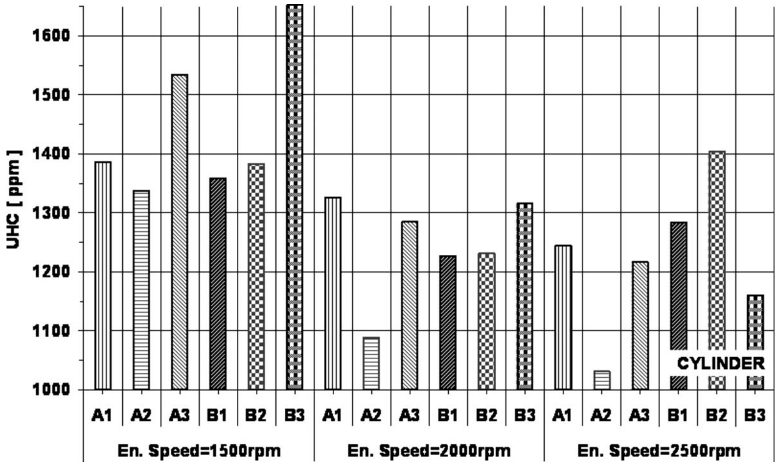

Fig. 8 Unburned hydrocarbons CTCV for the V6 test engine

Downloaded 02 Jun 2010 to 171.66.16.109. Redistribution subject to ASME license or copyright; see http://www.asme.org/terms/Terms_Use.cfm

Table 2 Effect of changes in fuel injector pulse width on individual cylinder performance

Pulse width PW-B (μs)	PW-B3 adjustment (μs)	Effective PW-B3 (μs)	NMEP (bar)			dP/dCA (bar/CA deg)		
			B1	B2	B3	B1	B2	B3
873	0	873	4.64	4.99	4.61	1.4	1.92	2.04
928	150	778	4.72	5.02	4.45	1.32	1.71	1.91
932	200	732	4.72	5.03	4.42	1.31	1.7	1.78
961	250	711	4.73	5.03	4.29	1.32	1.54	1.49

Engine speed=1500 rpm, IVO=80CAaTDC, and EVC=96CAbTDC

been mentioned earlier, differences in compression pressure between cylinders are below 0.3 bar, which make them insignificant. Thereafter other parameters will take primary role. The differences in inlet air temperature do not exceed 2°C, which, in turn, makes AFR and heat losses the main factors responsible for CTCV. As has been observed during the presented tests cylinder B3 is always operating with AFR close to stoichiometric or slightly below (richer). Cylinder B1 operates with the lowest AFR on the engine bank B. In addition, as mentioned earlier, cylinder B3 is the last in the coolant path, which makes heat losses the lowest.

The worst performing cylinder from all six is cylinder A1; combustion phasing is the worst there and this cylinder has the following as well: the lowest inlet and exhaust temperature, the lowest peak in-cylinder pressure during combustion and in motoring mode, the rate of pressure rise is the lowest (which will be an advantage at high load), and this cylinder is the first in the coolant path. Cylinder A1 seems to be the worst in all parameters; this is why it is the first to misfire, and this cylinder defines the lower boundary of HCCI for the whole engine. As has been observed during tests, misfire could occur as the first one on cylinder A2 and B1 as well. However, trends between all parameters affecting auto-ignition are not as clear for these two cylinders as for the cylinder A1. This is why describing the influence of all of the parameters on general behavior of a cylinder in HCCI require a look into each specific case.

The above discussion does not explain all the doubts, which can arise after data analysis. Some aspects of CTCV have to be investigated further with the support of more advanced measurements and modeling. This will involve a closer look into mixture preparation processes, internal fuel reforming effects (especially with regard to the effect of temperature, pressure and fuel amount), the amount of trapped residuals, and geometric details of the cylinder.

5 CTCV Compensation

It has been widely discussed that multicylinder engines will require active cylinder balancing to counteract natural variations between cylinders. During the presented work three methods have been tested: adjusting the amount of fuel injected into each cylinder by changing the pulse width (PW), utilizing split injections, and addition of spark.

Balancing CTCV by Fuel Quantity. In order to be able to adjust the fuel quantity the closed-loop lambda controller was modified. A control block, which allows manual decrease in the pulse width, was implemented in order to modify the pulse-width calculated by the closed-loop lambda controller. By this method the fuel quantity for all individual cylinders may be modified. This leads to the fact that if there is no additional manual adjustment, the default amount of fuel injected into each cylinder will be that calculated by closed-loop lambda controller. The results for the case with valve timing, which supports relatively low rate of pressure rise (low load) are presented in Table 2. Cylinder B3 has been adjusted in order to decrease the engine noise and to balance the cylinder-to-cylinder variations. When changes in pulse width are below 150 μs (roughly below 15% of the nominal pulse width), there are no significant differences in-cylinder performance. If the changes increase above 15%, the changing pulse width for one cylinder immediately affects the other cylinders within the engine bank.

Analysis of the data presented in Table 2 reveals that decreasing the amount of fuel injected into one cylinder affects the equilibrium set by the closed-loop controller. The controller immediately will adjust the fuel quantity to achieve the new operational point. Since the amount of fuel for cylinder B3 has been reduced, the calculated overall pulse width will increase. However, the effective pulse width (including the effect of change from the controller) for cylinder B3 decreased from 873 μs to 711 μs when the manual adjust reached minus 250 μs. Reduction in the fuel quantity increased the value of lambda, which, in turn, decreased the load and the rate of pressure rise (see cylinder B3 in Table 2). As the result of cylinder B3 adjustment, cylinders B1 and B2 will now operate with lower lambda (below stoichiometric). This leads to retarded combustion and, as has been observed during other tests, increased UHC emissions and reduction in NO_x emissions. NO_x emissions are due to the decrease in in-cylinder temperature (mainly due to increased cooling by the injected fuel) and to the decreased amount of available oxygen for cylinders with air-to-fuel ratio lower than stoichiometric. Reduction in available oxygen leads to higher UHC emissions due to incomplete combustion. Load increases for cylinder B1 suggest its operation with slightly higher lambda (larger amount of fuel injected).

Unfortunately, as has been presented in Fig. 9, the reduction in fuel quantity does not yield expected results. Even more, cylinder B1 (and B2, not shown) shows better response in combustion phasing than the adjusted cylinder B3. This leads to increased CTCV and worse engine operation (e.g., increased unnecessary and unwanted engine noise). The adjusted cylinder B3 did not change its combustion phasing at all when other cylinders retarded their combustion phasing by approximately 3 CA deg. These differences tend to increase with increasing engine load.

All the facts mentioned above suggest that one of the best ways to balance CTCV by adjusting the fuel quantity is to use individual lambda sensors for each cylinder. Some other methods such as map of pulse-width coefficients for individual cylinders might be used as well. In the early stage of the authors' work, an attempt was made to implement a previously optimized function, which will adjust the amount of fuel individually for each cylinder (within engine bank) based on one lambda sensor. Unfortunately when engine was operated for a longer time on one set condition, this resulted in unstable fuelling and this approach was not effective. However with a fully optimized engine, it might be possible to use a predefined map of coefficients.

Balancing CTCV by Split Fuel Injection. The aim of the second group of tests was to establish the applicability split injection for active cylinder balancing. Two sets of tests were carried out, of which one will be discussed here. The tests presented have been performed for the same valve timing as that discussed earlier for the discussion of fuel quantity (IVO=80CAaTDC, EVC

Downloaded 02 Jun 2010 to 171.66.16.109. Redistribution subject to ASME license or copyright; see http://www.asme.org/terms/Terms_Use.cfm

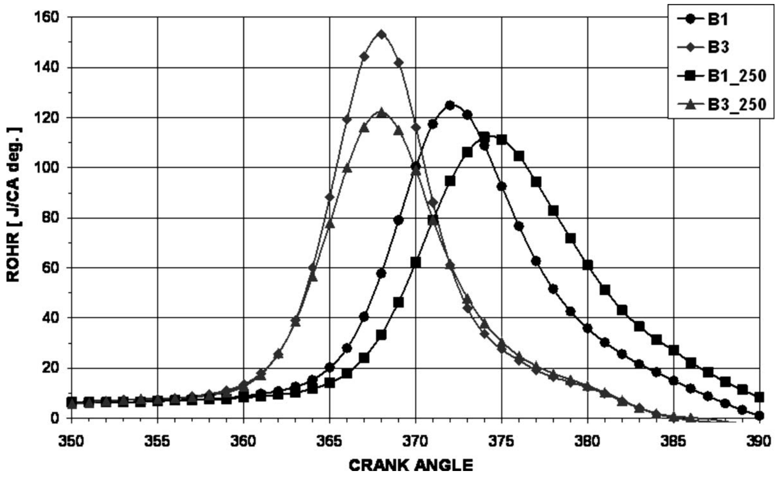

Fig. 9 Rate of heat release for fuel quantity adjustments

=96CAbTDC) and for the same engine speed (1500 rpm). However, these tests have been performed with few days time separation hence small difference in load will be present (due to differences in ambient temperature and humidity). Fuel for all cylinders has been injected at 350 CAbTDC combustion. Only the adjusted cylinder (A3) will have split fuel injection at 220 CAbTDC combustion. Tests have been carried out with stoichiometric air-to-fuel ratio. Adjustment has been carried out to an extent necessary to achieve a satisfactory MFB50% improvement.

The test described as C1 is a base (reference) test where all fuel has been injected at 350 CAbTDC. Test marked as C2 represents a point where only cylinder A3 has been adjusted and 30% of fuel has been injected during the induction part of the cycle with the end of injection at 220 CAbTDC. During test C2 the main effort was to change combustion phasing for cylinder A3, which as can be seen in Fig. 10 shows much earlier combustion than the other cylinders. It was noticed as well that load for this cylinder is lower and the rate of pressure rise is higher than for other cylinders. The results are presented in Table 3. In order to increase the load and reduce the rate of pressure rise, it has been decided to inject the fuel during the induction part of the cycle close to IV MOP. This is done to reduce the effect of internal fuel reforming for cylinder A3. The amount of fuel injected at IV MOP has been adjusted until the MFB50% did reach value similar, as for cylinders A1 and A2.

The results for test C2 in Table 3 show that when split injection adjustment has been done, load and rate of pressure rise become the same for all cylinders within the engine bank. Figures 10 and 11 present the rate of heat release and the MFB before split injection adjustments (test _C1) and when 30% of fuel for cylinder A3

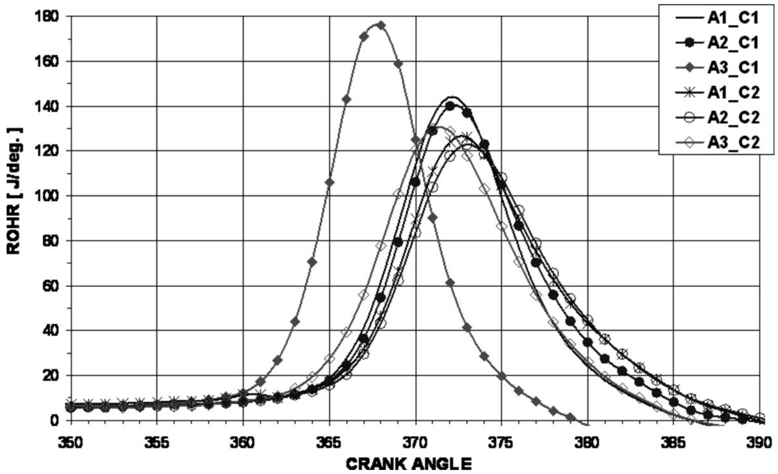

Fig. 10 Rate of heat release for engine bank A when split injection was applied

Table 3 Effect of split injection on individual cylinder performance

	Parameters							
	NMEP (bar)			dP/dCA (bar/CA deg)			HC (ppm)	NO_x (ppm)
Cylinder	A1	A2	A3	A1	A2	A3	-	-
No split injection (C1)	4.41	4.53	4.25	1.55	1.54	2.45	1648	33
A3—30% of fuel injected at 220 CAbTDCc (C2)	4.45	4.53	4.49	1.54	1.41	1.71	1609	33

Downloaded 02 Jun 2010 to 171.66.16.109. Redistribution subject to ASME license or copyright; see http://www.asme.org/terms/Terms_Use.cfm

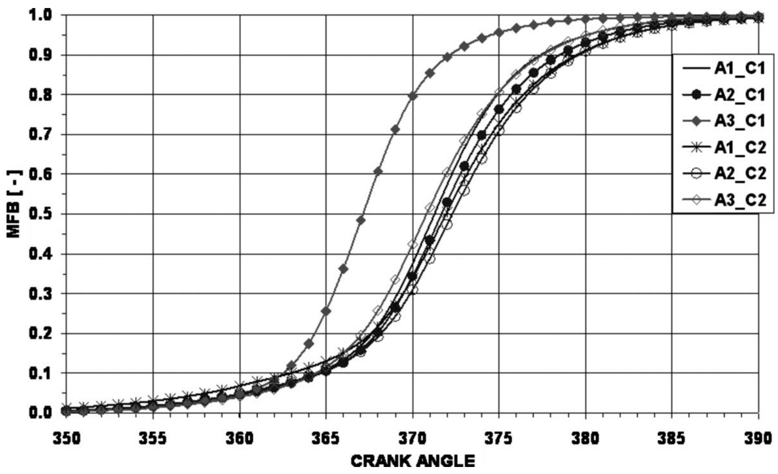

Fig. 11 MFB for bank A of the engine when split injection was applied

has been injected during induction part of the cycle (test _C2). It is clear that when split injection strategy has been implemented the cylinder-to-cylinder variations have been significantly decreased. Variations in MFB50% have been decreased below 2 CA. There is no visible difference in the emissions of UHC and NO_x.

Balancing CTCV by Spark Assistance. The last set of tests was to apply the spark-assisted HCCI for cylinder balancing. Many researchers have proven that spark-assisted HCCI has a wider operating envelope at the lower load end where the spark helps to maintain stable HCCI. Experiments have been performed for two engine speeds, 1500 rpm and 2500 rpm. Exhaust valve timing was set at 96 CAbTDC for both engine speeds. Inlet valve timing was set at 70 CAaTDC for 1500 rpm and in order to avoid misfires was retarded to 78 CAaTDC for 2500 rpm. As has been observed during tests, changing the spark phasing across a wide range does not cause major changes in the NMEP. In general, total changes of NMEP were between the 0.1 bar limit. Figure 12 shows increase in peak pressure when the spark is advanced. However, advanced combustion phasing increase in-cylinder pressure before TDC therefore increases compression work losses. A quick look at Fig. 13 will show that retarding the spark from 50 CAbTDC to 10 CAbTDC can decrease the rate of pressure rise by 0.5 bar/deg.

As shown in Figs. 14 and 15, the spark does not cause major changes in the rate of heat release but advance combustion phasing. From data analysis it can be observed that CTCV in the rate of heat release will reach 50 J/CA deg. The change in the rate of heat release (ROHR) caused by spark phasing is insignificant and does not exceed the maximum of 20 J/CA deg. Spark phasing is demonstrating its potential in the case of adjusting the combustion phasing.

Figure 16 shows MFB10%, MFB50%, and MFB90% for cylinder B1 and it is clear that from the situation when spark is considered as OFF (100 CAaTDC) to the spark timing of 50 CAbTDC the effect on combustion phasing is about 5 CA deg advance. In the presented tests spark was applied to all cylinders. However, applying spark only to selected cylinders does not change the observed trend, and the spark can be used as a powerful tool for combustion phasing control. Spark-assisted mode of HCCI can be divided into two regimes in terms of emissions. When the spark is advanced from TDC up to 20 CAbTDC, there is no visible change in either UHC or NO_x emissions. Further spark advance will lead to a progressive reduction in UHC emissions and an increase in NO_x emissions. The NO_x increased by approximately 14% from 59 ppm compared with the reference sample. Reduction in UHC emission is approximately 10% from 1322 ppm for the reference sample. Unfortunately, benefits resulting from the addition of spark assistance cannot be sustained for higher engine speed.

Figure 17 presents reduction in CTCV achieved by the spark-assisted HCCI. Differences in MFB50% have been reduced from 3.5 CA deg to below 1 CA deg when spark was applied at 40

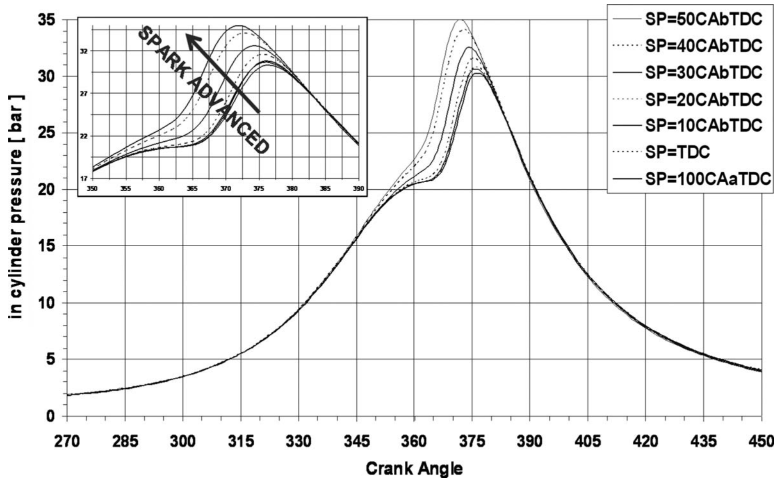

Fig. 12 Cylinder B1 pressure with spark addition at 1500 rpm

Downloaded 02 Jun 2010 to 171.66.16.109. Redistribution subject to ASME license or copyright; see http://www.asme.org/terms/Terms_Use.cfm

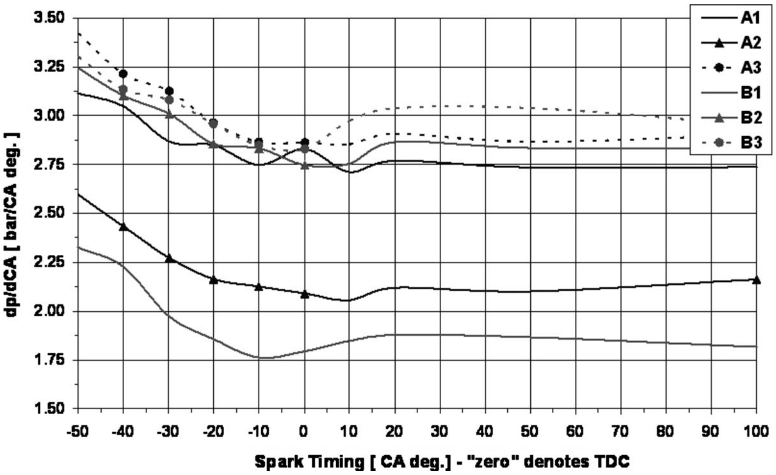

Fig. 13 Rate of pressure rise with spark addition at 1500 rpm

CAbTDCc for cylinder B1. However, the timings of MFB10% and MFB90% maintain the same differences compared with the base case. However after adjustment they are advanced instead of being retarded. This means that in reverse to the split injection adjustment, the assistance of spark addition generally promotes combustion. Since combustion phasing was advanced, there is an increase in rate of pressure rise by about 0.5 bar/CA deg. The load change is insignificant (0.08 bar increase in NMEP). As has been mentioned above, the UHC emissions have been reduced by 50 ppm while NO_x emissions increased by approximately 5 ppm.

Figure 18 presents the rate of heat release for cylinder B1 at

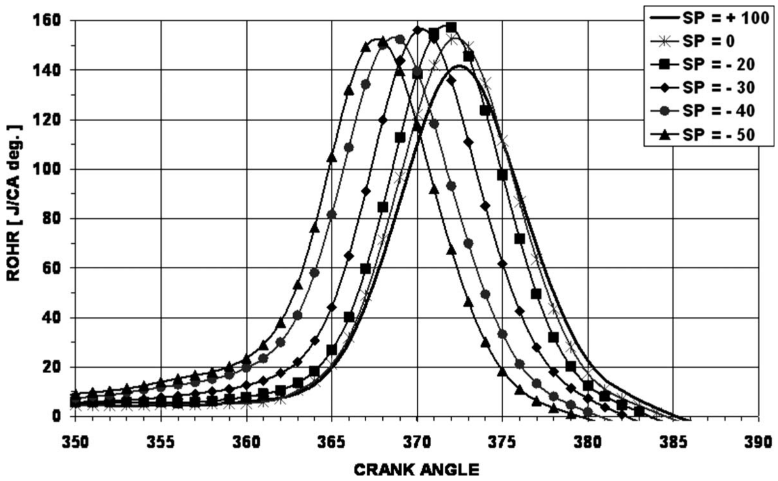

Fig. 14 Rate of heat release for cylinder B1 with spark addition at 1500 rpm

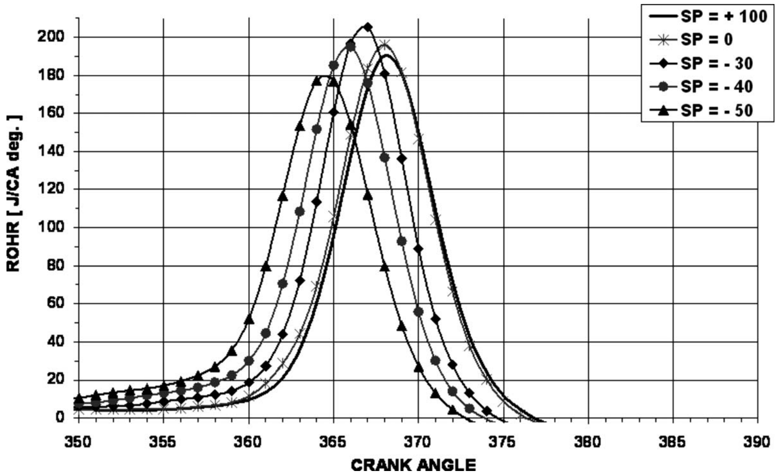

Fig. 15 Rate of heat release for cylinder B3 with spark addition at 1500 rpm

Downloaded 02 Jun 2010 to 171.66.16.109. Redistribution subject to ASME license or copyright; see http://www.asme.org/terms/Terms_Use.cfm

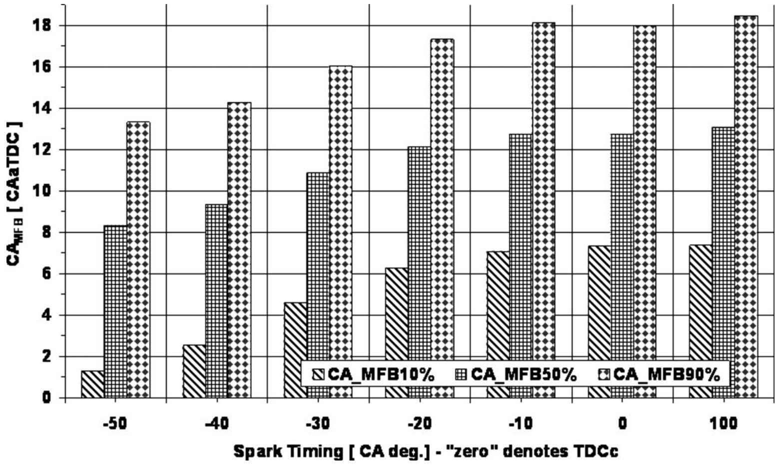

Fig. 16 MFB50% for cylinder B1 with spark addition at 1500 rpm

2500 rpm. Changing the spark phasing within wide range from 60 CAbTDC to TDC does not bring any changes in combustion phasing or rate of heat release. At this point it is worth explaining the nature of spark-assisted HCCI. When spark is applied there is a flame propagation, which generates additional energy for auto-ignition. The presence of EGR in HCCI engine will slow down the flame speed and extend the time during which sufficient energy is generated [18]. This will lead to two conclusions. First, spark-assisted HCCI is only important when engine is running at the low load boundary, and second at higher engine speeds the flame speed reduction resulting from high presence of EGR might lead to insufficient energy release. It is thought that the condition at which engine has run with the speed of 2500 rpm is an example of calling for the second conclusion described above. The impact

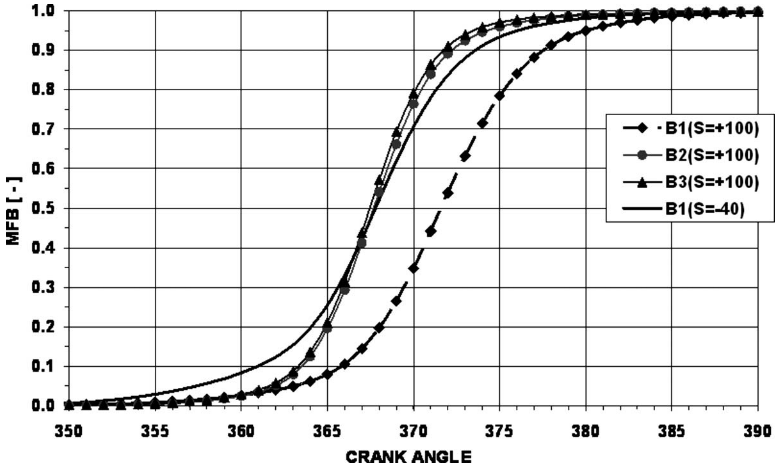

Fig. 17 Effect of spark adjustments on combustion phasing in-cylinder B1

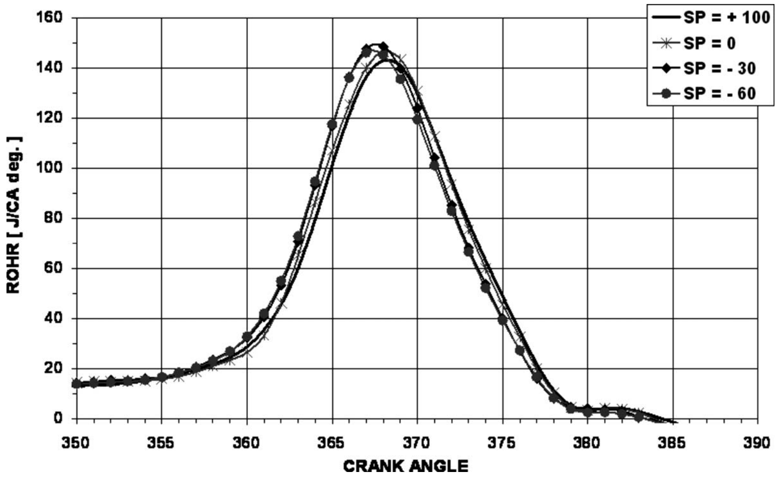

Fig. 18 Rate of heat release for cylinder B1 for spark addition on 2500 rpm

Downloaded 02 Jun 2010 to 171.66.16.109. Redistribution subject to ASME license or copyright; see http://www.asme.org/terms/Terms_Use.cfm

of EGR on the spark-assisted HCCI has not yet been properly defined. It is going to be the subject of future studies on the presented research engine.

All the tests presented have been recorded during steady-state operation. However, for most of its lifetime an engine is in transition between a series of steady-state conditions. For HCCI combustion one of the most challenging transient processes is the switching between SI and HCCI mode. This problem involves the effect of many other parameters, which have not been discussed and are beyond the scope of this publication. Detailed investigations on the transient operation of this HCCI engine are being carried out in the authors' laboratory and the results will be reported in separate publications.

6 Conclusions

In this paper, cylinder-to-cylinder variations in HCCI engines in terms of NMEP have been presented and discussed. It has been found that the cylinder, which is the most prone to misfire, will have the lowest inlet and exhaust temperature, the lowest in-cylinder pressure during combustion and motoring, and in addition, will be the first in the coolant path.

In order to balance the NMEP variations three methods have been implemented and investigated: fuel quantity adjustment, split injection correction, and spark-assisted HCCI combustion.

- Balancing CTCV by the adjustment of fuel quantity supplied to individual cylinders will be the most effective way, if individual lambda sensors for each cylinder can be installed. The use of one lambda sensor for each engine bank and a predefined table of coefficients is also considered as an alternative.
- Balancing CTCV using split injection allows reducing CTCV to a minimum.
- When split injection is in use there are no significant changes in emissions.
- The variety of possible settings for split injection makes it a time-consuming task to identify the best strategy for CTCV balancing.
- Spark-assistance is a very useful tool for the reduction of CTCV in HCCI engines for operating conditions close to low load boundary and at lower engine speeds.
- Utilizing spark will lead to a reduction in UHC but some increase in NO_x emissions.

Acknowledgment

The authors wish to show their great appreciation to Jaguar Cars Ltd. for their financial support and to the technical staff at the university for their valuable assistance in the laboratory.

References

[1] Chen, Z., and Mitsuru, K., 2003, "How to Put the HCCI Engine to Practical Use: Control the Ignition Timing by Compression Ratio and Increase the Power Output by Supercharge," SAE Paper No. 2003-01-1832.
[2] Helmantel, A., Gustavsson, J., and Denbratt', I., 2005, "Operation of a DI Diesel Engine With Variable Effective Compression Ratio in HCCI and Conventional Diesel Mode," SAE Paper No. 2005-01-0177.
[3] Mendiratta, R., and Singh, D., 2004, "Effect of Base Oil and Additives on Combustion Chamber and Intake Valve Deposits Formation in IC Engine," SAE Paper No. 2004-28-0089.
[4] Wang, Z., Wang, J., Shuai, S., and Ma, Q., 2005, "Effect of Spark Ignition and Stratified Charge on Gasoline HCCI Combustion With Direct Injection," SAE Paper No. 2005-01-0137.
[5] Wagner, R., Edwards, K. D., Daw, C. S., Green, J., and Bunting, B., 2006, "On the Nature of Cyclic Dispersion in Spark Assisted HCCI Combustion," SAE Paper No. 2006-01-0418.
[6] Hyvönen, J., Haraldsson, G., and Johansson, B., 2004, "Balancing Cylinder to Cylinder Variations in a Multi Cylinder VCR-HCCI Engine," SAE Paper No. 2004-01-1897.
[7] Haraldsson, G., Tunestål, P., Johansson, B., and Hyvönen, J., 2002, "HCCI Combustion Phasing in a Multi Cylinder Engine Using Variable Compression Ratio," SAE Paper No. 2002-01-2858.
[8] Flowers, D., Aceves, S., Martinez-Frias, J., Smith, J., Au, M., Girard, J., and Dibble, R., 2001, "Operation of a Four Cylinder 1.9l Propane-Fueled Homogeneous Charge Compression Ignition Engine Basic Operating Characteristics and Cylinder to Cylinder Effects," SAE Paper No. 2001-01-1895.
[9] Andreae, M. M., Cheng, W. K., Kenney, T., Yang, J., 2007, "Effect of Air Temperature and Humidity on Gasoline HCCI Operating in the Negative-Valve-Overlap Mode," SAE Paper No. 2007-01-0221.
[10] Iida, M., Aroonsrisopon, T., Hayashi, M., Foster, D., and Martin, J., 2001, "The Effect of Intake Air Temperature, Compression Ratio and Coolant Temperature on the Start of Heat Release in an HCCI (Homogeneous Charge Compression Ignition) Engine," SAE Paper No. 2001-01-1880/4278.
[11] Güralp, O., Hoffman, M., Assanis, D., Filipi, Z., Kuo, T., Najt, P., and Rask, R., 2006, "Characterizing the Effect of Combustion Chamber Deposits on a Gasoline HCCI Engine," SAE Paper No. 2006-01-3277.
[12] Persson, H., Pfeiffer, R., Hultqvist, A., Johansson, B., and Ström, H., 2005, "Cylinder to Cylinder and Cycle to Cycle Variations at HCCI Operation With Trapped Residuals," SAE Paper No. 2005-01-0130.
[13] Milovanovic, N., Blundell, D., Pearson, R., Turner, J., and Chen, R., 2005, "Enlarging The Operational Range Of A Gasoline HCCI Engine By Controlling The Coolant Temperature," SAE Paper No. 2005-01-0157.
[14] Jonkers, R., Bardon, M., and Gardiner, D., 2002, "Techniques for Predicting Combustion Chamber Deposits in a Direct Injection Diesel Engine," SAE Paper No. 2002-01-2673.
[15] Cheng, S., 2000, "The Impact of Engine Operating Conditions and Fuel Compositions on the Formation of Combustion Chamber Deposits," SAE Paper No. 2000-01-2025.
[16] Gharahbaghi, S., Wilson, T., Xu, H., Cryan, S., Richardson, S., Wyszynski, M. L., and Misztal, J., 2006, "Modelling and Experimental Investigations of Supercharged HCCI Engines," SAE Paper No. 2006-01-0634.
[17] Ashur, M., Misztal, J., Wyszynski, M. L., Tsolakis, A., Xu, H. M., Qiao, J., and Golunski, S., 2007, "On Board Exhaust Gas Reforming of Gasoline Using Integrated Reformer & TWC," SAE Paper No. 2007-24-0078.
[18] Persson, H., Hulqvist, A., Johansson, B., and Remon, A., 2007, "Investigation of the Early Flame Development in Spark Assisted HCCI Combustion Using High Speed Chemiluminescence Imaging," SAE Paper No. 2007-01-0212.

Downloaded 02 Jun 2010 to 171.66.16.109. Redistribution subject to ASME license or copyright; see http://www.asme.org/terms/Terms_Use.cfm

Peter L. Perez

Andre L. Boehman[1]
Professor of Fuel Science and Materials Science
and Engineering
e-mail: boehman@ems.psu.edu

Pennsylvania State University,
411 Academic Activities Building,
University Park, PA 16802-2308

Experimental Study of Oxygen-Enriched Diesel Combustion Using Simulated Exhaust Gas Recirculation

The techniques of design of experiments were applied to study the best operational conditions for oxygen-enriched combustion in a single-cylinder direct-injection diesel engine in order to reduce particulate matter (PM) emissions, with minimal deterioration in nitrogen oxide (NO_x) emissions, by controlling fuel injection timing, carbon dioxide (CO_2) and O_2 volume fractions in intake air. The results showed that CO_2 addition reduced average combustion temperatures and minimized the rate of increase in NO_x emissions observed during oxygen-enriched conditions. It was also observed that oxygen enrichment minimized the deterioration in brake-specific fuel consumption and hydrocarbon and PM emissions that occurred at the highest level of CO_2 addition.
[DOI: 10.1115/1.3077647]

Keywords: oxygen enrichment, exhaust gas recirculation, design of experiments, brake-specific fuel consumption, HC, CO, NO_x, and PM emissions

1 Introduction

The use of oxygen-enriched air to improve the combustion process in internal combustion engines has been recognized for a long time. The study by Karim and Ward [1] showed that a higher oxygen concentration in the intake air resulted in reduced smoke emissions, higher peak cylinder pressures, and reduced ignition delay. Improvements in power output were observed when the increase in oxygen concentration was accompanied by an increase in the fueling rate and retardation of fuel injection [1]. Higher rates of heat release for higher oxygen concentrations were also observed, with a significant reduction in the heat release due to premixed combustion [1]. The effects of oxygen enrichment on other regulated pollutants and brake-specific fuel consumption (BSFC) were not addressed in this initial study.

Wartinbee [2] reported significant increases in NO emissions, significant reductions in hydrocarbon (HC) and no effects on carbon monoxide (CO) emissions when using oxygen-enriched air (up to 39.5 vol % O_2) in a spark-ignition engine. The benefits of oxygen enrichment for the control of HC emissions were recognized, but it was suggested that the increase in NO emissions would require the use of exhaust gas recirculation (EGR), which might offset the benefits on HC emissions [2]. Similar results on emissions have been reported for diesel engines, with significant reductions in HC, CO, and smoke emissions, increases in nitrogen oxide (NO_x) emissions, and shortening of ignition delays [3–7]. In some cases, slight improvements in brake-specific fuel consumption and thermal efficiency have been observed by manipulation of fuel injection timing (FIT) [4–6].

Since HC and CO emissions are not a concern for diesel engines, most of the applications of oxygen enrichment to diesel engines have focused on the reduction in smoke and soot (particulate matter (PM)) emissions, and the benefits of burning low-quality fuels [8,9]. Desai et al. [8] observed that the increase in NO_x emissions could be controlled by optimization of the oxygen concentration and fuel injection timing. The works of Sekar et al. [10,11] addressed the optimization process using analytical models and incorporating techniques of quality control, such as the use of Taguchi designs. Virk et al. [12] achieved reductions of 20–30% in smoke and particulate emissions with no increase in NO_x emissions and no degradation in engine performance by increasing oxygen concentration to 22.5% and retarding fuel injection timing. They recognized the importance of optimization of fuel injection timing and other operating conditions to control the increase in NO_x emissions, but the interaction among those factors were not addressed. Donahue and Foster [13] also reported that most of the reduction benefits on PM emissions were observed when increasing the oxygen concentration in air from 21% to 22%, while for 23% O_2 the increase in NO_x emissions outweighed the benefits of PM reductions.

Oxygen enrichment has also been achieved via fuel oxygenation, in an attempt to realize the reductions in PM emissions in diesel engines without the adverse impact in NO_x emissions. Previous works by Boehman and co-workers [14–18] have demonstrated PM reductions with different kinds of oxygenated fuels. Song et al. [16] observed slight increases in NO_x emissions at high loads, and suggested that simultaneous reductions in both NO_x and PM were possible by combining high EGR ratios with the appropriate oxygen addition. By comparing both methods of oxygen enrichment (oxygenated fuel versus oxygen-enriched air), it was concluded that fuel oxygenation with glycol ethers resulted in similar PM reductions to the obtained with oxygen-enriched air (23% O_2), but the increase in NO_x emissions was lower for the oxygenated fuel [17]. Other oxygenated fuels, such as diethylene glycol diethyl ether (DGE) [19] and diethyl ether (DEE) [20], have been successfully used for the simultaneous reduction in PM and NO_x emissions, in combination with charge dilution and manipulation of fuel injection [19] or with exhaust gas recirculation [20].

Despite of the extensive work on oxygen-enriched combustion published in scientific literature, there is still interest in this topic [21–28]. This might be due to the recent developments in the technologies for air separation and NO_x control [25,26], the technical barriers for the introduction of oxygenated fuels, such as engine operational costs and fuel distribution infrastructure [29], and the inconclusive information regarding the interaction of the

---

[1] Corresponding author.

Manuscript received January 15, 2008; final manuscript received December 23, 2008; published online April 9, 2009. Review conducted by Margaret Wooldridge.

Copyright © 2009 by ASME

Downloaded 02 Jun 2010 to 171.66.16.109. Redistribution subject to ASME license or copyright; see http://www.asme.org/terms/Terms_Use.cfm

Table 1 Specifications of test engine

Parameters		Unit	L70EE-DE
Type		-	Single-cylinder, 4 cycle diesel
Cooling system		-	Forced air cooling by flywheel fan
Combustion system		-	Direct injection
Starting system		-	Starting motor with recoil starter
Bore × stroke		mm	78 × 64
Displacement		L	0.306
Output	Continuous		4.3
	Maximum	kW	4.8
Rated engine speed		rpm	3600
Compression ratio		-	20.2
Fuel system	Fuel injection pump	-	Bosch type Yanmar PFE-M type
	Fuel injection timing	deg	15.0 ± 0.5 deg bTDC
	Fuel injection nozzle	-	VCO nozzle Bosch made
	Fuel injection pressure	MPa	19.6
Governor		-	All speed type mechanical

oxygen enrichment level with relevant operational parameters such as engine speed, engine load, EGR level and fuel injection timing. In the present work, the techniques of design of experiments (DOE) were used for the systematic study of the main effects and interactions among oxygen concentration, simulated EGR level (by carbon dioxide (CO_2) addition to the intake), and fuel injection timing on the performance of a small single-cylinder direct-injection diesel engine. Even though it appears that a strong interaction exists, the quantification of such interactions by robust experimental methods is still a matter for further research.

2 Experimental Methods

2.1 Test Engine. The test engine was a single-cylinder, naturally aspirated, air-cooled, and direct-injected diesel engine (Yanmar L70EE) with a maximum power output of 4.8 kW at 3600 rpm. The engine was instrumented with a piezoelectric pressure transducer (Kistler 6052B) to measure cylinder pressure and a Hall effect proximity sensor to measure needle lift in the fuel injector. A shaft encoder (AVL 364) installed on the engine crankshaft along with a high-speed data acquisition board (Keithley DAS 1800) were used to record cylinder pressure and needle-lift signals with a crank angle resolution of 0.1 deg. Detailed specifications for the test engine are shown in Table 1. The engine has a mechanically-driven low-pressure fuel injection system (maximum of 200 bars), thus, the results in this work might not be relevant to modern engines with high-pressure fuel injection systems (e.g., common rail fuel injection).

The parameters used to describe the engine performance were maximum average (bulk-gas) combustion temperature, brake-specific fuel consumption, unburned hydrocarbon emissions, carbon monoxide emissions, nitrogen oxide emissions, and particulate matter emissions. Peak bulk-gas temperatures and rates of heat release (ROHR) were calculated from the acquired cylinder pressure using the expressions derived by Heywood [30] from first-law principles and the ideal gas law. Logged data on fuel mass and power output as a function of time were used to compute the brake-specific fuel consumption. Exhaust gas emissions were measured using an AVL CEB-II emissions bench. Particulate matter was collected from diluted exhaust on preweighed 90 mm Pallflex® membrane filters using a Sierra Instruments BG-2 partial flow sampling system. PM mass accumulated was determined by weighing the filter after sampling and stabilization in a humidity chamber in a weigh scale with a resolution of 0.001 mg (Sartorius M5P).

2.2 Oxygen Enrichment of Intake Air. The oxygen concentration in the intake air was increased by adding pure oxygen (purity minimum of 99.5%) from gas bottles to the engine intake system. The oxygen gas was introduced early in the intake system (before the intake surge tank) in order to allow sufficient time for mixing. A high-precision flowmeter attached to the oxygen gas bottle was used to control the oxygen concentration at volume fractions from 21% (baseline) to 23% (high level).

2.3 Simulation of Exhaust Gas Recirculation. Exhaust gas recirculation was simulated by injecting pure carbon dioxide from gas bottles (purity minimum of 99.8%) into the air intake system. Three volume fractions of CO_2 were considered: 0 vol %, 5 vol %, and 10 vol %, corresponding to simulated EGR levels of 0%, 55%, and 65%, respectively. This was the maximum value of CO_2 concentration that could be used in this engine without shutting down or severe deterioration of combustion stability. The percentage of simulated EGR was calculated as [31]

$$\%\mathrm{EGR} = \frac{\mathrm{CO}_2^{\mathrm{intake}} - \mathrm{CO}_2^{\mathrm{ambient}}}{\mathrm{CO}_2^{\mathrm{exhaust}} - \mathrm{CO}_2^{\mathrm{ambient}}} \times 100 \tag{1}$$

where $\mathrm{CO}_2^{\mathrm{intake}}$ is the volume fraction of CO_2 in the intake, $\mathrm{CO}_2^{\mathrm{exhaust}}$ is the CO_2 volume fraction measured in the exhaust gases, and $\mathrm{CO}_2^{\mathrm{ambient}}$ corresponds to the CO_2 volume fraction measured in the ambient air. The CO_2 concentration measured in the ambient air was of the order of the experimental error (below 0.02%), so it was not considered in this calculation.

2.4 Experimental Design and Data Analysis. The experiments were executed in two steps. First, a Taguchi-style screening design [32] was used to estimate the main effects of engine load and speed on the peak bulk-gas temperatures. The objective was to keep the peak bulk-gas temperatures below 1500 K, a region where both soot and NO_x formation rates have been reported to be minimized [33,34]. In this step, fuel injection timing, engine load, engine speed, and CO_2 volume fraction were the variable factors of interest. The Taguchi design allows the estimation of the main effects by fitting a linear model of the kind [32]

$$Y = \beta_0 + \sum \beta_i X_i \tag{2}$$

where Y is the estimated response variable, β_i represents the estimated coefficients (β_0 is the intercept), and X_i represents the predictor variables for the main effects. As can be seen, this screening design does not allow the study of the interactions among factors, but the interest at this stage was in finding the starting conditions

Downloaded 02 Jun 2010 to 171.66.16.109. Redistribution subject to ASME license or copyright; see http://www.asme.org/terms/Terms_Use.cfm

Table 2 Taguchi design for screening of operational parameters

Run no.	Fuel injection timing (deg bTDC)	Engine load (% of full load)	Engine speed (rpm)	CO_2 volume fraction (%)	Peak bulk-gas temperature (K)
1	8.8	25	1500	0	1113
2	8.8	50	2100	5	1311
3	8.8	75	2700	10	1410
4	7.5	25	2100	10	1126
5	7.5	50	2700	0	1316
6	7.5	75	1500	5	Not achieved[a]
7	4.6	25	2700	5	1158
8	4.6	50	1500	10	1192
9	4.6	75	2100	0	1183

[a] The engine shut down at these experimental conditions.

from which to start the optimization process.

Once the starting conditions for low bulk-gas temperatures were established, a central composite design (CCD) with fuel injection timing and CO_2 and O_2 volume fractions as variable factors was used to fit the response surface models for the parameters of engine performance. Central composite designs allow fitting second-order response surface models [32] such as

$$Y = \beta_0 + \sum \beta_i X_i + \sum \beta_{ii} X_i X_i + \sum \beta_{ij} X_i X_j \qquad (3)$$

where Y is the estimated response variable, X_i represents the variable factors, and β_i, β_{ii}, and β_{ij} represent the estimated regression coefficients for the main, quadratic, and interaction effects, respectively.

A statistical software package was used to design the experimental matrix, perform the diagnostic analyses on data, analysis of variance (ANOVA), and the estimation of coefficients and statistical significance of the terms in the fitted models. The confidence level chosen for all the significance tests (including ANOVA diagnostics) was 95%, and the terms that resulted to be not significant at this confidence level were removed from the model.

3 Results and Discussion

3.1 Reduction in Peak Bulk-Gas Temperatures. The reduction in average (bulk-gas) combustion temperatures can be achieved by reducing the fuel mass injected (low loads), reducing compression temperatures (lower engine speeds), or by diluting the cylinder charge (exhaust gas recirculation). Modern combustion modes approaches, such as low temperature combustion (LTC), achieve simultaneous reduction in NO_x and PM emissions by additionally improving fuel-air mixing with high fuel injection pressures and employing late fuel injection to increase ignition delays [34,35]. As mentioned before, the engine used in this study has a low-pressure fuel injection system, and fuel injection timing cannot be sufficiently retarded to achieve conditions for a true LTC mode.

Table 2 shows the Taguchi design used in the first set of experiments and the computed peak bulk-gas temperature. The experimental error was estimated by replicating run nos. 2–4 and 7 (not shown in Table 2). Fuel injection timing was retarded from its standard value of 15 deg before top dead center (bTDC) (see Table 1) at three levels, on which also three levels of engine load (25%, 50%, and 75%), three levels of engine speed (1500 rpm, 2100 rpm, and 2700 rpm), and three levels of CO_2 (0%, 5%, and 10%) were tested. Note that at the high-load low-speed condition (75% load, 1500 rpm), the engine shut down with even 5% CO_2, which means that pressure trace data were not collected.

Table 3 shows the coefficients and p-values for the main effect terms after fitting a linear model. Only the terms with p-values lower than 0.05 (at the 95% confidence level) are statistically significant. According to the p-values, engine load, engine speed, and fuel injection timing appear to be the statistically significant factors, while CO_2 volume fraction was not significant.

Figure 1 shows the main effect plots for the peak bulk-gas temperatures. Considering the magnitude of the error bars (represented by the pooled standard error), it is evident that only engine load, as expected, affected bulk-gas temperatures in a magnitude above the experimental error. The trend to lower peak bulk-gas temperatures at retarded fuel injection and lower engine speeds were not important, in spite of their statistical significance. According to these results, further retardation of fuel injection timing was required in order to affect the bulk-gas temperatures in a significant manner. However, the mechanical limitations of the engine used in this study did not allow achievement of retardations beyond top dead center.

This study is interested in the medium-to-high load conditions, where most of the benefits on PM reduction have been observed [4,6,12], so the 50% load (brake-mean effective pressure (BMEP) of 0.22 MPa) was chosen as the baseline condition. Although lower bulk-gas temperatures were observed at an engine speed of 1500 rpm, this speed was not convenient due to the unstable operation at 50% load. Thus, the experiments of the second stage were performed at 2100 rpm and 50% load (BMEP of 0.22 MPa). Further retardation of fuel injection timing was also sought, but with limited success.

3.2 Optimization of Oxygen-Enriched Diesel Combustion. The effect of using EGR to reduce NO_x emissions during oxygen-enriched diesel combustion was further studied by using a CCD with fuel injection timing, carbon dioxide, and oxygen volume fractions in the intake air as variable factors. The objective was to take advantage of the higher flame temperatures and shorter ignition delays when using oxygen-enriched air to control combustion phasing and to maintain adequate combustion rates when high rates of EGR were used to control NO_x emissions [33,35]. Table 4 shows the experimental matrix used for these experiments (replicates not shown). Fuel injection timing was retarded to the most that was possible in the Yanmar L70EE engine from the standard fuel injection timing of 15 deg bTDC, but it was never possible to reach fuel injection past TDC. The CO_2 volume fraction in the intake air could not be increased over 10% if the 50% load level was to be sustained. The maximum oxygen volume fraction in intake air was 23%, which has been shown to be the limit to minimize the adverse impact on NO_x emissions [12,13,17]. Note

Table 3 Results from fitting linear model to screening design

Term	Coefficient	SE coefficient	p-value
Constant	831.2	38.74	0.000
Fuel injection timing (FIT)	7.516	3.169	0.045
Engine load (LOAD)	447.5	29.45	0.000
Engine speed (RPM)	0.075	0.013	0.000
CO_2 volume fraction (CO2)	−212.5	147.1	0.187

Downloaded 02 Jun 2010 to 171.66.16.109. Redistribution subject to ASME license or copyright; see http://www.asme.org/terms/Terms_Use.cfm

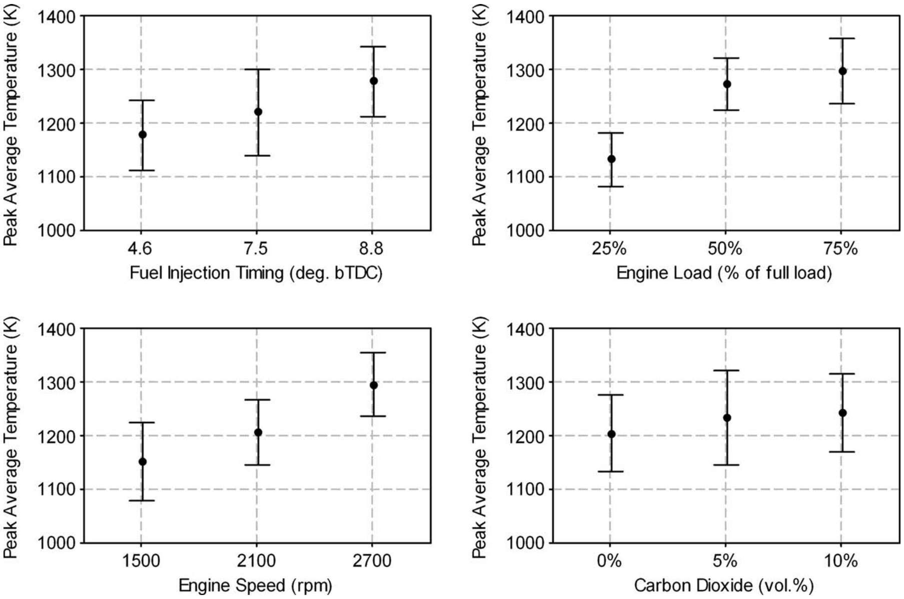

Fig. 1 Peak bulk-gas temperature versus FIT, load, speed, and CO_2

that oxygen enrichment was used whenever CO_2 was injected in order to compensate for the dilution of oxygen in the intake. This allowed studying the effects of CO_2 at constant O_2 concentration, as well as the effects of O_2 enrichment at constant CO_2 concentration (simulated EGR).

The operational conditions summarized in Table 5 represent the average values for the equivalence ratios, mass air flow, and mass fuel flow that were used in the design of experiment. Note that the combustion in the engine was lean, in general, for which the effects of low levels of oxygen enrichment on engine performance were not expected to be very significant.

Table 4 Design of experiments to study oxygen-enriched diesel combustion

Treatment	Fuel injection timing (deg bTDC)	CO_2 volume fraction (%)	O_2 volume fraction (%)
1	3.0	0.0	21.0
2	3.0	10.0	21.0
3	3.0	0.0	23.0
4	3.0	10.0	23.0
5	3.0	5.0	22.0
6	5.8	0.0	22.0
7	5.8	10.0	22.0
8	5.8	5.0	21.0
9	5.8	5.0	23.0
10	5.8	5.0	22.0
11	8.4	0.0	21.0
12	8.4	10.0	21.0
13	8.4	0.0	23.0
14	8.4	10.0	23.0
15	8.4	5.0	22.0

Table 5 Average operational conditions during oxygen-enriched diesel combustion

Operational parameter	Average value
Engine speed, rpm	2100
Engine load, MPa	0.44
Power output, kW	1.22
Mass fuel flow, g/s	0.10 ± 0.01
Mass air flow, g/s	5.1 ± 0.1
Overall equivalence ratio	0.29 ± 0.04

3.2.1 Combustion Analysis. The diagnosis of the combustion during the oxygen enrichment experiments were performed by using the bulk-gas cylinder gas temperature and rate of apparent net heat release calculated from the measured cylinder pressure. Bulk gas temperatures were computed assuming ideal gas behavior of the cylinder charge gas

$$T_{\mathrm{gas}} = \frac{P_{\mathrm{cyl}} V_{\mathrm{cyl}}}{m_{\mathrm{gas}} \bar{R}_{\mathrm{air}}} \tag{4}$$

where P_{cyl} and V_{cyl} are the instantaneous pressure and volume of the cylinder, respectively, m_{gas} is the total cylinder mass trapped per cycle (fuel plus air), and $\bar{R}_{\mathrm{air}}$ is the specific gas constant assuming that the charge mixture consists only of air. Cylinder pressure was acquired over the complete cycle, with a resolution of 0.1 deg crank angles. Cylinder volume at each crank angle degree was computed using the well-known Slider–Crank model [30]. From the pressure-volume relations, the apparent net heat release was computed as [30]

$$\frac{dQ_{\mathrm{net}}}{d\theta} = \frac{\gamma}{\gamma - 1} P \frac{dV}{d\theta} + \frac{1}{\gamma - 1} V \frac{dP}{d\theta} \tag{5}$$

where γ is the ratio of specific heats for air (C_p/C_v).

Figure 2 shows that oxygen enrichment increased the peak combustion pressures, with a corresponding increase in bulk-gas temperatures, but the magnitude of these effects depends on the fuel injection timing. At the latest FIT (3.0 deg bTDC), an increase of about 50 K was observed in the peak bulk-gas temperatures after combustion, when the oxygen concentration was increased from 21% (baseline) to 23% (0% CO_2), though the combustion phasing remained unchanged. When CO_2 concentration was increased to 10% (at 21% O_2), not only the peak bulk-gas temperature was reduced by 100 K (compared with baseline), but also the position of the peak bulk-gas temperature was retarded by 16 deg, reflecting the increase in ignition delay and the decrease in the rate of heat release caused by CO_2. Increasing oxygen concentration to 23% (with 10% CO_2) was effective to re-establish the combustion characteristics of the baseline. At the

Downloaded 02 Jun 2010 to 171.66.16.109. Redistribution subject to ASME license or copyright; see http://www.asme.org/terms/Terms_Use.cfm

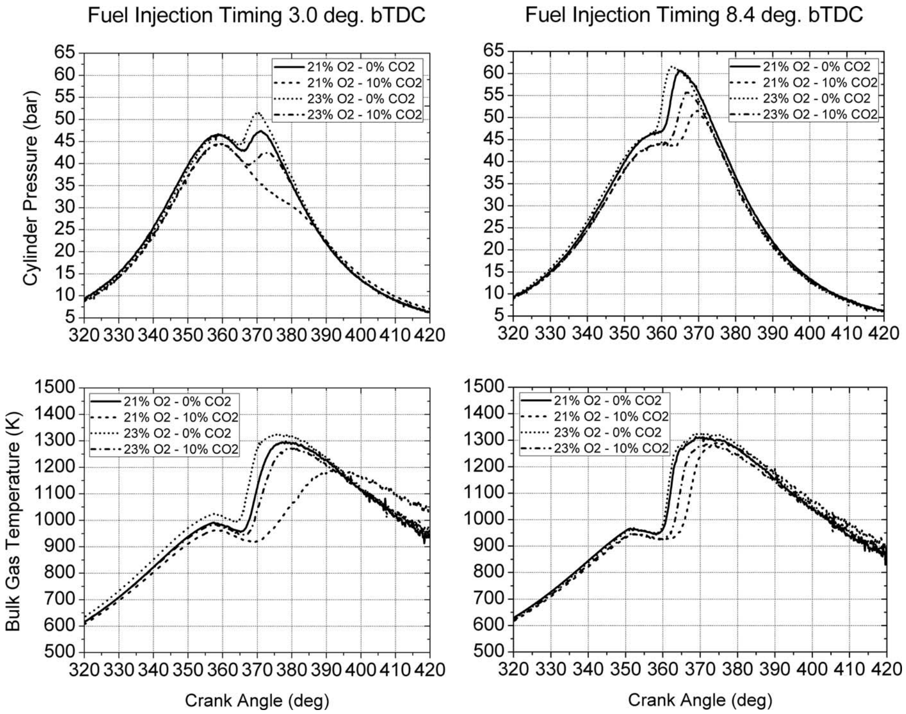

Fig. 2 Cylinder pressure and bulk-gas temperatures at the latest (3.0 deg bTDC) and earliest (8.4 deg bTDC) fuel injection timing (2100 rpm, 50% load)

earliest FIT (8.4 deg bTDC), the effects of oxygen enrichment and CO_2 addition are smaller, probably because the increase in available time for combustion outweighs that for the small changes in ignition delay observed in both cases. This is in agreement with prior works, in which the most benefits from oxygen enrichment were observed with substantial retardation of fuel injection (see for example [25]).

The rates of heat release and cumulative heat release in Fig. 3 corroborate the effects of oxygen enrichment and CO_2 on combustion phasing, which are more important at retarded fuel injection. With the latest fuel injection, oxygen enrichment (23% O_2,

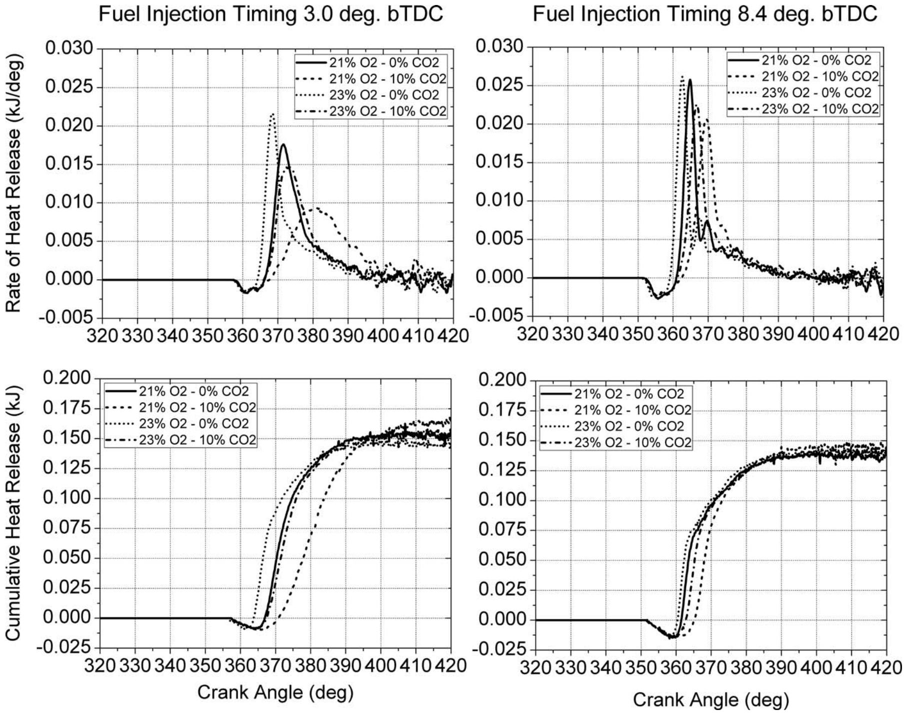

Fig. 3 Rate and cumulative heat release at the latest (3.0 deg bTDC) and earliest (8.4 deg bTDC) fuel injection timing (2100 rpm, 50% load)

Downloaded 02 Jun 2010 to 171.66.16.109. Redistribution subject to ASME license or copyright; see http://www.asme.org/terms/Terms_Use.cfm

Table 6 Response surface model fit for BSFC versus FIT, CO_2, and O_2 volume fractions

Term	Coefficient	Std. error of coefficient	*p*-value
Constant	301.6	6.291	0.000
Fuel injection timing (FIT)	−6.320	7.385	0.399
CO_2 volume fraction (CO2)	16.99	7.521	0.032
O_2 volume fraction (O2)	−7.341	7.773	0.353
$CO_2 \times O_2$	−19.36	8.302	0.027

0% CO_2) advanced the start of combustion (SOC) by 4 deg with respect to the baseline and increased the rate of heat release, while simulated EGR (10% CO_2, 21% O_2) caused a retardation in SOC of 5 deg, a decrease in the peak heat release rate, and an increase in the combustion duration. At the condition of 23% O_2 with 10% CO_2, the heat release characteristics were similar to those of the baseline condition.

The effects of O_2 enrichment observed were mainly due to the reduction in ignition delay that resulted from the increase in the burn rates at the higher oxygen concentration [1], since the thermophysical properties of the oxygen-enriched air will not change too much at low O_2 levels [1,21]. On the other hand, the use of EGR affects engine performance by three mechanisms: (1) dilution of oxygen concentration, (2) thermal effects due to the higher heat capacity of combustion gases (CO_2 and H_2O), and (3) chemical effects due to dissociation of combustion gases and their reactions [36–38]. Among these, the dilution effects, both from CO_2 and H_2O, are by far the most important [36–38]. The isolation of these effects was not attempted in the present work, but it is expected that most of the effects observed were related to the thermal effects of CO_2 (at fixed O_2 level). It can be anticipated that greater effects would be observed with real EGR due to the higher specific heat capacity of H_2O compared with CO_2 [37]. In fact, it has also been observed that the maximum EGR levels are lower when using real exhaust gas instead of pure CO_2 [31].

3.2.2 Brake-Specific Fuel Consumption. The coefficients and *p*-values from the analysis of the data on brake-specific fuel consumption are presented in Table 6. The *p*-values indicate that only CO_2 volume fraction and the interaction term CO2 × O2 were the statistically significant factors. The coefficient of the interaction term CO2 × O2 is of the same order of magnitude that the coefficient for CO_2 but has a negative sign, which means that there was an antagonistic relationship between both factors.

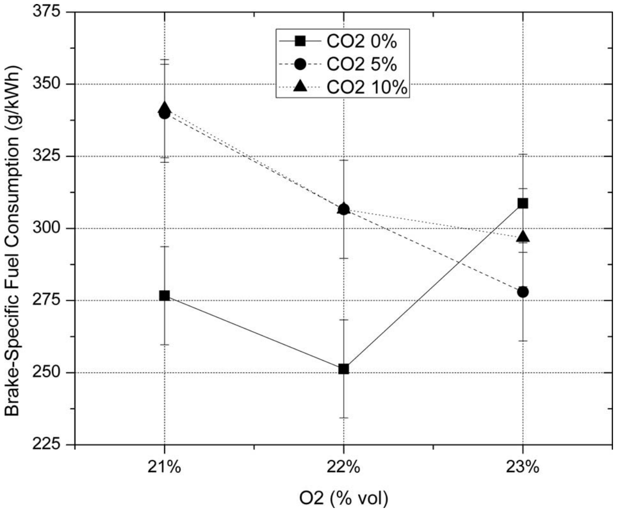

Fig. 5 Interaction plot for BSFC versus CO_2 and O_2 volume fractions (2100 rpm, 50% load)

Figure 4 corroborates that BSFC increased to a magnitude just above the experimental error when the CO_2 volume fraction was 5%, but no additional increase was observed at 10% CO_2. It is also clear that the neither fuel injection timing nor oxygen volume fraction caused changes in the average magnitude of BSFC, as shown by the ANOVA table. The interaction term can be better appreciated in the interaction plot of BSFC versus CO_2 and O_2 volume fractions (Fig. 5). In this plot one can observe that increasing O_2 concentration to 23% while also injecting CO_2 resulted in a reduction in BSFC of about 14% (averaging reductions for 5% and 10% CO_2). In fact, at 5% CO_2, the BSFC can be restored to baseline levels by increasing O_2 concentration to 23%. Figure 5 also shows that oxygen enrichment alone might not be beneficial, since there is a slight increase in BSFC for 23% O_2,

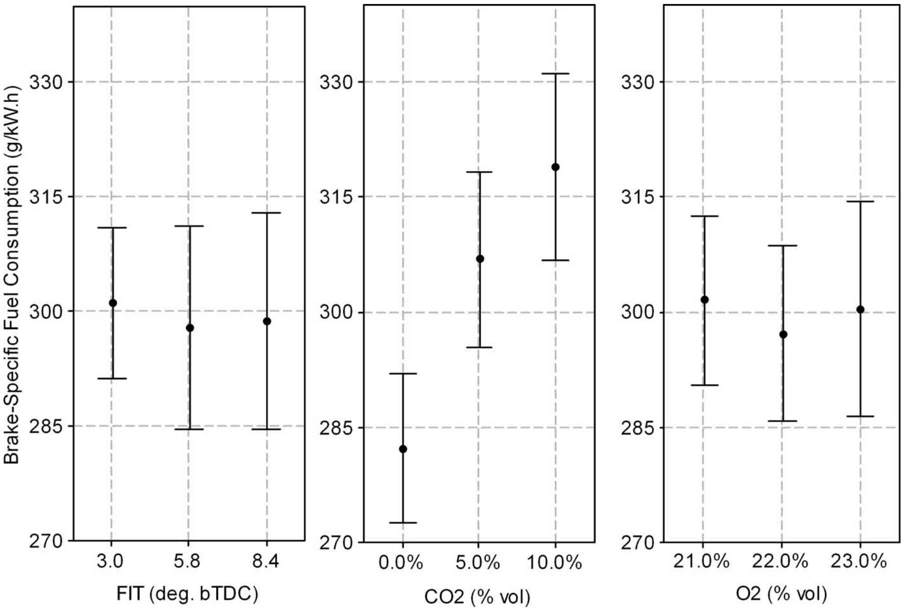

Fig. 4 BSFC versus FIT, CO_2, and O_2 (2100 rpm, 50% load)

Downloaded 02 Jun 2010 to 171.66.16.109. Redistribution subject to ASME license or copyright; see http://www.asme.org/terms/Terms_Use.cfm

Table 7 Response surface model fit for HC versus FIT, CO_2, and O_2

Term	Coefficient	Std. error of coefficient	p-value
Constant	8.7487	0.2369	0.000
Fuel injection timing (FIT)	−0.7366	0.2801	0.014
CO_2 volume fraction (CO2)	−0.1353	0.2928	0.648
O_2 volume fraction (O2)	−0.5245	0.2930	0.085
FIT × CO_2	−0.9484	0.3203	0.006
$CO_2 \times O_2$	−1.1276	0.3117	0.001

which might be due to the increase in heat transfer at the higher bulk-gas temperatures [8]. Similar results were observed by Desai et al. [8] and Donahue and Foster [13], who also observed that retardation of fuel injection timing for maximum brake torque (MBT) was necessary to maintain fuel conversion efficiency during oxygen enrichment [13].

3.2.3 Brake-Specific Exhaust Emissions

3.2.3.1 Unburned hydrocarbons. The fitting of the response surface model for unburned hydrocarbon emissions and the corresponding ANOVA indicated a significant effect (at the 95% confidence level) from fuel injection timing and the interaction terms FIT × CO2 and CO2 × O2, as shown in Table 7. The interaction terms that were not statistically significant were removed from the model.

Figure 6 shows graphically the magnitude of the main effects, where the experimental error bars correspond to the pooled standard error. CO_2 and O_2 would affect HC emissions through the changes in ignition delay that these gases would produce, since HC emissions increase or decrease with ignition delay [30]. As seen in Fig. 3, the changes in ignition delay caused by oxygen enrichment and CO_2 addition were not more than 5 deg crank angles, which were not enough to affect overall HC emissions. However, retardation of fuel injection timing favors undermixing of fuel with the consequent increase in HC emissions [30], which seemed to be the main mechanism operating in these experiments.

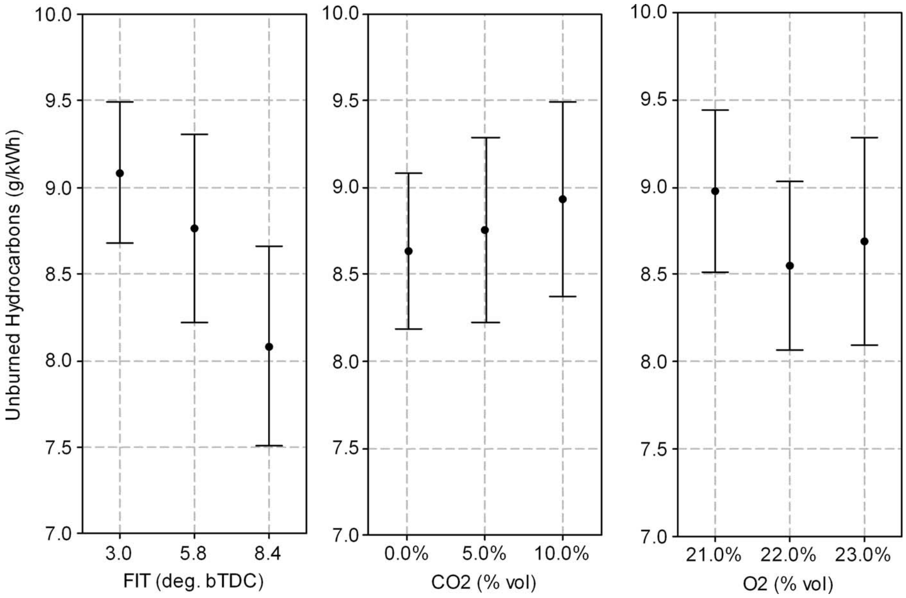

Fig. 6 HC emissions versus O_2 and CO_2 volume fractions (2100 rpm, 50% load)

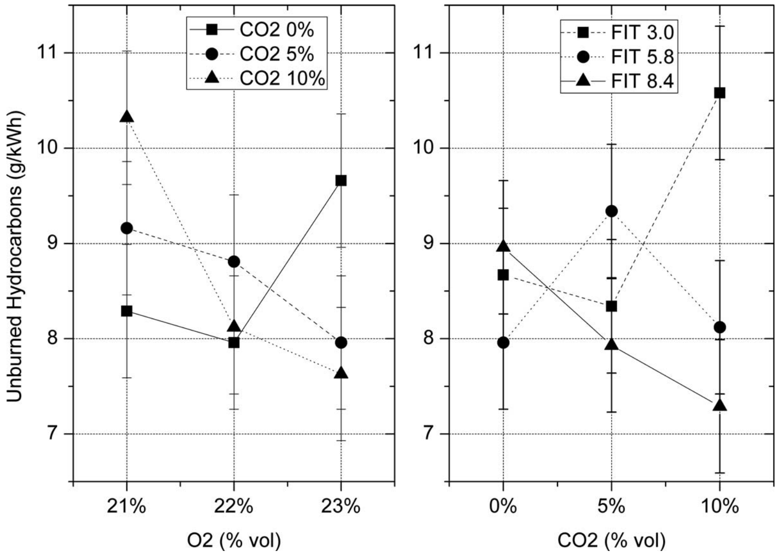

Fig. 7 Interaction plots for HC emissions (2100 rpm, 50% load)

Downloaded 02 Jun 2010 to 171.66.16.109. Redistribution subject to ASME license or copyright; see http://www.asme.org/terms/Terms_Use.cfm

Table 8 Response surface model fit for CO versus FIT, CO_2, and O_2

Term	Coefficient	Std. error of coefficient	*p*-value
Constant	19.823	0.4815	0.000
Fuel injection timing (FIT)	0.5636	0.5634	0.325
CO_2 volume fraction (CO2)	2.0088	0.5677	0.001
O_2 volume fraction (O2)	0.0062	0.5805	0.992

Table 9 Response surface model fit for NO_x versus FIT, CO_2, and O_2

Term	Coefficient	Std. error of coefficient	*p*-value
Constant	7.696	0.720	0.000
Fuel injection timing (FIT)	1.833	0.493	0.001
CO_2 volume fraction (CO2)	−7.960	0.501	0.000
O_2 volume fraction (O2)	6.124	0.521	0.000
$CO_2 \times CO_2$	2.497	0.881	0.009
$CO_2 \times O_2$	−4.616	0.551	0.000

The interaction plots in Fig. 7 show that there was indeed an increase of 25% in HC emissions with 10% CO_2, but the increase was offset by increasing O_2 concentration to 23%. The interaction between injection timing and CO_2 concentration is more difficult to explain, but this suggests that the response of HC emissions to CO_2 has opposite behavior at the latest and earliest fuel injection timing.

3.2.3.2 Carbon monoxide. Since diesel engines normally operate under lean conditions, carbon monoxide emissions have never been a concern [30]. However, with inert gas addition (such as CO_2), part of the air is replaced, which reduces the air/fuel ratio, thus increasing CO emissions [30]. This phenomenon was captured by the regression analysis, where only CO_2 volume fraction was statistically significant to CO emissions, as shown in Table 8. The main effects plot in Fig. 8 shows an increase of 24% in CO emissions when CO_2 concentration was increased to 10%. It can also be seen that oxygen enrichment did not have any impact on CO emissions.

3.2.3.3 Nitrogen oxides. The analysis of data (Table 9) indicated that all three variable factors (FIT, CO_2, and O_2) were statistically significant to NO_x emissions, as well as the interaction between CO_2 and O_2 volume fractions.

Past studies have shown that NO_x levels can be kept at the baseline levels as long as oxygen enrichment was limited to 21.5–22.5% [26]. However, Fig. 9 shows that average NO_x emissions in the Yanmar L70EE increased by more than 80% for oxygen volume fractions as low as 22%. CO_2 addition also had a big influence on NO_x emissions, which were reduced by 55% with only 5% CO_2. At 10% CO_2 and NO_x emissions were reduced by 87%. Note that fuel injection timing was not influential to NO_x emissions, as has been reported in literature [25,26]. The reason is that there was a mechanical limitation in the maximum degree of retardation or advancing that could be achieved in the Yanmar L70EE. Although the engine was well retarded compared with the standard fuel injection (15 deg bTDC), it was never possible to achieve fuel injection past top dead center. The interaction between CO_2 and O_2 (Fig. 10) demonstrates that adding CO_2 attenuated the rate of increase in NO_x emissions observed with oxygen enrichment. Note that NO_x emissions at the condition 23% O_2-10% CO_2 were reduced by 46% compared with the baseline. This result is important because it means that higher levels of oxygen enrichment could be achieved with essentially no impact, or even a reduction, on NO_x emissions.

3.2.3.4 Particulate matter. Particulate matter was collected on a Pallflex® membrane filter from diluted exhaust using a Sierra Instruments BG-2 sampling dilution system. The total mass collected was determined by weighing the filter before and after sample collection with a high-precision weight scale. The analysis of data (Table 10) indicated that fuel injection timing, CO_2 and O_2 volume fractions, and their interactions were all statistically significant to PM emissions.

Figure 11 shows that PM emissions increased by 52% at 10% CO_2, while a reduction of 33% was obtained when oxygen concentration was increased to 23%. The reducing effect of CO_2 on bulk-gas temperatures seemed to govern the soot oxidation rates in these experiments. A careful inspection of Fig. 12 suggests that the significant increase in PM emissions at 10% CO_2 dominated the interaction effects, but it seems clear that the PM emission levels of the baseline condition can be restored by using oxygen

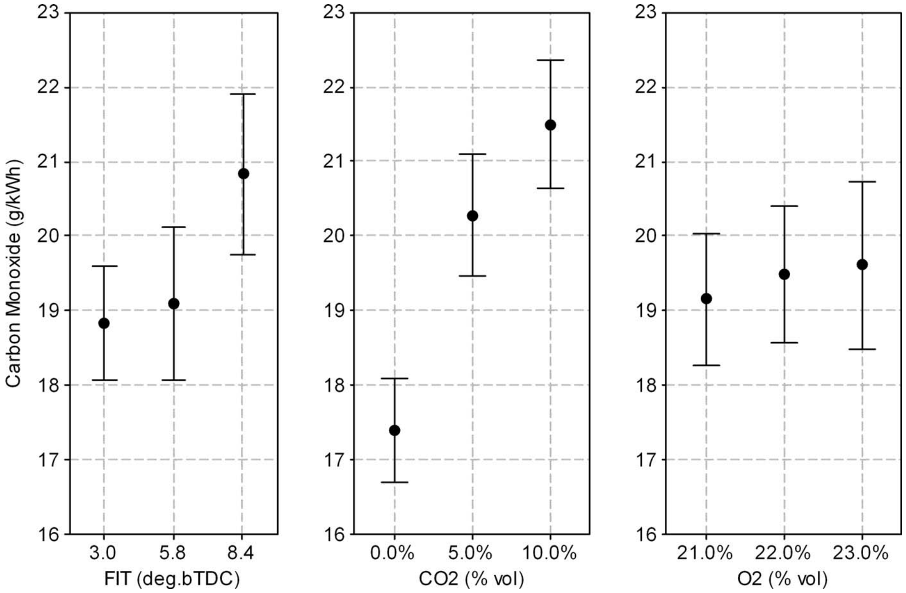

Fig. 8 CO emissions versus FIT, O_2, and CO_2 volume fractions (2100 rpm, 50% load)

Downloaded 02 Jun 2010 to 171.66.16.109. Redistribution subject to ASME license or copyright; see http://www.asme.org/terms/Terms_Use.cfm

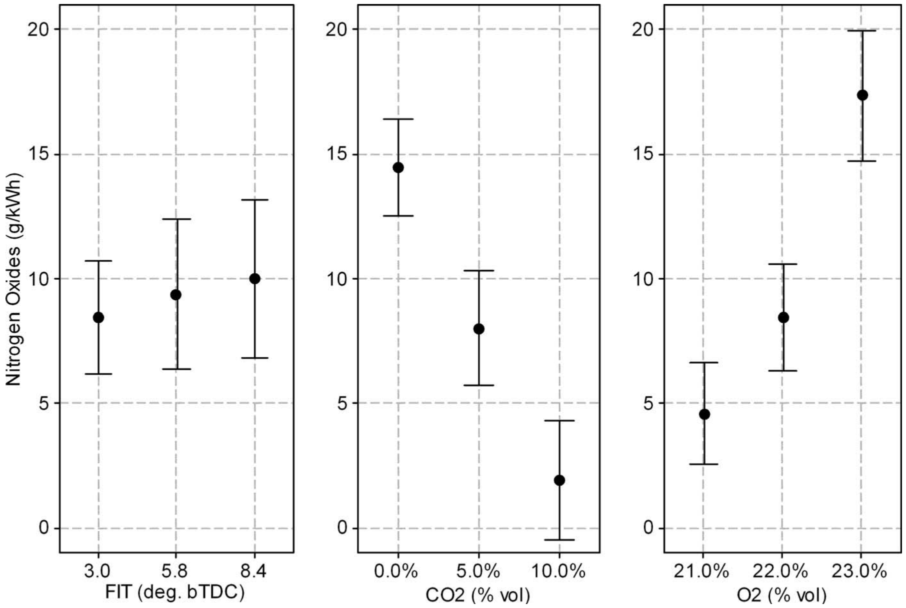

Fig. 9 **NO_x emissions versus FIT, O_2, and CO_2 volume fractions (2100 rpm, 50% load)**

enrichment.

An overall review of the results of this study reveals that oxygen enrichment might have some potential uses in diesel engines, but retardation of fuel injection timing beyond the limits achieved in this study are required. Low levels of oxygen enrichment were found to offset the effects on cylinder pressure, bulk-gas temperatures, and ignition delay caused by high levels of simulated EGR. This might be useful for modern combustion approaches that use high levels of EGR to simultaneously reduce NO_x and PM emissions, such as modulated kinetics [39] and smokeless rich diesel combustion [33].

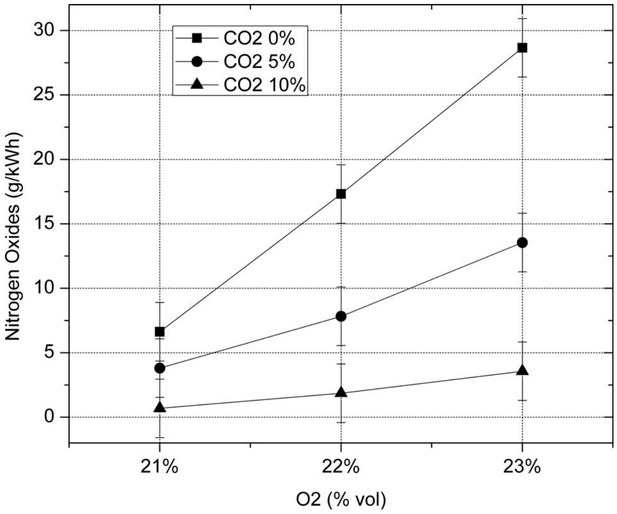

Fig. 10 **Interaction plot for NO_x emissions versus CO_2 and O_2 (2100 rpm, 50% load)**

Table 10 **Response surface model fit for PM versus FIT, CO_2, and O_2**

Term	Coefficient	Std. error of coefficient	*p*-value
Constant	0.9568	0.0683	0.000
Fuel injection timing (FIT)	−0.2422	0.0842	0.009
CO_2 volume fraction (CO2)	0.3828	0.0839	0.000
O_2 volume fraction (O2)	−0.2145	0.0892	0.026
FIT × CO_2	−0.2975	0.0955	0.005
FIT × O_2	0.2612	0.0958	0.013
CO_2 × O_2	−0.2990	0.0954	0.005

4 Conclusions

Cylinder pressures and bulk-gas temperatures increased with oxygen enrichment and decreased with CO_2 addition. The effects were stronger at the most retarded fuel injection timing (3 deg bTDC), where the peak bulk-gas temperature increased by 50 K with 23% O_2 and decreased by 100 K with 10% CO_2. At the condition 23% O_2-10% CO_2, cylinder pressures and computed bulk-gas temperatures are similar to those of the baseline condition.

The computed heat release rates showed that, at the most retarded fuel injection (3 deg bTDC), oxygen enrichment (23% O_2, 0% CO_2) advanced the SOC by 4 deg with respect to the baseline and increased the rate of heat release, while simulated EGR (10% CO_2, 21% O_2) caused a retardation in SOC of 5 deg, a decrease in the peak heat release rate, and an increase in the combustion duration. At the condition 23% O_2 with 10% CO_2, the heat release characteristics were restored to those of the baseline condition, with similar combustion phasing and similar peak heat release rate. At the earliest fuel injection timing, the same trends were observed, but the magnitude of the effects was smaller.

Brake-specific fuel consumption increased by 23% with the addition of 10% CO_2 (21% O_2). the average BSFC of the baseline condition was restored by the oxygen concentration to 23% (10% CO_2).

Although the main effects of O2 and CO2 were not statistically significant, the response surface model indicated that there was a statistically significant interaction between O_2 and CO_2. HC emissions increased by 25% with the addition of 10% CO_2. This increase was offset by increasing oxygen concentration to 23%.

CO emissions increased by 24% when CO_2 concentration was increased to 10%. Oxygen enrichment did not have any impact on CO emissions.

NO_x emissions increased in more than 80% for oxygen volume fractions as low as 22%. Adding CO_2 attenuated the rate of increase in NO_x emissions observed with oxygen enrichment. In

Downloaded 02 Jun 2010 to 171.66.16.109. Redistribution subject to ASME license or copyright; see http://www.asme.org/terms/Terms_Use.cfm

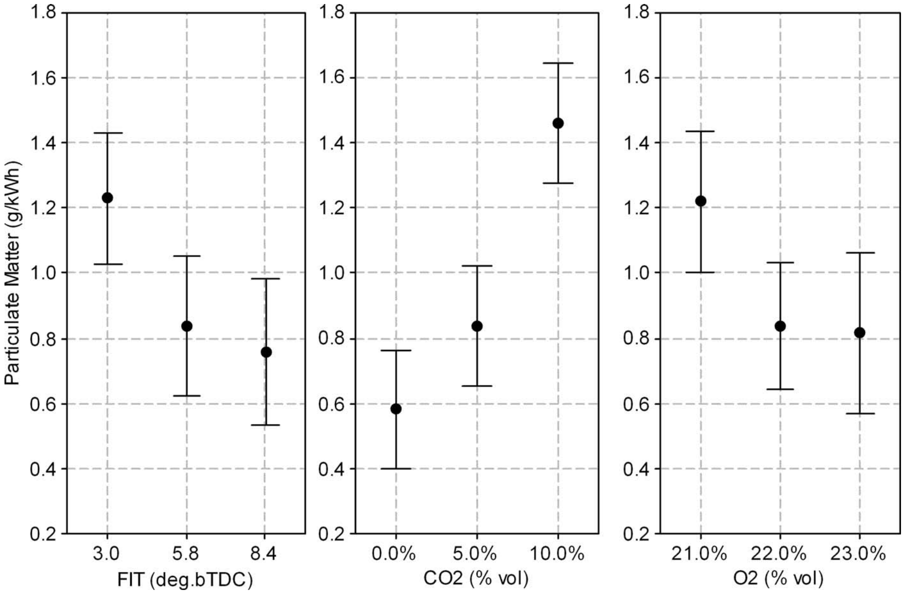

Fig. 11 PM emissions versus O_2 and CO_2 volume fractions (2100 rpm, 50% load)

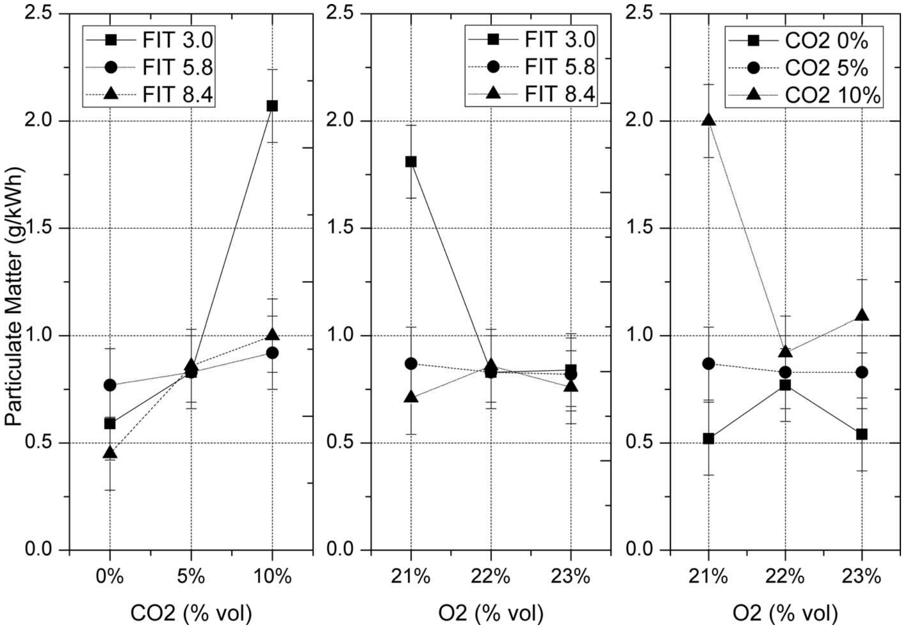

Fig. 12 Interaction plots for PM emissions (2100 rpm, 50% load)

fact, at the condition 23% O_2-10% CO_2, NO_x emissions were reduced by 46% with respect to the baseline condition. This result was considered one of the most important because it means that higher levels of oxygen enrichment could be achieved with essentially no impact on NO_x emissions.

PM emissions increased by 52% at 10% CO_2, while a reduction of 33% was observed when oxygen concentration was increased to 23%. It seemed clear that the PM emission levels of the baseline condition can be restored by using oxygen enrichment.

Acknowledgment

This work was funded by eVionyx, Inc. and the Defense Advanced Research Projects Agency (DARPA) through the Subcontract OSP No. 109298. The authors wish to thank Dr. Sadeg Faris of Reveo/eVionyx and Dr. William Coblentz of DARPA for their input and technical support during this project.

References

[1] Karim, G. A., and Ward, G., 1968, "The Examination of the Combustion Processes in a Compression-Ignition Engine by Changing the Partial Pressure of Oxygen in the Intake Charge," SAE Technical Paper No. 680767.

[2] Wartinbee, W. J., Jr., 1971, "Emissions Study of Oxygen Enriched Air," SAE Technical Paper No. 710606.

[3] Ghojel, J., Hilliard, J. C., and Levendis, Y. A., 1983, "Effect of Oxygen Enrichment on the Performance and Emissions of IDI Diesel Engines," SAE Technical Paper No. 830245.

[4] Iida, N., Suzuki, Y., Sato, G. T., and Sawada, T., 1986, "Effects of Intake Oxygen Concentration on the Characteristics of Particulate Emissions From a D.I. Diesel Engine," SAE Technical Paper No. 861233.

[5] Assanis, D. N., Baker, D., Sekar, R. R., Siambekos, C. T., Cole, R. L., and Marciniak, T. J., 1990, "Simulation Studies of Diesel Engine Performance With Oxygen Enriched Air and Water Emulsified Fuels," Argonne National Laboratory, Report No. CONF-900102-6.

[6] Watson, H. C., Milkins, E. E., and Rigby, G. R., 1990, "A New Look at Oxygen Enrichment: 1) The Diesel Engine," SAE Technical Paper No. 900344.

Downloaded 02 Jun 2010 to 171.66.16.109. Redistribution subject to ASME license or copyright; see http://www.asme.org/terms/Terms_Use.cfm

[7] Sekar, R., Marr, W. W., Schaus, J. E., Cole, R. L., Marciniak, T. J., and Eustis, J. N., 1990, "Cylinder Pressure Analysis of a Diesel Engine Using Oxygen-Enriched Air and Emulsified Fuels," SAE Technical Paper No. 901565.

[8] Desai, R. R., Gaynor, E., Watson, H. C., and Rigby, G. R., 1993, "Giving Standard Diesel Fuels Premium Performance Using Oxygen-Enriched Air in Diesel Engines," SAE Technical Paper No. 932806.

[9] Marr, W. W., Sekar, R., Cole, R. L., Marciniak, T. J., and Longman, D. E., 1993, "Oxygen-Enriched Diesel Engine Experiments With a Low-Grade Fuel," SAE Technical Paper No. 932805.

[10] Sekar, R. R., Marr, W. W., Schaus, J. E., Cole, R. L., and Marciniak, T. J., 1990, "Diesel Engine Experiments With Oxygen Enrichment, Water Addition and Lower-Grade Fuel," *Proceedings of the 25th Intersociety Energy Conversion Engineering Conference*, Vol. 4.

[11] Sekar, R. R., Marr, W. W., Cole, R. L., Marciniak, T. J., Assanis, D. N., and Schaus, J. E., 1990, "Oxygen-Enriched Diesel Engine Performance: A Comparison of Analytical and Experimental Results," Argonne National Laboratory, Report No. CONF-901038-1.

[12] Virk, K. S., Kokturk, U., and Bartels, C. R., 1993, "Effects of Oxygen-Enriched Air on Diesel Engine Exhaust Emissions and Engine Performance," SAE Technical Paper No. 931004.

[13] Donahue, R. J., and Foster, D. E., 2000, "Effects of Oxygen Enhancement on the Emissions From a DI Diesel Via Manipulation of Fuels and Combustion Chamber Gas Composition," SAE Technical Paper No. 2000-01-0512.

[14] Hess, H. S., Boehman, A. L., Tijm, P. J. A., and Waller, F. J., 2000, "Experimental Studies of the Impact of Cetaner on Diesel Combustion and Emissions," SAE Technical Paper No. 2000-01-2886.

[15] Chapman, E. M., Boehman, A. L., Tijm, P. J. A., Waller, F. J., and Bhide, S. V., 2000, "Emission Characteristics of a Navistar 7.3l Turbodiesel Fueled With Blends of Oxygenates and Diesel," SAE Technical Paper No. 2000-01-2887.

[16] Song, J. H., Cheenkachorn, K., Wang, J. G., Perez, J., Boehman, A. L., Young, P. J., and Waller, F. J., 2002, "Effect of Oxygenated Fuel on Combustion and Emissions in a Light-Duty Turbo Diesel Engine," Energy Fuels, **16**(2), pp. 294–301.

[17] Song, J., Zello, V., Boehman, A. L., and Waller, F. J., 2004, "Comparison of the Impact of Intake Oxygen Enrichment and Fuel Oxygenation on Diesel Combustion and Emissions," Energy Fuels, **18**(5), pp. 1282–1290.

[18] Litzinger, T., Stoner, M., Hess, H., and Boehman, A., 2000, "Effects of Oxygenated Blending Compounds on Emissions From a Turbocharged Direct Injection Diesel Engine," Int. J. Engine Res., **1**, pp. 57–70.

[19] Upatnieds, A., and Mueller, C. J., 2005, "Clean, Controlled DI Diesel Combustion Using Dilute, Cool Charge Gas and a Short-Ignition-Delay, Oxygenated Fuel," SAE Technical Paper No. 2005-01-0363.

[20] Anand, R., and Mahalakshmi, N. V., 2007, "Simultaneous Reduction of NO_x and Smoke From a Direct-Injection Diesel Engine With Exhaust Gas Recirculation and Diethyl Ether," Proc. Inst. Mech. Eng., Part D (J. Automob. Eng.), **221**(1), pp. 109–116.

[21] Lahiri, D., Mehta, P. S., Poola, R. B., and Sekar, R., 1997, "Utilization of Oxygen-Enriched Air in Diesel Engines: Fundamental Considerations."

[22] Poola, R., and Stork, K., 1998, "Membrane-Based Air Composition Control for Light-Duty Diesel Vehicles: A Benefit and Cost Assessment," Argonne National Laboratory, Report No. ANL/ESD/TM-144.

[23] Poola, R. B., Longman, D. E., Stork, K. C., Sekar, R., Nemser, S., and Callaghan, K., 2000, "Membrane-Based Nitrogen-Enriched Air for NO_x Reduction in Light-Duty Diesel Engines," SAE Technical Paper No. 2000-01-0228.

[24] Assanis, D. N., Poola, R. B., Sekar, R., and Cataldi, G. R., 2001, "Study of Using Oxygen-Enriched Combustion Air for Locomotive Diesel Engines," ASME J. Eng. Gas Turbines Power, **123**(1), pp. 157–166.

[25] Poola, R. B., and Sekar, R., 2003, "Reduction of NO_x and Particulate Emissions by Using Oxygen-Enriched Combustion Air in a Locomotive Diesel Engine," ASME J. Eng. Gas Turbines Power, **125**(2), pp. 524–533.

[26] Rakopoulos, C. D., Hountalas, D. T., Zannis, T. C., and Levendis, Y. A., 2004, "Operational and Environmental Evaluation of Diesel Engines Burning Oxygen-Enriched Intake Air or Oxygen-Enriched Fuels: A Review," SAE Technical Paper No. 2004-01-2924.

[27] Xiao, G. F., Qiao, X. Q., Huang, Z., and Chen, Z. P., 2007, "Improvement of Startability of Direct-Injection Diesel Engines by Oxygen-Enriched Intake Air," Proc. Inst. Mech. Eng., Part D (J. Automob. Eng.), **221**(11), pp. 1453–1465.

[28] Caton, J. A., 2005, "Use of a Cycle Simulation Incorporating the Second Law of Thermodynamics: Results for SI Engines Using Oxygen-Enriched Combustion Air," SAE Technical Paper No. 2005-01-1130.

[29] Zannis, T. C., Pariotis, E. G., Hountalas, D. T., Rakopoulos, D. C., and Levendis, Y. A., 2007, "Theoretical Study of DI Diesel Engine Performance and Pollutant Emissions Using Comparable Air-Side and Fuel-Side Oxygen Addition," Energy Convers. Manage., **48**(11), pp. 2962–2970.

[30] Heywood, J. B., 1988, *Internal Combustion Engine Fundamentals* (McGraw-Hill Series in Mechanical Engineering), McGraw-Hill, New York, p. 510.

[31] Zheng, M., Reader, G. T., and Hawley, J. G., 2004, "Diesel engine Exhaust Gas Recirculation—A Review on Advanced and Novel Concepts," Energy Convers. Manage., **45**(6), pp. 883–900.

[32] Kutner, M. H., Nachtsheim, C. J., Neter, J., and Li, W., 2005, *Applied Linear Statistical Models*, 5th ed., McGraw-Hill, Irwin, Boston.

[33] Akihama, K., Takatori, Y., Inagaki, K., Sasaki, S., and Dean, A., 2001, "Mechanism of the Smokeless Rich Diesel Combustion by Reducing Temperature," SAE Technical Paper No. 2001-01-0655.

[34] Jacobs, T. J., and Assanis, D. N., 2007, "The Attainment of Premixed Compression Ignition Low-Temperature Combustion in a Compression Ignition Direct Injection Engine," Proc. Combust. Inst., **31**(2), pp. 2913–2920.

[35] Lee, T., and Reitz, R. D., 2003, "Response Surface Method Optimization of a High-Speed Direct-Injection Diesel Engine Equipped With a Common Rail Injection System," ASME J. Eng. Gas Turbines Power, **125**(2), pp. 541–546.

[36] Ladommatos, N., Abdelhalim, S. M., Zhao, H., and Hu, Z., 1998, "The Effects of Carbon Dioxide in Exhaust Gas Recirculation on Diesel Engine Emissions," Proc. Inst. Mech. Eng., Part D (J. Automob. Eng.), **212**(1), pp. 25–42.

[37] Ladommatos, N., Abdelhalim, S., and Zhao, H., 1998, "Control of Oxides of nitrogen From Diesel Engines Using Diluents While Minimising the Impact on Particulate Pollutants," Appl. Therm. Eng., **18**(11), pp. 963–980.

[38] Zhao, H., Hu, J., and Ladommatos, N., 2000, "In-Cylinder Studies of the Effects of CO_2 in Exhaust Gas Recirculation on Diesel Combustion and Emissions," Proc. Inst. Mech. Eng., Part D (J. Automob. Eng.), **214**(D4), pp. 405–419.

[39] Kimura, S., Aoki, O., Ogawa, H., and Muranaka, S., and Enomoto, Y., 1999, "New Combustion Concept for Ultra-Clean and High-Efficiency Small DI Diesel Engines," SAE Technical Paper No. 1999-01-3681.

Downloaded 02 Jun 2010 to 171.66.16.109. Redistribution subject to ASME license or copyright; see http://www.asme.org/terms/Terms_Use.cfm

System Analysis of Nuclear-Assisted Syngas Production From Coal

E. A. Harvego

M. G. McKellar

J. E. O'Brien

Idaho National Laboratory,
2525 North Fremont Avenue,
MS 3885,
Idaho Falls, ID 83415

A system analysis has been performed to assess the efficiency and carbon utilization of a nuclear-assisted coal gasification process. The nuclear reactor is a high-temperature helium-cooled reactor that is used primarily to provide power for hydrogen production via high-temperature electrolysis. The supplemental hydrogen is mixed with the outlet stream from an oxygen-blown coal gasifier to produce a hydrogen-rich gas mixture, allowing most of the carbon dioxide to be converted into carbon monoxide, with enough excess hydrogen to produce a syngas product stream with a hydrogen/carbon monoxide molar ratio of about 2:1. Oxygen for the gasifier is also provided by the high-temperature electrolysis process. The results of the analysis predict 90.5% carbon utilization with a syngas production efficiency (defined as the ratio of the heating value of the produced syngas to the sum of the heating value of the coal plus the high-temperature reactor heat input) of 64.4% at a gasifier temperature of 1866 K for the high-moisture-content lignite coal considered. Usage of lower moisture coals such as bituminous can yield carbon utilization approaching 100% and 70% syngas production efficiency.

[DOI: 10.1115/1.3095805]

1 Introduction

Deepening concerns about energy security, especially with regard to liquid fuels for transportation, have motivated consideration of alternate methods for producing synthetic liquid fuels [1,2]. Indirect coal liquefaction technology consumes coal, steam, and oxygen in a gasification process to produce hydrogen and carbon monoxide that can be converted to liquid fuels via the Fischer–Tropsch catalytic synthesis process as follows:

$$nCO + (2n+1)H_2 \rightarrow C_nH_{2n+2} + nH_2O \qquad (1)$$

In addition to the Fischer–Tropsch process for production of liquid fuels, syngas is also the starting point for the production of many useful chemicals [3]. However, the traditional process for producing syngas also produces significant quantities of carbon dioxide that must be sequestered or released to the atmosphere. In fact, with traditional coal-to-liquid (CTL) technology, only about one-third of the carbon in the coal feedstock ends up in the liquid fuel product [4]. If supplemental hydrogen is available, nearly all of the carbon in the coal can end up in the liquid fuel product. Supplemental hydrogen for this process should be obtained from an efficient noncarbon-emitting process such as high-temperature electrolysis (HTE) of steam powered by nuclear energy [5,6]. The coupling of the HTE process to CTL is particularly appealing because it is more efficient than conventional electrolysis and because it provides both hydrogen and oxygen at elevated temperature. The oxygen can be fed directly to the gasifier and the hydrogen can be used to reduce the excess carbon dioxide produced in a gasifier, via the reverse shift reaction.

Nuclear-assisted CTL was analyzed in a recent study [7] for a particular advanced reactor-gasifier combination. The authors found that the most effective role for the reactor was in powering a high-temperature electrolysis process for the production of hydrogen and oxygen, both of which can be used directly in the gasification and shift reactor processes. Direct integration of reactor thermal energy into the process was not found to be beneficial. The results of that study indicated that very high carbon utilization is achievable with this concept.

This paper presents results of a general system analysis that examines the details of coupling an advanced high-temperature nuclear reactor to an HTE system and a coal gasifier for the production of syngas. The conversion of the syngas to a liquid fuel using the Fischer–Tropsch process is not considered herein. Overall system performance is characterized over a range of gasifier temperatures and coal moisture contents. Coal consumption and syngas production rates are determined based on maximizing carbon utilization with the available hydrogen from a 600 MW_t advanced reactor operating at a reactor outlet temperature of 900°C. Overall syngas production efficiency is determined as a ratio of the heating value of the produced syngas to the sum of the heating value of the coal plus the high-temperature reactor heat input.

2 System Model Description

UNISIM [8] process analysis software was used to evaluate the syngas production system performance. UNISIM software is a derivative of the HYSYS process analysis software. Using this code, a detailed process flow sheet has been developed that includes the major components that would be present in an actual syngas production plant such as pumps, compressors, heat exchangers, turbines, etc. These devices are included as standard UNISIM components. However, since the electrolyzer is not a standard UNISIM component, a custom electrolysis model was developed to handle steam electrolysis [9] for incorporation into the overall process flow sheet. UNISIM inherently ensures mass and energy balances across all components and it includes thermodynamic data for all chemical species. Figure 1 shows a process flow diagram for a nuclear-reactor-driven HTE process coupled to a syngas production plant. The process flow diagram presented in Fig. 1 is taken directly from the UNISIM graphical user interface.

A very-high-temperature-gas reactor (VHTGR) with a helium recuperated Brayton power cycle operating at a 53.2% electrical conversion efficiency was selected as the power source for the combined electrolysis and syngas production plant [10]. The model for the power cycle is shown at the bottom right of Fig. 1. The primary helium coolant (stream 11) exits the reactor

---

Manuscript received October 21, 2008; final manuscript received November 10, 2008; published online April 14, 2009. Review conducted by Dillip R. Ballal. Paper presented at the Fourth International Topical Meeting on High Temperature Reactor Technology (HTR2008), Washington, DC, September 28–October 1, 2008.

Copyright © 2009 by ASME

Downloaded 02 Jun 2010 to 171.66.16.109. Redistribution subject to ASME license or copyright; see http://www.asme.org/terms/Terms_Use.cfm

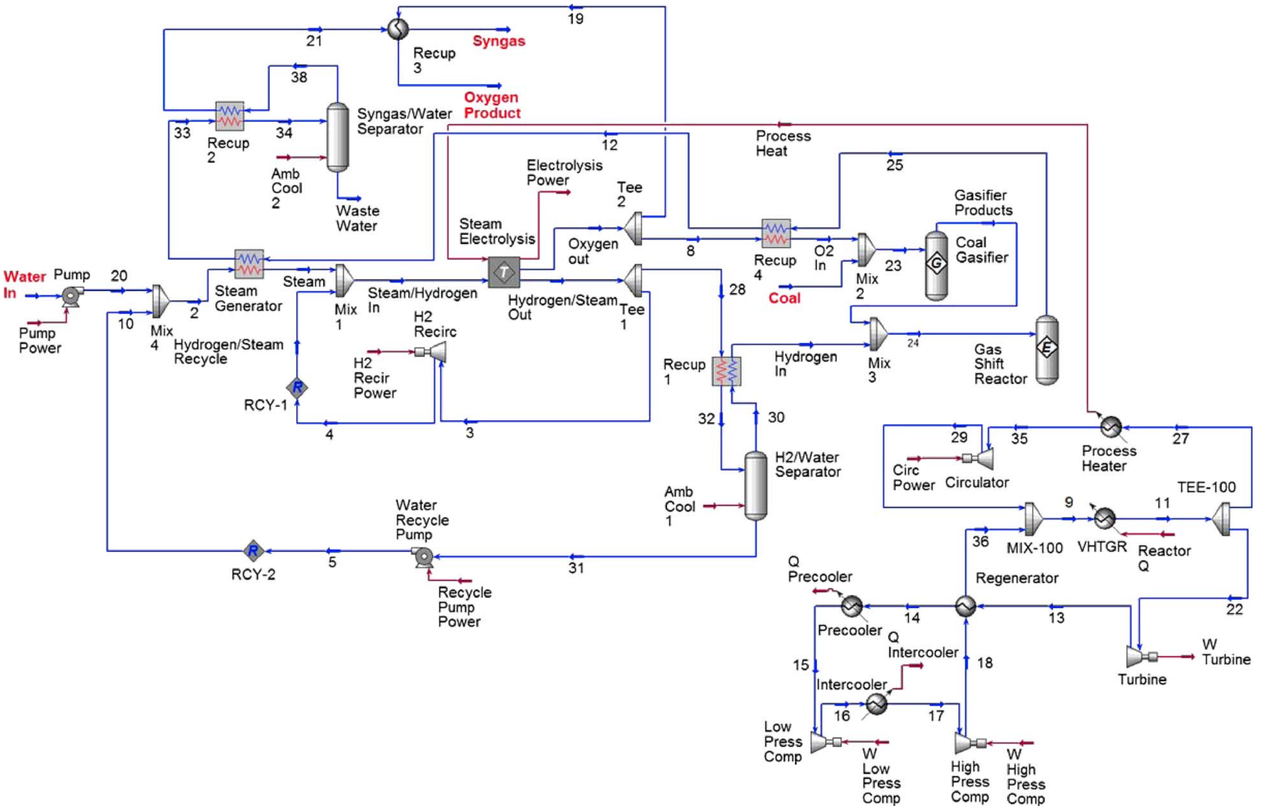

Fig. 1 Process flow diagram for helium-cooled reactor/direct Brayton/HTE syngas production plant

(VHTGR) at 900°C and is split at TEE-100, with approximately 95% of the flow going to the power cycle and the remainder ($\leq 5\%$) diverted to a process heater that supplies heat directly to the electrolysis stack to maintain the electrolyzer operating temperature of 800°C. The cooler helium leaving the process heater (stream 35) is compressed to the reactor inlet pressure and mixed with the primary coolant returning to the reactor. The helium flow from TEE-100 to the power cycle passes through a power turbine, producing electricity to drive the electrolysis process. This helium exits the power turbine at a reduced pressure and temperature and then passes through a recuperator and precooler where it is further cooled before entering the low-pressure compressor. To improve compression efficiency, the helium is again cooled in an intercooler before entering the high-pressure compressor. The helium exits the high-pressure compressor at a pressure that is slightly higher than the reactor operating pressure of 7 MPa. The coolant then circulates back through the recuperator where the recovered heat raises its temperature to the reactor inlet temperature of 540°C, completing the power cycle.

The water that feeds the electrolysis process enters at the left of Fig. 1 at a temperature of 15.6°C and is pressurized to the process pressure of approximately 2.9 MPa. Downstream of the pump, the feed water flow is combined with recycled condensate from the H_2/water separator tank (Mix 4) and vaporized in a steam generator. At Mix 1, recycled hydrogen and steam from the electrolyzer outlet is added to the electrolysis feed stream to maintain reducing conditions at the steam-hydrogen electrode. The inlet steam-hydrogen mixture (90% steam by volume) then enters the solid oxide electrolysis cell (SOEC) stack, where the steam is electrolytically reduced, yielding hydrogen and oxygen.

The electrolyzer model used in UNISIM was developed by the INL specifically for the analysis of HTE hydrogen production processes and related concepts being developed and evaluated at the laboratory [9]. The model calculates the electrolyzer heat requirements, hydrogen and oxygen production rates, and associated product stream conditions. An embedded spreadsheet is used to calculate the Nernst potential, operating voltage, and current and electrolysis powers based on an integral electrolyzer model.

Downstream of the electrolyzer, a portion of the oxygen product (stream 8) passes through a recuperative heat exchanger and is mixed with the coal feedstock entering the gasifier where the coal is gasified to produce a mixture of hydrogen, carbon monoxide, carbon dioxide, steam, and trace amounts of other gas contaminates. The remaining oxygen (approximately 38%) passes through a recuperator (Recup 3) where a portion of its heat is utilized to heat the syngas product stream. This excess oxygen product stream is a valuable commodity that can either be sold or used for other process applications.

The hydrogen and steam mixture leaving the electrolyzer is split at Tee 1 with a little over 11% of the total flow recycled back to the electrolyzer inlet to maintain reducing conditions at the steam electrode as described earlier. The remaining flow (approximately 89%) passes through a recuperator (Recup 1) where the hydrogen and steam mixture is cooled prior to entering the hydrogen/water separator (stream 32). Condensate from the hydrogen/water separator is recycled (water recycle pump) back to the process inlet where it is combined with the feed water flow (Mix 1). Dry hydrogen from the hydrogen/water separator (stream 30) then passes back through the recuperative heat exchanger (Recup 1) where a portion of the heat lost in the condensation process is recovered. This hydrogen stream is then mixed with the product gas from the coal gasifier (Mix 3) to produce a hydrogen-rich gas mixture (stream 24). This hydrogen-enriched gas mixture then passes through the reverse shift reaction where the majority of excess carbon dioxide is converted to carbon monoxide and steam, with plenty of hydrogen remaining. The resulting syngas stream exiting the gas shift reactor (stream 25) has a hydrogen-to-carbon monoxide molar ratio of about 2:1, with less than 10% of the total carbon (on a mass basis) in the form of carbon dioxide. The hydrogen-rich syngas mixture then passes through a recupera-

Downloaded 02 Jun 2010 to 171.66.16.109. Redistribution subject to ASME license or copyright; see http://www.asme.org/terms/Terms_Use.cfm

tor (Recup 4) where a portion of its heat is transferred to the oxygen feeding the coal gasifier. The syngas then passes through the steam generator where it is further cooled by transferring its heat to the electrolyzer feed water as described earlier. After leaving the steam generator, the syngas/steam mixture (stream 33) passes through another recuperative heat exchanger where it is cooled prior to entering the syngas/water separator, where most of the water is condensed to achieve the desired low moisture content for the final syngas product stream. After exiting the syngas/water separator tank, the syngas again passes through the syngas recuperative heat exchangers (Recup 2 and 3) where the syngas is heated to the desired temperature of approximately 450°F (232°C) for the production of liquid fuel using the Fisher–Tropsch synthesis process.

3 Parametric Studies

Parametric studies were performed to investigate the impact of gasifier temperature and coal moisture content on carbon utilization and syngas production efficiency. These two studies and their results are discussed separately below.

3.1 Gasifier Temperature. A parametric study was performed in which the gasification temperature was varied from 1477 K to 1866 K. For this temperature range, chemical equilibrium was assumed during the gasification process and the gasifier is modeled as a Gibbs reactor. A number of potential products were considered for the gasifier including nitrates, sulfates, and natural gas components, but the primary products were water, hydrogen, oxygen, carbon monoxide, and carbon dioxide with trace amounts of nitrogen, hydrogen sulfide, and ammonia.

For the parametric study, the following constraints were applied.

- All heat exchangers have a minimum approach of 20°C except Recup 4, which was set to 50°C by adjusting the temperature of the oxygen into the coal gasifier.
- The adiabatic efficiency for the power cycle turbine is 93%, the power cycle compressors have efficiencies of 88%, and all other compressors and pumps have efficiencies of 75%.
- The mass flow of the coal was adjusted until the molar ratio of hydrogen to carbon monoxide in the syngas product was 2.0.
- The steam electrolysis process is isothermal with an operating temperature of 800°C, cell area specific resistance of 0.4 Ω cm^2, a current density of 0.24, and a cell area of 225 cm^2.
- All of the 600 MW$_t$ heat from the reactor is dedicated for syngas production, with an associated requirement of 110,000 electrolysis cells.
- The stream entering the electrolysis process is 90% steam and 10% hydrogen by mole fraction.
- The streams exiting the process are 10% steam and 90% hydrogen on the cathode side and 100% oxygen on the anode side.

To optimize the process, two figures of merit were considered: syngas production efficiency and carbon utilization. The syngas production efficiency is defined as the ratio of the heating value of the syngas produced by the process to the sum of the heat addition to the process (total thermal power rating of the reactor for a fully dedicated plant) plus the heating value of the coal that is consumed in the process.

$$\eta_{\rm syn} = \frac{\dot{N}_{\rm H_2}\mathrm{LHV}_{\rm H_2} + \dot{N}_{\rm CO}\mathrm{LHV}_{\rm CO}}{\dot{Q}_{\rm th,reactor} + \dot{N}_{\rm coal}\mathrm{LHV}_{\rm coal}} \qquad (2)$$

For this analysis the lower heating value (LHV) of the coal and the syngas are used to calculate the thermal power of each.

The second figure of merit for the process is the carbon utilization, defined as the mass percentage of carbon from the coal that is ultimately transferred to the carbon monoxide in the syngas. The mass flow rate of the carbon in the coal is found as the product of the mass flow rate of the dry ash-free coal, the number of carbon moles per mole of dry ash-free coal, and the molecular weight of carbon divided by the molecular weight of the dry-ash free coal.

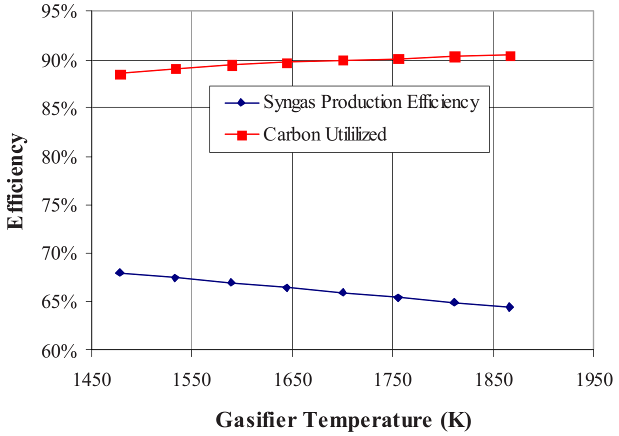

Fig. 2 Syngas production efficiency and carbon utilization as a function of gasification temperature

$$\dot{m}_{\rm C,coal} = \dot{m}_{\rm coal\text{-}dry,af}\, n_{\rm C\rightarrow coal\text{-}dry,af}\left(\frac{\mathrm{MW_C}}{\mathrm{MW_{coal\text{-}dry,af}}}\right) \qquad (3)$$

Similarly, the carbon flow in the syngas is found as the product of the mass flow of the carbon monoxide in the syngas, the number of moles of carbon per mole of carbon monoxide and the molecular weight of carbon divided by the molecular weight of carbon monoxide.

$$\dot{m}_{\rm C,syngas} = \dot{m}_{\rm CO,syngas}\, n_{\rm C\rightarrow CO}\left(\frac{\mathrm{MW_C}}{\mathrm{MW_{CO}}}\right) \qquad (4)$$

Finally, the carbon utilization is found by dividing Eq. (4) with Eq. (3) as follows:

$$U_{\rm C} = \frac{\dot{m}_{\rm C,syngas}}{\dot{m}_{\rm C,coal}} = \left(\frac{\dot{m}_{\rm CO,syngas}}{\dot{m}_{\rm coal\text{-}dry,af}}\right)\left(\frac{\mathrm{MW_{coal\text{-}dry,af}}}{\mathrm{MW_{CO}}}\right)\left(\frac{n_{\rm C\rightarrow CO}}{n_{\rm C\rightarrow coal\text{-}dry,af}}\right) \qquad (5)$$

For this analysis the number of moles of carbon per mole of dry ash-free coal and the number of moles of carbon per mole of carbon dioxide are both equal to 1.0, and Eq. (5) reduces to

$$U_{\rm C} = \left(\frac{\dot{m}_{\rm CO,syngas}}{\dot{m}_{\rm coal\text{-}dry,af}}\right)\left(\frac{\mathrm{MW_{coal\text{-}dry,af}}}{\mathrm{MW_{CO}}}\right) \qquad (6)$$

The coal type assumed for this analysis is lignite. The lignite and ash are modeled as hypothetical components in UNISIM. The lignite UNISIM component has a specified atomic breakdown of the carbon, hydrogen, oxygen, nitrogen, and sulfur. The heat of combustion for the lignite is also known. This information is sufficient to break down the lignite in the gasifier to produce the expected products. The ash is modeled as silica with a known heat capacity. It is used to capture heat in the gasifier that would otherwise be used for gasification of the lignite. The ash remains in the gasifier.

3.2 Gasifier Temperature Sensitivity Results. The results of the gasifier temperature parametric study are presented in Fig. 2, which shows the syngas production efficiency and carbon utilization as a function of gasification temperature. As the gasification temperature increases, the syngas production efficiency decreases slightly from 68.0% to 64.4%. The decrease in efficiency is primarily due to increased heat losses in the system. The exit tem-

Downloaded 02 Jun 2010 to 171.66.16.109. Redistribution subject to ASME license or copyright; see http://www.asme.org/terms/Terms_Use.cfm

perature of the syngas increases from 460 K to 578 K. The ambient cooling load at the syngas/water separator increases from 20 MW to 30 MW as the temperature increases.

Carbon utilization increases slightly from 88.6% to 90.5% as the temperature increases. At higher gasification temperatures, more carbon dioxide breaks down to carbon monoxide. Also, the syngas has a higher percentage of hydrogen at higher gasification temperatures. The mole fraction of hydrogen increases from 0.635 to 0.640. The mole fraction of carbon monoxide increases from 0.318 to 0.320 and carbon dioxide decreases from 0.040 to 0.034.

Although contaminants such as hydrogen sulfide and ammonia are formed, in this analysis contaminant removal is not considered. The process was designed to prevent contaminants from entering the electrolysis process.

The current analysis assumed a lignite coal feedstock with relatively high-moisture-content (approximately 36.2% by mass). This relatively high-moisture-content, compared with other U.S. coals makes it more difficult to fully utilize the carbon content of the coal. In the current analyses, the coal was gasified without attempting to remove any of the moisture from the coal or product gas from the gasifier. Dry hydrogen was then mixed with the product gas from the coal gasifier and was fed to the reverse gas shift reactor. This process resulted in 90.5% carbon utilization with a syngas production efficiency of 64.4% at a gasifier temperature of 1866 K. At this syngas production efficiency, approximately 55% of the energy input to the process (denominator of Eq. (2)) is provided by the nuclear reactor, and the remaining 45% is the heating value of the coal consumed in the process. In terms of carbon utilization, these results are extremely good compared with conventional processes, where only about 30% of the carbon in the coal ends up in the product syngas (i.e., close to 70% is converted to carbon dioxide that must be either sequestered or released to the environment). However, significantly higher carbon utilization (~97% or greater) can be achieved by reducing the moisture content of the feed to the reverse gas shift reactor. With less moisture (H_2O) in the feed stream, more carbon dioxide and hydrogen combine to produce equilibrium carbon monoxide and H_2O in the syngas exiting the reverse shift gas reactor. To achieve higher carbon utilization and syngas efficiencies, with high-moisture-content coals, the coal would either have to be dried before gasification or another step has to be added to the syngas production process to remove the water from the gasifier product stream.

3.3 Coal Moisture Content. To evaluate the influence of coal moisture content on carbon utilization and syngas production efficiency, the UNISIM process flow model in Fig. 1 and the process constraints identified previously were again used, but in this case, the moisture content of the coal fed to the gasifier was varied between 16.1% and 36.2%. For coal moisture contents of 16.1%, 30.4%, and 36.2%, actual coal analyses from Ref. [11], corresponding to bituminous, sub-bituminous, and lignite coals from various regions within the United States were used. To fill the gap in moisture content between 16.1% and 30.4%, the moisture content of the sub-bituminous coal was reduced from 30.4% to values of 25% and 20% to allow evaluation of the impact of moisture content in this intermediate range.

In each of the calculations, the reactor power was again fixed at 600 MW with a reactor outlet temperature of 900°C. All of the hydrogen produced in the electrolysis process was again used in the reverse shift reaction to convert carbon dioxide to carbon monoxide, and any oxygen not used by the gasifier is assumed to be used to heat the syngas product stream and then stored for sale as a valuable commodity. The initial gasifier temperature was fixed at 1700 K (1427°C) but, as discussed below, was gradually increased as the moisture content of the coal decreased to allow reasonable operating conditions for the heat exchangers used in the process. In all the analyses a hydrogen-to-carbon monoxide molar ratio of 2:1 was maintained for the syngas.

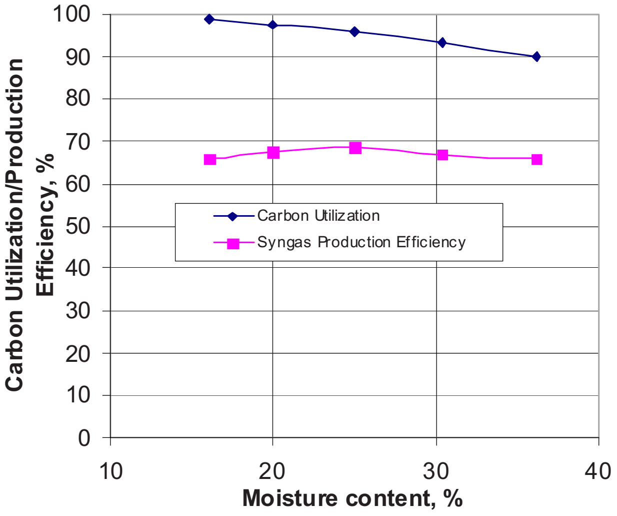

Fig. 3 Carbon utilization and syngas production efficiency as a function of coal moisture content

3.4 Coal Moisture Content Sensitivity Results. Figure 3 shows the influence of the coal moisture content on carbon utilization and syngas production efficiency. As seen in Fig. 3, carbon utilization increases with decreased moisture content, reaching a value of 98.8% for a moisture content of 16.1%. The syngas production efficiency shown in Fig. 3 also appears to increase as the moisture content is reduced, but peaks at about 68.8% for a coal moisture content of 25%. The drop in syngas production efficiency as the coal moisture content is reduced below 25% is the result of the need to increase the gasifier temperature to maintain a minimum heat exchanger approach temperature for the steam generator of approximately 20°C. This drop in syngas production efficiency is consistent with the early results in Fig. 2, which also show a drop in syngas production efficiency as the gasifier temperature increased.

Figure 4 shows the calculated gasifier and syngas outlet temperature as a function of coal moisture content. As seen in the figure, the gasifier temperature can be maintained at 1700 K at moisture contents above 25%, but must be increased as the moisture content drops below 25% to maintain a minimum approach temperature of 20°C for the steam generator. Figure 4 also shows that the syngas outlet temperature drops from 510 K at a coal

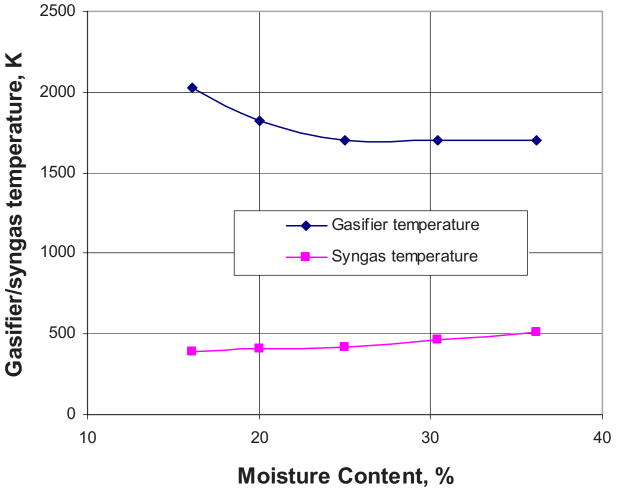

Fig. 4 Gasifier and syngas temperatures as a function of coal moisture content

Downloaded 02 Jun 2010 to 171.66.16.109. Redistribution subject to ASME license or copyright; see http://www.asme.org/terms/Terms_Use.cfm

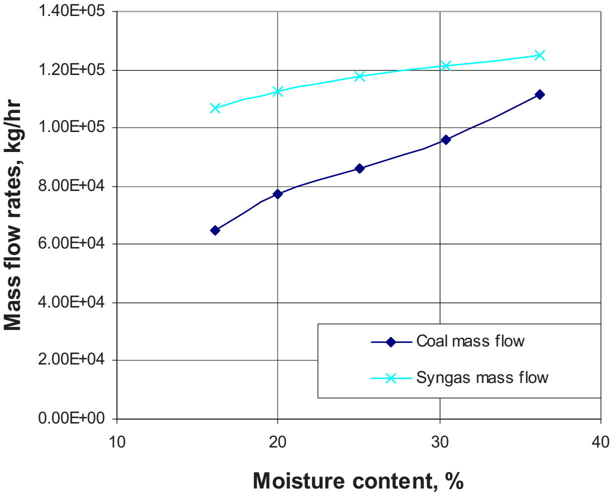

Fig. 5 Coal and syngas mass flow rates as a function of coal moisture content

moisture content of 36.2% to 392 K at a coal moisture content of 16.1%. This calculated temperature decrease was necessary to maintain a minimum approach temperature of 20°C at the Recup 4 heat exchanger shown in Fig. 1. Nevertheless, this temperature range for the syngas product stream is still within the acceptable temperature range of the Fischer–Tropsch synthesis process.

Finally, Fig. 5 shows the mass flow rates for coal and syngas as a function of coal moisture content. For a fixed reactor power and a fixed number of electrolysis cells, the overall syngas production rate increases with increased coal moisture content, but at the expense of a reduction in carbon utilization and syngas production efficiency (as shown previously in Fig. 3). The reduction in syngas production efficiency is also apparent in Fig. 5, which shows that the mass flow of syngas being produced increases at a slower rate than the mass flow of coal being consumed as the moisture content of the coal increases.

4 Conclusions

Production of syngas from coal with supplemental hydrogen and oxygen from nuclear reactor has been analyzed. The nuclear reactor under consideration is a high-temperature helium-cooled reactor that is used primarily to provide power for hydrogen production via high-temperature electrolysis. The supplemental hydrogen enables conversion of most of the carbon dioxide to carbon monoxide, with enough excess hydrogen to produce a syngas product stream with a hydrogen/carbon monoxide molar ratio of about 2:1, ideal for subsequent conversion to liquid fuel via the Fischer–Tropsch process with a cobalt catalyst. Oxygen for the gasifier is also provided by the high-temperature electrolysis process. The results of the analysis predict 90.5% carbon utilization with a syngas production efficiency of 64.4% at a gasifier temperature of 1866 K for the high-moisture-content lignite coal considered.

Parametric studies show that carbon utilization increases with increased gasifier temperature, while syngas production efficiency decreases slightly with increased gasifier temperature. Carbon utilization was also found to increase with lower moisture coals. A maximum carbon utilization value of 98.8% was obtained for the low moisture content bituminous coal (16.1% moisture) at a gasifier temperature of 2030 K and a syngas production efficiency of 65.7%.

Acknowledgment

This work was supported by the Idaho National Laboratory, Laboratory Directed Research and Development program and by the U.S. Department of Energy, Office of Nuclear Energy, Nuclear Hydrogen Initiative Program. This manuscript has been authored by Battelle Energy Alliance, LLC under Contract No. DE-AC07-05ID14517 with the U.S. Department of Energy.

Nomenclature

η_{syn} = syngas production efficiency
$\dot{m}$ = mass flow rate, kg/s
MW = molecular weight, gm/mol
$\dot{N}$ = molar flow rate, mol/s
LHV = low heating value, J/mol
$\dot{Q}_{\mathrm{th,reactor}}$ = reactor thermal power, MW
U_{C} = carbon utilization

References

[1] Forsberg, C. W., 2005, "Nuclear Hydrogen for Production of Liquid Hydrocarbon Transport Fuels," *Proceedings of the AIChE Annual Meeting*, pp. 7988–7995.
[2] Schultz, K., Bogart, S. L., and Noceti, R. P., 2007, "Synthesis of Hydrocarbon Fuels Using Renewable and Nuclear Energy," *Proceedings of the International Topical Meeting on the Safety and Technology of Nuclear Hydrogen Production, Control, and Management*, ANS Embedded Topical.
[3] Smith, R. G., 2000, "Eastman Chemical Company Kingsport Plan Chemicals From Coal Operations 1983–2000," 2000 Gasification Technologies Conference, San Francisco, CA, Oct. 8–11.
[4] Forsberg, C. W., 2007, "Is Hydrogen the Future of Nuclear Energy?" *Proceedings of the International Topical Meeting on the Safety and Technology of Nuclear Hydrogen Production, Control, and Management*, ANS Embedded Topical.
[5] O'Brien, J. E., Stoots, C. M., Herring, J. S., Lessing, P. A., Hartvigsen, J. J., and Elangovan, S., 2005, "Performance Measurements of Solid-Oxide Electrolysis Cells for Hydrogen Production From Nuclear Energy," ASME J. Fuel Cell Sci. Technol., **2**, pp. 156–163.
[6] O'Brien, J. E., Stoots, C. M., Herring, J. S., and Hartvigsen, J. J., 2006, "Hydrogen Production Performance of a 10-Cell Planar Solid-Oxide Electrolysis Stack," ASME J. Fuel Cell Sci. Technol., **3**, pp. 213–219.
[7] Cherry, R. S., and Wood, R. A., 2006, "Use of a Nuclear High-Temperature Gas Reactor in a Coal-to-Liquids Process," INL External Report No. INL/EXT-06-11667.
[8] UNISIM Design, R360 Build 12073, Honeywell International Inc.
[9] O'Brien, J. E., Stoots, C. M., and Hawkes, G. L., 2005, "Comparison of a One-Dimensional Model of a High-Temperature Solid-Oxide Electrolysis Stack With CFD and Experimental Results," ASME International Mechanical Engineering Congress and Exposition, Orlando, FL, Nov. 5–11.
[10] O'Brien, J. E., McKellar, M. G., and Herring, J. S., 2008, "Commercial-Scale Performance Predictions for High-Temperature Electrolysis Plants Coupled to Three Advanced Reactor Types," *Proceeding of the 2008 International Congress on Advances in Nuclear Power Plants*, ICAPP08, Anaheim, CA, June.
[11] Probstein, R. F., and Hicks, R. E., 2006, *Synthetic Fuels*, Dover, Mineola, NY.

Downloaded 02 Jun 2010 to 171.66.16.109. Redistribution subject to ASME license or copyright; see http://www.asme.org/terms/Terms_Use.cfm

Development of High-Temperature Transport Technologies for Liquid Cadmium in Pyrometallurgical Reprocessing

Takatoshi Hijikata

Tadafumi Koyama

Nuclear Technology Research Laboratory,
Central Research Institute of Electric Power
Industry (CRIEPI),
2-11-1 Iwado Kita, Komae-shi,
Tokyo 201-8511, Japan

Pyrometallurgical reprocessing is one of the most promising technologies for the advanced fuel cycle with favorable economic potential and intrinsic proliferation-resistance. The feasibility of pyrometallurgical reprocessing has been studied through many laboratory-scale experiments. Hence the development of the engineering technology necessary for pyrometallurgical reprocessing is a key issue for its industrialization. The development of high-temperature transport technologies for molten salt and liquid cadmium is crucial for pyrometallurgical processing; however, there have been a few transport studies on high-temperature fluids. In this study, a metal transport test rig was installed in an argon glove box with the aim of developing technologies for transporting liquid cadmium at approximately 773 K. The transport of liquid Cd using gravity was controlled by adjusting the valve. The liquid Cd was transported by a suction pump against a 0.93 m head and the transport amount of Cd was well controlled with the Cd amount and the position of the suction tube. The transportation of liquid cadmium at approximately 700 K could be controlled at a rate of 0.5–2.5 dm^3/min against a 1.6 m head using a centrifugal pump. [DOI: 10.1115/1.3079608]

1 Introduction

Dry (i.e., nonaqueous) processing technologies are currently being focused on in many countries for removing actinides from the fuel cycle because of their favorable economic potential [1] and intrinsic proliferation-resistance due to the inherent difficulty of using these technologies to extract weapons-usable plutonium [2]. Pyrometallurgical reprocessing is one of the most attractive dry processing technologies because Pu is not separated from the other actinides at any step of the process [3,4]. This property enables us to enhance the intrinsic proliferation-resistance and to recover long-lived transuranium elements for transmutation in fast reactors without further treatment. CRIEPI has been studying these processes since 1985 and has carried out joint studies with groups including ANL, JRC-ITU, and JAEA. The feasibility of pyrometallurgical reprocessing has been demonstrated through many laboratory-scale experiments [5–7].

The development of the engineering technology required for pyrometallurgical reprocessing is a key issue for its industrial realization. The development of high-temperature transport technologies for molten salt and liquid cadmium (Cd) is a crucial prerequisite; however, there have been a few transport studies on high-temperature fluids [8–12].

In this study, the transport characteristic of liquid cadmium was determined using experimental setups that consisted of pumps, inclined transportation pipes, and tanks.

2 Transport Technologies of High Temperature Fluids for Pyrometallurgical Reprocessing

Pyrometallurgical reprocessing mainly involves electrorefining, cathode processing, and injection casting, and a salt treatment system (waste management), as shown in Fig. 1. The electrorefining is carried out to dissolve spent fuel and to recover the actinides on the cathodes. Uranium metal and uranium-plutonium-cadmium alloy are deposited on the cathodes. These deposits are entrained with salt and cadmium, respectively. The cathode processing separates the salt or Cd from the deposits by distillation. The injection casting produces the metallic fuel by casting a uranium-plutonium-zirconium alloy. The salt treatment system separates the fission products (FPs) from the molten salt in the electrorefiner for recycle use. The removed FPs are occluded in zeolite and are solidified with glass matrix.

In the pyrometallurgical reprocessing, the transport technologies of high-temperature fluids are required for the electrorefiner and the salt treatment system (the reductive extraction and the zeolite column). As for the molten salt transport, the molten salt with FPs is transported from the electrorefiner to the zeolite column through the reductive extraction. The treated salt is transported back from the zeolite column to the electrorefiner through back extraction. As for the liquid Cd transport, the liquid Cd-actinide alloy in the Cd cathode is transported to the distillation crucible of the cathode processor while pure Cd, obtained by the distillation of Cd-actinide alloy, is transported back to the cathode crucible [13].

As for the molten salt transport, the flow rate and the head among the processes were evaluated based on the design of the feasibility study on commercialized fast reactor cycle system [14]. 67 dm^3 of molten salt needs to be transported from the electrorefiner to the reductive extraction every 6 days. If the molten salt could be transported to the reductive extraction within 1 h, the flow rate would be approximately 1 dm^3/min against a 2 m head. In the reductive extraction, if the molten salt could be treated within 1 day, the flow rate would be from 30 cm^3/min to 45 cm^3/min against a 1 m head. In the zeolite column, if 56 dm^3 of the treated salt in the reductive extraction could be treated within 1 day, the flow rate would be approximately 40 cm^3/min.

Manuscript received September 29, 2008; final manuscript received October 15, 2008; published online April 15, 2009. Review conducted by Dilip R. Ballal. Paper presented at the 16th International Conference on Nuclear Engineering (ICONE16), Orlando, FL, May 12–15, 2008.

Copyright © 2009 by ASME

Downloaded 02 Jun 2010 to 171.66.16.109. Redistribution subject to ASME license or copyright; see http://www.asme.org/terms/Terms_Use.cfm

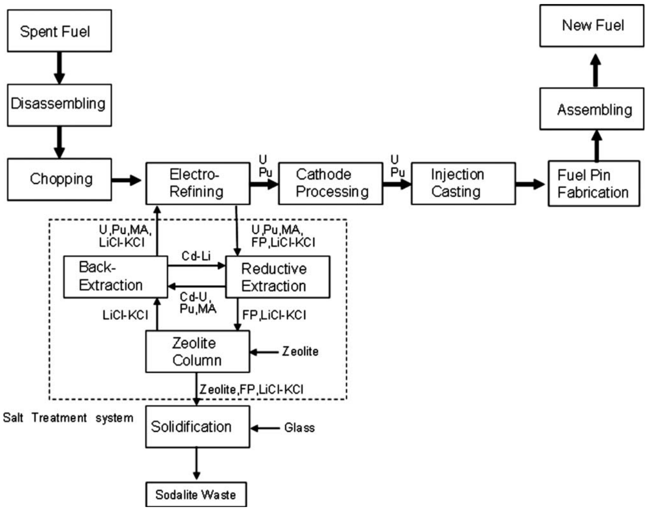

Fig. 1 Flow diagram of pyrometallurgical reprocessing

3 m of the maximum head is required because the column length is 0.61 m and the depth of the electrorefiner is 1 m [14].

As for the liquid Cd transport, the flow rate and the head were evaluated between the electrorefiner and the cathode processor based on the design of the feasibility study [14]. The Cd cathode recovers 5.6 kg of actinide everyday. The concentration of actinides must be less than the saturation limit in order to transport the Cd-actinide alloy in the liquid phase. The amount of Cd required would be 35 dm^3 since the actinide has a concentration of 2 wt % in Cd. If this alloy should be transported to the cathode process within 1 h, the flow rate and the maximum head of the pump are evaluated at approximately 0.6 $\mathrm{dm}^3/\mathrm{min}$ and 3 m, respectively.

Consequently, in the pyrometallurgical reprocessing, the required transport capacities for both molten salt and liquid Cd are evaluated to be >1 $\mathrm{dm}^3/\mathrm{min}$ against a 3 m head.

The transport technologies for high-temperature fluids were compared in Table 1. In addition to these pumps, the gravitational transport was considered as basic methods for transports.

The suction pump and the electromagnetic pump were favorable because they have no moving parts to be the maintenance. However, the capacity of the electromagnetic pump was too big to apply for pyrometallurgical reprocessing. The suction pump was employed to be applicable; however, there are no experiment.

Table 1 Comparison of the pump-based transport methods for high-temperature fluids

Type		Fluid	Flow rate head
Nonmachinery pump	Suction pump	Cd	- <1.3 m [a]
		Salt	- <6.5 m [a]
	Electromagnetic pump	LM[b]	<227 $\mathrm{m}^3/\mathrm{min}$ 1.7 MPa [15]
		Salt	
Machinery pump	Centrifugal pump	Cd	- -
		Salt	4–5.5 $\mathrm{dm}^3/\mathrm{min}$ 1.5 m [8]
	Reciprocating pump	Cd	- -
		Salt	14–2 $\mathrm{dm}^3/\mathrm{min}$ 0.02–0.07 MPa [12]

[a] The theoretical maximum head was calculated from the vacuum pressure and density.

[b] LM denotes liquid metal.

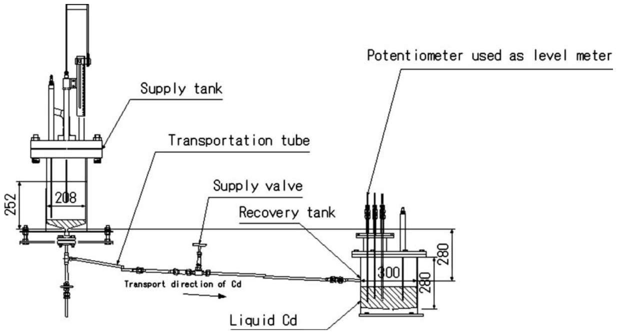

Fig. 2 Apparatus used in gravitation transport experiments

As for the machinery pumps, the centrifugal pump and the reciprocating pump were applied for molten salt [8,12]. However, long-term integrity of checking the valve against high-temperature liquid is a concern for the reciprocating pump, and the centrifugal pump is considered as a favorable method of machinery pump.

Consequently, the transport of the molten salt and the liquid Cd were tested for gravity, suction pump, and centrifugal pump. The results for molten salt have been reported elsewhere [16]. Here the results for liquid Cd will be reported.

3 Experiments on Liquid Cadmium Transport Using Gravity

3.1 Experimental. *Reagents*. Cadmium with purity greater than 99.99% was purchased from Nippon Mining & Metal Co. (Tokyo, Japan).

Experimental apparatus. The gravitation transportation experiments for liquid cadmium were carried out with the apparatus shown in Fig. 2. It should be noted that the figure ignored heaters and these insulators around the tanks, the valve, and the tubes.

The apparatus was installed in a large argon glove box (W: 7 m, D: 2 m, and H: 2.5–3 m). The liquid Cd was transported from the supply tank to the recovery tank. The supply tank had a 208 mm inner diameter and is 252 mm high. The recovery tank had a 300 mm inner diameter and is 280 mm high. The center of the bottom of the supply tank was connected to the transportation tube, which had a 10.1 mm inner diameter. The transportation tube had a down ward slope of 2 deg. A supply valve (Swagelok SS-8-UW) was installed to control the flow. The height from the bottom of the supply tank to the outlet was 280 mm and the length of the tube was 2.2 m. The supply tank, the recovery tank, and the transportation tube were maintained at approximately 773 K. The temperature of the liquid Cd was measured in the supply tank. The level of liquid Cd in the recovery tank was measured using potentiometer. The flow rate in the tube was measured by the change in the liquid level.

Experimental procedure. 3.9–6.2 dm^3 of liquid Cd was loaded in the supply tank. The supply tank, the recovery tank, and the transportation tube were heated at approximately 773 K. The liquid Cd in the supply tank was maintained at the desired temperature, and then the supply valve was opened by the desired number of turns. The flow rate was measured using a level meter. Table 2 shows the condition of the gravitation transportation experiment.

3.2 Results and Discussion. *Controllability of the flow rate by adjusting the valve opening*. Figure 3 shows the average flow rate of liquid Cd by the gravity. The average flow rate of liquid Cd was controlled between 0.8 $\mathrm{dm}^3/\mathrm{min}$ and 2.6 $\mathrm{dm}^3/\mathrm{min}$ by adjusting the valve opening.

The flow rate could be evaluated using Eq. (1) and the flow coefficient (C_V) [15].

Downloaded 02 Jun 2010 to 171.66.16.109. Redistribution subject to ASME license or copyright; see http://www.asme.org/terms/Terms_Use.cfm

Table 2 Condition of the gravitation transportation experiments

Run	Volume (dm^3)	Cd (K)	Valve opening (turns)	Repeat
G-1	4.5–6.2	740–763	0.5	2
G-2	5.8	751	1.5	1
G-3	4.2–5.6	698–756	2	11
G-4	3.9–5.8	750–760	2.5	3

$$Q = \frac{C_V}{1.17}\sqrt{\frac{P}{\rho}} \tag{1}$$

where Q represents the flow rate (m^3/h), C_V is the flow coefficient, ρ is the relative density of the fluid, and P is the differential pressure of the valve (kg/cm^2).

The differential pressure of the valve was 0.12 kg/cm^2 and C_V was obtained from the data of Swagelok valve in the catalog [17]. The calculated flow rate is shown by the broken line in Fig. 2 and is in good agreement with the experiment data. This suggests that the flow rate can be well controlled by adjusting the valve opening.

The flow was considered to be turbulent because the Reynolds number became between 7800 and 25,000.

Liquid Cd temperature dependence of the flow rate. The relationship between the average flow rate and liquid Cd temperature is shown in Fig. 4. At an opening of 2 turns, the average flow rate was approximately 2.4 dm^3/min and did not change with the decrease in temperature from 756 K to 698 K. This suggests that the liquid Cd temperature has a small effect on the flow rate at an operating temperature of 698–756 K by gravitation transport.

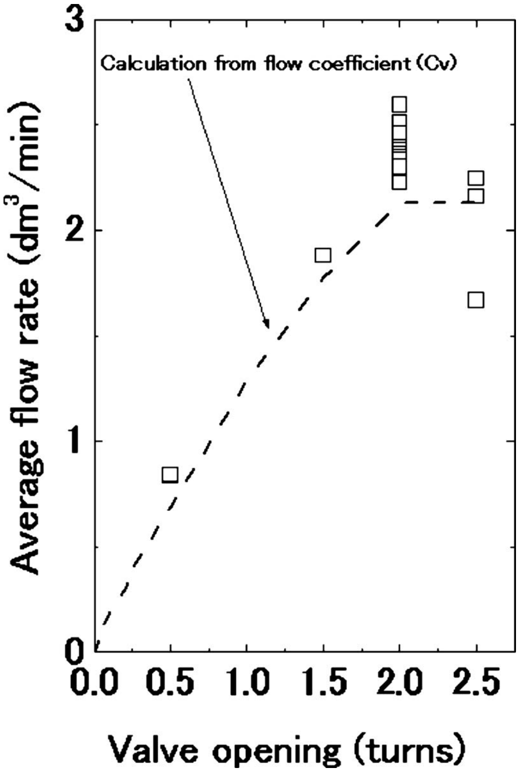

Fig. 3 Relationship between the average flow rate and the valve opening by the gravity

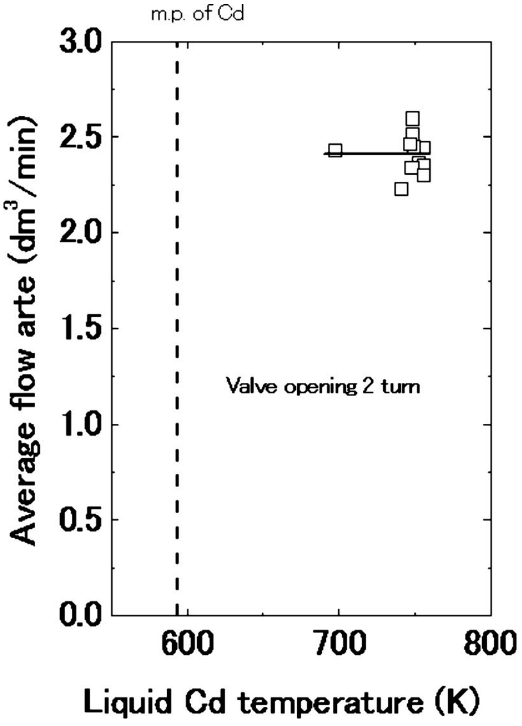

Fig. 4 Relationship between the average flow rate and the liquid Cd temperature with valve opening of 2 turns

4 Experiments on Liquid Cadmium Transport Using Suction Pump

4.1 Experimental. *Reagents.* Cadmium with purity greater than 99.99% was purchased from Nippon Mining & Metal Co.

Experimental apparatus. The transportation experiment for liquid Cd employed the apparatus shown in Fig. 5. It should be noted that the figure ignored heaters and these insulators around the tanks, the valve, and the tubes. The apparatus was installed in a large argon glove box. The apparatus consisted of an outer container, a lifter, a crucible, a division, a vacuum tank, a filter tank, a suction tube, a supply valve, a connecting valve, a vacuum valve, and an argon valve. The vacuum tank had a 220 mm inner diameter and is 295 mm high. The crucible had a 270 mm inner diameter and is 160 mm deep. The suction tube of 10.1 mm inner diameter was immersed in liquid Cd in the crucible. The crucible went up and down to move the position of the suction tube by the lifter. The outer container, the vacuum tank, and the suction tube were maintained at the temperature between 673 K and 773 K by a heater, and the filter tank was not heated. The liquid Cd was pumped up from the crucible to the vacuum tank. The temperature of the liquid Cd was measured in the crucible. The level of the liquid Cd in the crucible was measured using level meter. The height from the inlet of the suction tube to the outlet in the vacuum tank was 930 mm.

Experimental procedure. 1.9–7 dm^3 of liquid Cd was loaded in the crucible. The outer container, the vacuum, and the suction tube were heated at the desired temperature. The crucible was moved to the desired position of the suction tube. The supply valve and the argon valve were closed, and the vacuum valve was opened. After the filter tank was evacuated, the connecting valve was opened for evacuating the vacuum. The vacuum tank was maintained at less than 1 kPa. Then the supply valve was opened by 2.5 turns (fully open) quickly to transport the liquid Cd to the vacuum tank. The flow rate and transport amount were calculated from the change in the liquid Cd level in the crucible. Table 3 shows the condition of the suction transportation experiment.

The evacuated time means the time required for evacuating the

Downloaded 02 Jun 2010 to 171.66.16.109. Redistribution subject to ASME license or copyright; see http://www.asme.org/terms/Terms_Use.cfm

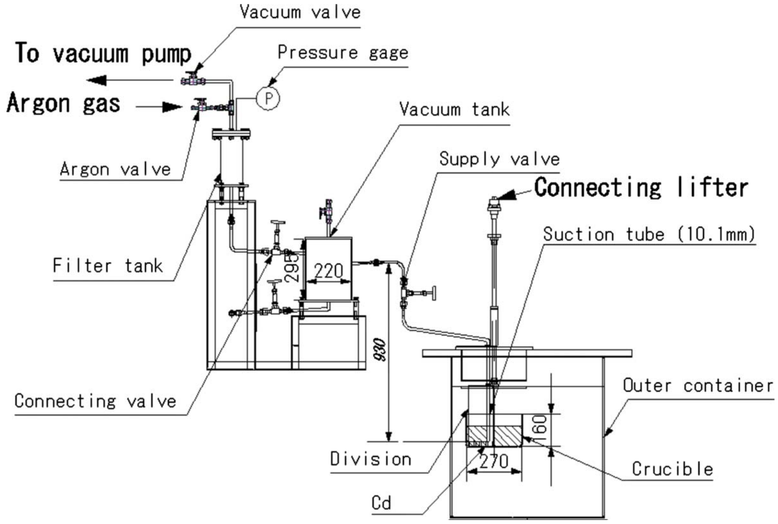

Fig. 5 Apparatus used in suction transport experiments

Table 3 Condition of the suction transportation experiment (position refers to the distance between the inlet of the tube and the bottom of the crucible)

Run	Volume (dm^3)	Cd (K)	Vacuum tank (K)	Position (mm)	Evacuated time (min)	Repeat
V-1	3.3–6.6	718–739	673–773	23	18–98	7
V-2	2.5–7.0	719–739	723–773	33	12–88	9
V-3	1.9–6.7	693–723	723–773	8	65–93	4
V-4	3.3–7.0	718–740	673–723	23	47–170	5
V-5	2.5–7.0	719–741	673–723	33	46–299	10
V-6	2.7–7.0	724–741	673–723	43	45–84	6

vacuum tank. In runs V-3–V-6, the flow rate and the transport amount of the liquid Cd were measured at various distances between the inlet of the suction tube and the bottom of the crucible.

4.2 Results and Discussion. *Theoretical pump head of suction pump*. The theoretical pump head was evaluated by using Eq. (2). The physical properties of the liquid Cd were compared with those of molten LiCl–KCl eutectic salt in Table 4. The density of liquid Cd is much greater than that of molten salt though they had similar viscosities. The boiling point of liquid Cd is lower than that of LiCl or KCl.

$$H_{\text{th}} = \frac{10.2}{\rho} \cdot \left(101 - \left(\frac{P \cdot V_V + 101 \cdot V_T}{V_V + V_T} + P_{\text{Cd}}\right)\right) \tag{2}$$

where H_{th} is the theoretical pump head (cm), ρ is the density of Cd (g/cm^3), P represents the pressure in vacuum tank (kPa), V_V is the volume of the vacuum tank (10.7 dm^3), V_T is the volume of the suction tube (0.10 dm^3), and P_{Cd} is the vapor pressure of Cd (kPa).

Figure 6 shows the relationship between pressure in the vacuum

Table 4 Physical properties of the liquid Cd and molten salt

	Cd [18]	LiCl–KCl
Melting point (K)	594	625 [19]
Boiling point (K)	1040	1655 (LiCl) [19] 1710 (KCl) [19]
Temperature (K)	773	
Density (g/cm^3)	7.8	1.6 [20]
Viscosity (MPa s)	1.6	2.2 [20]

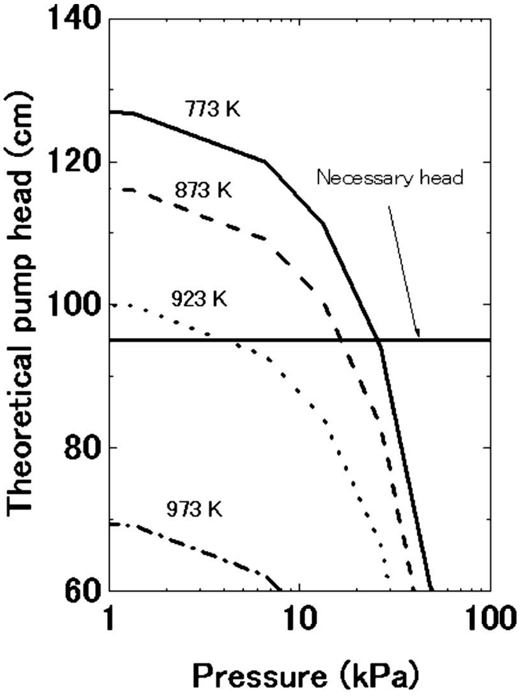

Fig. 6 Relationship between the pressure in vacuum tank and the theoretical pump head in the liquid Cd temperature from 773 K to 973 K

Downloaded 02 Jun 2010 to 171.66.16.109. Redistribution subject to ASME license or copyright; see http://www.asme.org/terms/Terms_Use.cfm

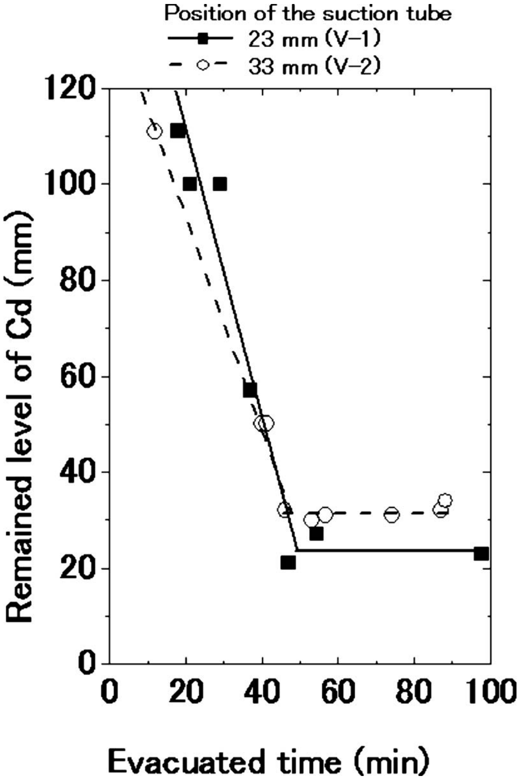

Fig. 7 Relationship between the evacuated time in vacuum tank and the remained level of Cd in the crucible after the transport of Cd at 730 K

tank and theoretical pump head. At 773 K of liquid Cd, the pressure in the vacuum tank should be less than 25 kPa for obtaining the necessary head, which was the height from the inlet of the suction tube to the outlet in the vacuum tank.

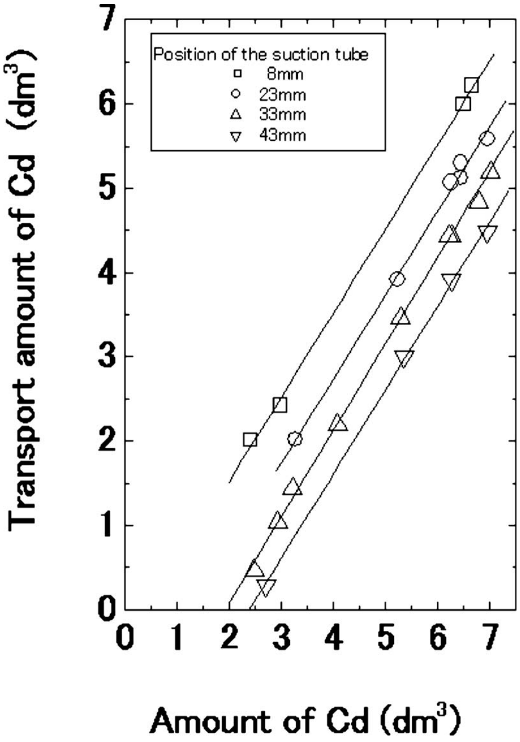

Fig. 8 Relationship between the amount of Cd in the crucible and the transport amount of Cd at 730 K

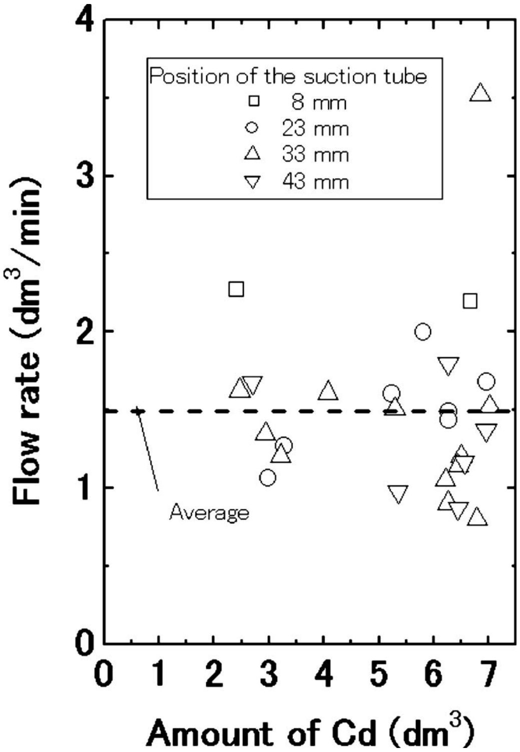

Fig. 9 Relationship between the amount of Cd in the crucible and the flow rate at 730 K

Evacuated time in the vacuum tank. The relationship between the evacuated time in the vacuum tank and the remained level of the liquid Cd in the crucible were measured in runs V-1 and V-2, as shown in Fig. 7. When the evacuated time was more than 45 min, the remained level became a constant level at the positions of 23 mm or 33 mm. This suggests that more than 45 min of evacuated time is required for transporting the liquid Cd by the suction pump. As the suction pump has enough capacity to evacuate the vacuum tank in less than 10 min, the additional time can be attributed to the vaporization of residual Cd in the vacuum tank, the valve, and the tube, and to the pressure loss in the valve and the tube.

Transport amount of Cd and the position of the suction tube. Figure 8 shows the relationship between the amount of Cd in the crucible and the transport amount of Cd.

The transport amount of Cd was increased with the increase in Cd amounts in the crucible. The slope of these relations had 0.55 at all positions of the suction tube (8–43 mm). The transport amount of Cd was controlled with the amount of Cd and the position of the suction tube.

Consequently, the suction pump had a good reproducibility and controllability in the liquid Cd transport.

Flow rate of the suction pump. The relationship between the amount of Cd in the crucible and the flow rate is shown in Fig. 9. The flow rate was scattered from 0.8 dm^3/min to 3.5 dm^3/min, though the supply valve was opened as quickly as possible to minimize the pressure loss of the valve. Consequently, it is difficult to control the flow rate by adjusting the valve.

5 Experiments on Liquid Cadmium Transport Using Centrifugal Pump

5.1 Experimental. *Reagents*. Cadmium with purity greater than 99.99% was purchased from Nippon Mining & Metal Co.

Experimental apparatus. The transportation experiments for liquid cadmium employed the apparatus shown in Fig. 10. It should be noted that the figure ignored heaters and these insulators

Downloaded 02 Jun 2010 to 171.66.16.109. Redistribution subject to ASME license or copyright; see http://www.asme.org/terms/Terms_Use.cfm

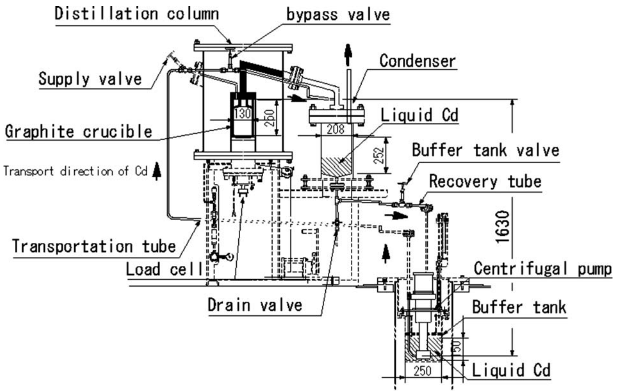

Fig. 10 Apparatus used in the liquid Cd transportation experiment

around the tanks, the valves, and the tubes. The apparatus was installed in a large argon glove box. The apparatus has two combined functions: the distillation of Cd and the transportation of liquid Cd. The liquid Cd was transported to the condenser or the graphite crucible from the buffer tank. The buffer tank had a 250 mm inner diameter and was 150 mm high. The condenser had a 208 mm inner diameter and was 252 mm high. The graphite crucible had a 130 mm inner diameter and was 250 mm high. The centrifugal pump (MAE-V) was manufactured by Sanwa Hydrotech Co. (Osaka, Japan). The impeller had a 50 mm diameter and the rotation speed could be varied between 2100 rpm and 3000 rpm. The transportation tube and drain tube had a 10.1 mm inner diameter and the head was 1.63 m. The buffer tank, condenser, distillation column, and all tubes were maintained at a temperature between 673 K and 923 K by a heater. The temperature of the liquid Cd was measured in the buffer tank. The liquid levels in the buffer tank and the condenser were measured using potentiometers. The flow rate in the tube was measured by the change in the liquid level. Also, during the transport of Cd to the graphite crucible, the flow rate was measured by weighing the crucible using a load cell.

Experimental procedure. 30–60 kg of Cd was loaded into the buffer tank. The buffer tank was heated at 723 K to melt the Cd. The recovery tube, transportation tube, and distillation column were heated at approximately 773 K. The liquid Cd in the buffer tank was maintained at the desired temperature, and then the centrifugal pump was activated after setting the rotation speed. During the transport to the condenser, the bypass valve was opened by the desired number of turns. The flow rate was measured using a level meter. During the transportation to the graphite crucible, the supply valve was opened by a quarter turn and the flow rate was calculated from the weight of the crucible. After transport, the Cd in the condenser was returned to the buffer tank. Table 5 shows the conditions of the Cd transportation experiment. In runs P-1–P-6, the flow rates were measured at a pump rotation speed of 3000 rpm with the valve opened by different numbers of turns. In runs P-7–P-16, the flow rates were measured at various rotation speeds. In run P-17, the liquid Cd was transported to the crucible in the distillation column.

5.2 Results and Discussion. *Controllability of the flow rate by adjusting the valve opening*. At the constant head of 1.63 m, the flow rate was controlled by turning the valve. Figure 11 shows the average flow rate of liquid Cd against the valve opening at the rotation speed of 3000 rpm.

The average flow rate of liquid Cd was controlled between 0.5 $\mathrm{dm}^3/\mathrm{min}$ and 2.5 $\mathrm{dm}^3/\mathrm{min}$ by adjusting the valve. The flow rate was evaluated using Eq. (1) and the flow coefficient (C_V). The differential pressure of the valve was 0.16 $\mathrm{kg}/\mathrm{cm}^2$ and C_V was obtained from the data of the Swagelok valve in the catalog [17]. The calculated flow rate is shown by the broken line in Fig. 11 and is in good agreement with the experiment data. This suggests that the flow rate can be well controlled by adjusting the valve opening.

The flow was considered to be turbulent because the Reynolds number was between 3700 and 24,000. Consequently, the flow of liquid Cd became turbulent in spite of its low velocity. The transportation of a high-density fluid tends to impose a strong shock on the graphite crucible. However, in run P-17, the valve was opened by a quarter turn, and the liquid Cd was transported to the graphite crucible at a rate of 1.3 $\mathrm{dm}^3/\mathrm{min}$ without breaking the crucible.

Controllability of the flow rate by the rotation speed. The relationship between the average flow rate and the rotation speed is shown in Fig. 12. When the valve was opened by more than 1.5 turns, the flow rate could be controlled between 1.0 $\mathrm{dm}^3/\mathrm{min}$ and 2.5 $\mathrm{dm}^3/\mathrm{min}$ by changing the rotation speed. When the valve was opened by 1 turn, the flow rate was between 0.3 $\mathrm{dm}^3/\mathrm{min}$ and 1.5 $\mathrm{dm}^3/\mathrm{min}$ depending on the rotation speed. Also, the liquid Cd was not able to flow at a valve opening of less than 1.0 turn or a rotation speed of less than 2400 rpm because Cd has a high density. Consequently, the flow rate of liquid Cd was controlled at the rotation speed from 2400 rpm to 3000 rpm and by adjusting the valve opening from 1 turn to 2.5 turns.

Table 5 Conditions of Cd transportation experiment

Run	Destination	Volume (dm^3)	Cd (K)	Valve opening (turns)	Rotation speed (rpm)	Repeat
P-1	Condenser	5.7–7.5	676–719	0.25	3000	7
P-2	Condenser	5.2–7.7	678–755	0.5	3000	13
P-3	Condenser	7.1–7.4	689–732	1	3000	4
P-4	Condenser	7.0–7.4	716–735	1.5	3000	3
P-5	Condenser	7.2–7.5	700–720	2	3000	3
P-6	Condenser	7.0–7.5	690–730	2.5	3000	3
P-7	Condenser	7.4	735	0.5	2700	2
P-8	Condenser	7.1–7.4	725–737	1	2700	3
P-9	Condenser	7.1–7.3	728–737	1.5	2700	2
P-10	Condenser	7.4	718–729	2	2700	2
P-11	Condenser	7.4	712	2.5	2700	1
P-12	Condenser	7.3	726	1	2400	1
P-13	Condenser	7.1–7.2	730–733	1.5	2400	2
P-14	Condenser	7.2–7.3	727–738	2	2400	2
P-15	Condenser	7.3–7.4	722–740	2.5	2400	2
P-16	Condenser	7.3	748	2.5	2100	1
P-17	Crucible	3.8	693	0.25	3000	1

Downloaded 02 Jun 2010 to 171.66.16.109. Redistribution subject to ASME license or copyright; see http://www.asme.org/terms/Terms_Use.cfm

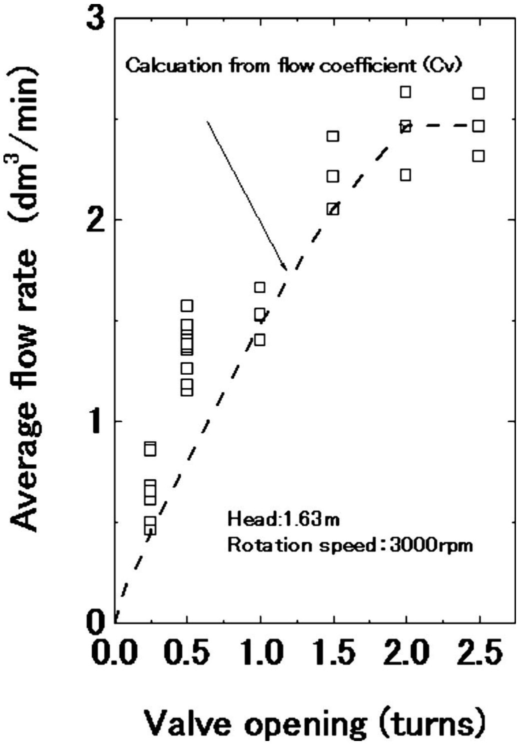

Fig. 11 Relationship between the average flow rate and the valve opening

Liquid Cd temperature dependence of the flow rate. The relationship between the average flow rate and the liquid Cd temperature is shown in Fig. 13. At an opening of a half turn and a rotation speed of 3000 rpm, the average flow rate was approximately 1.4 dm^3/min and did not change with the decrease in temperature from 755 K to 683 K. This suggests that the liquid Cd temperature has a small effect on the flow rate at operating temperatures from 683 K to 755 K.

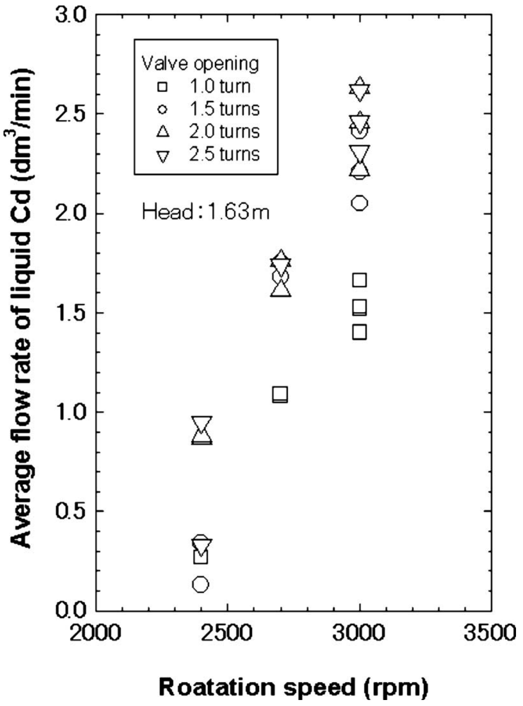

Fig. 12 Relationship between the average flow rate and the rotation speed of the centrifugal pump for rotation speeds of 2400 rpm, 2700 rpm, and 3000 rpm

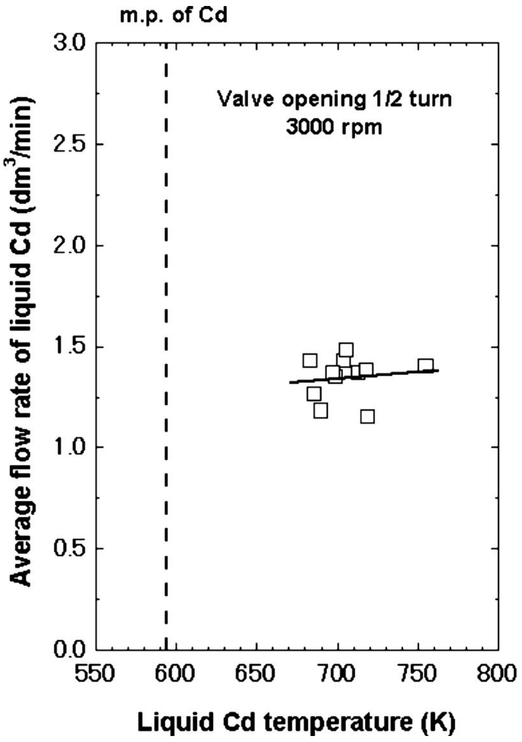

Fig. 13 Relationship between flow rate and liquid Cd temperature at rotation speed of 3000 rpm and valve opening of 0.5 turn

6 Conclusions

These different transport technologies—the gravity, the suction pump, and the centrifugal pump—were applied for the liquid Cd at approximately 773 K. The measured transport behaviors were concluded as follows.

(1) The liquid Cd was transported by gravity at 280 mm height. The flow rate of liquid Cd was well controlled between 0.8 dm^3/min and 2.6 dm^3/min by adjusting the valve opening. The liquid Cd temperature had a negligible effect on the flow rate in the operating temperature range of 698–756 K.
(2) The liquid Cd was transported by a suction pump against a 0.93 m head. The transport amount of Cd was well controlled with the Cd amount and the position of the suction tube by the suction pump.
(3) 0.5–2.5 dm^3/min of liquid Cd by adjusting the valve opening was transported against a 1.63 m head with the centrifugal pump. The liquid Cd temperature had a negligible effect on the flow rate in the operating temperature range of 683–755 K.

Acknowledgment

The present study is the result of the “development of engineering technology basis for electrometallurgical pyroprocess equipment” entrusted to the Central Research Institute of Electric Power Industry (CRIEPI) by the Ministry of Education, Culture, Sports, Science and Technology of Japan (MEXT).

References

[1] Tanaka, H., Kawamura, F., Nishimura, T., and Kamiya, M., 2001, “Design Study on Advanced Reprocessing Systems for FR Fuel Cycle,” *Proceedings of GLOBAL2001*, Paris, Sept.

Downloaded 02 Jun 2010 to 171.66.16.109. Redistribution subject to ASME license or copyright; see http://www.asme.org/terms/Terms_Use.cfm

[2] USDOE, 2001, TOPS Task Force of the Nuclear Energy Research Advisory Committee (NERAC), “Technological Opportunities to Increase the Proliferation Resistance of Global Civilian Nuclear Power Systems.”

[3] Chang, Y. I., 1989, “The Integral Fast Reactor,” Nucl. Technol., **88**, pp. 129–138.

[4] Garcia, H. E., Lineberry, M. J., Aumeier, S. E., and McFarlane, H. F., 2001, “Proliferation Resistance of Advanced Sustainable Nuclear Fuel Cycles,” *Proceedings of GLOBAL2001*, Paris, Sept.

[5] Inoue, T., 2002, “Actinide Recycling by Pyro-Processing With Metal Fuel FBR for Future Nuclear Fuel Cycle System,” Prog. Nucl. Energy, **40**(3–4), pp. 547–554.

[6] Koyama, T., Kinoshita, K., Inoue, T., Ougier, M., Glatz, J.-P., and Koch, L., 2002, “Study of Electrorefining of U–Pu–Zr Alloy Fuel,” J. Nucl. Sci. Technol., **3**, pp. 765–768.

[7] Koyama, T., Hijikata, T., Usami, T., Kitawaki, S., Shinozaki, T., and Fukushima, M., 2007, “Integrated Experiments of Electrometallurgical Pyroprocessing Using Plutonium Oxide,” J. Nucl. Sci. Technol., **44**(3), pp. 382–392.

[8] Carls, E. L., Blaskovitz, R. J., Johnson, T. R., and Ogata, T., 1993, “Tests of Prototype Salt Stripper System for IFR Fuel Cycle,” *Proceedings of GLOBAL1993*, Seattle, Sept.

[9] Hanson, B., Hopins, P., and Donaldson, N., 2003, “Pyrochemistry: A Program for Industrialization,” *Proceedings of GLOBAL2003*, New Orleans, Nov.

[10] Huntley, W. R., and Silverman, M. D., 1976, “System Design Description of Forced-Convection Molten-Salt Corrosion Loops MSR-FCL-3 and MSR-FCL-4,” Paper No. ONRL/TM-5540.

[11] Barth, D. L., Pacheco, J. E., Kolb, W. J., and Rush, E. E., 2002, “Development of a High-Temperature, Long-Shafted Molten Salt Pump for Power Tower Applications,” ASME J. Sol. Energy Eng., **124**, pp. 170–175.

[12] Watanabe, H., Hashimoto, H., Katagiri, I. K., and Tang, B., 1996, “Improvement of Performance of Vibration Pump for Molten Salt at High Temperature,” Trans. Jpn. Soc. Mech. Eng., Ser. B, **602**, pp. 3649–3653.

[13] Koyama, T., Hijikata, T., Yokoo, T., and Inoue, T., 2007, “Development of Engineering Technology Basis for Industrialization of Pyrometallurgical Reprocessing,” *Proceedings of the GLOBAL2007*, Boise, Sept.

[14] Advance Nuclear System Research and Development Directorate, 2006, “Feasibility Study on Commercialized Fast Reactor Cycle Systems Technical Study Report of Phase II-(2) Nuclear Fuel Cycle System,” JAEA-Research No. 2006-043.

[15] Karassik, I. J., Krutzsch, W. C., Fraser, W. H., and Messina, J. P., 1976, *Pump Handbook*, McGraw-Hill, New York.

[16] Hijikata, T., and Koyama, T., 2009, “Development of High Temperature Molten Salt Transport Technology for Pyrometallurgical Reprocessing,” J. Power Energy Syst., **3**(1), pp. 170–181.

[17] 2003, Swagelok Company Catalog, Bellows Sealed Valve U-Series.

[18] Brandes, E. A., and Brook Smithhells, G. B., 1992, *Metals Reference Book*, 7th ed., Butterworth-Heinemann, Oxford.

[19] Kubachewski, O. K., and Alock, C. B., 1979, *Metallurgical Thermochemistry*, 5th ed., Pergamon, New York.

[20] George, J. J., 1988, “Thermodynamic and Transport Properties for Molten Salts: Correlation Equation for Critically Evaluated Density, Surface Tension, Electrical Conductance, and Viscosity Data,” J. Phys. Chem. Ref. Data, The American Chemical Society (Washington, DC) and the American Institute of Physics (New York) for the National Bureau of Standards.

Downloaded 02 Jun 2010 to 171.66.16.109. Redistribution subject to ASME license or copyright; see http://www.asme.org/terms/Terms_Use.cfm

The Influence of the Grain Structure Size on Microstructurally Short Cracks

Igor Simonovski

Leon Cizelj
e-mail: leoncizelj@ijs.si

Reactor Engineering Division,
"Jožef Stefan" Institute,
Jamova cesta 39,
SI-1000 Ljubljana Slovenia

The dominant processes in the initialization and propagation of microstructurally short cracks include microstructural features such as crystallographic orientations of grains, grain boundaries, inclusions, voids, material phases, etc. The influence of the microstructural features is expected to vanish with distance from the crack tip. Also, the influence of the nearby microstructural features is expected to be smaller for a long than for a small crack. Finally, a crack of sufficient length can be modeled using classical fracture mechanic methods. In this paper the approach to estimate the crack length with vanishing influence from the microstructural feature is proposed. To achieve this, a model containing a large number of randomly sized, shaped, and oriented grains is employed. The random grain structure is modeled using a Voronoi tessellation. A series of cracks of lengths from about 1 to 7 grain lengths is inserted into the model, extending from a grain at the surface toward the interior of the model. The crack tip opening displacements are estimated and statistically analyzed for a series of random crystallographic orientation sets assigned to the grains adjacent to the crack. Anisotropic elasticity and crystal plasticity constitutive models are employed at the grain size scale. It is shown that the standard deviation of the crack tip opening displacement decreases from about 20% for a short surface crack embedded within a single grain to about 7% for a surface crack extending through seven grains. From the engineering point of view, a crack extending through less than about ten grain sizes is therefore considered to strongly depend on the neighboring microstructural features. [DOI: 10.1115/1.3079610]

Keywords: short cracks, crack tip opening displacement, polycrystalline material, crystal plasticity

1 Introduction

Aging and damage in materials could play a significant role in the long term safe operation of nuclear power plants. Vast knowledge about aging and damage has accumulated over the years. There are, however, some remaining issues calling for better explanation. These include initialization and propagation of microstructurally short cracks, which account for a rather significant proportion of a component's lifetime.

The dominant processes in the initialization and propagation of microstructurally short cracks include microstructural features such as crystallographic orientations of grains, grain boundaries, inclusions, voids, material phases, etc. [1–3]. It has been noted, for example, that the crack growth rate can be decreased when the crack approaches the grain boundary [3–5]. Also, short cracks tend to closely follow the slip plane. The crack therefore changes the direction when crossing the grain boundary [6]. This often results in zigzag patterns [7]. Different crystallographic orientations of the grains may also accelerate, decelerate, or even arrest the crack growth [8,9]. The crack tip loading in the highly variable deformation field caused by the inhomogeneous grain structure is therefore generally mixed-mode with strong shear component. The size of the plastic zone around the crack tip grows comparable to the crack length already at relatively small loads, therefore severely thwarting the applicability of linear elastic fracture mechanics.

In this paper, the approach to estimate the crack length with vanishing influence from the microstructural feature is proposed. To achieve this, a model containing a large number of randomly sized, shaped, and oriented grains is employed. The random grain structure is modeled using a Voronoi tessellation. A series of transgranular cracks of lengths from about 1 to 7 grain lengths is inserted into the model, extending from a grain at the surface and kinking across grain boundaries toward the interior of the model. Anisotropic elasticity and crystal plasticity constitutive models are employed at the grain size scale with grain boundaries modeled simply as a discontinuity in the lattice orientation between neighboring grains. Dislocations are not modeled, although it is acknowledged that they are important, especially near the grain boundaries [10,11]. The proposed approach builds on the previous work on the modeling of short cracks by the authors [12,13].

Crack tip opening displacement (CTOD) values are calculated for a series of stationary cracks under monotonic uniaxial tensile load. Different sets of random crystallographic orientations are applied to enable statistical analysis of the variability of CTOD values due to the surrounding crystallographic orientations.

The material properties used in this paper are typical for the American Iron and Steel Institute (AISI) 316L austenitic stainless steel, which is extensively used in nuclear industry (e.g., pipes) and has also been selected for a number of components of the International Thermonuclear Experimental Reactor (ITER) (vacuum vessel and ports, blanket shield modules, thin walled tubes for the first wall, cooling manifolds, diverter body, etc.) [14].

2 Model

The structural model includes a planar rectangular polycrystalline aggregate with 5027 randomly sized and shaped grains, outlined in Fig. 1. The finite elements are omitted from Fig. 1 to minimize the clutter. The planar grain structure is approximated using a planar Voronoi tessellation, generated using the VORTESS

Manuscript received October 1, 2008; final manuscript received October 6, 2008; published online April 15, 2009. Review conducted by Dilip R. Ballal. Paper presented at the 16th International Conference on Nuclear Engineering (ICONE16), Orlando, FL, May 12–15, 2008.

Copyright © 2009 by ASME

Downloaded 02 Jun 2010 to 171.66.16.109. Redistribution subject to ASME license or copyright; see http://www.asme.org/terms/Terms_Use.cfm

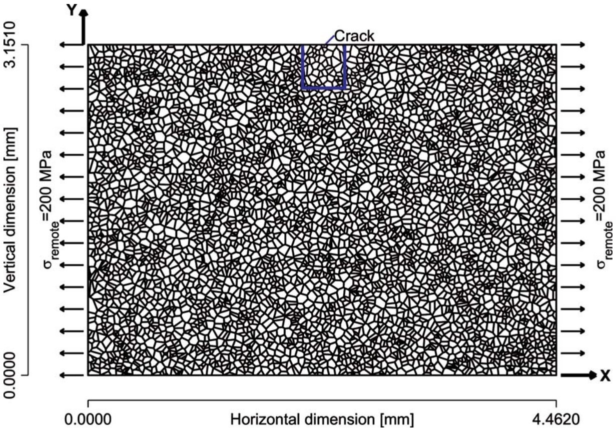

Fig. 1 The outline of the finite element model

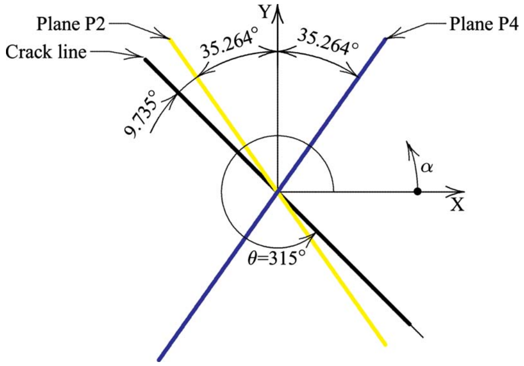

Fig. 3 Angles between the slip planes and the crack plane for crystallographic orientation $\alpha=0$ deg and crack direction $\theta=315$ deg

code [15]. In order to facilitate the finite element meshing, a Voronoi tessellation with reasonably small aspect ratios of cord lengths has been selected [16].

The applied loading and boundary conditions are illustrated in Fig. 1. The left and right edges are monotonically loaded in macroscopic uniaxial tension (with zero shear traction) up to a maximum load of 200 MPa, which is equivalent to about 80% of the yield strength of the material (240 MPa). This load is sufficient to trigger significant slip systems activity in all analyzed cases. The upper and lower edges are traction free. Prevention of rigid body movement is also imposed.

Each grain is assumed to behave as a randomly oriented monocrystal governed by the anisotropic elasticity and crystal plasticity models, described in Sec. 2.1. Crystallographic orientations are defined by the following.

- Setting the angle between the crystallographic [100] direction and the macroscopic *X* direction of all crystals in the model to 135 deg, as shown in Fig. 2. This results in a planar slip system model compatible with the planar macroscopic model; the projections of the primary and conjugate slip planes are depicted in Fig. 3.
- Setting random rotation of the lattice in individual grains about the global *Z*-axis. The angle of this random rotation is hereafter referred to as crystallographic orientation α (see Fig. 3)

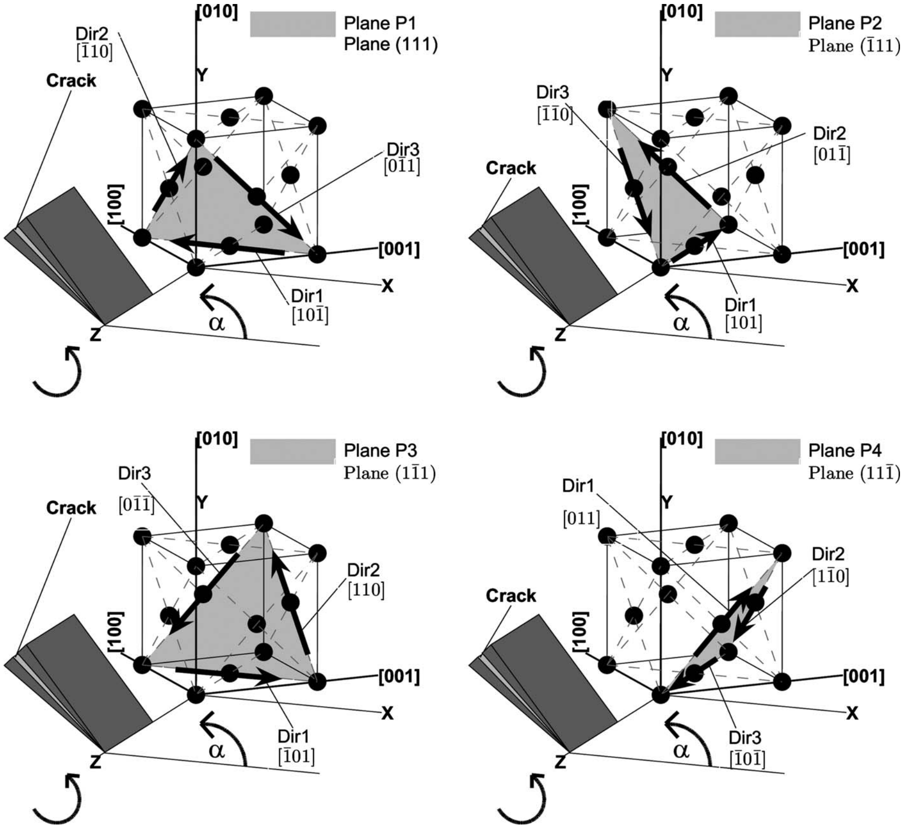

Fig. 2 Relation between the slip systems of a face centered cubic crystal and the crack for crystallographic orientation $\alpha=0$ deg and crack direction $\theta=315$ deg

Downloaded 02 Jun 2010 to 171.66.16.109. Redistribution subject to ASME license or copyright; see http://www.asme.org/terms/Terms_Use.cfm

A set of short surface cracks of different lengths, all of them representative of a Stage I fatigue crack, is introduced into the model at the free surface as denoted at the middle upper part of Fig. 1. Detailed description follows in Sec. 2.3.

2.1 Constitutive Model. The main features of the elastoplastic constitutive model of monocrystal are briefly explained below. Each crystal grain in the polycrystalline aggregate is assumed to behave as an anisotropic continuum. Random orientations of crystal lattice differ from grain to grain. Constitutive relations in linear elasticity are given by generalized Hooke's law, as follows:

$$\sigma_{ij} = C_{ijkl} \cdot \varepsilon_{kl} \tag{1}$$

where σ_{ij} represents the second rank stress tensor, C_{ijkl} represents the fourth rank stiffness tensor, and ε_{ij} represents the second rank strain tensor. Indices i, j, k, and l are running from 1 to 3. The inverse of the stiffness tensor, the compliance tensor D_{ijkl}, is defined as

$$\varepsilon_{ij} = D_{ijkl} \cdot \sigma_{kl} \tag{2}$$

Crystal plasticity used in the proposed model follows the pioneering work of Taylor [17] and Hill and Rice [18]. It is assumed that the plastic deformation is a result of crystalline slip only. The crystalline slip is driven by the resolved shear stress $\tau^{(\alpha)}$ [19]:

$$\tau^{(\alpha)} = m_i^{(\alpha)} \cdot \sigma_{ij} \cdot s_j^{(\alpha)} \tag{3}$$

where αth slip system is defined by a combination of slip plane (determined by normal $m_i^{(\alpha)}$) and slip direction ($s_j^{(\alpha)}$). The number of slip systems and their orientations depend on the crystal lattice (e.g., 48 in the body and 12 in the face centered cubic lattice). The stress rate can be defined as

$$\dot{\sigma}_{ij} = C_{ijkl} \cdot (\dot{\varepsilon}_{kl} - \dot{\varepsilon}_{kl}^{p}) = C_{ijkl} \cdot \left(\dot{\varepsilon}_{kl} - \sum_{\alpha} \tfrac{1}{2} \dot{\gamma}^{(\alpha)} (s_i^{(\alpha)} m_j^{(\alpha)} + s_j^{(\alpha)} m_i^{(\alpha)}) \right) \tag{4}$$

where $\dot{\sigma}_{ij}$ is the stress rate tensor, $\dot{\varepsilon}_{kl}$ is the strain rate tensor, $\dot{\varepsilon}_{kl}^{p}$ is the plastic strain rate tensor, and $\dot{\gamma}^{(\alpha)}$ is the slipping rate of the αth slip system. The slipping rate $\dot{\gamma}^{(\alpha)}$ is assumed to be governed by the resolved shear stress $\tau^{(\alpha)}$ in a viscoplastic framework [20], as follows:

$$\dot{\gamma}^{(\alpha)} = \dot{a}^{(\alpha)} \left(\frac{\tau^{(\alpha)}}{g^{(\alpha)}} \right) \left(\left| \frac{\tau^{(\alpha)}}{g^{(\alpha)}} \right| \right)^{n-1} \tag{5}$$

where $\dot{a}^{(\alpha)}$ is reference strain rate, n is the strain rate sensitivity parameter, and $g^{(\alpha)}$ is the current strain hardened state of the crystal. In the limit as n approaches infinity this power law approaches that of a rate-independent material. The current strain hardened state $g^{(\alpha)}$ is defined by

$$\dot{g}^{(\alpha)} = \sum_{\beta} h_{\alpha\beta} \dot{\gamma}^{(\beta)} \tag{6}$$

where $h_{\alpha\beta}$ are the slip-hardening moduli. Different proposals of hardening moduli could be found in literature, most of them relying on empirical models. The hardening law of Peirce et al. [21] is used in the numerical example. Self-($h_{\alpha\alpha}$) and latent-hardening moduli ($h_{\alpha\beta}$) are defined as

$$h_{\alpha\alpha} = h(\gamma) = h_0 \,\mathrm{sech}^2 \left| \frac{h_0 \gamma}{\tau_S - \tau_0} \right|, \quad h_{\alpha\beta} = q h(\gamma), \quad (\alpha \neq \beta) \tag{7}$$

where h_0 is the initial hardening modulus; τ_0 is the yield stress, which equals the initial value of the current strength $g^{(\alpha)}(0)$; τ_S is the breakthrough stress where large plastic flow initiates; γ is the cumulative slip; and q is the hardening factor.

A user subroutine [20], which incorporates anisotropic elasticity and crystal plasticity with finite-strain and finite-rotation formulations, was used in the commercially available finite element code ABAQUS.

2.2 Material Parameters. The following elastic constants for the AISI 316L face centered cubic crystal are used: C_{iiii} $=163{,}680$ MPa, $C_{iijj}=110{,}160$ MPa, and $C_{ijij}=100{,}960$ MPa [22]. Crystal plasticity parameters have been optimized from the macroscopic plastic response of AISI 316L polycrystal [22]: h_0 $=330$ MPa, $\tau_s=270$ MPa, $\tau_0=90$ MPa, $n=55$, $q=1.0$, and $a^{(\alpha)}$ $=0.001$. With these parameters the proposed plain strain model is deemed sufficiently accurate to provide a correct qualitative representation of the macroscopic response [22]. The reference calculations with isotropically elastic and plastic material models have been carried out using a Young modulus of 192 GPa, a Poisson ratio of 0.3, a yield strength of 240 MPa, and a hardening modulus of 1,118 MPa.

2.3 Layout of Cracks. A set of short surface cracks of different lengths, all of them representative of a Stage I fatigue crack, is introduced into the model (Fig. 4). The shortest crack is completely embedded in the Grain No. 4854. The crack is placed in the slip plane denoted as P2 in Fig. 2. Increasing the crack length requires crossing the grain boundaries and kinking of the crack direction, which is assumed to follow the slip plane also in the newly damaged grain.

In the model, the crack path was assumed arbitrarily, keeping in mind that the growing crack would finally tend toward the pure mode I loading. The assumed path of the crack and the assumed coincidence of the crack with slip plane P2 (Fig. 2) also required that the orientations of the lattice in grains along the crack path are fixed accordingly. It follows from Fig. 2 that the crack with the direction θ, measured in the counterclockwise direction, will coincide with the slip plane P2 in the lattice with orientation α when

$$\theta = 90 \text{ deg} + 25.264 \text{ deg} + \alpha + 180 \text{ deg} \tag{8}$$

Table 1 lists the crystallographic orientations α and crack directions θ for all grains along the assumed crack path. The orientation of all remaining grains in the model is random with uniform distribution in the range between 0 and 2π.

The shape of the crack assessed in this paper is rather complex. It is therefore useful to introduce a suitable effective crack shape with the available linear elastic fracture mechanics (LEFM) solution. Two immediate purposes of the effective crack shape and length come in mind:

- availability of reliable reference values of (CTOD)
- proportionality of the CTOD to the crack length in LEFM

Two crack shapes with available solutions [23] have been selected—kinked and oblique cracks emanating from a surface of a semi-infinite plate, as depicted in Fig. 5. It turns out that the difference in stress intensity factors between kinked and oblique cracks in similar configurations (see Fig. 5) is of the order of 1% or less. A simpler oblique crack has been therefore selected as the representative effective crack. The appropriate lengths of effective cracks are listed in Table 1. It should be noted here that the physical crack length is not always a good measure of the CTOD: crack ending in Grain No. 88 is physically longer than crack ending in Grain No. 4956 but nevertheless results in much lower elastic CTOD.

2.4 Crack Tip Opening Displacement. For each case the CTODs are calculated at a distance of 2.5% of the average grain size behind the crack tip (i.e., $0.025 \times 52.9 = 1.3$ μm), as depicted in Fig. 6. Such definition of CTOD was taken from the author's previous work where the effect of the grain boundary on the crack tip was evaluated [22]. Calculating CTOD at a larger distance behind the crack tip would diminish the observable effect of the grain boundary and would result in the linear increase in the CTOD with increased load, since the material far behind the crack tip is deformed elastically. The definition of the CTOD is also consistent with examples found in the literature [24,25].

Downloaded 02 Jun 2010 to 171.66.16.109. Redistribution subject to ASME license or copyright; see http://www.asme.org/terms/Terms_Use.cfm

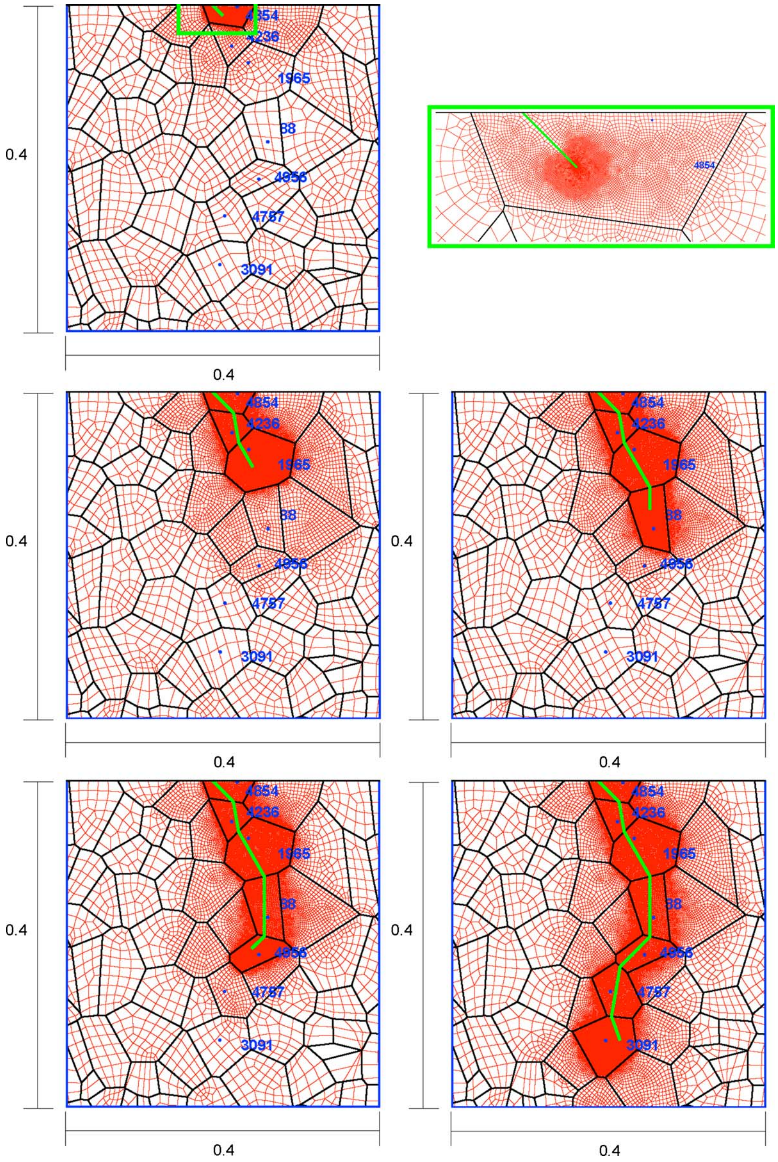

Fig. 4 Details of the crack tip meshes for different crack lengths. The numbers indicate the grains containing the crack. Please refer to Fig. 1 for the global position of the crack in the model.

3 Results

Before embarking on the discussion of the results obtained with rather complex models containing randomly oriented crystal grains (monocrystals), it may be useful to give some insight in the constitutive response of anisotropic monocrystals. Changing the orientation of the lattice in the monocrystal with respect to the uniaxial load directly influences the stiffness of the monocrystal (individual grain) in the direction of the macroscopic loading

Table 1 Crack and crystal orientations and effective crack lengths

Grain No.	Crystal orientation α (deg)	Crack direction θ (deg)	Crack length Physical (mm)	Physical perpendicular to load (mm)	Effective (mm)	CTOD calculated
4854	9.375	315	0.0187	0.0132	0.0093	Yes
4236	−25.264	280	0.0578	0.0465	0.0569	No
1965	−5.264	300	0.1114	0.0951	0.0929	Yes
88	−35.264	270	0.1693	0.1490	0.1874	Yes
4956	−80.264	225	0.2398	0.2127	0.1495	Yes
4757	−45.264	260	0.2974	0.2609	0.3193	No
3091	−15.264	290	0.3671	0.3281	0.3694	Yes

Downloaded 02 Jun 2010 to 171.66.16.109. Redistribution subject to ASME license or copyright; see http://www.asme.org/terms/Terms_Use.cfm

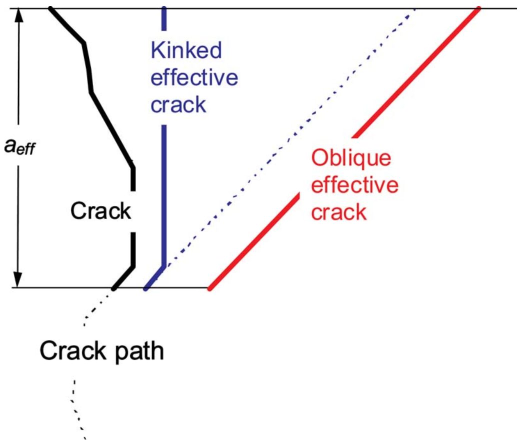

Fig. 5 Possible effective crack shapes and effective crack length

(σ_{11}=240 MPa, see also Fig. 7 and Ref. [13]). The contribution from the anisotropic elasticity (dashed line in Fig. 7) is notable, but moderate. The largest contribution comes from the crystal plasticity: First, the stiffness in crystal plasticity is defined by the Schmid factors (Eq. (4)) and second by the power law dependence of the shear rate (Eq. (5)). Due to the rather high exponent in Eq. (5), directions with slightly smaller Schmid factors will exhibit significantly smaller shear rate. The combination of the two factors results in very distinct directions with stiff and soft response of the monocrystal.

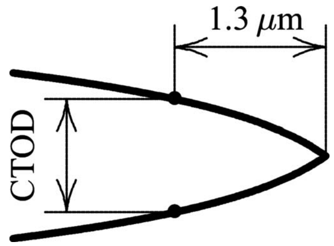

Fig. 6 Definition of crack tip opening displacement CTOD

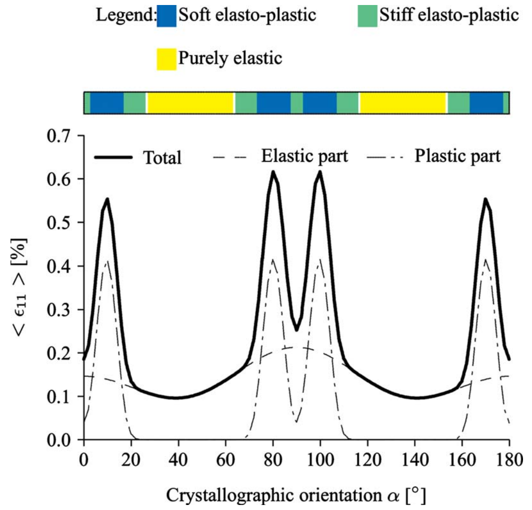

Fig. 7 Strain ε_{11} in a single crystal as a function of crystallographic orientation

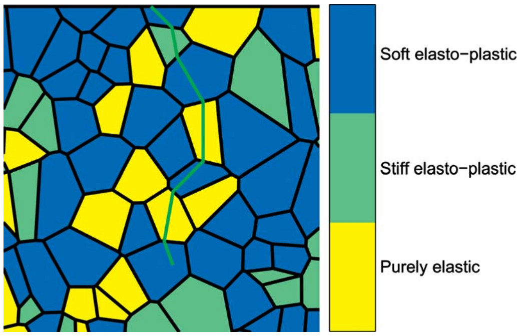

Fig. 8 Grain stiffness for an arbitrarily selected set of crystallographic orientations. Orientations of the crack-containing grains were kept constant for all analyses reported in this paper

Three somewhat arbitrary levels of the stiffness in the directional response of the monocrystal are defined here for illustrative purposes: (1) purely elastic response, (2) stiff elastic-plastic with $0 \leq \varepsilon_{11}^{\mathrm{pl}} < 0.1\%$, and (3) soft elastic-plastic response with $0.1\% \leq \varepsilon_{11}^{\mathrm{pl}}$. Stiffness of the crack-containing grains with respect to the uniaxial loading is depicted in Fig. 8. It is noted here that the fourth and sixth grains on the crack path (grains Nos. 88 and 4757) would, without a crack, remain elastic under the applied remote loading and consequently represent notable resistance toward local deformation.

The role of grain orientations is basically twofold. Obviously, the "softness" of the grains in the vicinity of the crack has a major influence on the CTOD. Additionally, if clusters of "soft" grains are present in the vicinity of the crack tip, the macroscopic bands of localized strain could coincide with the crack tip, resulting in large CTOD values. On the contrary, when clusters of soft grains form far from the crack tip, the bands of localized strain could form elsewhere, which could significantly reduce the CTOD values [12]. Such effects could become even more pronounced in textured materials.

A set of 30 models with different random grain orientations were generated for the five different crack lengths depicted in Fig. 4 and detailed in Table 1. For each of the crack lengths, the average and standard deviation values of CTOD were then calculated. The 30 input values are sufficient to obtain statistically reasonably stable estimates of averages and standard deviations. It was expected that, with increasing crack length, the CTOD would depend less on the surrounding microstructural features. Consequently, since the scatter of the CTOD is caused by the random orientations of the grains in the model, the value of the CTOD standard deviation is expected to decrease.

Figure 9 displays CTOD values as a function of effective crack length. The effective crack length is discussed in Sec. 2.3 and has been introduced to minimize the impact of the crack shape on the discussion of the results. As expected, the CTOD values obtained using isotropic linear elastic material, are nearly proportional to the effective crack length. The small amount of nonproportionality is believed to be caused by a rather complex crack shape, which could not be entirely captured by the effective crack approximation.

The mean values of the CTOD obtained using crystal plasticity and randomly oriented grains increase with the effective crack length. The exception is the stable CTOD value between the cracks with an effective length of 0.1495 mm (crack tip in Grain No. 4956) and 0.1874 mm (crack tip in Grain No. 88). Please note here that the crack with an effective crack length of 0.15 mm is physically longer than the crack with the effective crack length of 0.19 mm (Table 1). In addition, the relative stiffness of the grain containing the tip of the crack with a_{eff}=0.19 mm is much higher than the relative stiffness of the grain containing the tip of the crack with a_{eff}=0.15 mm (see Fig. 8).

The CTOD value obtained by the isotropic plasticity model is

Downloaded 02 Jun 2010 to 171.66.16.109. Redistribution subject to ASME license or copyright; see http://www.asme.org/terms/Terms_Use.cfm

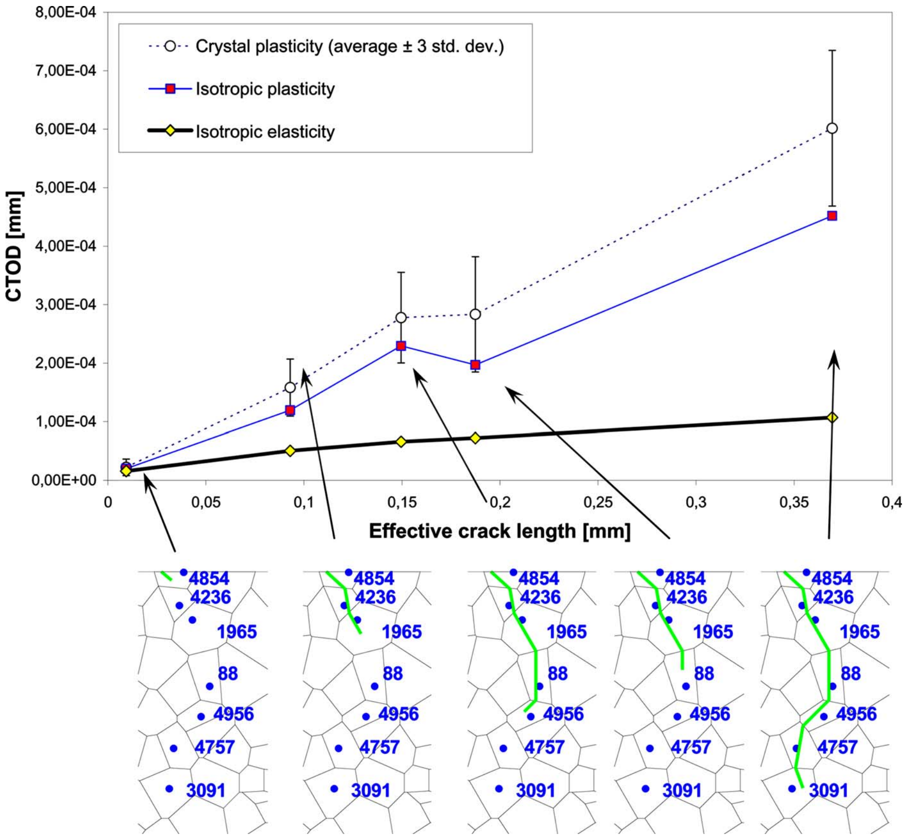

Fig. 9 Scatter of the CTOD values due to the random nature of crystallographic orientations of the surrounding grains

shown to represent an approximate lower limit. Both the isotropic elastic and isotropic plastic models are shown to significantly underestimate the CTOD values.

The scatter of the CTOD is indicated in Fig. 9 with error bars denoting the range of ±3 standard deviations (~99% of all random realizations) and increases with the effective crack length.

The normalized scatter of the CTOD is depicted in Fig. 10 using the standard deviation as a measure of the scatter. A rather sharp decrease in scatter from above 20% to about 10% is noted for very short cracks. Further moderate decrease in scatter is seen with increasing the effective crack length. For the longest crack analyzed, which extends through seven grains, the standard deviation of the CTOD values is 7.3%.

The decrease of scatter was less pronounced than expected. Some possible reasons for this include the following.

- The crack was always placed in the P2 slip plane. In some cases, placing the crack in the P4 slip plane would result in the crack being more perpendicular to the external load, resulting in larger CTOD due to the remote load, which could mask some part of the scatter. This aspect was, however, not explored in this work. The emphasis was put on the evaluation of the scatter of the CTOD due to the crystallographic orientation.
- A microcrack usually forms at surface extrusions/inclusions or along slip bands. The formation and position of these structures depends significantly on the crystallographic orientations of the grains. For different sets of crystallographic orientations the position of these structures differs and the initial position of the crack should follow this. In our case the initial position of the crack is, however, fixed.
- The crack extending through seven grains could be too short to become independent of the surrounding microstructural features. However, the longest crack in the model is longer than 10% of the model height. Longer cracks would require model with larger number of grains, which is currently beyond our computational capabilities.

Based on the limited experience already gained with the 3D simulations [26], qualitatively similar results are expected for a 3D model, with possible quantitative changes in the amount of scatter. Additional work is currently underway to verify this.

4 Conclusions

In this paper, the approach to estimate the crack length with vanishing influence from the microstructural feature is proposed. This is achieved through a model containing a large number of randomly sized, shaped, and oriented grains.

A series of transgranular cracks of lengths from 1 to 7 typical grain lengths is inserted into the model, extending from a grain at the surface and kinking across grain boundaries toward the interior of the model. Anisotropic elasticity and crystal plasticity constitutive models are employed at the grain size scale with grain boundaries modeled simply as discontinuity in the lattice orientation between neighboring grains. Although the loading was monotonic, a number of key observations may be relevant for the fatigue case.

The CTOD values obtained show rather high scatter. The isotropic plasticity model is shown to represent an approximate lower limit of those scattered values. Both the isotropic elastic and isotropic plastic models are shown to significantly underestimate the CTOD values.

The scatter of the CTOD is measured using the standard deviation. It decreases rapidly from 20% for a crack embedded in a single grain to about 10% for cracks spanning 2–3 grains. Slower decrease to 7% for crack spanning seven grains is observed.

Downloaded 02 Jun 2010 to 171.66.16.109. Redistribution subject to ASME license or copyright; see http://www.asme.org/terms/Terms_Use.cfm

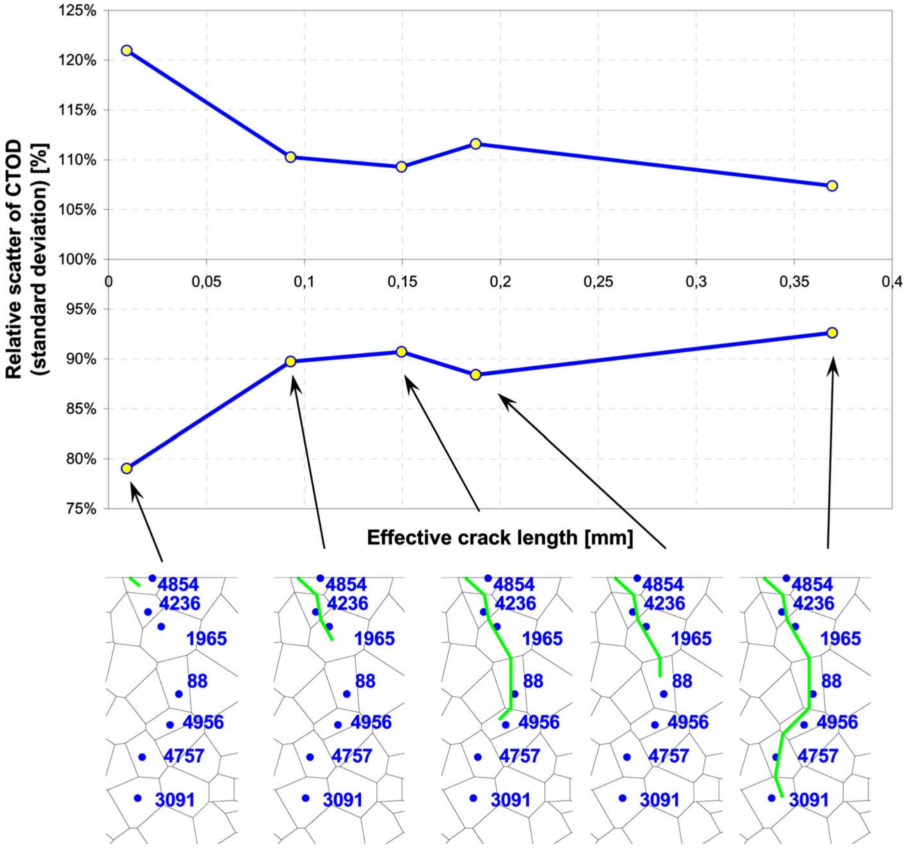

Fig. 10 Normalized scatter of the CTOD values due to the random nature of crystallographic orientations of the surrounding grains

From the engineering point of view, cracks extending through more than about ten grains may be analyzed with classical continuum mechanics approaches with reasonable accuracy. Shorter cracks may however require more sophisticated multiscale approaches.

The proposed approach is deemed useful for the understanding of the initiation and coalescence of the multiple stress corrosion cracks. A model of such cracks is currently under development with emphasis on the appropriate grain boundary properties, which have been disregarded in the presented work.

Acknowledgment

Financial support of the Slovene Research Agency (www.arrs.si) through Grant Nos. P2-0026, J2-9168, and V2-0375 (cosponsored by the Slovene Nuclear Safety Administration www.ursjv.si) is gratefully acknowledged.

Nomenclature

C_{ijkl} = stiffness tensor
D_{ijkl} = compliance tensor
$\dot{a}^{(\alpha)}$ = strain rate in slip system α
$\dot{g}^{(\alpha)}$ = current strain hardened state in slip system α
$g^{(\alpha)}$ = current strength in slip system α
h_0 = initial hardening modulus
$h_{\alpha\alpha}$ = self-hardening moduli
$h_{\alpha\beta}$ = slip-hardening moduli
$m_i^{(\alpha)}$ = slip plane normal
n = strain rate sensitivity parameter
q = hardening factor
$s_j^{(\alpha)}$ = slip direction
α = grain's crystallographic orientation
$\dot{\gamma}^{(\alpha)}$ = slipping rate in slip system α
ε_{ij} = strain tensor
$\dot{\varepsilon}_{kl}$ = strain rate tensor
$\dot{\varepsilon}_{kl}^{p}$ = plastic strain rate tensor
θ = crack direction
σ_{ij} = stress tensor
$\dot{\sigma}_{ij}$ = stress rate tensor
τ_0 = yield stress
$\tau^{(\alpha)}$ = Taylor's resolved shear stress

References

[1] Miller, K. J., 1987, "The Behaviour of Short Fatigue Cracks and Their Initiation. Part II: A General Summary," Fatigue Fract. Eng. Mater. Struct., **10**(2), pp. 93–113.

[2] Hussain, K., 1997, "Short Fatigue Crack Behaviour and Analytical Models: A Review," Eng. Fract. Mech., **58**(4), pp. 327–354.

[3] Hussain, K., de los Rios, E., and Navarro, A., 1993, "A Two-Stage Micromechanics Model for Short Fatigue Cracks," Eng. Fract. Mech., **44**(3), pp. 425–436.

[4] Morris, W. L., Buck, O., and Marcus, H. L., 1976, "Fatigue Crack Initiation and Early Propagation in Al 2219–T851," Metall. Trans. A, **7**(7), pp. 1161–1165.

[5] Zhang, Y. H., and Edwards, L., 1994, "On the Blocking Effect of Grain Boundaries on Small Crystallographic Fatigue Crack Growth," Mater. Sci. Eng., A, **188**(1–2), pp. 121–132.

[6] Düber, O., Künkler, B., Krupp, U., Christ, H.-J., and Fritzen, C.-P., 2006, "Experimental Characterization and Two-Dimensional Simulation of Short-Crack Propagation in an Austenitic-Ferritic Duplex Steel," Int. J. Fatigue, **28**(9), pp. 983–992.

[7] Suresh, S., 1991, *Fatigue of Materials*, Cambridge University Press, Cambridge.

[8] Tvergaard, V., Wei, Y., and Hutchinson, J. W., 2001, "Edge Cracks in Plastically Deforming Surface Grains," Eur. J. Mech. A/Solids, **20**(5), pp. 731–738.

[9] Zhai, T., Wilkinson, A. J., and Martin, J. W., 2000, "A Crystallographic Mechanism for Fatigue Crack Propagation Through Grain Boundaries," Acta Mater., **48**(20), pp. 4917–4927.

[10] Watanabe, T., 1984, "Approach to Grain Boundary Design for Strong and

Downloaded 02 Jun 2010 to 171.66.16.109. Redistribution subject to ASME license or copyright; see http://www.asme.org/terms/Terms_Use.cfm

Ductile Polycrystals," Res. Mech., **11**(1), pp. 47–84.

[11] Lehockey, E. M., Brennenstuhl, A. M., and Thompson, I., 2004, "On the Relationship Between Grain Boundary Connectivity, Coincident Site Lattice Boundaries, and Intergranular Stress Corrosion Cracking," Corros. Sci., **46**(10), pp. 2383–2404.

[12] Simonovski, I., Nilsson, K., and Cizelj, L., 2007. "Crack Tip Displacements of Microstructurally Small Cracks in 316l Steel and Their Dependence on Crystallographic Orientations of Grains," Fatigue Fract. Eng. Mater. Struct., **30**(6), pp. 463–478.

[13] Simonovski, I., Nilsson, K.-F., and Cizelj, L., 2007, "The Influence of Crystallographic Orientation on Crack Tip Displacements of Microstructurally Small, Kinked Crack Crossing the Grain Boundary," Comput. Mater. Sci., **39**(4), pp. 817–828.

[14] Kalinin, G., Barabash, V., Fabritsiev, S., Kawamura, H., Mazul, I., Ulrickson, M., Wu, C., and Zinkle, S., 2001, "ITER R&D: Vacuum Vessel and In-Vessel Components: Materials Development and Test," Fusion Eng. Des., **55**(2–3), pp. 231–246.

[15] Riesch-Oppermann, H., 1999, "VorTess Generation of 2D Random Poisson–Voronoi Mosaics as Framework for Micromechanical Modeling of Polycrystalline Materials-Algorithm and Subroutines Description," Technical Report No. FZKA 6325.

[16] Weyer, S., Fröhlich, A., Riesch-Oppermann, H., Cizelj, L., and Kovač, M., 2002, "Automatic Finite Element Meshing of Planar Voronoi Tessellations," Eng. Fract. Mech., **69**(8), pp. 945–958.

[17] Taylor, G. I., 1938, "Plastic Strain in Metals," J. Inst. Met., **62**, pp. 307–324.

[18] Hill, R., and Rice, J. R., 1972, "Constitutive Analysis of Elastic-Plastic Crystals at Arbitrary Strain," J. Mech. Phys. Solids, **20**(6), pp. 401–413.

[19] Rice, J. R., 1970, "On the Structure of Stress-Strain Relations of Time-Dependent Plastic Deformation in Metals," ASME J. Appl. Mech., **3**(7), pp. 728–737.

[20] Huang, Y., 1991, "A User-Material Subroutine Incorporating Single Crystal Plasticity in the ABAQUS Finite Element Program," Division of Applied Sciences, Harvard University, http://www.columbia.edu/1jk2079/fem/umat documentation.pdf.

[21] Peirce, D., Asaro, R. J., and Needleman, A., 1983, "Material Rate Dependence and Localized Deformation in Crystalline Solids," Acta Metall., **31**(12), pp. 1951–1976.

[22] Simonovski, I., Nilsson, K.-F., and Cizelj, L., 2005, "Material Properties Calibration for 316L Steel Using Polycrystalline Model," 13th International Conference on Nuclear Engineering, Beijing, China, May 16–20.

[23] Murakami, Y., 1987, *The Stress Intensity Factor Handbook*, Pergamon, New York.

[24] Potirniche, G. P., and Daniewicz, S. R., 2003, "Analysis of Crack Tip Plasticity for Microstructurally Small Cracks Using Crystal Plasticity Theory," Eng. Fract. Mech., **70**(13), pp. 1623–1643.

[25] Bennett, V. P., and McDowell, D. L., 2003, "Crack Tip Displacements of Microstructurally Small Surface Cracks in Single Phase Ductile Polycrystals," Eng. Fract. Mech., **70**(2), pp. 185–207.

[26] Cizelj, L., and Simonovski, I., 2008, "Simulated Planar Polycrystals With Planar and Spatial Random Lattice Orientations," Proceedings of the Ninth Biennial ASME Engineering Systems Design and Analysis Conference, Haifa, Israel, July 7–9, 2008.

Downloaded 02 Jun 2010 to 171.66.16.109. Redistribution subject to ASME license or copyright; see http://www.asme.org/terms/Terms_Use.cfm

Corrosion of the Materials in Sulfuric Acid

Hong Pyo Kim

Dong-Jin Kim[1]
e-mail: djink@kaeri.re.kr

Hyuk Chul Kwon

Ji Yeon Park

Yong Wan Kim

Korea Atomic Energy Research Institute (KAERI),
1045 Daedeok-daero,
Yuseong-gu, Daejeon, 305-353, Korea

A program for a hydrogen production by using a high temperature nuclear heat has been launched in Korea since 2004. Iodine sulfur (IS) process is one of the promising processes for a hydrogen production because it does not generate carbon dioxide and a massive hydrogen production may be possible. However, the highly corrosive environment of the process is a barrier to its application in the industry. Therefore, corrosion behaviors of various materials were evaluated in sulfuric acid to select appropriate materials compatible with the IS process. The materials used in this work were Ni based alloys, Fe–Si alloys, Ta, Au, Pt, Zr, SiC, and so on. The test environments were boiling 50 wt % sulfuric acid without/with HI as an impurity and 98 wt % sulfuric acid. The surface morphologies and cross-sectional areas of the corroded materials were examined by using the scanning electron microscopy (SEM) equipped with energy dispersive X-ray spectroscopy (EDS). From the results of the weight loss and potentiodynamic experiments, it was found that a Si enriched oxide is attributable to a corrosion resistance for materials including Si in boiling 98 wt % sulfuric acid. Moreover, the passive Si enriched film thickness increased with the immersion time leading to an enhancement of the corrosion resistance. Corrosion behaviors of the material tested are discussed in terms of the chemical composition of the materials, the corrosion morphology, and the surface layer's composition. [DOI: 10.1115/1.3095808]

1 Introduction

Hydrogen, which can be stored and transported for a long distance with a lower loss when compared with electricity, is one of the promising major energy sources in the future. Moreover, a necessity for hydrogen as a clean energy source is increasing more due to significant climate changes [1,2].

Iodine sulfur (IS) process, which splits water thermochemically, can produce a large amount of hydrogen without an emission of greenhouse gases by using a high temperature nuclear energy with a thermal efficiency above 40% [3].

IS process, which was first proposed by General Atomics [4] and demonstrated as a closed cycle at JAEA [5], is composed of the following three chemical reactions:

$$I_2 + SO_2 + 2H_2O = 2HI + H_2SO_4 \tag{1}$$

$$2HI = H_2 + I_2 \tag{2}$$

$$H_2SO_4 = H_2O + SO_2 + 1/2O_2 \tag{3}$$

Here, reaction (1) is known as the Bunsen reaction, where gaseous sulfur dioxide reacts with iodine and water producing an aqueous solution of iodic acid and sulfuric acid. Thermal decomposition of hydrogen iodide (2) and that of sulfuric acid (3) produces hydrogen and oxygen, respectively. By carrying out these three reactions sequentially, as a net material balance of the process, water can be decomposed into hydrogen and oxygen [6].

Sulfuric acid from a Bunsen reactor is purified and concentrated and then it is decomposed into SO_3 and SO_2, thus producing oxygen again. Therefore, materials composing an IS process should withstand a high temperature up to 950°C and highly concentrated sulfuric acid environments up to 98 wt %. Moreover, a normal high pressure operating condition elevates the boiling temperature and sulfuric acid decomposition temperature, which accelerates the corrosion process of materials.

Therefore, considering that the IS process is operated under very severe environments of iodic and sulfuric acids at a wide temperature range from room temperature to 950°C, a material corrosion must be an important issue for an accomplishment of a successful IS process. Especially, a corrosion resistant material applicable to a highly concentrated sulfuric acid environment of a high temperature should be found.

In the present work, corrosion behaviors of some commercial materials and fabricated materials were investigated in boiling 50 wt % sulfuric acid without/with HI as an impurity and 98 wt % sulfuric acid.

2 Experimental Details

Corrosion tests of various materials were performed in a 50 wt % boiling sulfuric acid condition at 125°C and a 98 wt % sulfuric acid condition at 320°C. Moreover, a corrosion test for materials showing a good corrosion resistance in a 50 wt % boiling sulfuric acid condition was conducted in a 50 wt % boiling sulfuric acid including HI of 0.5 mol, when considering HI as an impurity.

Materials such as Alloy 690, Hastelloy C276, Hastelloy X, Haynes 556, Ta, Zr, Au, Fe-xSi alloys(x=6%, 10%, and 13%), and SiC were tested. The dimension of the specimen was $20\times20\times1$ mm^3 with a 5 mm diameter circular hole to be held over the specimen holder.

Corrosion cell made of a Pyrex glass flask with a capacity of 1 l was used. The corrosion cell was heated on a hot plate to maintain a stable boiling condition. Evaporated sulfuric acid was liquidified in a reflux condenser to minimize the evaporation loss. The immersion period was defined as the time between the moment when the boiling begins and the moment when the heater is shut off.

The weight before and after the immersion test was measured using an electronic balance of the Metler model AT261. Specimens were washed ultrasonically in acetone for 5 min before weighing them and then dried. Corrosion rate was calculated by dividing the weight loss by both the specimen surface area and the immersion period. The surface morphologies of the corroded ma-

---

[1] Corresponding author.

Manuscript received October 22, 2008; final manuscript received October 23, 2008; published online April 16, 2009. Review conducted by Dilip R. Ballal. Paper presented at the Fourth International Topical Meeting on High Temperature Reactor Technology (HTR 2008), Washington, DC, September 28–October 1, 2008.

Copyright © 2009 by ASME

Downloaded 02 Jun 2010 to 171.66.16.109. Redistribution subject to ASME license or copyright; see http://www.asme.org/terms/Terms_Use.cfm

Table 1 Chemical composition for the corrosion tested specimen

Specimen	Fe	Ni	Cr	Mo	Co	W
Alloy 690	7	Bal.	30		-	-
Hastelloy C276	5	Bal.	15	15	-	3
Hastelloy X	18	Bal.	22	9	2	-
Haynes 556	Bal.	20	22	3	18	2

Table 2 Corrosion rate for various materials in boiling 50 wt % sulfuric acid without/with 0.5 mol HI and in boiling 98 wt % sulfuric acid

Specimen	Corrosion rate without HI (50 wt %) (mm/yr)	Corrosion rate with HI (50 wt %) (mm/yr)	Corrosion rate (98 wt %) (mm/yr)
Alloy 690	194	N/A	4
Hastelloy C276	1.3	Dissolved	1
Hastelloy X	8	Dissolved	0.4
Haynes 556	9	N/A	7
Ta	0.003	0.01	41
Zr	0.02	0.1	Dissolved
Au	0.001	22.8	0.04
SiC	0.1	N/A	0.1

terials were examined by using the scaning electron microscopy (SEM) equipped with energy dispersive X-ray spectroscopy (EDS) (JSM6360).

3 Results and Discussion

Table 1 shows the chemical compositions of the major alloying elements for the various materials used for the corrosion test. Pure Ta, Zr, Au, and Fe-xSi alloys ($x=6\%$, 10%, and 13%) were also tested.

Table 2 shows the corrosion rates for the various materials tested in boiling 50 wt % boiling sulfuric acid. A surface of Alloy 690 was corroded relatively severely indicating that the relatively high Cr content, which provides most Fe–Cr alloys and Ni based alloys with a corrosion resistance, was not affected. It seems that the corrosion resistance in boiling 50 wt % sulfuric acid is improved by alloying some Mo rather than Cr. Ta, Zr, Au, and SiC showed an excellent corrosion resistance in boiling 50 wt % sulfuric acid.

Figure 1 illustrates the micrographs obtained from the SEM for the specimens in the boiling 50 wt % sulfuric acid. For Hastelloy C276, it seems that a general corrosion including a little grain boundary attack occurred and a pit was observed at a triple point where three grains were intersected. For Hastelloy X and Haynes 556, a similar appearance was observed, showing some spots like pits. On the other hand, surface appearances of Ta, Au, and SiC were very clean indicating a corrosion resistance in boiling 50 wt % H_2SO_4 at 125°C. It is notable that there was a pit on the surface of Zr in spite of its excellent corrosion resistance.

From the Bunsen reactor, HI can be incorporated into a low temperature sulfuric acid part as an impurity level. Therefore, some materials were tested in boiling 50 wt % sulfuric acid with

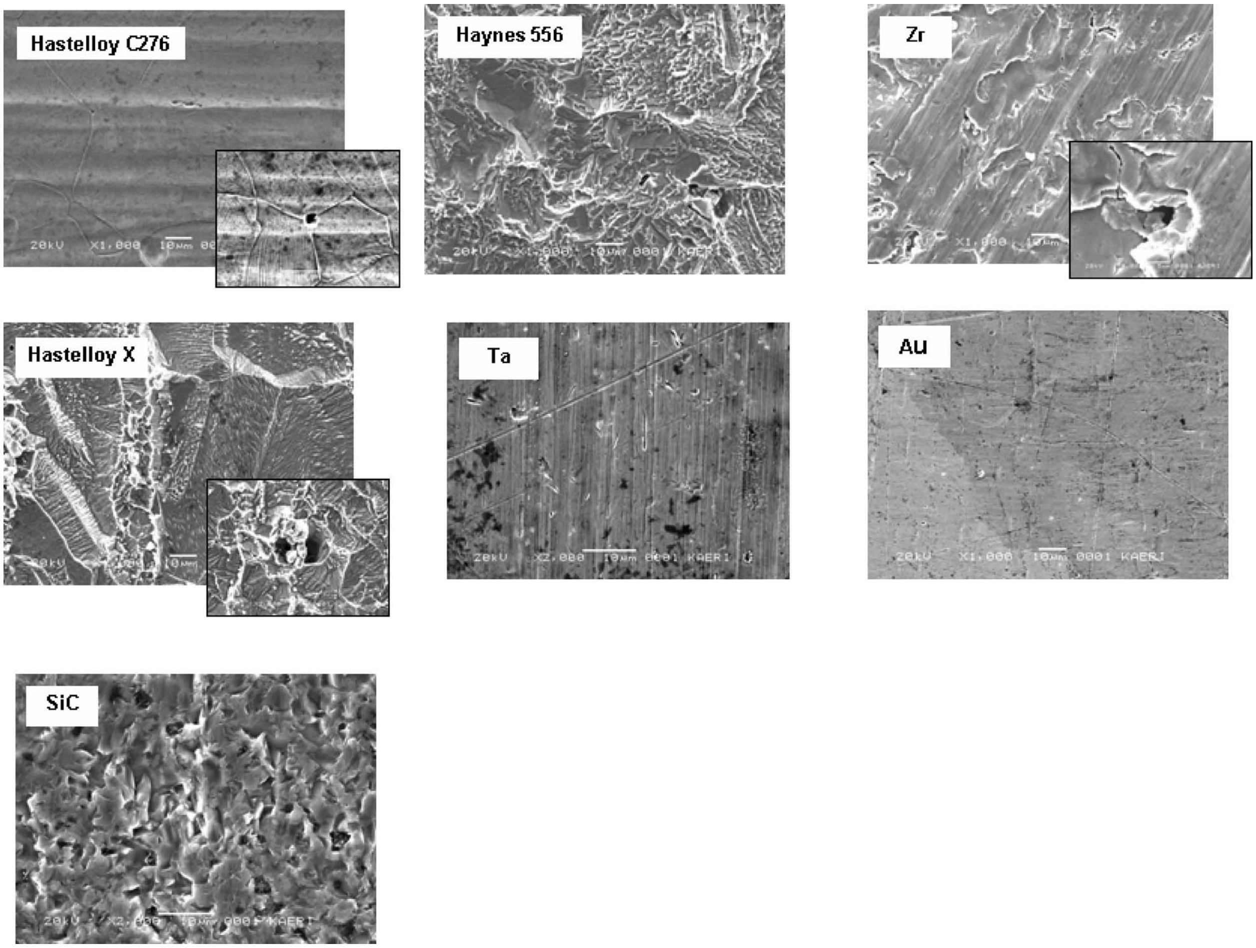

Fig. 1 Micrographs obtained from SEM for the specimens in 50 wt % sulfuric acid

Downloaded 02 Jun 2010 to 171.66.16.109. Redistribution subject to ASME license or copyright; see http://www.asme.org/terms/Terms_Use.cfm

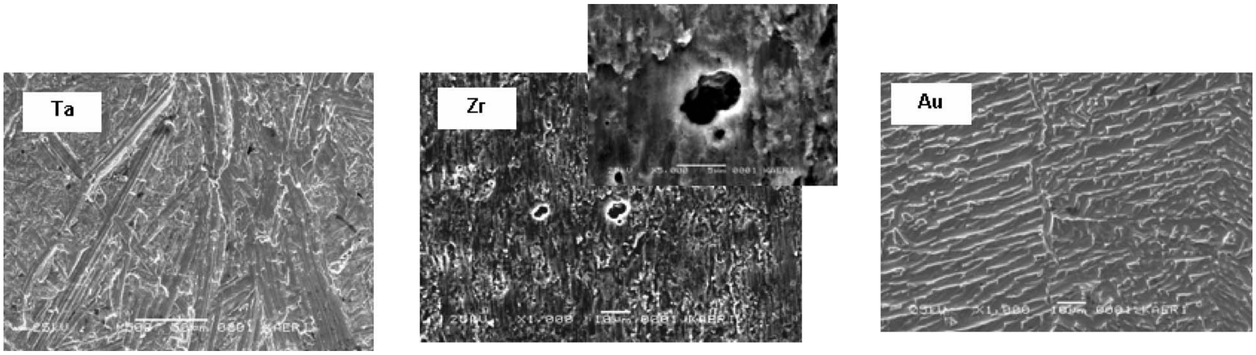

Fig. 2 Micrographs obtained from SEM for the specimens in 50 wt % sulfuric acid with 0.5 mol HI

0.5 mol HI as an impurity. The test results were also shown in Table 2. Ta and Zr still showed an excellent corrosion resistance, while Hastelloy C276, Hastelloy X, and Au showed a poor corrosion resistance indicating that HI accelerated the corrosion rate of these materials.

Figure 2 shows the micrographs obtained from the SEM for the specimens in boiling 50 wt % sulfuric acid with 0.5 mol HI. Surface appearance of Ta was very clean indicating a corrosion resistance in boiling 50 wt % $H_2SO_4+0.5$ mol HI. It should be noted for an application that a pit, which had been observed in 50 wt % sulfuric acid without HI, was enlarged and developed in the presence of HI. There was a change in the surface appearance by a corrosion of Au, which had shown an excellent corrosion resistance of 50 wt % sulfuric acid without HI.

Corrosion rates for various materials in boiling 98 wt % sulfuric acid are also presented in Table 2. When comparing the results in boiling 50 wt % sulfuric acid, the tendency of a corrosion resistance in 98 wt % sulfuric acid was different from the corrosion tendency in 50 wt % sulfuric acid. In previous works [7,8] for the Fe–Cr alloys, the corrosion rate was increased with a decreasing Cr content. The high corrosion resistance of the Fe–Cr alloys in most corrosive environments is attributed to an enrichment of the Cr in the passive film on the Fe–Cr alloys [3].

Commercially, pure Ni is highly resistant in many corrosive media, especially in reducing environments like a nonaerated solution of sulfuric acid, where the surface of a passive Ni oxide film is usually stable. In many cases, the corrosion resistance of Ni can be improved by alloying it with Cu, Cr, Mo, or W. In Cr–Ni alloys, the tendency to form a stable Cr_2O_3 surface film provides an appropriate stability for the Ni based alloys [9]. However, the Cr contents of Ni based alloys were not correlated with the corrosion resistance in this work. It seems that a certain amount of Mo is related to an improvement of the corrosion resistance in 98 wt % sulfuric acid as well as in 50 wt % sulfuric acid.

Au and SiC also showed an excellent corrosion resistance in boiling 98 wt % sulfuric acid, while Ta showed a poor corrosion resistance.

Figure 3 presents the micrographs obtained from the SEM for the specimens in 98 wt % sulfuric acid. For Alloy 690, a severe grain boundary attack and numerous pits within the grains were observed, which were responsible for large corrosion rate of 4 mm/yr. For Hastelloy C276, an oxide, which was confirmed by using EDS (not shown here), was clearly observed, which can be related to a passivation of Hastelloy C276 for the 98 wt % sulfuric acid. For Hastelloy X, an oxide was formed on the surface leading to an appropriate corrosion resistance. For Haynes 556, a general corrosion occurred. For Ta, a general corrosion was observed apart from an excellent corrosion resistance in 50 wt % sulfuric acid. Oxides were observed on the surfaces of Au and SiC, which led to an excellent corrosion resistance in the 50 wt % and 98 wt % sulfuric acids.

Figures 4(*a*) and 4(*b*) present the corrosion rate for SiC obtained as a function of the immersion test duration and that for Fe–Si alloys as a function of the Si content in boiling 98 wt % of sulfuric acid, respectively. It was found that the corrosion rate for SiC was decreased up to a weight gain with the test duration, and the corrosion rate for Fe–Si alloys was decreased with Si content indicating that Si is very essential to a corrosion resistance in boiling 98 wt % sulfuric acid.

Figures 5(*a*)–5(*c*) are micrographs obtained from the SEM for the SiC in boiling 98 wt % sulfuric acid as a function of the immersion test duration. After a 10 day immersion, silicon oxide was observed on the SiC surface. The coverage and size of the passive oxide on SiC were increased with the immersion time. It seems that Si is enriched on the SiC surface with the immersion time and silicon oxide is formed, and the coverage of the oxide increases with the time leading to a corrosion resistance of SiC.

Figure 6 presents the potentiodynamic curves for Fe–6Si, Fe–10Si, and Fe–13Si in 50 wt % sulfuric acid at room temperature with a scan rate of 5 mV/s. At -0.4 V (SCE, saturated calomel electrode), a corrosion potential was observed, irrespective of the Si amount, which was consistent with the equilibrium potential of an Fe dissolution [10]. At this corrosion potential, passive SiO_2 was thermodynamically stable according to the E-pH diagram. In the active-passive transition region and the passive region, the measured current was decreased with an increase in the Si amount. Additionally, a passive current has been measured above about 0.4 V (SCE), where Fe_2O_3 is formed [10].

At this corrosion potential, Fe dissolves and exposes a Si enriched surface. Exposed Si is oxidized to a passive SiO_2, which is thermodynamically stable at this potential. As the applied potential increases, it is expected that the surface coverage of the passive SiO_2 is increased with an increase in the Si amount leading to a decrease in the measured current in the active-passive transition region and the passive region. For the Fe–13Si specimen, an active-passive transition caused by an Fe_2O_3 formation was less obvious, which could be due to the large coverage of SiO_2 already formed on the surface during an anodic sweep of the applied potential.

From these results, it is plausible that the coverage of the passive SiO_2 is increased with an increase in the Si amount in the Fe-*x*Si during an immersion in 98 wt % boiling sulfuric acid. Corrosion resistance of Fe–Si with the Si amount, as shown in Fig. 4(*b*), is caused by a coverage and thickness increase in the passive SiO_2 as a function of the Si amount.

In spite of the excellent corrosion resistance of SiC and Fe-*x*Si ($x>10$) alloys, their brittle property is a drawback for an application. Table 3 presents the corrosion rate for Fe–Si alloys after a thermal heat treatment at 1100°C in boiling 98 wt % sulfuric acid. Corrosion rates for Fe–10Si and Fe–13Si are much lower than those of Fig. 4(*b*), and are decreased with the immersion time. Corrosion rate for Fe–6Si, which is more or less formable, is

Downloaded 02 Jun 2010 to 171.66.16.109. Redistribution subject to ASME license or copyright; see http://www.asme.org/terms/Terms_Use.cfm

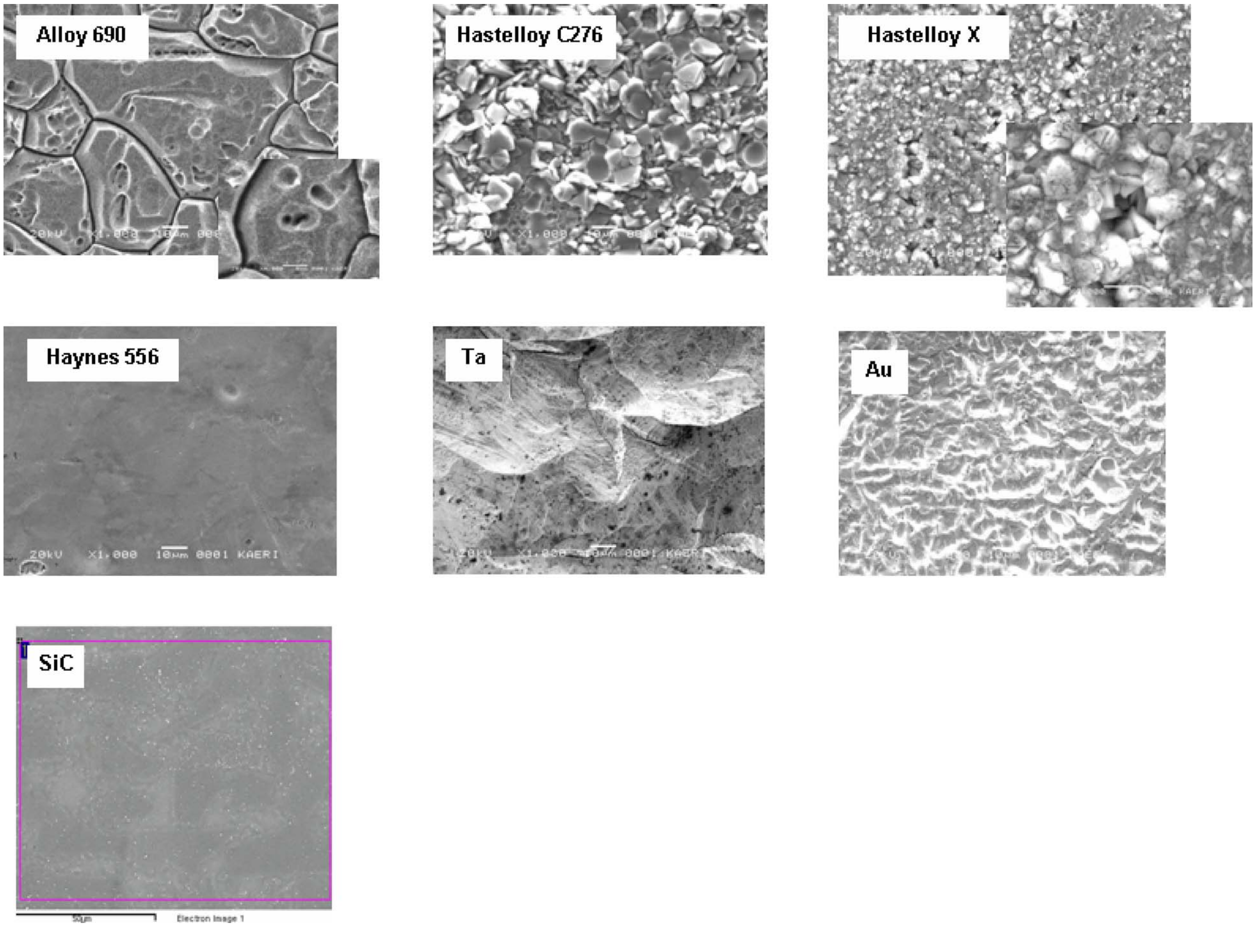

Fig. 3 Micrographs obtained from SEM for the specimens in 98 wt % sulfuric acid

Duration (day)	Specimen	SiC
1	Weight change(g)	-0.0004
	Corr. rate(mm/year)	0.0763
10	Weight change(g)	+0.0002
	Corr. rate(mm/year)	-
30	Weight change(g)	+0.0016
	Corr. rate(mm/year)	-
60	Weight change(g)	+0.0258
	Corr. rate(mm/year)	-
90	Weight change(g)	+0.0354
	Corr. rate(mm/year)	-
120	Weight change(g)	+0.0595
	Corr. rate(mm/year)	-

(*a*)

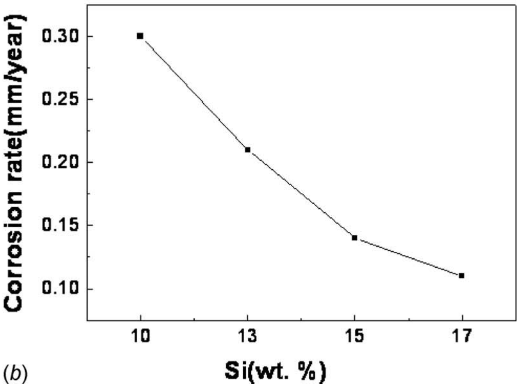

(*b*)

Fig. 4 (*a*) Corrosion rate for SiC obtained as a function of the immersion test duration and (*b*) that for Fe–Si alloys obtained as a function of the Si content in boiling 98 wt % sulfuric acid

Downloaded 02 Jun 2010 to 171.66.16.109. Redistribution subject to ASME license or copyright; see http://www.asme.org/terms/Terms_Use.cfm

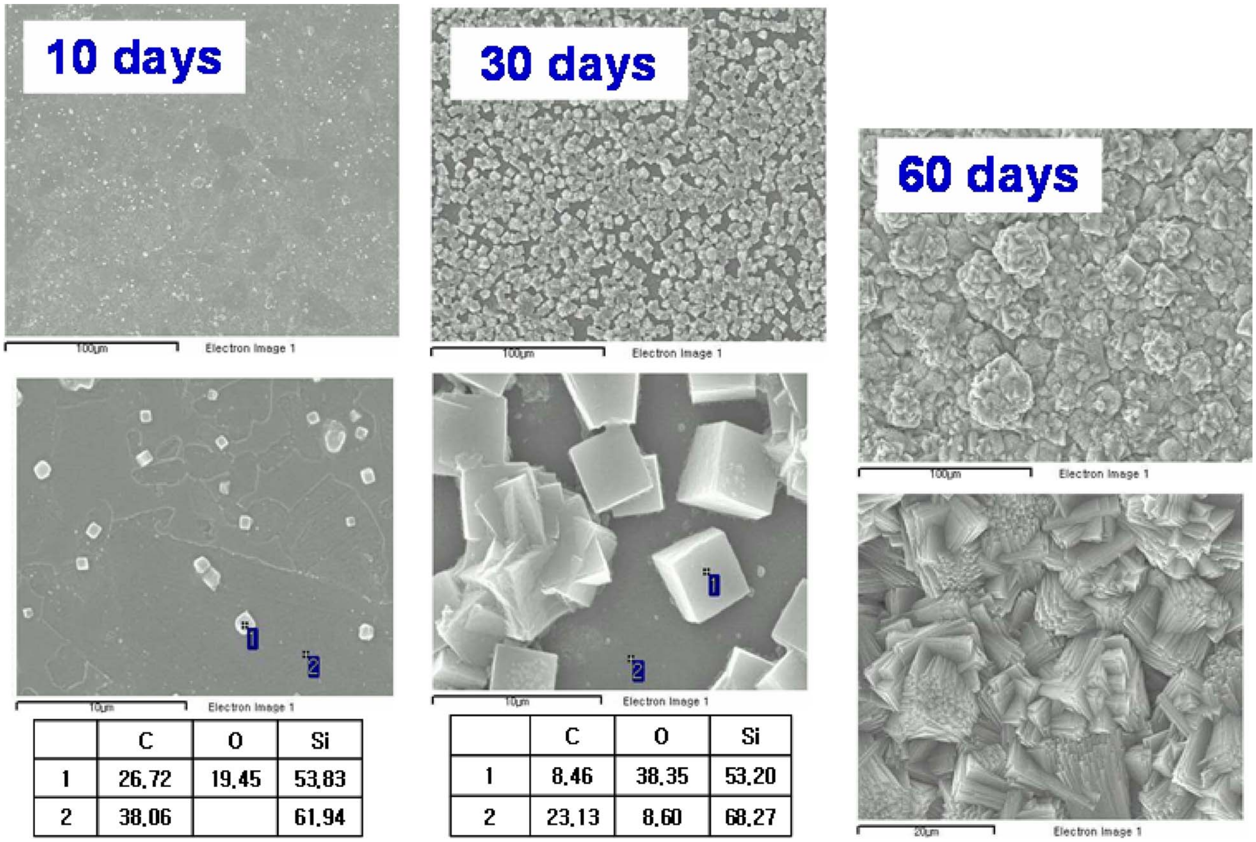

	C	O	Si
1	26.72	19.45	53.83
2	38.06		61.94

(*a*)

	C	O	Si
1	8.46	38.35	53.20
2	23.13	8.60	68.27

(*b*)

(*c*)

Fig. 5 Micrographs obtained from SEM for the SiC in boiling 98 wt % sulfuric acid after (*a*) 10 day immersion, (*b*) 30 day immersion, and (*c*) 60 day immersion

decreased drastically with the immersion time, while the corrosion rate for the specimen without a thermal treatment is about 20 mm/yr. Moreover, the corrosion rate is as high as 20 mm/yr after polishing of a thermal treated specimen indicating that a surface modification during a heat treatment greatly affects the corrosion resistance.

Figures 7(*a*) and 7(*b*) show the micrographs obtained from the SEM for the Fe–6Si without and with a thermal treatment in boiling 98 wt % sulfuric acid, respectively. For Fe–6Si with a thermal treatment, Si rich oxide is observed after the immersion test in boiling 98 wt % sulfuric acid, while there is no oxygen on the

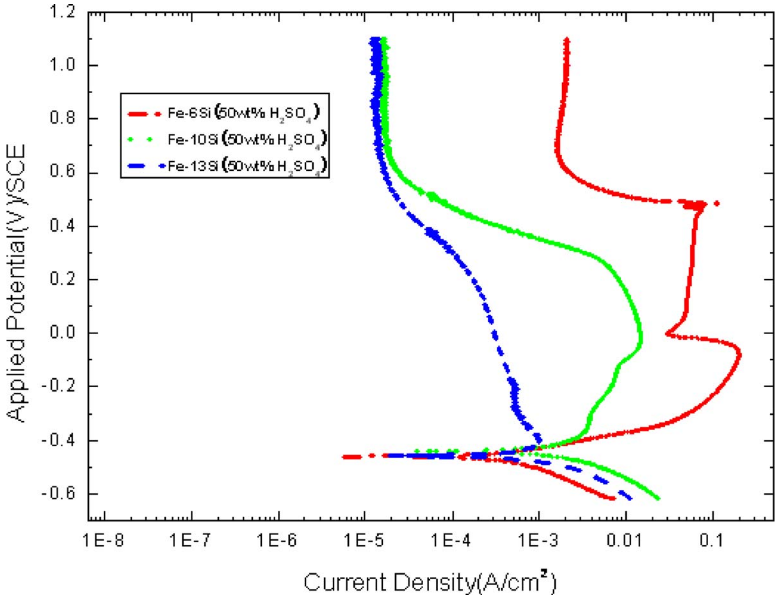

Fig. 6 Potentiodynamic curves for Fe–6Si, Fe–10Si, and Fe–13Si in 50 wt % sulfuric acid at room temperature with a scan rate of 5 mV/s

Downloaded 02 Jun 2010 to 171.66.16.109. Redistribution subject to ASME license or copyright; see http://www.asme.org/terms/Terms_Use.cfm

Table 3 Corrosion rate for Fe–Si alloys after thermal heat treatment in boiling 98 wt % sulfuric acid

mm/yr	Fe–6Si	Fe–10Si	Fe–13Si
	1.3	0.09	0.06
	0.9	0.08	0.06
1 day	1.0	-	0.03
	0.16	0.008	0.016
	0.43	0.016	0.003
10 days	0.71	0.009	0.003
	0.05	0.0005	−0.0023(weightgain)
	0.04	−0.0018(weightgain)	−0.0033(weightgain)
30 days	0.18	0.0015	−0.011 (weightgain)

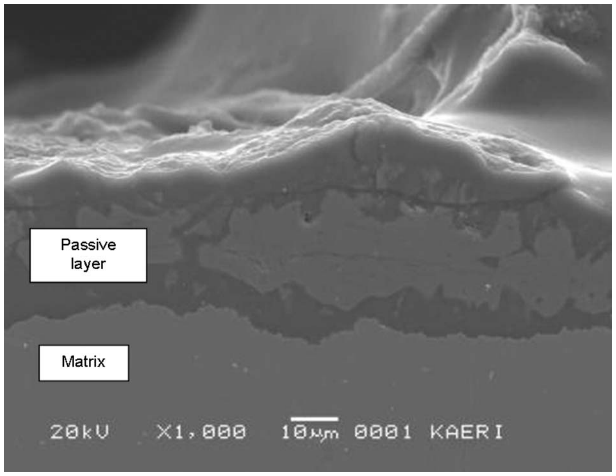

Fig. 8 Micrograph obtained from SEM for the Fe-6Si with thermal treatment after a 30 day immersion in boiling 98 wt % sulfuric acid

Fe–6Si surface without a thermal treatment. It is expected that the passivity of the Si rich oxide is related to the corrosion resistance of the Fe–6Si with a thermal treatment.

Figure 8 presents the micrograph obtained from the SEM for the Fe–6Si with a thermal treatment after a 30 day immersion in boiling 98 wt % sulfuric acid. A 30 μm thick passive layer, which is well adherent to matrix alloy, is observed.

Figure 9 represents the chemical composition as a function of the depth of a passive layer. On the outermost surface of a passive layer, silicon and oxygen are observed, while an iron is not observed. Iron is observed at an interface of a passive layer and the matrix. It is plausible that Si, which is more oxidative than Fe, is selectively oxidized during a heat treatment. At an early immersion time in boiling 98 wt % sulfuric acid, an aqueous solution penetrates into the matrix through silicon oxide leading to a dissolution of Fe, and the dissolved Fe ion is transported through the silicon oxide film leaving a Si enriched matrix. Silicon oxide grows through an oxidation of the Si enriched matrix to become a steady state. Therefore, it is concluded that the silicon oxide layer formed during a heat treatment and grown during an immersion provides the corrosion resistance for Fe–6Si.

4 Summary

For an application of low concentration and low temperature part, Ta, Zr, Au, and SiC showed an excellent corrosion resistance in 50 wt % boiling sulfuric acid, which was selected as an experimental condition by considering the feeding part of the sulfuric

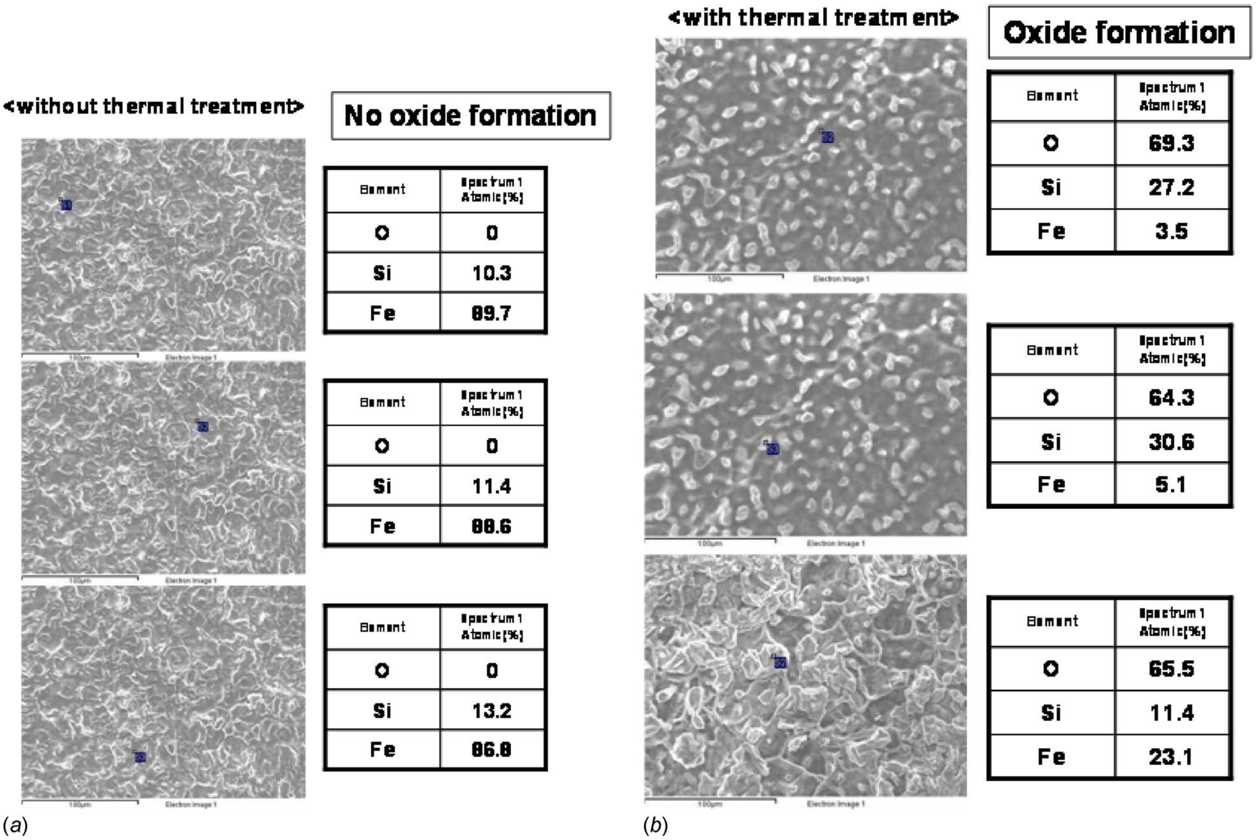

Element	Spectrum 1 Atomic[%]
O	0
Si	10.3
Fe	89.7

Element	Spectrum 1 Atomic[%]
O	0
Si	11.4
Fe	88.6

Element	Spectrum 1 Atomic[%]
O	0
Si	13.2
Fe	86.8

Element	Spectrum 1 Atomic[%]
O	69.3
Si	27.2
Fe	3.5

Element	Spectrum 1 Atomic[%]
O	64.3
Si	30.6
Fe	5.1

Element	Spectrum 1 Atomic[%]
O	65.5
Si	11.4
Fe	23.1

Fig. 7 Micrographs obtained from SEM for the Fe–6Si (*a*) without and (*b*) with thermal treatment in boiling 98 wt % sulfuric acid, respectively

Downloaded 02 Jun 2010 to 171.66.16.109. Redistribution subject to ASME license or copyright; see http://www.asme.org/terms/Terms_Use.cfm

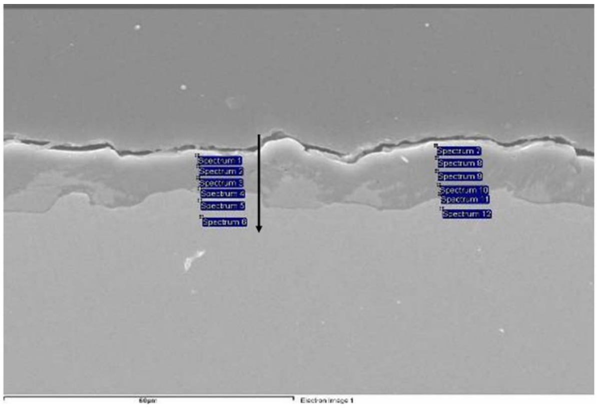

Element	1 Atomic(%)	2 Atomic(%)	3 Atomic(%)	4 Atomic(%)	5 Atomic(%)	6 Atomic(%)
O	75.27	67.66	68.48	61.89	0	0
Si	24.73	32.34	31.52	28.01	8.32	6.58
Fe	0	0	0	10.09	91.68	93.42

Fig. 9 Chemical composition as a function of the depth of a passive layer

acid coming from the Bunsen reactor. However, the corrosion resistance of Au was degraded by adding 0.5 mol HI, which can be incorporated into the sulfuric acid as an impurity.

Au and SiC showed an excellent corrosion resistance in boiling 98 wt % sulfuric acid, which was selected as an experimental condition by considering the concentrator and evaporator required for a concentrated liquid sulfuric acid. Oxides were observed on the surfaces of Au and SiC, which could lead to an excellent corrosion resistance in the 50 wt % and 98 wt % sulfuric acids, while Ta showed a poor corrosion resistance in boiling 98 wt % sulfuric acid.

With regard to Fe-xSi ($x=6\%$, 10%, and 13%), the corrosion rates for Fe–6Si, Fe–10Si, and Fe–13Si in 98 wt % boiling sulfuric acid were decreased with an increase in the Si amount. It is expected that the corrosion resistance of Fe–Si is attributed to a passive SiO_2 formation on the surface, which was explained reasonably well by analyzing the results of the potentiodynamic curves and E-pH diagram.

After an appropriate thermal treatment, the corrosion rate for Fe–6Si was drastically decreased and its corrosion rate was decreased with the immersion time. It seems that a surface modification during a thermal treatment provides passivity against corrosion.

Acknowledgment

This work was financially supported by the Ministry of Education, Science and Technology (MEST) of Korea.

References

[1] IPCC, 2007, “The Physical Science Basis-Summary for Policymakers,” Climate Change 2007.
[2] Chang, J. H., Kim, Y. W., Lee, K. Y., Lee, Y. W., Lee, W. J., Noh, J. M., Kim, M. H., Lim, H. S., Shin, Y. J., Bae, K. K., and Jung, K. D., 2007, “A Study of a Nuclear Hydrogen Production Demonstration Plant,” Nucl. Eng. Tech., **39**(2), pp. 111–122.
[3] Ota, H., Kubo, S., Hodotsuka, M., Inatomi, T., Kobayashi, M., Terada, A., Kasahara, S., Hino, R., Ogura, K., and Maruyama S., 2005, “Conceptual Design Study on Sulfuric-Adic Decomposer for Thermo-Chemical Iodine-Sulfur Process,” 13th International Conference on Nuclear Engineering, Beijing, China, pp. 1–7.
[4] Norman, J., Besenbruch, G., Brown, L., O’Keefe, D. and Allen, C., 1982, “Thermochemical Water-Splitting Cycle Bench-Scale Investigations and Process Engineering,” Paper No. GA-A16713.
[5] Nakajima, H., Sakurai, M., Ikenoya, K., Hwang, G. J., Onuki, K., and Shimizu, S., 1999, “A Study on a Closed-Cycle Hydrogen Production by Thermochemical Water-Splitting IS Process,” ICONE-7, Tokyo, Japan, Paper No. ICONE-7104.
[6] Onuki, K., Nakajima, H., Ioka, I., Futakawa, M. and Shimizu, S., 1994, “IS Process for Thermochemical Hydrogen Production,” JAERI Report No. 94–006.
[7] Kim, D. J., Lee, H. H., Kim, H. P., Yi, Y. S., Ryu, W. S., and Kim, Y. W., 2006, “Corrosion Test of Various Materials in Sulfuric Acid for IS Process,” 14th Asia-Pacific Corrosion Control Congress, Shanghai, China.
[8] Kim, D. J., Lee, H. H., Kwon, H. C., Kim, H. P., and Hwang, S. S., 2007, “Corrosion of Selected Materials in Boling Sulfuric Acid for the Nuclear Power Industries,” Corros. Sci. Technol., **6**, pp. 37–43.
[9] Lu, G., and Zangari, G., 2002, “Corrosion Resistance of Ternary Ni–P Based Alloys in Sulfuric Acid Solutions,” Electrochim. Acta, **47**, pp. 2969–2979.
[10] Pourbaix, M., 1966, *Atlas of Electrochemical Equilibria in Aqueous Solutions*, Pergamon Press, Oxford.

Downloaded 02 Jun 2010 to 171.66.16.109. Redistribution subject to ASME license or copyright; see http://www.asme.org/terms/Terms_Use.cfm

E. López-Honorato

P. J. Meadows

J. Tan

Y. Xiang

P. Xiao[1]
e-mail: ping.xiao@manchester.ac.uk

Materials Science Centre,
School of Materials,
University of Manchester,
Grosvenor Street,
Manchester M1 7HS, UK

Deposition of TRISO Particles With Superhard SiC Coatings and the Characterization of Anisotropy by Raman Spectroscopy

In this work we have deposited silicon carbide (SiC) at 1300°C with the addition of small amounts of propylene. The use of propylene and high concentrations of methyltrichlorosilane (9 vol %) allowed the deposition of superhard SiC coatings (42 GPa). The superhard SiC could result from the presence of a SiC–C solid solution, undetectable by X-ray diffraction but visible by Raman spectroscopy. Another sample obtained by the use of 50 vol % Argon, also showed the formation of SiC with good properties. The use of a flat substrate together with the particles showed the importance of carrying out the analysis on actual particles rather than in flat substrates. We show that it is possible to characterize the anisotropy of pyrolytic carbon by Raman spectroscopy.

[DOI: 10.1115/1.3095804]

1 Introduction

The ever increasing worries produced by climate change, political instabilities in important oil producing countries, and the continuous increase in oil prices have sparked a long awaited interest in nuclear energy. This interest in nuclear technology has brought back the development of the high temperature reactor (HTR). The HTR is considered one of the most promising candidates for the production of nuclear energy due to a series of features, which include the enclosure of its fuel kernel with several layers of ceramics [1]. This type of fuel, known as tristructural isotropic (TRISO) coated fuel particle, is made of three layers of pyrolytic carbon (PyC)—buffer, inner pyrolytic carbon, and outer pyrolytic carbon—and one of silicon carbide.

The development of the HTR technology started with the creation of the Dragon project in the UK in 1959 (criticality achieved in August 1963) [2]. Their results provided an invaluable amount of data and experience that helped in the future development of HTRs in other countries. Among other achievements, their experimental work on the deposition of pyrolytic carbon and silicon carbide helped to establish the basis for the creation of the bistructural isotropic (BISO) and TRISO fuel particles [3–6].

Despite the considerable achievements made in the past, current improvements in the understanding of the deposition of PyC and SiC, together with the availability of new and better characterization techniques, could lead to the production of SiC and PyC coatings with tailored characteristics thus ensuring maximum performance [7].

In this paper we show some of the work currently done in the development of TRISO fuel particles, especially on the deposition of SiC coatings and the characterization of anisotropy of PyC by Raman spectroscopy.

2 Experimental

2.1 Sample Preparation. PyC and SiC were deposited in a fluidized bed chemical vapor deposition (CVD) coater as described in Ref. [8]. A 30 g load of Al_2O_3 particles 500 μm in diameter was initially fluidized by argon in spouted mode at atmospheric pressure. SiC was deposited on top of a high density PyC coating produced at 1250°C with 25 vol % acetylene/propylene. SiC was deposited at 1400°C with 1.3 vol % methyltrichlorosilane (MTS) and 50 vol % argon, and at 1300°C with 9 vol % MTS and 0.5 vol % propylene in a pure hydrogen environment. Pieces of graphite $4 \times 5 \times 4$ mm (length, width, and height) were also introduced in some experiments. A more detailed description of the deposition of PyC can be found elsewhere [8].

2.2 Sample Characterization. Samples were mounted in a copper-loaded resin and ground with successive grades of SiC paper to the cross section of the sample and were polished up to $\frac{1}{4}$ μm diamond paste and silica solution. For the sample produced at 1300°C it was not possible to use SiC paper due to the high hardness of the SiC layer; instead diamond disks were used to grind the samples. Coatings were characterized using Raman spectroscopy (Renishaw 1000 Raman system with a 514 nm Ar-ion laser source). Raman analysis was performed by single spot measurements, using a 50× objective lens.

Measurements were generally performed every 5 μm. PyC samples were ground in a mortar and pestle. Texture was quantified by measuring the orientation angle (OA) obtained from azimuthal intensity scans of selected area electron diffraction (SAED) patterns using a similar method to that of Refs. [9,10]. SAED were recorded in the transmission electron microscope (TEM, FEI Tecnai G2 F30) operating at 300 kV using a Gatan digital camera. For the measurement of the orientation angle, the smallest selected area aperture (SA1 diameter 200 nm) was employed. Other microstructural features were observed by analyzing fractured particles with scanning electron microscopy (Philips XL30 FEG-SEM). X-ray microtomography was carried out using a X-Tek HMX-225 instrument and a charge coupled device (CCD) camera equipped with a beryllium detector. Young's modulus and the hardness of each layer were obtained by nanoindentation (Nanoindenter XP, MTS systems) using continuous stiffness measurement (CSM) and a Berkovich indenter. A maximum penetration depth of 500 nm was established and indentations within each array were typically 10 μm apart from each other on polished cross sections.

---

[1] Corresponding author.

Manuscript received October 22, 2008; final manuscript received October 24, 2008; published online April 16, 2009. Review conducted by Dilip R. Ballal. Paper presented at the Fourth International Topical Meeting on High Temperature Reactor Technology (HTR2008), Washington, DC, September 28–October 01, 2008.

Copyright © 2009 by ASME

Downloaded 02 Jun 2010 to 171.66.16.109. Redistribution subject to ASME license or copyright; see http://www.asme.org/terms/Terms_Use.cfm

Table 1 Young's modulus and hardness of SiC coatings measured by nanoindentation

Sample	Young's modulus (GPa)	Hardness (GPa)
SiC/propylene	448	42
SiC/argon	415	39
SiC/argon/flat	173	23

3 Results and Discussion

3.1 Superhard SiC Coating. The good quality of the SiC coating produced by the addition of 0.5 vol % propylene was evident even during sample preparation, since SiC paper was incapable of grinding the sample due to its high hardness. Young's modulus and the hardness of this sample are shown in Table 1. The hardness of 42 GPa is higher than the hardness obtained by nanoindentation on standard SiC of around 30 GPa. The value of hardness obtained is similar to other superhard SiC previously reported to be around 41 GPa [11].

High concentrations of MTS, which could result in coating rates above the usual 0.2 μm/min [12], are desirable since they could considerably reduce coating times. Figure 1 shows that despite the SiC coating having a coating rate of 1.2 μm/min, it was capable of penetrating the IPyC and forming the rough interface necessary for a good bonding between layers. This rough interface was also clearly identified by the use of X-ray microtomography. Figure 2 shows the isosurface (3D contour or surface within a volumetric data) of the SiC coating, in which the internal section (Inner SiC), corresponding to the IPyC/SiC interface, was considerably rough compared with the outer shell (SiC/OPyC interface). which was relatively flat. No internal defects (soot inclusions or fractures) were identified with X-ray microtomography on different particles, suggesting that the coatings were of good quality. Although not explored here, the use of tomography images could be used not only for the identification of defects, coating thickness, density, and sphericity, but also this type of images could be useful for the modeling of the TRISO particles since it would include features such as roughness and roundness, which are generally omitted.

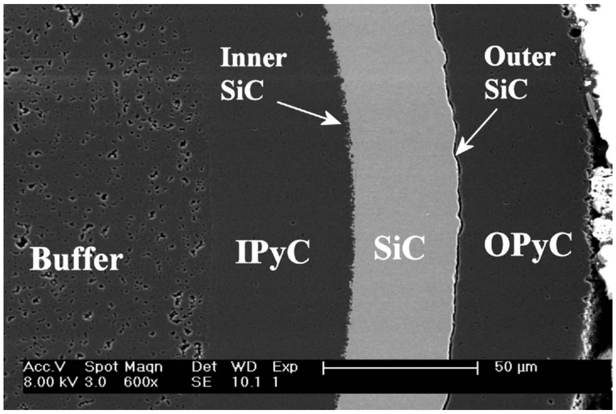

Fig. 1 SEM image of SiC produced at 1300°C and 9 vol % MTS and 0.5 vol % propylene

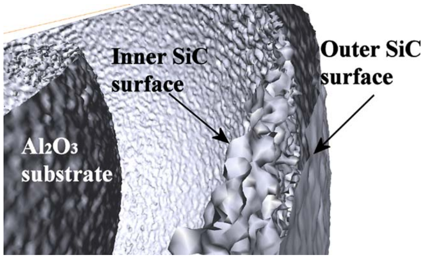

Fig. 2 3D image obtained by X-ray microtomography showing the isosurface of the IPyC/SiC interface and the SiC/OPyC interface. PyC coatings are not shown.

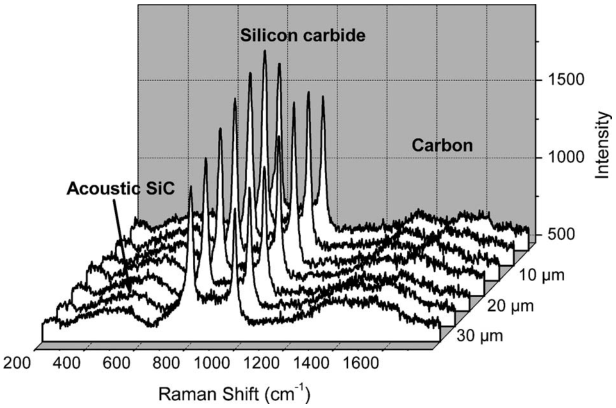

Fig. 3 Phase composition obtained by Raman spectroscopy of the SiC coating deposited at 1300°C

Phase composition was carried out by X-ray diffraction (XRD) and Raman spectroscopy (Fig. 3). As it has been previously reported [7], Raman spectroscopy was capable of detecting small amounts of carbon excesses across the coating, while XRD only showed the formation of stoichiometric β-SiC (spectra not shown). The signals between 1200 cm^{-1} and 1700 cm^{-1}, corresponding to excess carbon, might suggest the presence of diamondlike carbon, which could be partially responsible for the high hardness and Young's modulus shown in Table 1 [11].

3.2 Deposition of SiC Coatings With the Addition of Argon and on Flat Substrates. Another way to control the microstructure is by the use of argon in addition to hydrogen during the deposition of SiC [13]. Furthermore, in order to facilitate the characterization of the coatings, small flat pieces of graphite were also added in addition to the alumina particles into the CVD machine, similar to other experiments performed in the past [13] (Fig. 4).

Figure 5 shows that the addition of 50% Ar was effective in the formation of stoichiometric SiC coatings on the particles. However, there is a clear difference between the coatings produced on the particles and the flat substrate. Figure 5 shows that contrary to the coatings on the particles, the SiC produced on the flat substrate contained considerably high concentrations of excess silicon in

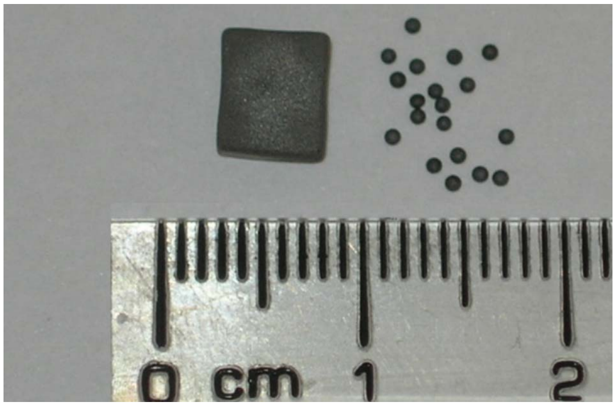

Fig. 4 Flat substrate and coated particles obtained during the deposition of SiC at 1400°C

Downloaded 02 Jun 2010 to 171.66.16.109. Redistribution subject to ASME license or copyright; see http://www.asme.org/terms/Terms_Use.cfm

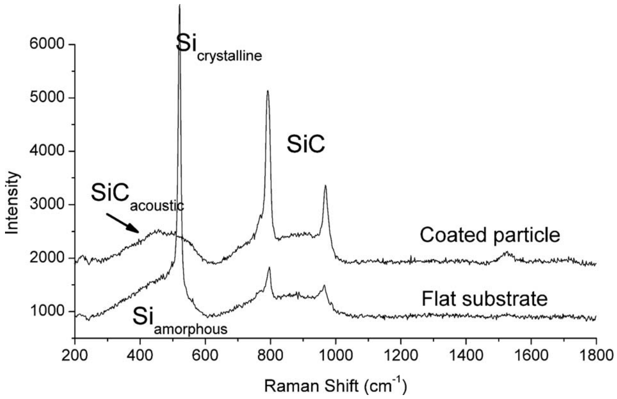

Fig. 5 Differences in stoichiometry between SiC coatings produced on alumina particles and flat substrates

amorphous and crystalline phases.

The mechanical properties between these two samples were considerably different (Table 1). The coated particles gave a Young's modulus and hardness of 415 GPa and 39 GPa, whereas the flat substrate gave 173 GPa and 23 GPa, respectively. The considerably low values of hardness and Young's modulus were due to the excess Si [14].

The deposition of excess Si results from the differences in fluidization and the temperature gradient within the CVD coater. Due to differences in weight and shape, flat substrates do not fluidize as efficiently as particles do. This results in the flat substrate moving slowly and spending longer times at lower sections of the crucible, where the temperature can be 200°C lower than that at the hot zone. This deposition at lower temperatures (i.e., 1200°C) produces the deposition of excess Si due to the low sticking coefficient of carbon intermediate molecules [7].

3.3 Anisotropy Measured by Raman Spectroscopy. The anisotropy of PyC is one of the most important properties of this material since it determines the probability of failure under irradiation. The current nomenclature for PyC divides this material into four categories depending on its texture or anisotropy: high texture (HT), medium texture (MT), low texture (LT), and isotropic (ISO) [15]. Texture was obtained by measuring the orientation angle from SAED patterns (Fig. 6). Using bespoke software, the digital images were converted into plots of intensity versus angle by considering the intensity within a ring enclosing the 002 diffracted arcs (Fig. 6). Following baseline correction, the two peaks obtained were fitted to Gaussian curves of which the full width at half maximum (FWHM) was determined. The orientation angle of each pattern was taken as an average for the two peaks, and the OA for each sample was obtained from an average of 10–25 random diffraction patterns from across the specimen.

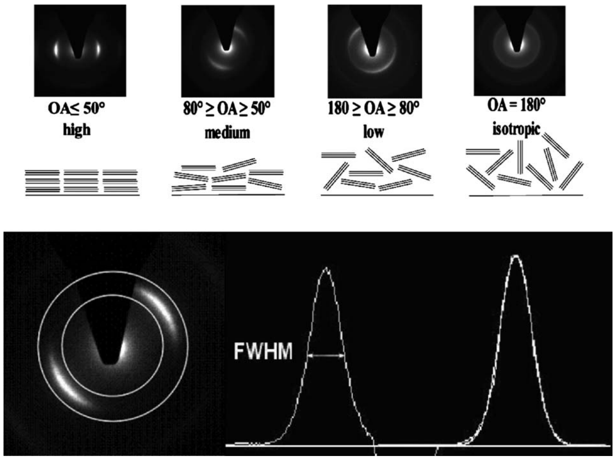

Fig. 6 Measurements of OA from FWHM of azimuthal intensity scan of selected area electron diffraction pattern

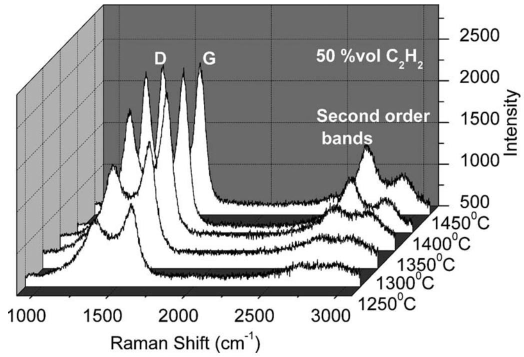

Fig. 7 Changes in the Raman spectra of PyC depending on the deposition conditions

We have produced and analyzed a wide range of structures from high to low texture carbons produced by fluidized bed CVD [8,10]. Figure 7 shows that the intensities of the Raman signal changed with deposition temperature and the level of tortuosity of PyC [10]. In order to establish a fast and easy way to characterize not only the microstructure but also the anisotropy of PyC, we combined the measurements of texture by transmission electron microscopy and the changes observed by Raman spectroscopy. Figure 8 shows that Raman spectroscopy can provide the texture of PyC for medium and low textured carbons. Further details on the application of this technique for the characterization of PyC can be found elsewhere [10,16].

4 Conclusions

The microstructure and mechanical properties of the SiC coatings can be controlled by the use of propylene and/or argon. Superhard SiC coatings were obtained in coatings with small amounts of excess carbon as detected by Raman spectroscopy. The use of X-ray microtomography for the characterization of SiC was also shown. It has also been observed that the deposition of SiC flat pieces of graphite is not suitable since the coating produced was considerably different to that obtained in actual particles. The use of flat substrates could lead to erroneous interpretations in the performance of coated particles, since the SiC studied in the flat substrate would be different from that actually used in coated fuel, thus giving the wrong impression that certain

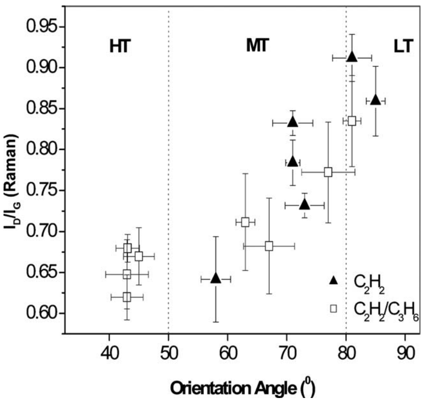

Fig. 8 Texture obtained by TEM and its correlation to Raman signals

Downloaded 02 Jun 2010 to 171.66.16.109. Redistribution subject to ASME license or copyright; see http://www.asme.org/terms/Terms_Use.cfm

microstructures or compositions have better or worst properties. Furthermore, we have established a way to measure the anisotropy of PyC by Raman spectroscopy.

Acknowledgment

The authors would like to thank Francisco A. García Pastor for his help on the processing of tomography images.

References

[1] Lohnert, G. H., Nabielek, H., and Schenk, W., 1988, "The Fuel Element of the HTR-Module, a Prerequisite of an Inherently Safe Reactor," Nucl. Eng. Des., **109**, pp. 257–263.

[2] Rennie, C. A., 1978, "Achievements of the Dragon Project," Ann. Nucl. Energy, **5**, pp. 305–320.

[3] Gough, J. R. C., and Kern, D., 1967, "Studies on the Coating of Fuel Particles for the 'Dragon' Reactor Experiment," J. Nucl. Energy, **21**, pp. 623–642.

[4] Voice, E. H., 1971, "The Formation and Structure of Silicon Carbide Pyrolytically Deposited in a Fluidised Bed of Microspheres," Ph.D. thesis, Bath University, Bath, England.

[5] Dayton, R. W., Oxley, J. H., and Townley, C. W., 1964, "Ceramic Coated Particle Nuclear Fuels," J. Nucl. Mater., **11**, pp. 1–31.

[6] Ford, L. H., Hibbert, N. S., and Martin, D. G., 1972, "Recent Developments of Coatings for GCFR and HTGCR Fuel Particles and Their Performance," J. Nucl. Mater., **45**, pp. 139–149.

[7] López-Honorato, E., Meadows, P. J., Tan, J., and Xiao, P., 2008, "Control of Stoichiometry, Microstructure and Mechanical Properties in SiC Coatings Produced by Fluidized Bed Chemical Vapor Deposition," J. Mater. Res., **23**, pp. 1785–1796.

[8] López-Honorato, E., Meadows, P. J., Xiao, P., Marsh, G., and Abram, T. J., 2008, "Structure and Mechanical Properties of Pyrolytic Carbon Produced by Fluidized Bed Chemical Vapor Deposition," Nucl. Eng. Des., **238**, pp. 3121–3128.

[9] Bourrat, X., Trouvat, B., Limousin, G., and Vignoles, G., 1999, "Pyrocarbon Anisotropy as Measured by Electron Diffraction and Polarized Light," J. Mater. Res., **15**, pp. 92–101.

[10] López-Honorato, E., Meadows, P. J., and Xiao, P., 2008, "Fluidized Bed Chemical Vapor Deposition of Pyrolytic Carbon—I. Effect of Deposition Conditions on Microstructure," Carbon, **47**, pp. 396–410.

[11] Mykhaylyk, O. O., and Gadzira, M., 2001, "Superhard Materials Based on the Solid Solution SiC–C," J. Mater. Chem., **11**, pp. 217–222.

[12] Petti, D. A., Buongiorno, J., Maki, J. T., Hobbins, R. R., and Miller, G. K., 2003, "Key Differences in the Fabrication, Irradiation and High Temperature Accident Testing of US and German TRISO-Coated Particle Fuel, and Their Implications on Fuel Performance," Nucl. Eng. Des., **222**, pp. 281–297.

[13] Minato, K., and Fukuda, K., 1987, "Chemical Vapor Deposition of Silicon Carbide for Coated Fuel Particles," J. Nucl. Mater., **149**, pp. 233–246.

[14] Yeheskel, J., and Dariel, M. S., 1995, "Codeposition of Free Silicon During CVD of Silicon Carbide," J. Am. Ceram. Soc., **78**, pp. 229–232.

[15] Reznik, B., and Huttinger, K. J., 2002, "On the Terminology for Pyrolytic Carbon," Carbon, **40**, pp. 621–624.

[16] Meadows, P. J., Lopez-Honorato, E., and Xiao, P., 2008, "Fluidized Chemical Vapor Deposition of Pyrolytic Carbon—II. Effect of Deposition Conditions on Anisotropy," Carbon, **47**, pp. 251–262.

Downloaded 02 Jun 2010 to 171.66.16.109. Redistribution subject to ASME license or copyright; see http://www.asme.org/terms/Terms_Use.cfm

H.-J. Kretzschmar[2]
Department of Technical Thermodynamics,
Zittau/Goerlitz University of Applied Sciences,
P.O. Box 1455,
D-02754 Zittau, Germany
e-mail: hj.kretzschmar@hs-zigr.de

A. H. Harvey
National Institute of Standards and Technology,
Physical and Chemical Properties Division,
Boulder, CO 80305

K. Knobloch
Department of Technical Thermodynamics,
Zittau/Goerlitz University of Applied Sciences,
P.O. Box 1455,
D-02754 Zittau, Germany

R. Mareš
Department of Technical Thermodynamics,
University of West Bohemia,
CZ 306 14 Plzeň, Czech Republic

K. Miyagawa
4-12-11-628 Nishiogu, Arakawa-ku,
Tokyo 116-0011, Japan

N. Okita
Thermal Plant Systems Project Department,
Toshiba Corporation,
Yokohama 230-0045, Japan

R. Span
Chair of Thermodynamics
Ruhr-University Bochum,
D-44780 Bochum, Germany

I. Stöcker
Department of Technical Thermodynamics,
Zittau/Goerlitz University of Applied Sciences,
P.O. Box 1455,
D-02754 Zittau, Germany

W. Wagner
Chair of Thermodynamics
Ruhr-University Bochum,
D-44780 Bochum, Germany

I. Weber
Siemens AG,
Fossil Power Generation,
D-91050 Erlangen, Germany

Supplementary Backward Equations $v(p,T)$ for the Critical and Supercritical Regions (Region 3) of the IAPWS Industrial Formulation 1997 for the Thermodynamic Properties of Water and Steam[1]

When steam power cycles are modeled, thermodynamic properties as functions of pressure and temperature are required in the critical and supercritical regions (region 3 of IAPWS-IF97). With IAPWS-IF97, such calculations require cumbersome iterative calculations, because temperature and volume are the independent variables in the formulation for this region. In order to reduce the computing time, the International Association for the Properties of Water and Steam (IAPWS) adopted a set of backward equations for volume as a function of pressure and temperature in region 3. The necessary numerical consistency is achieved by dividing the region into 20 subregions, plus auxiliary subregions near the critical point in which the consistency requirements are relaxed due to the singular behavior at the critical point. In this work, we provide complete documentation of these equations, along with a discussion of their numerical consistency and the savings in computer time. The numerical consistency of these equations should be sufficient for most applications in heat-cycle, boiler, and steam-turbine calculations; if even higher consistency is required, the equations may be used to generate guesses for iterative procedures. [DOI: 10.1115/1.3028630]

1 Introduction

The International Association for the Properties of Water and Steam (IAPWS) adopted the IAPWS Industrial Formulation 1997 for the Thermodynamic Properties of Water and Steam (IAPWS-IF97) [1–3] as the standard for calculation of thermodynamic properties of water and steam in the power industry in 1997 and extended it in 2007. It contains basic equations, saturation equations, and equations for the commonly used "backward" functions $T(p,h)$ and $T(p,s)$ valid in the liquid region 1 and the vapor region 2; see Fig. 1.

In 2001, IAPWS-IF97 was supplemented by "Backward Equations for Pressure as a Function of Enthalpy and Entropy $p(h,s)$ to the IAPWS Industrial Formulation 1997 for the Thermodynamic Properties of Water and Steam" [4,5], referred to here as IAPWS-IF97-S01. These equations are valid in regions 1 and 2.

An additional supplementary release "Backward Equations for

---

[1] Partial contribution of the National Institute of Standards and Technology, not subject to copyright in the U.S.

[2] Corresponding author.

Manuscript received May 20, 2008; final manuscript received July 1, 2008; published online April 13, 2009. Review conducted by Dilip R. Ballal.

Copyright © 2009 by ASME

Downloaded 02 Jun 2010 to 171.66.16.109. Redistribution subject to ASME license or copyright; see http://www.asme.org/terms/Terms_Use.cfm

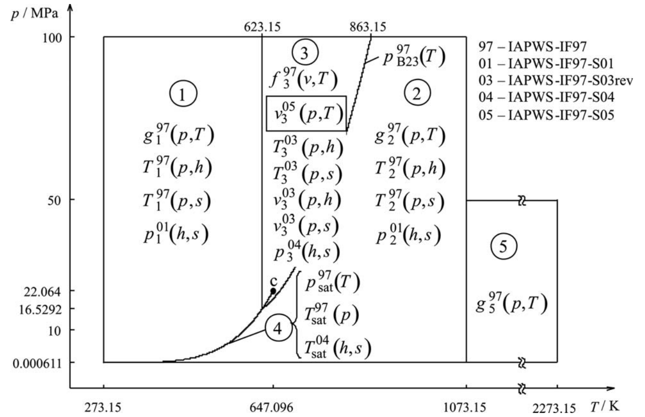

Fig. 1 Regions and equations of IAPWS-IF97, IAPWS-IF97-S01, IAPWS-IF97-S03rev, IAPWS-IF97-S04, and the equations $v_3(p,T)$ of this work adopted as IAPWS-IF97-S05

the Functions $T(p,h)$, $v(p,h)$ and $T(p,s)$, $v(p,s)$ for Region 3 of the IAPWS Industrial Formulation 1997 for the Thermodynamic Properties of Water and Steam" [6,7], referred to here as IAPWS-IF97-S03rev, was adopted by IAPWS in 2003 and extended in 2004.

In 2004, IAPWS-IF97 was supplemented by "Supplementary Release on Backward Equations $p(h,s)$ for Region 3, Equations as a Function of h and s for the Region Boundaries, and an Equation $T_{sat}(h,s)$ for Region 4 of the IAPWS Industrial Formulation 1997 for the Thermodynamic Properties of Water and Steam" [8,9], referred to here as IAPWS-IF97-S04.

The basic equation $f_3(\rho,T)$ is used in region 3 of IAPWS-IF97. This equation, along with the backward equations $v(p,h)$, $T(p,h)$, $v(p,s)$, $T(p,s)$, and $p(h,s)$, can be used to calculate all thermodynamic properties as a function of (p,h), (p,s), and (h,s) without iteration. However, in modeling modern steam power cycles, properties as a function of the variables (p,T) are required for region 3. Such calculations from the basic equation $f_3(\rho,T)$ are cumbersome, because they require iteration of v for given values of p and T using the relation $p(v,T)$ with $v=1/\rho$ derived from $f_3(\rho,T)$.

In order to avoid such iteration, this paper provides backward equations $v_3(p,T)$ for region 3 as shown in Fig. 1. With the specific volume v calculated from the backward equations $v_3(p,T)$, all other properties in region 3 can be calculated without iteration from the basic equation $f_3(\rho,T)$ with $\rho=1/v_3$.

For process calculations, the numerical consistency requirements for the backward equations $v_3(p,T)$ are very strict. Since the specific volume on the v-p-T surface has a complicated structure including an infinite slope at the critical point, region 3 had to be divided into 26 subregions. The first 20 subregions and their associated backward equations, described in Sec. 4, cover nearly all of region 3 and fully meet the consistency requirements given in Sec. 2. For a small area very near the critical point, it was not possible to meet the consistency requirements completely. This near-critical region is covered with reasonable consistency by six subregions with auxiliary equations that are described in Sec. 5.

This set of backward and auxiliary equations was adopted by IAPWS in 2005, referred to here as IAPWS-IF97-S05 [10]. The purpose of this paper is to fully document IAPWS-IF97-S05.

The entire system of supplementary backward equations adopted by IAPWS is summarized in Ref. [11] and described in detail in Ref. [12].

2 Numerical Consistency Requirements

In region 3, any property calculation from the basic equation $f_3(\rho,T)$ for given values of p and T requires the determination of the density by iteration. The permissible numerical consistency of the equations for specific volume with the IAPWS-IF97 fundamental equation was determined based on the required accuracy of the iteration otherwise used. The iteration accuracy depends on thermodynamic process calculations. To obtain specific enthalpy or entropy from pressure and temperature in region 3 with a maximum deviation of 0.001% from IAPWS-IF97, and isobaric heat capacity or speed of sound with a maximum deviation of 0.01%, the inconsistencies in v between the backward equations $v_3(p,T)$ and the basic equation $f_3(\rho,T)$ had to be less than 0.001%, and for some parts of region 3 even smaller. The consistency requirements for all of these properties are summarized in Table 1.

Table 1 Permissible numerical inconsistencies in the properties v, h, s, c_p, and w, when v is calculated first via iteration with the basic equation $f_3(\rho,T)$ for given inputs of p and T, and second directly from the backward equation $v_3(\rho,T)$. Based on these two (slightly different) v values, the properties h, s, c_p, and w are obtained from the basic equation $f_3(\rho,T)$. (The values for v are calculated from the backward equations $v_3(\rho,T)$.)

Permissible inconsistencies				
$\lvert\Delta v/v\rvert_{perm}$	$\lvert\Delta h/h\rvert_{perm}$	$\lvert\Delta s/s\rvert_{perm}$	$\lvert\Delta c_p/c_p\rvert_{perm}$	$\lvert\Delta w/w\rvert_{perm}$
0.001%	0.001%	0.001%	0.01%	0.01%

In the near-critical region, there are no defined numerical consistency requirements for the auxiliary equations, but the inconsistencies should be as small as possible.

3 Range of Validity of the Backward and Auxiliary Equations

The range of validity of the entire set of backward equations $v_3(p,T)$ corresponds to region 3 of IAPWS-IF97, which is defined by the following range of temperature and pressure:

$$623.15\ \text{K} < T < 863.15\ \text{K and } p_{B23}(T) < p \leqslant 100\ \text{MPa}$$

with $p_{B23}(T)$ defined by the B23-equation [1,2] as shown in Fig. 1.

The numerical consistency requirement of 0.001% for $v_3(p,T)$ proved to be infeasible to achieve with simple functional forms in the region

$$p_{sat}(643.15\ \text{K}) < p \leqslant 22.5\ \text{MPa}, \quad T_{3qu}(p) < T \leqslant T_{3rx}(p)$$

where $p_{sat}(643.15\ \text{K})=21.03436732$ MPa. This region is marked in gray in Fig. 2, which also shows the temperature and pressure range of the boundary equations $T_{3qu}(p)$ and $T_{3rx}(p)$. The boundary equations themselves are given in Sec. 4.2, and $p_{sat}(643.15\ \text{K})$ is calculated from the IAPWS-IF97 saturation-pressure equation.

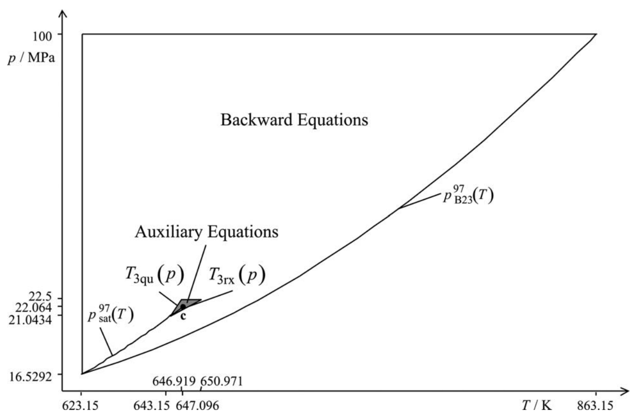

Fig. 2 Range of validity of the backward and auxiliary equations. The area in gray is not to scale but is enlarged to make the small area more visible.

Downloaded 02 Jun 2010 to 171.66.16.109. Redistribution subject to ASME license or copyright; see http://www.asme.org/terms/Terms_Use.cfm

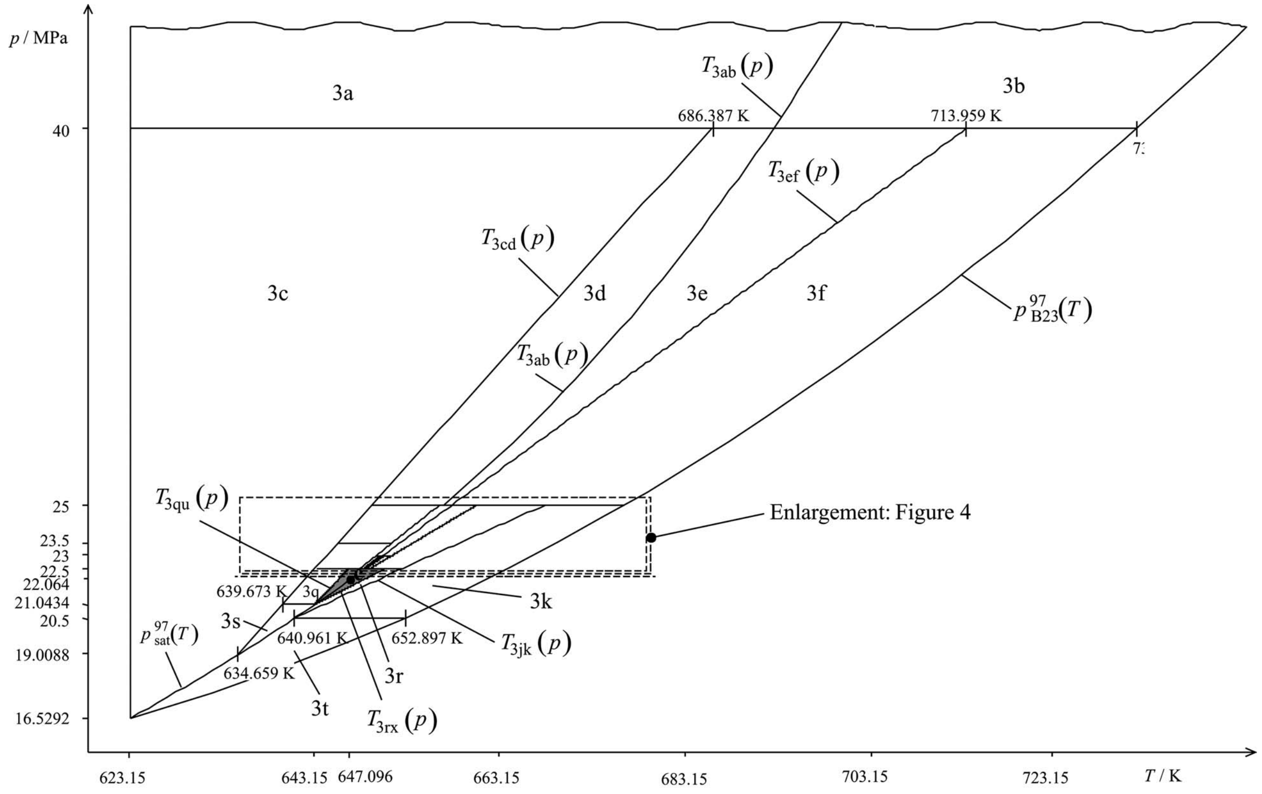

Fig. 3 Division of region 3 into subregions for the backward equations $v_3(p,T)$

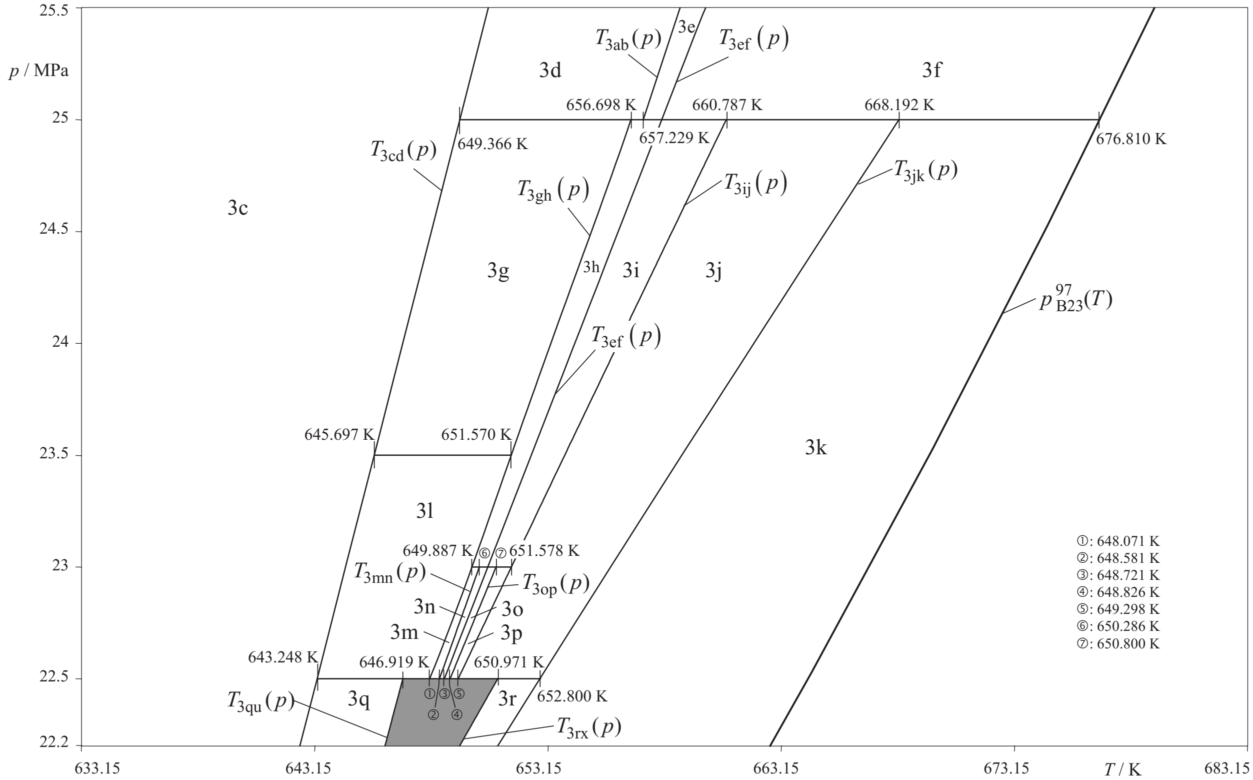

Fig. 4 Enlargement from Fig. 3 for the subregions 3c–3r for the backward equation $v(p,T)$

Downloaded 02 Jun 2010 to 171.66.16.109. Redistribution subject to ASME license or copyright; see http://www.asme.org/terms/Terms_Use.cfm

The reason for excluding the near-critical region (gray area in Fig. 2) from the range of validity of the backward equations $v_3(p,T)$ is based on the complex structure of this region on the v-p-T surface with the infinite slope $(\partial v/\partial p)_T$ at the critical point. In order to not exclude any region completely from the equations $v(p,T)$, Sec. 5 contains equations for this small region very close to the critical point. These equations exhibit larger inconsistencies with the basic equation $f_3(\rho,T)$ and are called auxiliary equations in this work.

4 Backward Equations $v(p,T)$ for Subregions 3a–3t

4.1 Development of the Equations $v(p,T)$. A major motivation for the development of IAPWS-IF97 and its supplementary backward equations was to reduce the time for computing thermodynamic properties. As shown previously [13], the following functional form is effective for this purpose:

$$\frac{Z(X,Y)}{Z^*} = \sum_i n_i \left(\frac{X}{X^*} + a \right)^{I_i} \left(\frac{Y}{Y^*} + b \right)^{J_i} \tag{1}$$

where the reducing parameters Z^*, X^*, and Y^* are typically maximum values of the corresponding property within the range of validity of the equation. The shifting parameters a and b were determined by nonlinear optimization. The exponents I_i and J_i and coefficients n_i were determined from the structure optimization method of Wagner [14] and Setzmann and Wagner [15], which chooses the optimal terms from a bank of terms with various

Table 2 Numerical values of the coefficients of the equations for subregion boundaries (except $T_{3\mathrm{ef}}(p)$)

Equation	i	I_i	n_i
$T_{3\mathrm{ab}}(p)$	1	0	$0.154793642129415 \times 10^{4}$
	2	1	$-0.187661219490113 \times 10^{3}$
	3	2	$0.213144632222113 \times 10^{2}$
	4	−1	$-0.191887498864292 \times 10^{4}$
	5	−2	$0.918419702359447 \times 10^{3}$
$T_{3\mathrm{cd}}(p)$	1	0	$0.585276966696349 \times 10^{3}$
	2	1	$0.278233532206915 \times 10^{1}$
	3	2	$-0.127283549295878 \times 10^{-1}$
	4	3	$0.159090746562729 \times 10^{-3}$
$T_{3\mathrm{gh}}(p)$	1	0	$-0.249284240900418 \times 10^{5}$
	2	1	$0.428143584791546 \times 10^{4}$
	3	2	$-0.269029173140130 \times 10^{3}$
	4	3	$0.751608051114157 \times 10^{1}$
	5	4	$-0.787105249910383 \times 10^{-1}$
$T_{3\mathrm{ij}}(p)$	1	0	$0.584814781649163 \times 10^{3}$
	2	1	-0.616179320924617
	3	2	0.260763050899562
	4	3	$-0.587071076864459 \times 10^{-2}$
	5	4	$0.515308185433082 \times 10^{-4}$
$T_{3\mathrm{jk}}(p)$	1	0	$0.617229772068439 \times 10^{3}$
	2	1	$-0.770600270141675 \times 10^{1}$
	3	2	0.697072596851896
	4	3	$-0.157391839848015 \times 10^{-1}$
	5	4	$0.137897492684194 \times 10^{-3}$
$T_{3\mathrm{mn}}(p)$	1	0	$0.535339483742384 \times 10^{3}$
	2	1	$0.761978122720128 \times 10^{1}$
	3	2	-0.158365725441648
	4	3	$0.192871054508108 \times 10^{-2}$
$T_{3\mathrm{op}}(p)$	1	0	$0.969461372400213 \times 10^{3}$
	2	1	$-0.332\,500170441278 \times 10^{3}$
	3	2	$0.642\,859598466067 \times 10^{2}$
	4	−1	$0.773845935768222 \times 10^{3}$
	5	−2	$-0.152313732937084 \times 10^{4}$
$T_{3\mathrm{qu}}(p)$	1	0	$0.565603648239126 \times 10^{3}$
	2	1	$0.529062258221222 \times 10^{1}$
	3	2	-0.102020639611016
	4	3	$0.122240301070145 \times 10^{-2}$
$T_{3\mathrm{rx}}(p)$	1	0	$0.584561202520006 \times 10^{3}$
	2	1	$-0.102961025163669 \times 10^{1}$
	3	2	0.243293362700452
	4	3	$-0.294905044740799 \times 10^{-2}$

Table 3 Pressure ranges and corresponding subregion-boundary equations for determining the correct subregion, 3a to 3t, for the backward equations $v_3(p,T)$

Pressure range	Subregion	Temperature range
40 MPa $< p \leq$ 100 MPa	3a	$T \leq T_{3\mathrm{ab}}(p)$
	3b	$T > T_{3\mathrm{ab}}(p)$
25 MPa $< p \leq$ 40 MPa	3c	$T \leq T_{3\mathrm{cd}}(p)$
	3d	$T_{3\mathrm{cd}}(p) < T \leq T_{3\mathrm{ab}}(p)$
	3e	$T_{3\mathrm{ab}}(p) < T \leq T_{3\mathrm{ef}}(p)$
	3f	$T > T_{3\mathrm{ef}}(p)$
23.5 MPa $< p \leq$ 25 MPa	3c	$T \leq T_{3\mathrm{cd}}(p)$
	3g	$T_{3\mathrm{cd}}(p) < T \leq T_{3\mathrm{gh}}(p)$
	3h	$T_{3\mathrm{gh}}(p) < T \leq T_{3\mathrm{ef}}(p)$
	3i	$T_{3\mathrm{ef}}(p) < T \leq T_{3\mathrm{ij}}(p)$
	3j	$T_{3\mathrm{ij}}(p) < T \leq T_{3\mathrm{jk}}(p)$
	3k	$T > T_{3\mathrm{jk}}(p)$
23 MPa $< p \leq$ 23.5 MPa	3c	$T \leq T_{3\mathrm{cd}}(p)$
	3l	$T_{3\mathrm{cd}}(p) < T \leq T_{3\mathrm{gh}}(p)$
	3h	$T_{3\mathrm{gh}}(p) < T \leq T_{3\mathrm{ef}}(p)$
	3i	$T_{3\mathrm{ef}}(p) < T \leq T_{3\mathrm{ij}}(p)$
	3j	$T_{3\mathrm{ij}}(p) < T \leq T_{3\mathrm{jk}}(p)$
	3k	$T > T_{3\mathrm{jk}}(p)$
22.5 MPa $< p \leq$ 23 MPa	3c	$T \leq T_{3\mathrm{cd}}(p)$
	3l	$T_{3\mathrm{cd}}(p) < T \leq T_{3\mathrm{gh}}(p)$
	3m	$T_{3\mathrm{gh}}(p) < T \leq T_{3\mathrm{mm}}(p)$
	3n	$T_{3\mathrm{mm}}(p) < T \leq T_{3\mathrm{ef}}(p)$
	3o	$T_{3\mathrm{ef}}(p) < T \leq T_{3\mathrm{op}}(p)$
	3p	$T_{3\mathrm{op}}(p) < T \leq T_{3\mathrm{ij}}(p)$
	3j	$T_{3\mathrm{ij}}(p) < T \leq T_{3\mathrm{jk}}(p)$
	3k	$T > T_{3\mathrm{jk}}(p)$
$p_{\mathrm{sat}}(643.15\ \mathrm{K})^{\mathrm{a}} < p \leq$ 22.5 MPa	3c	$T \leq T_{3\mathrm{cd}}(p)$
	3q	$T_{3\mathrm{cd}}(p) < T \leq T_{3\mathrm{qu}}(p)$
	3r	$T_{3\mathrm{rx}}(p) < T \leq T_{3\mathrm{jk}}(p)$
	3k	$T > T_{3\mathrm{jk}}(p)$
20.5 MPa $< p \leq p_{\mathrm{sat}}(643.15\ \mathrm{K})^{\mathrm{a}}$	3c	$T \leq T_{3\mathrm{cd}}(p)$
	3s	$T_{3\mathrm{cd}}(p) < T \leq T_{\mathrm{sat}}(p)$
	3r	$T_{\mathrm{sat}}(p) \leq T \leq T_{3\mathrm{jk}}(p)$
	3k	$T > T_{3\mathrm{jk}}(p)$
$p_{3\mathrm{cd}}{}^{\mathrm{b}} < p \leq$ 20.5 MPa	3c	$T \leq T_{3\mathrm{cd}}(p)$
	3s	$T_{3\mathrm{cd}}(p) < T \leq T_{\mathrm{sat}}(p)$
	3t	$T \geq T_{\mathrm{sat}}(p)$
$p_{\mathrm{sat}}(623.15\ \mathrm{K})^{\mathrm{c}} < p \leq p_{3\mathrm{cd}}{}^{\mathrm{b}}$	3c	$T \leq T_{\mathrm{sat}}(p)$
	3t	$T \geq T_{\mathrm{sat}}(p)$

[a] $p_{\mathrm{sat}}(643.15\ \mathrm{K}) = 21.04336732$ MPa.
[b] $p_{3\mathrm{cd}} = 19.00881189$ MPa.
[c] $p_{\mathrm{sat}}(623.15\ \mathrm{K}) = 16.52916425$ MPa.

Downloaded 02 Jun 2010 to 171.66.16.109. Redistribution subject to ASME license or copyright; see http://www.asme.org/terms/Terms_Use.cfm

Table 4 Temperature values calculated from the subregion-boundary equations for selected pressures

Equation	p (MPa)	T (K)
$T_{3\mathrm{ab}}(p)$	40	6.930341408×10^{2}
$T_{3\mathrm{cd}}(p)$	25	6.493659208×10^{2}
$T_{3\mathrm{ef}}(p)$	40	7.139593992×10^{2}
$T_{3\mathrm{gh}}(p)$	23	6.498873759×10^{2}
$T_{3\mathrm{ij}}(p)$	23	6.515778091×10^{2}
$T_{3\mathrm{jk}}(p)$	23	6.558338344×10^{2}
$T_{3\mathrm{mn}}(p)$	22.8	6.496054133×10^{2}
$T_{3\mathrm{op}}(p)$	22.8	6.500106943×10^{2}
$T_{3\mathrm{qu}}(p)$	22	6.456355027×10^{2}
$T_{3\mathrm{rx}}(p)$	22	6.482622754×10^{2}

values of I_i and J_i. The final equations were developed using the approximation algorithm developed in previous work [16–19].

In the approximation process, the backward equations were fitted to v-p-T values, with p calculated from the IAPWS-IF97 basic equation $f_3(\rho,T)$ for values of $\rho=1/v$ and T distributed over the range of validity. The computing time is considered in the optimization. Details of the fitting processes are given in Refs. [11,16].

4.2 Division of Region 3 into Subregions and the Subregion-Boundary Equations. Preliminary investigations showed that it was not possible to meet the numerical consistency requirements with only a few subregions. Therefore, the main part of region 3 was divided into 20 subregions 3a–3t, as illustrated in Figs. 3 and 4.

The following subscripts mark the boundaries that separate the adjacent subregions:

3ab:	boundary between subregions	3a/3b and 3d/3e
3cd:	boundary between subregions	3c/3d, 3c/3g, and 3c/3l
3ef:	boundary between subregions	3e/3f, 3h/3i, and 3n/3o
3gh:	boundary between subregions	3g/3h and 3l/3m
3ij:	boundary between subregions	3i/3j and 3p/3j
3jk:	boundary between subregions	3j/3k and 3r/3k
3mn:	boundary between subregions	3m/3n
3op:	boundary between subregions	3o/3p
3qu:	boundary between subregions	3q/3u
3rx:	boundary between subregions	3r/3x
3uv:	boundary between subregions	3u/3v
3wx:	boundary between subregions	3w/3x
B23:	boundary between regions	2/3

These subregion boundaries are also shown in Figs. 3 and 4.

The subregion-boundary equations, except for the equations $T_{3\mathrm{ab}}(p)$, $T_{3\mathrm{ef}}(p)$, and $T_{3\mathrm{op}}(p)$, have the dimensionless form

$$\frac{T(p)}{T^*}=\theta(\pi)=\sum_{i=1}^{N} n_i \pi^{I_i} \qquad (2)$$

where $\theta=T/T^*$ and $\pi=p/p^*$ with $T^*=1$ K and $p^*=1$ MPa.

The equations $T_{3\mathrm{ab}}(p)$ and $T_{3\mathrm{op}}(p)$ have the form

Table 5 Reducing quantities v^*, p^*, and T^*, the number of coefficients N, the nonlinear parameters a and b, and exponents c, d, and e of the backward equations $v(p,T)$ of subregions 3a–3t

Subregion	v^* (m^3 kg^{-1})	p^* (MPa)	T^* (K)	N	a	b	c	d	e
3a	0.0024	100	760	30	0.085	0.817	1	1	1
3b	0.0041	100	860	32	0.280	0.779	1	1	1
3c	0.0022	40	690	35	0.259	0.903	1	1	1
3d	0.0029	40	690	38	0.559	0.939	1	1	4
3e	0.0032	40	710	29	0.587	0.918	1	1	1
3f	0.0064	40	730	42	0.587	0.891	0.5	1	4
3g	0.0027	25	660	38	0.872	0.971	1	1	4
3h	0.0032	25	660	29	0.898	0.983	1	1	4
3i	0.0041	25	660	42	0.910	0.984	0.5	1	4
3j	0.0054	25	670	29	0.875	0.964	0.5	1	4
3k	0.0077	25	680	34	0.802	0.935	1	1	1
3l	0.0026	24	650	43	0.908	0.989	1	1	4
3m	0.0028	23	650	40	1.000	0.997	1	0.25	1
3n	0.0031	23	650	39	0.976	0.997	—	—	—
3o	0.0034	23	650	24	0.974	0.996	0.5	1	1
3p	0.0041	23	650	27	0.972	0.997	0.5	1	1
3q	0.0022	23	650	24	0.848	0.983	1	1	4
3r	0.0054	23	650	27	0.874	0.982	1	1	1
3s	0.0022	21	640	29	0.886	0.990	1	1	4
3t	0.0088	20	650	33	0.803	1.020	1	1	1

Table 6 Values of the specific volume calculated from the backward equations $v(p,T)$ of subregions 3a–3t for selected values of pressure and temperature

Equation	p (MPa)	T (K)	v (m^3 kg^{-1})
$v_{3\mathrm{a}}(p,T)$	50	630	1.470853100×10^{-3}
	80	670	1.503831359×10^{-3}
$v_{3\mathrm{b}}(p,T)$	50	710	2.204728587×10^{-3}
	80	750	1.973692940×10^{-3}
$v_{3\mathrm{c}}(p,T)$	20	630	1.761696406×10^{-3}
	30	650	1.819560617×10^{-3}
$v_{3\mathrm{d}}(p,T)$	26	656	2.245587720×10^{-3}
	30	670	2.506897702×10^{-3}
$v_{3\mathrm{e}}(p,T)$	26	661	2.970225962×10^{-3}
	30	675	3.004627086×10^{-3}
$v_{3\mathrm{f}}(p,T)$	26	671	5.019029401×10^{-3}
	30	690	4.656470142×10^{-3}
$v_{3\mathrm{g}}(p,T)$	23.6	649	2.163198378×10^{-3}
	24	650	2.166044161×10^{-3}
$v_{3\mathrm{h}}(p,T)$	23.6	652	2.651081407×10^{-3}
	24	654	2.967802335×10^{-3}
$v_{3\mathrm{i}}(p,T)$	23.6	653	3.273916816×10^{-3}
	24	655	3.550329864×10^{-3}
$v_{3\mathrm{j}}(p,T)$	23.5	655	4.545001142×10^{-3}
	24	660	5.100267704×10^{-3}
$v_{3\mathrm{k}}(p,T)$	23	660	6.109525997×10^{-3}
	24	670	6.427325645×10^{-3}
$v_{3\mathrm{l}}(p,T)$	22.6	646	2.117860851×10^{-3}
	23	646	2.062374674×10^{-3}
$v_{3\mathrm{m}}(p,T)$	22.6	648.6	2.533063780×10^{-3}
	22.8	649.3	2.572971781×10^{-3}
$v_{3\mathrm{n}}(p,T)$	22.6	649.0	2.923432711×10^{-3}
	22.8	649.7	2.913311494×10^{-3}
$v_{3\mathrm{o}}(p,T)$	22.6	649.1	3.131208996×10^{-3}
	22.8	649.9	3.221160278×10^{-3}
$v_{3\mathrm{p}}(p,T)$	22.6	649.4	3.715596186×10^{-3}
	22.8	650.2	3.664754790×10^{-3}
$v_{3\mathrm{q}}(p,T)$	21.1	640	1.970999272×10^{-3}
	21.8	643	2.043919161×10^{-3}
$v_{3\mathrm{r}}(p,T)$	21.1	644	5.251009921×10^{-3}
	21.8	648	5.256844741×10^{-3}
$v_{3\mathrm{s}}(p,T)$	19.1	635	1.932829079×10^{-3}
	20	638	1.985387227×10^{-3}
$v_{3\mathrm{t}}(p,T)$	17	626	8.483262001×10^{-3}
	20	640	6.227528101×10^{-3}

Downloaded 02 Jun 2010 to 171.66.16.109. Redistribution subject to ASME license or copyright; see http://www.asme.org/terms/Terms_Use.cfm

$$\frac{T(p)}{T^*} = \theta(\pi) = \sum_{i=1}^{N} n_i (\ln \pi)^{I_i} \tag{3}$$

and $T_{3\mathrm{ef}}(p)$ has the form

$$\frac{T_{3\mathrm{ef}}(p)}{T^*} = \theta(\pi) = \left.\frac{\mathrm{d}\theta}{\mathrm{d}\pi}\right|_{\mathrm{c}} (\pi - 22.064) + 647.096 \tag{4}$$

where the derivative of the IAPWS-IF97 saturation-temperature equation at the critical point is $\mathrm{d}\theta/\mathrm{d}\pi|_{\mathrm{c}} = 3.727888004$.

The coefficients n_i and exponents I_i of these subregion-boundary equations are listed in Table 2.

With the help of the ranges of pressure and temperature given in Table 3, any (p,T) point can be assigned to the corresponding subregions 3a–3t as given in Figs. 3 and 4; the subregion-boundary equations $T_{3\mathrm{ab}}(p)$ to $T_{3\mathrm{rx}}(p)$ are defined in Eqs. (2)–(4) in combination with Table 2.

The information given above completely documents the equations for these subregion boundaries. Some of the equations are designed to approximate specific physical relationships such as isentropes. This is discussed in more detail elsewhere [10,11].

To assist the user in computer-program verification of the equations for the subregion boundaries, Table 4 contains test values for calculated temperatures.

4.3 Backward Equations $v(p,T)$. The backward equations $v(p,T)$ for subregions 3a–3t, except for 3n, have the dimensionless form

$$\frac{v(p,T)}{v^*} = \omega(\pi,\theta) = \left[\sum_{i=1}^{N} n_i [(\pi - a)^c]^{I_i} [(\theta - b)^d]^{J_i} \right]^e \tag{5}$$

The equation for subregion 3n has the form

$$\frac{v_{3\mathrm{n}}(p,T)}{v^*} = \omega(\pi,\theta) = \exp\left[\sum_{i=1}^{N} n_i (\pi - a)^{I_i} (\theta - b)^{J_i} \right] \tag{6}$$

where $\omega = v/v^*$, $\pi = p/p^*$, and $\theta = T/T^*$. The reducing quantities v^*, p^*, and T^*, the number of coefficients N, the nonlinear parameters a and b, and the exponents c, d, and e are listed in Table 5. The coefficients n_i and exponents I_i and J_i of these equations are given in the Appendix.

To assist the user in computer-program verification of the backward equations $v(p,T)$, Eqs. (5) and (6), for subregions 3a–3t, Table 6 contains test values for calculated specific volumes.

4.4 Calculation of Properties Utilizing the Backward Equations $v(p,T)$. The backward equations $v_{3\mathrm{a}}(p,T)$–$v_{3\mathrm{t}}(p,T)$, described in Sec. 4.3, along with the IAPWS-IF97 basic equation $f_3(\rho,T)$, make it possible to determine all thermodynamic properties, e.g., specific enthalpy, specific entropy, specific isobaric heat capacity, and speed of sound, for given values of pressure p and temperature T in region 3 without iteration.

The following steps should be made.

- Identify the subregion (3a–3t) for the given values of the pressure p and temperature T following the instructions in Sec. 4.2 in conjunction with Table 3 and Figs. 3 and 4. Then, calculate the specific volume v for the subregion with the corresponding backward equation $v(p,T)$, Eq. (5) or Eq. (6).
- Calculate the desired property for the previously calculated specific volume v and the given temperature T by use of the relation of this property to the basic equation $f_3(\rho,T)$, where $\rho = 1/v$ is determined from the corresponding backward equation, Eq. (5) or Eq. (6).

Table 7 Maximum and root-mean-square inconsistencies in v, h, s, c_p, and w, when these properties are calculated from the basic equation $f_3(\rho,T)$ after ρ is determined by iteration and when ρ is calculated directly from the backward equations $v(p,T)$ of regions 3a–3t

	Inconsistencies in v, h, s, c_p, and w (%)									
	$\lvert\Delta v/v\rvert$		$\lvert\Delta h/h\rvert$		$\lvert\Delta s/s\rvert$		$\lvert\Delta c_p/c_p\rvert$		$\lvert\Delta w/w\rvert$	
Subregion	max	rms	max	rms	max	rms	max	rms	max	rms
3a	0.00061	0.00031	0.00018	0.00008	0.00026	0.00011	0.0016	0.0006	0.0015	0.0006
3b	0.00064	0.00035	0.00017	0.00008	0.00016	0.00008	0.0012	0.0003	0.0008	0.0003
3c	0.00080	0.00038	0.00026	0.00012	0.00025	0.00011	0.0059	0.0016	0.0023	0.0010
3d	0.00059	0.00025	0.00018	0.00008	0.00014	0.00006	0.0035	0.0010	0.0012	0.0004
3e	0.00072	0.00033	0.00018	0.00009	0.00014	0.00007	0.0017	0.0005	0.0006	0.0002
3f	0.00068	0.00020	0.00018	0.00005	0.00013	0.00004	0.0015	0.0003	0.0002	0.0001
3g	0.00047	0.00016	0.00014	0.00005	0.00011	0.00004	0.0032	0.0011	0.0010	0.0003
3h	0.00085	0.00044	0.00022	0.00012	0.00017	0.00009	0.0066	0.0018	0.0006	0.0002
3i	0.00067	0.00028	0.00018	0.00008	0.00013	0.00006	0.0019	0.0006	0.0002	0.0001
3j	0.00034	0.00019	0.00009	0.00005	0.00007	0.00004	0.0020	0.0006	0.0002	0.0001
3k	0.00034	0.00012	0.00008	0.00003	0.00007	0.00002	0.0018	0.0003	0.0002	0.0001
3l	0.00033	0.00019	0.00010	0.00006	0.00008	0.00005	0.0035	0.0015	0.0008	0.0004
3m	0.00057	0.00031	0.00015	0.00009	0.00011	0.00006	0.0062	0.0030	0.0006	0.0002
3n	0.00064	0.00029	0.00017	0.00008	0.00012	0.00006	0.0050	0.0013	0.0002	0.0001
3o	0.00031	0.00015	0.00008	0.00004	0.00006	0.00003	0.0007	0.0002	0.0001	0.0001
3p	0.00044	0.00022	0.00012	0.00006	0.00009	0.00005	0.0026	0.0010	0.0002	0.0001
3q	0.00036	0.00018	0.00012	0.00006	0.00009	0.00005	0.0040	0.0016	0.0010	0.0005
3r	0.00037	0.00007	0.00010	0.00002	0.00008	0.00002	0.0030	0.0004	0.0002	0.0001
3s	0.00030	0.00016	0.00010	0.00005	0.00007	0.00004	0.0033	0.0015	0.0009	0.0005
3t	0.00095	0.00045	0.00022	0.00010	0.00018	0.00008	0.0046	0.0015	0.0004	0.0002
Permissible values	0.001		0.001		0.001		0.01		0.01	

Downloaded 02 Jun 2010 to 171.66.16.109. Redistribution subject to ASME license or copyright; see http://www.asme.org/terms/Terms_Use.cfm

Table 8 Numerical values of the coefficients of the equations $T_{3uv}(p)$ and $T_{3wx}(p)$ for subregion boundaries

Equation	i	I_i	n_i
$T_{3uv}(p)$	1	0	$0.528199646263062 \times 10^{3}$
	2	1	$0.890579602135307 \times 10^{1}$
	3	2	-0.222814134903755
	4	3	$0.286791682263697 \times 10^{-2}$
$T_{3wx}(p)$	1	0	$0.728052609145380 \times 10^{1}$
	2	1	$0.973505869861952 \times 10^{2}$
	3	2	$0.147370491183191 \times 10^{2}$
	4	−1	$0.329196213998375 \times 10^{3}$
	5	−2	$0.873371668682417 \times 10^{3}$

4.5 Numerical Consistency. The numerical inconsistencies between the backward equations $v(p,T)$, Eqs. (5) and (6), and the basic equation $f_3(\rho,T)$ in comparison with the permissible inconsistencies given in Table 1 are listed in Table 7. In addition to the inconsistencies in specific volume v itself, the effects of these inconsistencies with regard to the inconsistencies in specific enthalpy, specific entropy, specific isobaric heat capacity, and speed of sound are also given; the calculation of these properties based on the calculation of v from the backward equations $v(p,T)$, Eqs. (5) and (6), is described in Sec. 4.4.

Table 7 shows that the inconsistencies in specific volume v, specific enthalpy h, and specific entropy s are less than 0.001% when v is calculated from the backward equations $v(p,T)$ given in Sec. 4.3 and from the basic equation $f_3(\rho,T)$. The corresponding inconsistencies in the specific isobaric heat capacity c_p and in the speed of sound w are less than 0.01%. Thus, all inconsistencies are less than the permissible values. The values for v, h, and s calculated only from the basic equation $f_3(\rho,T)$ (with iteration of $\rho=1/v$) are represented to within five significant figures by values determined from the basic equation $f_3(\rho,T)$, where $\rho=1/v$ is calculated from the backward equations $v(p,T)$ (i.e., without iteration). The corresponding values of c_p and w are represented to within four significant figures.

Comprehensive tests [11] have shown that the maximum inconsistencies between the backward equations $v(p,T)$ of adjacent subregions are less than 0.001%. Moreover, the inconsistencies in h, s, c_p, and w along subregion boundaries, when these properties are calculated one time with the help of the backward equations $v(p,T)$ and the other time with the basic equation $f_3(\rho,T)$ alone, are also less than the permissible values given in Table 1; this is valid for subregion boundaries, isobars, and lines defined by the subregion-boundary equations according to Eqs. (2)–(4).

5 Auxiliary Equations $v(p,T)$ for the Near-Critical Region

5.1 Range of Validity, Division Into Subregions, and Subregion-Boundary Equations. The auxiliary equations $v(p,T)$ for subregions 3u–3z are valid in the temperature and pressure range given by

$$T_{3qu}(p) < T \le T_{3rx}(p) \text{ and } p_{sat}(643.15\ \text{K}) < p \le 22.5\ \text{MPa}$$

where $p_{sat}(643.15\ \text{K}) = 21.04336732$ MPa is calculated from the saturation-pressure equation of IAPWS-IF97.

The subregion-boundary equation $T_{3uv}(p)$ has the form of Eq. (2), and the equation $T_{3wx}(p)$ has the form of Eq. (3). The coefficients n_i and the exponents I_i of these two boundary equations are listed in Table 8. The numerical information on the subregion-boundary equation $T_{3ef}(p)$ is given in Sec. 4.2. The description of the use of the subregion-boundary equations is summarized in Table 9, where the subregion boundaries are shown in Fig. 5.

The information given above completely documents the equations for these subregion boundaries. Some of the equations are designed to approximate specific physical relationships such as isochores. This is discussed in more detail elsewhere [10,11].

To assist the user in computer-program verification of the equations for the subregion boundaries, Table 10 contains test values for calculated temperatures.

5.2 Auxiliary Equations $v(p,T)$ for Subregions 3u–3z. The auxiliary equations $v(p,T)$ for subregions 3u–3z have the dimensionless form of Eq. (5). The reducing quantities v^*, p^*, and T^*, the number of coefficients N, the nonlinear parameters a and b, and the exponents c, d, and e are listed in Table 11. The coefficients n_i and exponents I_i and J_i are given in the Appendix.

Table 9 Pressure ranges and corresponding-subregion boundary equations for determining the correct subregion, 3u–3z, for the auxiliary equations $v(p,T)$

	Subcritical pressure region ($p \le p_c$)		
Temperature range	Pressure range	Subregion	Temperature range
$T \le T_{sat}(p)$ (liquid)	$p_{sat}(0.00264\ \text{m}^3\ \text{kg}^{-1})^{a} < p \le 22.064$ MPa	3u	$T_{3qu}(p) < T \le T_{3uv}(p)$
		3y	$T_{3uv}(p) < T$
	$p_{sat}(643.15\ \text{K}) < p \le p_{sat}(0.00264\ \text{m}^3\ \text{kg}^{-1})^{a}$	3u	$T_{3qu}(p) < T$
$T \ge T_{sat}(p)$ (vapor)	$p_{sat}(0.00385\ \text{m}^3\ \text{kg}^{-1})^{b} < p \le 22.064$ MPa	3z	$T \le T_{3wx}(p)$
		3x	$T_{3wx}(p) < T \le T_{3rx}(p)$
	$p_{sat}(643.15\ \text{K}) < p \le p_{sat}(0.00385\ \text{m}^3\ \text{kg}^{-1})^{b}$	3x	$T \le T_{3rx}(p)$

	Supercritical pressure region ($p > p_c$)	
Pressure range	Subregion	Temperature range
22.064 MPa $< p \le$ 22.11 MPa	3u	$T_{3qu}(p) < T \le T_{3uv}(p)$
	3z	$T_{3ef}(p) < T \le T_{3wx}(p)$
	3y	$T_{3uv}(p) < T \le T_{3ef}(p)$
	3x	$T_{3wx}(p) < T \le T_{3rx}(p)$
22.11 MPa $< p \le$ 22.5 MPa	3u	$T_{3qu}(p) < T \le T_{3uv}(p)$
	3w	$T_{3ef}(p) < T \le T_{3wx}(p)$
	3v	$T_{3uv}(p) < T \le T_{3ef}(p)$
	3x	$T_{3wx}(p) < T \le T_{3rx}(p)$

[a] $p_{sat}(0.002\,64\ \text{m}^3\ \text{kg}^{-1}) = 21.93161551$ MPa.

[b] $p_{sat}(0.003\,85\ \text{m}^3\ \text{kg}^{-1}) = 21.90096265$ MPa.

Downloaded 02 Jun 2010 to 171.66.16.109. Redistribution subject to ASME license or copyright; see http://www.asme.org/terms/Terms_Use.cfm

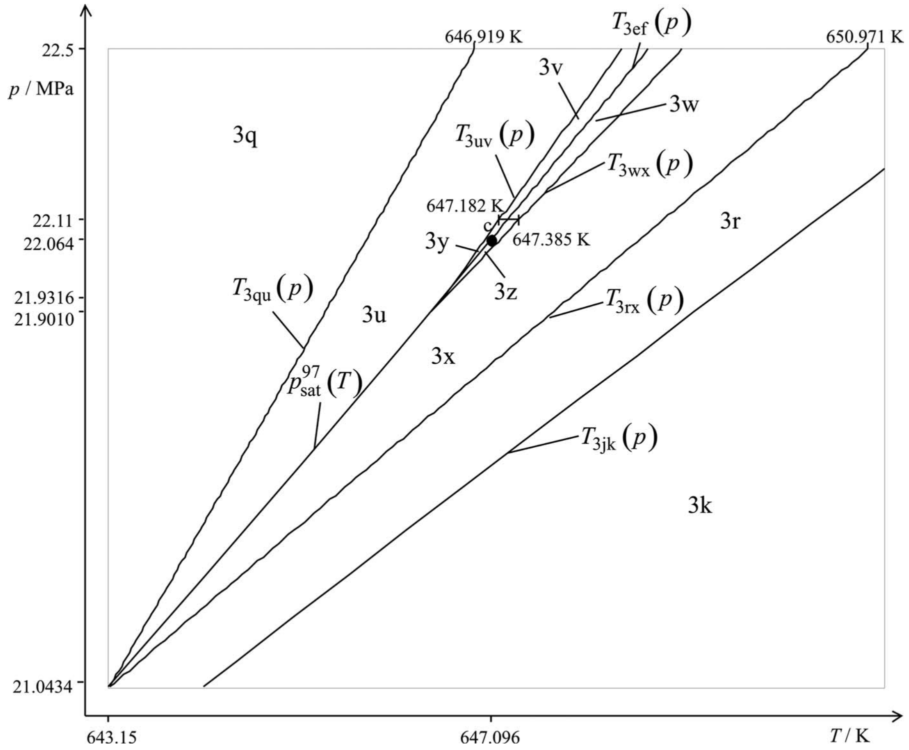

Fig. 5 Division of region 3 into subregions 3u–3z for the auxiliary equations

To assist the user in computer-program verification of these auxiliary equations, Table 12 contains test values for calculated specific volumes.

5.3 Calculation of Properties Utilizing the Auxiliary Equations $v(p,T)$. In order to calculate the thermodynamic properties in the range very close to the critical point with the help of the auxiliary equations $v(p,T)$ for regions 3u–3z, the description given in Sec. 4.4 must be applied analogously to the auxiliary equations $v(p,T)$.

5.4 Numerical Consistency. The numerical inconsistencies between the auxiliary equations $v(p,T)$ for subregions 3u–3z and the basic equation $f_3(\rho,T)$ are listed in Table 13. This table shows that the maximum inconsistencies in specific volume between these equations are less than 0.1%. Only in a small region at pressures less than 22.11 MPa, see Fig. 5, the maximum inconsistencies with the basic equation $f_3(\rho,T)$ approach 2%.

The maximum inconsistencies in specific volume between the auxiliary equations $v(p,T)$ of adjacent subregions along subregion

Table 10 Temperature values calculated from the subregion-boundary equations $T_{3uv}(p)$ and $T_{3wx}(p)$ for selected pressures

Equation	p (MPa)	T (K)
$T_{3uv}(p)$	22.3	6.477996121×10^2
$T_{3wx}(p)$	22.3	6.482049480×10^2

Table 11 Reducing quantities v^*, p^*, and T^*, number of coefficients N, nonlinear parameters a and b, and exponents c, d, and e of the auxiliary equations $v(p,T)$, Eq. (5), of subregions 3u–3z

Subregion	v^* (m^3 kg^{-1})	p^* (MPa)	T^* (K)	N	a	b	c	d	e
3u	0.0026	23	650	38	0.902	0.988	1	1	1
3v	0.0031	23	650	39	0.960	0.995	1	1	1
3w	0.0039	23	650	35	0.959	0.995	1	1	4
3x	0.0049	23	650	36	0.910	0.988	1	1	1
3y	0.0031	22	650	20	0.996	0.994	1	1	4
3z	0.0038	22	650	23	0.993	0.994	1	1	4

Table 12 Values of the specific volume calculated from the auxiliary equations $v(p,T)$ for subregions 3u–3z

Equation	p (MPa)	T (K)	v (m^3 kg^{-1})
$v_{3u}(p,T)$	21.5	644.6	$2.268366647 \times 10^{-3}$
	22.0	646.1	$2.296350553 \times 10^{-3}$
$v_{3v}(p,T)$	22.5	648.6	$2.832373260 \times 10^{-3}$
	22.3	647.9	$2.811424405 \times 10^{-3}$
$v_{3w}(p,T)$	22.15	647.5	$3.694032281 \times 10^{-3}$
	22.3	648.1	$3.622226305 \times 10^{-3}$
$v_{3x}(p,T)$	22.11	648.0	$4.528072649 \times 10^{-3}$
	22.3	649.0	$4.556905799 \times 10^{-3}$
$v_{3y}(p,T)$	22.0	646.84	$2.698354719 \times 10^{-3}$
	22.064	647.05	$2.717655648 \times 10^{-3}$
$v_{3z}(p,T)$	22.0	646.89	$3.798732962 \times 10^{-3}$
	22.064	647.15	$3.701940010 \times 10^{-3}$

Table 13 Maximum and root-mean-square inconsistencies in specific volume between the auxiliary equations $v(p,T)$ for subregions 3u–3z and the basic equation $f_3(\rho,T)$

Subregion	$\|\Delta v/v\|$ (%) max	$\|\Delta v/v\|$ (%) rms
3u	0.097	0.058
3v	0.082	0.040
3w	0.065	0.023
3x	0.090	0.050
3y	1.77	1.04
3z	1.80	0.921

Downloaded 02 Jun 2010 to 171.66.16.109. Redistribution subject to ASME license or copyright; see http://www.asme.org/terms/Terms_Use.cfm

boundaries are as follows: Along subregion boundaries that are isobars, the inconsistencies are less than 0.1% for all subregions except for the boundaries between subregions 3v/3y and 3w/3z, where the inconsistencies amount to 1.7%. Along boundaries defined by the subregion-boundary equations given in Sec. 5.1, the inconsistencies are also less than 0.1%, except for the boundaries between subregions 3u/3v and 3u/3y ($T_{3\mathrm{uv}}(p)$), 3y/3z ($T_{3\mathrm{ef}}(p)$), and 3z/3x ($T_{3\mathrm{wx}}(p)$), where the maximum inconsistencies are 0.14%, 1.8%, 3.5%, and 1.8%, respectively.

6 Computing Time Relative to IAPWS-IF97 Iteration

A very important motivation for the backward equations $v(p,T)$ was reducing the computing time to obtain thermodynamic properties for the given variables (p,T) in region 3. With the $v(p,T)$ equations, time-consuming iteration of IAPWS-IF97 can be avoided. The calculation speed is then about 17 times faster than that using only the basic equation. In this comparison, the basic equation is applied in combination with a one-dimensional Newton iteration with convergence tolerances corresponding to the consistency requirements for the backward equations given in Sec. 2.

7 Application of the Equations

The numerical consistency of the backward equations $v(p,T)$ presented in Sec. 4 with the IAPWS-IF97 basic equation is sufficient for most applications in heat-cycle and boiler calculations. For applications where the demands on numerical consistency are extremely high, iteration using the IAPWS-IF97 basic equation $f_3(\rho,T)$ may be necessary. In these cases, the backward and auxiliary equations $v(p,T)$ can be used to calculate very accurate starting values to reduce the time required for convergence of an iterative process.

In comparison with the backward equations $v(p,T)$, the corresponding numerical consistency of the auxiliary equations $v(p,T)$ for the range very close to the critical point is clearly worse. Nevertheless, for many applications, this consistency is satisfactory.

The backward and auxiliary equations $v(p,T)$ should only be used in their ranges of validity described in Sec. 4. They should not be used for determining any thermodynamic derivatives. They should also not be used together with the fundamental equation in iterative calculations of other backward functions such as $T(p,h)$ or $T(p,s)$. Iteration of backward functions can only be performed by using the fundamental equations.

8 Summary

Backward and auxiliary equations $v(p,T)$ for water in IAPWS-IF97 region 3 have been developed. The numerical consistency of specific volume calculated from the backward equations $v(p,T)$ with the IAPWS-IF97 basic equation are sufficient for most applications in heat-cycle and boiler calculations. The new backward equations are 17 times faster than iterative calculation from IAPWS-IF97. For applications where the demands on numerical consistency are extremely high, iteration using the IAPWS-IF97 equations may still be necessary. In these cases, the equations presented here can be used for calculating very accurate starting values.

Further details of the numerical consistency of all backward and region-boundary equations are in the dissertation of Knobloch [11] and the book of Wagner and Kretzschmar [12]. Computer code for the equations presented in this paper may be obtained from the corresponding author (H.-J.K.).

Acknowledgment

The authors are indebted to other members of the IAPWS Working Groups “Industrial Requirements and Solutions” and “Thermophysical Properties of Water and Steam.” They are grateful to all of their IAPWS colleagues who contributed to the project of the development of supplementary equations for IAPWS-IF97. Two of the authors (H.-J.K. and K.K.) are particularly grateful to the Saxony State Ministry of Science and Art in Germany for its financial support.

Nomenclature

Thermodynamic Quantities

a, b = shifting parameters
c_p = specific isobaric heat capacity (kJ kg^{-1} K^{-1})
f = specific Helmholtz free energy (kJ kg^{-1})
h = specific enthalpy (kJ kg^{-1})
I, J = exponent
n = coefficient
p = pressure (MPa)
s = specific entropy (kJ kg^{-1} K^{-1})
T = absolute temperature (K) on the International Temperature Scale of 1990 (ITS-90)
v = specific volume (m^3 kg^{-1})
w = speed of sound (m s^{-1})
θ = reduced temperature $\theta = T/T^*$
π = reduced pressure, $\pi = p/p^*$
ω = reduced volume, $\omega = v/v^*$
Δ = difference in any quantity

Subscripts

1–5 = regions 1–5
3a–3z = subregion 3a–3z
3ab = boundary between subregions 3a, 3d and 3b, 3e
3cd = boundary between subregions 3c and 3d, 3g, 3l, 3q, 3s
3ef = boundary between subregions 3e, 3h, 3n and 3f, 3i, 3o
3gh = boundary between subregions 3g, 3l and 3h, 3m
3ij = boundary between subregions 3i, 3p and 3j
3jk = boundary between subregions 3j, 3r and 3k
3mn = boundary between subregions 3m and 3n
3op = boundary between subregions 3o and 3p
3qu = boundary between subregions 3q and 3u
3rx = boundary between subregions 3r and 3x
3uv = boundary between subregions 3u and 3v
3wx = boundary between subregions 3w and 3x
B23 = boundary between regions 2 and 3
c = critical point
max = maximum value of a quantity
perm = permissible inconsistency
rms = root-mean-square value of a quantity (see below)
sat = saturation state
root-mean-square value = $\Delta z_{\mathrm{rms}} = \sqrt{1/m\sum_{i=1}^{m}(\Delta z_i)^2}$, where Δz_i can be either absolute or percentage differences of the corresponding property z and m is the number of Δz_i values (depending on the property, between 10^7 and 10^8 points uniformly distributed over the range of validity)

Superscripts

97 = quantity or equation of IAPWS-IF97
01 = equation of IAPWS-IF97-S01
03 = equation of IAPWS-IF97-S03rev
04 = equation of IAPWS-IF97-S04
05 = equation of IAPWS-IF97-S05
$*$ = reducing quantity
$'$ = saturated liquid state
$''$ = saturated vapor state

Downloaded 02 Jun 2010 to 171.66.16.109. Redistribution subject to ASME license or copyright; see http://www.asme.org/terms/Terms_Use.cfm

Appendix

Coefficients for backward equations are shown in Tables 14–33. Coefficients for auxiliary equations are shown in Tables 34–39.

Table 14 Coefficients and exponents of the backward equation $v_{3a}(p,T)$ for subregion 3a

i	I_i	J_i	n_i
1	−12	5	$0.110879558823853\times10^{-2}$
2	−12	10	$0.572616740810616\times10^{3}$
3	−12	12	$-0.767051948380852\times10^{5}$
4	−10	5	$-0.253321069529674\times10^{-1}$
5	−10	10	$0.628008049345689\times10^{4}$
6	−10	12	$0.234105654131876\times10^{6}$
7	−8	5	0.216867826045856
8	−8	8	$-0.156237904341963\times10^{3}$
9	−8	10	$-0.269893956176613\times10^{5}$
10	−6	1	$-0.180407100085505\times10^{-3}$
11	−5	1	$0.116732227668261\times10^{-2}$
12	−5	5	$0.266987040856040\times10^{2}$
13	−5	10	$0.282776617243286\times10^{5}$
14	−4	8	$-0.242431520029523\times10^{4}$
15	−3	0	$0.435217323022733\times10^{-3}$
16	−3	1	$-0.122494831387441\times10^{-1}$
17	−3	3	$0.179357604019989\times10^{1}$
18	−3	6	$0.442729521058314\times10^{2}$
19	−2	0	$-0.593223489018342\times10^{-2}$
20	−2	2	0.453186261685774
21	−2	3	$0.135825703129140\times10^{1}$
22	−1	0	$0.408748415856745\times10^{-1}$
23	−1	1	0.474686397863312
24	−1	2	$0.118646814997915\times10^{1}$
25	0	0	0.546987265727549
26	0	1	0.195266770452643
27	1	0	$-0.502268790869663\times10^{-1}$
28	1	2	-0.369645308193377
29	2	0	$0.633828037528420\times10^{-2}$
30	2	2	$0.797441793901017\times10^{-1}$

Table 15 Coefficients and exponents of the backward equation $v_{3b}(p,T)$ for subregion 3b

i	I_i	J_i	n_i
1	−12	10	$-0.827670470003621\times10^{-1}$
2	−12	12	$0.416887126010565\times10^{2}$
3	−10	8	$0.483651982197059\times10^{-1}$
4	−10	14	$-0.291032084950276\times10^{5}$
5	−8	8	$-0.111422582236948\times10^{3}$
6	−6	5	$-0.202300083904014\times10^{-1}$
7	−6	6	$0.294002509338515\times10^{3}$
8	−6	8	$0.140244997609658\times10^{3}$
9	−5	5	$-0.344384158811459\times10^{3}$
10	−5	8	$0.361182452612149\times10^{3}$
11	−5	10	$-0.140699677420738\times10^{4}$
12	−4	2	$-0.202023902676481\times10^{-2}$
13	−4	4	$0.171346792457471\times10^{3}$
14	−4	5	$-0.425597804058632\times10^{1}$
15	−3	0	$0.691346085000334\times10^{-5}$
16	−3	1	$0.151140509678925\times10^{-2}$
17	−3	2	$-0.416375290166236\times10^{-1}$
18	−3	3	$-0.413754957011042\times10^{2}$
19	−3	5	$-0.506673295721637\times10^{2}$
20	−2	0	$-0.572212965569023\times10^{-3}$
21	−2	2	$0.608817368401785\times10^{1}$
22	−2	5	$0.239600660256161\times10^{2}$
23	−1	0	$0.122261479925384\times10^{-1}$
24	−1	2	$0.216356057692938\times10^{1}$
25	0	0	0.398198903368642
26	0	1	-0.116892827834085
27	1	0	-0.102845919373532
28	1	2	-0.492676637589284
29	2	0	$0.655540456406790\times10^{-1}$
30	3	2	-0.240462535078530
31	4	0	$-0.269798180310075\times10^{-1}$
32	4	1	0.128369435967012

Table 16 Coefficients and exponents of the backward equation $v_{3c}(p,T)$ for subregion 3c

i	I_i	J_i	n_i
1	−12	6	$0.311967788763030\times10^{1}$
2	−12	8	$0.276713458847564\times10^{5}$
3	−12	10	$0.322583103403269\times10^{8}$
4	−10	6	$-0.342416065095363\times10^{3}$
5	−10	8	$-0.899732529907377\times10^{6}$
6	−10	10	$-0.793892049821251\times10^{8}$
7	−8	5	$0.953193003217388\times10^{2}$
8	−8	6	$0.229784742345072\times10^{4}$
9	−8	7	$0.175336675322499\times10^{6}$
10	−6	8	$0.791214365222792\times10^{7}$
11	−5	1	$0.319933345844209\times10^{-4}$
12	−5	4	$-0.659508863555767\times10^{2}$
13	−5	7	$-0.833426563212851\times10^{6}$
14	−4	2	$0.645734680583292\times10^{-1}$
15	−4	8	$-0.382031020570813\times10^{7}$
16	−3	0	$0.406398848470079\times10^{-4}$
17	−3	3	$0.310327498492008\times10^{2}$
18	−2	0	$-0.892996718483724\times10^{-3}$
19	−2	4	$0.234604891591616\times10^{3}$
20	−2	5	$0.377515668966951\times10^{4}$
21	−1	0	$0.158646812591361\times10^{-1}$
22	−1	1	0.707906336241843
23	−1	2	$0.126016225146570\times10^{2}$
24	0	0	0.736143655772152
25	0	1	0.676544268999101
26	0	2	$-0.178100588189137\times10^{2}$
27	1	0	-0.156531975531713
28	1	2	$0.117707430048158\times10^{2}$
29	2	0	$0.840143653860447\times10^{-1}$
30	2	1	-0.186442467471949
31	2	3	$-0.440170203949645\times10^{2}$
32	2	7	$0.123290423502494\times10^{7}$
33	3	0	$-0.240650039730845\times10^{-1}$
34	3	7	$-0.107077716660869\times10^{7}$
35	8	1	$0.438319858566475\times10^{-1}$

Table 17 Coefficients and exponents of the backward equation $v_{3d}(p,T)$ for subregion 3d

i	I_i	J_i	n_i
1	−12	4	$-0.452484847171645\times10^{-9}$
2	−12	6	$0.315210389538801\times10^{-4}$
3	−12	7	$-0.214991352047545\times10^{-2}$
4	−12	10	$0.508058874808345\times10^{3}$
5	−12	12	$-0.127123036845932\times10^{8}$
6	−12	16	$0.115371133120497\times10^{13}$
7	−10	0	$-0.197805728776273\times10^{-15}$
8	−10	2	$0.241554806033972\times10^{-10}$
9	−10	4	$-0.156481703640525\times10^{-5}$
10	−10	6	$0.277211346836625\times10^{-2}$
11	−10	8	$-0.203578994462286\times10^{2}$
12	−10	10	$0.144369489909053\times10^{7}$
13	−10	14	$-0.411254217946539\times10^{11}$
14	−8	3	$0.623449786243773\times10^{-5}$
15	−8	7	$-0.221774281146038\times10^{2}$
16	−8	8	$-0.689315087933158\times10^{5}$
17	−8	10	$-0.195419525060713\times10^{8}$
18	−6	6	$0.316373510564015\times10^{4}$
19	−6	8	$0.224040754426988\times10^{7}$
20	−5	1	$-0.436701347922356\times10^{-5}$
21	−5	2	$-0.404213852833996\times10^{-3}$
22	−5	5	$-0.348153203414663\times10^{3}$
23	−5	7	$-0.385294213555289\times10^{6}$
24	−4	0	$0.135203700099403\times10^{-6}$
25	−4	1	$0.134648383271089\times10^{-3}$
26	−4	7	$0.125031835351736\times10^{6}$
27	−3	2	$0.968123678455841\times10^{-1}$
28	−3	4	$0.225660517512438\times10^{3}$
29	−2	0	$-0.190102435341872\times10^{-3}$
30	−2	1	$-0.299628410819229\times10^{-1}$
31	−1	0	$0.500833915372121\times10^{-2}$
32	−1	1	0.387842482998411
33	−1	5	$-0.138535367777182\times10^{4}$
34	0	0	0.870745245971773
35	0	2	$0.171946252068742\times10^{1}$
36	1	0	$-0.326650121426383\times10^{-1}$
37	1	6	$0.498044171727877\times10^{4}$
38	3	0	$0.551478022765087\times10^{-2}$

Downloaded 02 Jun 2010 to 171.66.16.109. Redistribution subject to ASME license or copyright; see http://www.asme.org/terms/Terms_Use.cfm

Table 18 Coefficients and exponents of the backward equation $v_{3e}(p,T)$ for subregion 3e

i	I_i	J_i	n_i
1	−12	14	$0.715815808404721 \times 10^{9}$
2	−12	16	$-0.114328360753449 \times 10^{12}$
3	−10	3	$0.376531002015720 \times 10^{-11}$
4	−10	6	$-0.903983668691157 \times 10^{-4}$
5	−10	10	$0.665695908836252 \times 10^{6}$
6	−10	14	$0.535364174960127 \times 10^{10}$
7	−10	16	$0.794977402335603 \times 10^{11}$
8	−8	7	$0.922230563421437 \times 10^{2}$
9	−8	8	$-0.142586073991215 \times 10^{6}$
10	−8	10	$-0.111796381424162 \times 10^{7}$
11	−6	6	$0.896121629640760 \times 10^{4}$
12	−5	6	$-0.669989239070491 \times 10^{4}$
13	−4	2	$0.451242538486834 \times 10^{-2}$
14	−4	4	$-0.339731325977713 \times 10^{2}$
15	−3	2	$-0.120523111552278 \times 10^{1}$
16	−3	6	$0.475992667717124 \times 10^{5}$
17	−3	7	$-0.266627750390341 \times 10^{6}$
18	−2	0	$-0.153314954386524 \times 10^{-3}$
19	−2	1	0.305638404828265
20	−2	3	$0.123654999499486 \times 10^{3}$
21	−2	4	$-0.104390794213011 \times 10^{4}$
22	−1	0	$-0.157496516174308 \times 10^{-1}$
23	0	0	0.685331118940253
24	0	1	$0.178373462873903 \times 10^{1}$
25	1	0	-0.544674124878910
26	1	4	$0.204529931318843 \times 10^{4}$
27	1	6	$-0.228342359328752 \times 10^{5}$
28	2	0	0.413197481515899
29	2	2	$-0.341931835910405 \times 10^{2}$

Table 19 Coefficients and exponents of the backward equation $v_{3f}(p,T)$ for subregion 3f

i	I_i	J_i	n_i
1	0	−3	$-0.251756547792325 \times 10^{-7}$
2	0	−2	$0.601307193668763 \times 10^{-5}$
3	0	−1	$-0.100615977450049 \times 10^{-2}$
4	0	0	0.999969140252192
5	0	1	$0.214107759236486 \times 10^{1}$
6	0	2	$-0.165175571959086 \times 10^{2}$
7	1	−1	$-0.141987303638727 \times 10^{-2}$
8	1	1	$0.269251915156554 \times 10^{1}$
9	1	2	$0.349741815858722 \times 10^{2}$
10	1	3	$-0.300208695771783 \times 10^{2}$
11	2	0	$-0.131546288252539 \times 10^{1}$
12	2	1	$-0.839091277286169 \times 10^{1}$
13	3	−5	$0.181545608337015 \times 10^{-9}$
14	3	−2	$-0.591099206478909 \times 10^{-3}$
15	3	0	$0.152115067087106 \times 10^{1}$
16	4	−3	$0.252956470663225 \times 10^{-4}$
17	5	−8	$0.100726265203786 \times 10^{-14}$
18	5	1	$-0.149774533860650 \times 10^{1}$
19	6	−6	$-0.793940970562969 \times 10^{-9}$
20	7	−4	$-0.150290891264717 \times 10^{-3}$
21	7	1	$0.151205531275133 \times 10^{1}$
22	10	−6	$0.470942606221652 \times 10^{-5}$
23	12	−10	$0.195049710391712 \times 10^{-12}$
24	12	−8	$-0.911627886266077 \times 10^{-8}$
25	12	−4	$0.604374640201265 \times 10^{-3}$
26	14	−12	$-0.225132933900136 \times 10^{-15}$
27	14	−10	$0.610916973582981 \times 10^{-11}$
28	14	−8	$-0.303063908043404 \times 10^{-6}$
29	14	−6	$-0.137796070798409 \times 10^{-4}$
30	14	−4	$-0.919296736666106 \times 10^{-3}$
31	16	−10	$0.639288223132545 \times 10^{-9}$
32	16	−8	$0.753259479898699 \times 10^{-6}$
33	18	−12	$-0.400321478682929 \times 10^{-12}$
34	18	−10	$0.756140294351614 \times 10^{-8}$
35	20	−12	$-0.912082054034891 \times 10^{-11}$
36	20	−10	$-0.237612381140539 \times 10^{-7}$
37	20	−6	$0.269586010591874 \times 10^{-4}$
38	22	−12	$-0.732828135157839 \times 10^{-10}$
39	24	−12	$0.241995578306660 \times 10^{-9}$
40	24	−4	$-0.405735532730322 \times 10^{-3}$
41	28	−12	$0.189424143498011 \times 10^{-9}$
42	32	−12	$-0.486632965074563 \times 10^{-9}$

Table 20 Coefficients and exponents of the backward equation $v_{3g}(p,T)$ for subregion 3g

i	I_i	J_i	n_i
1	−12	7	$0.412209020652996 \times 10^{-4}$
2	−12	12	$-0.114987238280587 \times 10^{7}$
3	−12	14	$0.948180885032080 \times 10^{10}$
4	−12	18	$-0.195788865718971 \times 10^{18}$
5	−12	22	$0.496250704871300 \times 10^{25}$
6	−12	24	$-0.105549884548496 \times 10^{29}$
7	−10	14	$-0.758642165988278 \times 10^{12}$
8	−10	20	$-0.922172769596101 \times 10^{23}$
9	−10	24	$0.725379072059348 \times 10^{30}$
10	−8	7	$-0.617718249205859 \times 10^{2}$
11	−8	8	$0.107555033344858 \times 10^{5}$
12	−8	10	$-0.379545802336487 \times 10^{8}$
13	−8	12	$0.228646846221831 \times 10^{12}$
14	−6	8	$-0.499741093010619 \times 10^{7}$
15	−6	22	$-0.280214310054101 \times 10^{31}$
16	−5	7	$0.104915406769586 \times 10^{7}$
17	−5	20	$0.613754229168619 \times 10^{28}$
18	−4	22	$0.802056715528378 \times 10^{32}$
19	−3	7	$-0.298617819828065 \times 10^{8}$
20	−2	3	$-0.910782540134681 \times 10^{2}$
21	−2	5	$0.135033227281565 \times 10^{6}$
22	−2	14	$-0.712949383408211 \times 10^{19}$
23	−2	24	$-0.104578785289542 \times 10^{37}$
24	−1	2	$0.304331584444093 \times 10^{2}$
25	−1	8	$0.593250797959445 \times 10^{10}$
26	−1	18	$-0.364174062110798 \times 10^{28}$
27	0	0	0.921791403532461
28	0	1	-0.337693609657471
29	0	2	$-0.724644143758508 \times 10^{2}$
30	1	0	-0.110480239272601
31	1	1	$0.536516031875059 \times 10^{1}$
32	1	3	$-0.291441872156205 \times 10^{4}$
33	3	24	$0.616338176535305 \times 10^{40}$
34	5	22	$-0.120889175861180 \times 10^{39}$
35	6	12	$0.818396024524612 \times 10^{23}$
36	8	3	$0.940781944835829 \times 10^{9}$
37	10	0	$-0.367279669545448 \times 10^{5}$
38	10	6	$-0.837513931798655 \times 10^{16}$

Table 21 Coefficients and exponents of the backward equation $v_{3h}(p,T)$ for subregion 3h

i	I_i	J_i	n_i
1	−12	8	$0.561379678887577 \times 10^{-1}$
2	−12	12	$0.774135421587083 \times 10^{10}$
3	−10	4	$0.111482975877938 \times 10^{-8}$
4	−10	6	$-0.143987128208183 \times 10^{-2}$
5	−10	8	$0.193696558764920 \times 10^{4}$
6	−10	10	$-0.605971823585005 \times 10^{9}$
7	−10	14	$0.171951568124337 \times 10^{14}$
8	−10	16	$-0.185461154985145 \times 10^{17}$
9	−8	0	$0.387851168078010 \times 10^{-16}$
10	−8	1	$-0.395464327846105 \times 10^{-13}$
11	−8	6	$-0.170875935679023 \times 10^{3}$
12	−8	7	$-0.212010620701220 \times 10^{4}$
13	−8	8	$0.177683337348191 \times 10^{8}$
14	−6	4	$0.110177443629575 \times 10^{2}$
15	−6	6	$-0.234396091693313 \times 10^{6}$
16	−6	8	$-0.656174421999594 \times 10^{7}$
17	−5	2	$0.156362212977396 \times 10^{-4}$
18	−5	3	$-0.212946257021400 \times 10^{1}$
19	−5	4	$0.135249306374858 \times 10^{2}$
20	−4	2	0.177189164145813
21	−4	4	$0.139499167345464 \times 10^{4}$
22	−3	1	$-0.703670932036388 \times 10^{-2}$
23	−3	2	-0.152011044389648
24	−2	0	$0.981916922991113 \times 10^{-4}$
25	−1	0	$0.147199658618076 \times 10^{-2}$
26	−1	2	$0.202618487025578 \times 10^{2}$
27	0	0	0.899345518944240
28	1	0	-0.211346402240858
29	1	2	$0.249971752957491 \times 10^{2}$

Downloaded 02 Jun 2010 to 171.66.16.109. Redistribution subject to ASME license or copyright; see http://www.asme.org/terms/Terms_Use.cfm

Table 22 Coefficients and exponents of the backward equation $v_{3i}(p,T)$ for subregion 3i

i	I_i	J_i	n_i
1	0	0	$0.106905684359136 \times 10^{1}$
2	0	1	$-0.148620857922333 \times 10^{1}$
3	0	10	$0.259862256980408 \times 10^{15}$
4	1	−4	$-0.446352055678749 \times 10^{-11}$
5	1	−2	$-0.566620757170032 \times 10^{-6}$
6	1	−1	$-0.235302885736849 \times 10^{-2}$
7	1	0	-0.269226321968839
8	2	0	$0.922024992944392 \times 10^{1}$
9	3	−5	$0.357633505503772 \times 10^{-11}$
10	3	0	$-0.173942565562222 \times 10^{2}$
11	4	−3	$0.700681785556229 \times 10^{-5}$
12	4	−2	$-0.267050351075768 \times 10^{-3}$
13	4	−1	$-0.231779669675624 \times 10^{1}$
14	5	−6	$-0.753533046979752 \times 10^{-12}$
15	5	−1	$0.481337131452891 \times 10^{1}$
16	5	12	$-0.223286270422356 \times 10^{22}$
17	7	−4	$-0.118746004987383 \times 10^{-4}$
18	7	−3	$0.646412934136496 \times 10^{-2}$
19	8	−6	$-0.410588536330937 \times 10^{-9}$
20	8	10	$0.422739537057241 \times 10^{20}$
21	10	−8	$0.313698180473812 \times 10^{-12}$
22	12	−12	$0.164395334345040 \times 10^{-23}$
23	12	−6	$-0.339823323754373 \times 10^{-5}$
24	12	−4	$-0.135268639905021 \times 10^{-1}$
25	14	−10	$-0.723252514211625 \times 10^{-14}$
26	14	−8	$0.184386437538366 \times 10^{-8}$
27	14	−4	$-0.463959533752385 \times 10^{-1}$
28	14	5	$-0.992263100376750 \times 10^{14}$
29	18	−12	$0.688169154439335 \times 10^{-16}$
30	18	−10	$-0.222620998452197 \times 10^{-10}$
31	18	−8	$-0.540843018624083 \times 10^{-7}$
32	18	−6	$0.345570606200257 \times 10^{-2}$
33	18	2	$0.422275800304086 \times 10^{11}$
34	20	−12	$-0.126974478770487 \times 10^{-14}$
35	20	−10	$0.927237985153679 \times 10^{-9}$
36	22	−12	$0.612670812016489 \times 10^{-13}$
37	24	−12	$-0.722693924063497 \times 10^{-11}$
38	24	−8	$-0.383669502636822 \times 10^{-3}$
39	32	−10	$0.374684572410204 \times 10^{-3}$
40	32	−5	$-0.931976897511086 \times 10^{5}$
41	36	−10	$-0.247690616026922 \times 10^{-1}$
42	36	−8	$0.658110546759474 \times 10^{2}$

Table 23 Coefficients and exponents of the backward equation $v_{3j}(p,T)$ for subregion 3j

i	I_i	J_i	n_i
1	0	−1	$-0.111371317395540 \times 10^{-3}$
2	0	0	$0.100342892423685 \times 10^{1}$
3	0	1	$0.530615581928979 \times 10^{1}$
4	1	−2	$0.179058760078792 \times 10^{-5}$
5	1	−1	$-0.728541958464774 \times 10^{-3}$
6	1	1	$-0.187576133371704 \times 10^{2}$
7	2	−1	$0.199060874071849 \times 10^{-2}$
8	2	1	$0.243574755377290 \times 10^{2}$
9	3	−2	$-0.177040785499444 \times 10^{-3}$
10	4	−2	$-0.259680385227130 \times 10^{-2}$
11	4	2	$-0.198704578406823 \times 10^{3}$
12	5	−3	$0.738627790224287 \times 10^{-4}$
13	5	−2	$-0.236264692844138 \times 10^{-2}$
14	5	0	$-0.161023121314333 \times 10^{1}$
15	6	3	$0.622322971786473 \times 10^{4}$
16	10	−6	$-0.960754116701669 \times 10^{-8}$
17	12	−8	$-0.510572269720488 \times 10^{-10}$
18	12	−3	$0.767373781404211 \times 10^{-2}$
19	14	−10	$0.663855469485254 \times 10^{-14}$
20	14	−8	$-0.717590735526745 \times 10^{-9}$
21	14	−5	$0.146564542926508 \times 10^{-4}$
22	16	−10	$0.309029474277013 \times 10^{-11}$
23	18	−12	$-0.464216300971708 \times 10^{-15}$
24	20	−12	$-0.390499637961161 \times 10^{-13}$
25	20	−10	$-0.236716126781431 \times 10^{-9}$
26	24	−12	$0.454652854268717 \times 10^{-11}$
27	24	−6	$-0.422271787482497 \times 10^{-2}$
28	28	−12	$0.283911742354706 \times 10^{-10}$
29	28	−5	$0.270929002720228 \times 10^{1}$

Table 24 Coefficients and exponents of the backward equation $v_{3k}(p,T)$ for subregion 3k

i	I_i	J_i	n_i
1	−2	10	$-0.401215699576099 \times 10^{9}$
2	−2	12	$0.484501478318406 \times 10^{11}$
3	−1	−5	$0.394721471363678 \times 10^{-14}$
4	−1	6	$0.372629967374147 \times 10^{5}$
5	0	−12	$-0.369794374168666 \times 10^{-29}$
6	0	−6	$-0.380436407012452 \times 10^{-14}$
7	0	−2	$0.475361629970233 \times 10^{-6}$
8	0	−1	$-0.879148916140706 \times 10^{-3}$
9	0	0	0.844317863844331
10	0	1	$0.122433162656600 \times 10^{2}$
11	0	2	$-0.104529634830279 \times 10^{3}$
12	0	3	$0.589702771277429 \times 10^{3}$
13	0	14	$-0.291026851164444 \times 10^{14}$
14	1	−3	$0.170343072841850 \times 10^{-5}$
15	1	−2	$-0.277617606975748 \times 10^{-3}$
16	1	0	$-0.344709605486686 \times 10^{1}$
17	1	1	$0.221333862447095 \times 10^{2}$
18	1	2	$-0.194646110037079 \times 10^{3}$
19	2	−8	$0.808354639772825 \times 10^{-15}$
20	2	−6	$-0.180845209145470 \times 10^{-10}$
21	2	−3	$-0.696664158132412 \times 10^{-5}$
22	2	−2	$-0.181057560300994 \times 10^{-2}$
23	2	0	$0.255830298579027 \times 10^{1}$
24	2	4	$0.328913873658481 \times 10^{4}$
25	5	−12	$-0.173270241249904 \times 10^{-18}$
26	5	−6	$-0.661876792558034 \times 10^{-6}$
27	5	−3	$-0.395688923421250 \times 10^{-2}$
28	6	−12	$0.604203299819132 \times 10^{-17}$
29	6	−10	$-0.400879935920517 \times 10^{-13}$
30	6	−8	$0.160751107464958 \times 10^{-8}$
31	6	−5	$0.383719409025556 \times 10^{-4}$
32	8	−12	$-0.649565446702457 \times 10^{-14}$
33	10	−12	$-0.149095328506000 \times 10^{-11}$
34	12	−10	$0.541449377329581 \times 10^{-8}$

Table 25 Coefficients and exponents of the backward equation $v_{3l}(p,T)$ for subregion 3l

i	I_i	J_i	n_i
1	−12	14	$0.260702058647537 \times 10^{10}$
2	−12	16	$-0.188277213604704 \times 10^{15}$
3	−12	18	$0.554923870289667 \times 10^{19}$
4	−12	20	$-0.758966946387758 \times 10^{23}$
5	−12	22	$0.413865186848908 \times 10^{27}$
6	−10	14	$-0.815038000738060 \times 10^{12}$
7	−10	24	$-0.381458260489955 \times 10^{33}$
8	−8	6	$-0.123239564600519 \times 10^{-1}$
9	−8	10	$0.226095631437174 \times 10^{8}$
10	−8	12	$-0.495017809506720 \times 10^{12}$
11	−8	14	$0.529482996422863 \times 10^{16}$
12	−8	18	$-0.444359478746295 \times 10^{23}$
13	−8	24	$0.521635864527315 \times 10^{35}$
14	−8	36	$-0.487095672740742 \times 10^{55}$
15	−6	8	$-0.714430209937547 \times 10^{6}$
16	−5	4	0.127868634615495
17	−5	5	$-0.100752127917598 \times 10^{2}$
18	−4	7	$0.777451437960990 \times 10^{7}$
19	−4	16	$-0.108105480796471 \times 10^{25}$
20	−3	1	$-0.357578581169659 \times 10^{-5}$
21	−3	3	$-0.212857169423484 \times 10^{1}$
22	−3	18	$0.270706111085238 \times 10^{30}$
23	−3	20	$-0.695953622348829 \times 10^{33}$
24	−2	2	0.110609027472280
25	−2	3	$0.721559163361354 \times 10^{2}$
26	−2	10	$-0.306367307532219 \times 10^{15}$
27	−1	0	$0.265839618885530 \times 10^{-4}$
28	−1	1	$0.253392392889754 \times 10^{-1}$
29	−1	3	$-0.214443041836579 \times 10^{3}$
30	0	0	0.937846601489667
31	0	1	$0.223184043101700 \times 10^{1}$
32	0	2	$0.338401222509191 \times 10^{2}$
33	0	12	$0.494237237179718 \times 10^{21}$
34	1	0	-0.198068404154428
35	1	16	$-0.141415349881140 \times 10^{31}$
36	2	1	$-0.993862421613651 \times 10^{2}$
37	4	0	$0.125070534142731 \times 10^{3}$
38	5	0	$-0.996473529004439 \times 10^{3}$
39	5	1	$0.473137909872765 \times 10^{5}$
40	6	14	$0.116662121219322 \times 10^{33}$
41	10	4	$-0.315874976271533 \times 10^{16}$
42	10	12	$-0.445703369196945 \times 10^{33}$
43	14	10	$0.642794932373694 \times 10^{33}$

Downloaded 02 Jun 2010 to 171.66.16.109. Redistribution subject to ASME license or copyright; see http://www.asme.org/terms/Terms_Use.cfm

Table 26 Coefficients and exponents of the backward equation v_{3m} (p,T) for subregion 3m

i	I_i	J_i	n_i
1	0	0	0.811384363481847
2	3	0	$-0.568199310990094 \times 10^{4}$
3	8	0	$-0.178657198172556 \times 10^{11}$
4	20	2	$0.795537657613427 \times 10^{32}$
5	1	5	$-0.814568209346872 \times 10^{5}$
6	3	5	$-0.659774567602874 \times 10^{8}$
7	4	5	$-0.152861148659302 \times 10^{11}$
8	5	5	$-0.560165667510446 \times 10^{12}$
9	1	6	$0.458384828593949 \times 10^{6}$
10	6	6	$-0.385754000383848 \times 10^{14}$
11	2	7	$0.453735800004273 \times 10^{8}$
12	4	8	$0.939454935735563 \times 10^{12}$
13	14	8	$0.266572856432938 \times 10^{28}$
14	2	10	$-0.547578313899097 \times 10^{10}$
15	5	10	$0.200725701112386 \times 10^{15}$
16	3	12	$0.185007245563239 \times 10^{13}$
17	0	14	$0.185135446828337 \times 10^{9}$
18	1	14	$-0.170451090076385 \times 10^{12}$
19	1	18	$0.157890366037614 \times 10^{15}$
20	1	20	$-0.202530509748774 \times 10^{16}$
21	28	20	$0.368193926183570 \times 10^{60}$
22	2	22	$0.170215539458936 \times 10^{18}$
23	16	22	$0.639234909918741 \times 10^{42}$
24	0	24	$-0.821698160721956 \times 10^{15}$
25	5	24	$-0.795260241872306 \times 10^{24}$
26	0	28	$0.233415869478510 \times 10^{18}$
27	3	28	$-0.600079934586803 \times 10^{23}$
28	4	28	$0.594584382273384 \times 10^{25}$
29	12	28	$0.189461279349492 \times 10^{40}$
30	16	28	$-0.810093428842645 \times 10^{46}$
31	1	32	$0.188813911076809 \times 10^{22}$
32	8	32	$0.111052244098768 \times 10^{36}$
33	14	32	$0.291133958602503 \times 10^{46}$
34	0	36	$-0.329421923951460 \times 10^{22}$
35	2	36	$-0.137570282536696 \times 10^{26}$
36	3	36	$0.181508996303902 \times 10^{28}$
37	4	36	$-0.346865122768353 \times 10^{30}$
38	8	36	$-0.211961148774260 \times 10^{38}$
39	14	36	$-0.128617899887675 \times 10^{49}$
40	24	36	$0.479817895699239 \times 10^{65}$

Table 27 Coefficients and exponents of the backward equation v_{3n} (p,T) for subregion 3n

i	I_i	J_i	n_i
1	0	−12	$0.280967799943151 \times 10^{-38}$
2	3	−12	$0.614869006573609 \times 10^{-30}$
3	4	−12	$0.582238667048942 \times 10^{-27}$
4	6	−12	$0.390628369238462 \times 10^{-22}$
5	7	−12	$0.821445758255119 \times 10^{-20}$
6	10	−12	$0.402137961842776 \times 10^{-14}$
7	12	−12	$0.651718171878301 \times 10^{-12}$
8	14	−12	$-0.211773355803058 \times 10^{-7}$
9	18	−12	$0.264953354380072 \times 10^{-2}$
10	0	−10	$-0.135031446451331 \times 10^{-31}$
11	3	−10	$-0.607246643970893 \times 10^{-23}$
12	5	−10	$-0.402352115234494 \times 10^{-18}$
13	6	−10	$-0.744938506925544 \times 10^{-16}$
14	8	−10	$0.189917206526237 \times 10^{-12}$
15	12	−10	$0.364975183508473 \times 10^{-5}$
16	0	−8	$0.177274872361946 \times 10^{-25}$
17	3	−8	$-0.334952758812999 \times 10^{-18}$
18	7	−8	$-0.421537726098389 \times 10^{-8}$
19	12	−8	$-0.391048167929649 \times 10^{-1}$
20	2	−6	$0.541276911564176 \times 10^{-13}$
21	3	−6	$0.705412100773699 \times 10^{-11}$
22	4	−6	$0.258585887897486 \times 10^{-8}$
23	2	−5	$-0.493111362030162 \times 10^{-10}$
24	4	−5	$-0.158649699894543 \times 10^{-5}$
25	7	−5	-0.525037427886100
26	4	−4	$0.220019901729615 \times 10^{-2}$
27	3	−3	$-0.643064132636925 \times 10^{-2}$
28	5	−3	$0.629154149015048 \times 10^{2}$
29	6	−3	$0.135147318617061 \times 10^{3}$
30	0	−2	$0.240560808321713 \times 10^{-6}$
31	0	−1	$-0.890763306701305 \times 10^{-3}$
32	3	−1	$-0.440209599407714 \times 10^{4}$
33	1	0	$-0.302807107747776 \times 10^{3}$
34	0	1	$0.159158748314599 \times 10^{4}$
35	1	1	$0.232534272709876 \times 10^{6}$
36	0	2	$-0.792681207132600 \times 10^{6}$
37	1	4	$-0.869871364662769 \times 10^{11}$
38	0	5	$0.354542769185671 \times 10^{12}$
39	1	6	$0.400849240129329 \times 10^{15}$

Table 28 Coefficients and exponents of the backward equation v_{3o} (p,T) for subregion 3o

i	I_i	J_i	n_i
1	0	−12	$0.128746023979718 \times 10^{-34}$
2	0	−4	$-0.735234770382342 \times 10^{-11}$
3	0	−1	$0.289078692149150 \times 10^{-2}$
4	2	−1	0.244482731907223
5	3	−10	$0.141733492030985 \times 10^{-23}$
6	4	−12	$-0.354533853059476 \times 10^{-28}$
7	4	−8	$-0.594539202901431 \times 10^{-17}$
8	4	−5	$-0.585188401782779 \times 10^{-8}$
9	4	−4	$0.201377325411803 \times 10^{-5}$
10	4	−1	$0.138647388209306 \times 10^{1}$
11	5	−4	$-0.173959365084772 \times 10^{-4}$
12	5	−3	$0.137680878349369 \times 10^{-2}$
13	6	−8	$0.814897605805513 \times 10^{-14}$
14	7	−12	$0.425596631351839 \times 10^{-25}$
15	8	−10	$-0.387449113787755 \times 10^{-17}$
16	8	−8	$0.139814747930240 \times 10^{-12}$
17	8	−4	$-0.171849638951521 \times 10^{-2}$
18	10	−12	$0.641890529513296 \times 10^{-21}$
19	10	−8	$0.118960578072018 \times 10^{-10}$
20	14	−12	$-0.155282762571611 \times 10^{-17}$
21	14	−8	$0.233907907347507 \times 10^{-7}$
22	20	−12	$-0.174093247766213 \times 10^{-12}$
23	20	−10	$0.377682649089149 \times 10^{-8}$
24	24	−12	$-0.516720236575302 \times 10^{-10}$

Table 29 Coefficients and exponents of the backward equation v_{3p} (p,T) for subregion 3p

i	I_i	J_i	n_i
1	0	−1	$-0.982825342010366 \times 10^{-4}$
2	0	0	$0.105145700850612 \times 10^{1}$
3	0	1	$0.116033094095084 \times 10^{3}$
4	0	2	$0.324664750281543 \times 10^{4}$
5	1	1	$-0.123592348610137 \times 10^{4}$
6	2	−1	$-0.561403450013495 \times 10^{-1}$
7	3	−3	$0.856677401640869 \times 10^{-7}$
8	3	0	$0.236313425393924 \times 10^{3}$
9	4	−2	$0.972503292350109 \times 10^{-2}$
10	6	−2	$-0.103001994531927 \times 10^{1}$
11	7	−5	$-0.149653706199162 \times 10^{-8}$
12	7	−4	$-0.215743778861592 \times 10^{-4}$
13	8	−2	$-0.834452198291445 \times 10^{1}$
14	10	−3	0.586602660564988
15	12	−12	$0.343480022104968 \times 10^{-25}$
16	12	−6	$0.816256095947021 \times 10^{-5}$
17	12	−5	$0.294985697916798 \times 10^{-2}$
18	14	−10	$0.711730466276584 \times 10^{-16}$
19	14	−8	$0.400954763806941 \times 10^{-9}$
20	14	−3	$0.107766027032853 \times 10^{2}$
21	16	−8	$-0.409449599138182 \times 10^{-6}$
22	18	−8	$-0.729121307758902 \times 10^{-5}$
23	20	−10	$0.677107970938909 \times 10^{-8}$
24	22	−10	$0.602745973022975 \times 10^{-7}$
25	24	−12	$-0.382323011855257 \times 10^{-10}$
26	24	−8	$0.179946628317437 \times 10^{-2}$
27	36	−12	$-0.345042834640005 \times 10^{-3}$

Downloaded 02 Jun 2010 to 171.66.16.109. Redistribution subject to ASME license or copyright; see http://www.asme.org/terms/Terms_Use.cfm

Table 30 Coefficients and exponents of the backward equation $v_{3q}\ (p,T)$ for subregion 3q

i	I_i	J_i	n_i
1	−12	10	$-0.820433843259950 \times 10^{5}$
2	−12	12	$0.473271518461586 \times 10^{11}$
3	−10	6	$-0.805950021005413 \times 10^{-1}$
4	−10	7	$0.328600025435980 \times 10^{2}$
5	−10	8	$-0.356617029982490 \times 10^{4}$
6	−10	10	$-0.172985781433335 \times 10^{10}$
7	−8	8	$0.351769232729192 \times 10^{8}$
8	−6	6	$-0.775489259985144 \times 10^{6}$
9	−5	2	$0.710346691966018 \times 10^{-4}$
10	−5	5	$0.993499883820274 \times 10^{5}$
11	−4	3	-0.642094171904570
12	−4	4	$-0.612842816820083 \times 10^{4}$
13	−3	3	$0.232808472983776 \times 10^{3}$
14	−2	0	$-0.142808220416837 \times 10^{-4}$
15	−2	1	$-0.643596060678456 \times 10^{-2}$
16	−2	2	$-0.428577227475614 \times 10^{1}$
17	−2	4	$0.225689939161918 \times 10^{4}$
18	−1	0	$0.100355651721510 \times 10^{-2}$
19	−1	1	0.333491455143516
20	−1	2	$0.109697576888873 \times 10^{1}$
21	0	0	0.961917379376452
22	1	0	$-0.838165632204598 \times 10^{-1}$
23	1	1	$0.247795908411492 \times 10^{1}$
24	1	3	$-0.319114969006533 \times 10^{4}$

Table 31 Coefficients and exponents of the backward equation $v_{3r}(p,T)$ for subregion 3r

i	I_i	J_i	n_i
1	−8	6	$0.144165955660863 \times 10^{-2}$
2	−8	14	$-0.701438599628258 \times 10^{13}$
3	−3	−3	$-0.830946716459219 \times 10^{-16}$
4	−3	3	0.261975135368109
5	−3	4	$0.393097214706245 \times 10^{3}$
6	−3	5	$-0.104334030654021 \times 10^{5}$
7	−3	8	$0.490112654154211 \times 10^{9}$
8	0	−1	$-0.147104222772069 \times 10^{-3}$
9	0	0	$0.103602748043408 \times 10^{1}$
10	0	1	$0.305308890065089 \times 10^{1}$
11	0	5	$-0.399745276971264 \times 10^{7}$
12	3	−6	$0.569233719593750 \times 10^{-11}$
13	3	−2	$-0.464923504407778 \times 10^{-1}$
14	8	−12	$-0.535400396512906 \times 10^{-17}$
15	8	−10	$0.399988795693162 \times 10^{-12}$
16	8	−8	$-0.536479560201811 \times 10^{-6}$
17	8	−5	$0.159536722411202 \times 10^{-1}$
18	10	−12	$0.270303248860217 \times 10^{-14}$
19	10	−10	$0.244247453858506 \times 10^{-7}$
20	10	−8	$-0.983430636716454 \times 10^{-5}$
21	10	−6	$0.663513144224454 \times 10^{-1}$
22	10	−5	$-0.993456957845006 \times 10^{1}$
23	10	−4	$0.546491323528491 \times 10^{3}$
24	10	−3	$-0.143365406393758 \times 10^{5}$
25	10	−2	$0.150764974125511 \times 10^{6}$
26	12	−12	$-0.337209709340105 \times 10^{-9}$
27	14	−12	$0.377501980025469 \times 10^{-8}$

Table 32 Coefficients and exponents of the backward equation $v_{3s}(p,T)$ for subregion 3s

i	I_i	J_i	n_i
1	−12	20	$-0.532466612140254 \times 10^{23}$
2	−12	24	$0.100415480000824 \times 10^{32}$
3	−10	22	$-0.191540001821367 \times 10^{30}$
4	−8	14	$0.105618377808847 \times 10^{17}$
5	−6	36	$0.202281884477061 \times 10^{59}$
6	−5	8	$0.884585472596134 \times 10^{8}$
7	−5	16	$0.166540181638363 \times 10^{23}$
8	−4	6	$-0.313563197669111 \times 10^{6}$
9	−4	32	$-0.185662327545324 \times 10^{54}$
10	−3	3	$-0.624942093918942 \times 10^{-1}$
11	−3	8	$-0.504160724132590 \times 10^{10}$
12	−2	4	$0.187514491833092 \times 10^{5}$
13	−1	1	$0.121399979993217 \times 10^{-2}$
14	−1	2	$0.188317043049455 \times 10^{1}$
15	−1	3	$-0.167073503962060 \times 10^{4}$
16	0	0	0.965961650599775
17	0	1	$0.294885696802488 \times 10^{1}$
18	0	4	$-0.653915627346115 \times 10^{5}$
19	0	28	$0.604012200163444 \times 10^{50}$
20	1	0	-0.198339358557937
21	1	32	$-0.175984090163501 \times 10^{58}$
22	3	0	$0.356314881403987 \times 10^{1}$
23	3	1	$-0.575991255144384 \times 10^{3}$
24	3	2	$0.456213415338071 \times 10^{5}$
25	4	3	$-0.109174044987829 \times 10^{8}$
26	4	18	$0.437796099975134 \times 10^{34}$
27	4	24	$-0.616552611135792 \times 10^{46}$
28	5	4	$0.193568768917797 \times 10^{10}$
29	14	24	$0.950898170425042 \times 10^{54}$

Table 33 Coefficients and exponents of the backward equation $v_{3t}(p,T)$ for subregion 3t

i	I_i	J_i	n_i
1	0	0	$0.155287249586268 \times 10^{1}$
2	0	1	$0.664235115009031 \times 10^{1}$
3	0	4	$-0.289366236727210 \times 10^{4}$
4	0	12	$-0.385923202309848 \times 10^{13}$
5	1	0	$-0.291002915783761 \times 10^{1}$
6	1	10	$-0.829088246858083 \times 10^{12}$
7	2	0	$0.176814899675218 \times 10^{1}$
8	2	6	$-0.534686695713469 \times 10^{9}$
9	2	14	$0.160464608687834 \times 10^{18}$
10	3	3	$0.196435366560186 \times 10^{6}$
11	3	8	$0.156637427541729 \times 10^{13}$
12	4	0	$-0.178154560260006 \times 10^{1}$
13	4	10	$-0.229746237623692 \times 10^{16}$
14	7	3	$0.385659001648006 \times 10^{8}$
15	7	4	$0.110554446790543 \times 10^{10}$
16	7	7	$-0.677073830687349 \times 10^{14}$
17	7	20	$-0.327910592086523 \times 10^{31}$
18	7	36	$-0.341552040860644 \times 10^{51}$
19	10	10	$-0.527251339709047 \times 10^{21}$
20	10	12	$0.245375640937055 \times 10^{24}$
21	10	14	$-0.168776617209269 \times 10^{27}$
22	10	16	$0.358958955867578 \times 10^{29}$
23	10	22	$-0.656475280339411 \times 10^{36}$
24	18	18	$0.355286045512301 \times 10^{39}$
25	20	32	$0.569021454413270 \times 10^{58}$
26	22	22	$-0.700584546433113 \times 10^{48}$
27	22	36	$-0.705772623326374 \times 10^{65}$
28	24	24	$0.166861176200148 \times 10^{53}$
29	28	28	$-0.300475129680486 \times 10^{61}$
30	32	22	$-0.668481295196808 \times 10^{51}$
31	32	32	$0.428432338620678 \times 10^{69}$
32	32	36	$-0.444227367758304 \times 10^{72}$
33	36	36	$-0.281396013562745 \times 10^{77}$

Downloaded 02 Jun 2010 to 171.66.16.109. Redistribution subject to ASME license or copyright; see http://www.asme.org/terms/Terms_Use.cfm

Table 34 Coefficient and exponents of the auxiliary equation $v_{3u}(p,T)$ for subregion 3u

i	I_i	J_i	n_i
1	−12	14	$0.122088349258355\times10^{18}$
2	−10	10	$0.104216468608488\times10^{10}$
3	−10	12	$-0.882666931564652\times10^{16}$
4	−10	14	$0.259929510849499\times10^{20}$
5	−8	10	$0.222612779142211\times10^{15}$
6	−8	12	$-0.878473585050085\times10^{18}$
7	−8	14	$-0.314432577551552\times10^{22}$
8	−6	8	$-0.216934916996285\times10^{13}$
9	−6	12	$0.159079648196849\times10^{21}$
10	−5	4	$-0.339567617303423\times10^{3}$
11	−5	8	$0.884387651337836\times10^{13}$
12	−5	12	$-0.843405926846418\times10^{21}$
13	−3	2	$0.114178193518022\times10^{2}$
14	−1	−1	$-0.122708229235641\times10^{-3}$
15	−1	1	$-0.106201671767107\times10^{3}$
16	−1	12	$0.903443213959313\times10^{25}$
17	−1	14	$-0.693996270370852\times10^{28}$
18	0	−3	$0.648916718965575\times10^{-8}$
19	0	1	$0.718957567127851\times10^{4}$
20	1	−2	$0.105581745346187\times10^{-2}$
21	2	5	$-0.651903203602581\times10^{15}$
22	2	10	$-0.160116813274676\times10^{25}$
23	3	−5	$-0.510254294237837\times10^{-8}$
24	5	−4	-0.152355388953402
25	5	2	$0.677143292290144\times10^{12}$
26	5	3	$0.276378438378930\times10^{15}$
27	6	−5	$0.116862983141686\times10^{-1}$
28	6	2	$-0.301426947980171\times10^{14}$
29	8	−8	$0.169719813884840\times10^{-7}$
30	8	8	$0.104674840020929\times10^{27}$
31	10	−4	$-0.108016904560140\times10^{5}$
32	12	−12	$-0.990623601934295\times10^{-12}$
33	12	−4	$0.536116483602738\times10^{7}$
34	12	4	$0.226145963747881\times10^{22}$
35	14	−12	$-0.488731565776210\times10^{-9}$
36	14	−10	$0.151001548880670\times10^{-4}$
37	14	−6	$-0.227700464643920\times10^{5}$
38	14	6	$-0.781754507698846\times10^{28}$

Table 35 Coefficient and exponents of the auxiliary equation $v_{3v}(p,T)$ for subregion 3v

i	I_i	J_i	n_i
1	−10	−8	$-0.415652812061591\times10^{-54}$
2	−8	−12	$0.177441742924043\times10^{-60}$
3	−6	−12	$-0.357078668203377\times10^{-54}$
4	−6	−3	$0.359252213604114\times10^{-25}$
5	−6	5	$-0.259123736380269\times10^{2}$
6	−6	6	$0.594619766193460\times10^{5}$
7	−6	8	$-0.624184007103158\times10^{11}$
8	−6	10	$0.313080299915944\times10^{17}$
9	−5	1	$0.105006446192036\times10^{-8}$
10	−5	2	$-0.192824336984852\times10^{-5}$
11	−5	6	$0.654144373749937\times10^{6}$
12	−5	8	$0.513117462865044\times10^{13}$
13	−5	10	$-0.697595750347391\times10^{19}$
14	−5	14	$-0.103977184454767\times10^{29}$
15	−4	−12	$0.119563135540666\times10^{-47}$
16	−4	−10	$-0.436677034051655\times10^{-41}$
17	−4	−6	$0.926990036530639\times10^{-29}$
18	−4	10	$0.587793105620748\times10^{21}$
19	−3	−3	$0.280375725094731\times10^{-17}$
20	−3	10	$-0.192359972440634\times10^{23}$
21	−3	12	$0.742705723302738\times10^{27}$
22	−2	2	$-0.517429682450605\times10^{2}$
23	−2	4	$0.820612048645469\times10^{7}$
24	−1	−2	$-0.188214882341448\times10^{-8}$
25	−1	0	$0.184587261114837\times10^{-1}$
26	0	−2	$-0.135830407782663\times10^{-5}$
27	0	6	$-0.723681885626348\times10^{17}$
28	0	10	$-0.223449194054124\times10^{27}$
29	1	−12	$-0.111526741826431\times10^{-34}$
30	1	−10	$0.276032601145151\times10^{-28}$
31	3	3	$0.134856491567853\times10^{15}$
32	4	−6	$0.652440293345860\times10^{-9}$
33	4	3	$0.510655119774360\times10^{17}$
34	4	10	$-0.468138358908732\times10^{32}$
35	5	2	$-0.760667491183279\times10^{16}$
36	8	−12	$-0.417247986986821\times10^{-18}$
37	10	−2	$0.312545677756104\times10^{14}$
38	12	−3	$-0.100375333864186\times10^{15}$
39	14	1	$0.247761392329058\times10^{27}$

Table 36 Coefficients and exponents of the auxiliary equation $v_{3w}(p,T)$ for subregion 3w

i	I_i	J_i	n_i
1	−12	8	$-0.586219133817016\times10^{-7}$
2	−12	14	$-0.894460355005526\times10^{11}$
3	−10	−1	$0.531168037519774\times10^{-30}$
4	−10	8	0.109892402329239
5	−8	6	$-0.575368389425212\times10^{-1}$
6	−8	8	$0.228276853990249\times10^{5}$
7	−8	14	$-0.158548609655002\times10^{19}$
8	−6	−4	$0.329865748576503\times10^{-27}$
9	−6	−3	$-0.634987981190669\times10^{-24}$
10	−6	2	$0.615762068640611\times10^{-8}$
11	−6	8	$-0.961109240985747\times10^{8}$
12	−5	−10	$-0.406274286652625\times10^{-44}$
13	−4	−1	$-0.471103725498077\times10^{-12}$
14	−4	3	0.725937724828145
15	−3	−10	$0.187768525763682\times10^{-38}$
16	−3	3	$-0.103308436323771\times10^{4}$
17	−2	1	$-0.662552816342168\times10^{-1}$
18	−2	2	$0.579514041765710\times10^{3}$
19	−1	−8	$0.237416732616644\times10^{-26}$
20	−1	−4	$0.271700235739893\times10^{-14}$
21	−1	1	$-0.907886213483600\times10^{2}$
22	0	−12	$-0.171242509570207\times10^{-36}$
23	0	1	$0.156792067854621\times10^{3}$
24	1	−1	0.923261357901470
25	2	−1	$-0.597865988422577\times10^{1}$
26	2	2	$0.321988767636389\times10^{7}$
27	3	−12	$-0.399441390042203\times10^{-29}$
28	3	−5	$0.493429086046981\times10^{-7}$
29	5	−10	$0.812036983370565\times10^{-19}$
30	5	−8	$-0.207610284654137\times10^{-11}$
31	5	−6	$-0.340821291419719\times10^{-6}$
32	8	−12	$0.542000573372233\times10^{-17}$
33	8	−10	$-0.856711586510214\times10^{-12}$
34	10	−12	$0.266170454405981\times10^{-13}$
35	10	−8	$0.858133791857099\times10^{-5}$

Table 37 Coefficients and exponents of the auxiliary equation $v_{3x}(p,T)$ for subregion 3x

i	I_i	J_i	n_i
1	−8	14	$0.377373741298151\times10^{19}$
2	−6	10	$-0.507100883722913\times10^{13}$
3	−5	10	$-0.103363225598860\times10^{16}$
4	−4	1	$0.184790814320773\times10^{-5}$
5	−4	2	$-0.924729378390945\times10^{-3}$
6	−4	14	$-0.425999562292738\times10^{24}$
7	−3	−2	$-0.462307771873973\times10^{-12}$
8	−3	12	$0.107319065855767\times10^{22}$
9	−1	5	$0.648662492280682\times10^{11}$
10	0	0	$0.244200600688281\times10^{1}$
11	0	4	$-0.851535733484258\times10^{10}$
12	0	10	$0.169894481433592\times10^{22}$
13	1	−10	$0.215780222509020\times10^{-26}$
14	1	−1	-0.320850551367334
15	2	6	$-0.382642448458610\times10^{17}$
16	3	−12	$-0.275386077674421\times10^{-28}$
17	3	0	$-0.563199253391666\times10^{6}$
18	3	8	$-0.326068646279314\times10^{21}$
19	4	3	$0.397949001553184\times10^{14}$
20	5	−6	$0.100824008584757\times10^{-6}$
21	5	−2	$0.162234569738433\times10^{5}$
22	5	1	$-0.432355225319745\times10^{11}$
23	6	1	$-0.592874245598610\times10^{12}$
24	8	−6	$0.133061647281106\times10^{1}$
25	8	−3	$0.157338197797544\times10^{7}$
26	8	1	$0.258189614270853\times10^{14}$
27	8	8	$0.262413209706358\times10^{25}$
28	10	−8	$-0.920011937431142\times10^{-1}$
29	12	−10	$0.220213765905426\times10^{-2}$
30	12	−8	$-0.110433759109547\times10^{2}$
31	12	−5	$0.847004870612087\times10^{7}$
32	12	−4	$-0.592910695762536\times10^{9}$
33	14	−12	$-0.183027173269660\times10^{-4}$
34	14	−10	0.181339603516302
35	14	−8	$-0.119228759669889\times10^{4}$
36	14	−6	$0.430867658061468\times10^{7}$

Downloaded 02 Jun 2010 to 171.66.16.109. Redistribution subject to ASME license or copyright; see http://www.asme.org/terms/Terms_Use.cfm

Table 38 Coefficients and exponents of the auxiliary equation $v_{3y}(p,T)$ for subregion 3y

i	I_i	J_i	n_i
1	0	−3	$-0.525597995024633\times 10^{-9}$
2	0	1	$0.583441305228407\times 10^{4}$
3	0	5	$-0.134778968457925\times 10^{17}$
4	0	8	$0.118973500934212\times 10^{26}$
5	1	8	$-0.159096490904708\times 10^{27}$
6	2	−4	$-0.315839902302021\times 10^{-6}$
7	2	−1	$0.496212197158239\times 10^{3}$
8	2	4	$0.327777227273171\times 10^{19}$
9	2	5	$-0.527114657850696\times 10^{22}$
10	3	−8	$0.210017506281863\times 10^{-16}$
11	3	4	$0.705106224399834\times 10^{21}$
12	3	8	$-0.266713136106469\times 10^{31}$
13	4	−6	$-0.145370512554562\times 10^{-7}$
14	4	6	$0.149333917053130\times 10^{28}$
15	5	−2	$-0.149795620287641\times 10^{8}$
16	5	1	$-0.381881906271100\times 10^{16}$
17	8	−8	$0.724660165585797\times 10^{-4}$
18	8	−2	$-0.937808169550193\times 10^{14}$
19	10	−5	$0.514411468376383\times 10^{10}$
20	12	−8	$-0.828198594040141\times 10^{5}$

Table 39 Coefficients and exponents of the auxiliary equation $v_{3z}(p,T)$ for subregion 3z

i	I_i	J_i	n_i
1	−8	3	$0.244007892290650\times 10^{-10}$
2	−6	6	$-0.463057430331242\times 10^{7}$
3	−5	6	$0.728803274777712\times 10^{10}$
4	−5	8	$0.327776302858856\times 10^{16}$
5	−4	5	$-0.110598170118409\times 10^{10}$
6	−4	6	$-0.323899915729957\times 10^{13}$
7	−4	8	$0.923814007023245\times 10^{16}$
8	−3	−2	$0.842250080413712\times 10^{-12}$
9	−3	5	$0.663221436245506\times 10^{12}$
10	−3	6	$-0.167170186672139\times 10^{15}$
11	−2	2	$0.253749358701391\times 10^{4}$
12	−1	−6	$-0.819731559610523\times 10^{-20}$
13	0	3	$0.328380587890663\times 10^{12}$
14	1	1	$-0.625004791171543\times 10^{8}$
15	2	6	$0.803197957462023\times 10^{21}$
16	3	−6	$-0.204397011338353\times 10^{-10}$
17	3	−2	$-0.378391047055938\times 10^{4}$
18	6	−6	$0.972876545938620\times 10^{-2}$
19	6	−5	$0.154355721681459\times 10^{2}$
20	6	−4	$-0.373962862928643\times 10^{4}$
21	6	−1	$-0.682859011374572\times 10^{11}$
22	8	−8	$-0.248488015614543\times 10^{-3}$
23	8	−4	$0.394536049497068\times 10^{7}$

References

[1] International Association for the Properties of Water and Steam, 2007, Revised Release on the IAPWS Industrial Formulation 1997 for the Thermodynamic Properties of Water and Steam, available at www.iapws.org.

[2] Wagner, W., Cooper, J. R., Dittmann, A., Kijima, J., Kretzschmar, H.-J., Kruse, A., Mareš, R., Oguchi, K., Sato, H., Stöcker, I., Šifner, O., Tanishita, I., Trübenbach, J., and Willkommen, Th., 2000, "The IAPWS Industrial Formulation 1997 for the Thermodynamic Properties of Water and Steam," ASME J. Eng. Gas Turbines Power, **122**, pp. 150–182.

[3] Wagner, W., Dauber, F., Kretzschmar, H.-J., Mareš, R., Miyagawa, K., Parry, W. T., and Span, R., "The New Basic Equation for the Extended Region 5 of the Industrial Formulation IAPWS-IF97 for Water and Steam," ASME J. Eng. Gas Turbines Power, to be submitted.

[4] International Association for the Properties of Water and Steam, 2001, Supplementary Release on Backward Equations for Pressure as a Function of Enthalpy and Entropy $p(h,s)$ to the IAPWS Industrial Formulation 1997 for the Thermodynamic Properties of Water and Steam, available at www.iapws.org.

[5] Kretzschmar, H.-J., Cooper, J. R., Dittmann, A., Friend, D. G., Gallagher, J. S., Knobloch, K., Mareš, R., Miyagawa, K., Stöcker, I., Trübenbach, J., Wagner, W., and Willkommen, Th., 2006, "Supplementary Backward Equations for Pressure as a Function of Enthalpy and Entropy $p(h,s)$ to the Industrial Formulation IAPWS-IF97 for Water and Steam," ASME J. Eng. Gas Turbines Power, **128**, pp. 702–713.

[6] International Association for the Properties of Water and Steam, 2003, Supplementary Release on Backward Equations for the Functions $T(p,h)$, $v(p,h)$, and $T(p,s)$, $v(p,s)$ for Region 3 of the IAPWS Industrial Formulation 1997 for the Thermodynamic Properties of Water and Steam, available at www.iapws.org.

[7] Kretzschmar, H.-J., Cooper, J. R., Dittmann, A., Friend, D. G., Gallagher, J. S., Harvey, A. H., Knobloch, K., Mareš, R., Miyagawa, K., Okita, N., Stöcker, I., Wagner, W., and Weber, I., 2007, "Supplementary Backward Equations $T(p,h)$, $v(p,h)$, and $T(p,s)$, $v(p,s)$ for the Critical and Supercritical Regions (Region 3) of the Industrial Formulation IAPWS-IF97 for Water and Steam," ASME J. Eng. Gas Turbines Power, **129**, pp. 294–303.

[8] International Association for the Properties of Water and Steam, 2004, Supplementary Release on Backward Equations $p(h,s)$ for Region, 3, Equations as a Function of h and s for the Region Boundaries, and an Equation $T_{\text{sat}}(h,s)$ for Region 4 of the IAPWS Industrial Formulation 1997 for the Thermodynamic Properties of Water and Steam, available at www.iapws.org.

[9] Kretzschmar, H.-J., Cooper, J. R., Gallagher, J. S., Harvey, A. H., Knobloch, K., Mareš, R., Miyagawa, K., Okita, N., Span, R., Stöcker, I., Wagner, W., and Weber, I., 2007, "Supplementary Backward Equations $p(h,s)$ for the Critical and Supercritical Regions (Region 3), and Equations for the Two-Phase Region and Region Boundaries of the IAPWS Industrial Formulation 1997 for the Thermodynamic Properties of Water and Steam," ASME J. Eng. Gas Turbines Power, **129**, pp. 1125–1137.

[10] International Association for the Properties of Water and Steam, 2005, Supplementary Release on Backward Equations for Specific Volume as a Function of Pressure and Temperature $v(p,T)$ for Region 3 of the IAPWS Industrial Formulation 1997 for the Thermodynamic Properties of Water and Steam, available at www.iapws.org.

[11] Knobloch, K., 2006, *Gleichungen für thermodynamische Umkehrfunktionen von Wasser und Wasserdampf im kritischen und überkritischen Zustandsgebiet für energietechnische Prozessberechnungen (Equations for Thermodynamic Backward Functions of Water in the Critical and Supercritical Regions for Power Cycle Calculations)*, VDI-Verlag, Düsseldorf, Germany.

[12] Wagner, W., and Kretzschmar, H.-J., 2008, *International Steam Tables*, Springer-Verlag, Berlin.

[13] Kruse, A., and Wagner, W., 1998, *Neue Zustandsgleichungen für Industrielle Anwendungen im Technisch Relevanten Zustandsgebiet von Wasser (New Equations of State for Water for Industrial Use)*, Fortschr.-Ber. VDI, Reihe 6, Nr. 393, VDI-Verlag, Düsseldorf, Germany.

[14] Wagner, W., 1974, *Eine Mathematisch Statistische Methode zum Aufstellen Thermodynamischer Gleichungen—Gezeigt am Beispiel der Dampfdruckkurve Reiner Fluider Stoffe (A Mathematical Statistical Method for Developing Equations of State—Demonstration With the Vapor Pressure Curves of Pure Fluids)*, Fortschr.-Ber. VDI, Reihe 3, Nr. 39, VDI-Verlag, Düsseldorf, Germany.

[15] Setzmann, W., and Wagner, W., 1989, "A New Method for Optimizing the Structure of Thermodynamic Correlation Equations," Int. J. Thermophys., **10**, pp. 1103–1126.

[16] Trübenbach, J., 1999, *Ein Algorithmus zur Aufstellung Rechenzeitoptimierter Gleichungen für Thermodynamische Zustandsgrößen (An Algorithm for Developing Equations of State Optimized Regarding Their Computing Time Consumption)*, Fortschr.-Ber. VDI, Reihe 6, Nr. 417, VDI-Verlag, Düsseldorf, Germany.

[17] Willkommen, Th., Kretzschmar, H.-J., and Dittmann, A., 1995, "An Algorithm for Setting up Numerically Consistent Forward and Backward Equations for Process Modelling," *Physical Chemistry of Aqueous Systems, Proceedings of the 12th International Conference on the Properties of Water and Steam*, H. J. White Jr., J. V. Sengers, D. B. Neumann, and J. C. Bellows, eds., Begell House, New York, pp. 194–201.

[18] Willkommen, Th., 1995, "Ein Algorithmus zur Aufstellung Numerisch Konsistenter Gleichungen für die in Prozessmodellierungen Benötigten Thermodynamischen Umkehrfunktionen (An Algorithm for Developing Numerically Consistent Backward Equations for Use in Process Modeling)," Doctoral thesis, Faculty of Mechanical Engineering, Technical University of Dresden, Dresden.

[19] Kretzschmar, H.-J., 1990, "Zur Aufbereitung und Darbietung Thermophysikalischer Stoffdaten für die Energietechnik (The Preparation and Processing of Thermophysical Properties for Power Engineering)," Habilitation thesis, Faculty of Mechanical Engineering, Technical University of Dresden, Dresden.

Downloaded 02 Jun 2010 to 171.66.16.109. Redistribution subject to ASME license or copyright; see http://www.asme.org/terms/Terms_Use.cfm

The Effects of Changing Fuels on Hot Gas Path Conditions in Syngas Turbines

Adrian S. Sabau

Ian G. Wright

Materials and Science and Technology Division,
Oak Ridge National Laboratory,
Oak Ridge, TN 37831

Gas turbines in integrated gasification combined cycle power plants burn a fuel gas (syngas (SG)) in which the proportions of hydrocarbons, H_2, CO, water vapor, and minor impurity levels may differ significantly from those in natural gas (NG). Such differences can yield changes in the temperature, pressure, and corrosive species that are experienced by critical components in the hot gas path, with important implications for the design, operation, and reliability of the turbine. A new data structure and computational methodology is presented for the numerical simulation of a turbine thermodynamic cycle, with emphasis on the hot gas path components. The approach used allows efficient handling of turbine components and variable constraints due to fuel changes. Examples are presented for a turbine with four stages, in which the vanes and blades are cooled in an open circuit using air from the appropriate compressor stages. For an imposed maximum metal temperature, values were calculated for the fuel, air, and coolant flow rates and through-wall temperature gradients for cases where the turbine was fired with NG or SG. A NG case conducted to assess the effect of coolant pressure matching between the compressor extraction points and corresponding turbine injection points indicated that this is a feature that must be considered for high combustion temperatures. The first series of SG simulations was conducted using the same inlet mass flow and pressure ratios as those for the NG case. The results showed that higher coolant flow rates and a larger number of cooled turbine rows were needed for the SG case to comply with the imposed temperature constraints. Thus, for that case, the turbine size would be different for SG than for NG. A second series of simulations examined scenarios for maintaining the original turbine configuration (i.e., geometry, diameters, blade heights, angles, and cooling circuit characteristics) used for the SG simulations. In these, the inlet mass flow was varied while keeping constant the pressure ratios and the amount of hot gas passing the first vane of the turbine. The effects of turbine matching between the NG and SG cases were increases—for the SG case of approximately 7% and 13% for total cooling flows and cooling flows for the first-stage vane, respectively. In particular, for the SG case, the vanes in the last stage of the turbine experienced inner wall temperatures that approached the maximum allowable limit.

[DOI: 10.1115/1.3028566]

Keywords: syngas, turbine cooling, thermodynamics, simulation, metal temperature, thermal barrier coatings

Introduction

Future developments in integrated gasification combined cycle (IGCC) plants envision the use of syngas (SG), hydrogen, and oxygen in various proportions as an approach in minimizing CO_2 and NO_x emissions. For all fuel scenarios, the overall goal of IGCC plants is to produce maximum power at maximum efficiency, which typically translates to the use of the highest possible rotor inlet temperature (RIT). However, because advances in turbine technology to maximize RIT when burning NG have required that the advanced materials used for the critical hot section components are operated near their limits, changes in fuel characteristics that have the potential to modify the operating environment experienced by those components must be better understood to ensure that any possibly detrimental effects on the lifetime/reliability of the turbine can be assessed. Historically, as the RIT has been increased, the vane/blade temperatures have been maintained within acceptable limits through the use of various internal convection and external film cooling techniques, and the application of an external thermal barrier coating (TBC). This paper investigates how changes in fuel from NG to SG would affect the operation of a large, land-based gas turbine that was initially designed to run on NG. The fuel change effects examined so far include the variation in volume flow rates, the composition of the hot gas, and its thermophysical properties. Compared to NG, combustion of SG (or H_2) leads to a higher mass flow rate for a given turbine output and to changes in the composition of the product gases. For example, an increase in the water vapor content of the combustion gas influences the molecular weight and the specific heat of the mixture [1]. Oluyede and Phillips [2] reported a significant reduction in the lifetime of turbine hot section components that was attributed to increased heat transfer with increasing water vapor content of the combustion gas.

In most thermodynamic and aerodynamic models for the study of turbine behavior, the cooling of turbine blades typically is uncoupled from the turbine cycle [3–6]. In this study, vane and blade cooling from an open-loop system, and the actual temperature-dependent properties of the working fluid were considered. The expansion in each cooled row (vane or blade) was considered to involve three separate phenomena: cooling, mixing (with losses), and expansion. A computational methodology was developed for solving in a coupled manner the equations for the thermodynamic cycle and heat transfer through the airfoil due to cooling. The adoption of a modular structure for this model allowed straightforward implementation of submodels for consideration of, for instance, fuel composition, different combustion scenarios, and airfoil cooling. Three different cases (RIT values of approximately 1370°C, 1470°C, and 1570°C) were chosen to study the effects of fuel changes. No dilution was considered. The magnitudes of coolant flows for the open-loop circuit were obtained for each case. The temperatures of the surfaces and relevant interfaces of the hot gas path component were calculated as a function of fuel composition and combustion conditions. The effect of pressure matching for the coolant between the extraction and mixing points was studied by comparing the cooling flows obtained with and without pressure matching. The SG fuel composition considered in this study was from a Texaco gasifier [7].

Turbine Configuration and Methodology

Rather than using a generic turbine model, in which the gas generation [4] and power generation sections are considered as separate entities, the approach taken here was to try to account for all of the major features typical of a land-based turbine system [8]. Thus, the approaches developed by various research groups were reviewed and adapted. Young and Wilcock [9,10] indicated that to accurately estimate the turbine performance requires consideration of the detailed cooling of each row of airfoils. A review of the advancement of methodologies for estimating cooling requirements, presented by Torbidoni and Horlock [11], highlighted semi-empirical methodologies, such as those in Refs. [12,13], that have been widely used for convectively-cooled vanes and blades, and the work by Consonni [6] to extend previous work by Ainley [14] by considering the vane/blade and coolant flow as a heat

---

Manuscript received May 13, 2008; final manuscript received May 14, 2008; published online April 14, 2009. Review conducted by Dilip R. Ballal. Paper presented at the ASME Turbo Expo 2007: Land, Sea and Air (GT2007), May 14–17, 2007, Montreal, Quebec, Canada.

Copyright © 2009 by ASME

Downloaded 02 Jun 2010 to 171.66.16.109. Redistribution subject to ASME license or copyright; see http://www.asme.org/terms/Terms_Use.cfm

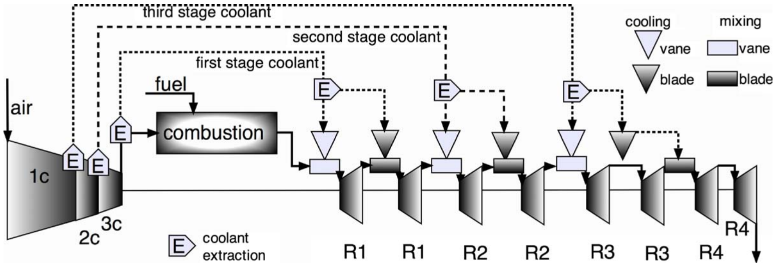

Fig. 1 Thermodynamic cycle for a four-stage turbine with open-loop cooling; six-row internal cooling and four-row film cooling

exchanger. For film-cooled blades, the coolant is considered to flow over the blade outer surface before mixing with the mainstream gas flow. The effect of the thickness of the airfoil wall and TBC typically has been considered through the use of two Biot numbers [9,10]. Cooling losses in gas turbines were addressed by Wilcock and co-workers [9,10,15], based on thermodynamic considerations.

The approach taken in this work first was to obtain results (without considering turbine matching) between the SG and the reference NG cases, by using the same airflow in the compressor for both cases. Compressor-turbine matching between the SG and NG cases was accomplished by estimating the SG airflow to the compressor such that the volumetric flow rate past the first vane of the turbine was the same for both NG and SG. The implementation was based on a turbine constant concept [8], in which the same value for the turbine constant for SG and NG cases ensures the same volume flow rate. Results for the coolant flows are presented and compared to those for NG cases. It was found that more coolant was required for the SG cases than for the NG cases. The fuel composition and the ensuing hot gas properties for the NG and SG cases were also compared. The intermediate results, which were obtained without coolant pressure matching for NG cases and without turbine-compressor matching between the SG and NG cases, were used to assess the influence of these features. Such data are useful for identifying the relevant features that must be included in the further development of turbine models when fuel change is considered.

Turbine Configuration. In this study, a four-stage turbine (with open-loop cooling) was considered, as shown schematically in Fig. 1. In open-loop cooling, coolant extracted from the compressor is injected into the component to be cooled, where it absorbs heat before leaving the component and mixing with the hot combustion gas flow. For modeling internal convective cooling, the following assumptions were made [11]: one cooling channel with three passes and a length equal to the height of the blade, and cooling hole of a radius of 1.6 mm. Thus, a total internal cooling area of 2262 mm^2 per airfoil was used. The assumed turbine dimensions were blade height (75 mm: in the absence of specific, physical data, the blade height was considered to be constant for all rows) [16], turbine hub diameter (1000 mm), chord (60/43 mm for vane/blade) [11], blade solidity 1.1 [17], and blade perimeter 120 mm. The stagger angles [17] were 40/15 deg and 25/15 deg for the first and the next vane/blade, respectively. The inlet and outlet flow angles for the vane/blade were 5/71 deg and 71/5 deg, respectively [11].

In film-cooled rotor rows, the expansion was divided into two equal parts, with cooling and mixing placed before the second expansion [8,18]. The efficiency of each rotor expansion was considered to be 0.9. As seen in the schematic representation in Fig. 1, in convectively-cooled rotor rows (which are not film cooled), the cooling was still considered to take place between the expansions, but with mixing taking place after the second expansion (since the coolant is not ejected over the blade surface). It was assumed that Stages 1 and 2 were film cooled, Stage 3 was internally cooled, and Stage 4 was uncooled, and that TBCs were present on the first two stages of vanes and blades, while the third and fourth stages were uncoated. For the sake of simplicity, the number of compressor stages was taken to be equal to the number of cooled turbine stages. The total compressor ratio was held fixed at 16.6 for all the simulations. The work extracted in each turbine stage was equally divided among the four stages. The airflow rate was chosen based on those used by Chiesa and Macchi [17]. The thermodynamic property data (including specific heat, enthalpy, and entropy) and the transport property data were those distributed with the CEA software [19,20]. The procedure for dealing with cooling effects involved correlations of experimental results and semitheoretical calculations [17].

Availability of data led to the choice of Nimonic 105 [21,22] for the airfoils, which were considered to have a wall thickness of 5 mm; the TBC was APS-YSZ. The ceramic layer of the TBC was considered to be air plasma-sprayed, yttria-partially stabilized zirconia (APS-YSZ). The thermal conductivity (k_{TBC}) of an as-deposited TBC can reach values of approximately 0.9 W/m K [23], increasing as the TBC degrades during service to, for example, 3.5 W/m K after approximately 32,000 h of service [24]. TBC thicknesses can vary from 0.15 mm to 0.6 mm, with the thicker TBCs on vanes, which are not subject to centrifugal forces. In order to ensure appropriate turbine function, the required cooling flow rates must be estimated for in-service conditions. Thus, the current simulations were mainly performed for conditions of $k_{\mathrm{TBC}}=3.5$ W/m K and $t_{\mathrm{TBC}}=0.15$ mm. The thermal conductivity of Nimonic 105 was taken as 17.5 W/m K, and the value of specific heat used for both metal and TBC was 1000 J/m K.

Computational Methodology. In order to develop thermodynamic models to analyze modern gas turbines, it is necessary not only to develop models for individual components but also to have data structures that allow a flexible arrangement of components. Torbidoni and Massardo [25] implemented a thermodynamic model for blade cooling into a FORTRAN subroutine and linked it with a commercial design software package (IPSEPRO) and its database [26]. As indicated earlier, one of the complicating factors in developing a model to describe the functioning of a gas turbine is the routing of coolant from the one component to another. Such intercomponent cooling affects the thermodynamic state of the components and *couples* the coolant source with the cooled component, which complicates the analysis of these systems. Thus, an *implicit* solver was considered in this study. Instead of combining equations to obtain fewer relationships for a component (as is usual for constant-temperature properties), in this study, the basic balance equations for energy, mass, and property calculations were used locally, i.e., for each component. Essentially, in the system of nonlinear equations in matrix notation, $f(x)=0$, where $x\equiv(x_1,x_2,\ldots,x_M)^T$ and $f\equiv(f_1,f_2,\ldots,f_M)^T$ are the unknown and equation column vectors, respectively, can be

Downloaded 02 Jun 2010 to 171.66.16.109. Redistribution subject to ASME license or copyright; see http://www.asme.org/terms/Terms_Use.cfm

Table 1 Expressions for the nonlinear system of equations

Function	f_i equations
Inlet coolant enthalpy	$x3-h(\times 2)=0$
Outlet coolant enthalpy	$x5-h(x4)=0$
Internal flow cooling	$\eta_c\ (x3-x6)=0$
Film cooling	$x7-x1+\eta_f\ (x1-x4)=0$
Heat removed from the blade	$x9-\alpha\ A\ (x7-x10)=0$
Heat removed by coolant	$x9-x8\ (x5-x3)=0$
Heat through TBC	$x9-k_{\mathrm{TBC}}\ (x10-T_{\mathrm{cr}})=0$
Heat through the metal	$x9-k_m\ (T_{\mathrm{cr}}-x6)=0$

solved by the Newton–Raphson technique, i.e., $\mathbf{J}\Delta x^{n+1}=-f(x^n)$ and $x^{n+1}=x^n+\Delta x^{n+1}$, where $J_{k,j}=\partial f_k/\partial x_j$ are the components of the Jacobian matrix, $\mathbf{J}$.

The construction of the component module consisted of setting up the functions and appropriate Jacobian elements. Each component was described by a series of equations as a function of variables such as enthalpy, entropy, pressures, temperatures, and flow rates (coolant, excess air, and combustion products). In order to ensure module flexibility, indices were used for ordering the variables, Nv, and equations, N_{eq}; N_v and N_{eq} were incremented with each introduction of a variable or equation, respectively. The Jacobian matrix was simple to obtain since there is a limited number of variables that contribute to each component. In order to account efficiently for coolant extraction and mixing, the hot gas was assumed to be a mixture of excess air and combustion products at the appropriate stoichiometric composition. The equations for each of the module variables depend on the set of *local* variables, such as those at the inlet of the component, intermediate state variables, and at the outlet from the component. Expressions for the nonlinear system of equations, $f=0$, are illustrated in Table 1 for the cooling module, and were based on the approach of Young and Wilcock [9,10], and Table 2 lists the order of the variables x# in the above equations. Also, $\eta_c=0.7$, $\eta_f=0.3$, A is the blade heat transfer area, α is the external heat transfer cofficient (HTC), and T_{cr} is the maximum temperature for the metal. The equations for variables $x1$ and $x2$ are in the expansion and compressor modules, respectively. The average heat transfer coefficient (α) on the outer side of the blade was evaluated based on a correlation developed by Louis et al. [18] and illustrated by Torbidoni and Horlock [11] for a given blade geometry.

Table 2 Notation for variables in the system of equations

No.	Variable
1	Mainstream gas recovery temperature
2	Coolant temperature at the inlet
3	Specific coolant enthalpy at the inlet
4	Coolant temperature at the outlet
5	Specific coolant enthalpy at the outlet
6	Metal temperature at the inner blade surface
7	Mean adiabatic wall temperature
8	Coolant mass
9	Heat flux removed
10	TBC surface temperature

The convergence criteria used to solve the linear system were $\max(|f_k^{n+1}|)<0.1$ and $\Delta\bar{x}=\max(|\Delta x^{n+1}/x^n|)<10^{-4}$. The small error bounds used for the convergence criteria ensured a numerical accuracy of approximately 0.01%. This worked well for problems without interstage cooling when the Jacobian matrix was block diagonal. When interstage cooling takes place, the coolant fractions at different components are needed so that the Jacobian matrix is not block diagonal and the convergence rate decreases. It was found that when coolant fractions were very high (above 10% of the compressor inlet), the classical Newton–Raphson relationship yielded values of approximately 0.1 for the criteria parameter $\Delta\bar{x}$ and finally did not converge. This was due to the fact that the combustion temperature depends strongly on the fuel to air ratio, which in turn is greatly affected by the coolant flows. The advantages of the methodology used here include the following: (a) temperature-dependent properties of the working fluids are used, (b) new constitutive equations can be inserted within existent modules, and (c) introduction of new modules into comprehensive thermodynamic cycles is straightforward.

Numerical Simulation Results

The types of simulations performed in this study, which is aimed at the accurate prediction of the temperature of the components as a function of fuel composition, combustion conditions, and ensuing cooling effects, are shown in Table 3. In order to study the effects of fuel change, three different cases were considered, with reference combustion temperatures spread approximately 100°C apart (1370°C, 1470°C, and 1570°C). Of particular interest was the effect of coolant flows in the turbine since the state properties of the turbine are influenced by the amount of coolant required to keep the blades and vanes at a given temperature.

Results for Natural Gas Combustion. First, numerical simulations were performed using only the compression and combustion modules without cooling (cases referred to as NGc). For an inlet compressor air flow rate m_a,NG=440 kg/s, and NG as fuel, the required fuel mass flow for the NGc cases required to attain combustion temperatures (T_{comb}) of 1362°C, 1451°C, and

Table 3 Simulation cases performed

ID	Simulation type	Fixed parameters	Data obtained
Natural gas cases			
NGc	Compression, combustion	m_a, T_{comb}	$m_{f,\mathrm{NG}}$
NG1	Coolant pressure not matched[a]	m_a, $m_{f,\mathrm{NG}}$	Minimum number of coolant rows, coolant flows, mixing pressure
NG2	Matched coolant pressure	m_a, $m_{f,\mathrm{NG}}$	Coolant flows
Syngas cases			
SGc	Compression, combustion	m_a, T_{comb}	$m_{f,\mathrm{SGc}}$
SG1	Matched coolant pressure, compressor-turbine not matched[b]	$m_a=m_{a,\mathrm{NG}}$; $m_{f,\mathrm{SGc}}$; same compressor[c]	Minimum number of coolant rows, coolant flows
SG2	matched coolant pressure,[b] matched compressor-turbine	T_{comb}, same compressor, $C_T=C_{T\mathrm{NG}}$	m_a, m_f, coolant flows

[a] $p_{\mathrm{compr,extr}}\neq p_{\mathrm{turb}}$, pressure between compressor extraction points and turbine.
[b] Includes turbine fluid dynamics matching between reference case (NG2) and the SG case.
[c] Includes the same pressure ratio for each stage and the same coolant extraction points.

Downloaded 02 Jun 2010 to 171.66.16.109. Redistribution subject to ASME license or copyright; see http://www.asme.org/terms/Terms_Use.cfm

Table 4 Case NG1 simulation results for T_{comb} and RIT to determine the minimum number and type of cooling rows (no pressure matching) (FC, film cooling: SC, solution convergence: A, convergent, acceptable solution; F, temperature in uncooled rows higher than acceptable limit; N, not convergent; S, slow convergence)

	No. of cooled rows				T_{comb} (°C)			
ID	Total	FC	TBC	AFR	Aim	Actual	RIT °C	SC
1a	2	2	2	50:1	1370	1302	1300	F
1b	3	2	2	49:1		1374	1369	F
1c	4	2	2	49:1		1375	1371	A
2a	4	2	2	34:1	1470	1705	1478	F
2b	5	2	2	32:1		1927	1848	N
2c	5	2	3	43:1		1488	1476	A
3a	6	2	3	36:1	1570	1691	1617	N
3b	6	3	3	34:1		1704	2100	N
3c	6	3	4	38:1		1605	1566	S
3d	6	4	4	39:1		1589	1557	A

Table 5 NG1 coolant flows (as percentage of total air flow) for vanes (V#) and blades (B#) (ID refers to target T_{comb}: 1 =1370°C; 2=1470°C; 3=1570°C)

ID	TC	V1	B1	V2	B2	V3	B3
1	1.4	0.6	0.3	0.4	0.1		
2	3.5	1.3	0.6	1.1	0.4	0.1	0
3	10.4	8.4	1.1	0.3	0.1	0.4	0.1

1537°C, was estimated to be 8.8 kg/s, 8.8 kg/s, and 10.8 kg/s, respectively. Thus, the air-to-fuel ratios were 50:1, 45:1, and 41:1, respectively. For the NGc and NG1 cases, the same compression ratio was considered for all stages. For the NG1 cases, numerical simulations for the entire turbine cycle were conducted using (a) the NGc flow rates for the fuel and inlet air and (b) equal compression ratios (thus, the pressures of the coolant at the extraction points in the compressor were not matched to those of the turbine mixing points). For the lowest-temperature cases, the number of compressor stages, $N_{c,\text{st}}$, was 2, and the compressor ratio per stage (r_c) for both cases was 4.1. For the other cases, $N_{c,\text{st}}=3$, and $r_c=2.56$.

The aim of the NG1 cases was to estimate the minimum number of cooled rows required to maintain a set value (T_{cr}) of 1000°C at the TBC-metal interface ($T_{\text{TBC},m}$) for each of the three combustion temperatures considered. The number of cooled rows was increased until an acceptable solution was attained (Table 4). For example, for $T_{\text{comb}}=1370°\text{C}$, when only three rows were cooled (Simulation NG1-1b) the solution was unacceptable since the fourth row had a higher temperature than T_{cr}. When four rows were considered to be cooled in NG1-1c, the problem converged to an acceptable solution.

For the second case (NG1-2, $T_{\text{comb}}=1470°\text{C}$), no acceptable solution was obtained with four cooled rows (Case NG1-2a). When three stages of cooling were considered (NG1-2b and NG1-2c), the results indicated that cooling of the sixth row was not necessary, demonstrating that the model has the capability of turning off the cooling for rows in which cooling is not required. By keeping the same number of cooled rows as for the NG1-2c case, Case NG1-3a ($T_{\text{comb}}=1570°\text{C}$) was not convergent, indicating that more coolant would be required. Thus, for $T_{\text{comb}}=1570°\text{C}$, it was found necessary to increase the number of film-cooled rows from two to four (NG1-3d) to obtain a satisfactory solution. The calculated coolant flows (as percentage of total air flow) for the vanes and blades for the NG1 simulations are summarized in Table 5. It is interesting to observe that the values of air-fuel mass ratio (AFR) for these cooling cases were larger than those for the simulation without cooling.

The NG2 cases were conducted to study the effect of coolant pressure matching. First, the compression ratios were obtained such that the pressures of the coolant at the extraction points in the compressor were equal to those of the turbine mixing points. The desired pressure ratios for each compressor stage were estimated, using the NG1 pressure values at the coolant mixing points in the vanes. For the lowest-temperature case (NG2-1), $N_{c,\text{st}}=2$ and $r_c=9.47$ and 1.76 for the first and second stages, respectively. For the higher-temperature NG2 cases, $N_{c,\text{st}}=3$ and $r_c=4.977$, 1.891, and 1.764 for the first, second, and third stages, respectively. For all the NG2 cases, the NGc flow rates and the new compression ratios were used, such that the coolant pressures were matched to those of the turbine. In fact, the values for AFR, T_{comb}, and RIT for the NG2 cases were very close to those for the NG1 cases. The distribution of the coolant to each row is shown in Table 6. With the exception of Case NG2-3 for $T_{\text{comb}}=1570°\text{C}$, slightly higher total cooling flow rates were required when coolant pressures were matched than when they were not matched. The results for Case NG1-3 ($T_{\text{comb}}=1570°\text{C}$, six cooled rows) in Table 5 show that where a high coolant fraction was needed, unrealistic results were obtained when the coolant pressures were not matched, indicating that pressure matching is a feature that must be considered for high T_{comb}.

Figure 2 illustrates the temperature distributions along the turbine for the case where $T_{\text{comb}}=1570°\text{C}$ (NG2-3). The variation in the metal temperature, $T_{m,\text{int}}$, mimicked that of the cooling fraction, but in the opposite direction. When the interface temperature between the metal and TBC ($T_{\text{TBC},m}$) was held constant at the

Table 6 NG2 coolant flows (as percentage of total air flow) for vanes and blades (with pressure matching); Case 3a is directly equivalent to Case SG1-3 in Table 7 (ID refers to target T_{comb}: 1=1370°C; 2=1470°C; 3, 3a=1570°C)

ID	TC	V1	B1	V2	B2	V3	B3
1	1.5	0.5	0.3	0.5	0.2		
2	3.8	1.2	0.6	1.4	0.4	0.2	
3	5.3	3.2	1.1	0.3	0.2	0.5	0.1
3a	4.0	2.1	0.9	0.3	0.2	0.5	0.1

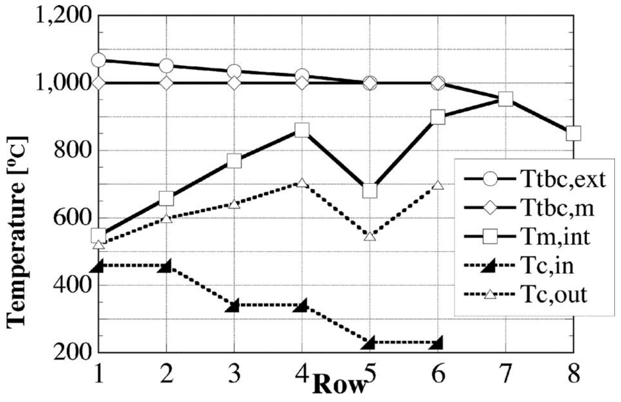

Fig. 2 Temperature profiles through each airfoil for combustion of NG at 1570°C, with pressure matching (Case NG2-3)

Downloaded 02 Jun 2010 to 171.66.16.109. Redistribution subject to ASME license or copyright; see http://www.asme.org/terms/Terms_Use.cfm

Table 7 SG1 coolant flows (as percentage of total air flow); with pressure matching (ID refers to target T_{comb}: 1=1370°C; 2=1470°C; 3=1570°C)

ID	TC	V1	B1	V2	B2	V3	B3
1	1.9	0.6	0.3	0.7	0.2	0.04	0
2	5.8	1.6	0.8	2.5	0.6	0.3	0
3	5.9	3.3	1.1	0.4	0.2	0.8	0.2

Table 8 SG2 coolant flows (as percentage of total air flow) for vanes and blade (with turbine matching) (ID refers to target T_{comb}: 1=1370°C; 2=1470°C; 3=1570°C)

ID	TC	V1	B1	V2	B2	V3	B3
1	2.2	0.7	0.4	0.8	0.3	0.06	0
2	5.1	1.5	0.8	2.0	0.6	0.3	0
3	5.5	2.8	1.2	0.4	0.2	0.7	0.2

maximum allowed value (1000°C), the inner wall metal temperature ($T_{m,\text{int}}$) on the cooled rows increased with row number. For Row 5, $T_{m,\text{int}}$ had a local minimum of 680°C due to the fact that the metal blade had only internal cooling, accomplished using coolant with the lowest temperature, while Rows 1–4 were cooled with a coolant at higher temperature. For the last two rows (which were uncooled) the vane/blade temperature was that of the hot gas. Interestingly, for the case considered, the vanes on the last stage (Row 7) experienced the highest inner wall metal temperature.

Results for Syngas Combustion. Neglecting H_2S, the SG compositions used were 35.91 CO, 26.91 H_2, 12.3 CO_2, 18.05 H_2O, and 6.83 N_2 (vol %) [7]. For all the SG cases, the compressor ratios were those determined for the NG2 cases. Similar to the NGc cases, numerical simulations were first performed using only the compression and combustion modules; cases referred to as SGc in Table 1. For SGc, the required fuel mass was estimated, such that the combustion temperature attained desired values at a given air flow rate into the compressor, i.e., $m_a = m_{a,\text{NG}}$. The required fuel mass flow rates for the SGc cases in order to attain combustion temperatures of 1362°C, 1451°C, and 1537°C were estimated to be 80.2 kg/s, 91.3 kg/s, and 102.6 kg/s, respectively, giving air-to-fuel ratios of 55:1, 48:1, and 43:1, respectively. Due to the differences in the heating values of SG and NG, the fuel mass flow rates (m_f) required to obtain the desired combustion temperature were higher for SG. The SGc and SG1 simulations were conducted with the same inlet mass flow and pressure ratios as those for NG, which is the first case that was considered by Jordal [8]. For this case, the turbine size would be different for SG than for NG, depending on how much of the compressor air would pass through the combustion chamber. This is the simplest case that can be analyzed when fuel composition is changed.

The results for Case SG1 (Table 7) illustrate that higher cooling flow rates were needed than for the NG cases, and, in fact, five instead of four rows (for NG) required cooling. For Case SG1-3 where $T_{\text{comb}} = 1570$°C, no acceptable solution was attained for $k_{\text{TBC}} = 3.5$ W/m K and $Z_{\text{TBC}} = 0.15$ mm (as used for the NG2-3 and the other SG cases. This was because these TBC properties yielded a relatively high metal temperature that could not be reduced with an appropriate amount of air from the compressor. In order not to alter the main turbine cooling features between the NG2-3 and SG1-3 cases, the thickness of the TBC was increased slightly to 0.20 mm in the SG-3 cases. In order to provide a direct comparison with these SG-3 cases, the results for NG firing using a $k_{\text{TBC}} = 3.5$ and $Z_{\text{TBC}} = 0.2$ are presented in Table 6 as Case NG2-3a. The air-to-fuel ratios for the two cases using a thicker TBC were estimated to be 39:1 (NG) and 4:1 (SG) in order to attain combustion temperatures of 1576°C and 1582°C, respectively, while the RIT was 1555°C for both cases.

Syngas Combustion With Turbine Matching. In order to retain most of the original turbine configuration (i.e., geometry, diameters, blade heights, angles, and cooling circuit characteristics) for the SG cases, it is usual to carry out a second series of simulations by varying the inlet mass flow, while keeping constant the pressure ratios and the turbine constant [8]. In practice, to attain high efficiency as the flow rate is varied, the turbine inlet area is changed by altering either the flow angle of the variable guide vanes or by physically changing the number of first-stage vanes [27,28]. Other modifications to handle multiple fuels involve oversizing the cooling channels for the reference fuel in anticipation that more coolant will be required for the alternative fuels. In this study, in order to illustrate major differences between the NG and SC cases, the inlet area of the turbine was kept the same for the SG and NG Cases.

A series of simulations for SG was carried out by varying the inlet mass flow, while keeping constant the pressure ratios and the turbine constant, which can be calculated from $m_4 = p_4/\sqrt{T_4 C_T}|_{\text{NG}}$ [8]. In order to ensure the same turbine constant for corresponding cases between the NG and SG simulations, i.e., Cases NG2-1 and SG2-1, the C_T from the NG calculations was used to formulate the following constraint on the mass flow rate of the hot gas through the first vane for the SG cases:

$$m_4 = \left. \frac{p_4}{\sqrt{T_4}} \sqrt{C_T \frac{R_{\text{ref}}}{R} \frac{k}{k_{\text{ref}}}} \right|_{\text{SG}} \tag{1}$$

where the subscript "ref" refers to properties of the hot gas from the corresponding NG2 case, i.e., Cases NG2-2 for the SG2-2. The m_a and m_f values were varied until the error between the actual m_4 and that given by the constraint was less than 1%. A constant value of the turbine constant ensures a constant volume flow past the first vane of the turbine for the NG and SG cases, respectively. This type of flow matching among the NG cases at the first vane was not conducted since little variation is expected for the R_{ref} and k_{ref} values among the NG cases. In order to ensure similar T_{comb} and RIT values for SG1 and SG2, respectively, the m_a and m_f values were varied such that AFR would have approximately the same values for SG1 and SG2. Thus, for SG2, m_f were 71 kg/s, 76.5 kg/s and 87.5 kg/s and m_a were 383 kg/s, 370 kg/s, and 375 kg/s for the three temperature cases considered.

The calculated cooling flow rates, shown in Table 8, indicate that the cooling flow rates for Case SG2 (with turbine matching) were slightly different than those for Case SG1, but were within 10% variation. A comparison of the cooling flow rates for the SG2-3 and NG2-3a Cases shows that for Rows 1–4, which employ film cooling and TBC s, approximately 30–40% more coolant would be required in the SG case than for the NG case. For Rows 5 and 6, which were internally (but not film) cooled, the coolant ratio increased; approximately 60% and 90% more coolant would be required for the third vane and third blade in the SG case than for the NG case. The temperature distributions for the case where $T_{\text{comb}} = 1570$°C (SG2-3) are shown in Fig. 3. The trend in temperature variation was essentially the same as that for NG. The most important differences were observed for the last two stages and, in particular, for the last-stage vane (Row 7), the temperature of which closely approached the set limit of 1000°C, with the exception that the internal metal temperatures were higher for Rows 1–4, 7, and 8 in the SG case.

Conclusions

A computational methodology is presented that allows an implicit coupling among different components in a gas turbine, such as between the compressor and turbine stages through the coolant

Downloaded 02 Jun 2010 to 171.66.16.109. Redistribution subject to ASME license or copyright; see http://www.asme.org/terms/Terms_Use.cfm

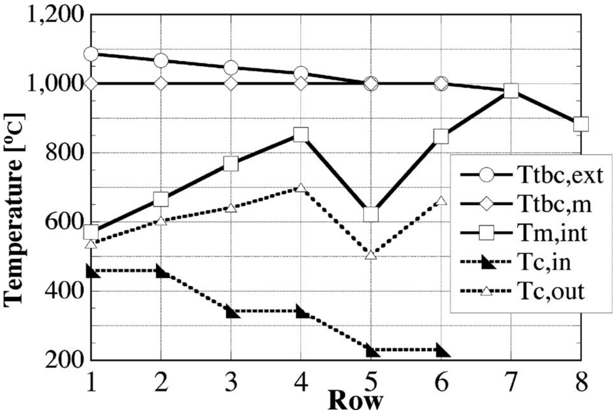

Fig. 3 Temperature profiles through each airfoil for combustion of SG at 1570°C, with pressure matching (Case SG2-3)

flows. Results are presented for several scenarios using a four-stage turbine with open-circuit airfoil cooling. The coolant flows required to maintain the temperature of the superalloy-bond coating interface below a preset value were calculated for conditions where the same combustion temperature and total air flow rate were maintained. Even for high combustion temperatures (for which the coolant flows are high and affect the state parameters in the compressor, combustion chamber, and turbine), solutions were found very efficiently (in approximately 10–20 iterations) due to implicit problem discretization.

It was found that, at lower combustion temperatures, the effect of considering coolant pressure matching could be neglected since its effect was approximately of 5°C and 7% on the RIT and total cooling flows, respectively. However, for high combustion temperatures (where high coolant flow fractions are needed), unrealistic results could be obtained when the coolant pressures were not matched. The effects of turbine matching between the NG and SG cases were approximately 7% and 13% for total cooling flows and cooling flows for the first vane, respectively. These results indicate that turbine-compressor matching, before and after fuel change, must be included in turbine models.

A comparison of the vane and blade temperatures indicated that higher metal temperatures were experienced on all rows for the SG cases and, in particular, those on the last (uncooled) stage approached the set limit. These findings suggest that this modeling approach, when supplied with appropriate parameters, can provide important insights for formulating materials requirements or turbine operating limits for the various fuel scenarios considered for turbines in integrated gasification combined cycle applications.

Acknowledgment

This research was sponsored by the Office of Coal and Power R&D, Office of Fossil Energy, U.S. Department of Energy under Contract No. DE-AC05-00OR22725 with UT-Battelle, LLC. The authors gratefully acknowledge the advice liberally provided by Dr. Paolo Chiesa of Politecnico di Milano, Italy on blade cooling models.

Nomenclature

C = turbine constant
h = enthalpy
k = thermal conductivity, W/m K (also index)
m = mass flow rate, kg/s
p = pressure
R = specific gas constant
t = time, s (also thickness, m)
T_{comb} = combustion temperature
T_g = hot gas temperature
$T_{\text{tbc,ext}}$ = TBC surface temperature
$T_{\text{tbc},m}$ = TBC-metal interface temperature
$T_{m,\text{int}}$ = metal temperature at the inner blade surface
$T_{c,\text{in}}$ = coolant temperature at inlet
$T_{c,\text{out}}$ = coolant temperature at outlet
TC = total coolant flows with respect to the total inlet air flow

Subscripts

a = air
g = hot gas
ref = reference case (NG1)
T = turbine
4 = turbine inlet

References

[1] Chiesa, P., Lozza, G., and Mazzocchi, L., 2005, "Using Hydrogen as Gas Turbine Fuel," ASME J. Eng. Gas Turbines Power, **127**, pp. 73–80.
[2] Oluede, E. O., and Phillips, J. N., 2007, "Fundamental Impact of Firing Syngas in Gas Turbines," ASME Paper No. GT2007-27385.
[3] Waters Mark and Associates, Inc., 1983, "Gas Turbine Evaluation (Gate) Computer Program (Thermodynamic Cycles), Methods, and Sample Cases," Final Report No. EPRI-AP-2871-CCM.
[4] Bathie, W. W., 1984, *Fundamentals of Gas Turbines*, Wiley, New York.
[5] Walsh, P. P., and Fletcher, P., 1998, *Gas Turbine Performance*, Blackwell Science, Oxford, UK.
[6] Consonni, S., 1992, "Performance Prediction of Gas/Steam Cycles for Power Generation," Ph.D. thesis, Princeton University, Princeton, NJ.
[7] Jazbec, M., Sendt, K., and Haynes, B. S., 2004, "Kinetic and Thermodynamic Analysis of the Fate of Sulphur Compounds in Gasification Products," Fuel, **83**, pp. 2133–2138.
[8] Jordal, K., 2001, "Modeling and Performance of Gas Turbine Cycles With Various Means of Blade Cooling," Ph.D. thesis, Lund University, Sweden.
[9] Young, J. B., and Wilcock, R. C., 2002, "Modelling the Air-Cooled Gas Turbine: Part 2-Coolant Flows and Losses," ASME J. Turbomach., **124**, pp. 214–221.
[10] Young, J. B., and Wilcock, R. C., 2002, "Modelling the Air-Cooled Gas Turbine: Part 1—General Thermodynamics," ASME J. Turbomach., **124**, pp. 207–213.
[11] Torbidoni, L., and Horlock, J. H., 2005, "A New Method to Calculate the Coolant Requirements of a High-Temperature Gas Turbine Blade," ASME J. Turbomach., **127**, pp. 191–199.
[12] Halls, G. A., 1969, "Air Cooling of Turbine Blades and Vanes," AGARDograph No. 120.
[13] Holland, M. J., and Thawke, T. F., 1980, "Rotor Blade Cooling in High Pressure Turbines," Int. J. Aircraft Eng., **17**, pp. 412–418.
[14] Ainley, D. G., "Internal Air Cooling for Gas Turbines," Aeronautical Research Council, R & M 3013.
[15] Wilcock, R. C., Young, J. B., and Horlock, J. H., 2005, "The Effect of Turbine Blade Cooling on the Cycle Efficiency of Gas Turbine Power Cycles," ASME J. Eng. Gas Turbines Power **127**(1), pp. 109–120.
[16] Kermanpur, A., Varahram, N., Davami, P., and Rappaz, M., 2000, "Thermal and Grain-Structure Simulation in a Land-Based Turbine Blade Directionally-Solidified With the Liquid Metal Cooling Process," Metall. Mater. Trans. B, **31**, pp. 1293–1304.
[17] Chiesa, P., and Macchi, E., 2002, "A Thermodynamic Analysis of Different Options to Break 60% Electric Efficiency in Combined Cycle Power Plants," ASME Paper No. GT-2002–30663.
[18] Louis, J. F., Hiraoka, K., and El-Masri, M. A., 1983, "A Comparative Study of the Infuence of Different Means of Turbine Cooling on Gas Turbine Performance," ASME Paper No. 83-GT-180.
[19] Gordon, S., and McBride, B. J., 1994, "Computer Program for Calculation of Complex Chemical Equilibrium Compositions and Applications: I. Analysis," NASA Report No. RP 1311.
[20] McBride, B. J., and Gordon, S., 1996, "Computer Program for Calculation of Complex Chemical Equilibrium Compositions and Applications: II. Users Manual and Program Description," NASA Report No. RP 1311.
[21] Powell, R. W., and Tye, R. P., 1960, "The Thermal and Electrical Conductivities of Some Nickel Chromium (Nimonic) Alloys," Engineer (London), **209**, pp. 729–732.
[22] Touloukian, Y. S. et al., 1979, Thermophysical Properties of Matter (now Thermophysical Properties of Matter Database), https://cindasdata.com
[23] Dinwiddie, R. B., Beecher, S. C., Porter, W. D., and Nagaraj, B. A., 1996, "The Effect of Thermal Aging on the Thermal Conductivity of Plasma Sprayed and EB-PVD Thermal Barrier Coatings." ASME Paper No. 96-GT-282.
[24] Sabau, A. S., and Wright, I. G., "Integration of Thermodynamic and Heat Transfer Models for Turbines Fired by Syngas and Hydrogen," *Materials in Clean Power Systems II: Fuel Cells, Solar, and Hydrogen-Based Technologies*, TMS Annual Meeting, Orlando, FL, Feb. 25–Mar. 1, TMS, Warrendale, PA, pp. 43–52.

Downloaded 02 Jun 2010 to 171.66.16.109. Redistribution subject to ASME license or copyright; see http://www.asme.org/terms/Terms_Use.cfm

[25] Torbidoni, L., and Massardo, A. F., 2004, “Analytical Blade Row Cooling Model for Innovative Gas Turbine Cycle Evaluations Supported by Semi-Empirical Air-Cooled Blade Data,” ASME J. Eng. Gas Turbines Power, **126**(3), pp. 498–506.
[26] Anon, 1998, “IPSEpro User Documentation,” Simtech Simulation Technology, Graz, Austria.
[27] Volshanik, V. V., and Étkin, A. G., 1994, “The “Ideal” Guide Vanes for a Reaction Turbine,” Power Technology and Engineering, **28**, pp. 540–546.
[28] Saravanamuttoo, H. I. H., Rogers, G. F. C., and Cohen, H., 2001, *Gas Turbine Theory*, 5th ed., Prentice-Hall, Harlow, England.

Downloaded 02 Jun 2010 to 171.66.16.109. Redistribution subject to ASME license or copyright; see http://www.asme.org/terms/Terms_Use.cfm